Small strain elastic behaviour of unsaturated soil investigated by bender/extender element testing

Ahmed M. Hasan

School of Engineering

University of Glasgow

A thesis submitted in fulfilment of the requirements for the Degree of Doctor of Philosophy

May 2016

Declaration

I declare that this thesis is a record of original work carried out by myself under the supervision of Professor Simon J. Wheeler in the Infrastructure & Environment Research Division of the School of Engineering at the University of Glasgow, United Kingdom. This research was undertaken during the period of May 2012 to May 2016. The copyright of this thesis belongs to the author under the terms of the United Kingdom Copyright Acts. Due acknowledgment must always be made of the use of any material contained in, or derived from, this thesis. The thesis has not been presented elsewhere in consideration for a higher degree.

Parts of the work have been published or are in the process of being published under joint authorship with the supervisor.

Hasan, A. M. & Wheeler, S. J., 2014. Influence of compaction procedure on elastic anisotropy. Proc. 5th International Conference on Unsaturated Soils, Sydney, Australia, Vol. 1, pp. 285-289.

Hasan, A. M. & Wheeler, S. J., 2015. Influence of unsaturated state variables on small strain elastic behavior. Proc. 6th Asia-Pacific Conference on Unsaturated Soils, Guilin, China, pp. 191–196.

Hasan, A. M. & Wheeler, S. J., 2015. Measuring travel time in bender/extender element tests. Proc. 16th European Conference on Soil Mechanics and Geotechnical Engineering, Edinburgh, UK, Vol. 6, pp. 3171-3176.

Hasan, A. M. & Wheeler, S. J., 2016. Interpreting measurements of small strain elastic shear modulus under unsaturated conditions. Proc. 3rd European Conference on Unsaturated Soils, Paris, France. September, Accepted.

Abstract

The aim of this project was to investigate very small strain elastic behaviour of soils under unsaturated conditions, using bender/extender element (BEE) testing. The behaviour of soils at very small strains has been widely studied under saturated conditions, whereas much less work has been performed on very small strain behaviour under unsaturated conditions.

A suction-controlled double wall triaxial apparatus for unsaturated soil testing was modified to incorporate three pairs of BEEs transmitting both shear and compression waves with vertical and horizontal directions of wave transmission and wave polarisation. Various different techniques for measuring wave travel time were investigated in both the time domain and the frequency domain and it was concluded that, at least for the current experimental testing programme, peak-to-first-peak in the time domain was the most reliable technique for determining wave travel time.

An experimental test programme was performed on samples of compacted speswhite kaolin clay. Two different forms of compaction were employed (i.e. isotropic and anisotropic). Compacted kaolin soil samples were subjected to constant suction loading and unloading stages at three different values of suction, covering both unsaturated conditions (s =50kPa and s =300kPa) and saturated conditions ($s = 0$). Loading and unloading stages were performed at three different values of stress ratio ($\eta \approx 0$, $\eta = 1$ and $\eta = -1$). In some tests a wetting-drying cycle was performed before or within the loading stage, with the wetting-drying cycles including both wetting-induced swelling and wetting-induced collapse compression. BEE tests were performed at regular intervals throughout all test stages, to measure shear wave velocity V_s and compression wave velocity V_p and hence to determine values of shear modulus G and constrained modulus M. The experimental test programme was designed to investigate how very small strain shear modulus G and constrained modulus M varied with unsaturated state variables, including how anisotropy of these parameters developed either with stress state (stress-induced anisotropy) or with previous straining (strain-induced anisotropy).

A new expression has been proposed for the very small strain shear modulus G of an isotropic soil under saturated and unsaturated conditions. This expression relates the

variation of G to only mean Bishop's stress p^* and specific volume v, and it converges to a well-established expression for saturated soils as degree of saturation approaches 1. The proposed expression for G is able to predict the variation of G under saturated and unsaturated conditions at least as well as existing expressions from the literature and it is considerably simpler (employing fewer state variables and fewer soil constants). In addition, unlike existing expressions from the literature, the values of soil constants in the proposed new expression can be determined from a saturated test.

It appeared that, in the current project at least, any strain-induced anisotropy of very small strain elastic behaviour was relatively modest, with the possible exception of loading in triaxial extension. It was therefore difficult to draw any firm conclusion about evolution of strain-induced anisotropy and whether it depended upon the same aspects of soil fabric as evolution of anisotropy of large strain plastic behaviour.

Stress-induced anisotropy of very small strain elastic behaviour was apparent in the experimental test programme. An attempt was made to extend the proposed expression for G to include the effect of stress-induced anisotropy. Interpretation of the experimental results indicated that the value of shear modulus was affected by the values of all three principal Bishop's stresses (in the direction of wave transmission, the direction of wave polarisation and the third mutually perpendicular direction). However, prediction of stress-induced anisotropy was only partially successful, and it was concluded that the effect of Lode angle was also significant.

Acknowledgments

Praise to Allah who gave me continual good health and opportunity to finish this project. I gratefully acknowledge the Ministry of Higher Education and Scientific Research of the Kurdistan Regional Government who undertook the financial support of this project, especially for the establishers and staff of the HCDP programme. The research was performed in the School of Engineering, University of Glasgow.

I am indebted to my supervisor Simon J. Wheeler, Cormack Professor of Civil Engineering, for his continual guidance and valuable suggestions throughout the period of this project. His clear explanations of complex issues related to many aspects of unsaturated soil mechanics, experimental testing and subsequent interpretation during our regular meetings created an indescribable atmosphere of comprehensive understanding. I will miss listening to these unrepeatable moments in my life.

I acknowledge Dr. Muayad Al-Sharrad (previous PhD student at the University of Glasgow) for his help in familiarization with the existing complex suction-controlled double wall triaxial apparatus. I would like to thank Dr.Zahur Ullah (post-doctoral researcher in Computational Engineering at the University of Glasgow) for his help in Matlab and also many thanks go to Dr. Rizgar M. Ahmed in the Department of Accounting at Salahaddin University-Erbil for his valuable help in familiarization with the SPSS software.

I would also like to thank Dr. Sean Rees from GDS Instruments for providing the BEAT software tool and the discussion of issues related to the installation of the bender/extender elements. I am also grateful to Mr. Nathan Vimalan, Mr. Qusai Al-Qudah and Mr. Adrian Rose from VJ Tech. Ltd. for their help related to upgrading the Clisp Studio CS software (the logging and control system). Special thanks go to the tireless laboratory technician Mr. Timothy Montgomery for his help with technical issues of the experimental programme. I would like also to thank Mrs. Elaine McNamara, Miss. Barbara Grant and Mrs. Karen Docherty for their administrative help.

Last but not least, my highly special appreciation goes to my parents, especially my mother for her endless spiritual support. I am also grateful to all my brothers especially Mshir, Amir, Sarhang and Adnan and also my colleague Mr.Zrar Seddiq for their help

in doing some tasks on my behalf in Erbil, related to my sponsorship. I am also deeply indebted to my wife Kafia Dzayi for her tireless support, encouragement and patience throughout the period of this project. Her continual support is unforgettable. I would like also to thank my daughters Aya, Ahi, Erena and Eman for being such wonderful children and creating an atmosphere of rejoicing for the family during our stay in Glasgow.

Contents

List of Symbols and Acronyms

α	Current inclination of the yield curve
p'_m	Current size of the yield curve
$\bar{\sigma}_r$	Radial net stress ($\bar{\sigma}_r = \sigma_r - u_a$)
$\bar{L}$	Micro-fabric orientation degree in the work of Mitaritonna et al., 2014
$\bar{p}$	Mean net stress
$\bar{p}_o$	Yield value of $\bar{p}$ at any suction s
$\bar{p}_o(0)$	Yield value of $\bar{p}_o$ in saturated conditions
β	Parameter giving the rate of change of compressibility with suction in the Barcelona Basic Model BBM
β_{hv}, β_{hh}	Stress ratio function in the shear modulus expressions
χ	Parameter related to degree of saturation
ΔH, ΔV	Increase in height and volume since the end of the equalization stage
δ_{ij}	Kronecker's delta
ϵ_a, ϵ_v, ϵ_r, ϵ_s	Axial strain, volumetric strain, radial strain and shear strain
ϵ_{xx}, ϵ_{yy}, ϵ_{zz}	Horizontal/horizontal/vertical strains in Cartesian co-ordinates
η	Stress path ratio ($\eta = q/\bar{p}$)
γ	Soil constant, taken as 0.55, in the model of Wong et al. (2014)
γ_{xy}, γ_{yz}, γ_{zx}	Shear strains in Cartesian coordinate system
κ	Gradient of elastic swelling lines in $v : ln\bar{p}$ plane (BBM) or $v : lnp^*$ plane (GCM)
κ^*	Gradient of swelling lines in $lnv : lnp'$ plot, as suggested by Butterfield (1979)

κ_s	Gradient of elastic shrinkage lines in $v : ln(s + p_a)$ in the BBM
λ	Wavelength of shear or compression waves
$\lambda(0)$	Value of $\lambda(s)$ at zero suction in the BBM
$\lambda(s)$	Slope of a constant suction normal compression line in the $v : ln\bar{p}$ plane in the BBM
λ^*	Gradient of normal compression line in $lnv : lnp'$ plot, as suggested by Butterfield (1979)
λ_p	Gradient of the water retention curve in the $lnS_r : lns$ plot in the model of Wong et al. (2014)
ν	Poisson's ratio
ν_u	Undrained Poisson's ratio
ν_{vh}, ν_{hv}, ν_{hh}	Vertical to horizontal, horizontal to vertical and horizontal to horizontal Poisson's ratios
ϕ'	Conventional friction angle for saturated conditions
ϕ^b	Friction angle with respect to suction under unsaturated conditions
ψ_o	Osmotic suction
ψ_T	Total suction
ρ	Bulk density of soil
σ_a	Axial stress
σ_{ij}	Total stress tensor
σ^*_{ij}	Bishop's stress tensor
σ'_{ij}	Effective stress tensor
σ'_i, σ'_j, σ'_k	Effective stresses in the directions of the wave transmission i, wave polarisation j and the third mutually perpendicular direction k
σ_r	Radial total stress or cell pressure
σ_{xx}, σ_{yy}, σ_{zz}	Horizontal/horizontal/vertical total stresses in Cartesian co-ordinates
σ'_h, σ'_h	Effective vertical/horizontal stresses
τ	Time shift in the cross-correlation function

τ_{xy}, τ_{yz}, τ_{zx}	Shear stresses in horizontal/vertical/vertical plane
ξ	Bonding state parameter, as suggested by Gallipoli et al. (2003b)
C, C_1, C_2	Soil constants in the expressions for shear modulus G
c'	Effective cohesion
C_{ij}	Soil constant in the expressions for shear modulus G, taking account of inherent (strain-induced) anisotropy, where i is the direction of wave transmission and j is the direction of wave polarisation
C_{pi}	Soil constant in the expressions for constrianed modulus M, accounting for inherent (strain-induced) anisotropy, where i is the direction of wave transmission
C_p, C_{p1}, C_{p2}	Soil constants in the expressions of constrained modulus M
$CC_{TR}(\tau)$	Cross-correlation function
$d\epsilon_v^e$	Elastic increment of volumetric strain
dS_r^e	Elastic increment of degree of saturation
E	Young's modulus
e	Void ratio
E_v, E_h	Vertical and horizontal Young's moduli
F	Deviator force on a soil sample
$f(e)$	Void ratio function
G, G_o	Elastic shear modulus
G'	Drained shear modulus
G_{hh}/G_{hv}	Shear modulus ratio
G_{ij}	Shear modulus measured from a shear wave velocity V_{sij}, where i is the direction of wave transmission and j is the direction of wave polarisation
G_s	Specific gravity of soil particles
G_u	Undrained shear modulus
G_{vh}, G_{hv}, G_{hh}	Vertical to horizontal, horizontal to vertical and horizontal to horizontal shear moduli

H_o, V_o	Height and volume of the sample at the end of the initial equalization stage
K	Bulk modulus
k	Soil constant (exponent of suction) in the model of Ng and Yung (2008)
k	Soil constant providing linear shift of the critical state line with suction in the $q : \bar{p}$ plane in the BBM
k, k_2	Exponent of OCR (soil constants)
K_u	Undrained bulk modulus
K_w	Bulk modulus of water
L_{tt}	Tip-to-tip distance between transmitter and receiver elements
M	Elastic constrained modulus
M	Gradient of a constant suction critical state line in the $q : \bar{p}$ plane
m	Exponent of void ratio (soil constant) in expressions for G
M^*	Gradient of critical state line in the $q : p^*$ plane
M'	Drained compression modulus
M_θ	Constrained modulus in an oblique direction
M_h/M_v	Constrained modulus ratio
M_s	Mass of solids in a soil sample
M_u	Undrained constrained modulus
M_v, M_h	Constrained moduli determined from the vertically and horizontally transmitted compression wave velocities
M_w	Molar mass of water vapour
n	Porosity
n, n_2	Exponent of stress (soil constants) in the expressions for G
$N(0)$	Value of $N(s)$ at zero suction in the BBM
$N(s)$	Specific volume on a constant suction normal compression line in the $v : ln\bar{p}$ plane at $\bar{p}$ =1kPa

n_i, n_j, n_k	Exponents of σ'_i, σ'_j and σ'_k in the directions of the wave transmission i, wave polarisation j and the third mutually perpendicular direction k
n_{pi}	Exponent of stress (soil constant) in the direction of wave transmission i in the expressions for M
n_p	Exponent of stress (soil constant) in the expressions for M
OCR	Overconsolidation ratio
p^*	Mean Bishop's stress
p'	Mean effective stress
p^c	Reference pressure in the BBM
p_a	Atmospheric pressure, taken as 100kPa
P_p	Partial water vapour pressure
p_r	Reference stress taken as either 1kPa or as atmospheric pressure p_a taken as 100kPa
P_s	Saturated water vapour pressure
q	Deviator stress on a soil sample
R	Radius of soil particles in Zhou (2014) expression
R	Universal gas constant
r	Parameter related to the minimum value of $\lambda(s)$ in the BBM
$R(t)$	Received wave
r_1, r_2	Principal radii of air-water interface
s	Matric suction
s^*	Modified suction
S_r	Degree of saturation
T	Absolute temperature
T	Total duration of recorded time for input and output signals in cross-correlation equation
t	Time

t	True travel time between a transmitter and a receiver bender elements passing through a soil sample
$T(t)$	Transmitted wave
t_d	Time delay between transmitter and receiver bender elements placed directly in contact
t_g	True group travel time
t_m	Measured travel time between a transmitter and a receiver bender elements passing through a soil sample
T_s	Surface tension
u_a	Pore air pressure
u_w	Pore water pressure
V	Wave velocity
v	Specific volume
V_p	Compression wave velocity
V_{shh}	Horizontally transmitted and horizontally polarized shear wave velocity
V_{shv}	Horizontally transmitted and vertically polarized shear wave velocity
V_{svh}	Vertically transmitted and horizontally polarized shear wave velocity
V_s	Shear wave velocity
V_s	Volume of solids in a soil sample
w	Water content
ABBM	Anisotropic model for unsaturated soil by Stropeit et al. (2008)
ABBM1	Anisotropic model for unsaturated soil by D'Onza et al. (2011a)
BBM	Barcelona Basic Model, the unsaturated model of Alonso et al. (1990)
BEE	Bender/extender element
GCM	Glasgow Coupled Model, the unsaturated mechanical/retension model of Wheeler et al. (2003b)
GDSBES	Global Digital Systems bender element software

LC	Loading collapse
LDT	Strain-gauged local axial displacement transducer
LVDT	Linear variable differential transducer
MCC	Modified Cam Clay, the saturated model of Roscoe and Burland (1968)
S-CLAY1	Anisotropic model for saturated soil by Wheeler et al. (2003a)
SEM	Scanning electron microscopy

Chapter 1

Introduction

1.1 Background

Ground movements in and around geotechnical structures often involve small or very small strains, particularly in stiff soils (Burland, 1989). Small strain behaviour of soils therefore plays a significant role if ground movements are to be accurately predicted in many geotechnical problems (e.g. tunnels, deep excavations, building foundations in urban area and other examples of soil-structure interaction). Many of these problems are likely to involve soil behaviour under saturated conditions, but some of them will involve soil behaviour under unsaturated conditions (e.g. shallow foundations, earth dams, landfills and highways). In arid, semi-arid or tropical regions, where unsaturated conditions can extend to considerable depth, even deep foundations and tunnels may be in the unsaturated zone. Whereas considerable research, over many decades, has been devoted to the small strain and very small strain behaviour of soils under saturated conditions, relatively little research has been devoted to small strain and very small strain behaviour of soils under unsaturated conditions. Anisotropy of this small strain and very small strain behaviour under unsaturated conditions may also be a significant issue, as it has been shown that predicted ground movements are significantly affected by soil anisotropy (Simpson et al., 1996 and Grammatikopoulou et al., 2014).

Bender/extender element (BEE) testing is an ideal method for investigating the very small strain elastic behaviour of soils in the laboratory (Lings & Greening, 2001). A pair of BEEs (one acting as a transmitter, the other acting as a receiver) can be used to measure shear wave velocity V_s and compression wave velocity V_p within a soil sample, and the values of V_s and V_p can in turn be used to calculate very small strain values of elastic shear modulus G and elastic constrained modulus M. Bender/extender element (BEE) testing has become increasingly popular (compared to other methods

for investigating small strain or very small strain behaviour), because BEEs can be relatively easily incorporated into a wide range of soil testing equipment (including the triaxial apparatus) and the BEEs can provide measurements of very small strain elastic stiffness even for soil samples subjected to very large plastic straining. BEEs are also ideally suited to the exploration of anisotropy of very small strain behaviour, by instrumenting a soil sample with several pairs of BEEs, with different directions of wave transmission and polarisation.

Many authors, such as Leong et al. (2009), have used BEE testing to investigate variations of very small strain elastic values of G and M for saturated sands, silts and clays and for dry sands. For isotropic conditions (isotropic soil fabric and isotropic stress state), various expressions have been proposed (i.e. Oztoprak & Bolton, 2013) to relate the variations of G and M to appropriate soil state variables for saturated or dry conditions (e.g. mean effective stress p' and void ratio e). For soils with anisotropic fabric or subjected to anisotropic stress states, the very small strain elastic behaviour can be anisotropic. This includes both strain-induced anisotropy, which can evolve during plastic straining (as the anisotropy of soil fabric evolves), and stress-induced anisotropy, which is attributable solely to the anisotropy of the current stress state. Anisotropy of very small strain elastic behaviour for saturated soils and dry sands has been investigated by authors such as Jovicic & Coop (2008) and Mitaritonna et al. (2014).

Much research has been conducted, over many decades, on the mechanical behaviour of soils under unsaturated conditions. However, the majority of the research has focused on large strain plastic behaviour, rather than behaviour at small or very small strains. Under unsaturated conditions, soil behaviour cannot be related solely to a unique single effective stress tensor. Instead, the mechanical behaviour can be related to two independent stress state variables (one tensor and one scalar). These are conventionally taken as the net stress tensor (where a normal net stress is the difference between the corresponding normal total stress and the pore air pressure) and the matric suction (the difference between pore air pressure and pore water pressure) (see, for example, Alonso et al., 1990). However, in recent years alternative combinations of unsaturated stress state variables have been suggested, including a pair known as "Bishop's stress" tensor and "modified suction" (see, for example, Wheeler et al., 2003b).

Triaxial testing of unsaturated soils involves additional complexity compared to equivalent testing under saturated conditions. Firstly, it is necessary to have a method for controlling matric suction within the soil sample (independent control of pore air pressure and pore water pressure). Secondly, a method is required for measuring volume

change of the soil sample (independently of the inflow or outflow of water to the sample).

The relatively few authors who have studied the behaviour of unsaturated soils at small strains or very small strains (e.g. Ng & Yung, 2008; Vassallo et al., 2007b; Biglari et al., 2011 and Wong et al., 2014) have attempted to interpret their results in terms of either conventional unsaturated stress variables (using net stress and suction as stress variables) or alternative combinations (e.g. including mean Bishop's stress). However the state of knowledge of this area is still highly uncertain, with limited experimental evidence available and somewhat conflicting proposals for interpretation.

1.2 Aims and objectives

The overall aims of this research were to use BEE testing to explore very small strain elastic behaviour of a compacted fine-grained soil under unsaturated conditions and to either confirm existing expressions from the literature for the variations of shear modulus G and constrained modulus M under unsaturated (and saturated) conditions or, if appropriate, to propose new expressions for the variations of G and M.

Specific objectives of the research project can be summarised as follows:

- To modify an existing suction-controlled double wall triaxial cell to incorporate three pairs of BEEs for measuring shear and compression wave velocities with different directions of wave transmission and polarization. The first pair of BEEs would transmit vertically through a soil sample, to provide measurements of shear wave velocity V_{svh} (where the second and third subscripts represent the transmission direction and polarisation direction respectively) and vertical compression wave velocity V_{pv}. The second and third pairs of BEEs would transmit horizontally across the sample, with one aligned to produce shear waves of vertical polarisation (giving V_{shv}) and the other aligned to produce shear waves with horizontal polarisation (giving V_{shh}). These second and third pairs would also provide two independent measurements of the horizontal compression wave velocity (V_{ph}).
- To perform preliminary tests to demonstrate successful use of the BEEs, and to determine suitable BEE wave frequencies and the most appropriate method of determining shear and compression wave travel times, through examining application of several methods from the literature.

- To perform tests on isotropically compacted samples under isotropic stress states, to explore the variations of shear modulus G and constrained modulus M under unsaturated (and saturated) conditions, when the soil is behaving as an isotropic material. Stress paths were to include isotropic loading and unloading at different values of suction (including large plastic volumetric strains during loading) and wetting-drying cycles (including both wetting-induced swelling and wetting-induced collapse compression). This would allow isotropic behaviour to be explored under the full range of possible states, including the influences of changes of void ratio and hysteresis in the water retention behaviour.

- To use the experimental results to propose expressions relating the variations of G and M under unsaturated (and saturated) conditions, for an isotropic soil, to appropriate unsaturated state variables. This should include interpretation of the results in terms of both conventional unsaturated stress state variables and alternative stress state variables. Existing expressions from the literature should be examined as well as, if appropriate, proposing new improved expressions.

- To perform tests on isotropically compacted samples under anisotropic stress states and tests on anisotropically compacted samples under isotropic and anisotropic stress states, to investigate anisotropy of very small strain elastic behaviour. This would include investigation of the role of both strain-induced anisotropy (including initial anisotropy due to anisotropic compaction as well as subsequent evolution during plastic straining) and stress-induced anisotropy (due to any anisotropy of the current stress state).

- To use the experimental results to propose expressions for the variations of G_{ij} and M_i (where the subscripts i and j are the directions of wave transmission and polarisation respectively), accounting for anisotropy, under unsaturated (and saturated) conditions, using conventional or alternative unsaturated state variables. These expressions should include the effect of strain-induced anisotropy or stress-induced anisotropy, as appropriate, on the basis of the experimental results.

- To explore whether any strain-induced changes of anisotropy of very small strain elastic behaviour follow similar patterns to the corresponding evolution of anisotropy of large strain plastic behaviour, in order to explore whether these two types of strain-induced anisotropy are related to the same aspects of anisotropy of soil fabric or to different aspects of anisotropy of fabric.

1.3 Thesis structure

This thesis consists of eight chapters, including this introduction chapter.

Chapter 2 is a literature review, covering the background relevant to the research topic. The first part of the chapter describes bender/extender element (BEE) testing and techniques for travel time determination in BEE tests. This is followed by a review of the behaviour of soils at very small strains under saturated conditions, including both isotropic and anisotropic behaviour and expressions for shear modulus G and constrained modulus M. The next part of the chapter reviews behaviour of soils under unsaturated conditions, covering general aspects, such as suction, stress state variables, mechanical behaviour and water retention behaviour, before focusing on very small strain behaviour under unsaturated conditions. Finally, evolution of large strain anisotropy under saturated and unsaturated conditions is reviewed, given that the last objective of the research was to investigate whether there is any relation between evolution of large strain anisotropy and evolution of strain-induced anisotropy of very small strain behaviour.

Chapter 3 describes the equipment used in the experimental investigation, including both the bender/extender element testing system and the suction-controlled double wall triaxial system. The chapter also describes in detail the modification of the suction-controlled double wall triaxial cell to incorporate three pairs of bender/extender elements. The calibration of the various devices is also presented.

Chapter 4 covers the procedures used in the experimental tests, including the way that isotropically compacted and anisotropically compacted samples were prepared. It also describes the setting-up procedures for saturated and unsaturated samples and procedures for all test stages. In addition, it covers data processing techniques for the single saturated test, all unsaturated tests and the bender/extender element testing. It also describes the stress paths followed in the research.

Chapter 5 describes preliminary tests performed on unsaturated samples using bender/extender elements to investigate and select the most appropriate technique for determining travel time for shear and compression waves. The chapter also covers some preliminary tests which provided some information on the influence of the two sample compaction procedures on initial anisotropy of very small strain elastic behaviour.

Chapter 6 provides the results of the main test programme. It shows results for all tests within the main programme, including initial discussion and interpretation of the

influences of, for example, stress paths, wetting/drying cycles and loading/unloading stages on the variations of G and M.

Chapter 7 describes interpretation of results, and the development of proposed expressions for the variations of G under unsaturated (and saturated) conditions, covering both isotropic and anisotropic stress states. Use of both conventional and alternative unsaturated state variables is investigated. The chapter also compares the proposed expression arising from the current study with other expressions from the literature.

Chapter 8 presents the conclusions from the research project and provides recommendations for future work.

Chapter 2

Literature review

This chapter, provides a literature review of topics relevant to the investigation of very small strain elastic behaviour under unsaturated conditions using bender/extender elements (BEEs), including the evolution of elastic anisotropy with stress state and with straining. The chapter begins with a review of bender/extender element testing (Section 2.1) and this is followed by a general review of very small strain elastic behaviour of soils under saturated conditions (Section 2.2). The chapter then moves on to cover the behaviour of soils under unsaturated conditions, initially on general aspects of mechanical behaviour (Section 2.3), and then focusing specifically on very small strain elastic behaviour (Section 2.4). The chapter concludes with a section on evolution of large strain anisotropy under saturated and unsaturated conditions (Section 2.5), because a specific objective of the project was to compare evolution of strain-induced anisotropy of very small strain elastic behaviour to evolution of anisotropy of large strain plastic behaviour, to see whether both could be related to the same evolution of soil fabric.

2.1 Bender/extender element testing

2.1.1 Development of bender/extender element testing

Bender/extender elements are piezoelectric transducers that can transmit and receive shear waves and compression waves in order to determine shear wave velocity V_s and compression wave velocity V_p. These wave velocities can then be used to determine very small strain elastic values of shear modulus G and constrained modulus M (defined in Section 2.2.2) as follows:

$$G = \rho V_s^2 \tag{2.1}$$

$$M = \rho V_p^2 \tag{2.2}$$

where ρ is the bulk density of the soil. The derivation of Equations 2.1 and 2.2 is given in, for example, Dobrin & Savit (1988). Note that, for transmission of compression waves in a three-dimensional continuum, the compression wave velocity V_p is dependent on the constrained modulus M (in contrast to one-dimensional transmission of a compression wave along a rod, which depends upon the Young's modulus E). In all cases, the wave velocity V (i.e. V_s or V_p) is determined from a measurement of travel time t and the known distance L_{tt} between transmitter and receiver elements:

$$V = \frac{L_{tt}}{t} \tag{2.3}$$

The development of bender/extender elements was preceded by development of shear-plate transducers (in the form of single piezoceramic elements), first used by Lawrence (1963, 1965) for determining shear wave velocity V_s in soils. These transducers required a high applied voltage in order to produce very low amplitude displacement. This produced a significant mismatch between the soil sample and the shear-plate characteristics, which limited their use in geotechnical laboratories. To avoid this mismatch between the shear-plate transducer and soil samples, Shirley (1978) and Shirley & Hampton (1978) developed a more efficient piezometric shear wave transducer called a bender element.

A bender element is an electro-mechanical transducer that deforms mechanically as an electrical field is applied or conversely produces electrical output when it is subjected to mechanical deformation. Each bender element consists of two thin piezoceramic plates, bound together using a metal shim (see Figure 2.1). The wiring configurations of standard transmitter and receiver bender elements are illustrated in Figure 2.1 (Dyvik and Madshus 1985). Two piezoceramic plates with the same polarization in parallel connection are required for a transmitter bender element, whereas two plates in series connection with opposite polarization are required for a receiver bender element. A shear wave can be transmitted and propagated in a soil sample by a bender element consisting of two piezoceramic plates with the same polarization direction, which are energized with alternating voltages that are exactly 180^o out of phase to produce contraction in one piezoelectric plate and extension in the other one, causing the element to bend (see Figure 2.2).

Bender element transducers are now widely used in various types of apparatus in geotechnical laboratories, due to their simplicity, ease of use and wide range of applications. Bender elements can be easily incorporated in the base pedestal and top cap of a triaxial apparatus and they have been frequently used in triaxial testing (e.g. Schultheiss, 1981 and Viggiani & Atkinson, 1995). Bender element transducers have also been incorporated within other devices, such as: shear box (Dyvik and Olsen, 1989); resonant column apparatus (Dyvik & Madshus 1985, Souto et al., 1994; Fam et al., 2002; Ferreira et al., 2007 and Yang & Gu, 2013); oedometer (Schultheiss, 1981; Thomann and Hryciw, 1990; Fam and Santamarina, 1995; Zeng and Ni, 1998; Grolewski and Zeng, 2001); centrifuge (Ismail and Hourani, 2003); hollow cylinder apparatus (Di Benedetto et al., 1999; Geoffroy et al., 2003) and cyclic triaxial apparatus (Huang et al., 2005 and Zhou, 2014).

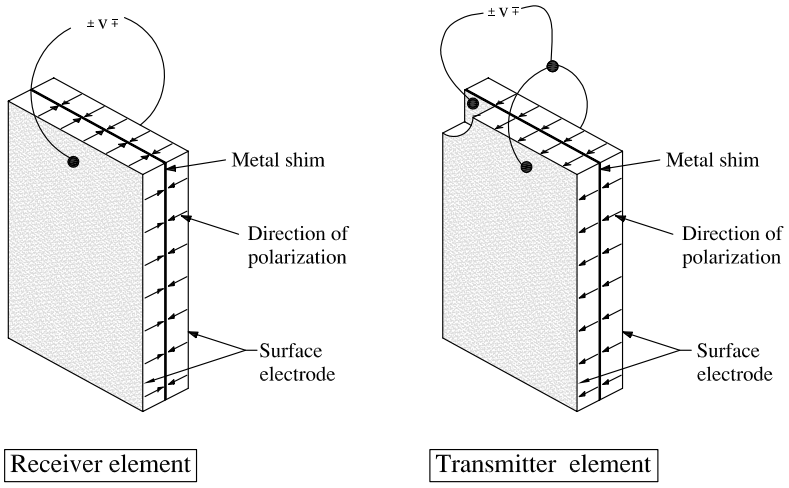

Figure 2.1: Bender element transmitter (parallel connection) and bender element receiver (series connection), BE wiring and polarization configuration (after Dyvik and Madshus, 1985)

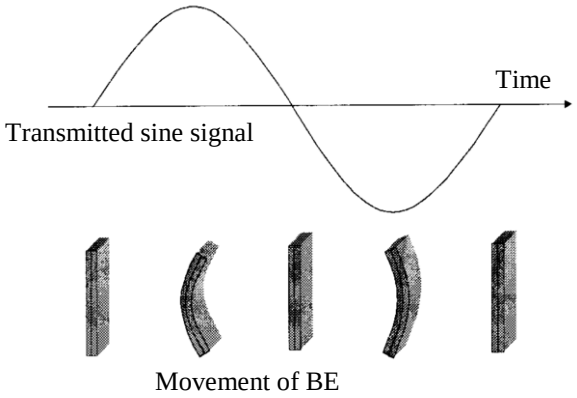

Figure 2.2: Movement of BE during energizing by a single sinusoidal pulse (Ferreira, 2008)

Lings and Greening (2001) modified the wiring configuration of a standard bender el-

ement (generating shear waves) to produce an extender element (generating compression waves) (see Figure 2.3). Compression waves are transmitted by two piezoceramic elements with opposite polarization directions, excited by voltages that are 180^o out of phase to cause simultaneous extension or compression in both plates. By switching between the two forms of wiring connection it is possible to use a single pair of elements for either shear waves or compression waves (with a given element being the transmitter in one case and the receiver in the other case). These type of elements are called Bender/Extender Elements (BEEs).

Leong et al. (2009), investigated the effects of the size of the bender/extender elements, the resolution of the signal recorder, and the excitation voltage frequency on the performance of bender/extender elements. They showed that it is possible to improve performance of bender/extender elements by using an appropriate high-resolution oscilloscope ($\geq$12bits, see Section 3.2.3), and by appropriately selecting the size of the bender/extender elements (relative to the size of the soil particle sizes) and the input excitation frequency (adopting a suitable ratio of wavelength λ to transmission path length L_{tt} (i.e. $\lambda/L_{tt}<0.3$)).

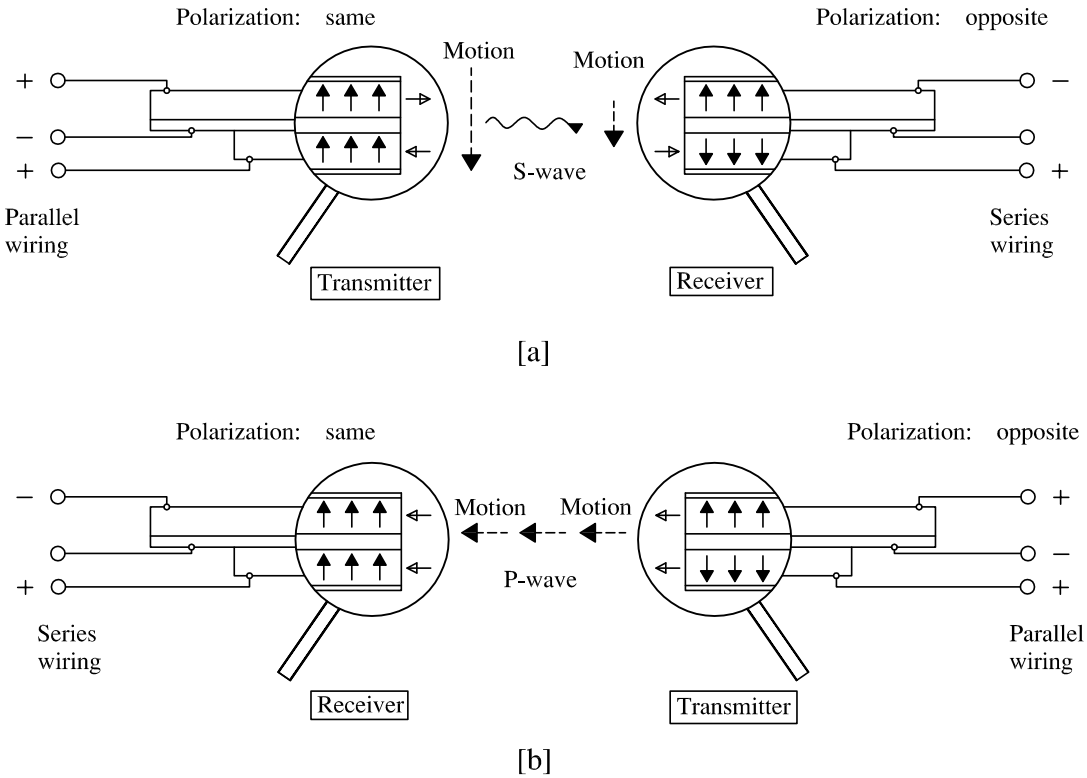

Figure 2.3: Wiring, polarization and displacement details for (a) bender element (b) extender element (after Lings and Greening, 2001)

An alternative to extender elements, for measuring compression wave velocity V_p, is compression disc transducers, consisting of a single piezoceramic element, usually prismatic (e.g. Valle-Molina & Stokoe, 2012). During voltage application on a compression

disc transducer, it will longitudinally expand and contract, to generate compression waves in the soil sample.

Some geotechnical researchers have used separate shear and compression wave transducers in the same base pedestal and top cap of a triaxial apparatus for testing saturated soil samples (e.g. Schultheiss, 1981; Bates 1989; Brignoli et al., 1996; Nakagawa et al., 1997; Fioravante & Capoferri, 2001; Ferreira 2008 and Valle-Molina & Stokoe 2012). However, one advantage of using combined BEE transducers (Lings & Greening, 2001) to measure both shear and compression wave velocities is that less space is required in the base pedestal and top cap. This is particularly important for testing under unsaturated conditions, where the designs of the base pedestal and top cap are typically very congested, because of the necessity of providing separate drainage connections and porous filters for control of pore water pressure u_w and pore air pressure u_a (see Section 3.3.3). It was therefore decided to use BEEs in the current project.

2.1.2 Determination of travel time

Measurement of wave travel time t in bender/extender element tests, for determination of shear or compression wave velocity (see Equation 2.3) can be challenging. Inspection of Figure 2.4 shows that the received signal is of much lower amplitude than the transmitted signal, due to energy-dissipation in the soil sample (Brignoli et al., 1996), and it is distorted due to dependency of the received signal on many phenomena, for example, near-field effects, as described in the next paragraphs (Sánchez-Salinero et al., 1986; Mancuso et al., 1989; Viggiani & Atkinson 1995; Jovičić et al. 1996; Brignoli et al 1996; Lee & Santimarena 2005, Arroyo et al., 2006). Wave travel time t also depends on the signal frequency relative to the resonant frequency of the sample (Valle-Malina & Stokoe 2012).

If BEE measurements are to be used to provide meaningful values of elastic moduli G and M, the measured travel time t must be sensibly independent of the chosen frequency of the transmitted wave, at least over an appropriate range of frequencies. For shear wave velocity measurements, this appropriate range of frequencies may be related to avoidance of the "near-field effect", where distortion of the received shear wave occurs because of the influence of an accompanying faster compression wave (Sanchez-Salinero et al., 1986). The near-field effect is likely to mask correct arrival time of the shear wave signal and therefore very commonly produces difficulties in identification of a shear wave travel time (Viggiani & Atkinson, 1995). This phenomenon has been studied theoretically (Sanchez-Salinero et al., 1986; Jovicic et al., 1996; Arroyo et al., 2006 and Leong et al., 2005, 2009) and experimentally (Brignoli et al., 1996; Arulnathan et al., 1998 and Arroyo et al., 2003).

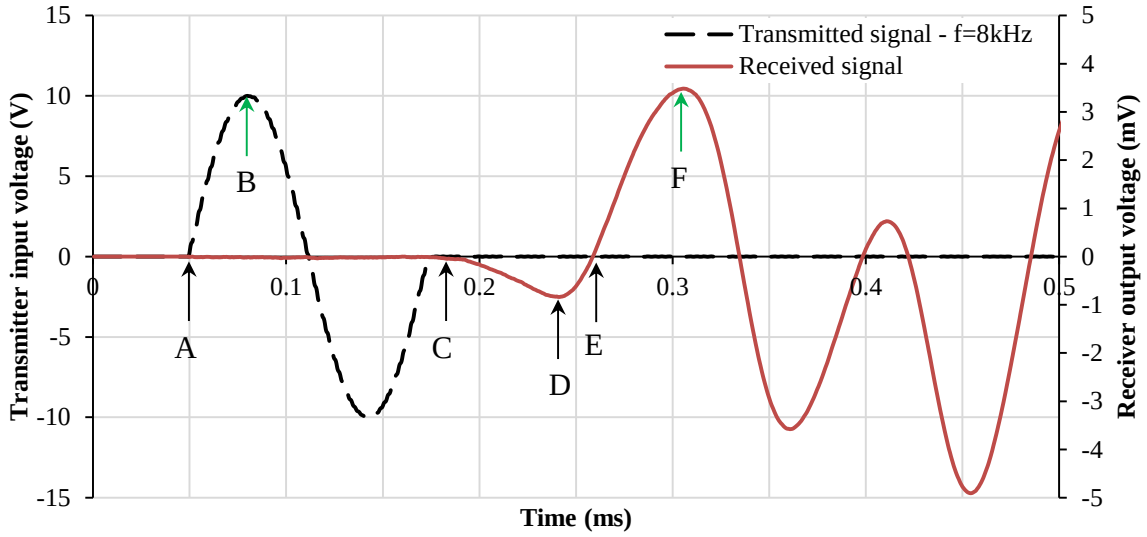

Figure 2.4: Typical waveforms of a single sinusoidal transmitted signal with its corresponding distorted received signal

Leong et al. (2005, 2009) stated that near-field effects could be minimised by using an input signal frequency, that ensured that the signal wavelength was less than 30% of the transmission path length of the signal.

The detection of travel time of a compression wave is much easier than for a shear wave, because arrival of the received compression wave is unaffected by any accompanying shear wave, because the shear wave travels more slowly. Therefore, defining or detecting correct travel time for a compression wave is less challenging than for a shear wave (Brignoli et al., 1996).

In attempting to produce a clear received shear wave signal, various different types of waveforms have been used and applied to transmitter bender elements, such as a square signal (Fam & Santamarina, 1995; Jamiolkowski et al., 1995 and Rampello et al., 1997), an impulse signal (Lee & Santamarina, 2005), a single sinusoidal signal (Leong et al., 2005); a 90^o phase shifted sine pulse (Pennington et al., 2001) and a distorted single sinusoidal signal (30^o phase shift) (Jovicic et al., 1996). These waveforms usually produced clearer received waves than a square waveform, due to the fact that the square wave includes a wide variety of frequencies (Jovicic et al., 1996), which produces difficulties in identifying a reliable arrival travel time due to strong near-field effects.

Various different techniques have been proposed for interpretation of the bender element received signal in order to determine correct travel time, because of the difficulty of identify a single technique that is best under all conditions. These interpretation

methods include techniques from the time-domain and the frequency domain. There is, however, considerable controversy within the literature about which of the various interpretation techniques gives the most reliable and consistent values of travel time (see, for example, Yamashita et al., 2009). In the following paragraphs the most common techniques are described.

a) Time-domain methods

Various time-domain methods are based on selecting a specific "characteristic point" on the received signal. Figure 2.4 shows a typical single sinusoidal transmitted (input) signal and a distorted received (output) signal, showing different types of characteristic point as they are described below.

First deflection, first bump and first zero-crossing point methods

In the first deflection technique, the travel time is taken from the start of the input signal wave (point A in Figure 2.4) to the first sharp upward or downward deflection of the output signal (point C in Figure 2.4). This technique was first used in geophysical field testing (Abbiss, 1981) and then in geotechnical laboratories (e.g. Nakagawa et al. 1997; Lings & Greening 2001; Valle-Molina & Stokoe, 2012; Yang & Liu, 2016). The first deflection of the output signal is, however, usually masked by traces of compression wave (near-field effect) (Brignoli et al., 1996 and Leong et al., 2009), as illustrated in Figure 2.5. This produces difficulties and doubt in picking the position of the first deflection and hence introduces subjectivity to the technique (Viggiani & Atkinson, 1995). Figure 2.5 illustrates the difficulty in selecting the first deflection for vertical, horizontal and oblique shear wave transmissions due to near-field effects.

Picking travel time between point A in Figure 2.4 on the input signal and point D on the output signal is known as the first bump technique (for example, Nash et al., 2007), whereas travel time from point A to point E (see Figure 2.4) is known as the first zero-crossing method (e.g. Kawaguchi et al., 2001; Kumar & Madhusudhan, 2010, Kang et al., 2014). Obviously, different travel times will be determined by using these three options (i.e. first deflection C, first bump D and first-crossing point E). Due to uncertainties involved in these techniques, they were not included in the preliminary investigation reported in Section 5.1.

Peak-to-first-peak method

Selecting travel time between point B on the transmitted signal (see Figure 2.4) and point F on the received signal is called the peak-to-first-peak technique (Viggiani &

Atkinson 1995). This method is very simple and popular (Yamashita et al., 2009) due to its simplicity, and it is used by many researchers (e.g. Callisto & Rampello, 2002 ; Ng & Yanug, 2008 and Chan et al., 2010). The advantage of this method is that over an appropriate range of input frequencies (sufficiently high frequencies that near-field effects are eliminated), the arrival time is found to be frequency-independent (e.g. Leong et al., 2009), thus providing a reliable value of travel time (Kawaguchi et al., 2001; Yamashita & Suzuki, 2001). The peak-to-first-peak method was included in the preliminary investigation reported in Section 5.1.

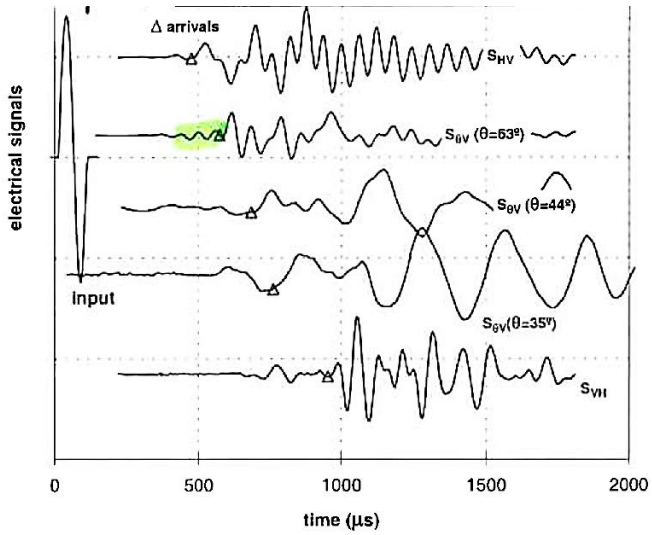

Figure 2.5: Arrival travel times in different directions and polarisations (Fioravante & Capoferri, 2001)

Cross-correlation method

In this technique, the cross-correlation function CC_{TR} (τ), which is a measure of the degree of correlation of two wave signals, is used as suggested by Viggiani & Atkinson (1995):

$$CC_{TR}(\tau) = \lim_{T\to\infty} \frac{1}{T} \int_{T} T(t+\tau)R(t)dt \tag{2.4}$$

where T is the total duration of recorded time for input and output signals. The cross-correlation function $CC_{TR}(\tau)$ is plotted against the time shift (τ). If the cross-correlation $CC_{TR}(\tau)$ of the transmitted wave $T(t)$ and the received wave $R(t)$ is calculated for different values of time shift τ, see Equation 2.4, the value of CC_{TR} (τ) should be a maximum at a value of time shift τ which is equal to the travel time (Viggiani & Atkinson, 1995 and Mohsin & Airey, 2003). Figure 2.6 shows the cross-correlation plot for the input and output signals from Figure 2.4, with the maximum

peak indicated. Lee & Santamarina (2006) stated that use of the maximum peak from the cross-correlation method produces correct travel time as long as the polarity and the shape of the input and output signals are the same, and Airey & Mohsin (2013) showed that it is feasible to automate the cross-correlation technique and produce reasonable values of travel time. Automating the process of travel time determination is useful when a large number of measurements have to be analysed. Airey & Mohsin (2013) recommended that if an automated version of the cross-correlation method is to be used, it must be clear that near-field effects are absent (Wang et al., 2007) and the transmission distance should be taken as the distance between the centres of the bender elements, instead of the tip-to-tip distance as is more common. The cross-correlation technique was included in the preliminary investigation reported in Section 5.1.

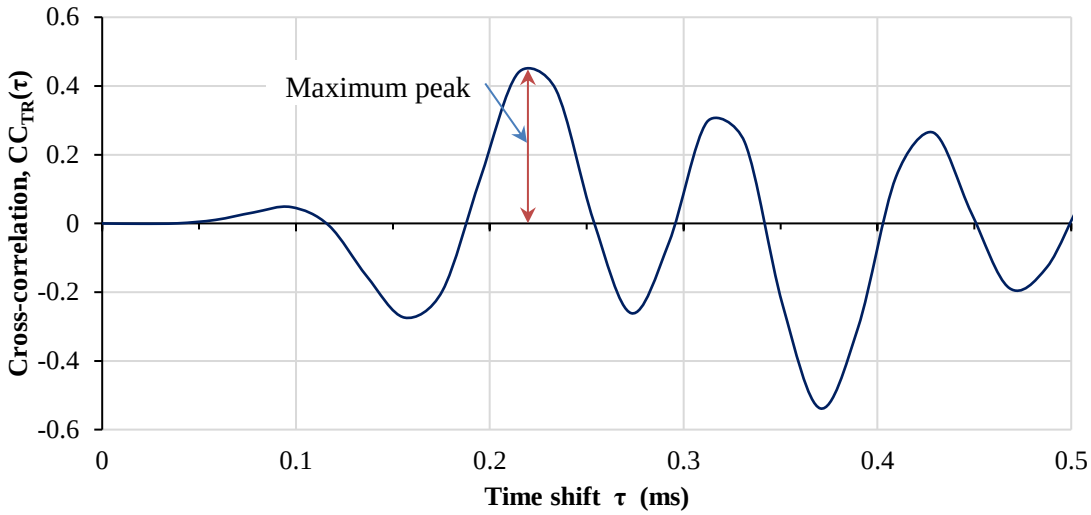

Figure 2.6: Typical cross-correlation plot

b) Frequency domain methods

Methods for determining travel time from the frequency domain include the cross-spectrum method, the discrete (π-point) method and the continuous method.

Cross-spectrum method

The cross-spectrum technique applies a single sinusoidal pulse as the input signal. Viggiani & Atkinson (1995) first introduced the cross-spectrum technique through applying fast Fourier transforms FFT to the transmitted signal $T(t)$ and received signal $R(t)$ (see Figure 2.4), to produce the linear spectrum for the signals, as shown in Figure 2.7. The linear spectrum is considered as a vector. The magnitude and the phase of this vector are the amplitude and the phase shift of each of the frequency

components of the signals, respectively. The product of the linear spectrum of the input signal and the complex conjugate of the output signal produces the cross-power spectrum. The magnitude and the phase of the cross-power spectrum for a specific frequency are the amplitude and the phase differences of the two signals respectively at that specific frequency. Figure 2.8 shows wrapped and unwrapped phase differences, for the two signals (taken from Figure 2.7) plotted against frequency. The slope of the unwrapped phase-frequency plot can be used to determine a group travel time t_g for a selected band window of frequency (Mancuso et al., 1989 and Viggiani & Atkinson, 1995) by:

$$t_g = \frac{1}{2\pi}\frac{d\theta}{df} \tag{2.5}$$

The value of t_g then used for t in Equation 2.3 to calculate the wave velocity.

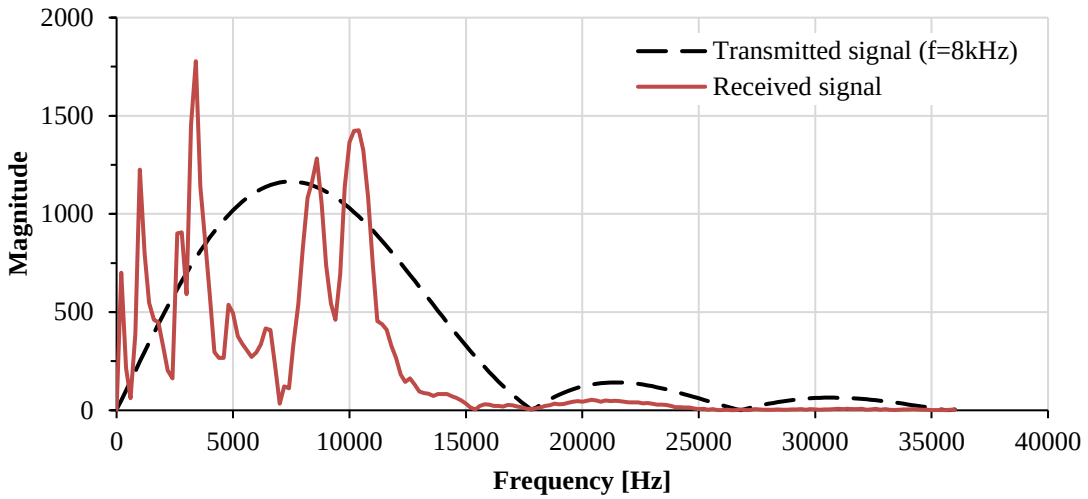

Figure 2.7: Typical Fast Fourier Transform for input and output signals in Figure 2.4

The cross-spectrum method can be automated through writing a code in MS Excel (Rees et al., 2013) or a code in Matlab (see Section 5.1.1). The cross-spectrum technique was one of the methods assessed in the preliminary tests described in Section 5.1.

b) Discrete (π-point) method

In the π-point method, the waveform of the input signal is selected as a continuous sinusoidal wave in order to produce less distortion in the received signal, because the transmitted signal has only a single frequency component (Blewett et al., 1999,

2000). Travel time cannot be measured in the time-domain with this type of input signal, because it is unclear which cycle of the received signal relates to a specified cycle of the transmitted signal. An oscilloscope is used to display the input and output signals, plotted against each other to form Lissajous figures, which indicate the phase difference between the two signals. The frequency of the transmmited signal is adjusted manually, recording each specific frequency when input and output signals are completely in-phase or completely out-of-phase, so the phase differences are multiples of π. Travel time is calculated from the slope of a straight line fitted to a number of π-points in the frequency-phase plot (see Figure 2.9), using Equation 2.5, and hence wave velocity can be determined using Equation 2.3.

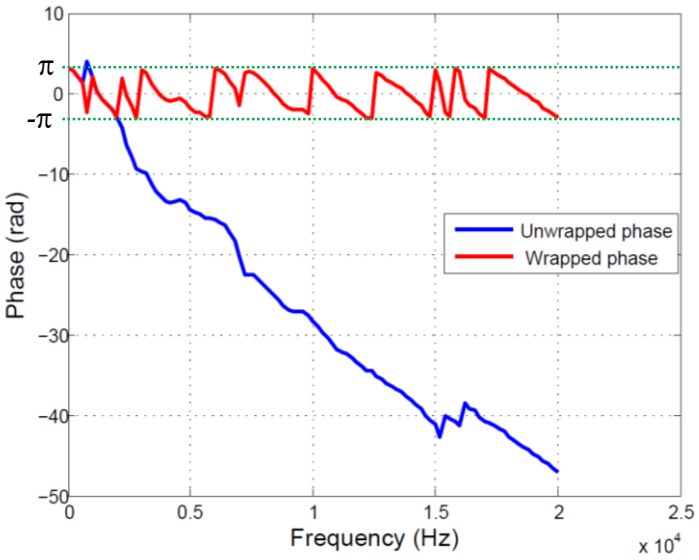

Figure 2.8: Typical wrapped and unwrapped phase-frequency relationship

The π-point method is very time consuming because of the need to manually apply input signals of various different frequencies in sequence (adjusting frequency each time until input and output signals are completely in-phase or completely out-of-phase). This would be time-consuming when using three separate pairs of bender/extender elements, as planned in the current project (see Section 3.2.3), and it was therefore decided not to include this method in the preliminary tests described in Section 5.1.

c) Continuous method

In this technique, a sinusoidal continuous sweep input signal and a spectrum analyser hardware (which converts analogue input and output signals to digital ones before applying FFT on the digitised signals) are used (Greening & Nash, 2004). The difference between this technique and the discrete method is that the continuous method is much faster in producing results than the discrete method due to the use of automated

continuous sweep of the input signal frequency and then use of the spectrum analyser for determining phase angle. The spectrum analyser also provides much useful information about the signals, such as the coherence between the input and output signals, which represents the level of correlation between the signals and how much the energy of the input signal affects the energy of the output signal (Hoffman et al., 2006).

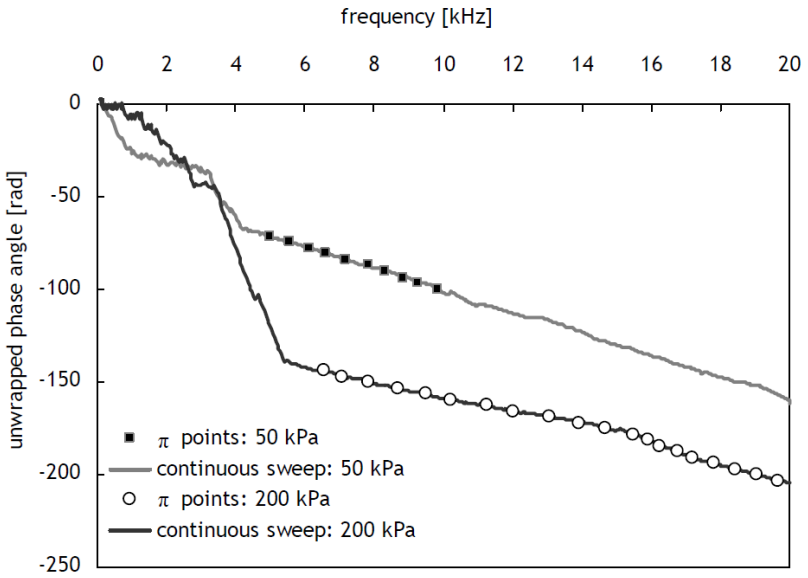

Figure 2.9: Typical unwrapped phase-frequency plots for continuous method superimposed with π-point method for different stress conditions (Ferreira, 2008)

The continuous method also uses the slope of the frequency-phase curve (see Figure 2.9) to determine travel time t (see Equation 2.5). Figure 2.9 shows a comparison between the π-point and continuous methods. Inspection of Figure 2.9 shows that there was excellent agreement between the results from the two methods under different stress conditions (Ferreira, 2008).

The continuous method was not investigated in the preliminary tests described in Section 5.1., because it is similar to the cross-spectrum method and it requires additional equipment that was not available and would have been expensive to purchase.

Some researchers including Viana da Fonseca et al. (2009), Styler and Howie (2013) and Camacho-Tauta et al. (2015) have argued that it is best to combine several interpretations methods (involving both time and frequency domains) in order to achieve the most reliable determination of time travel. However, combining sometimes conflicting measurements from different methods still needs robust judgment (see more details in Viana da Fonseca et al., 2009).

2.2 Behaviour of saturated soils at very small strains

2.2.1 Behaviour at small and very small strains

Ground movements in and around geotechnical structures often involve small or very small strains, particularly in stiff soils (Burland, 1989). Small strain behaviour of soils therefore plays a significant role if ground movements are to be accurately analysed and predicted in many geotechnical problems (e.g. tunnels, deep excavations, building foundations in urban area and other examples of soil-structure interaction). Small strain behaviour is also crucial in dynamic response of soils especially in earthquake engineering. Experimental evidence shows that the behaviour of soils at small strain is normally much stiffer than the behaviour at moderate strain as conventionally measured in, for example, triaxial tests. Therefore, if this issue is not taken into account, there would be overestimation of ground movements in serviceability limit state design calculations. Hence, incorporating the small strain behaviour in models to design geotechnical projects can lead to more efficient design and reduced costs (Jardine et al., 1991). Simpson et al. (1979) showed the importance of the small strain behaviour in calculating ground movements by showing that, for many geotechnical problems large zones of soil may experience only very low strains (see Figure 2.10), and hence correct assessment of the stiffness at these small strains may be crucial if ground movements are to be accurately predicted.

It is possible to investigate large strain behaviour of soils using conventional sample deformation measurement techniques in the triaxial apparatus, whereas it is not feasible to use conventional triaxial apparatus instrumentation for researching very small strain and small strain behaviour, because of problems with system compliance and bedding errors (Jardine et al., 1984). To avoid this issue, different local strain measuring devices have been developed, for fitting directly on soil samples within triaxial cells. These local strain measurement devices include linear variable differential transducers (LVDTs) (e.g Costa-Filho, 1985; Rowe & Barden, 1964; Cuccovillo & Coop, 1997 and Ackerley et al., 2016), inclinometer devices (e.g. Burland & Symes, 1982; and Ackerley et al., 1987), Hall Effect transducers (e.g Clayton & Khatrush, 1987; and Clayton et al., 1989), proximity transducer devices (e.g. Hird & Yung, 1987 and 1989) and strain-gauged local axial displacement transducers (LDTs) (e.g. Tatsuoka et al., 1990; and Goto et al.,1991). Scholey et al. (1995) provide a review of the various devices designed for accurate local measurement of small axial and radial strains in the triaxial apparatus. A number of researchers, for example Atkinson & Evans (1985); Lo Presti et al. (1993) and Zhou (2014), have investigated the differences between external and local strain measurements.

The resonant column device can be used to measure shear modulus G at strain levels

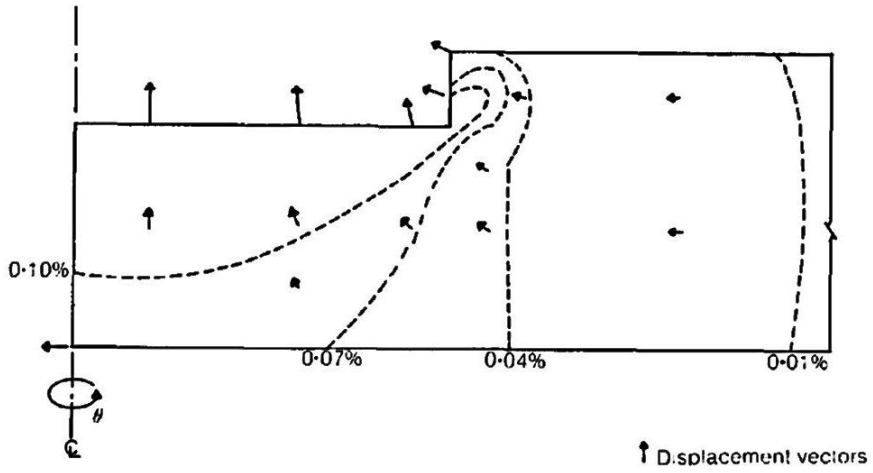

Figure 2.10: Shear strain contours around an excavation (Simpson et al., 1979)

down to even smaller than those that can be measured accurately with local strain measurement devices in the triaxial apparatus. The resonant column is a dynamic technique, which was introduced to soil mechanics laboratories in the 1960s (Hall & Richart, 1963 and Hardin & Black, 1968). In this technique, it is possible to determine the value of elastic shear modulus G by torsional vibration (Allen & Stokoe, 1982). A soil sample with one fixed end and the other free (Hall & Richart, 1963) is excited in torsion by motion of the free end to discover the resonant frequency. The shear wave velocity V_s can then be calculated from the resonant frequency f and the sample height h (ASTM D4015, 2000), and hence shear modulus G can be calculated from Equation 2.1.

Measurements of wave velocities, by devices such as bender/extender elements (see Section 2.1), provide a means to investigate soil behaviour at very small strains (less than 0.001%).

The full range of stress-strain behaviour of saturated soils was divided by Jardine et al. (1991) into three zones in stress space (see Figure 2.11). They proposed that the first zone (up to the Y_1 curve) is linear and elastic (recoverable), while the second zone (between Y_1 and Y_2) is non-linear but still essentially elastic (recoverable). Strains in the third zone (between Y_2 and Y_3) include a significant plastic (irrecoverable) component. In terms of strain levels, Atkinson & Sallfors (1991) divided soil behaviour into three zones of very small, small and large strains.

Atkinson et al. (1993) stated that the shear modulus G of a soil decreases significantly as the level of strain exceeds a critical strain of approximately 0.001%. Jardine et al. (1991) suggested that the precise value of this threshold strain depends on the plasticity index of the soil. Atkinson & Sallfors (1991) showed the typical variation of G for soils (see Figure 2.12). They also showed on the figure the idealised division of

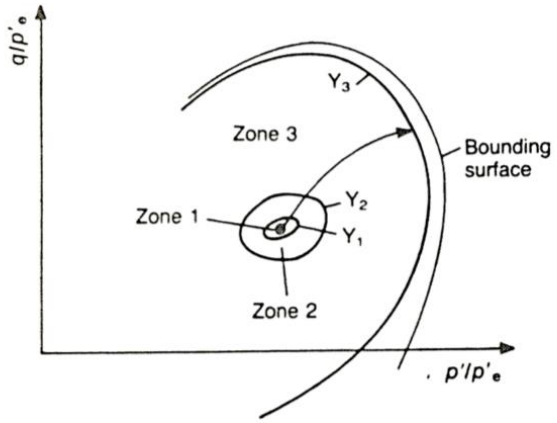

Figure 2.11: Three idealized zones in triaxial stress space (Jardine et al., 1991)

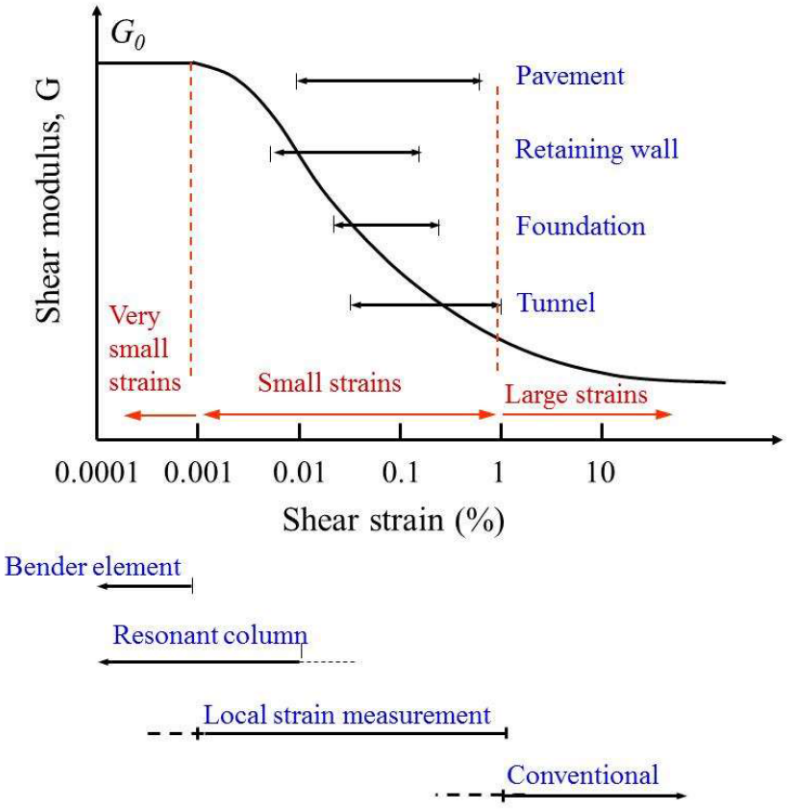

Figure 2.12: Typical variation of shear modulus with shear strain, with typical strain ranges encountered in engineering structures and in laboratory testing (Atkinson and Sallfors, 1991; Mair, 1993, cited by Zhou, 2014)

strains into very small, small and large strain regions (similar to Jardine et al., 1991 as described in the previous paragraph). In addition, on the same figure (i.e. Figure 2.12), Mair (1993) added typical corresponding ranges of strain for different types of structure.

In addition to depending upon strain amplitude, the value of shear stiffness G also depends on recent stress history (i.e. stress path rotations). Atkinson et al. (1990) performed specifically designed experimental stress path tests, as shown in Figure 2.13, to rigorously investigate the effect of recent stress history on the variation of soil stiffness. They concluded that at small strain, the stiffness significantly depends on any change of stress path direction and then this dependency gradually decreases and then erases with increase in strains, as shown in Figure 2.13. In contrast, at very small strains, within the truly elastic region (shear strain <0.001%), elastic shear modulus G measured by wave velocity methods is approximately independent of recent stress and strain history (for example, Lo Presti et al., 1993)

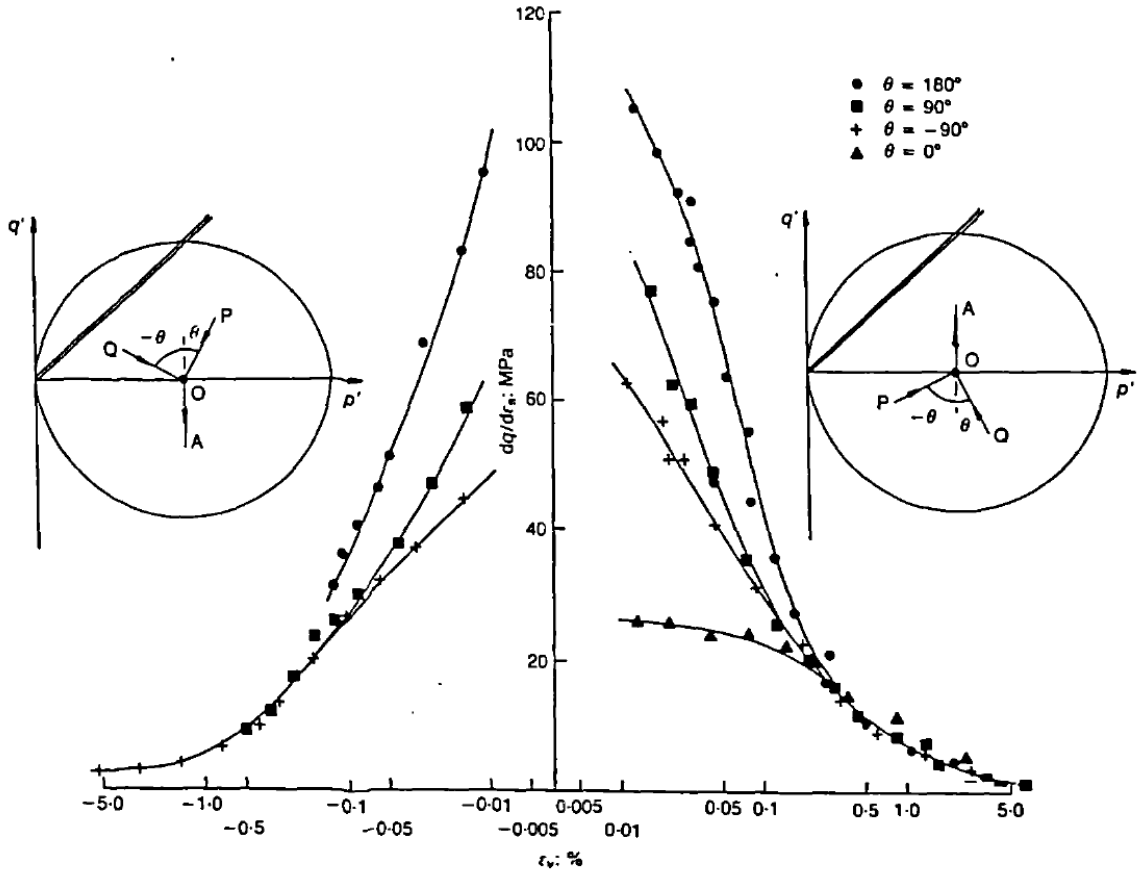

Figure 2.13: Recent stress history effect on shear modulus (after Atkinson et al. 1990, cited by Jovicic, 1997)

Some advanced constitutive models for saturated soils attempt to include appropriate modelling of small strain behaviour including, for example, smooth transition between

elastic behaviour and elasto-plastic behaviour, recent stress history effects and behaviour during cyclic loading-unloading. Advanced constitutive models intended to provide improved modelling of small strain behaviour whilst also accurately capturing large strain behaviour include multiple yield surface models (Mroz et al., 1979; Al-Tabbaa & Wood, 1989; Stallebrass et al., 1990; Stallebrass & Taylor, 1997; and Puzrin & Burland, 1998) and bounding surface models (e.g. Dafalias & Herrmann, 1982).

2.2.2 Very small strain elastic moduli of isotropic saturated soils

At very small strains, the behaviour of saturated soils can be treated as elastic. If the soil is isotropic, the elastic behaviour can be represented by two independent elastic properties, which are normally selected either as Young's modulus E and Poisson's ratio ν or as shear modulus G and bulk modulus K, where:

$$G = \frac{E}{2(1+\nu)} \tag{2.6}$$

$$K = \frac{E}{3(1-2\nu)} \tag{2.7}$$

For saturated soil, it can be helpful to choose to express the elastic properties in terms of G and K (rather than E and ν), because shear modulus G should be the same for both drained and undrained behaviour, and K is often considered as infinite for undrained behaviour. For linear elastic behaviour, G and K are constants, but soils often show non-linear elastic behaviour, with G and K varying with stress, strain or soil state.

Constrained modulus M is the elastic modulus (applied normal stress increment divided by normal strain increment in the same direction) for a condition where strain is prevented in both perpendicular directions. For an isotropic elastic soil, M can be expressed in terms of E and ν, or in terms of G and K:

$$M = \frac{E(1-\nu)}{(1-2\nu)(1+\nu)} \tag{2.8}$$

$$M = K + \frac{4}{3}G \tag{2.9}$$

Equations 2.1 and 2.2 show that the shear wave velocity V_s and compression wave velocity V_p measured in bender/extender elements BEE tests depend upon G (Equation 2.6) and M (Equation 2.8 or 2.9) respectively. BEE tests are high frequency dynamic measurements and hence they provide undrained values of shear and constrained moduli (G_u and M_u), rather than drained values G' and M'. For shear modulus G, this distinction has no significance, because there is no difference between drained and undrained values. For constrained modulus M, however, the distinction is crucial, because drained and undrained values are very different. Indeed, for saturated conditions, it is commonly assumed that the soil is incompressible under undrained conditions ($K_u = \infty$, ν_u=0.5), which would imply an infinite compression wave velocity V_p. In practice, saturated soils are not completely incompressible under undrained conditions, due mainly to the compressibility of the pore water, and this leads to finite (although very large) values of M_u and hence to high but finite values of compression wave velocity V_p. In contrast to saturated sands or clays, measurements of compression wave velocities in dry sands provide values of drained constrained modulus M', because the pore air is highly compressible (with a bulk modulus much lower than that of the soil skeleton).

There are many factors influencing the very small strain values of G and M of soils, such as grain and mineralogy characteristics (constant for a given soil), fabric, ageing, recent stress history, mean effective stress p', void ratio e, overconsolidation ratio OCR, temperature and others (Hardin & Black, 1969). The most important factors, which affect G and M for saturated soils under isotropic and anisotropic stress conditions are e, p' and OCR.

Experimental evidence shows that G increases when p' increases (e.g. Duffy et al., 1994; Viggiani & Atkinson, 1995; Jovicic & Coop, 1998; Callisto & Rampello, 2002 and Wang & Ng, 2005), e decreases (e.g. Hardin & Blanford, 1989) and OCR increases (e.g. Viggiani & Atkinson, 1995 and Houlsby & Wroth, 1991).

Some authors, such as Hardin and Black (1968) proposed that very small strain modulus G should be expressed as a function of e, p' and OCR:

$$G = f(e, p', OCR) \tag{2.10}$$

However, at least for fine-grained soils, the value of void ratio e can be related to p' and OCR for a given soil (using the equation of the normal compression line and the gradient of swelling lines). This means that it should be possible to simplify Equation

2.10 to a form where G depends upon only two of the three variables e, p' and OCR. Two possible forms instead of Equation 2.10 are therefore:

$$G = f(e, p') \tag{2.11}$$

or:

$$G = f(p', OCR) \tag{2.12}$$

Hardin (1978) correlated G to all three important variables (i.e. e, p' and OCR) through an expression that comes under the general form of Equation 2.10:

$$G = Cf(e) \left(\frac{p'}{p_r}\right)^n OCR^k \tag{2.13}$$

where C, n and k are soil constants, $f(e)$ is a function of void ratio e and p_r is a reference stress (a constant) to ensure dimensional consistency. The value of p_r is arbitrary, but it is typically taken as either 1kPa or as atmospheric pressure p_a (taken as 100kPa). The value of C depends upon the choice of p_r.

Experimental evidence from Shibuya et al. (1992), Jamiolkowski et al. (1995) and Santagata et al. (2005) showed that, provided a sensible form was selected for $f(e)$, the exponent k in Equation 2.13 was almost zero, so that OCR had negligible effect on the elastic shear modulus. Equation 2.13 therefore simplifies to a form suggested by many researchers (for example, Hardin & Black 1968; Shibuya et al, 1997; Salgado et al., 2000; Wang & Ng, 2005; Bui, 2009 and Oztoprak & Bolton, 2013):

$$G = Cf(e) \left(\frac{p'}{p_r}\right)^n \tag{2.14}$$

Equation 2.14 comes under the general form of Equation 2.11.

Generally, two main forms of $f(e)$ have been adopted in the literature for use in Equation 2.14. The first form, proposed mainly for sands by Hardin & Richart (1963) and many others, is given by:

$$f(e) = \frac{(a_1 - e)^2}{(1 + e)} = \frac{(a_2 - v)^2}{v} \tag{2.15}$$

where $a_1 = a_2 - 1$ is a soil constant, ranging from 1.46 to 7.32 for different soils (Bui,2009).

The second form of $f(e)$ for use in Equation 2.14 was mainly proposed for clays and was suggested by authors such as Jamiolkowski et al. (1991), Shibuya et al. (1997) and Lo Presti (1995):

$$f(e) = (1 + e)^{-m} = v^{-m} \tag{2.16}$$

where v is specific volume and m is a soil constant. Oztoprak & Bolton (2013) argued that the second form of $f(e)$ given in Equation 2.16 was preferable to the first form given in Equation 2.15, because it is simpler and because it resulted in less scatter when used to interpret experimental results from 343 tests involving 3860 data points. Use of Equation 2.16 in Equation 2.14 therefore leads to the following widely used expression for G:

$$G = Cv^{-m} \left(\frac{p'}{p_r} \right)^n \tag{2.17}$$

There has been much study of the value of the exponent n in Equation 2.17. According to Hertzian theory, G for a simple cubic packing of identical smooth elastic spheres should be proportional to cube root of the isotropic confining pressure $(p')^{1/3}$ and to the elastic stiffness of the spheres. This suggests that the value of the exponent n in Equation 2.17 should be 1/3. In practice, however, experimental evidence for sands and clays show that the value of the exponent n is approximately 0.5 (for example, Hardin & Black, 1966, 1968; Houlsby & Wroth, 1991; Shibuya & Tanaka, 1996 and Oztoprak & Bolton, 2013). This is attributed to the fact that natural soils contain a range of particle sizes and the particles are not perfect spheres (McDowell & Bolton, 2001).

For soils where the specific volume is approximately constant, such as dense sands and heavily overconsolidated clays (at stresses much lower than the yield condition), it may be possible to simplify Equation 2.17 to:

$$G = C_1 \left(\frac{p'}{p_r} \right)^n \tag{2.18}$$

This is the form of equation proposed for sands by Wroth & Houlsby (1985) and for all low compressibility soils by McDowell & Bolton (2001).

Rather than an expression relating G to e and p' (see the general form of Equation 2.11), some others such as Viggiani & Atkinson (1995), proposed expresions relating G to p' and OCR (see the general form of Equation 2.12). The particular form of expression proposed by Viggiani & Atkinson (1995) was:

$$G = C_2 \left(\frac{p'}{p_r} \right)^{n_2} OCR^{k_2} \tag{2.19}$$

where C_2, n_2 and k_2 are soil constants. Given the form of relationship typically found between v, p' and OCR, Equation 2.19 will normally be able to provide very similar predictions to Equation 2.17 (but note that, to achieve this, $C_2 \neq C$ and $n_2 \neq n$). In particular, if the soil behaviour can be idealised by a normal compression line that is a straight line in a $lnv : lnp'$ plot (as suggested by Butterfield, 1979) of gradient λ^*, with swelling lines as straight lines of gradient κ^* in the same plot (as in the soft soil elasto-plastic constitutive model in the widely-used FE program PLAXIS), then Equations 2.17 and 2.19 are directly equivalent. In this case, v is related to p' and OCR by:

$$v = \mu \left(\frac{p'}{p_r} \right)^{-\lambda^*} OCR^{-(\lambda^* - \kappa^*)} \tag{2.20}$$

where μ is a soil constant giving the value of v on the normal compression line when p' is equal to the reference pressure p_r. Insertion of Equation 2.20 into Equation 2.17 gives:

$$G = C\mu^{-m} \left(\frac{p'}{p_r} \right)^{n+m\lambda^*} OCR^{m(\lambda^* - \kappa^*)} \tag{2.21}$$

Comparison of Equation 2.21 with Equation 2.19 shows that, with this form of compression model for the soil, Equations 2.19 and 2.17 are directly equivalent, with the soil constants in Equation 2.19 (C_2, n_2 and k_2) related to those in Equation 2.17 (C, m and n) by:

$$C_2 = C\mu^{-m} \tag{2.22}$$

$$n_2 = n + m\lambda^* \tag{2.23}$$

$$k_2 = m(\lambda^* - \kappa^*) \tag{2.24}$$

For a case of normally consolidated soil ($OCR = 1$), Equation 2.19 simplifies to:

$$G = C_2 \left(\frac{p'}{p_r}\right)^{n_2} \tag{2.25}$$

This was the form of expression proposed for normally consolidated clays by Viggiani & Atkinson (1995), based on bender element test data from normally consolidated reconstituted speswhite kaolin samples. It is important to note that the exponent n_2 in Equation 2.25 (which applies for normally consolidated soils) is not the same as the exponent n in Equation 2.18 (which applies for incompressible soils), as indicated in Equation 2.23.

Anderson & Stokoe (1978) investigated the effect of ageing on very small strain shear modulus G. In tests where p' was held constant, they noted that G increased at a relatively rapid rate with the logarithm of time for normally consolidated clays, whereas the rate of increase of G with the logarithm of time was lower for overconsolidated clays and lower still for sands (see Figure 2.14). These ageing effects are probably partially attributable to reductions of specific volume caused by creep straining (noting that creep strains generally occur at a linear rate with the logarithm of time and are greatest in normally consolidated clays, smaller in overconsolidated clays and smallest of all in sands (see, e.g., Lambe & Whitman, 1979)), and hence the ageing effect on G may be partially represented by Equation 2.17 (through the reduction of v caused by creep strains). However, other fabric rearrangement effects with time (which do not involve any change of v) probably also contribute to the ageing-induced increases of G.

Less study has been performed on the factors controlling the constrained modulus M of saturated soils determined from measurements of compression wave velocity. This is essentially because it is generally sufficient in geotechnical design (with the exception of seismic design) to assume that the undrained bulk modulus K_u and hence undrained constrained modulus M_u (see Equation 2.9) of a saturated soil is infinite. In reality, saturated soils are not completely incompressible under undrained conditions, and this is mainly attributable to the compressibility of the pore water, because the bulk modulus of water K_w is generally significantly lower that the bulk modulus of

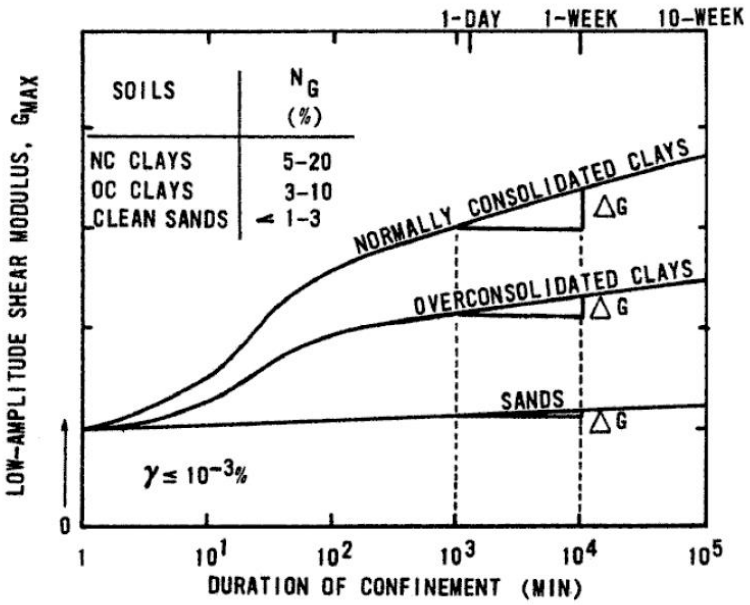

Figure 2.14: Ageing effect on shear modulus G (after Anderson & Stokoe 1978)

the minerals forming the soil particles. This means that the undrained constrained modulus M_u of a saturated soil should be mainly determined by the value of K_w (a constant) and the proportion of the soil volume occupied by voids. Hence, the expectation would be that M_u could be expressed simply as a function of void ratio:

$$M_u = f(e) \tag{2.26}$$

For dry sands, measurements of compression wave velocity can be used to determine the value of drained constrained modulus M'. By analogy with the shear modulus G (see Equation 2.11), the expectation would be that M' would be a function of e and p':

$$M' = f(e, p') \tag{2.27}$$

Based on measurements of compression wave velocity V_p in a dry sand, using source and receiver geophones in a test chamber, Stokoe et al. (1995) proposed the following expression for M':

$$M' = C_p \left(\frac{p'}{p_r} \right)^{n_p} \tag{2.28}$$

where C_p and n_p are soil constants. Equation 2.28 assumes that changes of void ratio

are negligible (compare with Equation 2.27). Figure 2.15 shows the predicted (using Equation 2.28) and measured values of V_p on sand samples from Valle-Molina & Stokoe (2012). It is clear from Figure 2.15 that there was very good agreement between the predicted and measured values of V_p. Clearly, Equation 2.28 would need modification for materials where changes of void ratio were significant. A possible form for this would be:

$$M' = C_p f(e) \left(\frac{p'}{p_r} \right)^{n_p} \tag{2.29}$$

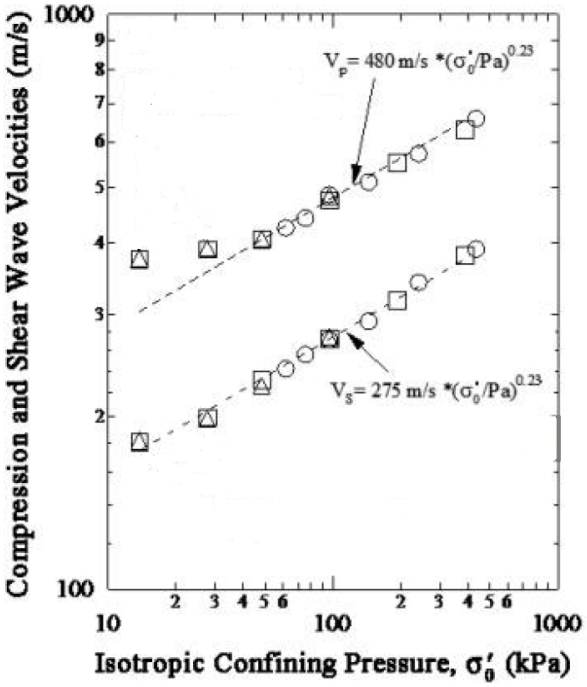

Figure 2.15: Comparison between measured and predicted V_p (after Valle-Molina & Stokoe, 2012)

2.2.3 Very small strain elastic moduli of anisotropic saturated soils

The importance of anisotropy of very small strain behaviour has been investigated by many authors such as Lee & Rowe (1989), Simpson et al. (1996), Wongsaroj et al. (2004) and Grammatikopoulou et al. (2014). They showed, using numerical analysis, that including anisotropy of G during the prediction of deformations of tunnelling in stiff clays (such as London clay) appeared to play a vital role.

The processes of deposition and consolidation in natural soils or compaction in fill materials will typically produce soils that are cross-anisotropic (also known as transversely

isotropic or orthotropic). This type of anisotropy is due to anisotropy of the soil fabric (the arrangement of soil particles). This anisotropy of soil fabric can evolve during plastic straining, leading to changes in the anisotropy of mechanical behaviour. These changes of anisotropy caused by changes of soil fabric are therefore termed "strain-induced anisotropy" (Jovicic & Coop, 1998). The initial anisotropy of the soil in it's in-situ condition is sometimes termed "inherent anisotropy" or "intrinsic anisotropy" (Ng & Yung, 2008). However, the term "inherent" or "intrinsic" may be rather misleading, because they suggest a permanent memory of this anisotropy, whereas the initial anisotropy in the in-situ condition is attributable simply to the soil fabric at that point in time. This initial anisotropy is therefore a form of "strain-induced anisotropy", produced by the previous history of deposition, consolidation, erosion, creep and ageing; and it can be changed subsequently by further changes of soil fabric arising during plastic straining, with a permanent loss of memory of this initial anisotropy.

In addition to the anisotropy of mechanical behaviour caused by anisotropy of the soil fabric, there can be anisotropy caused simply by the current stress state (independent of soil fabric). This type of anisotropy is attributable to changes of the distribution of inter-particle forces as the stress state changes (without significant movement of soil particles) and is known as "stress-induced anisotropy" (Stokoe et al., 1995 and Jovicic & Coop, 1998).

Very small strain elastic behaviour may be influenced both by anisotropy of fabric (strain-induced anisotropy) and by stress-induced anisotropy. In contrast, anisotropy of large strain plastic behaviour can be attributed solely to anisotropic of fabric (strain-induced anisotropy), because the concept of stress-induced anisotropy is already implicit in even isotropic plasticity (see Section 2.5).

Love (1927) showed that thermodynamic considerations mean that the stiffness matrix (and compliance matrix) of an elastic material must be symmetric. This means that the most general form of linear anisotropic elastic behaviour involves 21 (rather than 36) independent elastic constants (see Graham & Houlsby, 1983).

For a cross-anisotropic elastic material, with the same properties in all horizontal directions but different properties in vertical directions, symmetry of the stiffness and compliance matrices implies that:

$$\frac{\nu_{hv}}{E_h} = \frac{\nu_{vh}}{E_v} \tag{2.30}$$

where E_h and E_v are the Young's moduli in horizontal and vertical directions re-

spectively, ν_{hv} is the Poisson's ratio giving the ratio of vertical to horizontal strain increment caused by a uniaxial stress increment in the horizontal direction, and ν_{vh} is the Poisson's ratio giving the ratio of horizontal to vertical strain increment caused by a uniaxial stress increment in the vertical direction. Thermodynamic considerations also imply that for this cross-anisotropic material, the shear moduli G_{vh} , G_{hv} and G_{hh} are given by:

$$G_{hv} = G_{vh} \tag{2.31}$$

$$G_{hh} = \frac{E_h}{2(1+\nu_{hh})} \tag{2.32}$$

This means that, as shown by Graham & Houlsby (1983), the behaviour of a cross-anisotropic elastic material involves only 5 independent elastic constants, which can be taken as E_v, E_h, ν_{vh}, ν_{hh} and G_{vh}. The stress-strain relations of this cross-anisotropic elastic material can then be expressed as:

$$\begin{bmatrix} \Delta\epsilon_{xx} \\ \Delta\epsilon_{yy} \\ \Delta\epsilon_{zz} \\ \Delta\gamma_{xy} \\ \Delta\gamma_{yz} \\ \Delta\gamma_{zx} \end{bmatrix} = \begin{bmatrix} \frac{1}{E_h} & -\frac{\nu_{hh}}{E_h} & -\frac{\nu_{vh}}{E_v} & & & \\ -\frac{\nu_{hh}}{E_h} & \frac{1}{E_h} & -\frac{\nu_{vh}}{E_v} & & & \\ -\frac{\nu_{vh}}{E_v} & -\frac{\nu_{vh}}{E_v} & \frac{1}{E_v} & & & \\ & & & \frac{1}{G_{hv}} & & \\ & & & & \frac{1}{G_{hv}} & \\ & & & & & \frac{2(1+\nu_{hh})}{E_h} \end{bmatrix} \begin{bmatrix} \Delta\sigma'_{xx} \\ \Delta\sigma'_{yy} \\ \Delta\sigma'_{zz} \\ \Delta\tau_{xy} \\ \Delta\tau_{yz} \\ \Delta\tau_{zx} \end{bmatrix} \tag{2.33}$$

where x and y are horizontal directions, z is the vertical direction, $\Delta\sigma_{xx}$, $\Delta\sigma_{yy}$ and $\Delta\sigma_{zz}$ are normal stress increments, $\Delta\epsilon_{xx}$, $\Delta\epsilon_{yy}$ and $\Delta\epsilon_{zz}$ are corresponding normal strain increments, $\Delta\tau_{xy}$, $\Delta\tau_{yz}$ and $\Delta\tau_{zx}$ are shear stress increments and $\Delta\gamma_{xy}$, $\Delta\gamma_{yz}$ and $\Delta\gamma_{zx}$ are corresponding shear strain increments. In Equation 2.33 all zero terms in the compliance matrix have been omitted for clarity.

Due to the thermodynamic requirement that strain energy must be positive in elastic materials, the values of the five independent elastic constants are bounded. The values of E_v, E_h and G_{hv} must be positive (Pickering, 1970 and Lings 2001) and -1$<\nu_{hh}<$1 . The values of E_v, E_h, ν_{vh} and ν_{hh} must also satisfy an inequality (Pickering, 1970):

$$\frac{E_v}{E_h}(1-\nu_{hh})-2\nu_{vh}^2 \geqslant 0 \tag{2.34}$$

There is also a limit for the value of G_{hv} (Raymond, 1970), given by:

$$G_{hv} \leqslant \frac{E_v}{2\nu_{vh}(1+\nu_{hh})+2\left(\sqrt{\left[\frac{E_v}{E_h}(1-2\nu_{hh}^2)\left(1-\frac{E_h}{E_v}\nu_{hh}^2\right)\right]}\right)} \tag{2.35}$$

For a shear wave, the direction of motion of the soil particles (the wave polarisation) is perpendicular to the direction of wave transmission, as shown in Figure 2.16. Hence, different shear wave velocities can be measured, depending upon the direction of the wave transmission and the direction of the wave polarisation, e.g. V_{svh}, V_{shv} and V_{shh}, where the second subscript gives the wave transmission direction, the third subscript gives the wave polarisation direction and v and h represent vertical and horizontal respectively. For compression waves, the direction of particle motion (wave polarisation) is the same as the direction of wave transmission (see, Figure 2.16). By transmitting compression waves in vertical and horizontal directions, compression waves velocities V_{pv} and V_{ph} can be measured.

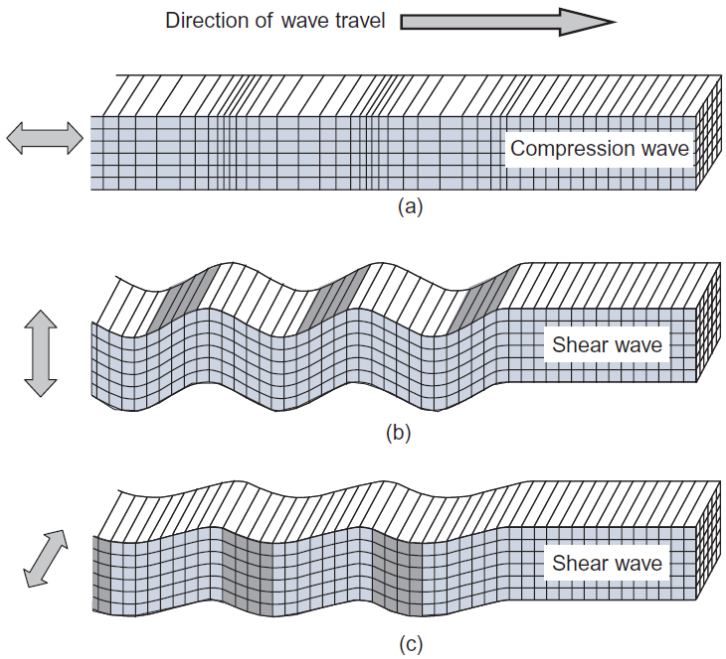

Figure 2.16: Compression and shear wave travel: (a) Compression wave with horizontal transmission, V_{ph} (b) Shear wave with horizontal transmission and vertical polarisation, V_{shv} (c) Shear wave with horizontal transmission and horizontal polarisation, V_{shh} (Clayton, 2011)

If a cross-anisotropic soil sample is fitted with three pairs of BEEs, one pair transmitting vertically and two pairs transmitting horizontally (one oriented to produce vertically polarised shear waves, the other oriented to produce horizontally polarised shear waves), these can therefore provide measurements of shear wave velocities V_{svh}, V_{shv} and V_{shh} and compression wave velocities V_{pv} and V_{ph}. These five velocities can then be used to determine the 5 elastic parameters G_{vh} , G_{hv} , G_{hh}, M_v and M_h, by using Equations 2.1 and 2.2. G_{vh} and G_{hv} should, however, be identical (see Equation 2.31), meaning that the BEE measurements provide values of 4 independent elastic constants, G_{vh}=G_{hv} , G_{hh}, M_v and M_h.

The constrained moduli M_v and M_h, determined from the vertical and horizontal compression wave velocities measured with BEEs, can be expressed in terms of E_v, E_h, ν_{vh} and ν_{hh} as follows:

$$M_v = \frac{E_v}{1 - 2\nu_{vh}\frac{E_h}{E_v}\frac{\nu_{vh}}{(1-\nu_{hh})}} \tag{2.36}$$

$$M_h = \frac{E_h(E_v - \nu_{vh}^2 E_h)}{(1-\nu_{hh}^2)E_v - 2\nu_{vh}^2(1+\nu_{hh})E_h} \tag{2.37}$$

Derivations of Equations 2.36 and 2.37 are presented in Appendix A. The 4 independent elastic parameters that can be determined by three pairs of BEEs (one transmitting vertically and two transmitting horizontally), G_{hv}=G_{vh} , G_{hh}, M_v and M_h, can therefore be related to the 5 independent elastic constants in the compliance matrix of Equation 2.33, E_v, E_h, ν_{vh}, ν_{hh} and G_{hv} by Equations 2.31, 2.32, 2.36 and 2.37.

The only one of the 5 independent elastic constants in the compliance matrix of Equation 2.33 that can be measured by the three pairs of BEEs described above is the shear modulus G_{hv}. Re-arranging and combining Equations 2.32, 2.36 and 2.37, the independent elastic constants E_v, E_h and ν_{vh} can be expressed in terms of the final constant ν_{hh} and the three other elastic moduli measured in the BEE tests i.e. G_{hh}, M_v and M_h:

$$E_h = 2(1+\nu_{hh})G_{hh} \tag{2.38}$$

$$E_v = \frac{(1+\nu_{hh})M_v G_{hh}}{(1-\nu_{hh})(M_h - G_{hh})} \tag{2.39}$$

$$\nu_{vh} = \frac{1}{2(M_h - G_{hh})} \left[\frac{M_v((1-\nu_{hh})M_h - 2G_{hh})}{(1-\nu_{hh})} \right]^{1/2} \tag{2.40}$$

Derivations of Equations 2.39 and 2.40 are presented in Appendix A. It is clear that BEE tests using the conventional arrangement of three pairs of BEEs (one transmitting vertically and two transmitting horizontally) provide only 4 independent measurements and hence cannot be used to determine all 5 independent elastic constants for a cross-anisotropic soil.

Stokoe et al. (1995) and Fioravante & Cappoferri (2001) showed that the 5 independent elastic constants of cross-anisotropic soils could be measured with bender and extender elements if an additional extender element was used to determine a constrained modulus M_θ in an oblique direction. Alternatively, Pennington (1999) showed how all 5 independent constants could be determined by combining bender element testing (to measure G_{hv} and G_{hh}) with local strain measurement on triaxial samples (to measure E_v, E_h and ν_{vh}). This does, however, have the drawback of combining two different types of measurement (at two different strain amplitudes).

Using the conventional arrangement of three pairs of BEEs (one transmitting vertically and two transmitting horizontally), the 4 independent elastic parameters that can be directly determined are G_{hv}, G_{hh}, M_v and M_h. The ratios G_{hh}/G_{hv} and M_h/M_v then provide two different measures of elastic anisotropy. In addition to G_{hh}/G_{hv} and M_h/M_v, a third ratio (such as ν_{hh}/ν_{hv}) would be required to fully characterise the anisotropy of a cross-anisotropic soil (giving that cross-anisotropic elasticity involves three more independent elastic constants than isotropic elasticity), but this additional ratio cannot be determined from the conventional arrangement of BEEs transmitting horizontally and vertically.

Jovicic & Coop (1998) showed (in Figure 2.17), that for the undisturbed London clays, under isotropic effective stress, the values of G_{hh} are greater than values of G_{hv} (i.e. G_{vh}), showing the elastic cross-anisotropic behaviour of the soil. Many other researchers have experimentally confirmed values of G_{hh}/G_{hv} greater than 1 for various different soils including, for example, reconstituted speswhite kaolin clays (Kuwano et al., 1999), natural Pisa clay (Jamiolkowski et al., 1995), completely decomposed tuff (Ng & Leung, 2007) and Chicago clay (Kim & Finno, 2012).

Jovicic & Coop (1998) investigated experimentally the evolution of elastic anisotropy (in terms of G_{hh}/G_{hv}) for initially anisotropic reconstituted London clay by conducting bender element tests as the sample was subjected to continuously increasing isotropic stress states in a high stress triaxial apparatus (i.e. they investigated strain-induced

changes of very small strain elastic anisotropy). They concluded that after yielding as indicated by a significant change of plastic strain increment ratio $\Delta\epsilon_r/\Delta\epsilon_a$ (see Figure 2.18), evolution of G_{hh}/G_{hv} occurred. However, even large plastic strains caused only relatively modest change of G_{hh}/G_{hv} (see Figure 2.18).

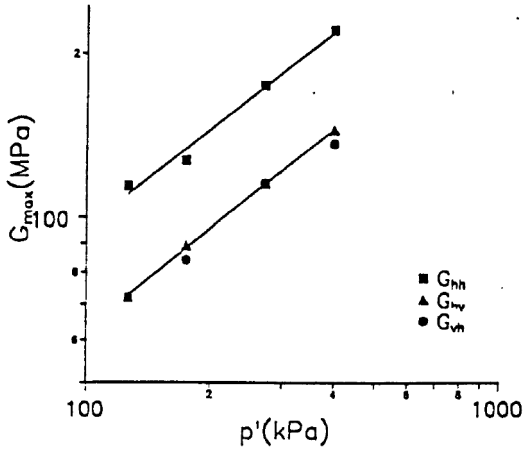

Figure 2.17: Bender element tests of undisturbed London clays (Jovicic & Coop, 1998)

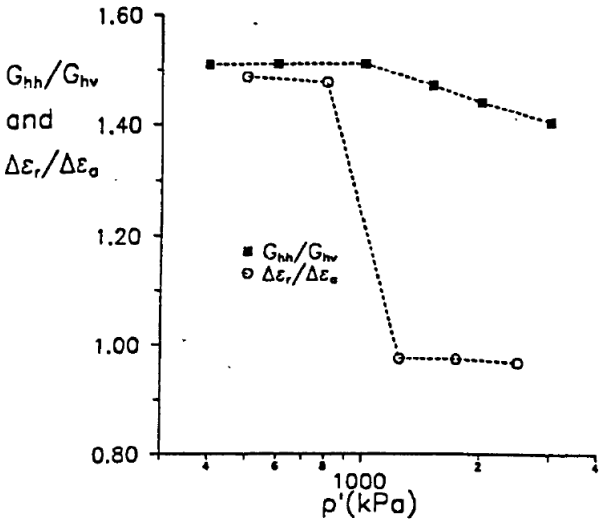

Figure 2.18: Strain-induced anisotropy of reconstituted London clay (Jovicic & Coop 1998)

Evolution of elastic anisotropy G_{hh}/G_{hv} was related to micro-fabric orientation degree, $\bar{L}$ using scanning electron microscopy (SEM) by Mitaritonna et al. (2014). They performed bender element testing and SEM imaging on reconstituted Lucera clay loaded along different stress paths (η>0). They found that plastic straining under high values of η changed micro-fabric orientation degree $\bar{L}$ (i.e. strain-induced anisotropy) and hence caused an increase of G_{hh}/G_{hv} (see Figure 2.19).

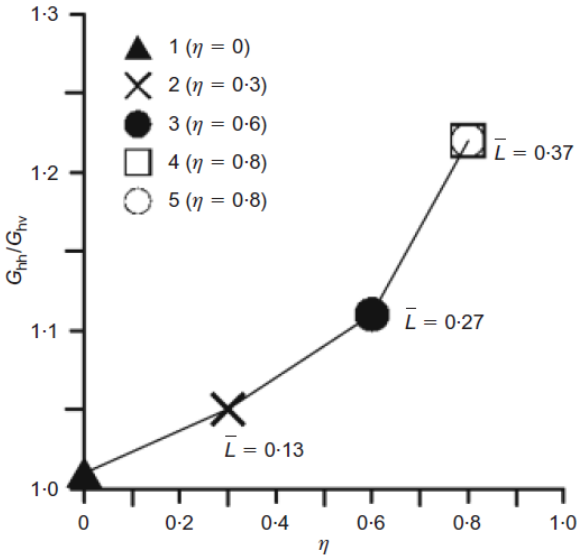

Figure 2.19: Anisotropy ratio G_{hh}/G_{hv} against η (Mitaritonna et al., 2014)

Equation 2.13, for the shear modulus of an isotropic soil, can be extended to include the possible effects of both inherent (strain-induced) anisotropy and stress-induced anisotropy:

$$G_{ij} = C_{ij} f(e) \left(\frac{\sigma'_i}{p_r}\right)^{n_i} \left(\frac{\sigma'_j}{p_r}\right)^{n_j} \left(\frac{\sigma'_k}{p_r}\right)^{n_k} OCR^k \tag{2.41}$$

In Equation 2.41, if G_{ij} is determined from a shear wave velocity V_{sij}, then subscript i represents the direction of wave transmission, subscript j represents the direction of wave polarisation and subscript k represents the third mutually perpendicular direction. If the values of C_{ij} are different for different directions, then this represents inherent anisotropy. Values of C_{ij} can evolve during plastic straining, as fabric anisotropy evolves (strain-induced anisotropy). If the three exponents n_i, n_j and n_k are not equal then the different dependencies on σ'_i, σ'_j and σ'_k in Equation 2.41 represent stress-induced anisotropy.

As stated in Section 2.2.2, if the function $f(e)$ is selected appropriately, then the inclusion of dependence on OCR in Equation 2.41 is unnecessary. The expression then simplifies to:

$$G_{ij} = C_{ij} f(e) \left(\frac{\sigma'_i}{p_r}\right)^{n_i} \left(\frac{\sigma'_j}{p_r}\right)^{n_j} \left(\frac{\sigma'_k}{p_r}\right)^{n_k} \tag{2.42}$$

In order for Equation 2.42 to converge to Equation 2.14 for isotropic stress states,

the exponents n_i, n_j and n_k in Equation 2.42 must be related to the exponent n in Equation 2.14 by:

$$n_i + n_j + n_k = n \tag{2.43}$$

Also, the fact that, by definition, $G_{ij} = G_{ji}$ means that:

$$C_{ij} = C_{ji} \tag{2.44}$$

and

$$n_j = n_i \tag{2.45}$$

Equation 2.43 then becomes:

$$2n_i + n_k = n \tag{2.46}$$

Inserting Equation 2.45, Equation 2.42 now becomes:

$$G_{ij} = C_{ij} f(e) \left(\frac{\sigma'_i}{p_r}\right)^{n_i} \left(\frac{\sigma'_j}{p_r}\right)^{n_i} \left(\frac{\sigma'_k}{p_r}\right)^{n_k} \tag{2.47}$$

This means that G_{hv} and G_{hh} are given by:

$$G_{hv} = C_{hv} f(e) \left(\frac{\sigma'_h}{p_r}\right)^{n_i+n_k} \left(\frac{\sigma'_v}{p_r}\right)^{n_i} \tag{2.48}$$

$$G_{hh} = C_{hh} f(e) \left(\frac{\sigma'_h}{p_r}\right)^{2n_i} \left(\frac{\sigma'_v}{p_r}\right)^{n_k} \tag{2.49}$$

Authors such as Rosler (1979), Hardin & Blandford (1989), Stokoe et al. (1995), Jamiolkowski et al. (1995), Shibuya et al. (1997) and Yamashita & Susuki (2001) have investigated experimentally the values of the exponents n_i, n_j and n_k in Equation 2.42, or the values of the corresponding exponents in Equations 2.48 and 2.49, for

both sands and clays. Most of these authors interpreted their results in terms of expressions that also included dependency on OCR (see Equation 2.41), even though this was probably unnecessary if the function of void ratio $f(e)$ had been selected appropriately (as discussed in Section 2.2.2).

Hardin & Blandford (1989), Stokoe et al. (1995), Jamiolkowski et al. (1995) and Shibuya et al. (1997) all concluded from their experimental results that $n_j = n_i$ (i.e. that the influence of the stress in the shear wave polarisation direction is the same as the influence of the stress in the shear wave transmission direction), as required by theory (see Equation 2.45). They also concluded that $n_k \approx 0$, i.e. that the stress in the third mutually perpendicular direction has no influence. For example, Figure 2.20b shows results from shear wave measurements by Stokoe et al. (1995) on a sand in a cubical true triaxial calibration chamber in which the principal stresses σ'_x and σ'_y were held constant while the principal stress σ'_z was gradually increased. The results in Figure 2.20b show that the increase of σ'_z had no influence on the shear wave velocity V_{sxy} (i.e. $n_k \approx 0$), whereas it produced similar increases in shear wave velocities V_{syz} and V_{szx} (i.e. $n_i = n_j$). In contrast, Jung et al. (2007) performed bender element measured of G_{hv} (actually they measured G_{vh}) on saturated Chicago clay samples and found that the exponent n_k was not zero, as they found that the exponent $n_i + n_k$ of σ'_h (see Equation 2.48) was three times higher than the exponent n_i of σ'_v (see Equation 2.48). This showed that, for clays, the stress in the third mutually perpendicular direction had an influence on G_{hv}. On the other hand, Viggiani & Atkinson (1995) found that the exponent n_k in Equation 2.48 was non-zero during triaxial extension tests on saturated speswhite kaolin clay samples but n_k in Equation 2.48 was approximately zero for triaxial compression tests on the same kaolin samples.

If $n_k = 0$, as suggested by several authors, then (taking account of Equation 2.46, Equation 2.47, 2.48 and 2.49 simplify to:

$$G_{ij} = C_{ij} f(e) \left(\frac{\sigma'_i}{p_r}\right)^{n/2} \left(\frac{\sigma'_j}{p_r}\right)^{n/2} \tag{2.50}$$

$$G_{hv} = C_{hv} f(e) \left(\frac{\sigma'_h}{p_r}\right)^{n/2} \left(\frac{\sigma'_v}{p_r}\right)^{n/2} \tag{2.51}$$

$$G_{hh} = C_{hh} f(e) \left(\frac{\sigma'_h}{p_r}\right)^{n} \tag{2.52}$$

These are the type of expressions proposed by, for example, Pennington (1999).

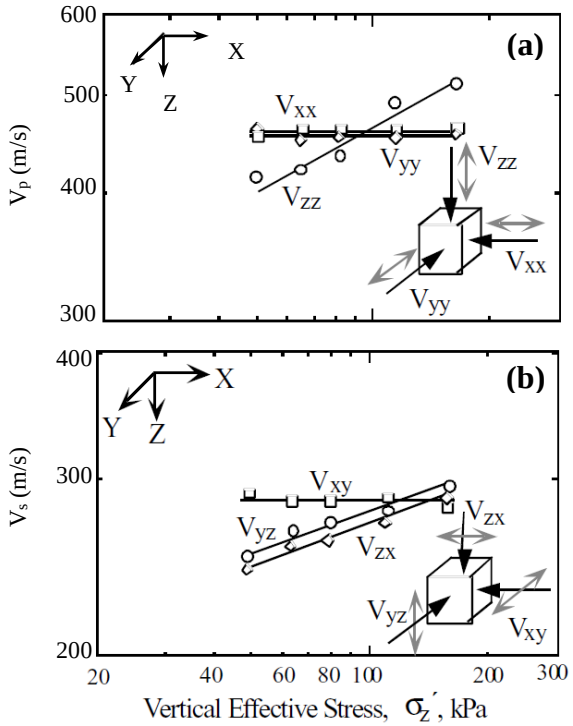

Figure 2.20: Variation of V_p and V_s along the three principal stress directions with only σ'_z changing (after Stokoe et al., 1995)

Authors such as Viggiani & Atkinson (1995), Rampello et al. (1997) and Pennington (1999) re-wrote Equations 2.51 and 2.52 in terms of mean effective stress p' and stress ratio η (where $\eta = q/p'$), instead of σ'_h and σ'_v. Noting that in a triaxial apparatus:

$$\sigma'_v = p'(1 + \frac{2\eta}{3}) \tag{2.53}$$

$$\sigma'_h = p'(1 - \frac{\eta}{3}) \tag{2.54}$$

Equations 2.51 and 2.52 become:

$$G_{hv} = C_{hv} f(e) \left(\frac{p'}{p_r}\right)^n \beta_{hv} \tag{2.55}$$

$$G_{hh} = C_{hh} f(e) \left(\frac{p'}{p_r}\right)^n \beta_{hh} \tag{2.56}$$

where:

$$\beta_{hv} = (1 - \frac{\eta}{3})^{n/2}(1 + \frac{2\eta}{3})^{n/2} \tag{2.57}$$

$$\beta_{hh} = (1 - \frac{\eta}{3})^{n} \tag{2.58}$$

If the exponent n_k is not zero in Equations 2.48 and 2.49, then the expressions for β_{hv} and β_{hh} in Equations 2.57 and 2.58 become:

$$\beta_{hv} = (1 - \frac{\eta}{3})^{(n+n_k)/2}(1 + \frac{2\eta}{3})^{(n-n_k)/2} \tag{2.59}$$

$$\beta_{hh} = (1 - \frac{\eta}{3})^{(n-n_k)}(1 + \frac{2\eta}{3})^{n_k} \tag{2.60}$$

Figure 2.21 shows the variations of β_{hv} and β_{hh} predicted by Equations 2.57 and 2.58 (for the case n =0.5) plotted against stress ratio η. It is clear from Figure 2.21 that use of Equations 2.57 and 2.58 in Equations 2.55 and 2.56 means that, at any given value of p', G_{hv} and G_{hh} are predicted to vary only modestly with stress ratio η, within the range of -1 < η < 1. It is also clear from Figure 2.21 that Equation 2.56 and 2.57 predict that for positive values of η (triaxial compression) G_{hv} will be greater than the value under isotropic stress states whereas G_{hh} will be less than the value under isotropic stress states, with the reverse situation for negative values of η (triaxial extension). Different patterns could be predicted by using the more general expressions of Equations 2.59 or 2.60 with $n_k \neq 0$.

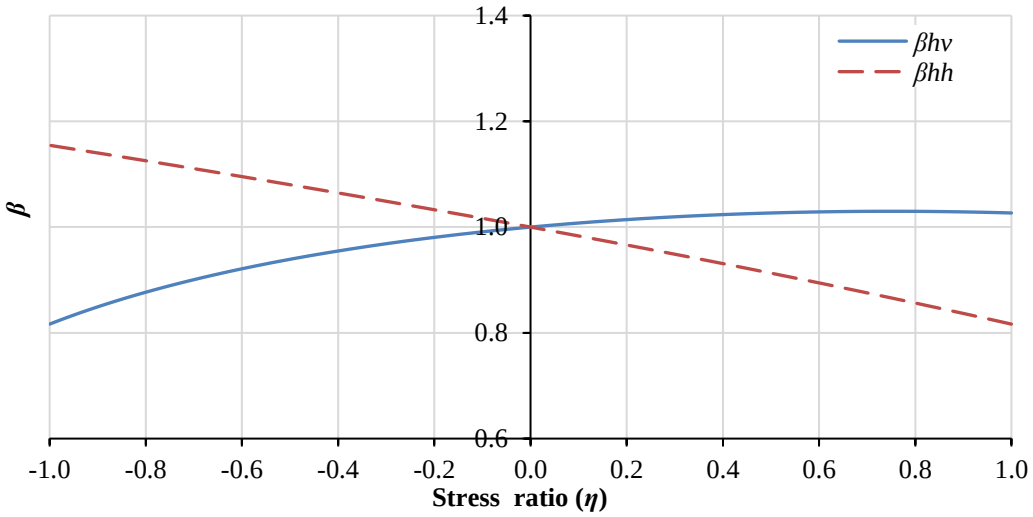

Figure 2.21: Variations of β_{hv} and β_{hh} with η when n_k =0 and n =0.5

Experimental investigations of the influence of η on G_{hv} and G_{hh} (e.g. Viggiani & Atkinson (1995), Rampello et al. (1997), Jovicic & Coop (1998), Pennington (1999) and Mitaritonna et al. (2014)) confirmed that the value of η had little or no influence on the values of G_{hv} and G_{hh}.

Viggiani & Atkinson (1995) concluded that η had no influence on G_{hv} (they actually measured G_{vh}) in kaolin samples (see Figure 2.22, where the values of G_o were measurements of G_{vh}). Jovicic & Coop (1998) concluded that η had negligible effect on both G_{hv} and G_{hh}. Rampello et al. (1997) found in tests on reconstituted Vallericca clay that values of G_{hv} (they actually measured G_{vh}) increased slightly with increase of η above zero, as predicted by Equation 2.55 (see Figure 2.21).

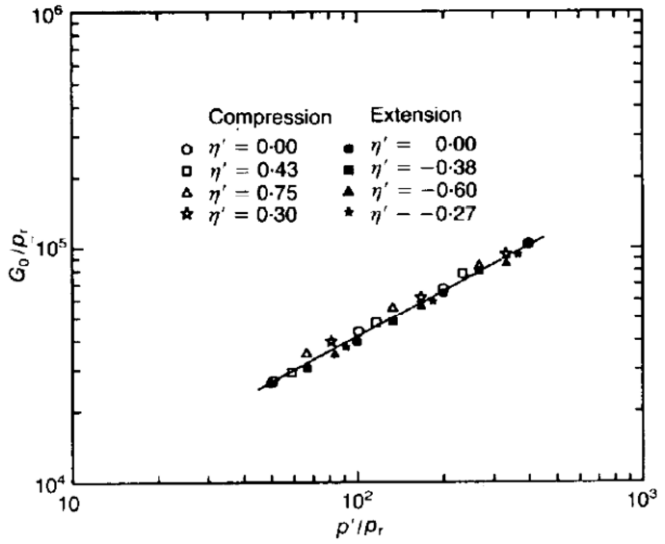

Figure 2.22: Variation of G with p' for normally consolidated kaolin samples at different stress ratios η (Viggiani & Atkinson, 1995)

The results from Mitaritonna et al. (2014) from tests on Lucera clay at values of p' up to 1400kPa are shown in Figure 2.23. These show no clear influence of η on G_{hv} (within the range $0 \leq \eta \leq 0.6$) and that G_{hh} was slightly greater at $\eta = 0.6$ than at $\eta = 0$ or $\eta = 0.3$ (this is actually the opposite of what would be predicted by Equation 2.58, as shown in Figure 2.21).

Much less work has been done on the influence of anisotropy on values of constrained modulus M than has been done for shear modulus G. As stated previously in Section 2.2.2, this is probably because for most geotechnical design it is normally acceptable to assume that K_u and M_u are infinite under saturated conditions.

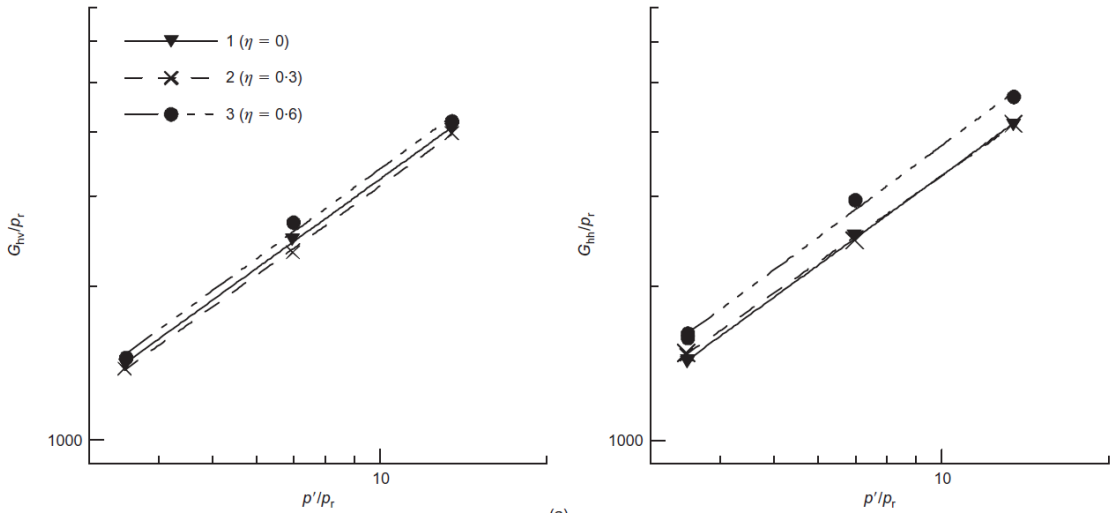

Figure 2.23: Influence of η on G_{hv} andG_{hh} (Mitaritonna et al., 2014)

There has been some study on the influence of stress-induced anisotropy on the very small strain drained constrained modulus determined from measurements of compression wave velocities in dry sands. Authors such as Bellotti et al. (1996) and Fioravante & Capoferri (2001) proposed an expression for the drained constrained modulus M'_i measured from a compression wave transmitting in direction i which is directly equivalent to the expression for shear modulus G_{ij} given in Equation 2.47:

$$M'_i = C_{pi} f(e) \left(\frac{\sigma'_i}{p_r}\right)^{n_{pi}} \left(\frac{\sigma'_j}{p_r}\right)^{n_{pj}} \left(\frac{\sigma'_k}{p_r}\right)^{n_{pk}} \tag{2.61}$$

If Equation 2.61 is to converge with Equation 2.29 for isotropic stress states:

$$n_{pi} + n_{pj} + n_{pk} = n_p \tag{2.62}$$

Also, symmetry requires that:

$$n_{pk} = n_{pj} \tag{2.63}$$

This means that M'_h and M'_v can be written as:

$$M'_h = C_{ph} f(e) \left(\frac{\sigma'_h}{p_r}\right)^{n_p - n_{pj}} \left(\frac{\sigma'_v}{p_r}\right)^{n_{pj}} \tag{2.64}$$

$$M'_v = C_{pv} f(e) \left(\frac{\sigma'_v}{p_r}\right)^{n_p - 2n_{pj}} \left(\frac{\sigma'_h}{p_r}\right)^{2n_{pj}} \tag{2.65}$$

Stokoe et al. (1995) presented experimental results of compression wave velocities in a dry sand measured in their cubical true triaxial calibration chamber, where they varied the principal stress σ'_z whilst holding σ'_x and σ'_y constant. Their results (see Figure 2.20a) indicated that variation of σ'_z affected the compression wave velocity V_{pz} but had no influence on the compression wave velocities V_{px} and V_{py}. This suggests that values of drained constrained modulus M' are unaffected by the stresses acting perpendicular to the direction of wave transmission ($n_{pj} = n_{pk} = 0$ in Equations 2.61 to 2.65). The expressions for M'_h and M'_v of Equations 2.64 and 2.65 then simplify to:

$$M'_h = C_{ph} f(e) \left(\frac{\sigma'_h}{p_r}\right)^{n_p} \tag{2.66}$$

$$M'_v = C_{pv} f(e) \left(\frac{\sigma'_v}{p_r}\right)^{n_p} \tag{2.67}$$

Bellotti et al. (1996) showed a slightly different pattern to Stokoe et al. (1995). They varied σ'_h whilst maintaining σ'_v constant during testing of dry sand in a large cylindrical calibration chamber, and they found that the values of M'_h increased substantially with increasing σ'_h but that the values of M'_v also decreased slightly with increasing σ'_h (see Figure 2.24). The latter is inconsistent with Equation 2.67 and would actually suggest a small negative value of n_{pj} in Equation 2.65. The values of very small strain Young's moduli E_v and E_h shown in Figure 2.24 were determined by Bellotti et al. (1996) by combining measurements of shear and compression wave velocities from conventional vertical and horizontal transmission with equivalent measurements of shear and compression wave velocities from oblique transmission (at 45^o to the axis of the test chamber).

2.3 Behaviour of unsaturated soils

2.3.1 Occurrence of unsaturated soils

Soils are composed of solids (soil particles) and pores (voids). These pores might be filled entirely with liquid (typically water), known as saturated conditions, entirely with gas (typically air), known as a dry condition, or with a mixture of liquid and gas, known as an unsaturated condition. Both natural and placed (fill) soils are often

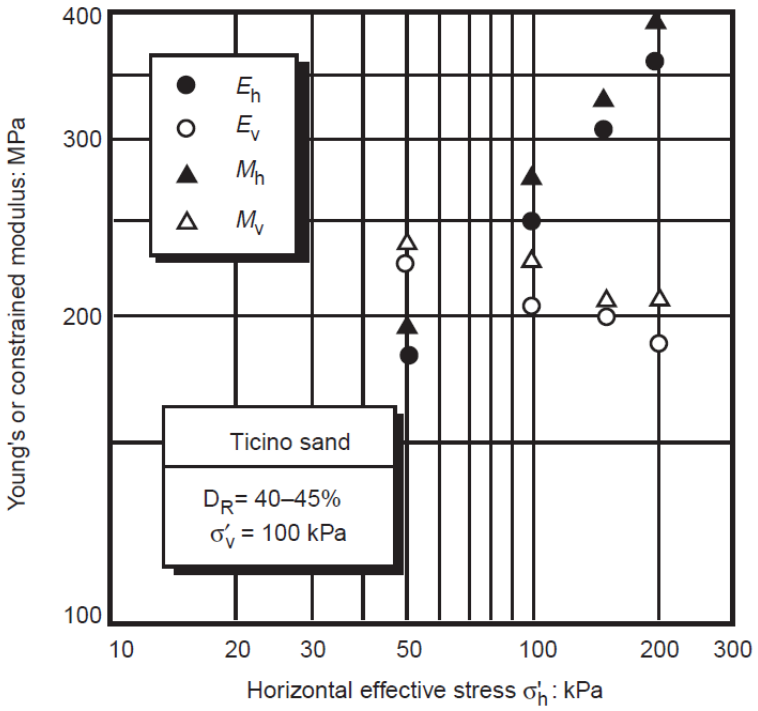

Figure 2.24: Influence of horizontal effective stress on E and M (Bellotti et al., 1996)

found in an unsaturated condition (see e.g. Alonso et al., 1995). Above the water table in natural soils there will be a capillary fringe of saturated soil with negative pore water pressure, and above this there will be unsaturated conditions. Placed soils, such as compacted fills for embankments, earth dams, earth retaining walls, landfills and highways, are typically in an unsaturated condition after placement and compaction. Because unsaturated soils are involved in many important infrastructure projects, as mentioned above, it is crucial to understand the behaviour of soils under unsaturated conditions.

2.3.2 Suction in unsaturated soils

Pore water pressures in unsaturated soils are generally negative relative to atmospheric pressure, hence the use of the term "suction". In the absence of a gravitational term, water flows through soils are driven by gradients of "total suction". Total suction is defined in terms of the total free energy of the pore water (per unit volume). If the pore water is in equilibrium across an air-water interface with air at a relative humidity P_p/P_s, Kelvin's law provides a relationship between the total suction ψ_T in the liquid water and the relative humidity P_p/P_s of the gas phase:

$$\psi_T = -\frac{RT}{M_w} ln \frac{P_p}{P_s} \tag{2.68}$$

where R is the universal gas constant (8.314J/mol K), T is absolute temperature, M_w is the molar mass of water, P_p is the partial pressure of the water vapour and P_s is the saturated water vapour pressure at the same temperature. The total suction can be expressed as the sum of matric suction s and osmotic suction ψ_o:

$$\psi_T = s + \psi_o \tag{2.69}$$

Matric suction s is the difference between the pore air pressure u_a and the pore water pressure u_w:

$$s = u_a - u_w \tag{2.70}$$

Matric suction s can be expressed in terms of surface tension T_s at the air-water interface and the curvature of this interface. Authors such as Fisher (1926) analysed the force equilibrium of this interface (see Figure 2.25) and showed that:

$$u_a - u_w = T_s \left(\frac{1}{r_1} + \frac{1}{r_2} \right) \tag{2.71}$$

where r_1 and r_2 are the principal radii of curvature of the air-water interface considered positive when the interface is concave on the air side.

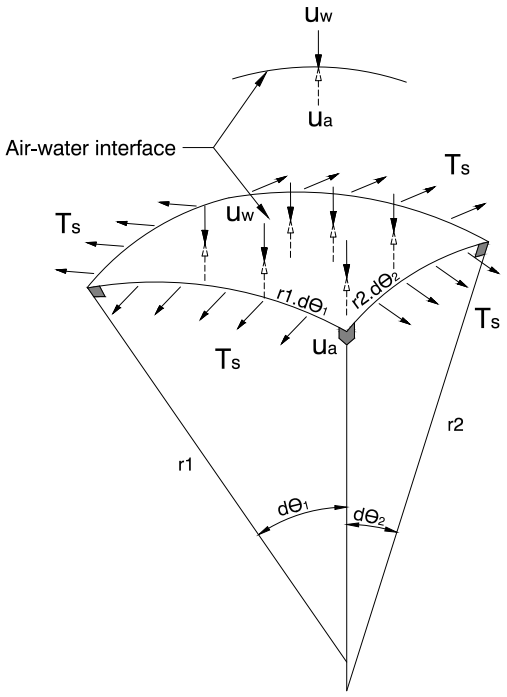

Figure 2.25: Equilibrium of an infinitesimally small element of air-water interface

2.3.3 The role of meniscus water bridges

Water within the pores of unsaturated soils has two forms: bulk water and meniscus water, as shown in Figure 2.26 (Wheeler et al., 2003b)(clays also contain water in a third form, as adsorbed water on the surface of the clay minerals). Bulk water occupies water-filled voids, whereas meniscus water is present as "bridges" at particle contacts around air-filled voids (see Figure 2.26). Negative pore water pressure u_w occurs in both types of water, but the pore water pressure within bulk water and the pore water pressure in meniscus water act on the soil skeleton in different ways. The pore water pressure in bulk water acts in the same way as in a saturated soil, so that a decrease of u_w (increase of suction) generates additional normal and tangential forces at inter-particle contacts, although in this case only at the particle contacts influenced by bulk water. In contrast, a decrease of u_w (increase of suction) within meniscus water generates only additional normal force at inter-particle contacts, which provides extra stability to the soil skeleton. The existence of additional normal forces at inter-particle contacts, due to the presence of meniscus water bridges means that when a soil is under unsaturated conditions it is more resistant to yielding than under saturated conditions (Alonso et al., 1987 and Wheeler & Sivakumar, 1995).

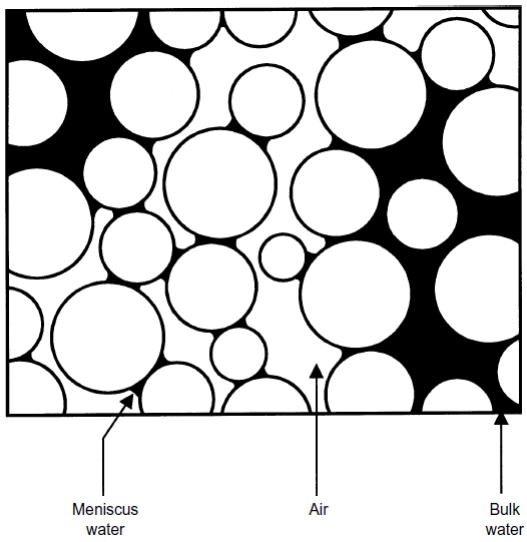

Figure 2.26: Bulk water and meniscus water (Wheeler et al., 2003b)

2.3.4 Stress state variables

Proper description of the mechanical behaviour of soils requires an appropriate numbers of stress state variables. Terzaghi (1936) introduced the "effective stress" tensor σ'_{ij} as the only stress state variable required for saturated soils:

$$\sigma'_{ij} = \sigma_{ij} - u_w \delta_{ij} \tag{2.72}$$

where σ_{ij} is the total stress tensor, u_w is the pore water pressure and δ_{ij} is Kronecker's delta. Equation 2.72 indicates that each normal effective stress is simply the difference between the corresponding normal total stress and the pore water pressure, whereas each effective shear stress is the same as the corresponding total shear stress. The mechanical behaviour of saturated soils can be expressed solely in terms of this single tensorial stress variable known as the "effective stress".

The validity and usefulness of the effective stress concept for saturated soils generated many efforts to suggest a corresponding effective stress definition for unsaturated soils. The most widely quoted proposal was by Bishop (1959) who suggested a single tensorial effective stress variable σ'_{ij} for unsaturated soils involving the total stress tensor σ_{ij}, the pore water pressure u_w and the pore air pressure u_a:

$$\sigma'_{ij} = \sigma_{ij} - [\chi u_w + (1 - \chi)u_a]\delta_{ij} \tag{2.73}$$

where χ was a weighting factor (between 0 and 1) the value of which depended upon the degree of saturation S_r. Subsequently, however, authors such as Jennings & Burland (1962) showed that key features of the mechanical behaviour of unsaturated soils (such as the possible occurrence of collapse compression on wetting, see Section 2.3.6) could not be explained by use of a single stress state variable such as Bishop's effective stress. Therefore, the idea of two independent stress state variables was introduced by Bishop and Blight (1963). The most commonly used pair of stress state variables (Bishop & Blight, 1963 and Fredlund & Morgenstern, 1977) are the net stress tensor $\bar{\sigma}_{ij}$ and the matric suction s (a scalar variable, see Equation 2.70), where $\bar{\sigma}_{ij}$ is defined as follow:

$$\bar{\sigma}_{ij} = \sigma_{ij} - u_a\delta_{ij} \tag{2.74}$$

Many authors have investigated and interpreted the mechanical behaviour of unsaturated soils in terms of these two stress state variables (e.g. Matyas & Radhakrishna, 1968; Fredlund & Morgenstern, 1977; Fredlund, Morgenstern & Widger, 1978; Alonso, Gens & Hight, 1987; Toll, 1990; and Wheeler & Sivakumar, 1995) or have developed constitutive models expressed using these stress state variables (e.g. Alonso, Gens & Josa, 1990). If net stress and matric suction are selected as stress state variables for unsaturated soils, then appropriate stress state variables for the triaxial test are mean net stress $\bar{p}$, deviator stress q, and matric suction s.

Other authors have proposed alternative pairs of stress state variables for unsaturated soils, typically involving one tensorial variable and an additional scalar variable.

Wheeler and Karube (1996), Gens (1996) and Sheng et al. (2008) provide reviews of many of these proposals.

A tensorial stress state variable σ^*_{ij} which has been proposed by several authors (Jommi & Di Prisco, 1994; Bolzon et al., 1996; Kohgo et al., 1993; Loret & Khalili, 2000; Houlsby, 1997; Jommi, 2000; Wheeler et al., 2003b; and Della Vecchia et al., 2012) and which has received widespread attention is very similar to Bishop's original effective stress proposal, and is termed either "Bishop's stress" (Bolzon et al., 1996 and Wheeler et al. 2003b) or "average soil skeleton stress" (Jommi, 2000) and takes the form:

$$\sigma^*_{ij} = \sigma_{ij} - [S_r u_w + (1 - S_r)u_a]\delta_{ij} = \bar{\sigma}_{ij} + S_r s \delta_{ij} \tag{2.75}$$

This tensorial stress state variable must be combined with a second (scalar) stress state variable and, based on energy input consideration, Houlsby (1997) and Wheeler et al. (2003b) argue that the most logical choice for this is the "modified suction" s^* defined by:

$$s^* = n(u_a - u_w) = ns \tag{2.76}$$

where n is the porosity. If Bishop's stress tensor (defined by Equation 2.75) and modified suction (defined by Equation 2.76) are selected as stress state variables for unsaturated soils, then appropriate stress state variables for the triaxial test are mean Bishop's stress p^*, deviator stress q and modified suction s^*, where p^* is given by:

$$p^* = p - S_r u_w - (1 - S_r)u_a = \bar{p} + S_r s \tag{2.77}$$

2.3.5 Laboratory testing of unsaturated soils

For triaxial testing of unsaturated soils, two additional requirements over those required for saturated testing are the need to control suction (i.e. separate control of u_a and u_w) and the need to monitor sample volume change independently of the inflow or outflow of water to the sample.

a) Suction control

In the field, pore water pressure u_w within unsaturated soils is usually negative relative to atmospheric pressure, with the pore air pressure ua at atmospheric. It is difficult to produce this situation within laboratory tests, because it is difficult to apply and control negative value of pore water pressure u_w. At a negative pore water pressure of approximately -100kPa, cavitation is likely to occur within the connecting water drainage line and associated water volume measurement equipment. To avoid this issue, several techniques have been developed to control matric suction s in laboratories, including the axis translation technique, the osmotic method and control through the vapour phase.

The axis translation technique was introduced to geotechnical laboratories by Hilf (1956). In order to avoid the need to apply and control negative values of u_w, this technique uses elevated values of total stress, pore air pressure u_a and pore water pressure u_w. A positive value of u_w is applied to the soil sample through a pore water drainage line, a higher value of u_a is applied through a separate pore air drainage line (to give the required value of suction), and then an even higher value of total stress is applied (to give the required value of net stress). In order to prevent pore air from the unsaturated sample (at pressure u_a) entering into the pore water drainage line (which is maintained at a lower pressure u_w), a saturated high air-entry (HAE) ceramic filter is used. HAE ceramic of various different air entry values (up to 1500kPa) are available, and this air entry value of the ceramic filter essentially determines the maximum achievable suction of the equipment.

The axis translation technique for controlling matric suction has been used by many researchers in many different types of laboratory equipment, such as triaxial apparatus (e.g. Matyas & Radhakrishna, 1968; Wheeler & Sivakumar, 1995), shear box apparatus (e.g. Escario & Saez, 1986) and oedometers (e.g. Alonso et al., 1995). The axis translation technique is popular, because it requires equipment that is relatively similar to that used for saturated testing. In addition, the axis translation technique is suitable for tests where it is necessary (or desirable) to vary suction in a continuous fashion (rather than as a series of step changes). A drawback of the axis translation technique is that it does not completely reproduce the field stress state and there is therefore a risk that some processes which might be occur in the field will not be observed in laboratory tests employing the axis translation technique. For example, de-saturation of soil in the field (change from a saturated condition to an unsaturated condition) may occur either by air entry from a boundary or by cavitation internally, whereas the latter possibility is excluded when using the axis translation technique in the laboratory (Tarantino & Mongiovi, 2000).

Matric suction within a soil sample can also be controlled by the osmotic method, where a semi-permeable membrane separates between the pore water within the soil sample and a drainage line containing polyethylene glycol PEG solution of controlled concentration. The semi-permeable membrane allows the passage of the small water molecules but prevents the passage of the large PEG molecules. Equilibrium (zero net flow of water across the semi-permeable membrane) occurs when the pore water pressure on one side of the membrane is substantially lower than the pressure of the PEG solution on the other side of the membrane, producing a tendency for water flow into the soil sample that exactly counterbalances the tendency for an osmotically induced water flow across the membrane in the reverse direction. Negative pore water pressure within the soil sample can therefore be controlled simply by controlling the concentration of the PEG solution, whilst keeping the PEG solution in the drainage line at atmospheric pressure.

The osmotic technique has been used successfully in geotechnical laboratories by a number of researchers such as Kassiff & Ben Shalom (1971); Delage et al. (1992) and Delage & Cui (2008). The advantages of the osmotic technique of controlling osmotic suction is that it properly reproduces the field situation of negative pore water pressure within the soil. The disadvantage of the technique is that it is difficult to vary suction in a continous fashion. Typically step changes of suction are applied by making step changes to the concentration of the PEG solution (by replacement of one PEG reservoir with another of different concentration).

The third method of controlling suction is through the vapour phase. Equation 2.68 states that, under equilibrium conditions across a liquid-gas interface, the total suction within the liquid phase is related to the relative humidity within the gas phase. This means that controlling the relative humidity of the pore air can lead to control of total suction. This control of relative humidity is achieved by circulating the air over a saturated solution of s selected salt (see e.g. Hoffmann et al., 2005 and Rojas et al., 2012). The total suction can be changed by changing the choice of salt, with saturated solutions of different salts producing different relative humidites and hence different values of total suction.

Like the osmotic method of controlling suction, an advantage of this method of controlling suction through the vapour phase is that it properly reproduces the field situation of negative values of pore water pressure within the soil. In addition, this technique can apply total suction values up to 1000MPa (by selecting a suitable salt), which is impossible with the other two methods of controlling suction. A disadvantage of this technique is that it can only be used to apply a limited set of suction values,

corresponding the relative humidities produced by saturated solutions of the various available salts.

A variant on the method of controlling suction through the vapour phase is to circulate dry (low humidity) air past the boundary of the soil sample and then to measure matric suction independently elsewhere on the sample using a tensiometer. By switching on and off the circulation of the dry air using a control system triggered by the measured value of suction it is possible to control suction to a desired value or vary it with time in any desired fashion (Ridley & Burland, 1993 and Lourenco et al., 2011)

b) Measurement of sample volume change

The measurement of sample volume change of saturated and unsaturated soil samples in the triaxial apparatus is entirely different. For saturated samples, the volume change of the sample is measured simply from the water outflow/inflow to the sample, whereas for unsaturated samples the measurement of sample volume change is not straightforward, because of changes of pore air volume which cannot simply be measured by the outflow/inflow of air, due to its high compressibility.

Various different techniques have been proposed to measure volume change of unsaturated soil samples. The first of these involves the measuring of water outflow/inflow to the surrounding triaxial cell. This technique is based on principles first introduced by Bishop & Donald (1961) and subsequent further developed by Wheeler (1986) and a number of subsequent authors. To achieve the necessary accuracy of sample volume change measurement, careful design of the cell is required, incorporating features such as a double wall construction (to avoid excessive change of inner cell volume with changes of cell pressure), use of an inner cell wall made of a material (such as glass) that does not adsorb water (unlike acrylic) and careful detailing to avoid any leaks from the cell or entrapment of air during filling of the cell. Even with these design features, careful calibration of the cell performance is required (see Section 3.5). Examples of successful use of this approach for measuring sample volume change include Bishop & Donald (1961), Josa (1988), Wheeler & Sivakumar (1995), Cui & Delage (1996), Ng et al. (2002) and Sivakumar (2007).

A second approach to measuring volume change of unsaturated triaxial test samples is to measure axial and radial strains directly on the soil sample, using local strain measurement devices (see Section 2.2.1). Researchers employing this approach include Zakaria (1994) and Ng & Yung (2008). This approach is highly accurate at small strains but becomes increasingly inappropriate at higher strains, as the sample becomes

highly distorted. There are also limitations of maximum travel for many of the local strain measurement devices.

The final approach to measuring volume change of unsaturated triaxial test samples is to scan the sample profile using either a laser system (e.g. Romero et al., 1997) or a conventional camera system accompanied by image processing (e.g. Gachet et al., 2007 and Rojas et al., 2012). This approach can be extremely accurate, but it typically involves considerable technical complexity and it may involve relatively expensive equipment.

2.3.6 Mechanical behaviour

Volume change

Distinctive features of volume change in unsaturated soils are that the yield stress during isotropic or one-dimensional loading increases with increasing suction (as the soil becomes more unsaturated) and that during wetting (reduction of suction) swelling is observed at low values of net stress whereas a reduction of volume (known as "collapse compression") is observed at high net stress. These two observations were first linked by Alonso et al. (1987) with the proposal of a Loading Collapse (LC) yield curve introduced in $s : \bar{p}$ space (see Figure 2.27), where $\bar{p}$ is the mean net stress. The LC yield curve concept indicated that plastic volume changes on loading (increase of $\bar{p}$, e.g. from D to C in Figure 2.27) and plastic volume changes on wetting (collapse compression caused by decrease of s , e.g. from B to C in Figure 2.27) are essentially the same process, with both corresponding to movement of a single yield curve.

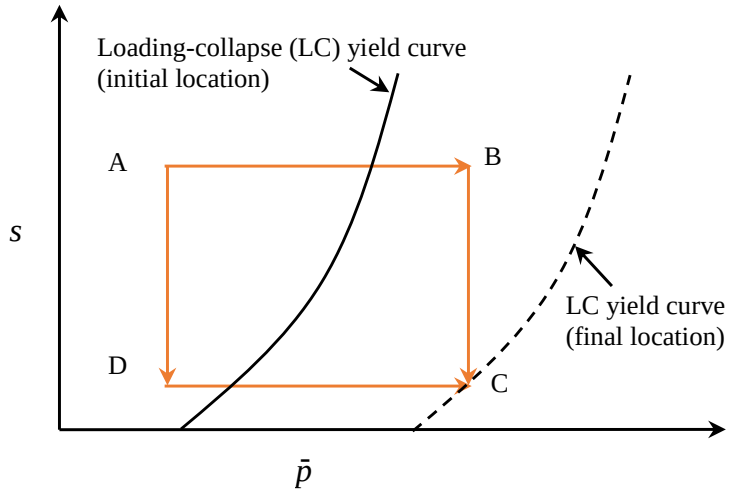

Figure 2.27: LC yield curve in $s : \bar{p}$ stress space (after Alonso et al., 1987)

On isotropic loading (increase of mean net stress $\bar{p}$) at constant s, once the LC yield

curve is reached and plastic straining commences, the compression curve follows a normal compression line in a plot of specific volume v against mean net stress $\bar{p}$, with a different normal compression line for each value of suction (see Figure 2.28). The equation of a normal compression line for a given value of suction is given by:

$$v = N(s) - \lambda(s) ln\bar{p} \tag{2.78}$$

where the gradient $\lambda(s)$ and intercept $N(s)$ are both functions of suction (Alonso et al., 1990 and Wheeler & Sivakumar, 1995). The variation of $\lambda(s)$ and $N(s)$ with suction can be linked to the shape of the yield curve and the way this shape develops as the LC yield curve expands during plastic straining (see Alonso et al., 1990 and Wheeler & Sivakumar, 1995).

Shear strength

Shear strength of a soil under unsaturated conditions is greater than under saturated conditions and strength generally increases as a soil becomes more unsaturated. Fredlund et al. (1978) proposed that the shear strength on a given failure plane under unsaturated conditions could be related to the net stress normal to the plane and to matric suction s by:

$$\tau_f = c' + (\sigma - u_a) tan\phi' + (u_a - u_w) tan\phi^b = c' + \bar{\sigma}.tan\phi' + s.tan\phi^b \tag{2.79}$$

where c' is the cohesion intercept, ϕ' is the conventional friction angle for saturated conditions and ϕ^b is a friction angle giving the increase of shear strength with suction. Equation 2.79 predicts a linear increase of shear strength with suction. Later researchers, including Escario & Saez (1986), Fredlund et al. (1987) and Gan & Fredlund (1988) showed however that the increase of shear strength with suction is non-linear (ϕ^b decreases as suction increases). Raveendiraraj (2009) argued that this is because the contribution of the additional inter-particle forces due to meniscus water bridges (see Section 2.3.3) increases in a non-linear fashion with suction.

Many researchers (such as Khalili & Khabbaz, 1998; Alonso et al., 2010; and Lloret-Cabot et al., 2013) have proposed expressions for shear strength in terms of an alternative stress variable, which is sufficient on its own to successfully capture shear strength behaviour.

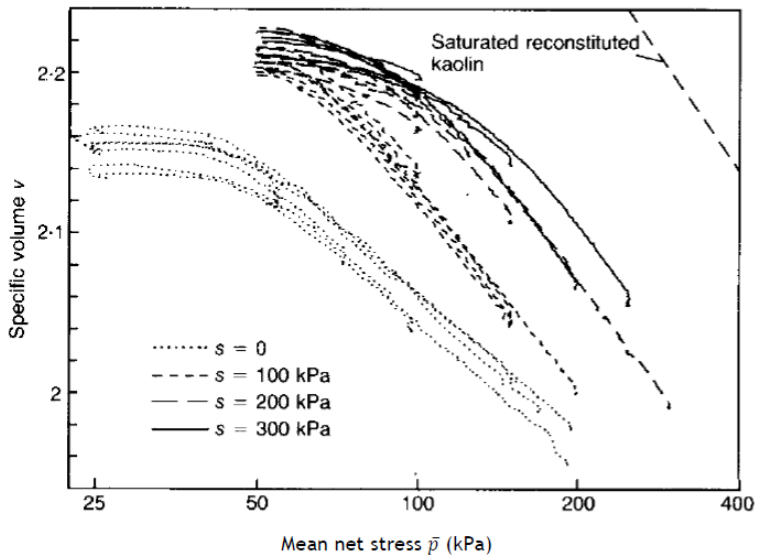

Figure 2.28: Variation of v at various suctions during isotropic compression (Wheeler & Sivakumar, 1995)

2.3.7 Water retention behaviour

Water retention behaviour can be defined as the relationship between degree of saturation S_r and suction s, as shown in Figure 2.29. The term "soil water characteristic curve" is also sometimes used for this relationship, although this term is now generally not preferred because it may (incorrectly) be taken to imply a single unique relationship between S_r and s for a given soil. On drying from a saturated condition the soil follows the "main drying curve" in the water retention plot (see Figure 2.29). Conversely, on wetting from a fully dry state the soil follows the "main wetting curve", which is different to the main drying curve (i.e. hysteresis in the water retention behaviour). Any other reversal of suction generates a scanning curve which lies between the main drying curve and the main wetting curve (see Figure 2.29). Hysteresis in the water retention behaviour occurs because the suction at which a void will empty during drying is governed by the radius of the narrow entry throat into the void, whereas the suction at which the same void will refill with water during wetting is governed by the radius of the void itself (see Buisson & Wheeler, 2000).

Many different mathematical expressions have been proposed for the form of a water retention curve in the S_r : s plot. (e.g. Brooks & Corey, 1964; Van Genuchten, 1980 and Fredlund & Xing, 1994). The mathematical forms of these expressions and their merits and drawbacks are reviewed by Leong & Rahardjo (1997). Use of a single water retention curve expression of this type fails to account for the influence of hysteresis (i.e. the differences between main drying curve, main wetting curve and the infinity of possible intermediate scanning curves). These classical water retention curve

expressions also fail to account for the fact that the entire water retention behaviour shown in Figure 2.29 shifts to higher values of suction if the soil undergoes a reduction of void ratio.

Models for water retention behaviour that attempt to include the influence of hysteresis include domain models (i.e. Philip (1964); Mualem (1974); Hanks et al. (1969)), which are based on the physical processes involved. Within the majority of the domain models, there is an assumption made involving two key values of suction for each pore. The first suction value controls the filling of the pore and the other suction value controls emptying of the pore. Within a limited range of suction, a group of pores is called a domain. Combination of some groups of these domains represents a porous system such as a soil. It is possible for these domains to be independent (i.e. each domain does not affect other domains) or dependent (i.e. affected by other domains such as air entry from adjacent domains). An alternative way of modelling hysteresis effects in water retention behaviour (i.e. main drying curve, main wetting curve and intermediate scanning curves) is on the basis of elasto-plasticity (e.g. Dangla et al. (1997) and Wheeler et al. (2003b)).

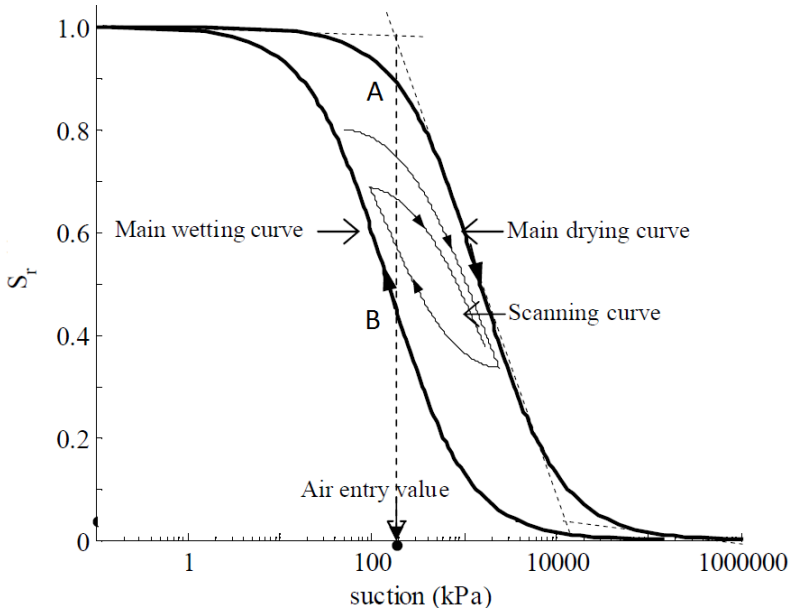

Figure 2.29: Typical water retention curves for fine-grained soils (after Raveendiraraj, 2009)

Water retention behaviour is influenced by changes of void ratio e, because if the void ratio reduces this means decreases in the sizes of voids and of the narrow "throats" between voids, implying that higher values of suction are now required to fill a void with water during wetting or empty a void of water during drying. Authors such as Gallipoli et al. (2003a), Tarantino (2009) and Hu et al. (2013) accounted for this effect, by proposing water retention expressions relating S_r to both s and e. The fact

that changes of void ratio affect water retention behaviour means that mechanical behaviour (i.e. volumetric strain) influences water retention behaviour (coupling).

In addition to influence of mechanical behaviour on retention behaviour, there is also coupling in the reverse direction, with retention behaviour (changes of S_r) influencing mechanical behaviour. In $S_r - s$ stress space and for a certain suction, the degree of saturation on drying path (see point A in Figure 2.29) is higher than the degree of saturation on the wetting path (see point B in Figure 2.29). Wheeler et al. (2003b) argued that this influence of S_r affects strongly the mechanical behaviour of a soil because of the presence of the additional meniscus water bridges at the lower degree of saturation (i.e. on the wetting path), which increase the mechanical stabilization of the soil (see Section 2.3.3).

2.3.8 Constitutive modelling

Many different constitutive models have been proposed for mechanical or mechanical-retention behaviour of unsaturated soils (see Wheeler & Karube (1996), Gens et al. (2006) and D'Onza et al. (2011b) for reviews). The focus here is on two key models, the Barcelona Basic Model (BBM) of Alonso, Gens and Josa (1990) and the Glasgow Coupled Model (GCM) of Wheeler, Sharma and Buisson (2003b).

Barcelona Basic Model (BBM)

Based on the idea of Alonso et al. (1987) to introduce a Loading Collapse (LC) yield curve to bring plastic compression on loading and plastic compression on wetting (collapse compression) into a single framework (see Section 2.3.6), Alonso, Gens and Josa (1990) developed the first elasto-plastic constitutive model for unsaturated soils, known as the Barcelona Basic Model (BBM). The BBM model uses net stresses and matric suction as stress state variables (see Equations 2.74 and 2.70 in Section 2.3.4), so that, for the conditions of the triaxial test, the stress state variables are mean net stress $\bar{p}$, deviator stress q and matric suction s. The BBM converges to the Modified Cam Clay (MCC) model (Roscoe & Burland, 1968) for saturated soils at s =0.

In the BBM, elastic volumetric strains are produced by changes of both mean net stress $\bar{p}$ and matric suction s:

$$d\epsilon_v^e = \frac{\kappa d\bar{p}}{v\bar{p}} + \frac{\kappa_s ds}{v(s+p_a)} \tag{2.80}$$

where κ and κ_s are two elastic parameters (soil constants). Atmospheric pressure p_a was (rather arbitrarily) included in the denominator of the second term in Equation 2.80 to avoid infinite elastic volumetric strain as suction approaches zero. Elastic shear strains are given, in the BBM, simply by assumption of a constant value of elastic shear modulus G. This, together with Equation 2.80, means that the BBM does not include proper modelling of the small-strain soil response, which is the main focus of this thesis.

The BBM assumes that isotropic normal compression lines for different values of suction are straight lines in the $v : ln\bar{p}$ plot, given by Equation 2.78, with gradient $\lambda(s)$ and intercept $N(s)$ related to the suction by:

$$\lambda(s) = \lambda(0)\left[r + (1-r)exp(-\beta s)\right] \tag{2.81}$$

$$N(s) = N(0) - \kappa_s ln\left(\frac{s+p_a}{p_a}\right) - (\lambda(0) - \lambda(s))lnp^c \tag{2.82}$$

where $\lambda(0)$ and $N(0)$ are the gradient and intercept of the saturated normal compression line (soil constants) and r, β and p^c are three further soil constants.

Alonso et al. (1990) showed that Equations 2.78, 2.80 and 2.82 mean that the form of the LC yield curve in the BBM, for isotropic stress states, is given by:

$$\left(\frac{\bar{p_o}}{p^c}\right) = \left(\frac{\bar{p}_o(0)}{p^c}\right)^{[\lambda(0)-\kappa]/[\lambda(s)-\kappa]} \tag{2.83}$$

where $\bar{p}_o$ is the yield value of $\bar{p}$ at any suction s and $\bar{p}_o(0)$ is the yield value at a saturated condition (s =0). Inspection of Equation 2.83 shows that the form of $N(s)$ assumed in Equation 2.82 has resulted in a relatively simple form for the LC yield curve, but this does mean that it can be challenging to fit normal compression lines for different values of suction to experimental results (see D'Onza et al., 2015).

For anisotropic stress states ($q \neq 0$), the LC yield curve is extended to form a LC yield surface in $q : \bar{p} : s$ space. The BBM assumes that constant suction cross-sections of this yield surface are elliptical in shape, equivalent to the MCC model for saturated soil, but with a tension intercept that increases linearly with suction. As a consequence, the BBM predicts critical state lines for different values of suction, defined in the $q : \bar{p}$ plane by:

$$q = M(\bar{p} + ks) \tag{2.84}$$

where M and k are soil constants. Equation 2.84 is directly equivalent to the linear shear strength expression of Equation 2.79.

The BBM is capable of predicting many important aspects of unsaturated soil behaviour, including wetting-induced swelling or wetting-induced collapse compression. Based on the framework of BBM, subsequent authors have proposed many alternative constitutive models for unsaturated soils employing mean net stresses and matric suction as stress state variables. These related models include Josa et al. (1992), Wheeler & Sivakumar (1995), Cui & Delage (1996), Alonso et al. (1999), Chiu & Ng (2003) and Sheng et al. (2008). Each of these subsequent models attempted to improve a specific shortcoming of the BBM or to incorporate an aspect of soil behaviour not included in the BBM.

Glasgow Coupled Model (GCM)

In more recent years, various authors have proposed constitutive models for unsaturated soils which employ stress state variables other than net stresses and suction. These include Wheeler et al. (2003b), Gallipoli et al. (2003b), Pereira et al. (2005), Khalili et al. (2008), Nuth & Laloui (2008) and Masin & Khalili (2008). The motivations of these authors was to capture aspects of unsaturated soil behaviour that are difficult or impossible to represent with constitutive models expressed in terms of net stresses and suction, such as the influence of degree of saturation (separately from the influence of suction) on mechanical behaviour. This includes proper representation of transition between saturated and unsaturated conditions, which in practice do not occur at zero suction and which occur at different values of suctions during drying and wetting (air entry and air exclusion points respectively).

One of the most interesting constitutive models of this type is the elasto-plastic model of Wheeler at al. (2003b), fully developed by Lloret-Cabot et al. (2013) and now known as the Glasgow Coupled Model (GCM). This model represents a significant development, because it combines modelling of mechanical behaviour and retention behaviour in a single model, including coupling in both directions (i.e. influence of changes of S_r on mechanical behaviour and influence of volumetric strains on retention behaviour).

The GCM uses "Bishop's stresses" and "modified suction" (see Equations 2.75 and 2.76 in Section 2.3.4) as the stress state variables. A key conceptual idea behind the

selection of these two alternative stress variables is that the first stress state variable (Bishop's stress tensor σ^*_{ij}), defined in Equation 2.75, can represent the effects of externally applied total stresses, pore water pressure in water-filled voids (i.e. bulk water) and pore air pressure within air-filled voids. As a consequence, some aspects of behaviour, such as elastic straining or shear strength, can be related solely to changes of this stress state variable. However, this variable does not include the stabilizing effect of meniscus water bridges and the important effect this has on yielding. Wheeler et al. (2003b) suggest that this stabilizing influence of meniscus water bridges can be related to the degree of saturation S_r (or more strictly to plastic changes of S_r), which can, in turn, be related to the variation of the second (scalar) stress state variable, modified suction s^*. For the conditions of the triaxial test, the required stress state variables are mean Bishop's stress p^*, deviator stress q and modified suction s^*.

In the GCM, elastic volumetric strains (mechanical behaviour) are related solely to changes of the mean Bishop's stress, not to any changes of modified suction:

$$d\epsilon^e_v = \frac{\kappa dp^*}{vp^*} \tag{2.85}$$

Elastic change of degree of saturation (retention behaviour) are related solely to changes of modified suction:

$$dS^e_r = \frac{-\kappa_s ds^*}{s^*} \tag{2.86}$$

κ and κ_s are two soil constants. Elastic shear strains are given by assumption of a constant value of elastic shear modulus G. This, together with Equation 2.85, means that the GCM (like the BBM) does not include proper modelling of the small-strain soil response, which is the main focus of this thesis.

In the GCM, plastic volumetric strains (mechanical behaviour) occur on a single mechanical (LC) yield surface which, for isotropic stress states, has an extremely simple form in the $s^* : p^*$ plane (see Figure 2.30). Plastic changes of degree of saturation (retention behaviour) occur on two retention (SI and SD) yield surfaces, which also take extremely simple forms (see Figure 2.30). Coupling between mechanical and retention behaviour is represented by coupled movements of the three yield surfaces, to capture the influence of plastic volumetric strains on retention behaviour and the influence of plastic changes of degree of saturation on mechanical behaviour.

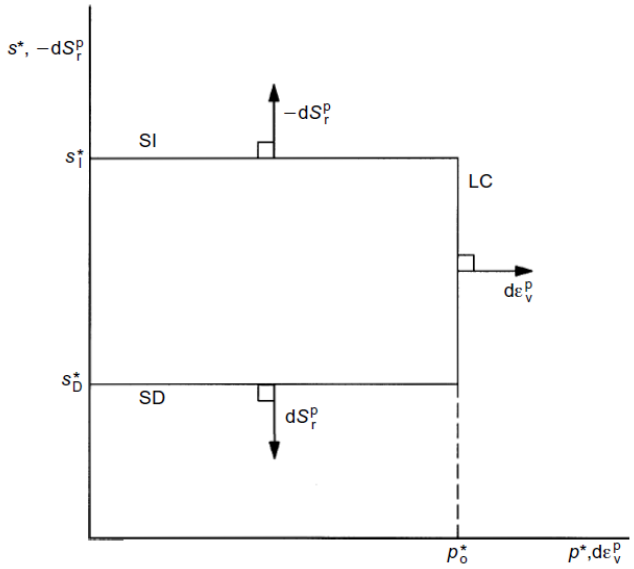

Figure 2.30: LC, SI and SD yield curves in the GCM for isotropic stress states (Wheeler et al., 2003b)

Lloret-Cabot et al. (2014) demonstrated a simulation of an experimental test (performed by Kato, 1998) to show the capability of the GCM in accurately predicting the variations of both e and S_r during drying, loading and wetting stages, where plastic compression occurred in all three test stages. They emphasized that the GCM accurately predicts the plastic changes of both e and S_r caused by all types of wetting, loading and drying stress paths.

2.4 Behaviour of unsaturated soils at very small strains

Although it has received less attention than large strain behaviour of unsaturated soils and very small strain behaviour of saturated soils, a number of researchers have investigated the very small strain behaviour of soils under unsaturated conditions using BEEs.

2.4.1 Influence of unsaturated state variables $\bar{p}$, s and S_r

Experimental evidence on very small strain elastic behaviour of unsaturated soils show that G and M are functions of $\bar{p}$, s , e and S_r (see, for example, Ng & Yung, 2008 and Alramahi et al., 2008).

A number of researchers have observed that values of G measured with bender elements increase as s increases (e.g. Marinho et al., 1995; Mendoza & Colmenares, 2006; Cabarkapa & Cuccovillo, 2005; Ng & Yung, 2008; Sawangsuriya et al., 2008; Nyunt et

al., 2011 and Han & Vanapalli, 2016) and as $\bar{p}$ increases (e.g. Mancuso et al., 2002; Vassallo et al., 2007a and Ng & Yung, 2008). Ng et al. (2009) observed that, during drying-wetting cycles, the values of G were consistently lower in drying stages than in wetting stages (see Figure 2.31). This suggests that degree of saturation S_r (which is higher during a drying stage than during a wetting stage) has an influence on G, in addition to $\bar{p}$ and s.

Heitor et al. (2013) observed for unsaturated silty sand, that G increases with increase of compaction energy. This suggests dependency of G on void ratio.

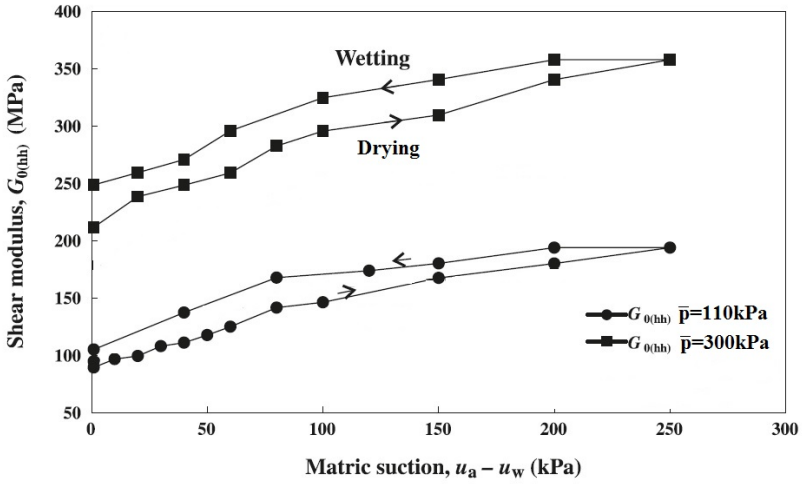

Figure 2.31: Shear modulus G_{hh} during drying and wetting tests (after Ng et al., 2009)

The influence of S_r on compression wave velocity V_p and hence constrained modulus M has been examined by Eseller-Bayat et al. (2013) on Ottawa sand under full range of S_r $(0 - 1.0)$ in a liquefaction box using bender/extender element testing. They found that a small reduction of S_r from 1.0 to 0.96 (see Figure 2.32) produced a substantial decrease of V_p, whereas further decrease of S_r from 0.96 to 0, produced only very minor further reduction of V_p. The fact that undrained constrained modulus increases dramatically as the degree of saturation approaches 1 is only to be expected, as it is often assumed that undrained bulk modulus and hence undrained constrained modulus (see Equation 2.9) is infinite under saturated conditions.

2.4.2 Anisotropic elasticity in unsaturated soils

As described in Section 2.2.3, very small strain elastic anisotropy of saturated soils has been investigated by many researchers (e.g. Mitaritonna et al., 2014), whereas very limited information is available on elastic anisotropy of unsaturated soils. Elastic anisotropy of two dynamically compacted unsaturated completely decomposed tuff soils (the samples were under isotropic stress states ($\bar{p}$ =110kPa and q =0 for the first

sample and $\bar{p}$ =300kPa and q =0 for the second sample) was investigated by Ng et al. (2009) using two pairs of bender elements to measure V_{shh} and V_{shv} (hence G_{hh} and G_{hv}, respectively). They found that the first and the second soil samples showed a very small value of initial elastic anisotropy (G_{hh}/G_{hv} ≈1.03 or 1.04, see Figure 2.33) when they were under saturated and isotropic stress states. These values of G_{hh}/G_{hv} of the two samples hardly changed during a drying path at s =250kPa (the values of G_{hh}/G_{hv} after drying were 1.038 and 1.05 for the two samples, see Figure 2.33). This lack of development of anisotropy was expected, because during the drying stage the samples were still under isotropic stress states, meaning that, there was no opportunity for either strain-induced anisotropy or stress-induced anisotropy to occur. At the end of a subsequent wetting stage, the values of G_{hh}/G_{hv} were still essentially unchanged.

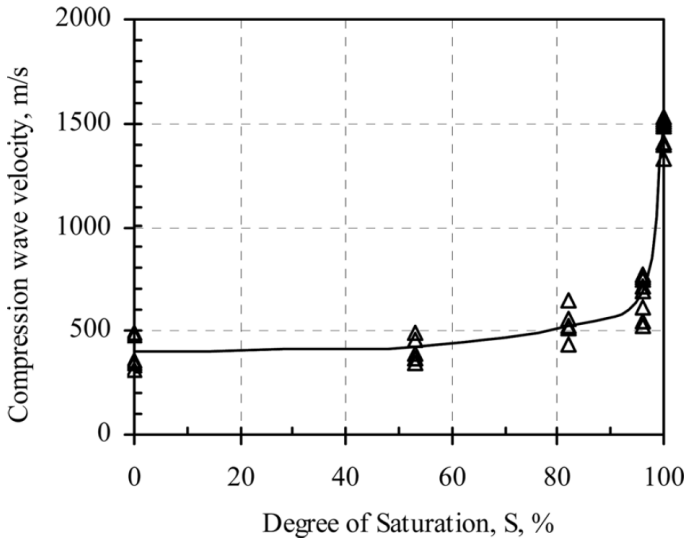

Figure 2.32: Variation of V_p against S_r (Eseller-Bayat et al., 2013)

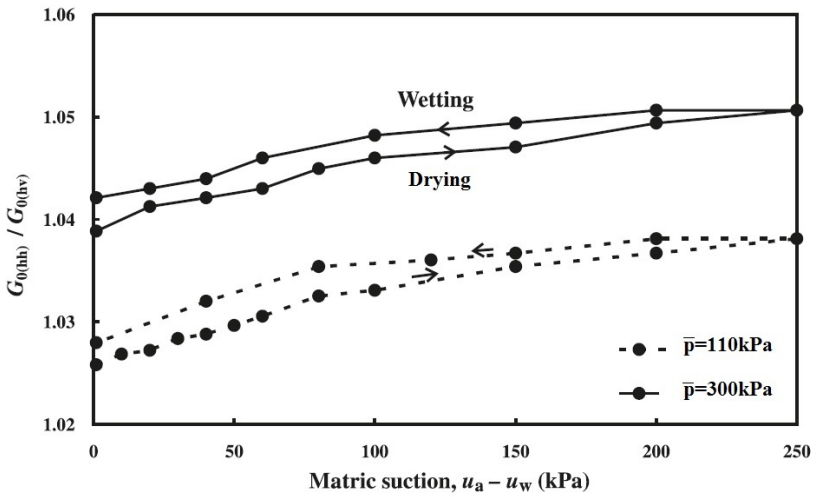

Figure 2.33: Variation of G_{hh}/G_{hv} during wetting-drying cycle (Ng et al., 2009)

In terms of the very small strain elastic anisotropy of constrained modulus M_h/M_v

under unsaturated conditions, as far as the author is aware, there is no record in the literature of any previous study of this topic.

2.4.3 Proposed expressions for shear modulus G

Expressions using conventional unsaturated stress state variables

For low plasticity unsaturated soils, under isotropic stress states, based on experimental results from resonant column and bender element tests, several researchers proposed mathematical expressions for very small strain elastic shear modulus G in terms of conventional unsaturated state variables $\bar{p}$, s and e (Mancuso et al., 2002; Leong et al., 2006; Vassallo et al., 2007b; Ng & Yung, 2008 and Sawangsuriya et al., 2009). Some of these expressions are relatively simple (e.g. Ng & Yung, 2008) and some of them complex (e.g. Vassallo et al., 2007b).

For example, Ng & Yung (2008) proposed a simple expression to predict G:

$$G = Cf(e)\left(\frac{\bar{p}}{p_r}\right)^n \left(\frac{p_r + s}{p_r}\right)^k \tag{2.87}$$

where p_r is a reference stress (taken as 1 kPa) and C, n and k are soil constants. The arbitrary addition of p_r within the numerator of the final part of Equation 2.87 was to allow the expression to be used down to s =0. Clearly, however, this means that the results predicted by Equation 2.87 can be highly sensitive to the choice of p_r.

Expressions using alternative stress state variables

Authors such as Biglari et al. (2011) and Zhou (2014) interpreted measurements of small strain shear modulus G in terms of alternative unsaturated state variables, such as mean Bishop's stress p^*, defined in Equation 2.77. Some other researchers including Khosravi & McCartney (2012) and Wong et al (2014), used other stress variables, in an attempt to represent variation of G under a full range of stress paths (including wetting-induced swelling and wetting-induced collapse compression).

For example, Wong et al. (2014) proposed a relatively complex expression for G based on use of a stress variable suggested by Khalili & Khabbaz (1998). The proposal of Wong et al. (2014) can be expressed as:

$$G = C(v-1)^{-m}\left(\frac{\bar{p} + S_r^{(\gamma/\lambda_p)}s}{p_r}\right)^n S_r^{(-k/\lambda_p)} \tag{2.88}$$

In Equation 2.88, v is the specific volume and γ takes a value of 0.55 for all soils (see Khalili & Khabbaz, 1998), whereas C, m , n, k and λ_p are soil constants, where λ_p is the gradient of the water retention curve in the $lnS_r : lns$ plot. Equation 2.88 would be difficult to use in practice because it involves a large number of variables ($\bar{p}$, s, v and S_r) and a large number of soil constants, some of which would be difficult to determine. Wong et al. (2014) suggested that the last term in Equation 2.88 (i.e. $S_r^{(-k/\lambda p)}$) represents additional stability at inter-particle contacts due to meniscus water bridges.

An alternative simpler expression to Equation 2.88 was proposed by Zhou (2014). He related G to specific volume v, mean Bishop's stress p^* and a bonding parameter ξ (representing the influence of the additional forces at inter-particle contacts due to meniscus water bridges) introduced by Gallipoli et al. (2003b), which depends upon both S_r and s:

$$\xi = f(s)(1 - S_r) \tag{2.89}$$

where $f(s)$ is the extra stabilizing force imposed by a single meniscus water bridge and $(1 - S_r)$ represents the proportion of particle contacts affected by water meniscus bridges. The value of $f(s)$ in Equation 2.89 can be related to s and the equivalent particle diameter, as shown in Gallipoli et al. (2003b) (see Section 7.1.5).

The expression for G proposed by Zhou (2014) is then given by:

$$G = C_1 v^{-m}\left[\left(\frac{p^*}{p_r}\right)^{n_1} + C_2\xi^{n_2}\right] \tag{2.90}$$

where C_1 and C_2 are soil constants, whereas Zhou (2014) suggested the values of the exponents m, n_1 and n_2 are 3, 0.5 and 0.5 respectively for all soils.

Recently, Dong et al. (2016) proposed an expression for G for unsaturated soils, given by:

$$G = C_3 \left(\frac{1}{S_e}\right)^{\beta} \left[\left(\frac{\sigma'}{p_r}\right) + 1\right]^{\gamma_o} \tag{2.91}$$

where

$$\sigma' = \bar{\sigma} + \left(\frac{S_e}{\alpha}\right) \left[S_e^{[n/(1-n)]} - 1\right]^{1/n} \tag{2.92}$$

and

$$S_e = \frac{S - S_r}{1 - S_r} = [1 + \alpha s^n]^{1/n-1} \tag{2.93}$$

where C_3, β, γ_o, α and n are soil constants (Dong et al. (2016) also suggested that γ_o is a function of n). Equation 2.92 is complex and in order to calibrate the parameters α and n a soil sample has to be subjected to a wetting or drying stage. Dong et al. (2016) verified their proposed expression in Equation 2.91 using different types of soil. They showed that their proposed expression was able to predict values of G for these soils successfully, however the test data did not include loading and unloading stages or wetting-drying cycles. In addition, Equation 2.91 has several limitations such as excluding dependency upon void ratio (i.e. it only applies to incompressible soils), whereas the majority of proposed expressions for G under both saturated conditions (e.g. see Equation 2.14) and unsaturated conditions (e.g. see Equation 2.88) include void ratio e as a variable.

Equations 2.87, 2.88, 2.90 and 2.91 should all be viewed, at this stage, as tentative proposals describing the variation of very small strain shear modulus under unsaturated conditions. Each of them includes some rather arbitrary assumptions about their form and each of them has not yet been tested against a wide range of experimental data. In addition, Equations 2.88, 2.90 and 2.91 are complex in form (when difficulty of calculating the value of bonding parameter ξ in Equation 2.90 is taken into account) and practical determination of the values of the various soil constants in Equations 2.88 and 2.91 is likely to be problematic.

2.4.4 Expressions for constrained modulus M

Little has been published on the variation of very small strain undrained constrained modulus M under unsaturated conditions. Pierce & Charlie (1990) proposed a very

simple expression for unsaturated sands in terms of $\bar{p}$ and s:

$$M = C_{p1}\bar{p} + C_{p2}s \tag{2.94}$$

where C_{p1} and C_{p2} are soil constants. The expression in Equation 2.94 was compared with experimental results for unsaturated Ottawa and Eglin sands by Pierce & Charlie (1990), as shown in Figure 2.34. They concluded that Equation 2.94 is only able to predict M for values of S_r between zero and 0.8. They concluded that Equation 2.94 was not able to predict the variation of M for higher values of degree of saturation (S_r>0.8), because the influence of S_r is so great (see Figure 2.32).

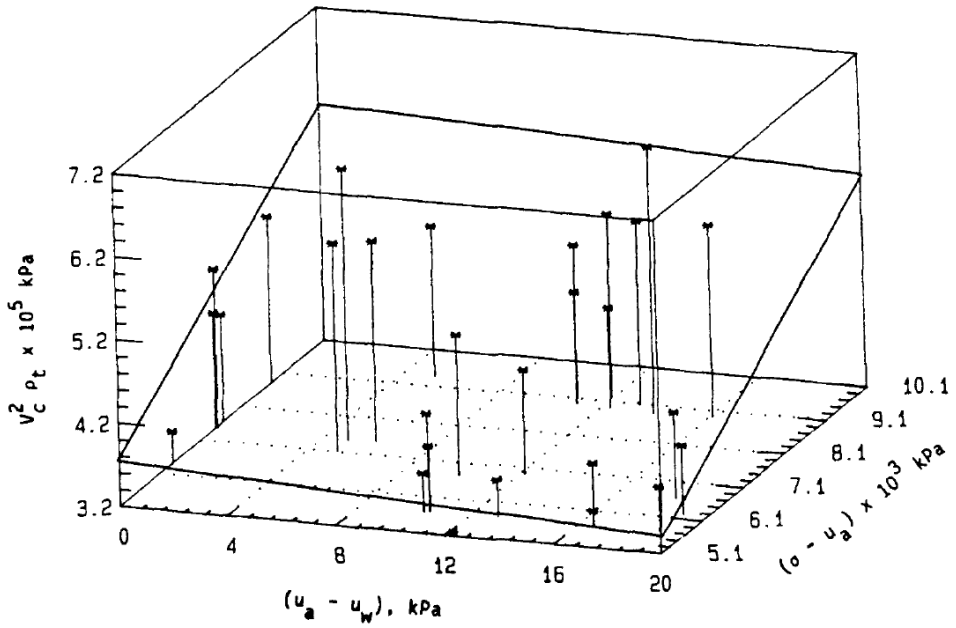

Figure 2.34: Variation of M against $\bar{p}$ and s for Eglin sand (Pierce & Charlie, 1990)

2.5 Evolution of large strain anisotropy in saturated and unsaturated soils

Evolution of anisotropy of large strain plastic behaviour has been previously explored under both saturated conditions (e.g. Dafalias, 1987 and Wheeler et al., 2003a) and unsaturated conditions (e.g Della Vecchia et al., 2012 and Al-Sharrad, 2013). This anisotropy of large strain plastic behaviour can be attributed solely to strain-induced anisotropy, because the concept of stress-induced anisotropy is inapplicable to plastic behaviour, giving that even an isotropic elasto-plastic model (such as Modified Cam Clay) will, through the basic concept of a flow rule, predict anisotropic plastic strain-

ing if the stress state is anisotropic (even if the stress change involves equal stress increments in all directions).

Evolution of small strain elastic behaviour (measured in bender element tests) caused by plastic straining (strain-induced anisotropy) has been investigated under saturated conditions by, for example, Kim & Finno (2012). The evolution of large strain plastic anisotropy and small strain elastic anisotropy have, however, generally been studied entirely independently, without any investigation of the linkages between them. As a consequence, one key question that remains unanswered is whether the variation of both plastic anisotropy and strain-induced elastic anisotropy can be related to a single fabric tensor or whether different fabric tensors control elastic and plastic behaviour. This issue was investigated in the current study. Therefore, experimental studies and constitutive models related to evolution of anisotropy of large strain plastic behaviour of saturated and unsaturated soils from the literature are briefly presented here, as relevant to the current study.

2.5.1 Anisotropy of large strain behaviour in saturated soils

The processes of deposition and consolidation in a natural soil generally form a soil fabric that is directionally dependent (anisotropic). One-dimensional deposition and consolidation will produce different properties in vertical and horizontal directions but the same properties in all horizontal directions, so that the soil is transversely isotropic (also known as cross-anisotropic). Any subsequent plastic straining can produce changes of soil fabric (the arrangement of soil particles and their contacts) and hence changes (evolution) of soil anisotropy. If this plastic straining involves a situation other than one-dimensional straining (as will occur, for example, in the formation of a slope or in the soil beneath a foundation or embankment of finite width or in the soil around a tunnel or excavation) the resulting soil fabric will no longer be transversely isotropic, and the soil behaviour will show a more general form of anisotropy.

Both small strain (elastic) behaviour and large strain (plastic straining and strength) behaviour are influenced by anisotropy. However, a lack of awareness of this key feature may lead to poor predictions of deformations in many important geotechnical engineering applications including embankments on soft soil deposits (Zdravkovic et al., 2002), slopes (Al-Karni & Al-Shamrani, 2000 and Wei, 2012), tunnels (Lee & Rowe, 1989 and Simpson et al., 1996) and deep excavations (Ng et al., 2004).

Anisotropy of large strain (plastic) behaviour of saturated soils is indicated by, amongst other things, inclination of the yield curve in $q : p'$ stress space (see Figure 2.35). This behaviour has been studied in triaxial tests on transversely isotropic samples by a

number of researchers (e.g. Graham et al., 1983; Korhonen & Lojander, 1987; Smith et al., 1992; Diaz-Rodriguez et al., 1992 and Wheeler et al., 2003a).

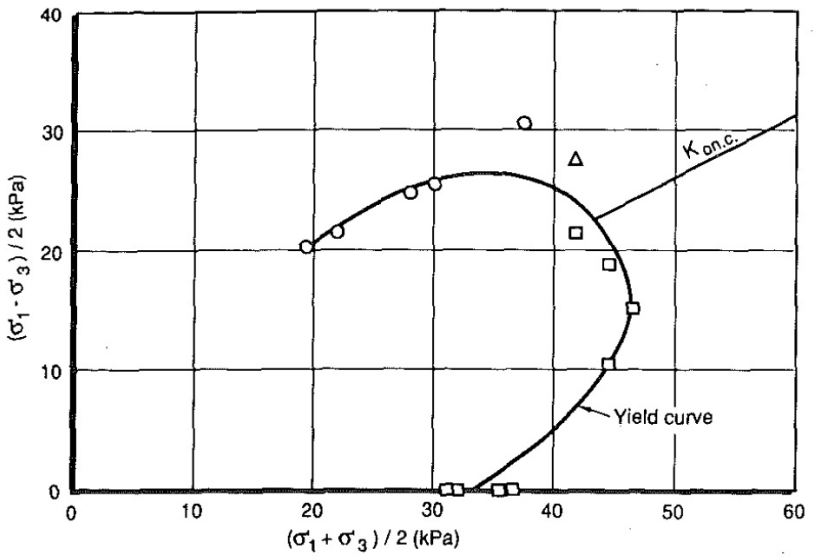

Figure 2.35: Experimental yielding points and yield curve of Mexico clay (Diaz-Rodriguez et al., 1992)

2.5.2 Evolution of anisotropy of large strain behaviour in saturated soils

In the development of elasto-plastic constitutive models incorporating anisotropy of large straining behaviour, the inclined yield curve is typically represented (for a transverselly isotropic soil) by either a rotated ellipse or a sheared (distorted) ellipse (e.g. Banerjee & Yousif, 1986), with the latter generally considered as more realistic and more mathematically elegant. A commonly employed form of sheared ellipse first proposed by Dafalias (1987) and Korhonen & Lojander (1987) and subsequently employed by Wheeler et al. (2003a) in the development of the S-CLAY1 constitutive model, is given by:

$$f = (q - \alpha p')^2 - (M^2 - \alpha^2)(p'_m - p')p' = 0 \tag{2.95}$$

In Equation 2.95, M is the critical state stress ratio (a soil constant), and p'_m and α are variables which describe the current size and inclination of the yield curve respectively (see Figure 2.36). Variation of anisotropy can be represented by variation of α. If α is zero, the soil is isotropic and Equation 2.95 corresponds to the conventional Modified Cam Clay (MCC) yield curve expression.

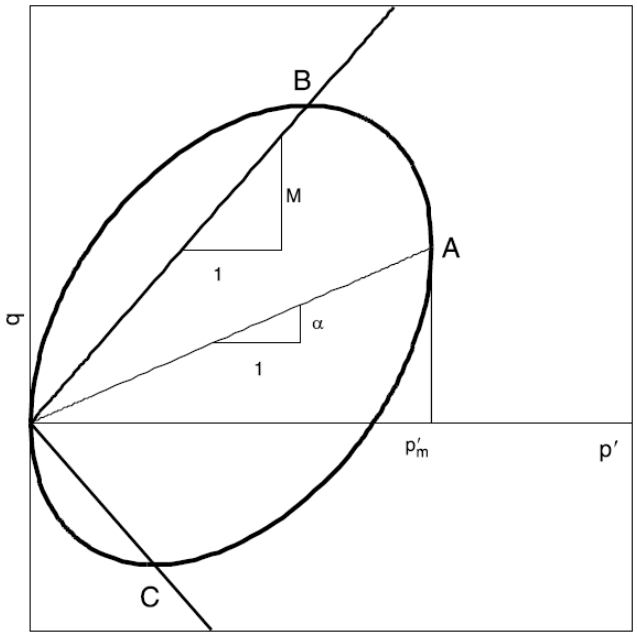

Figure 2.36: S-CLAY1 yield curve (Wheeler et al., 2003a)

Many researchers have attempted to model evolving anisotropy of large strain behaviour (Banerjee & Yousif, 1986; Dafalias, 1987; Davies & Newson, 1993; Whittle & Kavvadas, 1994 and Wheeler et al., 2003a). Many of these authors assumed that only plastic volumetric strains could produce changes of anisotropy, whereas Wheeler et al. (2003a) incorporated the influence of both plastic volumetric strains and plastic shear strains in the hardening law giving the change of inclination of the yield curve in the S-CLAY1 constitutive model. This is more realistic and Karstunen & Koskinen (2008) subsequently demonstrated that S-CLAY1 is able to accurately capture the evolution of large strain anisotropy of soft clays, at least for the relatively simple case of reconstituted clays.

In the S-CLAY1 model, two hardening laws are incorporated. The change of size p'_m of the yield curve is represented by the first hardening law, which is only related to plastic volumetric strain (the same as in MCC), whereas the second hardening law, representing the change of inclination α of the yield surface during plastic straining due to change in fabric anisotropy, is related to both plastic volumetric strain and plastic shear strain (and the stress state).

Yield stress identification

Various different techniques have been proposed to identify yield stresses for saturated and unsaturated soils, such as bi-linear approximation (e.g. Butterfield, 1970) in the

$v : lnp'$ plot or $v : ln\sigma'_v$ plot (in oedometer tests) and graphical or visual methods in the $v : ln\sigma'_v$ plot (e.g. Casagrande, 1936).

In the bi-linear technique, the intersection of two straight lines, which are plotted as extrapolations of the straight parts of the pre-yield and post-yield curves, is considered a yield stress. It is possible to estimate a yield stress using the bi-linear technique in the $v : p'$ and $q : \epsilon_a$ plots (Graham et al., 1983), and it is also possible to estimate it in the $\epsilon_v : p'$, $q : \epsilon_s$ and $\epsilon_v : \epsilon_s$ plots (Sultan et al., 2010). Estimating yield stress on each of these (logarithmic or linear scale) plots has its advantages and disadvantages, as explained in detail by Al-Sharrad (2013), along with other methods.

The bi-linear method is one of the simplest and most reliable methods in terms of estimating yield stress for different stress loading paths (Cui & Delage, 1996 and Al-Sharrad, 2013). Cui & Delage, (1996) and Al-Sharrad (2013) performed suction-controlled tests on unsaturated Jossigny silt and unsaturated speswhite kaolin clay respectively, by following different loading stress paths (such as isotropic loading and shearing at different stress ratios. Cui & Delage (1996) and Al-Sharrad (2013) deduced that the bi-linear method in the $v : ln\bar{p}$ plot gave the most consistent and reliable values of yield stress. However, the use of a bi-linear fit in this semi-logarithmic plot can still give false yield points, and confirmation of yield points from alternative plots using natural scales is always desirable.

2.5.3 Anisotropy of large strain behaviour in unsaturated soils

Cui & Delage (1996) performed a series of suction-controlled triaxial tests on statically compacted Jossigny silt, following different stress ratios (i.e. $\eta > 0$ and $\eta = 0$) in the $q : \bar{p}$ plane. They found that experimentally determined yield points demonstrated that constant-suction cross-sections of the yield surface all had the same inclination in the $q : \bar{p}$ plane (see Figure 2.37). They also attempted to fit rotated ellipses to these inclined yield curves.

Based on the BBM constitutive framework, Cui & Delage (1996) introduced the first anisotropic elasto-plastic constitutive model for unsaturated soils. They employed mean net stress, deviator stress and suction as stress variables (i.e. $\bar{p}$, q and s). The anisotropic model proposed by Cui & Delage (1996) did not, however, account for the evolution of anisotropy.

Al-Sharrad (2013) carried out a series of suction-controlled triaxial tests on statically compacted speswhite kaolin clay, following loading stress paths of different inclinations (i.e. $\Delta q/\Delta\bar{p} > 0$, $\Delta q/\Delta\bar{p} = 0$ and $\Delta q/\Delta\bar{p} < 0$) in the $q : \bar{p}$ plane. He discovered that the

soil showed anisotropy of large strain plastic behaviour through inclined constant-suction yield curves in the $q : \bar{p}$ plane and he attempted to fit sheared ellipses to these curves.

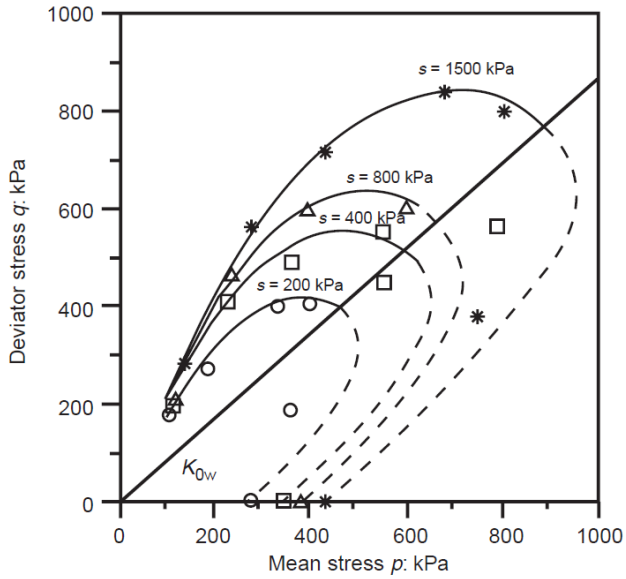

Figure 2.37: Experimental yield points and constant suction cross-sections yield surfaces in $q : \bar{p}$ plane (Cui & Delage, 1996)

2.5.4 Evolution of anisotropy of large strain behaviour in unsaturated soils

The evolution of anisotropy of large strain plastic behaviour of unsaturated soils has been experimentally investigated and modelled by a limited numbers of researchers, such as Stropeit et al. (2008); D'Onza et al. (2011a); Della Vecchia et al., 2012 and Al-Sharrad (2013).

In order to investigate the evolution of anisotropy of large strain plastic behaviour of unsaturated kaolin clay samples, Al-Sharrad (2013) loaded a number of samples along the same first loading path in the $q : \bar{p}$ plane, then unloaded each sample and finally re-loaded each sample along a different final probing path, to determine a yield point on the newly expanded yield curve. Figure 2.38a shows, an example of Al-Sharrad's results for a suction of 300kPa, showing the initial yield curve (dashed line) and the evolution of the yield curve (solid line) following a first loading stage at $\Delta q/\Delta\bar{p} = -1$. Figure 2.38b shows the same yield data plotted in the $q : p^*$ plane (where p^* is mean Bishop's stress). It is clear from Figures 2.38a and 2.38b that the first loading stage caused a significant change of yield curve inclination α. In this case, loading in triaxial extension caused a reduction of α from an initial positive value to a final small negative value. Al-Sharrad (2013) found that an advantage of plotting

in the $q : p^*$ plane (rather than the $q : \bar{p}$ plane) was that yield curves at all values of suction could be fitted through the origin.

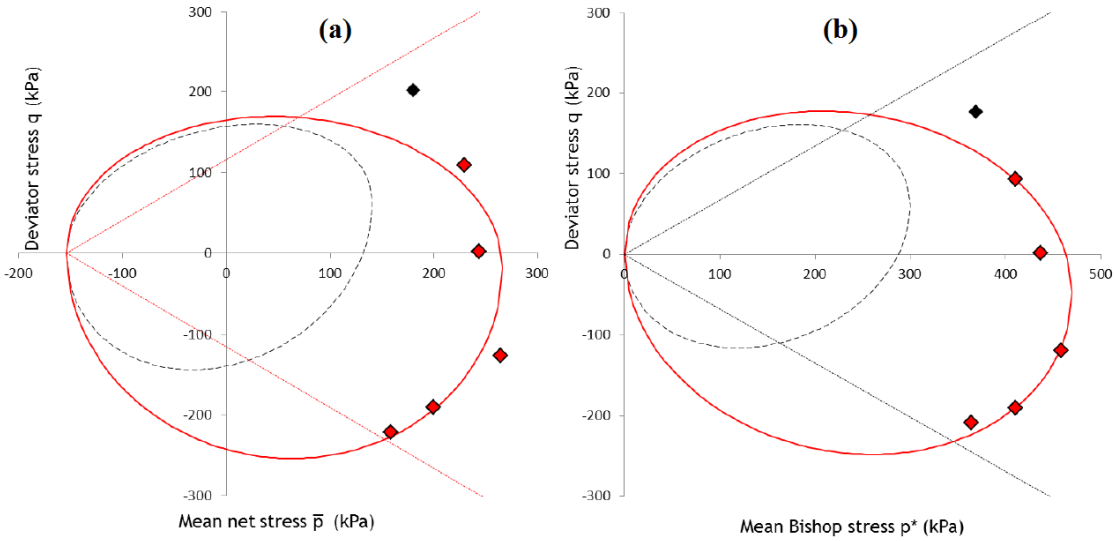

Figure 2.38: Evolution of anisotropy of constant suction (300kPa) cross-sections of yield surfaces in a) $q : \bar{p}$ plane and b) $q : p^*$ plane, following loading at $\Delta q/\Delta\bar{p} = -1$ (after, Al-Sharrad, 2013)

Combining the ideas of evolving anisotropy from the S-CLAY1 model for saturated soils (see Section 2.5.2) and the ideas from the BBM constitutive model for unsaturated soils (see Section 2.3.8), Stropeit et al. (2008) and D'Onza et al. (2011a) proposed anisotropic unsaturated elasto-plastic models: namely ABBM and ABBM1, respectively. Their models use $\bar{p}$, q and s as stress variables and both include evolution of anisotropy during plastic straining.

One of differences between ABBM and ABBM1 is that, in the ABBM model, the critical state line intersects the apex of the yield curve only when the value of yield curve inclination α reaches a unique critical state value, whereas in the ABBM1 model, the critical state line always intersects the apex of the yield curve, whatever the value of α (as in the saturated S-CLAY1 model). The ABBM1 yield surface expression of D'Onza et al. (2011a) is given by:

$$f = (q - \alpha\bar{p})^2 - (M^2 - \alpha^2)(\bar{p}_m(s) - \bar{p})(\bar{p} + \frac{M}{M - \alpha}f(s)) = 0 \qquad (2.96)$$

where α represents the current inclination of constant suction cross-sections of the yield surface and $\bar{p}_m(s)$ defines the current size of a cross-section of the yield surface at a suction s. M and $f(s)$ come from the definition of the critical state line in the $q : \bar{p}$ plane for a given value of suction:

$$q = M(\bar{p} + f(s)) \tag{2.97}$$

Equation 2.97 is similar to the BBM critical state line expression of Equation 2.84, except that it allows for the possibility of a non-linear increase of critical state strength with suction. Like the S-CLAY1 elasto-plastic model, both ABBM and ABBM1 models linked the evolution of yield curve inclination to both plastic volumetric strain and plastic shear strain, which allow the models to predict sensible evolution of anisotropy for all stress paths.

Al-Sharrad (2013) proposed an anisotropic unsaturated elasto-plastic constitutive model which used p^*, q and s as stress variables. The model involved a combination of features from the GCM isotropic model for unsaturated soils described in Section 2.3.8 (only features from the mechanical parts of the model, not the water retention parts of the model) and features from the S-CLAY1 model for saturated soils described in Section 2.5.2 (for the evolution of anisotropy). However, the model of Al-Sharrad (2013) was incomplete, because it did not include the coupled mechanical and water retention behaviour from the GCM model.

Chapter 3

Experimental equipment and calibration techniques

3.1 Introduction

In this PhD research, to meet the objectives described in Section 1.2, shear and compression wave velocities were determined for unsaturated (and saturated) soil samples using Bender/Extender Elements (BEEs). To use BEEs with the existing suction-controlled double wall triaxial equipment, which was inherited from a previous PhD student, modifications were required to some parts of the equipment; particularly the base pedestal and the top cap. In addition, both the inner and the outer base plates had to be modified to allow passage of six cables for three pairs of BEEs. Incorporating three pairs of BEEs within the existing system meant that it was possible to measure shear wave velocities V_{svh} ,V_{shv} and V_{shh} and compression wave velocities V_{pv} and V_{ph}. In this chapter both the BEE system and the modified suction-controlled double wall triaxial system are described.

3.2 Bender/extender elements system

In this section, the BEE system, provided by GDS Instruments (UK), is described. The system transmits and receives shear and compression waves using three pairs of BEEs; a vertical pair (incorporated into the base pedestal and the top cap) and two horizontal pairs (mounted horizontally on soil samples). Details of how bender/extender elements operate are provided in Section 2.1.1.

3.2.1 Vertical bender/extender elements

Each vertical bender/extender element was manufactured as an insert (see Figure 3.1). This insert can be mounted in a base pedestal or a top cap of a triaxial cell. Manufacturing BEEs as an insert allows the same pair of BEEs to be used in different triaxial cells or even in various different types of apparatus in laboratories, for example, oedometer and shear box tests. Figure 3.1 shows a typical vertical BEE insert before and after mounting in the modified base pedestal of the suction-controlled double wall triaxial cell (see Section 3.3.3).

In this study, the vertical BEE in the base pedestal was used to transmit shear waves and receive compression waves whereas the vertical BEE in the top cap was used to transmit compression waves and receive shear waves. The shear waves were transmitted in the vertical direction and involved horizontal polarization (movement of the soil was in the horizontal direction) and hence the shear wave velocity measured by this pair of BEEs was V_{svh}. The compression waves were transmitted and polarized in the vertical direction and hence the compression wave velocity measured by this pair of BEEs was V_{pv}. Figure 3.2 illustrates clearly both transmission direction and polarization direction of the shear and compression waves transmitted and received by the vertical BEEs.

Figure 3.1: Vertical BEEs

3.2.2 Horizontal bender/extender elements

Two pairs of horizontal BEEs were employed in the research. These were similar to the vertical BEEs in design and wiring configuration. However, the inserts for the horizontal BEEs were of smaller diameter than the vertical BEEs, because the horizontal BEEs were mounted directly on a soil sample without recourse to the base pedestal or the top cap and therefore minimization of weight was important. Figure 3.3 shows a horizontal BEE without and with a bracket, grommet and 'O' ring used for mounting on the soil sample. The bracket was designed to turn the cable through

90^o after exit from the BEE insert, to allow these horizontal BEEs to fit within the inner cell of the double wall triaxial cell (see later). The cable of each horizontal BEE was bent gently after warming by a hairdryer (to avoid any damage of the seal between the insert and the cable) and then the bracket was placed and crimped around the cable.

Figure 3.2 shows that one horizontal BEE pair was oriented to produce shear waves with horizontal transmission and vertical polarization (measuring shear wave velocity V_{shv}), whereas the second horizontal BEE pair was oriented to produce shear waves with horizontal transmission and horizontal polarization (measuring V_{shh}). Both horizontal BEE pairs produced compression waves with horizontal transmission providing two separate measurements (V_{ph1} and V_{ph2}) of the same compression wave velocity V_{ph}.

In theory, the values of shear wave velocities V_{svh} (measured by the vertical BEE pair) and V_{shv} (measured by the first horizontal BEE pair) should be identical, on the basis of thermodynamic requirements (Love, 1927). This means that, in principle, the 6 measurements of wave velocities from the three pairs provide 4 independent pieces of information ($V_{svh} = V_{shv}$, V_{shh} , V_{pv} and V_{ph}).

3.2.3 Equipment for measuring shear and compression wave velocities

To record both transmitted and received signals for shear and compression wave velocities, a high speed data acquisition card was required. A master control box and a slave control box were provided with three pairs of BEEs by GDS Instruments (see Figure 3.4). The master control box included a high speed data acquisition card. The main functions of the master control box were switching between shear and compression wave testing (see Figure 3.5), supplying power to the three pairs of BEEs and signal conditioning. Digital to analogue conversion of the transmitted signal and analogue to digital conversion of the received signal was performed by the high speed data acquisition card with 16 bit resolution. Leong et al. (2009) studied the effect of data acquisition resolution on the shear and compression received signals using two different data acquisitions with 5 bit and 12 bit resolutions. They stated that received signals were much clearer with 12 bit resolution of data acquisition than with 5 bit resolution. In this study, the resolutions of transmitted and received signals for both shear and compression waves were high (see Figure 3.6), because of using a high speed data acquisition card with 16 bit resolution.

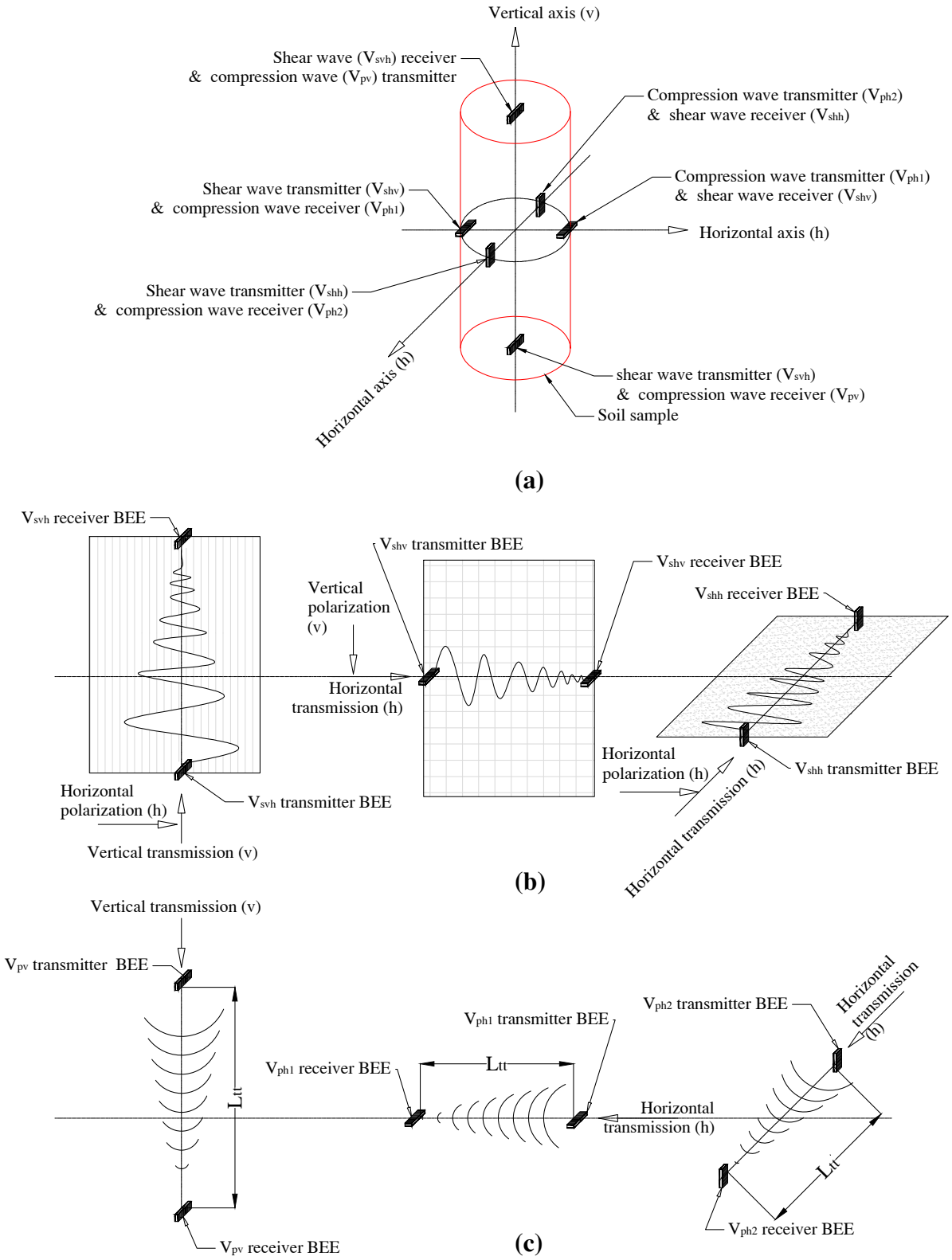

Figure 3.2: Multi-directional pairs of BEEs (a) arrangement of BEEs (b) shear waves (c) compression waves

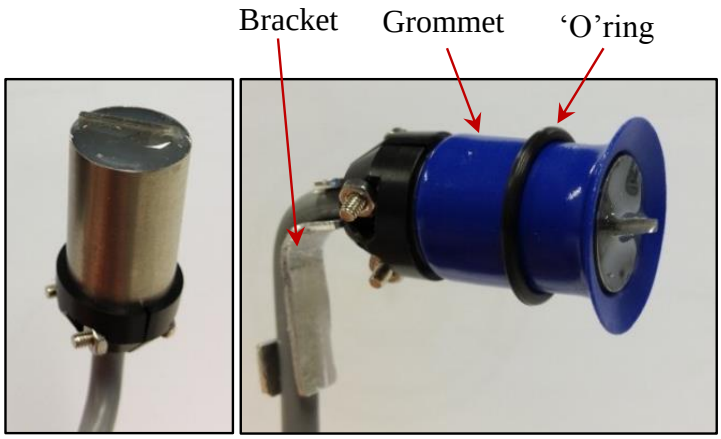

Figure 3.3: Horizontal BEEs without and with bracket, grommet and 'O' ring

The slave control box allows the BEE system to use a single data acquisition card (within the master control box) for all three BEE pairs, as shown in Figure 3.4 and Figure 3.5. Switching between the three BEE pairs is the main function of the slave box.

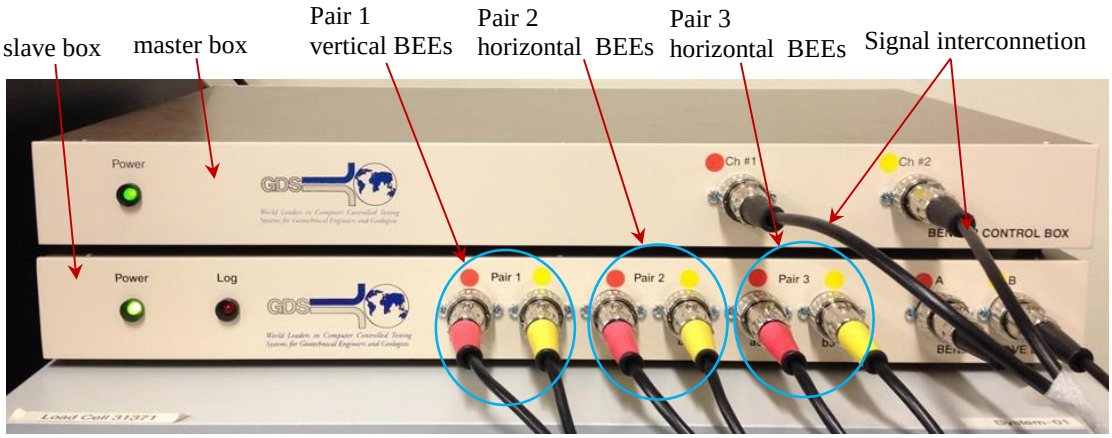

Figure 3.4: Master and slave control boxes

3.2.4 Logging and control system for BEEs

V_s and V_p measurements were performed using the GDSBES software package, provided by GDS Instruments UK with the BEE system. This software was used to control both shear and compression waves and to log data for further analysis. The GDSBES software is capable of measuring shear and compression wave velocities if it is supplied with the transmission distance L_{tt},which is the current tip-to-tip distance between a transmitter and a receiver BEE, see Figure 3.2, and the required waveform, wave frequency and amplitude. A wide range of waveforms (for example, sinusoidal single wave, square single wave and sinusoidal continuous wave) can be triggered by

pressing the trigger button after uploading the required waveform file, as shown in Figure 3.6. The travel time t can be measured from the transmitted and received waves (see Figure 3.6). Various different methods (using both time domain and frequency domain) were available for determining the travel time (as explained in Section 5.1).

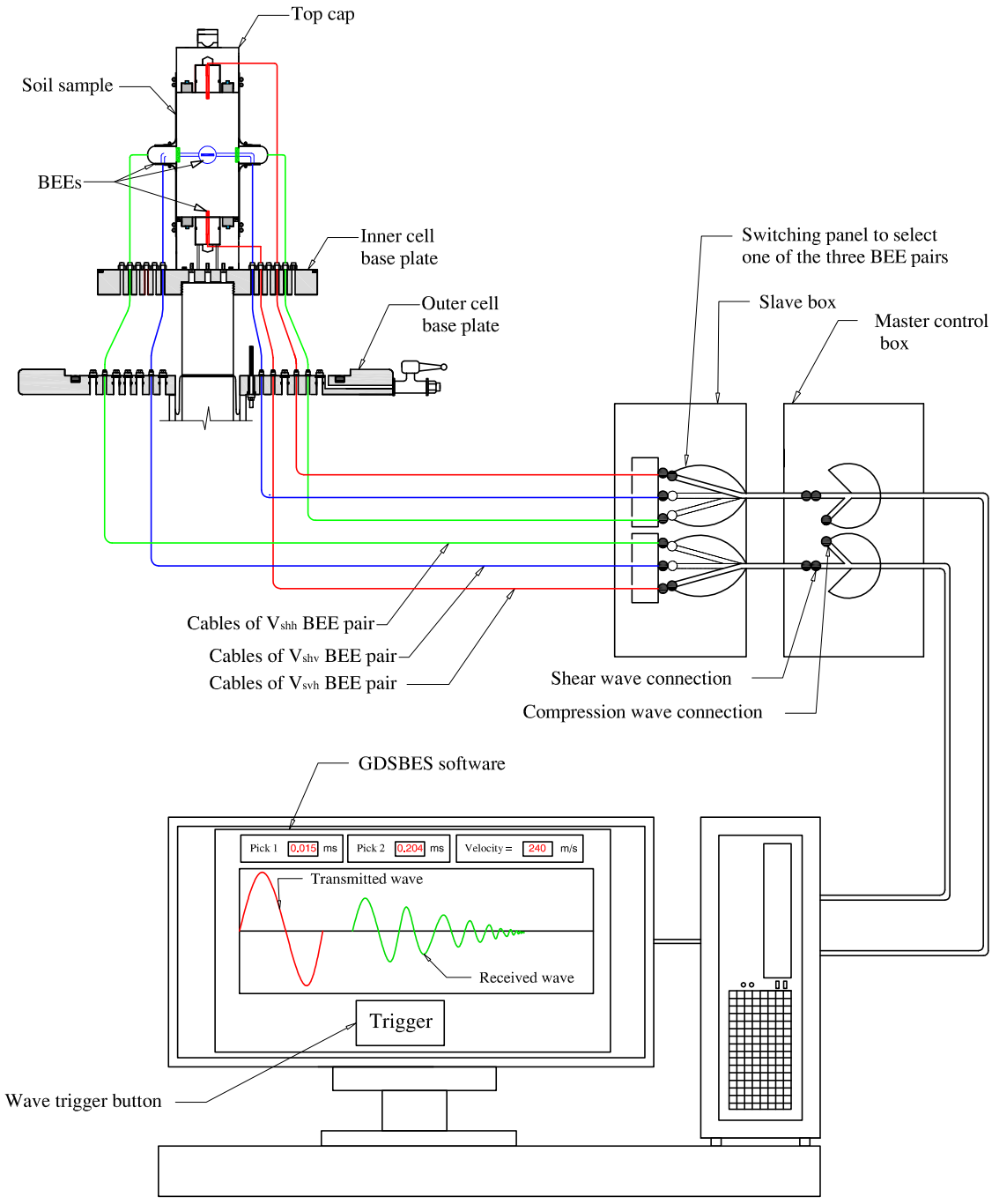

Figure 3.5: Layout of BEE system

3.2.5 Calibration of bender/extender elements

The measured travel time t_m between transmitted and received signals is greater than the true transmission time across the soil sample, because of the time delay associated with coating materials, ceramics and electronics (Brignoli et al. 1996). This time delay t_d is determined by measuring a travel time between transmitted and received signals when the transmitter and receiver elements are placed directly in contact. Figure 3.7 shows measurement of a typical time delay t_d of a pair of BEEs. True travel time t (which is used to calculate wave velocity V as in Equation 2.3) is determined by subtracting the delay time t_d from the measured travel time t_m:

$$t = t_m - t_d \tag{3.1}$$

Each pair of bender elements has an individual value of t_d, even though they are all supplied by the same manufacturer. This probably results from small differences in the dimensions of coating materials and/or ceramics. During measurement of shear wave velocities, t_d values for the three pairs of BEEs were $10.5\mu s$,$10\mu s$ and $8\mu s$ for the BEE pairs measuring V_{svh}, V_{shv} and V_{shh} respectively. During measurement of compression wave velocities, the t_d value was $7\mu s$ for all three pairs of BEEs. The fact that t_d had the same value for all three BEE pairs when they were used for measuring compression wave velocities was probably because the elements do not bend during this mode of operation and hence are less affected by the lateral coating materials.

It is essential that the only path for propagation of a wave from transmitter element to receiver element is through the soil sample. A possible unwanted transmission path, for the case of the vertical BEE pair, would be through the body of the triaxial cell (i.e. the top cap, the loading ram, the top plate, the cell wall or tie rods, the base plate and the base pedestal). A trial without a soil sample showed that no shear or compression waves could be detected by the receiver elements, thus confirming that the only transmission path was through the soil sample.

3.2.6 Performance of bender element pairs

The two horizontal BEE pairs were normally used to measure V_{shv} and V_{shh}. To ensure that these pairs were measuring consistently, initial tests were carried out on two isotropically compacted soil samples, with both pairs of horizontal bender elements aligned to measure V_{shh} (horizontal wave propagation and horizontal wave polarization). Table 3.1 shows the measured values of V_{shh} for both pairs of BEEs. It can be seen from the table that there is excellent consistency. This provided confidence that

any differences in the values of V_{shv}, and V_{shh} measured subsequently with the two horizontal BEE pairs when used in their normal arrangements were not simply due to difference in performance of the two pairs.

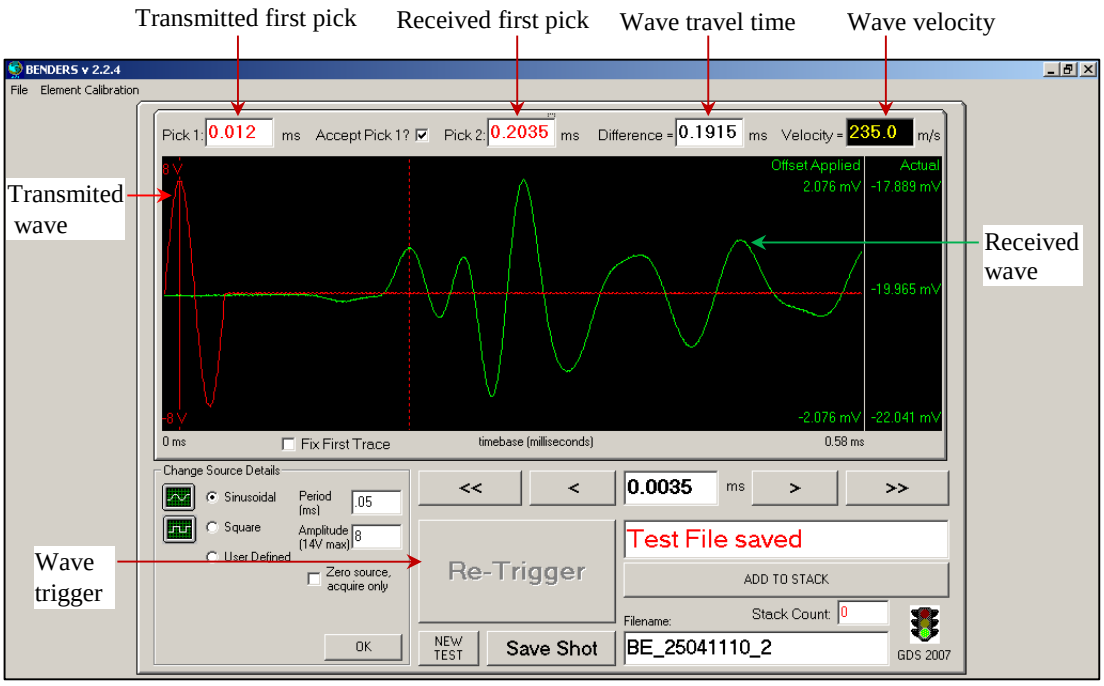

Figure 3.6: Typical interface of GDSBES software

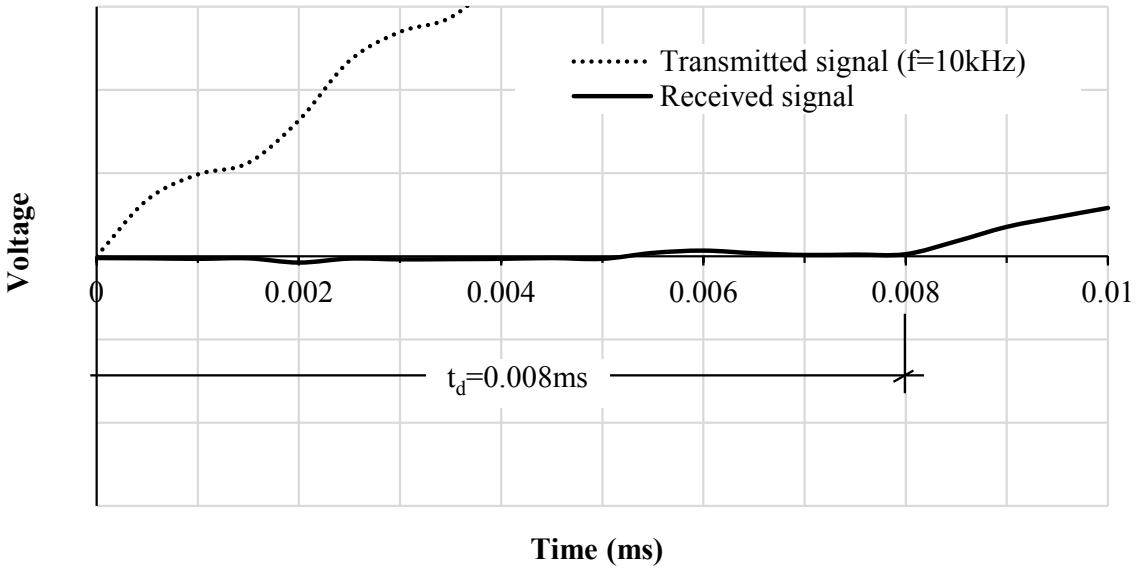

Figure 3.7: Measurement of delay time t_d for a typical BEE pair

Table 3.1: Results with horizontal wave polarization on both horizontal bender element pairs

Sample number	$V_{shh1}(pair1)$ (m/s)	$V_{shh2}(pair2)$ (m/s)	V_{shh1}/V_{shh2}
1	247.1	247.1	1.00
2	218.4	215.3	1.01

3.3 Suction-controlled double wall triaxial apparatus with modifications

As mentioned in Section 3.1, the existing suction-controlled double wall triaxial apparatus for testing unsaturated soil samples was inherited from a previous PhD student (Al-Sharrad, 2013), but this had to be modified for use in this research.

Wheeler (1986) designed the earliest version of this equipment. In this early design, the inner and the outer walls were made from acrylic; however, the inner cell wall material was changed to glass by Sivakumar et al. (2006) to minimize water absorption by the inner cell wall. The inner glass cell wall is equally pressurized on both sides (i.e. the same cell pressure is applied to the inner and outer cells); therefore no deformation of the inner glass cell occurs during application of cell pressure. Owing to no absorption and no deformation of the inner glass cell, it is possible to measure the volume change of a soil sample inside the cell by measuring the flow of water into or out of the inner cell using a volume change transducer (as described in Section 3.3.5) . The current double wall cell was manufactured by VJ Tech Ltd on the basis of a design developed by Sivakumar et al. (2006). In addition to the double wall cell, the system also includes various other equipment, such as automated pressure/volume controllers, a volume change transducer, a load cell and a data logger, which were also manufactured by VJ Tech Ltd.

3.3.1 Modified double wall cell

A schematic diagram of the modified double wall cell is shown in Figure 3.8, showing the inner glass cell wall and the outer acrylic cell wall, to enable changes of sample volume to be monitored by measuring the flow of water into or out of the inner cell. The maximum working pressure of the cell was 1600kPa and it was designed for testing samples of 50mm diameter.

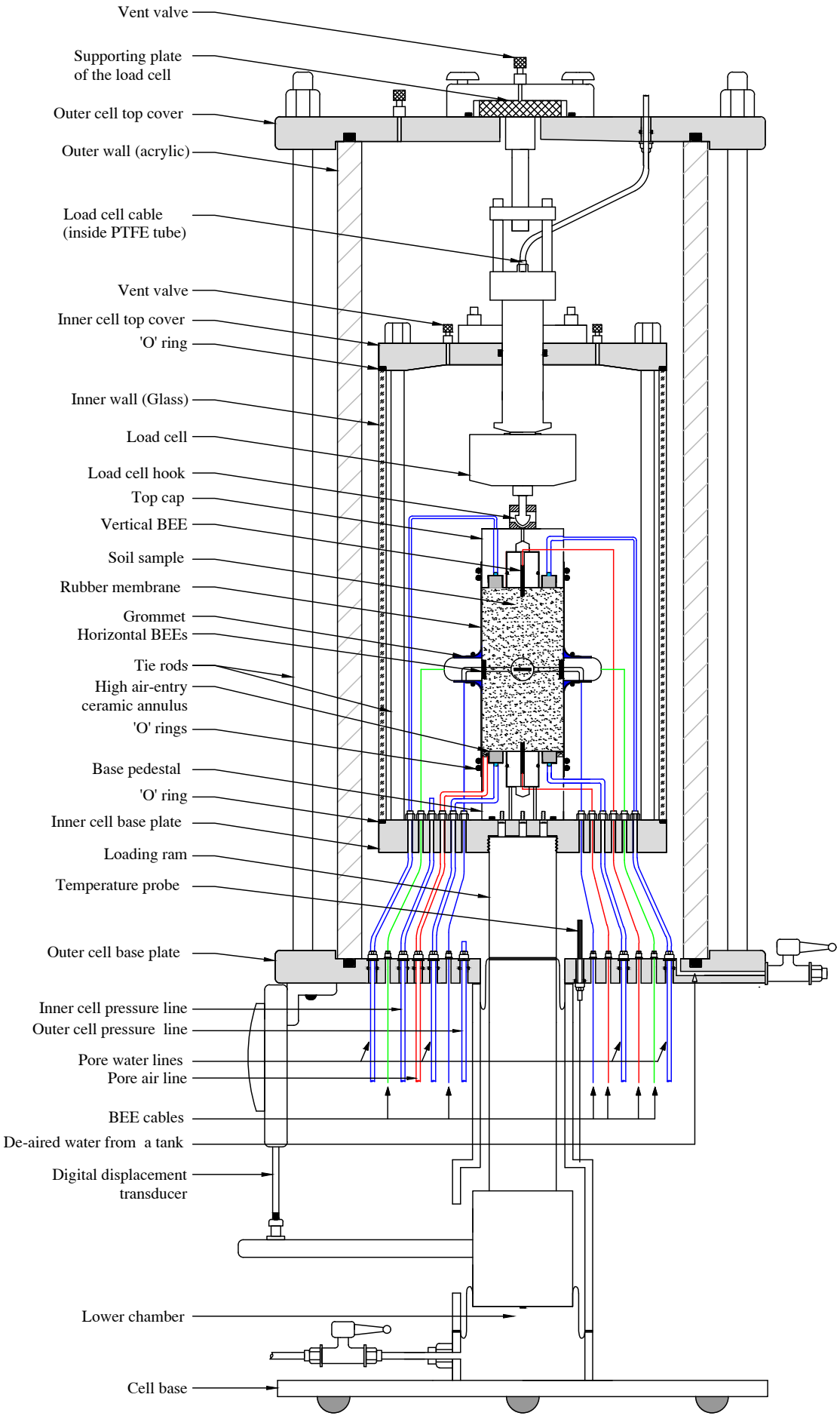

Figure 3.8: General layout of the modified double wall cell to accommodate BEEs

Suction control was achieved by the axis translation technique (Hilf, 1956), with both pore air pressure u_a and pore water pressure u_w maintained above atmospheric pressure (see Section 2.3.5). Suction-controlled triaxial testing of unsaturated fine-grained soils is notoriously slow, because the very low values of water permeability mean that very slow rates of testing are required to ensure proper equalization of pore water pressure (and hence suction) throughout the sample. To speed up the rate at which testing could be performed, the water drainage path length was minimized by controlling pore water pressure at both top and bottom of the sample (through the top cap and base pedestal respectively). In contrast, pore air pressure was controlled only at the bottom of the sample (through the base pedestal), because equalization of pore air pressure throughout the sample was relatively rapid.

As per objectives described in Section 1.2, the existing suction-controlled double wall triaxial system had to be modified to host three pairs of BEEs. To do this, the base pedestal, the top cap, the outer base plate and the inner base plate had to be modified. Prior to the modifications, the base plate of the outer cell accommodated nine push-in fitting outlets, the first six of which also passed through the inner cell base plate (see Figure 3.8). Two outlets were used to apply pore water pressure to the base of the soil sample through the base pedestal (provision of two connections allowed flushing of any diffused air, see Section 3.3.6). Similarly, a further two outlets were used to apply pore water pressure to the top of the soil sample through the top cap. Another outlet was used to apply pore air pressure to the base of the soil sample through the base pedestal (there was no application of pore air pressure at the top of the soil sample). One outlet was employed to fill, empty, and pressurize the inner cell. Another outlet was used for filling and emptying the outer cell, with a separate outlet for applying pressure to the outer cell. Finally, a temperature probe within the outer cell occupied the last outlet.

Six more outlets were required in the outer and inner cells to accommodate the three pairs of BEEs. Because of the limited space within the outer and inner cell bases, it was a great challenge to add six more outlets in addition to the existing nine in the outer cell base and six in the inner cell base. GDS Instruments provided the three BEE pairs with push-in fittings of 20mm diameter. The GDS fittings were changed to compression fittings of 10mm diameter, which were sufficiently small to allow fitting within the congested space available in both inner and outer base plates.

3.3.2 Application and measurement of deviator force

Deviator force was applied to the soil sample by applying hydraulic pressure from a ram pressure controller to a lower chamber which pushed up a loading ram and hence

moved upwards the entire inner cell and base pedestal. Reaction at the top of the soil sample was provided by a submersible internal load cell, with a capacity of 1kN mounted on the top cover of the outer cell. An O-ring provided a seal where the load cell passed through the inner cell top cover.

The load cell was supported by a detachable plate on the outer cell top cover, which allowed external adjustment of the load cell position (both height and rotation). The electrical cable of the load cell passed through a PTFE tube to prevent any leakage of water into the load cell. The axial displacement of samples was measured externally with a displacement transducer which attached to the outer cell base plate which measured the displacement of the loading ram (and hence the base pedestal). No corrections were made to the measured axial displacement for bedding errors or compression of the system, because the axial displacement measurement was not used to explore the small strain response of the soil (when errors caused by these effects would have been significant).

Attachment between the load cell and the top cap allowed either triaxial compression testing or triaxial extension testing. Figure 3.9a shows two stainless steel plates (the bottom plate with hemi-spherical recess and the top one with an opening at its centre) bolted to the top cap. An arrow-head hook was screwed to the end of the load cell (see Figure 3.9b). One of the important steps during setting up a soil sample was that the hook attached to the load cell was inserted into the top cap arrangement (see Figure 3.9b) and then rotated by 90^o (see Figure 3.9c). By performing this crucial step, the loading system (i.e. the load cell, the hook and the lower chamber) could be used to apply either a triaxial compression loading stage (see Figure 3.10a) or a triaxial extension loading stage (see Figure 3.10b). If no deviator stress was required on the soil sample (if the soil sample was to be subjected to isotropic loading) the load cell hook position had to be intermediate between those shown in Figure 3.10a and Figure 3.10b.

3.3.3 Re-designed base pedestal and top cap

To measure values of V_{svh} and V_{pv} using vertical BEEs, the base pedestal and the top cap had to be re-designed to incorporate the vertical BEE inserts.

Base pedestal first version design

It was a great challenge to design a base pedestal of only 50mm diameter to include the vertical BEE insert (20mm diameter) and drainage connections for both pore water

pressure and pore air pressure. The vertical BEE insert occupied significant area on the top surface of the base pedestal, leading to a great challenge in the design process.

(a) (b) (c)

Figure 3.9: Photograph of (a) top cap arrangement and (b) & (c) load cell hook rotation

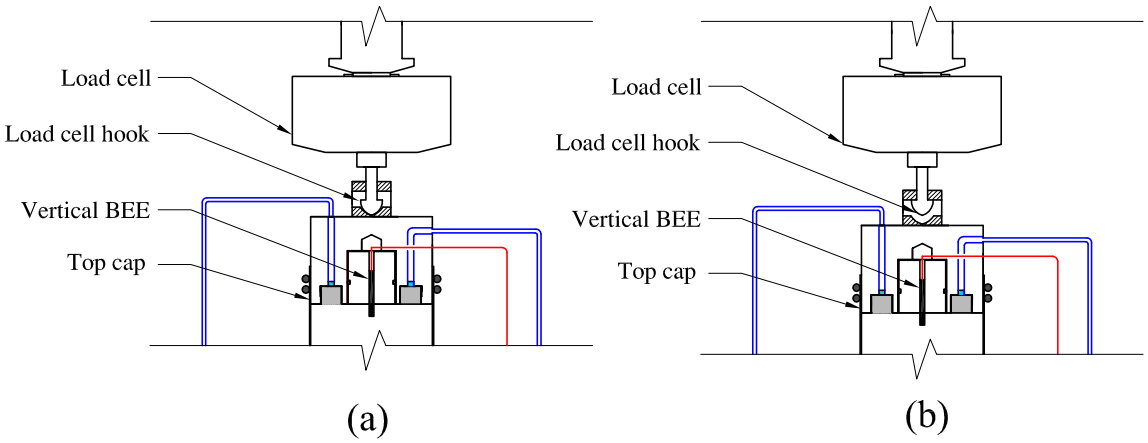

Figure 3.10: Load cell hook arrangements: (a) compression tests (b) extension tests

Figure 3.11 shows the design of the first version of modified base pedestal. Control of pore air pressure was through an outer sintered brass annulus with a low value of air entry pressure. This was simply placed on a shoulder of the stainless steel body of the base pedestal (it was not glued in position). Control of pore water pressure was through a high air entry (HAE) ceramic annulus, machined from a HAE ceramic disc with an air entry value of 500kPa, supplied by Soilmoisture Equipment Corp., USA through ELE Ltd., UK. The central hole in the annulus was drilled carefully using a carbide drill bit. The HAE ceramic annulus was thicker than the sintered brass outer annulus. The HAE ceramic annulus was glued within an annular seating in the top surface of base pedestal. Araldite 2011 glue was used for sealing between the steel body of the base pedestal and the HAE ceramic annulus. On the internal radius of

the HAE ceramic annulus, there was a thin annular upstand of stainless steel (part of the pedestal body) separating the HAE ceramic annulus from the BEE (see Figure 3.11). In contrast, the outer surface of HAE ceramic annulus abutted directly against the low air entry sintered brass annulus. This design was intended to maximize the plan area of the HAE ceramic annulus and to ease machining of the pedestal body. It meant that the HAE ceramic annulus was glued on its internal radius but on the outer radius it was unsupported over much of its height (it was a non-contact fit between the HAE ceramic annulus and the sintered brass annulus).

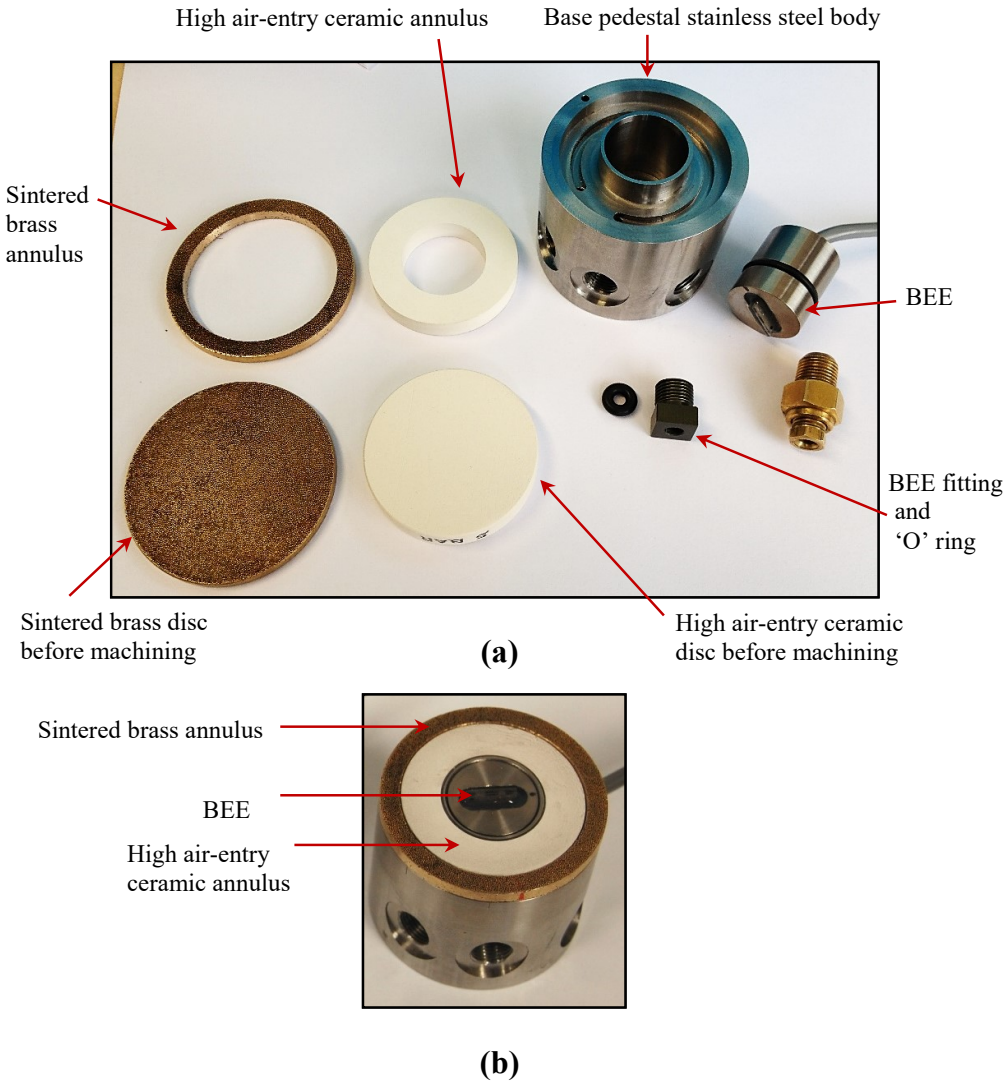

Figure 3.11: First version design of the base pedestal: (a) before assembly (b) after assembly

The base pedestal and the top cap (see later) were manufactured in the mechanical workshop of the School of Engineering at the University of Glasgow as per the designed details (see Figure 3.11) . Both the base pedestal and the top cap were used in several preliminary triaxial tests to check the performance of them during soil sample testing. Unfortunately, some months (nearly 3 months) after testing began, inspections showed that there was damage to the HAE filters, with major cracks in the filter of the base

pedestal (see Figures 3.12 and 3.13a). Although there was no cracks in the HAE filter in the top cap, there was however evidence of localized spalling (see Figure 3.13b).

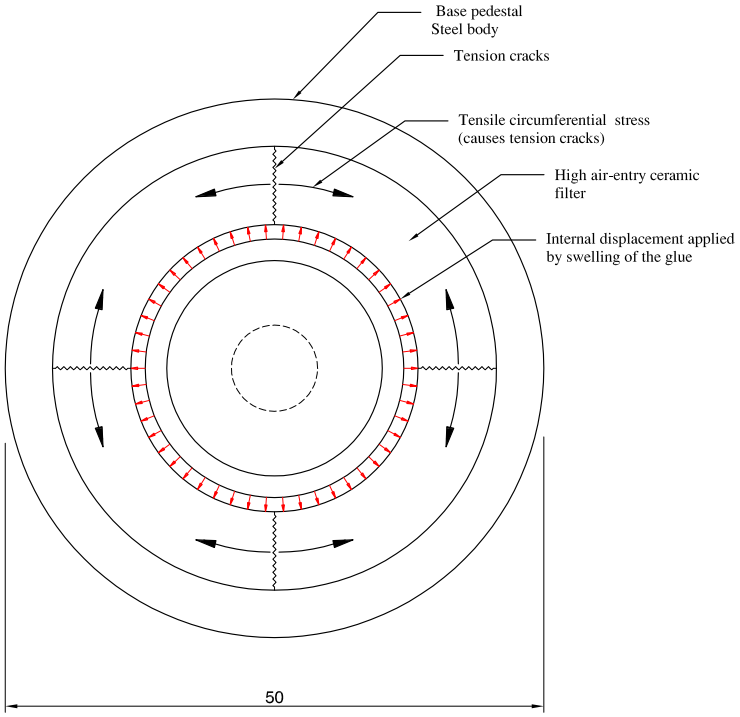

Figure 3.12: HAE ceramic filter crack mechanism

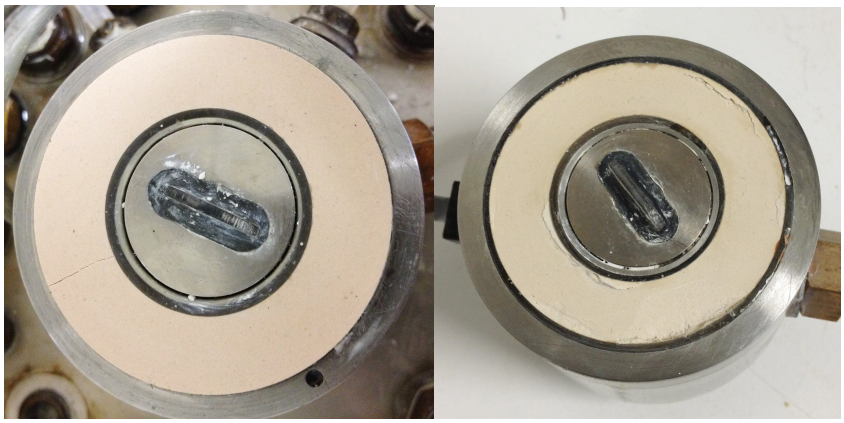

(a) (b)

Figure 3.13: Damage to HAE ceramic: (a) base pedestal tension cracks (b) top cap spalling

Initially, it was thought that the damage to the HAE ceramic filters might be due to damage caused when drilling the central hole in the HAE ceramic annulus to fit the vertical BEE inserts. To address this, pre-formed annular HAE filters were supplied by Soilmoisture Equipment Corp as a special order, so that no machining was required. However, it was subsequently discovered this was not the source of the problem. The problem was actually caused by time-dependent swelling of the glue (Araldite 2011)

which had been used for sealing the HAE ceramic filters on the recommendation of VJ Tech Ltd.. This explains the difference in behaviour in the base pedestal and the top cap, because in the top cap the HAE ceramic annulus was glued and restrained on both its inner and outer surfaces, as it was entirely set within the stainless steel body of the top cap. Expansion of the glue on both inner and outer radii would have generated significant compressive radial stresses, leading to surface spalling. In contrast, the HAE ceramic in the base pedestal was unrestrained on the outer radius over much of its height. Expansion of the glue on the inner radius thus led to outward radial displacement of the ceramic, leading to tensile circumferential strain, generation of tensile circumferential stress and hence formation of tension cracks (see Figure 3.12).

The above problem was solved by changing the original glue to a different one (Aluminum Putty), which was recommended by GDS Instruments. The latter type of glue does not swell when subjected to a wet environment for a long time. Also, to minimize even more the risk of cracking of the HAE ceramic filter, the design of the base pedestal was also modified to provide restraint on both inner and outer surfaces (as explained in the next paragraphs). It is worth reporting here that the swelling process of the original glue (on exposure to water) was a very slow process, lasting nearly 3 months and because of this it was difficult to diagnose the cause of the cracking in a short time. Three times HAE ceramics were damaged and changed to new ones for both base pedestal and the top cap, which consumed more than 10 months.

Base pedestal second version design

Figures 3.14, 3.15 and 3.16 show the second version of the base pedestal. Figure 3.14 shows a plan view of the stainless steel body of the pedestal and a cross-section of the entire base pedestal (including BEE insert, HAE ceramic annulus, O-rings, etc). Figure 3.15 shows two cross-sections of the stainless steel body of the pedestal and Figure 3.16 shows photographs of the base pedestal before and after assembly. As can be observed from Figures 3.14, 3.15 and 3.16, the design of the upper part of the base pedestal body was modified in such a manner to restrain over its full height the outer surface of the HAE ceramic annulus. It can also be seen from these figures that the sintered brass annulus used to apply pore air pressure in the first design was replaced by a stainless steel ring with 2mm thickness and 1.2mm height designed to fit within a groove on the top surface of the base pedestal. This stainless steel ring fitted loosely within the groove, so that pore air pressure was transmitted to the base of the soil sample around both inner and outer circumferences of the ring. A rough surface was created between the stainless steel body of the base pedestal and the glue on the inner and outer surfaces of the HAE ceramic annulus (see Figure 3.15) to provide a good bond and to help resist any tendency of the glue to swell in the vertical direction.

A significant challenge for the mechanical workshop staff in manufacturing the base pedestal was to provide a smooth path for passage of the cable of the vertical BEE (see Figure 3.15) in order to avoid risk of damage to the cable (i.e. sharp edges had to be avoided). As a consequence, the life of the BEE insert is prolonged as the insert is removed and replaced. Removing and replacing of the vertical BEEs is necessary, because it is likely that the vertical BEE pair will sometimes be used in other equipment in the laboratory (e.g. oedometer test).

A drainage groove (in the form of an incomplete circle) beneath the HAE ceramic annulus transmitted the applied pore water pressure to a significant part of the lower surface of the HAE ceramic and also allowed flushing of any diffused air bubbles between the two pore water drainage connections. Both pore water drainage connections and the single pore air drainage connection exited the base pedestal on the side of the pedestal (see Figures 3.14 to 3.16) and then exited the cell through both inner and outer base plates (see Figure 3.8). This arrangement was essentially the same as that used in the original base pedestal inherited from Al-Sharrad (2013). The cable for the BEE also exited on the side of the base pedestal (see Figures 3.14 to 3.16). The space directly beneath the BEE insert was connected to the inner cell pressure (via the passage taken by the BEE cable) and hence an O-ring was required on the outer surface of the BEE insert (see Figure 3.14) to prevent any leakage between the inner cell and the base of the soil sample.

Three threaded holes in the bottom of the pedestal (see Figure 3.16b) were used to attach the pedestal to the inner cell base plate. An outer O-ring on the bottom surface of the pedestal (see Figure 3.16b) was used to prevent leakage of water from the inner cell along the three corresponding bolt holes in the inner cell base plate. Two more holes in the bottom surface of the pedestal (see Figure 3.16b) connected to the space beneath the BEE. These two holes were used for two purposes. Firstly, they were used to bolt the BEE in place, to prevent any vertical displacement of the BEE as changes of deviator stress q were applied to the soil sample. Secondly, insertion of two small steel rods into these holes enabled the BEE insert to be pushed out of the pedestal body, if replacement, repair or removal of the BEE was required. O-rings on these two holes prevented any leakage of inner cell water from the space beneath the BEE insert and then through the bolt holes in the inner cell base plate.

A groove (1.2mmx2mm) on the top part of the outer surface of the base pedestal was provided to hold an O-ring (see Figure 3.14), which was used to carry a temporary slotted mould during setting up an unsaturated soil sample (see Section 4.2.2).

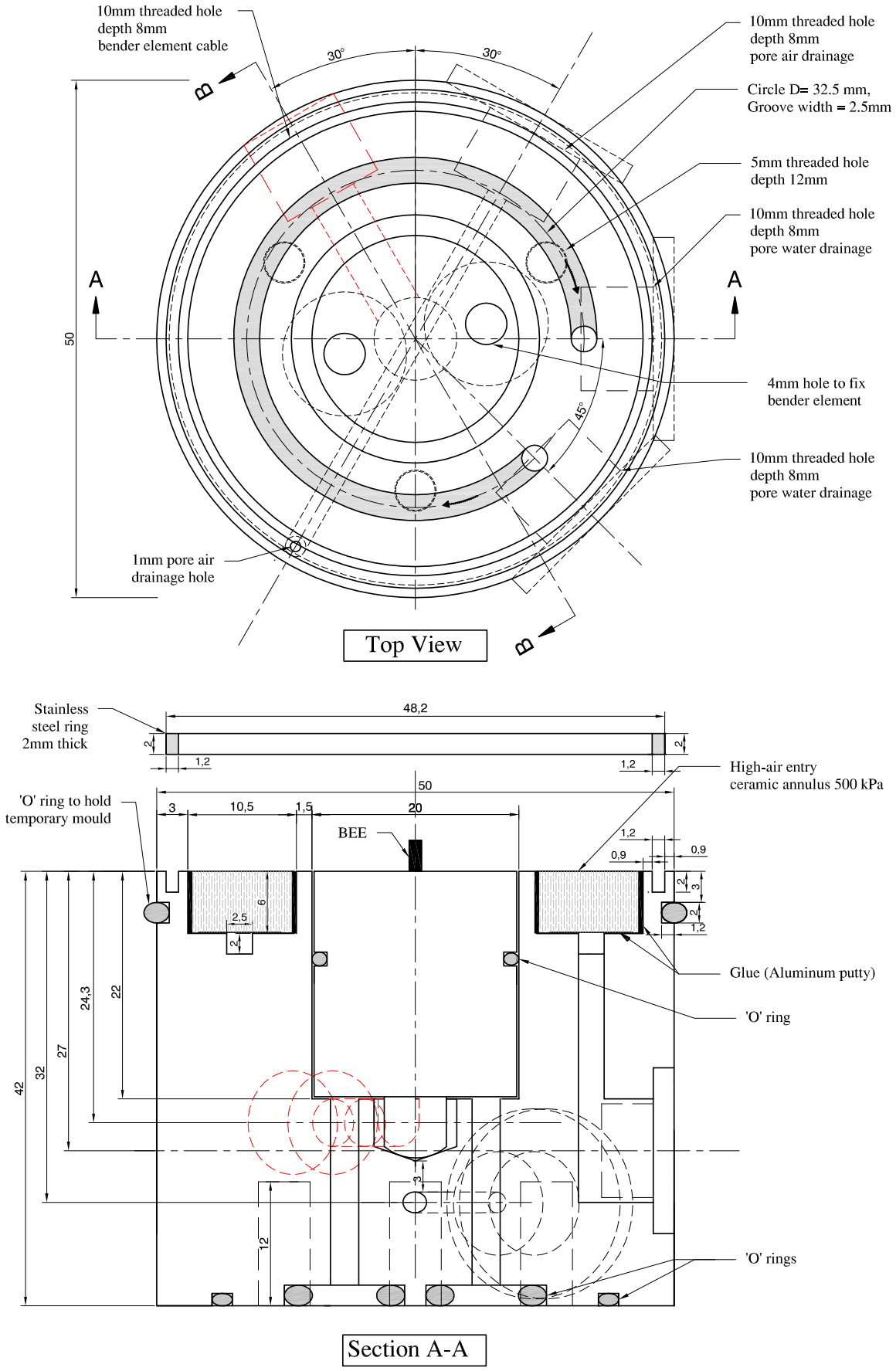

Figure 3.14: Second version of the base pedestal: top view of base pedestal body and section A-A of entire base pedestal assembly

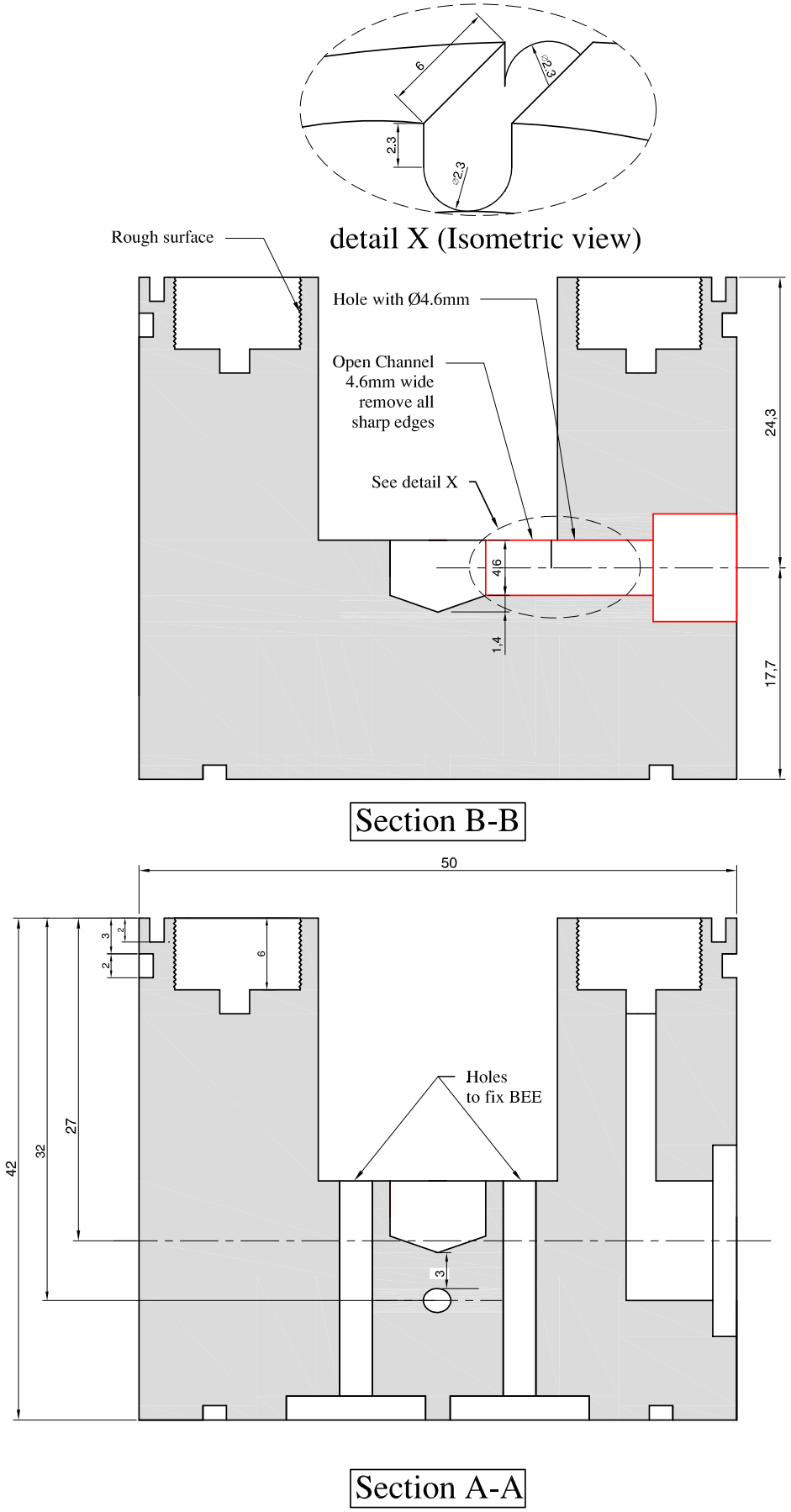

Figure 3.15: Second version of base pedestal: section A-A and section B-B of pedestal body

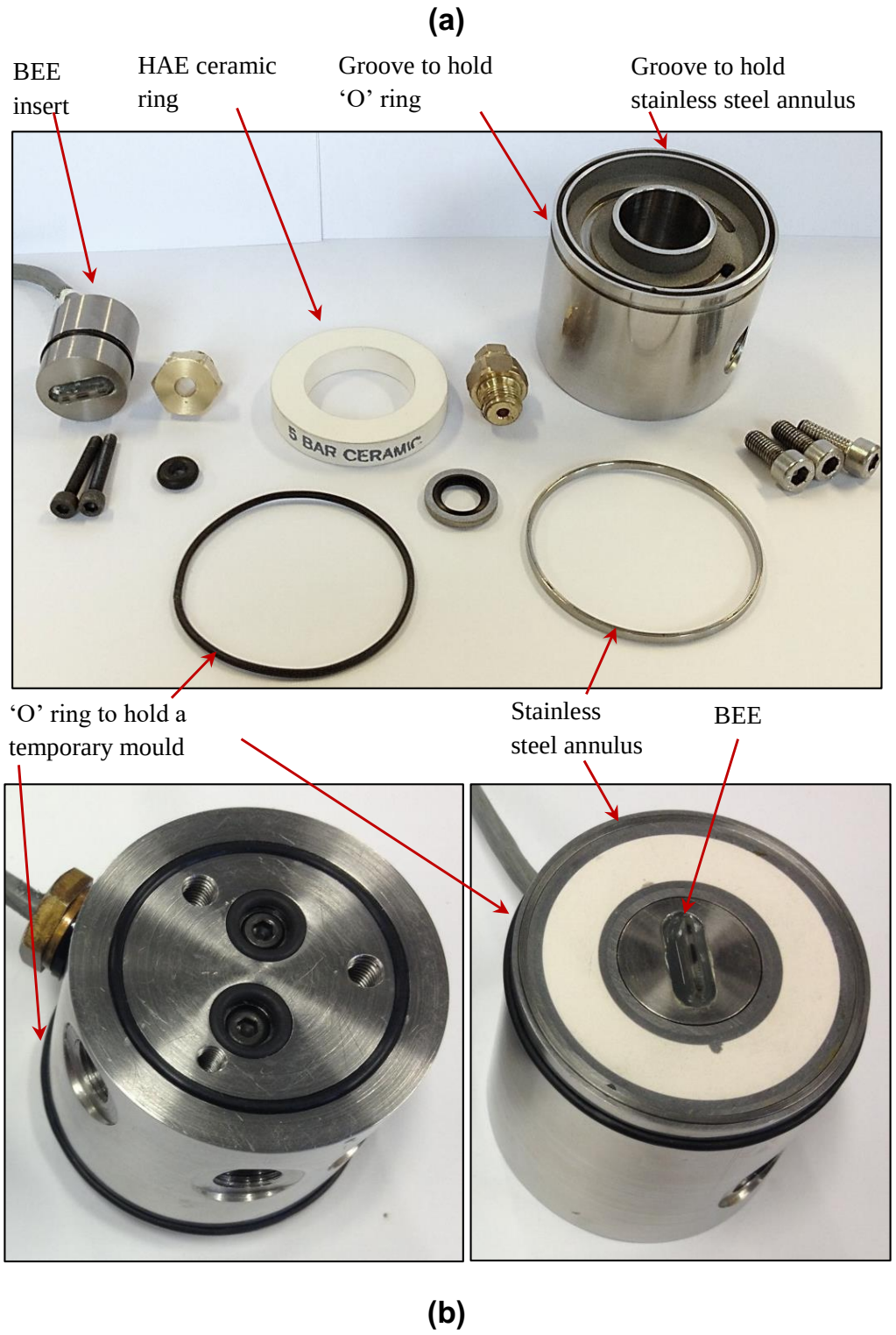

Figure 3.16: Second version of the base pedestal: (a) before assembly (b) after assembly

Details of re-designed top cap

Figures 3.17 and 3.18 show the top cap design details and a photograph of the parts before and after assembly, respectively. A crucial difference in design between the base

pedestal and the top cap was that there was no pore air pressure connection to the top cap and this made the design significantly easier.

A yoke arrangement was bolted to the top surface of the top cap (see Figures 3.17 and 3.18) to provide the connection for the load cell hook (see Figure 3.17), which allowed either triaxial compression testing or triaxial extension testing (see Section 3.3.2). This yoke was also used (with two O-rings) to seal the two holes connecting to the space above the BEE insert (used to bolt the BEE insert in place and also used when removing the BEE insert from the top cap).

One of the two pore water pressure connections exited at the top surface of the top cap, whereas the other pore water pressure connection and the cable for the vertical BEE exited on the side of the top cap (see Figures 3.17 and 3.18). This arrangement was chosen to provide reasonably balanced loading on the top cap during soil testing.

The glueing process of HAE ceramic annulus filters in both the base pedestal and the top cap was a great challenge, due to the very limited gaps between the inner and outer surfaces of the HAE ceramic annulus and the stainless steel body of the base pedestal or top cap. Air-entry value checks of both HAE ceramic filters (see next section) confirmed that the glued seals were successful.

3.3.4 Quality check for re-designed base pedestal and top cap

After finishing all work on the base pedestal and the top cap, the HAE ceramic filters were saturated using the saturation process described in Section 4.2.1. After the saturation process, the double wall triaxial cell was assembled with both base pedestal and top cap in place, but without a soil sample (the top cap was simply placed inside the triaxial cell). The cell was air-filled and was then connected to an air pressure controller in order to apply air pressure on the front surface of the filters during the seal and air-entry value checking process. The pore water drainage connections behind the filters were connected to a water pressure controller, to record directly any flow along the pore water drainage line caused by air flow from the cell either by leakage (past an O-ring or a glued seal) or by exceeding the air-entry value of the HAE ceramic.

The checking process was performed by gradually increasing the water pressure behind the filters to 200kPa and the air pressure in front of the filters to 800kPa or 900kPa. Both pressures were increased simultaneously at a rate of 2kPa/min starting from zero. This meant that the pressure difference $u_a - u_w$ across the filters remained at zero until the water pressure reached its target value of 200kPa, and $u_a - u_w$ then increased at 2kPa/min to a final value of 600kPa or 700kPa.

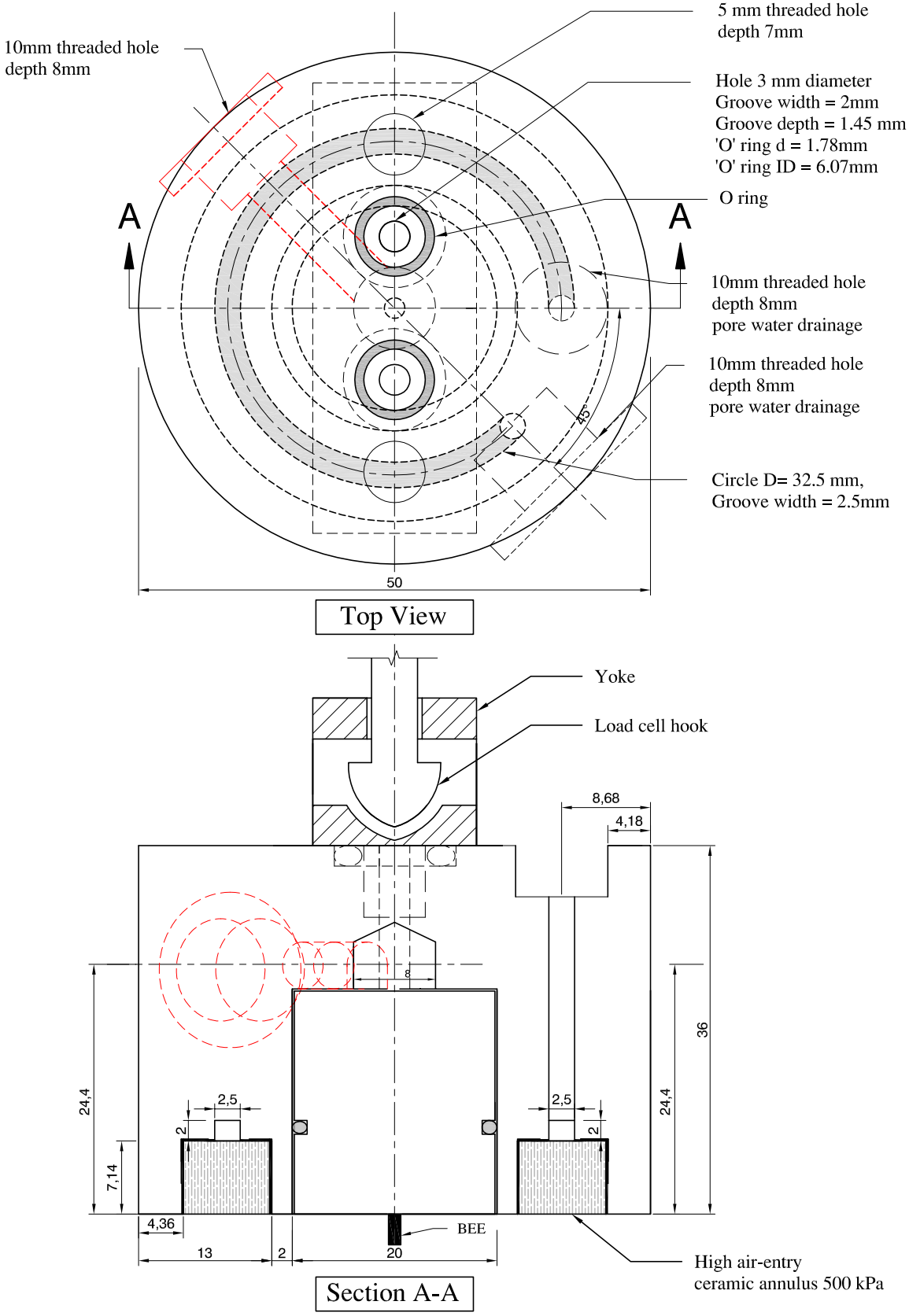

Figure 3.17: Top cap design details to accommodate BEE

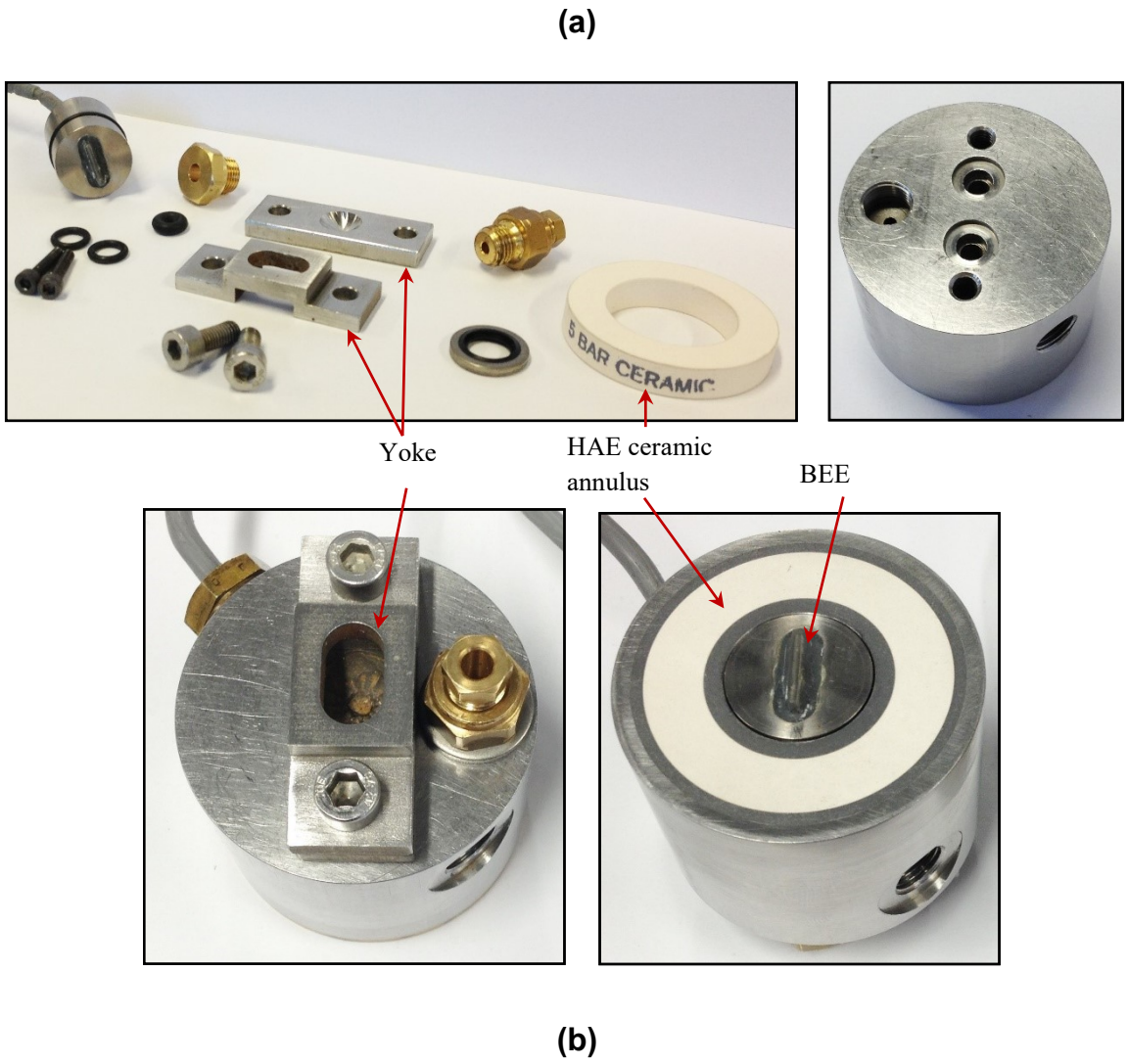

Figure 3.18: Top cap: (a) before assembly (b) after assembly

Figures 3.19 and 3.20 show the results of seal quality and air-entry value checks for the base pedestal and the top cap, respectively. The vertical section of the blue line at the start of each graph represents a small water inflow along the water drainage line as the equal air and water pressures of 200kPa were applied. This was attributed to expansion of the tube fittings and compression and dissolution of any trapped air bubbles. Results from the top cap showed no further measurement of flow on the water drainage line until the difference between air and water pressure was about 675kPa. This suggests that all seals were effective and that the air entry value of the HAE ceramic filter was 675kPa (higher than the manufacturer's quoted value of 500kPa). In contrast, the test on the base pedestal showed a water outflow of approximately 0.12cm^3 as $u_a - u_w$ was increased from about 30kPa to about 70kPa and then no further flow until $u_a - u_w$ reached 425kPa. The initial flow of 0.12cm^3 was attributed to the initial volume of water ponded on the top surface of the HAE ceramic of the base pedestal (not present in the case of the top cap, because ponding was not possible),

and the air entry value of the HAE ceramic filter appeared to be 425kPa (rather less than the manufacturer's quoted value of 500kPa).

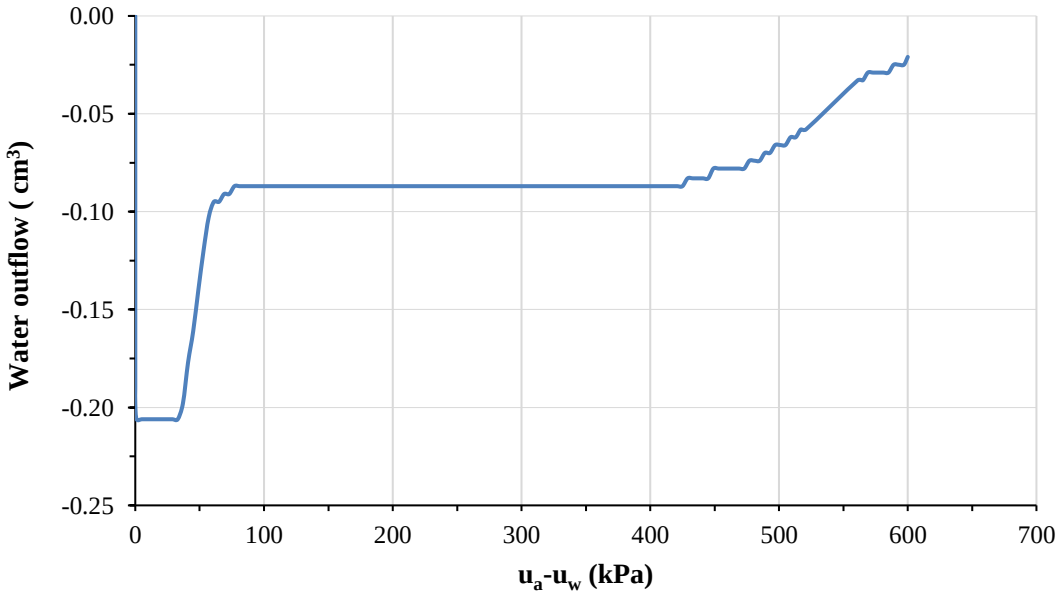

Figure 3.19: Air entry value and seal check of base pedestal

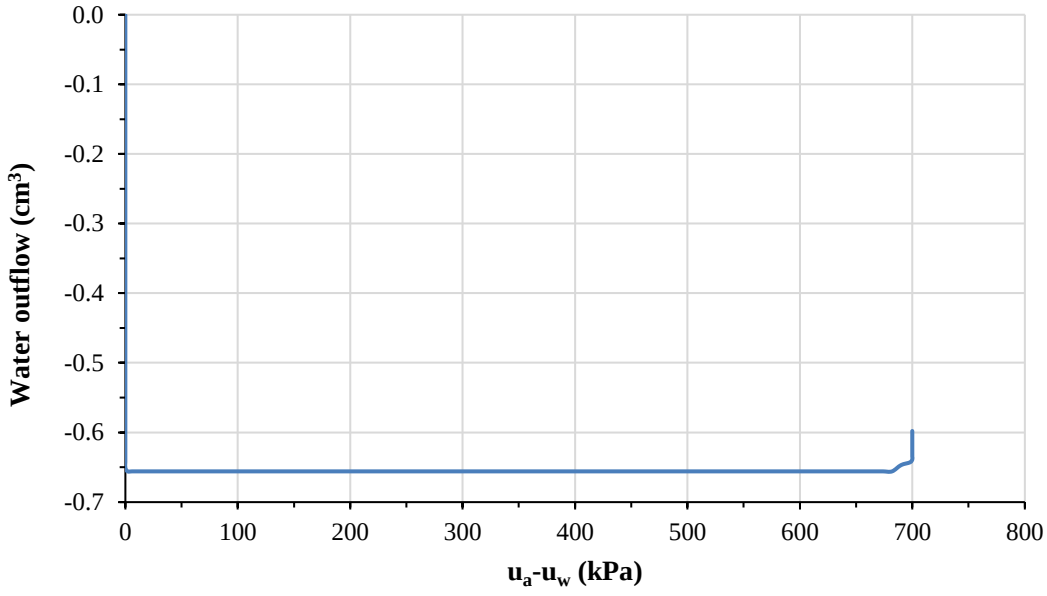

Figure 3.20: Air entry value and seal check of top cap

3.3.5 Pressure/volume controllers and measurement devices

Figures 3.21 and 3.22 show the general layout of the equipment.

Automated water pressure/volume controllers

In this work, three automated water pressure/volume controllers (AWPCs) manufactured by VJ Tech Ltd. were employed to control cell pressure, pore water pressure and ram pressure (see Figure 3.21). A fourth (much older) AWPC manufactured by GDS Instruments was used for the flushing system. Figure 3.23 shows a schematic diagram of a typical AWPC. The AWPCs were controlled together with other devices by the main computer control software (Clisp Studio), as explained in Section 3.6. A pressure transducer was fitted inside the stainless steel cylinder of each AWPC. The transducer was capable of measuring pressure up to 3000kPa with resolution of ±1kPa and it was connected to the AWPC's control panel (see Figure 3.23).

In order to ramp or set and maintain to a target value of pressure or water volume, the piston inside the cylinder was triggered by a stepper motor and gear box (also connected to the control panel) to move the piston forward or backward to obtain the target pressure or target water volume inside the cylinder. Each AWPC also provided measurement of water volume change. Each step movement of the piston corresponded to a certain amount of water volume which depended on the diameter of the piston and the magnitude of the displacement step. Each AWPC had a volume capacity of 250cm^3 and resolution of ±0.001cm^3. In all tests of the research programme the pore water drainage from or to the unsaturated soil samples was measured using the pore water pressure/volume controller.

Automated air pressure controller

Testing unsaturated soil samples requires a supply of pressurized air for control of pore air pressure. Air supplied from a compressed air line was regulated and controlled by an automated air pressure controller (AAPC) supplied by VJ Tech, which was equipped with an internal pressure transducer ranging from 0 to 1000kPa with resolution of ±1kPa and maximum inlet pressure of 1400kPa.

An air dryer was connected to the compressed air supply line close to the main compressor by the previous PhD student. Two additional air dryer/filters were connected to the main line inside the laboratory to provide clean, water-free air. The first dryer/filter was connected to the compressed air line just before the AAPC (see Figure 3.21).This was because the main line was subjected to change in temperature before reaching the AAPC inside the laboratory, which might cause water condensation inside the main line, which might damage the AAPC or prevent it from providing good regulation of the pore air pressure. The second dryer/filter was positioned between the pore air controller and the base pedestal (see Figure 3.21) to remove any humidity which might arise from the water inside the soil sample.

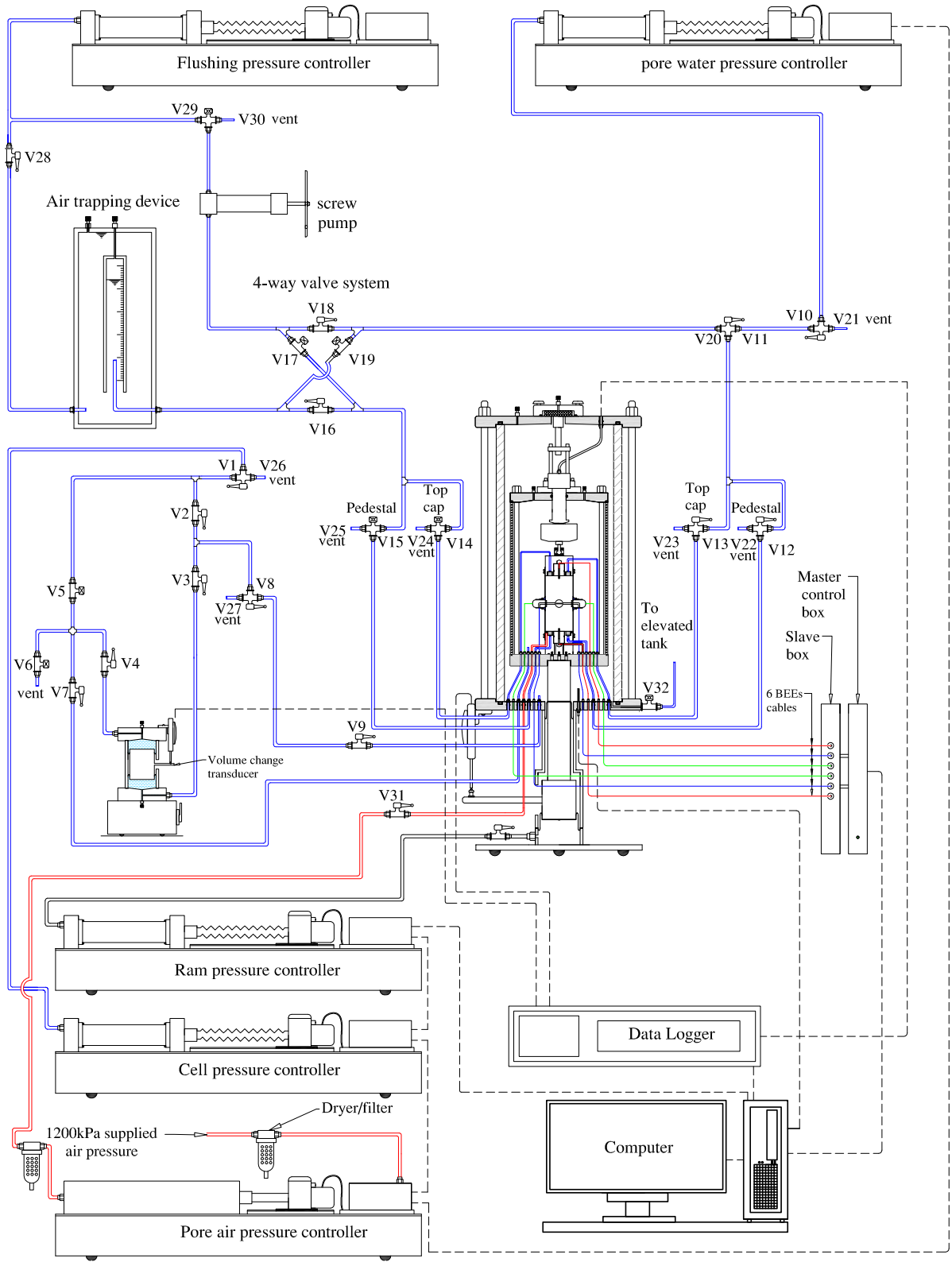

Figure 3.21: General layout of the equipment

Figure 3.22: Modified suction-controlled double wall triaxial cell and BEE systems

A disadvantage of the use of the dryer/filters was that provision of very low humidity air on the air drainage line to the soil sample resulted in continuous evaporation of pore water from the soil sample and then diffusion of water vapour along the pore air drainage line to the dryer/filter. This (unmeasured) loss of water from the soil sample produced errors in the measured water content w (and hence degree of saturation S_r) of the soil sample. However, the very small internal diameter of the pore air drainage line meant that the rate of vapour diffusion was expected to be very low. This was confirmed by the fact that the measured water content of each soil sample stabilized at the end of an initial equalization stage (see Section 6.2.1).

Volume change transducer

The cell pressure/volume controller provided the pressure supply to both inner and outer cells of the double wall triaxial cell (see Figure 3.21) and hence was unable to measure the volume of water flowing into the inner cell (which was required for measurement of sample volume change of the unsaturated soil samples). Hence, it was necessary to provide a separate volume change transducer on the inner cell pressure line (after bifurcation of the pressure lines to inner and outer cells, see Figure 3.21). Figure 3.24 shows a schematic diagram of the volume change transducer, which was manufactured by VJ Tech Ltd., on the basis of the Imperial College design.

The pressure from the cell pressure controller was applied to the water in the lower chamber of the volume change transducer, which acted on a piston and hence applied pressure to the water in the upper chamber, which was connected to the inner cell of the triaxial apparatus (see Figure 3.24). The movement of the piston was detected by a displacement transducer attached to the piston (see Figure 3.24). To convert piston

displacement to water volume change in the upper chamber a calibration exercise was performed on the volume change transducer (see Section 3.4).

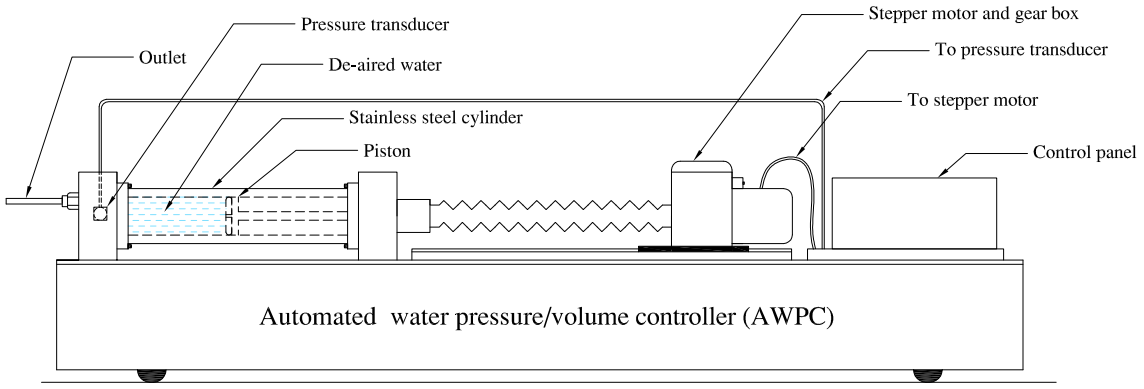

Figure 3.23: Automated water pressure/volume controller (AWPC)

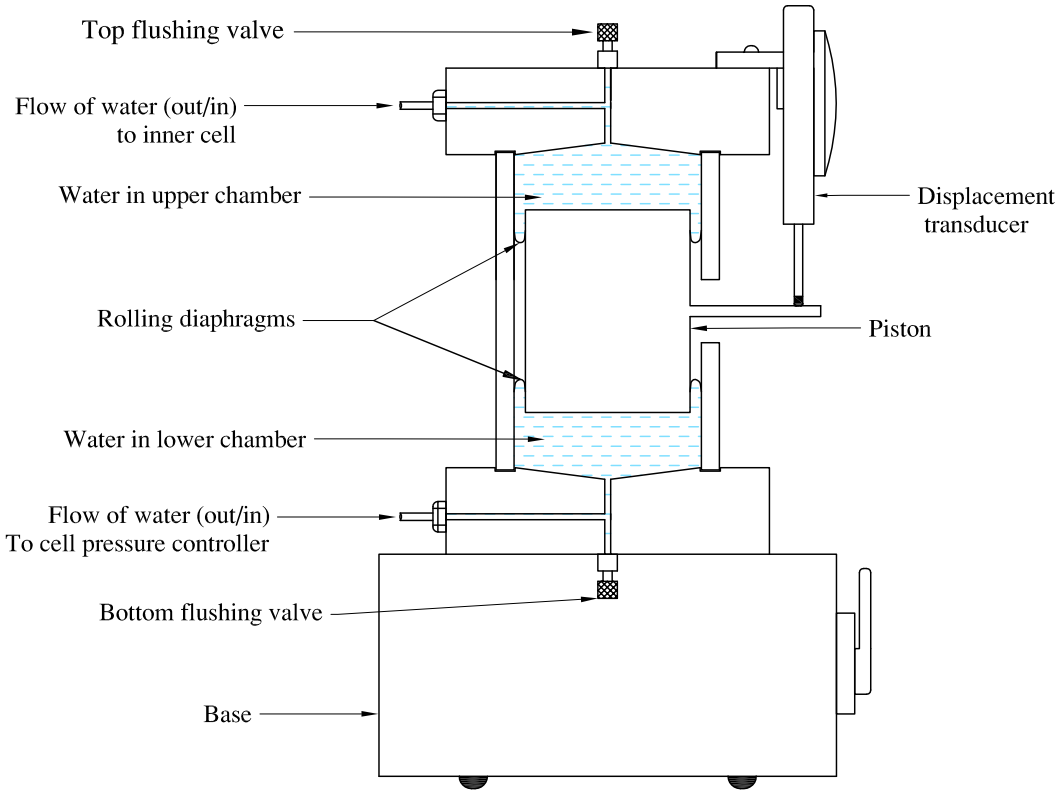

Figure 3.24: Volume change transducer

Load cell

A 1 kN submersible load cell with resolution of ±1N was used for triaxial compression and extension loading stages. After conducting some initial tests, it was discovered that the original 5 kN load cell (inherited from the previous PhD student) was faulty, as it gave spurious readings. A replacement 5 kN submersible load cell was purchased

from VJ Tech, after initial checking of the original load cell by VJ Tech indicated that it was not repairable. Subsequently, the 5kN load cell was replaced with a 1 kN load cell, in order to provide enhanced control and stability of deviator force.

Temperature probe

During testing of soil samples, the measured water inflow or outflow to the inner cell (which was used for monitoring volume change of the soil sample) had to be corrected for temperature fluctuation. A temperature sensor with resolution of $\pm 0.1^{o}$C was positioned within the outer cell base plate to measure temperature variation (see Figure 3.8). The effect of the change in temperature on the volume of water inside the inner cell was not eradicated completely after applying the temperature correction, because the temperature probe was located within the outer cell and not inside the inner cell (see details in Section 3.5.2).

Axial displacement transducer

To monitor the change of sample height throughout a test, a displacement transducer with a resolution of ± 0.001mm, attached to the outer cell base plate, was used to measure the displacement of the loading ram (see Figure 3.8). In this study, the change in sample height was not measured internally using for example Hall Effect transducers (Clayton & Khatrush, 1986), because these devices are unsuitable for measuring large displacements and the intention was to subject the soil samples to stress paths producing large strains (e.g axial strains of more than 17% were applied).

Essential laboratory infrastructure

Compressed air supply for the pore air pressure controller was provided by a 1200kPa compressor, with a second compressor as a back-up. This second compressor was triggered if pressure supply from the first compressor dropped.

De-aired water was produced within a Nold deaerator with 8 litre capacity, and then it was stored under vacuum (-96kPa) in an elevated tank in order to prepare a second 8 litres of de-aired water. This was because 12 litres of de-aired water was required to fill the double wall cell. 1.5 hours was sufficient to produce good quality de-aired water from the Nold deaerator. De-aired water was used to fill all the AWPCs and the sample volume change device (see Figure 3.24). It was also used to flush all water drainage lines in the system and to fill the double wall triaxial cell. Using de-aired water was important, in order to reduce errors in both measuring the pore water inflow or outflow to unsaturated samples and in measuring water inflow or outflow to

the inner cell. In addition, using de-aired water was also beneficial to avoid pressure fluctuation in the pore water pressure controller and the cell pressure controller.

Electrical devices including all the pressure/volume controllers, the data logging unit, the PC and the BEE system, were powered from an uninteruptable power supply (UPS), to avoid any power failure during soil testing.

The laboratory was temperature-controlled, in order to avoid large temperature-induced volume changes of the water within the inner cell. Temperature control of the laboratory was achieved within $\pm 1^{o}$C. The effect of the remaining change of temperature (i.e. $\pm 1^{o}$C) on the water volume change in the inner cell was corrected via temperature calibration (see Section 3.5.2).

3.3.6 Flushing system for diffused air

As explained in Section 3.3.4, the measured air-entry values for HAE ceramic filters for the base pedestal and the top cap were 425kPa and 675kPa respectively (compared to the ceramic manufacturer's quoted value of 500kPa). In this research, the maximum suction applied on soil samples was 300kPa. Under these conditions, it should be impossible for air to flow in gaseous form through a properly saturated HAE ceramic filter from the unsaturated soil sample to the water drainage lines. However, air dissolved within the water can diffuse through the HAE ceramic filters and then come out of solution to create air bubbles within the pore water drainage lines in the base pedestal or the top cap, leading to error in the measurement of inflow or outflow of pore water from the soil sample and perhaps also error in the suction applied to the soil sample. Therefore, a flushing system and air trapping device were proposed by Fredlund (1975) to remove and measure the volume of diffused air bubbles. The value of applied suction is the main factor affecting the rate of air diffusion (see Romero, 1999), with low diffusion rates at suctions of 300kPa and below and diffusion rates becoming very large at suctions above about 500kPa.

Figure 3.25 shows the diffused air flushing system. During a flushing operation, the pore water drainage lines were temporarily isolated from the pore water pressure controller, by closing valve V11, and pressure on the pore water drainage lines was provided by the flushing pressure controller, by opening valves V18, V20, V16 and V28 (with V29 closed). The pressure provided by the flushing controller was always set at the same value as that most recently provided by the pore water pressure controller. Flushing was achieved by manually displacing water from the screw pump (by turning the screw pump handle), through the pore water drainage lines in the base pedestal or top cap and then through the air trapping device to the flushing pressure

controller. Base pedestal and top cap were always flushed separately. Flushing of the base pedestal was achieved by opening valves V12 and V15 (with V13 and V14 closed), whereas flushing of the top cap was achieved by opening valves V13 and V14 (with V12 and V15 closed). During flushing of either base pedestal or top cap, the flow direction through the pedestal or the top cap was reversed several times, by using the 4-way valve system (see Figure 3.25). Valves V16 and V18 were opened (with V17 and V19 closed) to achieve flushing in one direction, whereas V17 and V19 were opened (with V16 and V18 closed) to achieve flushing in the reverse direction.

At the start of a test the screw pump and all the various drainage lines within the flushing system were carefully filled with de-aired water. This included pressurization (to dissolve any trapped air bubbles) followed by drainage of most of the water (to remove the dissolved air) and then replenishment with fresh de-aired water. The flushing procedure described above was then performed at the end of each test stage. After a flushing operation, the screw pump was re-filled by returning the de-aired water back from the flushing controller using valve V29 (with V17, V18 and V28 closed).

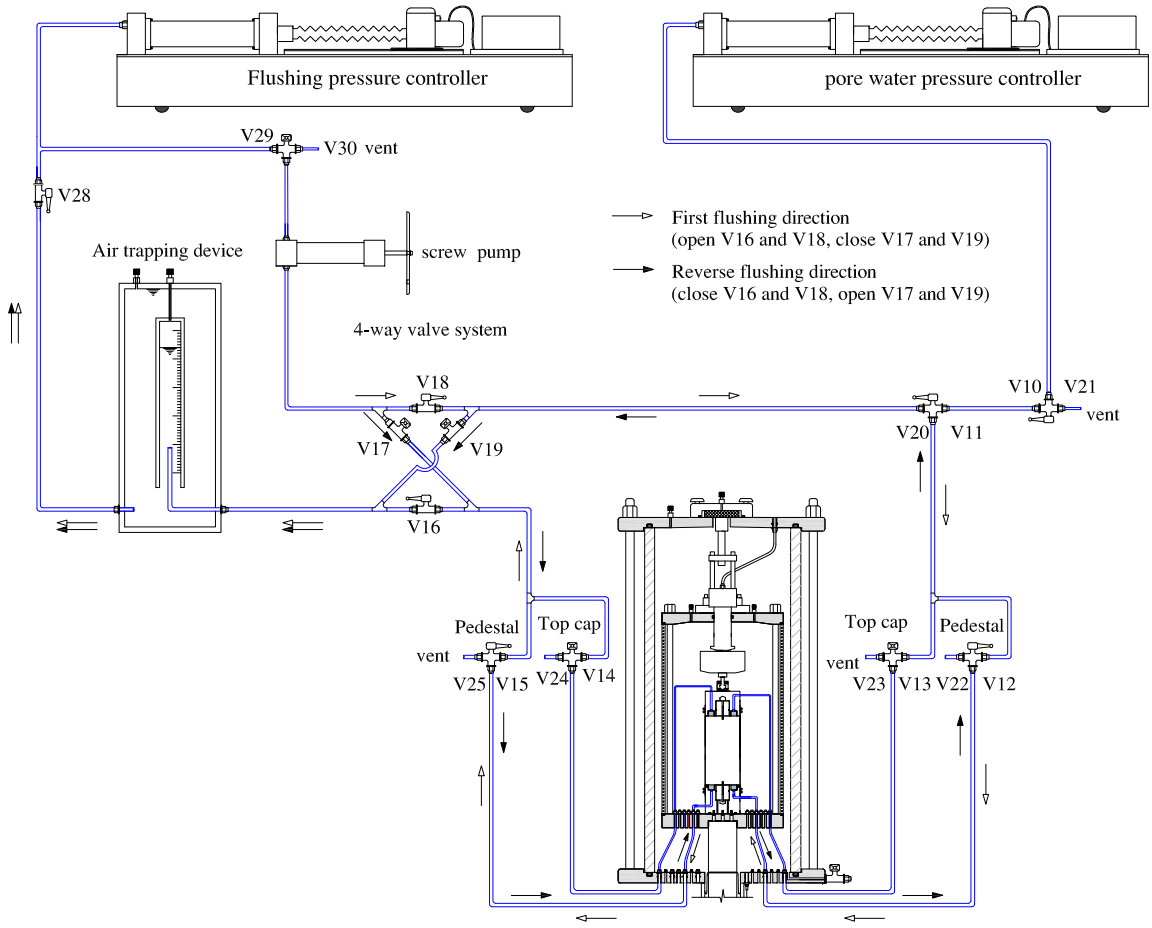

Figure 3.25: Diffused air flushing system

The intention was that the volume of flushed air would be measured in the air trapping device (see Figure 3.25). In practice, however, the flushing operations never produced any measurable quantities of air (because of the relatively low values of suction used within the test programme). Flushing was still performed at the end of each test stage, in order to remove dissolved air from the pore water lines (thus removing the risk of this dissolved air coming out of solution in a subsequent test stage).

3.4 Calibration of transducers

All transducers had been previously calibrated by VJ Tech Ltd., the manufacturer, and also by the previous PhD student (Al-Sharrad, 2013). After the first test from the main testing programme was conducted on an unsaturated sample, the main logging/control software programme (i.e. Clisp Studio CS) and the firmware of all the pressure/volume controllers were upgraded, and the controllers were re-calibrated by VJ Tech. In addition, some devices, such as the pore water pressure controller, the pore air pressure controller and the load cell were repaired by VJ Tech, because they had pressure fluctuation problems when they were instructed to set and maintain or ramp pressure (the controllers) or they indicated spurious readings (the load cell). Again these devices were re-calibrated by VJ Tech Ltd.

After all controllers were re-calibrated by VJ Tech Ltd., a simple check was performed that the pressure readings from the cell pressure controller, the pore water pressure controller and the pore air pressure controller were consistent, by checking them in turn against each other. This confirmed consistency within $\pm$1kPa.

The volume change transducer was not returned to VJ Tech Ltd., and hence they were unable to provide a calibration of this transducer after upgrading of the Clisp Studio CS logging/control programme. The volume change transducer was therefore calibrated by the author against volume change readings from the pore water pressure/volume controller, using the arrangement shown in Figure 3.26. This calibration was undertaken under a line pressure of 900kPa (provided by the cell pressure controller).

The influence of the pressure on the pore water drainage line on the measurements from the volume change transducer was investigated by the previous PhD student (Al-Sharrad, 2013), to see if changes of pressure caused any significant changes of reading from the volume change transducer (due to compression of water in the line or expansion of the tubing and tube connections). The results showed that the influence of the pressure on the pore water drainage line was insignificant and that there was no

need to include any calibration for this effect. Therefore, this check was not repeated here.

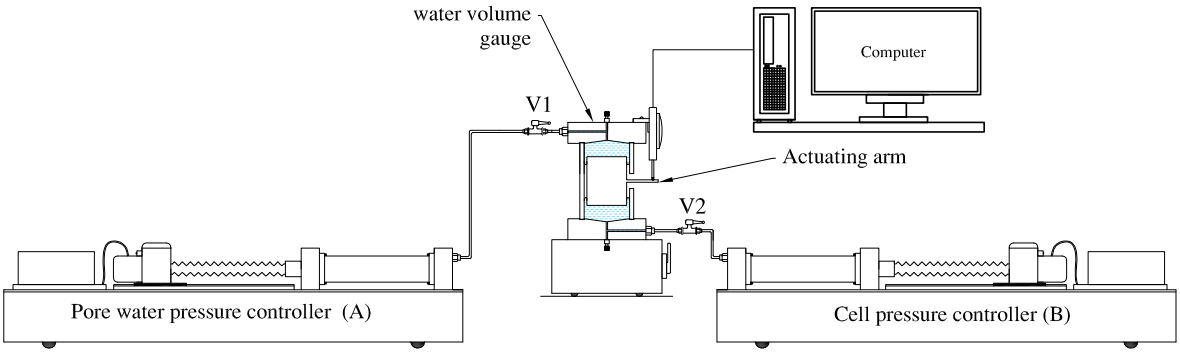

Figure 3.26: Volume change transducer calibration system

3.5 Calibration of suction-controlled triaxial cell

The suction-controlled double wall triaxial cell was designed to provide accurate measurements of the volume change of unsaturated soil samples, by monitoring the flow of water into or out of the inner cell. The double wall construction (with equal pressure in both inner and outer cells) should prevent any expansion of the inner cell wall with changing cell pressure, and the use of a glass inner cell wall (rather than acrylic) avoids water absorption by the inner cell wall. However, several important factors must still be taken into account before using the cell. Firstly, the influence of increasing and decreasing cell pressure (leading to compression or expansion of the water in the cell and expansion or contraction of the tubing and tube fittings) must be calibrated. Secondly, the effect of temperature fluctuations in the laboratory on expansion or contraction of the water inside the inner cell and the components of the inner cell should be carefully calibrated. Lastly, the volume displaced by movement of the load cell's loading ram into the inner cell (see Figure 3.8) must be calibrated.

3.5.1 Influence of changing cell pressure

Figure 3.27 shows the results of a calibration test, where a rapid change of cell pressure from zero to 750kPa was applied. In performing this calibration test there was no soil sample within the triaxial cell, but a dummy aluminum sample of similar size was included (enclosed in the same type of rubber membrane as used for soil testing). The dummy aluminium sample was effectively rigid, as it would have compressed less than 0.002cm^3 under the application of 750kPa pressure. All the other components that would normally be present within the inner cell during testing of soil samples were included in this calibration test. This included the base pedestal and top cap, the load

cell, the six BEEs and their cables (although these were not mounted on the dummy sample) and the various internal tubes providing pore water and pore air connections to the base pedestal and top cap (see Figure 3.8). Any displacement of the load cell's loading ram into the inner cell was avoided by the simple expedient of not fixing it to the upper supporting plate (see Figure 3.8).

Inspection of Figure 3.27 shows that the application of the rapid change in cell pressure from zero to 750kPa caused an immediate flow of approximately 9cm^3 of water into the inner cell. This was attributed to a combination of compression of the water within the cell (estimated at 2cm^3 from the bulk modulus of water), the initial compression of any air trapped within the cell or within any of the components inside the cell, the compression of any compressible elements inside the cell (such as the load cell, the BEEs and the tubes) and the expansion of the various tubes and tube connections external to the cell. The immediate inflow of 9cm^3 was followed by a further inflow of approximately 1.3cm^3 over the next 8 days (see Figure 3.27), after which there was no further significant inflow or outflow, other than small oscillations attributable to temperature fluctuations (see Section 3.5.2). The time-dependent water inflow over the first 8 days was attributed to dissolution of any remaining air within the inner cell or within any of the components inside the cell.

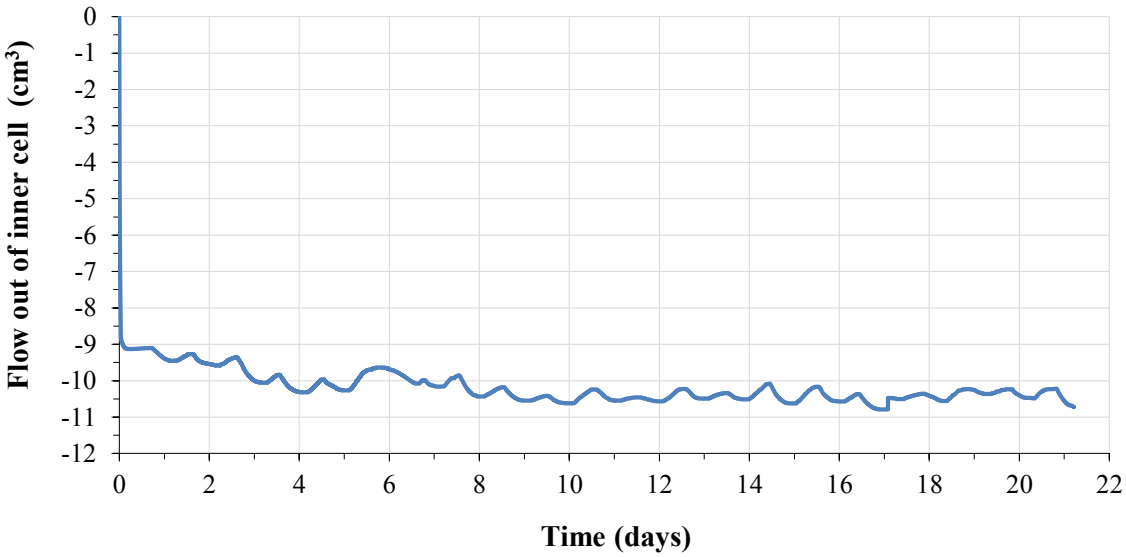

Figure 3.27: Influence of a step change of cell pressure

The immediate inflow of 9cm^3 shown in Figure 3.27 was larger than the equivalent figure reported by Al-Sharrad (2013), who used the same suction-controlled triaxial cell. This difference was attributed to the inclusion of the BEEs and their cables. Al-Sharrad (2013) and Raveendiraraj (2009) (who used a different suction-controlled

triaxial cell) both concluded that the immediate water inflow with change of cell pressure could not be accurately calibrated, as it was not repeatable. This lack of repeatability is probably attributable to factors such as variation of the volume of trapped air between one test and another. Al-Sharrad (2013) therefore decided to avoid the need for this calibration, by maintaining cell pressure constant in all tests whilst applying change of net stress and matric suction by varying pore air pressure and pore water pressure. It was decided to take the same approach in this work, by applying a constant cell pressure of 900kPa in all tests. This avoided the need for a calibration of water inflow to the inner cell with change of cell pressure. The procedure employed when initially applying the cell pressure of 900kPa to an unsaturated soil sample was designed to ensure that it was reasonable to assume negligible change of sample volume during cell pressure application (see Section 4.3.1).

By simply assuming no immediate change of soil sample volume during application of the cell pressure of 900kPa, the influence of the type of immediate inflow of water into the inner cell shown in Figure 3.27 could be removed. However, the type of subsequent time-dependent inflow shown over the next 8 days in Figure 3.27 would result in a corresponding error in the measurement of sample volume change over this initial period of a test. The magnitude of this error was estimated at approximately $1cm^3$ under a cell pressure of 900kPa (slightly less than under the cell pressure of 750kPa shown in Figure 3.27, because of the additional compression of air prior to dissolution at a higher pressure). This would result in an error of approximately 0.01 in the value of specific volume v of an unsaturated soil sample determined at the end of the initial equalization stage of a typical test (see Section 4.3.1).

During the calibration test shown in Figure 3.27, a number of step changes to the pore water pressure in the tubing within the inner cell were applied (see Section 3.5.4). These step changes of pore water pressure had no visible impact on the results in Figure 3.27, suggesting that any expansion of the lengths of tube within the inner cell with changing pressure was negligible, and that time-dependent effects such as water diffusion through the tube walls within the inner cell were also negligible. There was therefore no need to provide any correction for these effects on the measured inflow of water to the inner cell.

3.5.2 Calibration for temperature fluctuation

The testing laboratory was temperature controlled to $\pm 1^oC$ (as described in Section 3.3.5). However, the small remaining temperature fluctuations still had a noticeable effect on the water inflow or outflow to the inner cell, due to thermal expansion of the water within the cell and of the cell components. These effects are visible in the

"ripple" in the results of the calibration test shown in Figure 3.27. It was considered desirable to attempt to correct for this remaining temperature-induced effect, and hence a thermocouple was installed within the cell (see Figure 3.8).

By observing the water inflow and outflow to the inner cell when the laboratory temperature control was switched off, and there were significantly larger temperature fluctuations, it was concluded that the temperature effect was an outflow from the inner cell of approximately 0.65cm^3 for every 1^{o}C rise of temperature. Figure 3.28 shows the effect of applying this temperature correction of 0.65cm^3/^{o}C to the calibration test results shown in Figure 3.27 (when the laboratory temperature control was operating). Comparison of the green (corrected) line with the black (uncorrected) line in Figure 3.28 shows that the application of the temperature correction reduced the amplitude of oscillations in inflow/outflow to the inner cell, but significant oscillation still remained and additional shorter timescale "noise" had been introduced. This can be attributed to the fact that the thermocouple was measuring the temperature in the outer cell, whereas the inflow/outflow to the inner cell was affected by the temperature of the inner cell and the water within it. Siting of the thermocouple within the inner cell was not feasible, because of the congestion of the various connections through the inner cell base plate. The temperature correction of 0.65cm^3/^{o}C was applied to all test results, and it was concluded that the remaining temperature-induced oscillations, with an amplitude of approximate 0.15cm^3 (see Figure 3.28), were acceptable.

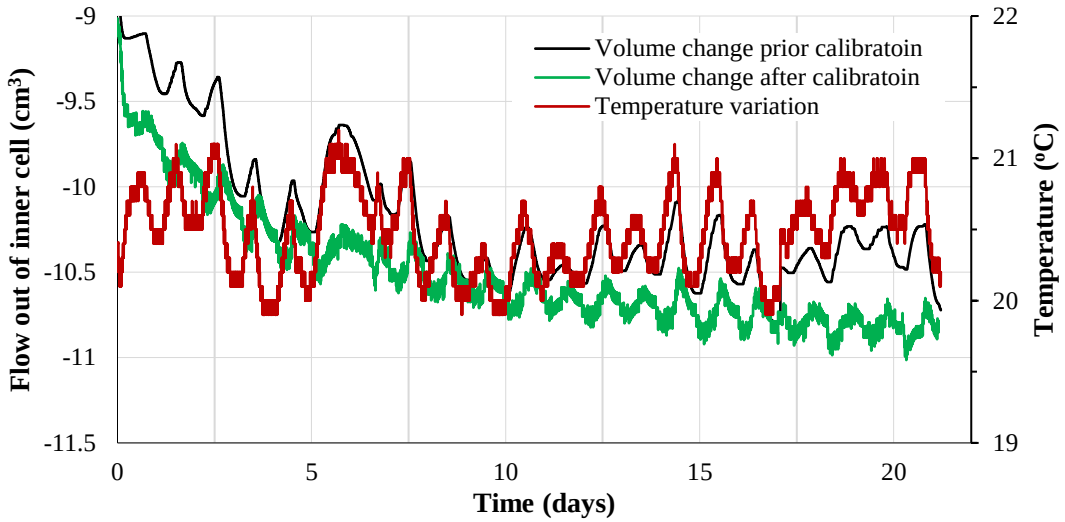

Figure 3.28: Influence of correction for temperature fluctuation

3.5.3 Calibration for load cell ram displacement

Application of deviator stress on soil samples during testing with the modified double wall triaxial cell was performed by vertical movements (upward for triaxial compression

loading and downward for triaxial extension loading) of the loading ram attached to the inner cell base plate (see Figure 3.8). This produced corresponding vertical penetration of the load cell and its loading ram into the top of the inner cell (see Figure 3.8). The water inflow/outflow to the inner cell therefore had to be corrected for this penetration of the load cell ram into the inner cell. Figure 3.29 shows the results of the calibration test for this effect giving a calibration factor of 0.4974 cm^3/mm (i.e. an effective ram area of 497.4mm^2).

3.5.4 Calibration of pore water drainage line

The pore water pressure/volume controller was used to measure the flow of water into or out of the soil sample. It was considered necessary to check whether this measurement needed to be corrected for any effects of varying the pressure in the pore water drainage line (given that tests on unsaturated soil samples were performed by holding the cell pressure constant and varying the pore air pressure and pore water pressure, see Section 3.5.1).

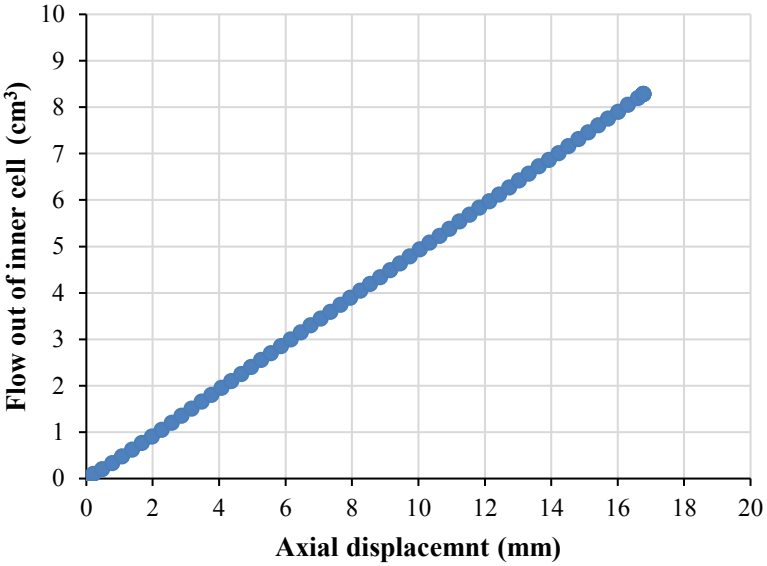

Figure 3.29: Calibration for loading ram movement

Calibration of this effect was performed as part of the same calibration test as used for checking the influence of cell pressure on inflow/outflow to the inner cell (i.e. the same test as shown in Figure 3.27). This was achieved by applying within the test a number of step decreases and step increases to the pressure within the pore water drainage line. During the test, the internal pore water drainage tubes were not connected to the base pedestal and the top cap (as they would be during testing of soil samples). Instead the two tubes normally connected to the base pedestal were replaced by a single tube (of equivalent length) connecting directly between the two relevant ports

in the inner cell base plate (see Figure 3.8). A similar arrangement replaced the two tubes normally connected to the top cap.

Figure 3.30 shows the results of this calibration test, with the values of pressure applied to the pore water drainage line included on the figure. It is clear that the step changes of pressure in the drainage line caused step changes in the volume measurements by the pore water pressure/volume controller. This can be attributed to the compression of the water in the lines and in the cylinder of the pressure/volume controller as well as to any expansion of the tubes and fittings. Figure 3.30 also indicates time-dependent changes of volume measurement. This can be attributed to diffusion of water through the external and internal PTFE tubes of the pore water drainage lines (although water diffusion rates through the PTFE tubes are significantly lower than through standard nylon tubes, they are not zero (Raveendiraraj, 2009)).

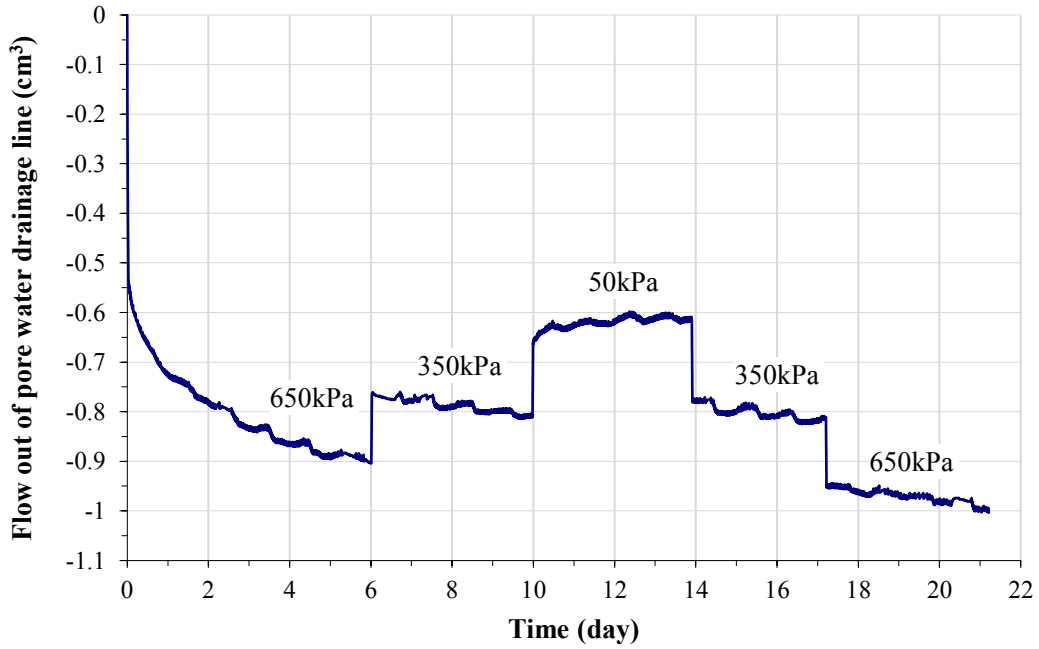

Figure 3.30: Calibration test of pore water drainage line

Inspection of Figure 3.30 shows that, under a constant pore water pressure condition, it was possible for the net diffusion of water through the PTFE tube walls of the pore water drainage line to be either into the drainage line (when the pore water pressure was 50kPa) or out of the drainage line (when the pore water pressure was 350kPa or 650kPa). Inward diffusion of water occurred over that part of the drainage line that was inside the triaxial cell, where the external pressure provided by the cell pressure of 750kPa was greater than the internal pressure provided by the pore water drainage line pressure of 650kPa, 350kPa or 50kPa. Conversely, outward diffusion of water occurred over that part of the drainage line that was outside the triaxial cell,

where the internal pore water drainage line pressure of 650kPa, 350kPa or 50kPa was greater than the external pressure corresponding to the atmospheric pressure in the laboratory (i.e zero). The relative importance of these two effects and hence the net rate of diffusion depended upon the value of pressure on the pore water drainage line.

Figure 3.30 suggested that average time-dependent diffusion rates of water into or out of the pore water drainage line would rarely exceed 0.01cm^3/day. Water diffusion at this rate would influence the calculated variation of degree of saturation S_r of a typical unsaturated soil sample by less than 0.001 over the duration of a typical test stage. Hence, it was decided that correction for the water diffusion into or out of the pore water drainage line was unnecessary.

Figure 3.31 shows calibration for the immediate inflow of water into the pore water drainage line due to the application of pressure on this pore water drainage line as the pressure was increased from 50kPa to 650kPa (purple line), decreased backed to 50kPa (blue line) and then increased again to 650kPa (red line). The data points shown in Figure 3.31 were taken from the vertical steps shown in Figure 3.30. Inspection of Figure 3.31 shows that there was an irreversible component of water inflow during the first pressure increase (this was attributed to the uptake of slackness in tube fittings, etc), whereas the outflow and inflow was essentially reversible during subsequent pressure decreases and increases. During tests on soil samples, the initial pressure on the pore water drainage line was high (see Section 4.3.1) and hence calibration for this effect was based on a linear regression through the reversible behaviour observed during the pressure decrease and second pressure increase in Figure 3.31. This gave a calibration factor of 0.0005cm^3/kPa.

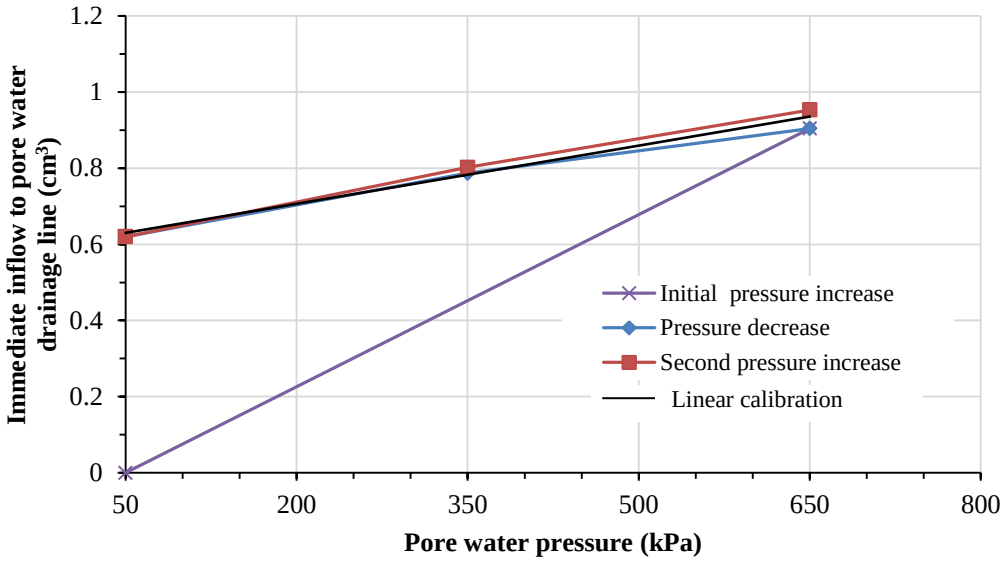

Figure 3.31: Calibration of pore water drainage line with pressure

3.6 Logging and control system

The main suction-controlled triaxial test system was logged and controlled by a data logger (Model MPX3000) and a PC using logging/control software (Clisp Studio CS) developed by VJ Tech Ltd. This included logging of the load cell, axial displacement gauge, volume change transducer and thermocouple, together with logging and control of the automated water pressure/volume controllers (for cell pressure, pore water pressure and ram pressure) and the automated air pressure controller (for pore air pressure) as shown in Figure 3.21. The BEEs were logged and controlled separately, as described in Section 3.2.4, using master and slave control boxes and the GDSBES software (which was mounted on the same PC as the main Clisp Studio software) as shown in Figure 3.21.

During a test on a soil sample, various different types of stress path or test stage could be controlled by the CS software. This included suction equalization stages, wetting or drying stages, isotropic loading or unloading stages and shearing stages using either stress control or strain control (see Section 4.3). The CS software logged the various transducers and controlled the various water pressure/volume controllers and the air pressure controller in order to follow the required stress path.

Existing code written within CS by the previous PhD student (Al-Sharrad, 2013), was replaced with a new version of the code, developed by the author, to meet the requirements of the main testing programme in this PhD. Prior to commencing any test stage, initial parameters for the stage (such as initial sample height, initial sample volume, initial deviator force and initial temperature) had to be fed into the CS software as input data. Using these input parameters and the measured outputs from all the various transducers and controllers, key variables were calculated within the CS software. These included matric suction s , deviator stress q and mean net stress $\bar{p}$. The CS software allowed users to save and use all input data, measured variables and calculated variables in MS Excel and Matlab spreadsheets for further analysis and assessment. Variables such as specific volume v , degree of saturation S_r , axial strain ε_a , volumetric strain ε_v and shear strain ε_s were only calculated subsequently in MS Excel spreadsheets.

As mentioned in Section 3.4, after performing the first test from the experimental programme, it was decided to send all the devices of the system (excluding the double wall cell) back to VJ Tech in Reading, UK, for repair (the pore water pressure controller and the load cell), re-calibration (all devices) and upgrading of the CS software and firmware of the controllers, due to some issues relating to the load cell (giving spurious readings) and both the pore air pressure controller and the pore water pressure controller (significant pressure fluctuations). After the process of repair, re-calibration

and upgrading was completed by VJ Tech, all devices for the system had to be reconnected (see Figure 3.21), redefined within CS and checked for any possible electronic problems. In addition, some devices such as the volume change transducer had to be re-calibrated from scratch as explained in Section 3.4.

Figure 3.32 shows a typical interface of the upgraded CS software. Details about the pressure and volume measurements from each of the 4 controllers and how they are currently being controlled are given in the left and the bottom of the screen, whereas, other measured and calculated variables are given in the top right and top centre of the screen.

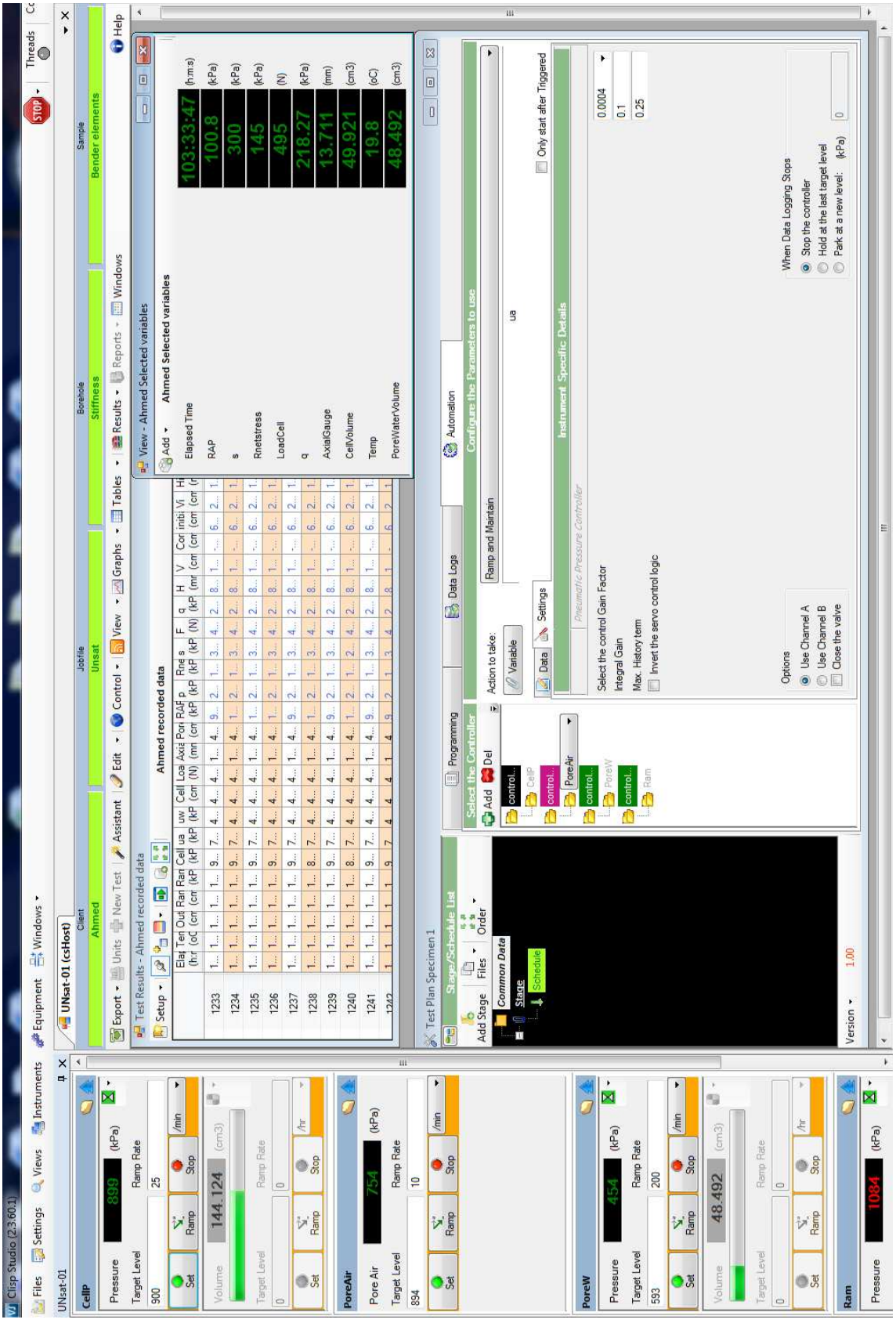

Figure 3.32: A typical interface for the upgraded CS software

Chapter 4

Sample preparation and experimental procedure

This chapter describes how isotropic and anisotropic soil samples were prepared and how saturated and unsaturated samples were set up and tested. In addition, the various different types of test stages are described, and methods of data processing for saturated tests, unsaturated tests and bender/extender element (BEE) testing are explained.

4.1 Sample preparation

4.1.1 Soil selection

Compacted speswhite kaolin clay was selected to be used in this experimental testing programme. Index properties of the speswhite kaolin clay are presented in Table 4.1. Figure 4.1 shows results from the standard Proctor compaction test, which was performed according to the British Standard (BS part 4:1990). It is clear from Figure 4.1 that the values of maximum dry unit weight and optimum water content were approximately 14.1kN/m^3 and 29%, respectively. One of the main reasons to select compacted speswhite kaolin clay was that it was possible to set the results from the current experimental study (focussing on small strain behaviour measured with BEEs) within the context of results from other researchers, who have studied other aspects of behaviour of this same soil, including volumetric behaviour and critical states (Sivakumar, 1993), coupling of mechanical behaviour and water retention behaviour (Raveendiraraj, 2009) and evolving anisotropy in large strain (plastic) behaviour (Al-Sharrad, 2013). With speswhite kaolin compacted dry of optimum, it was possible to produce samples with a relatively low air entry value (for a clay), which was compatible with the existing

Table 4.1: Index properties of compacted speswhite kaolin clay

Maximum dry unit weight (kN/m^3) (Standard Proctor Test)	14.1
Optimum water content (%)	29
Percentage of sand (%)	0
Percentage of silt (%)	25
Percentage of clay (%)	75
Specific gravity	2.60
Liquid limit (%)	68
Plastic limit (%)	36
Plasticity index (%)	32
Classification (USCS)	MH

suction-controlled triaxial apparatus, which is suitable for controlling suction in the range from 0 to 400kPa. In addition, it was possible to produce repeatable samples of this soil (see Section 6.1) in terms of initial conditions such as specific volume, degree of saturation and particle arrangements (fabric), which was crucial in researching soil behaviour. Finally, using compacted kaolin clay minimised the time involved in sample testing, compared to other unsaturated clays, because the rate of consolidation in the kaolin clay is faster than in most other clays. On the other side, the actual behaviour of natural clays might not be completely represented by the behaviour of the relatively homogenous compacted kaolin samples.

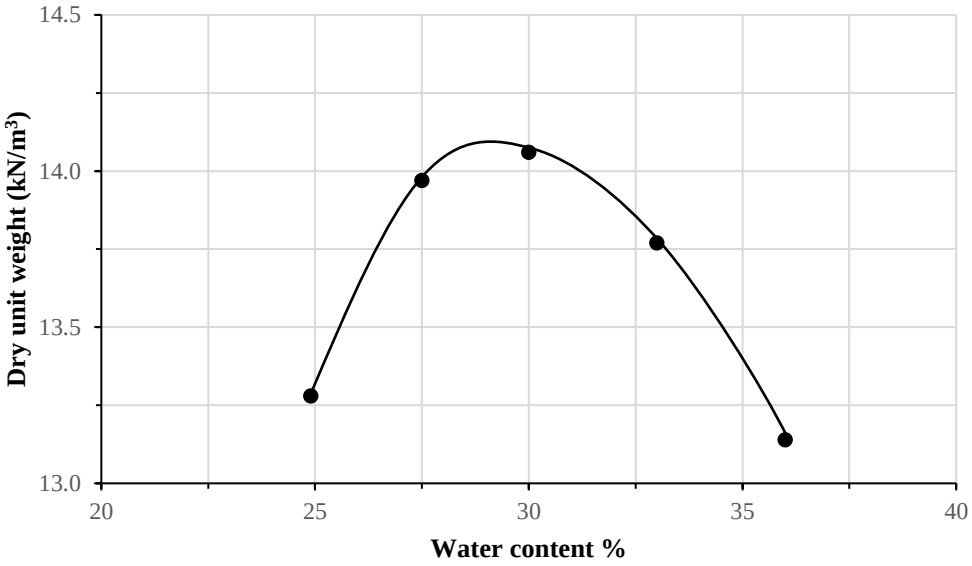

Figure 4.1: Standard Proctor compaction curve of the speswhite kaolin clay of the current project

4.1.2 Kaolin aggregate preparation

In order to prepare the kaolin for compaction, a measured amount of oven-dry kaolin clay powder (1000g for each isotropically compacted sample and 1200g for each anisotropically compacted sample) was manually mixed with tap water at a water content of 25% (approximately 4% dry of the optimum from the standard Proctor compaction test). This was the same compaction water content as employed by Sivakumar (1993), Raveendiraraj (2009) and Al-Sharrad (2013). The compaction water content of 25% was selected for the following reasons. Firstly, in order to compare results in the current study (small strain behaviour) with the results from the previous studies (mentioned above), it was sensible to use the same compaction water content (i.e. 25%), because using a different compaction water content would have produced soil with entirely different fabric and hence different mechanical behaviour (Sivakumar & Wheeler, 2000). Secondly, compaction of speswhite kaolin at a water content of 25% produced a bi-modal pore size distribution, with macro-pores between aggregates and micro-pores within these aggregates (i.e. between individual soil particles). This form of soil fabric provided compacted samples with relatively low air entry value, such that it was possible to cover a reasonably wide range of degree of saturation S_r (approximately $0.6 < S_r < 1.0$) using the rage of suction values achievable in the suction-controlled triaxial apparatus ($0 \leq s \leq 400$ kPa). Finally, this type of fabric produced by compaction dry of optimum is likely to produce a potential for larger magnitudes of collapse compression on wetting than the type of fabric produced by compaction wet of optimum.

After breaking up larger lumps of the kaolin/water mixture using a mortar and pestle, the mixture was then passed through a sieve with aperture of 2mm to create kaolin aggregates with a maximum size of 2mm (the same as Al-Sharrad, 2013). The maximum size of aggregates in the samples prepared by Sivakumar (1993) and Raveendiraraj (2009) was slightly smaller (1.18mm). The maximum aggregate size selected in this study was chosen for the following reasons. First, according to ASTM D2845 (1997), the maximum size of the aggregates should be smaller than $\lambda/3$, where λ is the wavelength of shear or compression waves used in the BEE tests, because larger aggregates would mean that the soil would not behave as a continuum in transmitting shear and compression waves and hence the wave velocities would not depend upon the bulk values of elastic moduli of the sample. Secondly, the size of the aggregates (2mm) compared to the diameter of the samples (50mm) was small enough to avoid any scaling effect on the mechanical behaviour of the samples. Thirdly, typical aggregates had to be sufficiently large to ensure relatively large macro-voids between aggregates and hence a relatively low air entry value for the soil samples. Finally, the maximum size of aggregates should not be too large, so that it was possible to perform tests within a manageable time scale. This issue arises because the time for equalization of pore

water pressure within the sample can depend upon the time required for water to flow between the interior of a low permeability aggregate and an adjacent macro-void.

The mixing and sieving process lasted about 45 minutes. After that the mixture was transferred to a plastic bag. To avoid any loss of moisture from the mixture, it was stored and sealed in two bags and kept inside a sealed container in a temperature-controlled room for 24 hours, which allowed the moisture to be equally distributed. The mixing process and all other steps, including soil compaction, sample coring and sample trimming (see Section 4.1.3), were performed in the same temperature-controlled room as the main testing programme, which ensured repeatable conditions during preparation of the samples. As a consequence the variation of the initial moisture content in all samples in this study did not exceed ±0.35% (see Section 6.1).

4.1.3 Preparation of isotropic and anisotropic samples

Sivakumar (1993) examined the effect of different types of compaction on repeatability and homogeneity of speswhite kaolin clay samples. He examined kneading, dynamic compaction and static compaction techniques. He concluded that static compaction was the most reliable method to produce repeatable and homogenous samples in terms of physical properties such as void ratio.

In the current project, all isotropic and anisotropic samples were compacted statically within a latex rubber membrane in a large triaxial cell (see next paragraphs). Sivakumar (2005) developed a technique to prepare isotropic compacted samples using a large triaxial cell. He placed the kaolin-water mixture within a 100mm diameter cylindrical latex membrane and then compressed this isotropically inside a large triaxial cell, allowing dissipation of pore air pressure through the base pedestal and the top cap. A smaller 50mm diameter cylindrical sample was then cored from the larger but rather irregular cylinder of soil created by this isotropic compaction. Sivakumar (2005) showed that this technique produced repeatable and homogenous isotropic samples. Al-Sharrad (2013) subsequently developed the technique to produce both isotropic and anisotropic statically compacted samples. For the anisotropic samples, radial stress and deviator stress were employed during initial compaction of the large sample in the triaxial apparatus. Hence, the anisotropic samples were prepared by compaction under a prescribed anisotropic stress path, rather than by more conventional one-dimensional compaction in a mould (which corresponds to a prescribed anisotropic strain path during compaction). The current study used similar methods to Al-Sharrad (2013) for preparing isotropic and anisotropic samples of compacted speswhite kaolin.

Figures 4.2 and 4.3 show the compaction apparatus used to produce isotropic and anisotropic samples. A triaxial cell for testing samples up to 100mm in diameter and a loading frame were used for preparing isotropic and anisotropic samples, with other tools including a cylindrical rubber membrane, a membrane stretcher, a perforated acrylic filter, two perforated rubber latex sheets, two unperforated rubber latex sheets, a top cap, four O-rings, silicon oil and a modified funnel. After putting a thin layer of silicon oil on the outer surface of the base pedestal, the bottom of the rubber membrane was fitted to the base pedestal by means of two O-rings. After that, the rubber membrane was inserted inside the membrane stretcher and the top of the membrane was folded over the stretcher. After removing trapped air between the stretcher and the membrane (by applying a small vacuum), the perforated acrylic filter and two perforated rubber latex sheets lubricated with silicon oil (to minimize end effects) were placed on the base pedestal to allow air to be expelled from the soil through the drainage connections in the base pedestal during the compaction process. The soil-water mixture was then placed evenly within the rubber membrane, using the funnel. After pouring the mix into the membrane, the top of the soil was levelled and then two lubricated (unperforated) rubber sheets and the top cap were carefully placed on top. The top of the membrane was then unfolded from the stretcher, the stretcher was removed and the top of the membrane was sealed on the top cap using two O-rings.

Figure 4.2: 100mm diameter triaxial cell and tools used for compacting samples

After assembling the triaxial cell, the cell was placed on the loading frame (see Figure 4.3). For isotropic compaction, compressed air was used to apply cell pressure, with

the pressure increased at a constant rate of 3 kPa/minute to the required final compaction value. For anisotropic compaction, deviator stress was applied with the compression frame by increasing axial displacement at a constant rate of 0.75mm/minute, with deviator force measured with an external proving ring (see Figure 4.3). The deviator stress q was then estimated (by assuming that the cross-sectional area remained unchanged during compaction) and the cell pressure (provided by compressed air) was then manually adjusted to keep the sample on a predefined stress path with $\eta = q/\bar{p} = 1.2$.

Figure 4.3: Loading frame and triaxial cell used for compacting samples

Figure 4.4 shows the compaction stress paths in the $q : \bar{p}$ plane. Anisotropic samples were prepared by an initial isotropic compaction stage ($\eta = q/\bar{p} = 0$) to $\bar{p} = 100$kPa, followed by an anisotropic compaction stage $\eta = q/\bar{p} = 1.2$ to $\bar{p} = 250$kPa, $q = 300$kPa. This second stage was achieved with a cell pressure σ_r of 150kPa and an axial stress σ_a of 450kPa, with the pore air pressure u_a assumed to be zero (given the high compressibility of air and the high value of air permeability, with air drainage allowed from the base of the sample during compaction). This form of anisotropic compaction procedure was identical to that used by Al-Sharrad (2013) and was found to give a specific volume v of approximately 2.17 (see Figure 4.5), consistent with the experience of Al-Sharrad (2013).

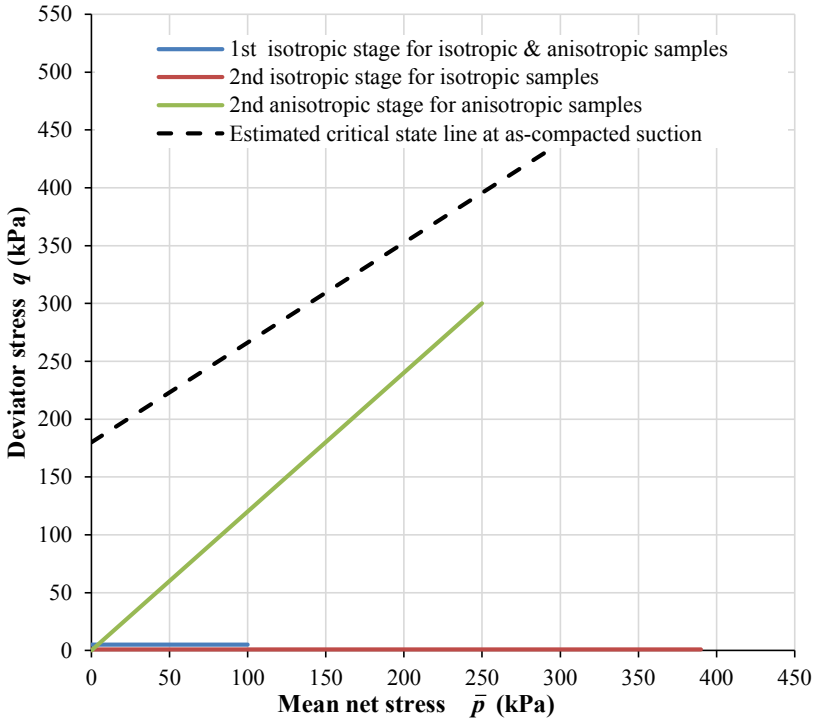

Figure 4.4: Stress paths for isotropic and anisotropic compaction

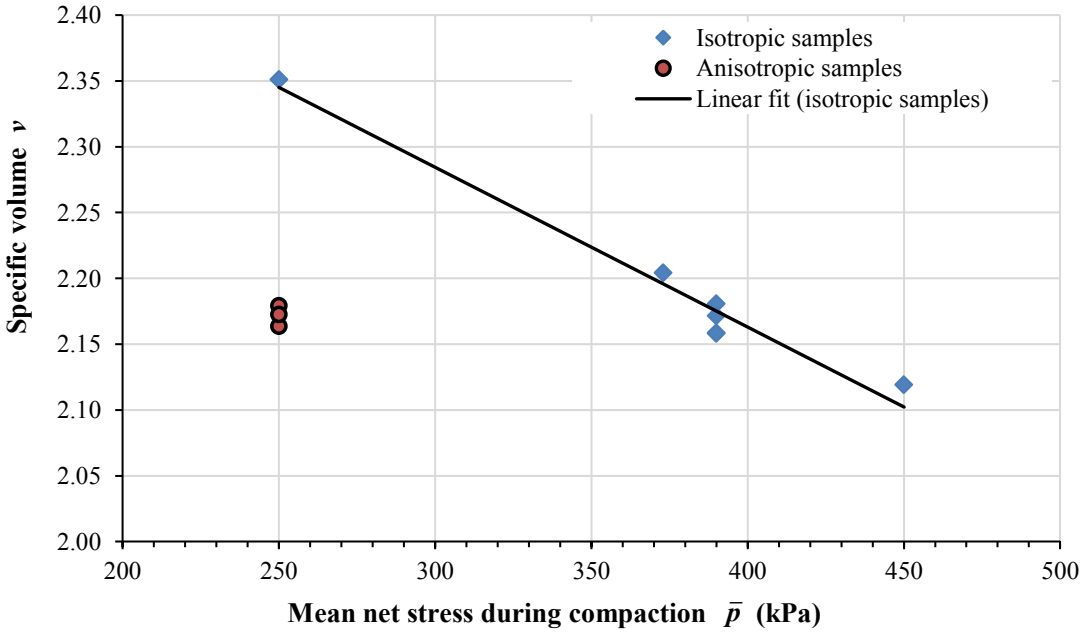

Figure 4.5: Isotropic and anisotropic compaction

Isotropic samples were prepared by an initial isotropic compaction stage ($\eta = q/\bar{p} = 0$) to $\bar{p}$ = 100kPa, followed by a second isotropic compaction stage ($\eta = q/\bar{p} = 0$) to a higher value of $\bar{p}$ (see Figure 4.4). The intention was to develop an isotropic compaction procedure that produced samples with the same initial specific volume as

the anisotropic compaction procedure described above ($v \approx 2.17$). Isotropic samples were therefore prepared using a variety of different values of $\bar{p}$ in the second compaction stage (see Figure 4.5) and, on the basis of the results, a value of $\bar{p} = 390$kPa was selected for isotropic compaction.

At the end of the compaction process (after unloading the sample), the large roughly cylindrical sample was removed from the triaxial cell and placed on the pedestal of a loading frame (see Figure 4.6). A cored sample with 50mm diameter was then taken by means of a standard 50mm oedometer ring attached to a cylindrical acrylic tube (with an internal diameter slightly larger than 50mm to avoid side friction) which was driven into the large soil sample at a rate of 5mm/minute. A split mould with 50mm diameter and 100mm height (see Figure 4.7) was then used to trim the height of the cored sample. Although the large compacted sample was sandwiched between two double lubricated latex sheets at the ends (to reduce end effects), the large sample was still not a perfect cylinder; therefore the split mould was placed at the middle of the cored sample to reduce end effects. Samples with height of 100mm were used for those tests involving isotropic loading or triaxial compression loading, whereas samples with the height of 75mm were used for those tests involving triaxial extension loading. This was because the loading ram travel in the suction-controlled triaxial cell was insufficient to allow triaxial extension testing of 100mm height samples.

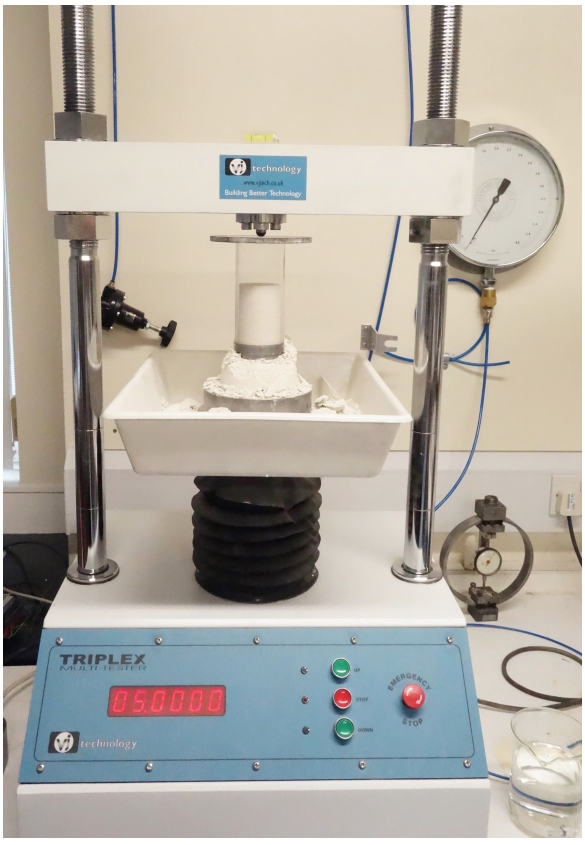

Figure 4.6: Taking a cored sample from the large sample

After trimming the ends of the sample, 6 slots (2 slots at the ends and 4 slots at the mid-height of the sample) were formed within the sample (see Figure 4.7), in order to mount the 3 pairs of BEEs on the sample without causing any damage to the BEEs. The slots were required because the soil samples were too strong to simply push the BEEs into the soil without resulting damage to the BEEs. The slots were formed by pushing dummy BEEs into the soil sample through the split mould (see Figure 4.7). The blades on the dummy BEEs were sized to produce slots that were slightly smaller (in width, height and depth) than the dimensions of the real BEEs. This was to ensure good contact between soil and BEEs when the latter were subsequently installed.

Figure 4.7: Special split mould for trimming and slotting samples, dummy BEEs and a fully prepared sample

4.2 Experimental procedure

4.2.1 Saturation of HAE ceramic filters

Before commencing any test on an unsaturated sample, the HAE ceramic filters were saturated with water to prevent air entering the pore water drainage lines from the unsaturated soil sample by passing through the HAE filters in gaseous form. The saturation of the filters was performed by carefully flushing all drainage lines with water, including the pore air drainage line (but prior to subsequently setting up a soil sample, the water inside the pore air drainage line was flushed with air using the pore air pressure controller), and then assembling the outer cell of the double wall triaxial cell including both the base pedestal and top cap with their HAE ceramic filters. The cell was filled with de-aired water and then a cell pressure of 900kPa was applied for 24 hours in order to dissolve any existing air bubbles within the HAE ceramic filters and the triaxial cell. For the same period of 24 hours, external sections of the pore water drainage lines were pressurized to 800kPa, to dissolve any air bubbles within these lines, but with the valves on the lines closed so that they were not connected to the base pedestal and top cap.

After 24 hours of pressurization, the valves on the various pore water drainage lines were opened, so that water flowed from the cell through the HAE ceramic filters and along the pore water drainage lines. This flow was generated by the pressure difference of 100kPa between the cell (at a pressure of 900kPa) and the pore water drainage lines (at a pressure of 800kPa). The flow was maintained for 24 hours, to remove the water containing dissolved air from the system, so that the air bubbles did not simply re-form when the pressure was subsequently reduced. After 24 hours, the pressure on the pore water drainage lines was gradually reduced to 50kPa generating a high pressure difference of 850kPa and hence a high flow of water from the cell to the pore water drainage lines. Finally both cell pressure and pore water drainage line pressure were reduced to zero. The saturation process was applied simultaneously for the HAE ceramic filters in both the base pedestal and the top cap.

At the end of the saturation process, the water inside the pore water pressure controller and the cell pressure controller was changed with freshly de-aired water before starting a test on a soil sample.

4.2.2 Setting up unsaturated samples

After saturation of the HAE ceramic filters, all valves on pore water drainage lines were closed. In order to avoid de-saturation of the HAE ceramic filters, the top cap was placed inside a container filled with water and a smear of water was maintained on the top surface of the base pedestal.

Care had to be taken to avoid de-saturation of the HAE ceramic filters when an unsaturated soil sample (with large negative pore water pressure) was placed directly on the HAE ceramic filters. To avoid this, some researchers, for example Sivakumar (1993) and Raveendiraraj (2009), used a piece of fuse wire to maintain a temporary separation between the HAE ceramic filters and the soil sample. Before starting the initial equalisation stage, they applied a relatively high mean net stress $\bar{p}$ of 50kPa on the sample in order to force the wires to penetrate into the sample to allow direct contact between the HAE filters and the sample. This penetration of the wires caused an error in measurement of specific volume of the sample. Sivakumar (1993) and Raveendiraraj (2009) concluded that it was not feasible to correct values of specific volume for this effect and they simply ignored it. This "fuse wire" technique was not used in the current study, because it was desirable to apply only a very low value of mean net stress ($\bar{p} = 10$kPa) during the equalization stage and this was insufficient to force the wires to penetrate into the soil sample. In addition, setting up samples in this research took approximately 4 times longer than previous studies by Sivakumar

(1993) and Raveendiraraj (2009), due to the time required for mounting the horizontal BEEs on the sample.

Al-Sharrad (2013) used a technique which was entirely different from the "fuse wire" technique. During setting up an unsaturated soil sample, he directly placed the sample on the HAE ceramic filter of the base pedestal but with all valves on the pore water drainage lines opened up to the pore water pressure controller (the controller was instructed to hold water volume constant, in order to monitor any change of water pressure occurring in the water drainage lines). Firstly, a vent valve was used to apply zero pressure (atmospheric pressure) in the pore water drainage lines. Once the unsaturated sample was placed on the HAE ceramic filter the pressure within the pore water drainage lines became increasingly negative as water was gradually extracted from the drainage lines into the sample, as a consequence of the large negative pore water pressure within the soil sample. Whenever the negative water pressure in the drainage lines reached -50kPa, the vent valve was opened for a second to bring the pressure in the line back to zero. The disadvantage of this technique was that a very small unmeasurable amount of water (less than $0.1cm^3$) was allowed to flow into the sample, which caused errors in the calculated initial values of water content and specific volume of the sample, given that the water content and the specific volume were assumed to be unchanged at the end of the setting up process.

In the current study, the technique of Al-Sharrad (2013) technique was used for avoiding de-saturation of the HAE ceramic filters when they came into contact with an unsaturated soil sample. However, it was crucial to ensure that the time duration over which this technique was employed was kept reasonably short, to ensure that the water inflow to the soil sample was small and hence that errors in the estimation of initial values of water content and specific volume were small. To ensure this, it was necessary to devise a procedure for attaching the horizontal BEEs to the rubber membrane (which was to enclose the soil sample) without the soil sample being in position. This procedure is described in the following paragraphs.

The process of setting up an unsaturated soil sample started by placing a slotted mould (see Figure 4.8) on the base pedestal. The slotted mould was supported on an O-ring which fitted in a groove on the base pedestal (see Figures 4.9a and 4.9b). Prior to this, the slotted mould has been lightly lubricated with silicon oil. A rubber membrane was then fitted to a membrane stretcher, which was then placed over the slotted mould (see Figure 4.9c). The bottom of the membrane was sealed on the base pedestal by two O-rings and the membrane stretcher was then removed (see Figure 4.9d). This was then followed by making four 5mm diameter holes in the rubber membrane for the horizontal BEEs. To make these holes a suitable tool was designed

and manufactured (see Figure 4.10). The 2 pairs of horizontal BEEs were dressed by means of blue grommets and an O-ring (see Figure 3.3), and they were then entered into the rubber membrane through the four holes by manually stretching out the membrane. To seal between the BEEs and the rubber membrane, four layers of liquid latex were applied (see Figure 4.9e) using a very soft brush. Each layer of liquid latex required approximately 30 minutes to dry before the next layer was applied. After the last layer of liquid latex had dried, an O-ring for each BEE was placed on the liquid latex layers to add an extra seal to the sealing process.

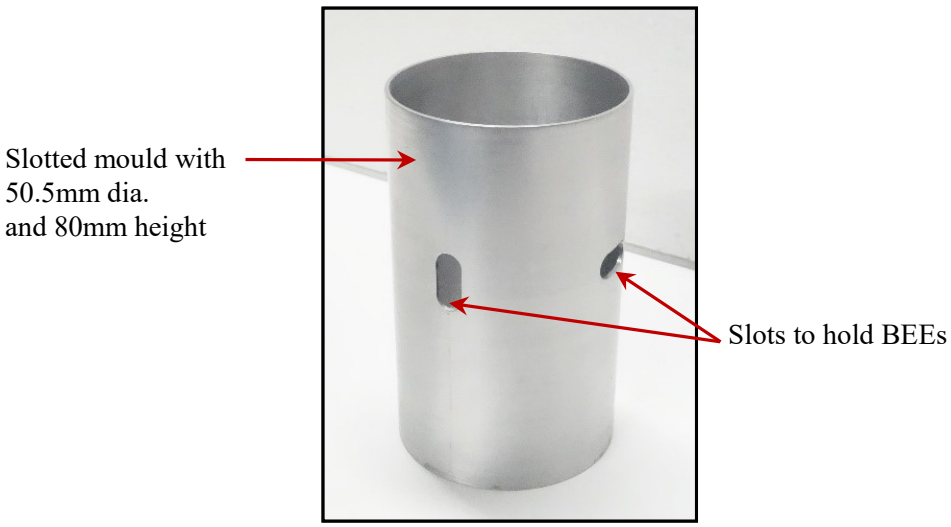

Figure 4.8: Slotted cylindrical mould

In order to lower a soil sample inside the slotted mould, the four horizontal BEEs were all pulled outwards slightly using four rubber bands attached to four vertical rods mounted on a metal frame (see Figure 4.9f). After folding the top part of the rubber membrane over the mould (see Figure 4.9f), the soil sample was lowered into place on the HAE filter of the base pedestal (all valves on the pore water drainage lines were opened up to the pore water controller at this point to avoid de-saturation of the HAE filter as described earlier). The next step was that the slotted mould was pulled out between the rubber membrane and the soil sample taking great care not to damage the soil sample. After ensuring that each of the four horizontal BEEs was properly aligned with the appropriate slot in the sample, the rubber bands were removed to allow the horizontal BEEs to insert into the slots. The top cap was then placed on top of the soil sample (all valves on the pore water drainage lines were opened up to the pore water controller) and the top of the rubber membrane was sealed on the top cap with two O- rings.

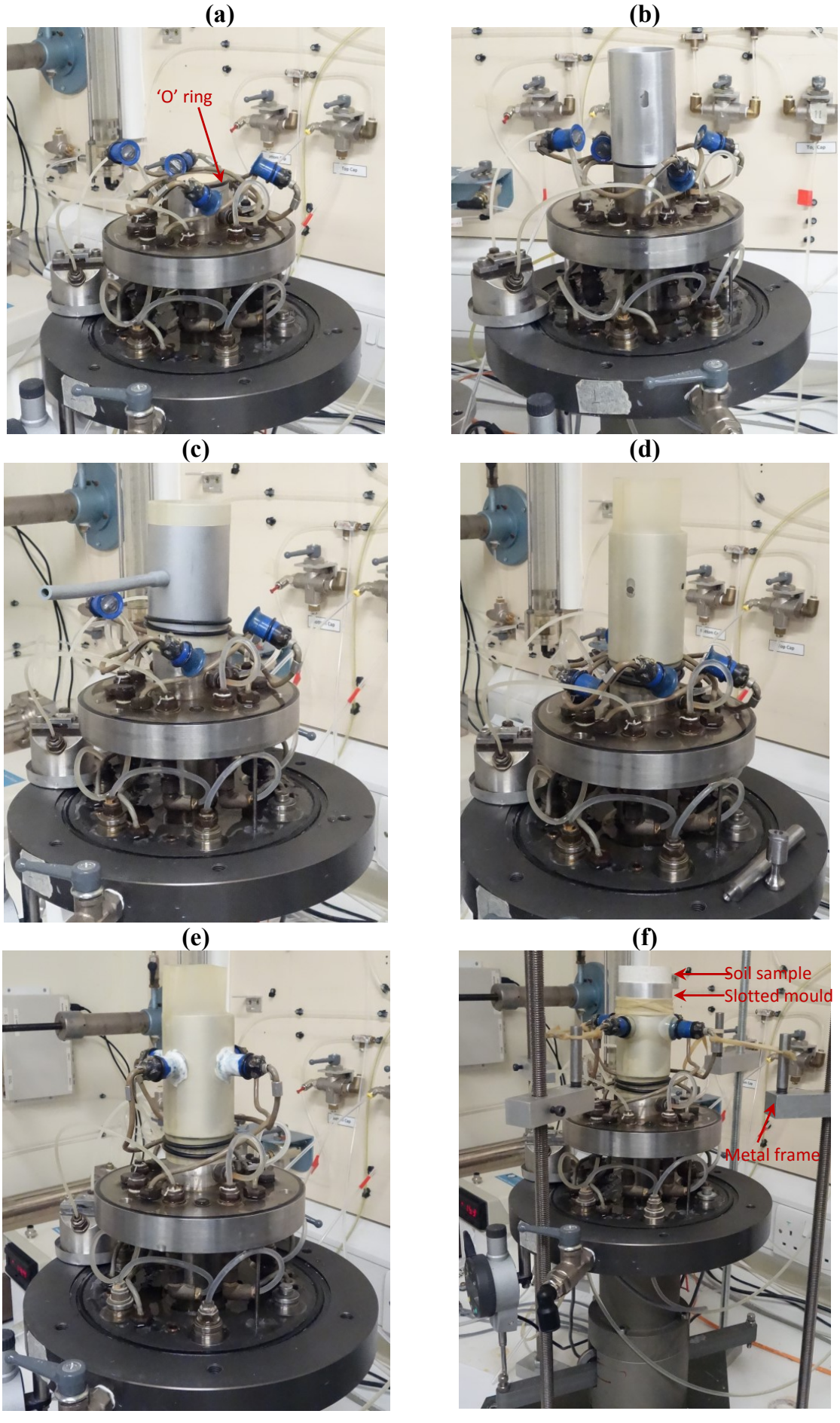

Figure 4.9: Setting up procedure

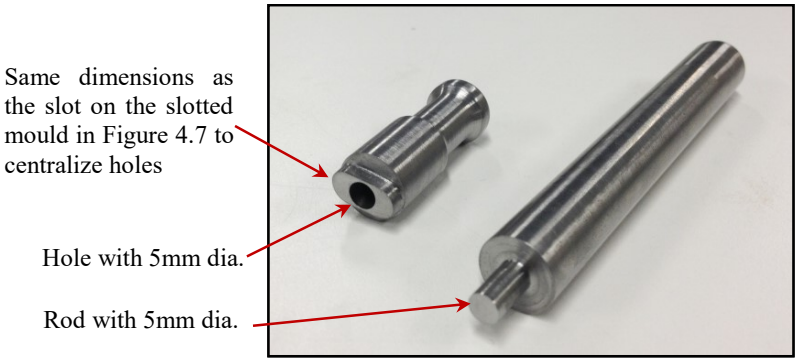

Figure 4.10: Tool used to make holes in rubber membrane

After installing the tie rods for inner and outer cells, the acrylic outer cell wall was placed on the base plate of the outer cell and temporarily clamped in place by using two pieces of acrylic at the top of the outer cell and 4 tie rods out of 6 existing tie rods (see Figure 4.11a). The outer cell was then filled with water until the 3 tie rods of the inner cell were submerged (see Figure 4.11a). After that, the glass inner cell wall was lowered carefully to be placed exactly on the O-ring of the inner cell base plate. This was followed by lowering the load cell (attached to the top cover of the inner cell) in a tilted way to remove any trapped air inside a hole on the load cell. The hook of the load cell was entered to the yoke and then rotated by 90^o, as described in Section 3.3.2. The top cover of the inner cell was then fixed (see Figure 4.11b) by tightening the 3 nuts at the top of the 3 tie rods and the 2 vent valves on the top cover of the inner cell were then closed.

After passing the electrical cable of the load cell through the top cover of the outer cell, the top cover was fixed using the 6 tie rods and nuts (see Figure 4.11c). Before adjusting the height of the load cell externally (using the supporting plate), all valves on the pore drainage lines to the inner cell were opened to apply a cell pressure of 12kPa to the inner cell, in order to prevent developing negative pressure in the inner cell. After fixing the supporting plate to the cover plate of the outer cell, the outer cell was filled with water and a cell pressure of 12kPa (the same as the inner cell) was applied to the outer cell. A pore air pressure of 2kPa was then applied to the sample. This meant that a mean net stress $\bar{p}$ of 10kPa was applied on the sample.

The cell pressure and the pore air pressure were both gradually increased at a rate of 25kPa/minute to 900kPa and 890kPa respectively, keeping a mean net stress $\bar{p}$ of 10kPa on the sample. The sample was maintained under this situation for 24 hours in order to dissolve any trapped air inside the inner cell, hence avoiding errors in measuring water inflow and outflow to the inner cell during the subsequent initial equalization stage.

If the test was to involve loading in triaxial compression, the loading ram was initially set close to its lowest position, whereas it was set close to its highest position if the test was to involve loading in triaxial extension. This was to allow maximum subsequent travel of the loading ram.

(a) (b) (c)

Figure 4.11: Assembling double-walled cell

4.2.3 Setting up saturated sample

One test on a saturated sample was performed using the same suction-controlled double wall triaxial apparatus, after some modifications to the drainage system. This was because initially an unsaturated sample was set up and then the sample was saturated by flushing water from the base pedestal to the top cap through the sample.

Several modifications to the drainage system were performed. Firstly, the pore air drainage line to the base pedestal was disconnected from the pore air pressure controller and then flushed with water and closed throughout the test, because testing under saturated conditions did not require any provision of pore air pressure. Secondly, the key feature of the modifications was that the original top cap, which contained the HAE ceramic filter, was replaced by another top cap with a low air entry sintered brass filter covered by a filter paper. This replacement was necessary in order to allow

flushing of water through the sample from the bottom to the top. The low air entry sintered brass filter and covering filter paper were initially placed in a dry condition, with the drainage line to the top cap (normally used as a pore water drainage line) filled with air.

To set up the saturated sample and to mount the 4 horizontal BEEs, similar procedures were followed as for unsaturated samples.

At the end of the setting up stage, the sample was in an unsaturated condition under a mean net stress $\bar{p}$ of 10kPa, which was applied by a cell pressure of 900kPa and a pore air pressure of 890kPa (applied at the top of the sample through the sintered brass filter). The saturation process was commenced by opening a valve on the pore water drainage line of the base pedestal to apply a pore water pressure of 898kPa at the base of the soil sample. Due to a pressure difference of 8kPa, the water was flushed from the bottom of the sample (898kPa) to the top of the sample (890kPa), exiting the sample through the sintered brass filter in the top cap and the connecting drainage line. The water flushing process was stopped when the water flowing from the top cap no longer contained air bubbles. This flushing process did not, however, completely saturate the sample, because many air bubbles were trapped within the sample.

On completion of the water flushing process, the drainage line to the top cap was flushed with water and connected to the pore water pressure controller (rather than the air pressure controller used previously). Trapped air bubbles were then forced to dissolve within the pore water in the sample, by maintaining a high pore water pressure within the sample for several days. During this process, the cell pressure was 900kPa and the pore water pressure (applied at both top and bottom of the sample) was 895kPa, giving an effective stress of 5kPa. The saturation process was finished when the rate of water inflow to the sample reduced to approximately 0.01cm^3/day. No measurement of B-value was performed at the end of the saturation stage (to confirm adequate saturation), because this would have required a change of cell pressure, whereas it had been decided to maintain cell pressure constant throughout each test, in order to achieve accurate measurement of sample volume change with the double wall cell (see Section 3.5.1).

4.3 Test stages

The main testing programme consisted of 11 tests, each following a different stress path (see Section 4.5), consisting of several test stages. Each stage was stress-controlled, involving variation of one or more of the radial net stress ($\bar{\sigma}_r = \sigma_r - u_a$), deviator

stress ($q = \sigma_a - \sigma_r$) and matric suction ($s = u_w - u_a$), along a predefined stress path. During all main tests, the cell pressure σ_r was held constant, so that changes of $\bar{\sigma}_r$ were achieved by varying u_a. Similarly, control of q was achieved by varying σ_a and control of s was performed by varying u_w.

4.3.1 Initial rest stage

After setting up a sample and prior to commencing the initial equalization stage, an initial rest period of 24 hours was applied to the sample, in order to dissolve any trapped air bubbles inside the inner cell (under the cell pressure of 900kPa). These air bubbles had to be dissolved in order to avoid errors in measuring sample volume change in the subsequent stage (i.e. initial equalization stage). No water inflow or outflow to the soil sample was allowed during the initial rest stage. In addition, a water pressure (590kPa for tests on unsaturated samples or 890kPa for the tests on saturated sample) was applied to the pore water drainage lines (the valves connecting to the base pedestal and top cap were closed, so this pressure was not applied to the soil sample). The purpose of applying this pressure on the drainage lines was to eliminate initial expansion of the fittings and tubes during the subsequent initial equalization stage. During the initial rest stage, the sample was under a low mean net stress of 10kPa (as explained in Section 4.2.2) and $q = 0$. It was assumed that no sample volume change occurred during this initial rest stage and no measurements of inflow or outflow of water to the inner cell were taken.

4.3.2 Initial equalization stage

After the initial rest stage and prior to commencing the initial equalization stage, all samples were brought to the desired initial stress state in the $q : \bar{p}$ plane (see Section 4.5.1), according to the test plan for the individual test. For unsaturated samples, the initial equalization stage was then immediately commenced by opening a valve on the pore water drainage lines, feeding simultaneously both the base pedestal and top cap with the pore water.

During the initial equalization stage, the intention was to wet the sample from the as-compacted suction (approximately 650kPa) to a lower target suction of 300kPa or 50kPa (see Section 4.5.1). Measurements of sample volume change and water inflow/outflow to the sample were recorded throughout the stage. When the rate of water inflow reduced to approximately 0.1cm^3/day, the stage was terminated. Generally, this required 7 to 11 days.

4.3.3 Loading and unloading stages

On completion of the initial equalization stage, loading and unloading stages (following isotropic or anisotropic stress paths) were conducted on the unsaturated samples. The stress paths followed in the different tests included $\eta \approx 0$, $\eta = 1$ and $\eta = -1$ (see Section 4.5), where $\eta = q/\bar{p}$.

For the unsaturated samples, the loading and unloading stages were carried out by holding the cell pressure σ_r constant, adjusting the pore air pressure u_a at an appropriate rate, to increase or decrease the radial net stress $\sigma_r - u_a$, and simultaneously adjusting the deviator stress q to follow the desired stress path in the $q : \bar{p}$ plane. The rate of variation of u_a was selected to result in a rate of increase or decrease of mean net stress $\bar{p}$ of 2kPa/hr or 1kPa/hr (as described in Section 4.3.5). In conventional triaxial testing, the cell pressure is usually varied and the pore pressure is held constant, but in this work the cell pressure was held constant to avoid any errors in the measurement of sample volume change caused by changes of cell pressure (see Section 3.5.1). For the saturated sample, isotropic loading and unloading stages were performed by decreasing or increasing the pore water pressure u_w whilst holding the cell pressure σ_r constant .

4.3.4 Wetting and drying stages

Some tests on unsaturated samples involved wetting or drying stages (variation of s) at constant mean net stress $\bar{p}$. Wetting and drying stages were performed under (almost) isotropic stress conditions, with a nominal deviator stress $q = 2$kPa to ensure contact between load cell and top cap and hence allow monitoring of axial displacement. For the first sample subjected to a wetting stage, an attempt was made to change suction at a constant rate of 2kPa/hr, in order to measure V_s and V_p at different values of suction throughout the wetting stage. However, at the end of the wetting stage, it was discovered that a very large water inflow occurred during a subsequent 24 hour rest period (see Figure 4.12) indicating that the rate of change of suction (i.e. 2kPa/hr) had been too fast to maintain approximately uniform suction throughout the sample. Time constraints meant that it was not feasible to apply significantly slower rates of suction change. Therefore, in subsequent tests which involved wetting or drying stages, a rapid change of suction was applied at the boundary, and then this was maintained until water inflow or outflow to the sample slowed to a low rate of approximately 0.1cm^3/day. Hence, measurements of V_s and V_p were only performed at the end of wetting and drying stages.

4.3.5 Rest stages

At the end of each loading or unloading stage, a rest period of 24 hours (an equalization stage) was applied to the sample to ensure that the pore water pressure was equalized throughout the sample. Measurements of water inflow/outflow and sample volume change during the rest period also indicated whether the rate of application of stress changes during the preceding stage was sufficiently slow (ideally, measured water inflow/outflow and sample volume change during the rest period should be negligible, indicating that any pore water pressure variation throughout the sample height during the preceding stage was small).

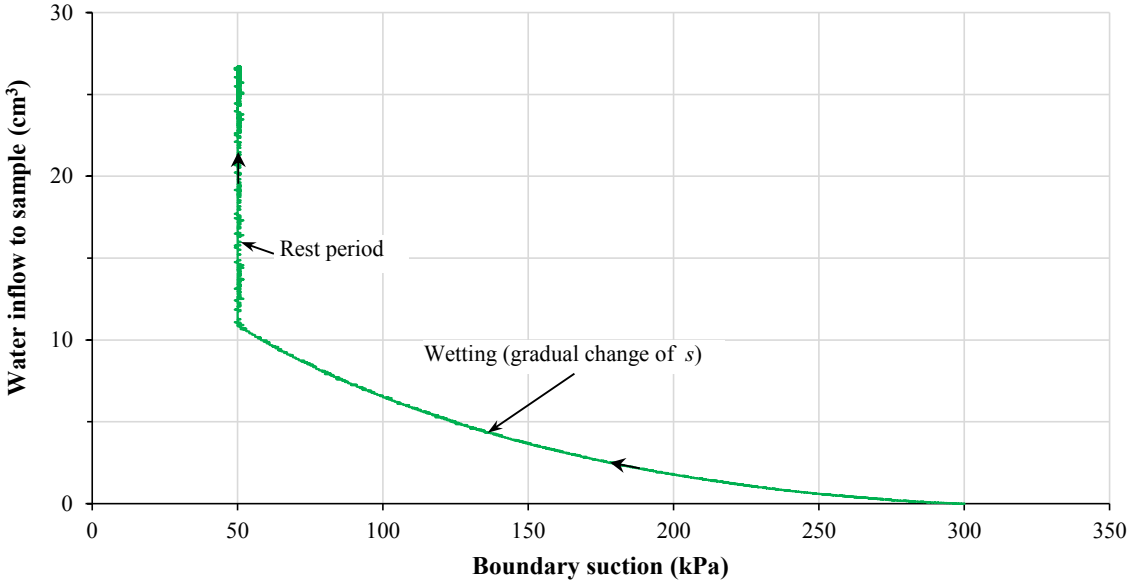

Figure 4.12: Water inflow to sample during wetting stage of first test involving wetting

Figure 4.13 shows the water inflow to the soil sample during the anisotropic loading stage and subsequent rest stage of a typical test, performed at $s = 300$kPa (Test B), with the loading stage performed with a rate of change mean net stress $d\bar{p}/dt$ of 2kPa/hr. Inspection of Figure 4.13 shows that the water inflow to the soil sample during the subsequent 24 hour rest period was much smaller than the inflow during the loading stage, indicating that the applied loading rate of 2kPa/hr was sufficiently slow. This rate of change of $\bar{p}$ was therefore used for all loading and unloading stages conducted at $s = 300$kPa.

For the loading and unloading stages performed at $s = 50$kPa or performed on the saturated sample, much larger water outflows and inflows were expected than during loading and unloading stages performed at $s = 300$kPa. Hence, it was decided that a lower rate of variation of mean net stress $d\bar{p}/dt$ of 1kPa/hr was appropriate in these loading and unloading stages performed at $s = 50$kPa or performed on the saturated

sample. Figure 4.14 shows the water outflow from the soil sample during the isotropic loading stage and subsequent rest stage of Test H, performed at $s = 50$kPa with $d\bar{p}/dt = 1$kPa/hr. Inspection of Figure 4.14 confirms that the water outflow during the subsequent 24 hr rest stage was much smaller than the outflow during the loading stage, confirming that the applied loading rate of 1kPa/hr was sufficiently slow. Note that isotropic loading at a constant suction of $s = 50$kPa produced outflow of water from the sample (see Figure 4.14), whereas isotropic loading at a higher constant suction of $s = 300$kPa produced inflow of water to the sample (see Figure 4.13). This is discussed further in Section 6.2.

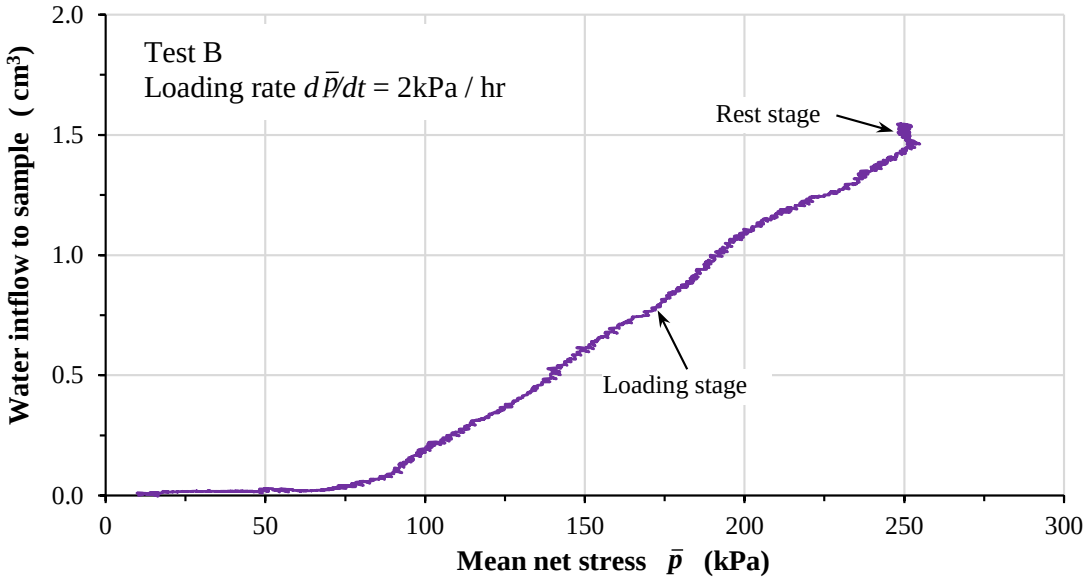

Figure 4.13: Loading stage and rest period stage at $s = 300$kPa

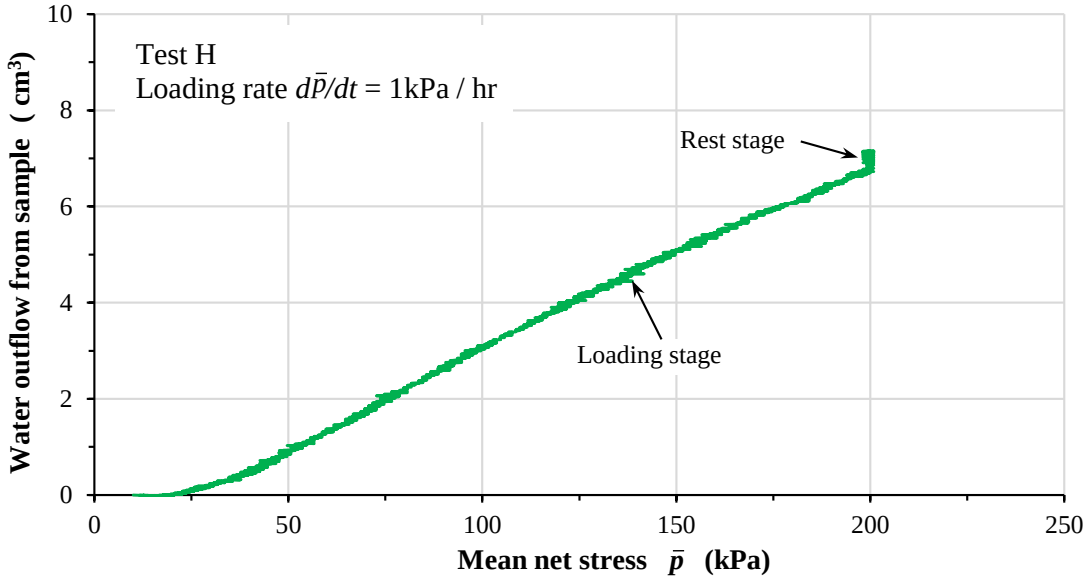

Figure 4.14: Loading stage and rest period stage at $s = 50$kPa

4.4 Data processing

4.4.1 Unsaturated tests

The calculations of the variables matric suction s , deviator stress q and mean net stress $\bar{p}$ were performed in the Clisp Studio CS logging/control software, using the following equations:

$$s = u_a - u_w \tag{4.1}$$

$$q = \frac{F}{V_o + \Delta V}(H_o + \Delta H) \tag{4.2}$$

$$\bar{p} = \sigma_r + \frac{q}{3} - u_a \tag{4.3}$$

where F is the deviator force measured from the load cell, H_o and V_o are the height and volume of the sample at the end of the initial equalization stage, and ΔH and ΔV are the increase in height and volume since the end of the equalization stage.

Values of specific volume v , water content w , degree of saturation S_r and mean Bishop's stress p^* were calculated subsequently in MS Excel using the equations set out below. Specific volume v was calculated by:

$$v = \frac{V_o + \Delta V}{V_s} \tag{4.4}$$

where V_s was the volume of solids in the sample, given by:

$$V_s = \frac{M_s}{G_s \rho_w} \tag{4.5}$$

where M_s was the mass of solids (measured at the end of the test, after drying the sample in an oven), G_s was the specific gravity of the soil particles ($G_s = 2.60$) and ρ_w was the density of water ($\rho_w = 1000\text{kg/m}^3$).

Water content w was calculated from:

$$w = \frac{\rho_w(V_{wo} + \Delta V_w)}{M_s} \tag{4.6}$$

where V_{wo} was the volume of water in the sample at the end of the initial equalization stage and ΔV_w was the water inflow to the sample since the end of the equalization stage. V_{wo} in Equation 4.6 was given by:

$$V_{wo} = V_{wi} - \Delta V_{wi} \tag{4.7}$$

where ΔV_{wi} was the water inflow to the sample during the initial equalization stage and V_{wi} was the volume of water in the sample at the time of setting up, given by:

$$V_{wi} = \frac{(M_i - M_s)}{\rho_w} \tag{4.8}$$

where M_i was the initial wet mass of the sample (measured just prior to setting up).

Degree of saturation S_r was calculated from:

$$S_r = \frac{(V_{wo} + \Delta V_w)}{(V_o + \Delta V - V_s)} \tag{4.9}$$

Mean Bishop's stress p^* was calculated from:

$$p^* = \bar{p} + S_r s \tag{4.10}$$

Axial strain ϵ_a , volumetric strain ϵ_v , radial strain ϵ_r and shear strain ϵ_s were calculated by:

$$\epsilon_a = -ln\left(\frac{H_o + \Delta H}{H_o}\right) \tag{4.11}$$

$$\epsilon_v = -ln\left(\frac{V_o + \Delta V}{V_o}\right) \tag{4.12}$$

$$\epsilon_r = \frac{1}{2}(\epsilon_v - \epsilon_a) \tag{4.13}$$

$$\epsilon_s = \frac{2}{3}(\epsilon_a - \epsilon_r) \tag{4.14}$$

Values of variables ϵ_a , ϵ_v , ϵ_r and ϵ_s were calculated as true strains rather than engineering strains (see Equations 4.11 and 4.12). Hence, Equations 4.13 and 4.14, relating the various strains, were rigorous even if strains were large. In this study, compressive strains were treated as positive (hence the negative signs in Equations 4.11 and 4.12). Note, from Equations 4.11 and 4.12, that the datum for strain measurement (i.e. the point corresponding to zero strain) was taken as the end of the initial equalization stage.

While a test was running, provisional values were calculated for the variables v , w and S_r , using an estimated value for the mass of solids M_s (and hence the volume of solids V_s), based on the measured water content of the trimmings and the initial wet mass of the sample. It was helpful to have these provisional values of v , w and S_r, to monitor the response of the sample during testing and plot provisional graphs such as the $v - ln\bar{p}$ curve. On completion of the test, correct values of v , w and S_r were calculated, using the measured value of M_s from the final measurement of the oven-dry mass of the sample.

4.4.2 Saturated tests

One test was performed on a saturated sample, which was loaded and unloaded isotropically. In the test, values of specific volume v , axial strain ϵ_a , volumetric strain ϵ_v , radial strain ϵ_r , and shear strain ϵ_s were performed in MS Excel using Equation 4.4 and Equations 4.11-4.14, whereas the mean effective stress p' was calculated in MS Excel as follows:

$$p' = \sigma_r + \frac{q}{3} - u_w \tag{4.15}$$

4.4.3 Bender/extender element results

In order to take measurements of V_s and V_p, it was necessary to know the current height and the current diameter of the sample in order to calculate the tip-to-tip distance L_{tt} between the transmitter and receiver BEEs in each pair. The current

height H (i.e. $H = H_o + \Delta H$) and the current diameter D (i.e. $D = (4V/\pi H)^{1/2}$ where $V = V_o + \Delta V$ is the current volume of the sample) were calculated in MS Excel from input and measured data. The tip-to-tip distance between transmitter and receiver BEEs, for vertical and horizontal BEE pairs, were then calculated respectively as:

$$L_{tt} = H - d_t - d_r \tag{4.16}$$

$$L_{tt} = D - d_t - d_r \tag{4.17}$$

where d_t and d_r were the depth of intrusion into the soil sample of the transmitter and receiver BEEs, respectively.

In calculating the value of D, and hence the value of L_{tt} from Equation 4.17, it was assumed that the soil sample deforms as a perfect cylinder during all stages, whereas in practice this is not the case, due to end effects at the top and bottom of the sample (shear stresses between the sample and the top cap and base pedestal). The change of diameter at the mid-height of the sample would be greater than the calculated change of diameter of a sample assumed to deform as a perfect cylinder. Moore (1966) showed that for a linear elastic sample, with a height-to-diameter of 2 and no slip between the sample and rigid top cap and base pedestal, the change of diameter at mid-height would be 14% greater than the average change of diameter (i.e. than the change of diameter calculated by assuming a perfect cylinder). In practice, the difference would probably be less than 14%, because there would be some slip between the sample and the top cap and base pedestal. At the end of the loading stage of a typical test (Test B, see Section 6.1), the calculated change of L_{tt} was 2.29mm and assuming the worst case of scenario that the true increase of diameter was 14% greater, this would suggest a true increase of diameter of 2.61mm with an initial sample diameter of 50mm, the resultant error in L_{tt} (and hence v) would be less than 0.7%. This is a worst case scenario, and typical errors in v due to this type of error in D would be smaller than 0.7%.

The shear wave velocity V_s was calculated from the shear wave travel time t_s (see Section 3.2.5) and the tip-to-tip distance L_{tt} between the transmitter and receiver BEEs:

$$V_s = \frac{L_{tt}}{t_s} \tag{4.18}$$

Three different shear wave velocities (V_{svh}, V_{shv} and V_{shh}) were measured, depending upon the directions of wave transmission and polarisation, where the second subscript gives the wave transmission direction, the third subscript gives the wave polarisation direction and v and h represent vertical and horizontal respectively. The corresponding elastic shear modulus G was then calculated from the shear wave velocity V_s :

$$G = \rho V_s^2 \tag{4.19}$$

where ρ is the density of the soil, given by:

$$\rho = \frac{M_s + \rho_w(V_{wo} + \triangle V_w)}{(V_o + \triangle V)} \tag{4.20}$$

Three different shear moduli (G_{vh}, G_{hv} and G_{hh}) were calculated from the three measured shear wave velocities.

The compression wave velocity V_p was calculated from the measured compression wave travel time t_p and the tip-to-tip distance between the transmitting and receiving BEEs:

$$V_p = \frac{L_{tt}}{t_p} \tag{4.21}$$

Three measurements of compression wave velocity (V_{pv}, V_{ph1} and V_{ph2}) were calculated with the three different BEE pairs. The horizontal compression wave velocity V_{ph} was then taken as the average of V_{ph1} and V_{ph2}. The elastic constrained modulus M was then calculated from the compression wave velocity V_p:

$$M = \rho V_p^2 \tag{4.22}$$

Two different constrained moduli (M_v and M_h) were calculated, from the measured values of V_{pv} and V_{ph} respectively.

4.5 Stress paths

4.5.1 Initial stress adjustment and initial equalization stage

Figure 4.15 shows stress paths in the $q : \bar{p}$ plane for the initial stages of all 11 tests in the main test programme.

At the end of the setting-up stage (Section 4.2.2 or Section 4.2.3), all unsaturated samples were at the as-compacted suction, a mean net stress $\bar{p}$ of 10kPa and deviator stress $q = 0$ (point X in Figure 4.15), whereas the single saturated sample I was at a mean effective stress p' of 5kPa and $q = 0$ (point Y in Figure 4.15). Setting-up was followed by an "initial stress adjustment", prior to the initial equalization stage.

Unsaturated samples A, D, H, J and K were to be subjected to "isotropic" loading and unloading stages, but a small deviator stress $q = 2$kPa was required to maintain contact between the load cell and the yoke on the top cap (see Section 3.3.2), in order to allow axial deformation of the sample to be monitored throughout these tests. The initial stress adjustment for these 5 tests therefore involved the application of a deviator stress of 2kPa. This application of a deviator stress was performed whilst maintaining mean net stress $\bar{p}$ at 10kPa, by suitable reduction of the radial net stress $\sigma_r - u_a$ (achieved by increasing u_a). The subsequent initial equalization stages of these 5 tests were therefore performed at $\bar{p} = 10$kPa, $q = 2$kPa (see points A_1, D_1, H_1, J_1 and K_1 in Figure 4.15, where the subscript 1 denotes the end of the initial equalization stage).

Unsaturated samples B, E and G were to be subjected to anisotropic loading and unloading stages in triaxial compression with $\eta = 1$. The initial stress adjustment for these 3 tests therefore involved the application of a deviator stress $q = 10$kPa whilst maintaining $\bar{p} = 10$kPa (by suitable adjustment of u_a), in order to bring the stress state to $\eta = 1$. The subsequent initial equalization stages of these 3 tests were therefore performed at $\bar{p} = 10$kPa, $q = 10$kPa (see points B_1, E_1 and G_1 in Figure 4.15).

Unsaturated samples C and F were to be subjected to anisotropic loading and unloading stages in triaxial extension with $\eta = -1$. The initial stress adjustment for these 2 tests therefore brought the stress state to $\bar{p} = 10$kPa, $q = -10$kPa (see points C_1 and F_1 in Figure 4.15).

The initial equalization stage for unsaturated samples A, B, C, D, E, F, G, J and K involved wetting the soil from the as-compacted value of s (approximately 650kPa) to

$s = 300$kPa, whereas the initial equalization stage for unsaturated sample H involved wetting to $s = 50$kPa.

The setting-up and saturation stages of saturated sample I (see Section 4.2.3) brought this sample to p'=5kPa, q=0 (point Y in Figure 4.15) and subsequent initial stress adjustment brought the sample to $p' = 5$kPa, $q = 2$kPa (point I_1 in Figure 4.15).

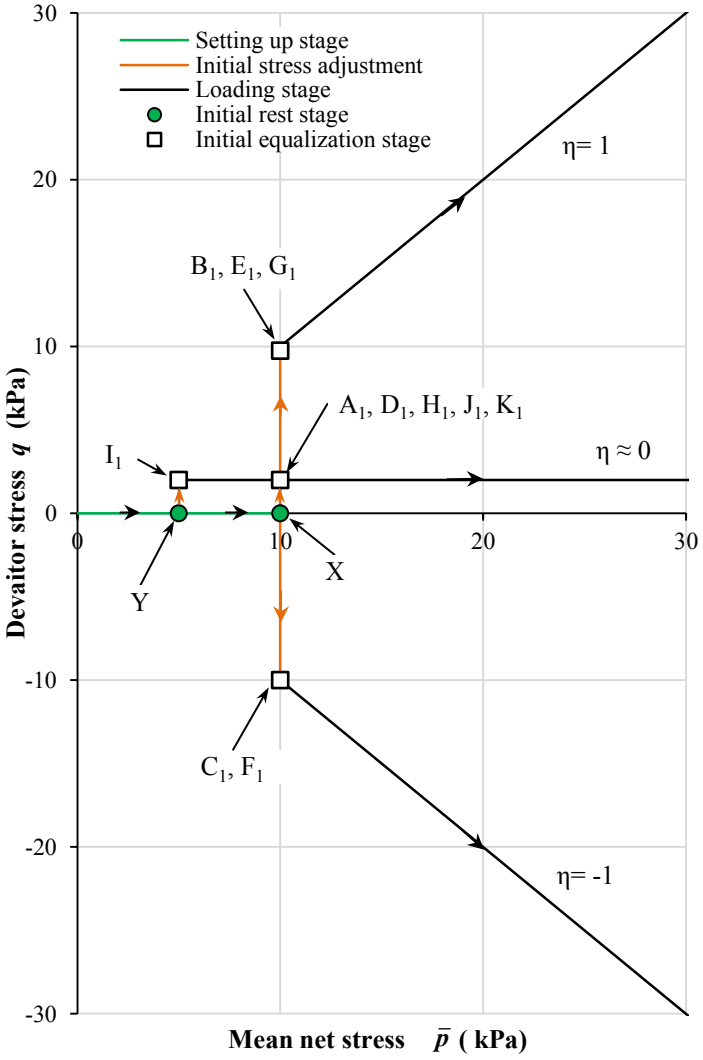

Figure 4.15: Initial stress adjustment

4.5.2 Loading/unloading stages and wetting/drying stages

Figure 4.16 shows the loading and unloading stages in the $q : \bar{p}$ plane for the 9 unsaturated samples tested at $s = 300$kPa. Three isotropically compacted samples (A, B and C) were loaded and unloaded at $\eta \approx 0$ (with q=2kPa), $\eta = 1$ and $\eta = -1$ respectively, with A_2, B_2 and C_2 representing the stress state at the end of the loading stages. Similarly, three anisotropically compacted samples (D, E and F) were loaded and unloaded at $\eta \approx 0$ (with $q = 2$kPa), $\eta = 1$ and $\eta = -1$ respectively (see points D_2, E_2 and

F_2 in Figure 4.16). Bender/extender element (BEE) measurements were performed at regular intervals throughout each loading and unloading stage. These 6 tests were designed to examine the influence of initial anisotropy and subsequent loading path on small strain elastic behaviour, under unsaturated conditions, including evolution of anisotropy. Test G was an additional test on an anisotropically compacted sample loaded at $\eta = 1$, but with a shorter loading stress path (see G_2 in Figure 4.16).

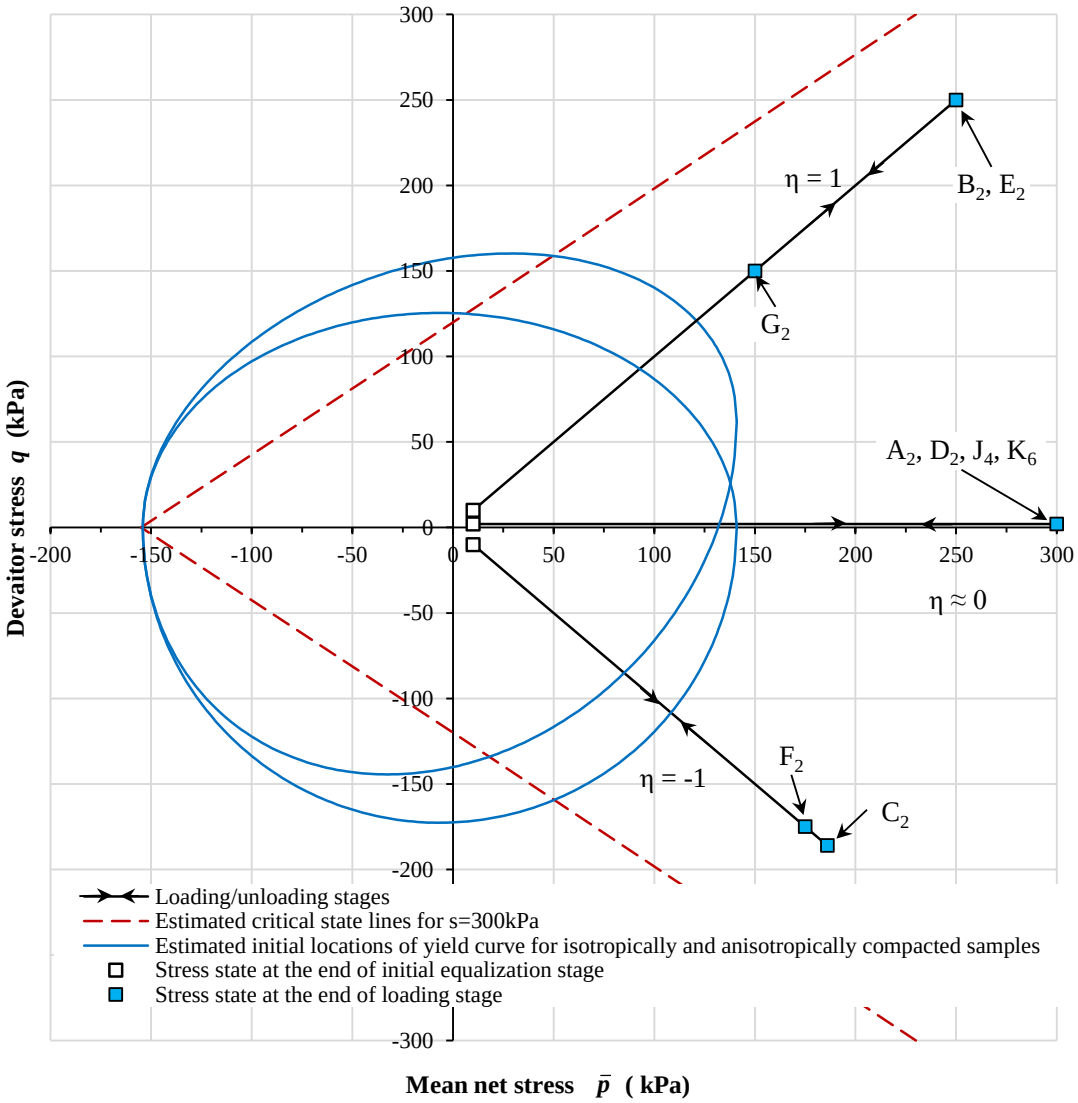

Figure 4.16: Loading and unloading stages at $s = 300$kPa

The values of $\bar{p}$ at the end of the loading stages in Tests A-F were $\bar{p} = 300$kPa for the two samples tested at $\eta \approx 0$, $\bar{p} = 250$kPa for the two samples tested at $\eta = 1$ and $\bar{p} = 175$kPa or 186kPa for the two samples tested at $\eta = -1$. The lengths of the stress paths for the various loading stages were selected based on three considerations.

1. Limitations of loading ram travel in the suction-controlled double wall triaxial cell.

2. A desire to ensure that the loading stress path extended significantly beyond the yield point and hence produced significant plastic straining. Figure 4.16 shows the estimated initial position of the cross-section of the yield surface at $s = 300$kPa for the anisotropically compacted samples and the isotropically compacted samples. The estimated initial position of the yield curve for the anisotropically compacted samples at $s = 300$kPa was taken from Al-Sharrad (2013) (he used an identical anisotropic compaction procedure). The estimated initial position of the yield curve for the isotropically compacted samples at $s = 300$kPa simply assumed that the yield curve was the same size (i.e. the same maximum value of $\bar{p}$) as for the anisotropically compacted samples, given that both groups of samples were compacted to the same value of v (see Section 4.1.3).

3. Needing to ensure that the anisotropic loading paths, at $\eta = 1$ and $\eta = -1$, did not reach the critical state lines in triaxial compression and triaxial extension respectively. Figure 4.16 shows the estimated positions of these critical state lines at $s = 300$kPa, taken from Al-Sharrad (2013).

Test H was a single test with loading and unloading stages performed at $s = 50$kPa. This test was conducted on an isotropically compacted sample and involved "isotropic" loading and unloading ($\eta \approx 0$, with $q = 2$kPa). The loading stage was continued to $\bar{p} = 200$kPa, compared to $\bar{p} = 300$kPa for the equivalent tests performed at $s = 300$kPa. The reduced length of the loading stress path at $s = 50$kPa was selected because the degree of saturation S_r in this test had increased to about 0.95 by $\bar{p} = 200$kPa, and there was concern that further increase of S_r (caused by continued loading) would result in non-equilibration of pore air pressure throughout the soil sample, due to the phenomenon of trapped air bubbles at very high values of S_r.

Test I was an equivalent test ($\eta \approx 0$, with $q = 2$kPa) performed on a saturated sample, although in this case the loading stage was continued to $\bar{p} = 300$kPa. Again, BEE measurements were performed at regular intervals throughout the loading and unloading stages of Tests H and I. Comparison of BEE results from Test A ($s = 300$kPa), Test H ($s = 50$kPa) and Test I (saturated, i.e. $s = 0$), all on isotropically compacted samples and with loading and unloading stages performed at $\eta \approx 0$ ($q =$2kPa), was intended to show the influence of suction s on small strain elastic behaviour.

Tests J and K were on isotropically compacted samples and involved "isotropic" loading and unloading stages ($\eta \approx 0$, with $q = 2$kPa) performed at $s = 300$kPa, but these two tests each involved a wetting-drying cycle, either at $\bar{p} = 10$kPa, before the loading stage (see $J_1J_2J_3$ in Figure 4.17) or at $\bar{p} = 100$kPa, within the loading stage (see $K_3K_4K_5$ in

Figure 4.17). Results from Tests J and K would be compared with the results from Test A, an equivalent test but without a wetting-drying cycle. The purpose of the wetting-drying cycles in Tests J and K was to ensure that during the subsequent "isotropic" loading and unloading stages the values of degree of saturation S_r were different for samples A, J and K, due to hysteresis in the water retention behaviour, even though the suction value was identical at 300kPa in all three cases. For Test K, the wetting was expected to produce collapse compression, whereas collapse compression was not expected in the wetting in Test J, so that the subsequent loading stages of Tests J and K were expected to be at different vales of v. Comparison of results from tests A, J and K was therefore expected to provide insight into the roles of S_r and v on small strain elastic behaviour (indicated by BEE tests), for tests where the suction value and stress path in the $q : \bar{p}$ plane were identical.

Detailed stress paths for each test are presented in the relevant sections of Chapter 6.

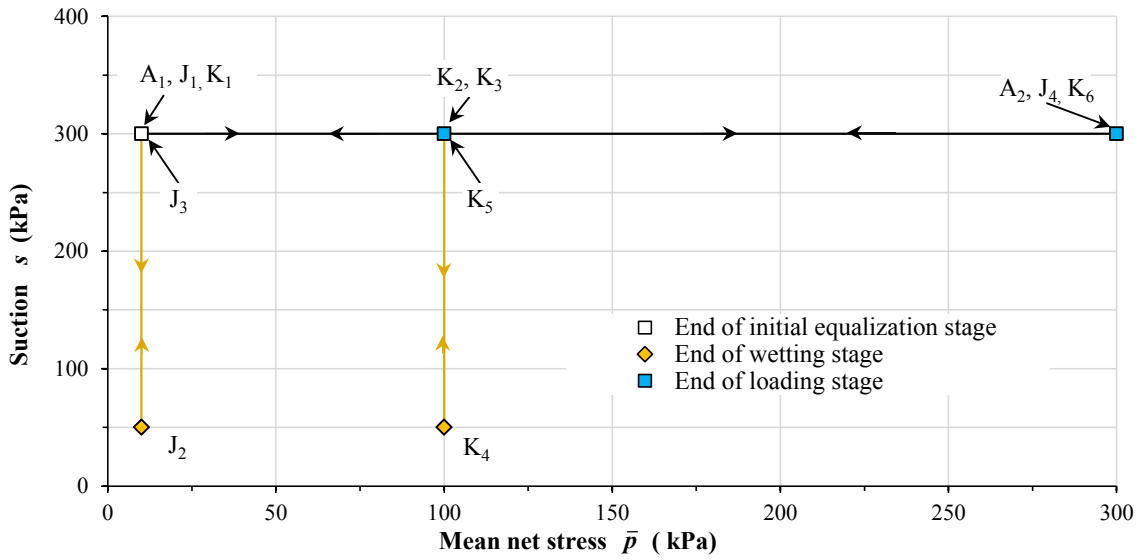

Figure 4.17: Stress paths for tests involving wetting and drying stages

Chapter 5

Preliminary tests

This chapter consists of two major sections. Each section describes preliminary test results. The first section presents tests performed to investigate four different techniques for measuring travel time in BEE tests, with a view to selecting the best method for travel time determination for the main test programme. The preliminary tests used for this investigation were performed on isotropically compacted samples and without suction control (at the as-compacted suction). The second section presents results from some preliminary tests (again, without suction control) on unsaturated samples prepared by a variety of different compaction procedures and also a single reconstituted saturated sample. These tests were intended to give some insight on the initial elastic anisotropy produced by different sample preparation procedures.

5.1 Investigation of methods of travel time determination

A series of preliminary tests investigated four different interpretation procedures (involving both time and frequency domains) for measuring travel times t_m in the bender/extender element tests. Various different techniques have been proposed for interpretation of the bender element signal (see Section 2.1.2). These include interpretation methods in either the time domain or the frequency domain. There is, however, considerable controversy within the literature about which of the various interpretation techniques gives the most reliable and consistent values of travel time (see, for example, Yamashita et al. 2009).

The four different interpretation procedures that were investigated were: peak-to-first-peak in the time domain; time to maximum peak in the cross-correlation plot; time to

first peak in the cross-correlation plot; and cross-spectrum in the frequency domain. Investigation of the reliability of each of the four different procedures for determining travel time was based on two criteria:

- whether (over an appropriate range of frequencies) the procedure provided a wave velocity that was frequency-independent (see Section 5.1.2);
- whether the procedure consistently provided equal wave velocities for different directions of wave transmission or wave polarisation in soil samples that had been specifically prepared to be isotropic in their properties (see Section 5.1.3).

In addition, the provisional choice for the travel time interpretation procedure was confirmed by a final check during the first test of the main test programme (see Section 5.1.4).

The preliminary tests were conducted on unsaturated samples of speswhite kaolin produced by the isotropic form of compaction described in Section 4.1.3. Samples were mounted in the suction-controlled double wall triaxial cell using the setting up procedures described in Section 4.2.2. Bender/extender element tests were performed at the as-compacted water content (i.e. there was no control of suction), under an isotropic total stress of 50kPa in order to provide reasonable contact between the 3 pairs of BEEs and the soil sample.

Transmitter bender/extender elements were excited by a single sinusoidal pulse (see Figure 5.1) and tests were conducted over a range of transmitted signal frequencies of $2 - 20$kHz for shear wave velocity V_s and $5 - 35$kHz for compression wave velocity V_p. These frequency ranges corresponded, in both cases, to signal wavelengths down to about 10mm (allowing for the difference in wave velocities V_s and V_p). Higher frequencies than these ranges (giving even shorter wavelengths) were found to produce very noisy received signals. Outputs were presented in both time domain (including a cross-correlation plot) and frequency domain (see Section 5.1.1).

Values of wave velocity were calculated from the tip-to-tip distance (i.e. L_{tt} see Section 4.4.3) between transmitter and receiver bender/extender elements and the travel times (t) determined using each of the four different interpretation procedures (see below), after correcting the measured value t_m by subtracting the delay time t_d (see Section 3.2.5).

5.1.1 Techniques to determine travel time

Time domain Techniques

Peak-to-first-peak

This technique simply involved measuring the travel time from the positive peak of the transmitted signal to the first significant positive peak of the received signal (see Figure 5.1).

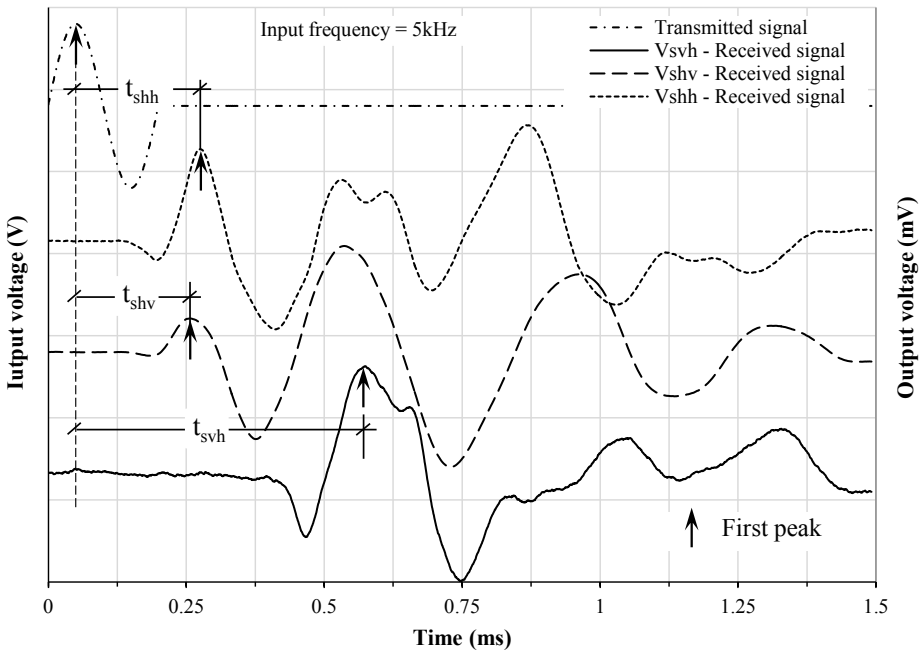

Figure 5.1: Peak-to-first-peak procedure

Maximum peak of cross-correlation plot

This technique used the cross-correlation plot in the time domain. The cross-correlation function $CC_{TR}(\tau)$ expresses the correlation between a transmitted wave $T(t)$ and a received wave $R(t)$, calculated for a given value of time shift (τ) (see Equation 2.4) (Viggiani & Atkinson, 1995). The cross-correlation function $CC_{TR}(\tau)$ is plotted against time shift (τ). The cross-correlation of the transmitted wave $T(t)$ and the received wave $R(t)$ should be a maximum at a time shift which is equal to the travel time.

The cross-correlation plot was produced by the Bender Element Analysis Tool BEAT (Rees et al., 2013), which was provided by GDS Instruments. In order to ensure that BEAT produced reliable results in plotting test data in the cross-correlation plot, Matlab code was written by the author to provide an independent cross-correlation plot. A set of data from BEE measurements on a soil sample was used for the comparison.

Figure 5.2 shows the comparison of the cross-correlation plots produced by the BEAT and the Matlab code. It can be seen from the figure that the BEAT and the Matlab code produced exactly the same cross-correlation plot. This confirmed that the BEAT produced highly accurate results.

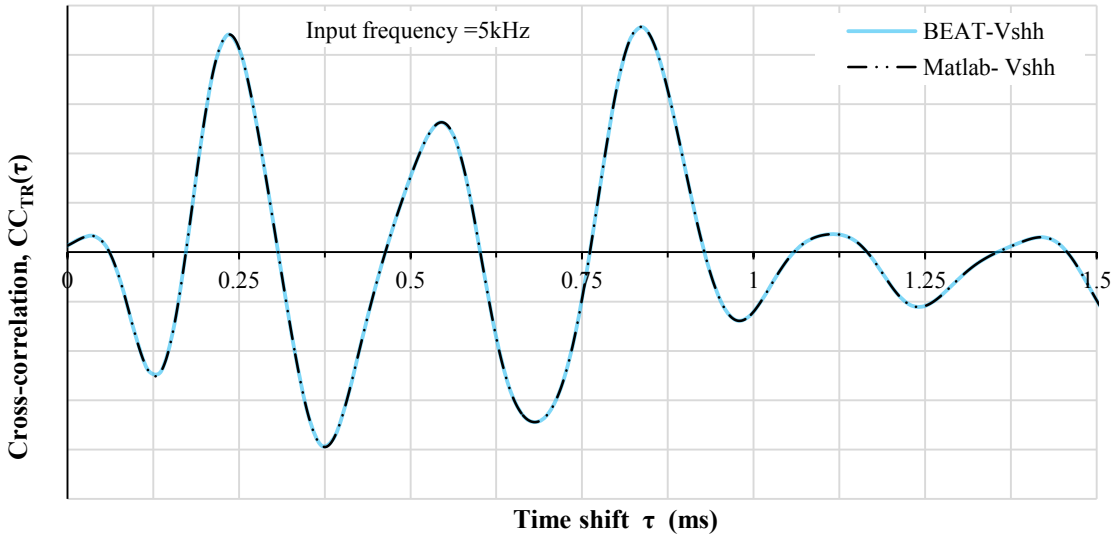

Figure 5.2: Comparison between BEAT and Matlab results for cross-correlation function

In the first of the two techniques employing the cross-correlation plot, the travel time was taken as the time shift corresponding to the maximum peak in the cross-correlation plot (see Figure 5.2). This value was provided automatically by the GDS Bender Element Analysis Tool BEAT.

First peak of cross-correlation plot

In this procedure, the travel time was taken as the time shift corresponding to the "first peak" in the cross-correlation plot, where "first peak" was defined as the first significant positive maximum that was preceded by a significant minimum (see Figure 5.3). This required manual interpretation of the cross-correlation plot. Inspection of Figures 5.3a and 5.3b (the cross-correlation plots for shear wave tests conducted at frequencies of 5kHz and 20kHz, respectively) shows that the "maximum peak" and "first peak" in the cross-correlation plot sometimes coincide and sometimes do not. When they do not coincide, the two cross-correlation procedures obviously give different values of travel time. Whether "maximum peak" and "first peak" coincide was found to be unpredictable, as it varied with frequency and with the directions of wave transmission and polarisation.

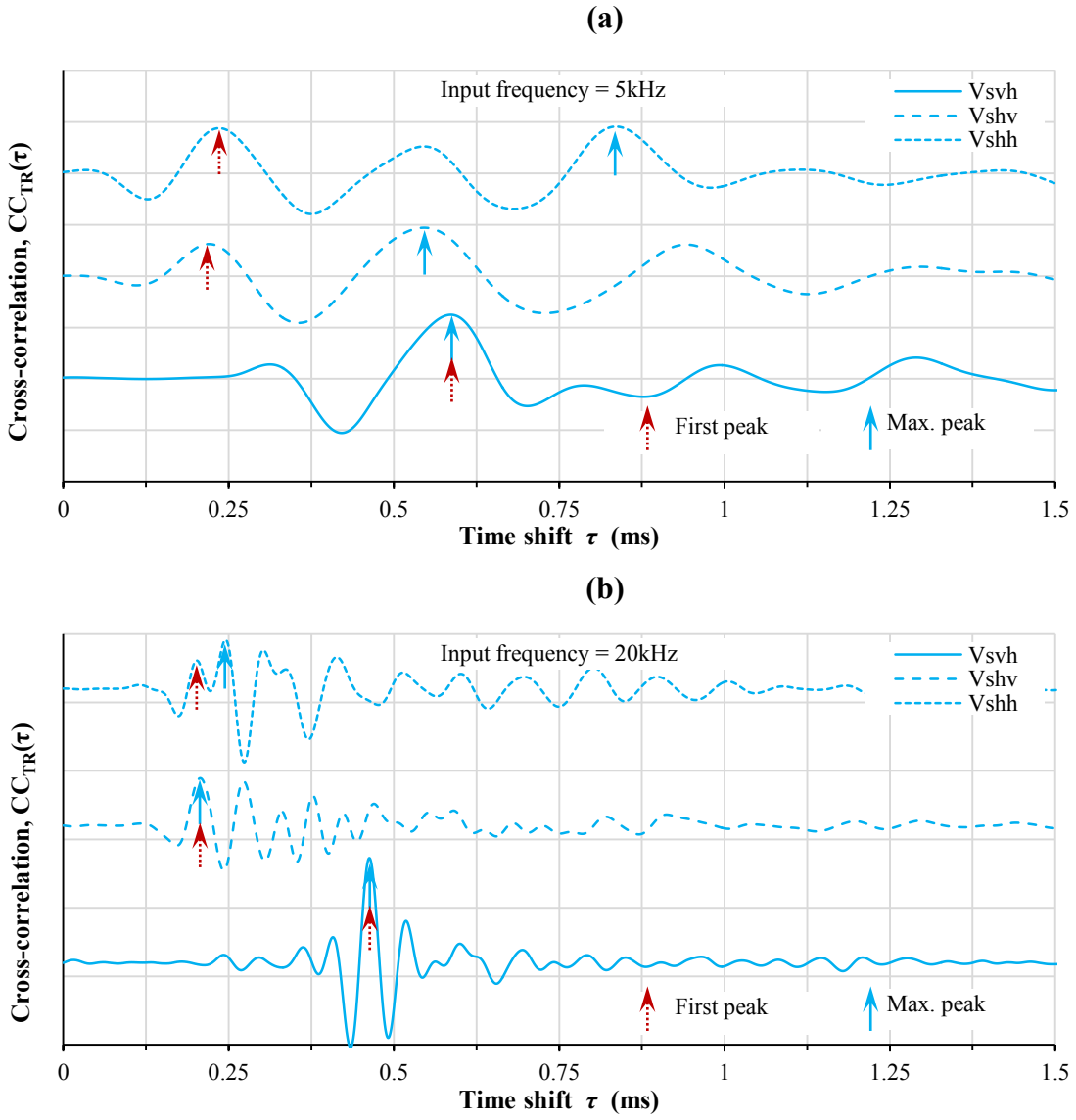

Figure 5.3: Cross-correlation results for frequencies (a) 5kHz (b) 20kHz

Frequency domain technique

Cross-spectrum

The final interpretation procedure used the cross-spectrum technique in the frequency domain (Greening & Nash, 2004). In this method, the measured travel time t_m is determined (as the group travel time) from the gradient of the phase-frequency diagram. The phase-frequency diagram is typically not a perfect straight line (see Figure 5.4), and hence the value of t_m determined by this method will depend upon the frequency range over which the gradient is measured. In the current work, this gradient was measured, using a function in the BEAT tool, over a frequency range from 0.8 to 1.2 times the transmitted wave frequency (Rees et al., 2013) as shown in Figure 5.4 for a test performed at a frequency of 5kHz.

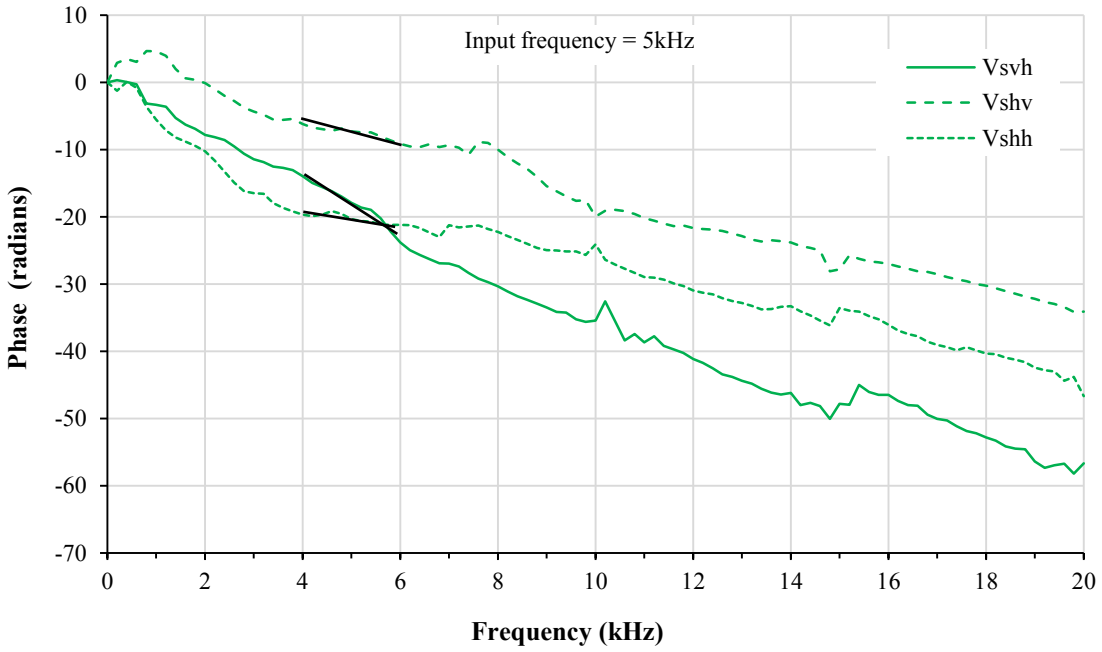

Figure 5.4: Cross-spectrum results for frequency of 5kHz

5.1.2 Independence of frequency

In order to produce true measurements of shear and constrained moduli, a method of travel time determination had to be used in which the measured value of V_s and V_p were frequency independent (at least over an appropriate range of frequency). If measurements of V_s and V_p depended upon the frequency of the transmitted wave, they produced rather meaningless measurements of G and M.

Figure 5.5 shows the variation of the three measured shear wave velocities (V_{svh}, V_{shv} and V_{shh}) with the frequency of the transmitted wave for each of the four different procedures for determining travel time. Figure 5.6 shows equivalent plots for the three measured compression wave velocities (V_{pv}, V_{ph1} and V_{ph2}).

Inspection of Figures 5.5 and 5.6 show that, of the four methods for measuring travel time, the simple measurement of peak-to-first-peak in the time domain (shown as "*pp*" in the figures) consistently gives results that are the least dependent on frequency for both shear and compression waves. For shear waves (Figure 5.5), this method gives wave velocity measurements with less than 2.5% variation with frequency for frequencies of 8-20kHz for vertical transmission (V_{svh}) and for frequencies of 16-20kHz for horizontal transmission (V_{shv} and V_{shh}). With a typical shear wave velocity of about 200 m/s, these frequency ranges correspond to wavelengths shorter than about 25% of the transmission path lengths. These results can be compared with the suggestions

of Leong et al. (2005), who recommended that shear wave measurements should be performed with wavelengths less than 30% of the transmission path length.

The results also show that for compression waves (Figure 5.6), the peak-to-first-peak in the time domain interpretation method gives wave velocity measurements showing less than 1% variation with frequency for frequencies of 5-35 kHz for vertical transmission (V_{pv}) and for frequencies of 10-35 kHz for horizontal transmission (V_{ph}). With a typical compression wave velocity of approximately 350 m/s, these frequency ranges correspond to wavelengths shorter than about 70% of the transmission path lengths.

Inspection of Figures 5.5 and 5.6 shows that use of the first peak in the cross-correlation plot (shown as "fcc" in the figures) often gives different results to use of the maximum peak in the cross-correlation plot ("cc" in the figures), indicating that in many cases the first peak and maximum peak in the cross-correlation plot did not coincide. It is also clear that the cc results typically show much more substantial and erratic variation with frequency than the fcc results, suggesting that the "first peak" in the cross-correlation plot is more meaningful than the "maximum peak". This has implications for attempts to automate determination of travel time from the cross-correlation plot (see, for example, Airey & Mohsin, 2013).

Figures 5.5 and 5.6 also show that the final interpretation procedure, using the cross-spectrum technique in the frequency domain (shown as "fd" in the figure) gives results that vary substantially and erratically with the frequency of the transmitted wave.

5.1.3 Ability to indicate isotropic behaviour of an isotropic sample

The second test of the reliability of the four different procedures for measuring travel times was whether each procedure was able to provide equal wave velocities for different directions of wave transmission or wave polarisation in a sample that had been specifically prepared to have isotropic properties.

In examining whether a given interpretation procedure provided equal wave velocities for different directions of wave transmission, a complicating factor was the possible influence of a difference in boundary conditions when transmitting vertically through the triaxial test specimen (between bender/extender elements fitted in the rigid base pedestal and top cap) and when transmitting horizontally across the specimen (between bender/extender elements fitted through the flexible rubber membrane). This issue had been previously examined by Pennington et al. (2001), but only for the case of shear waves.

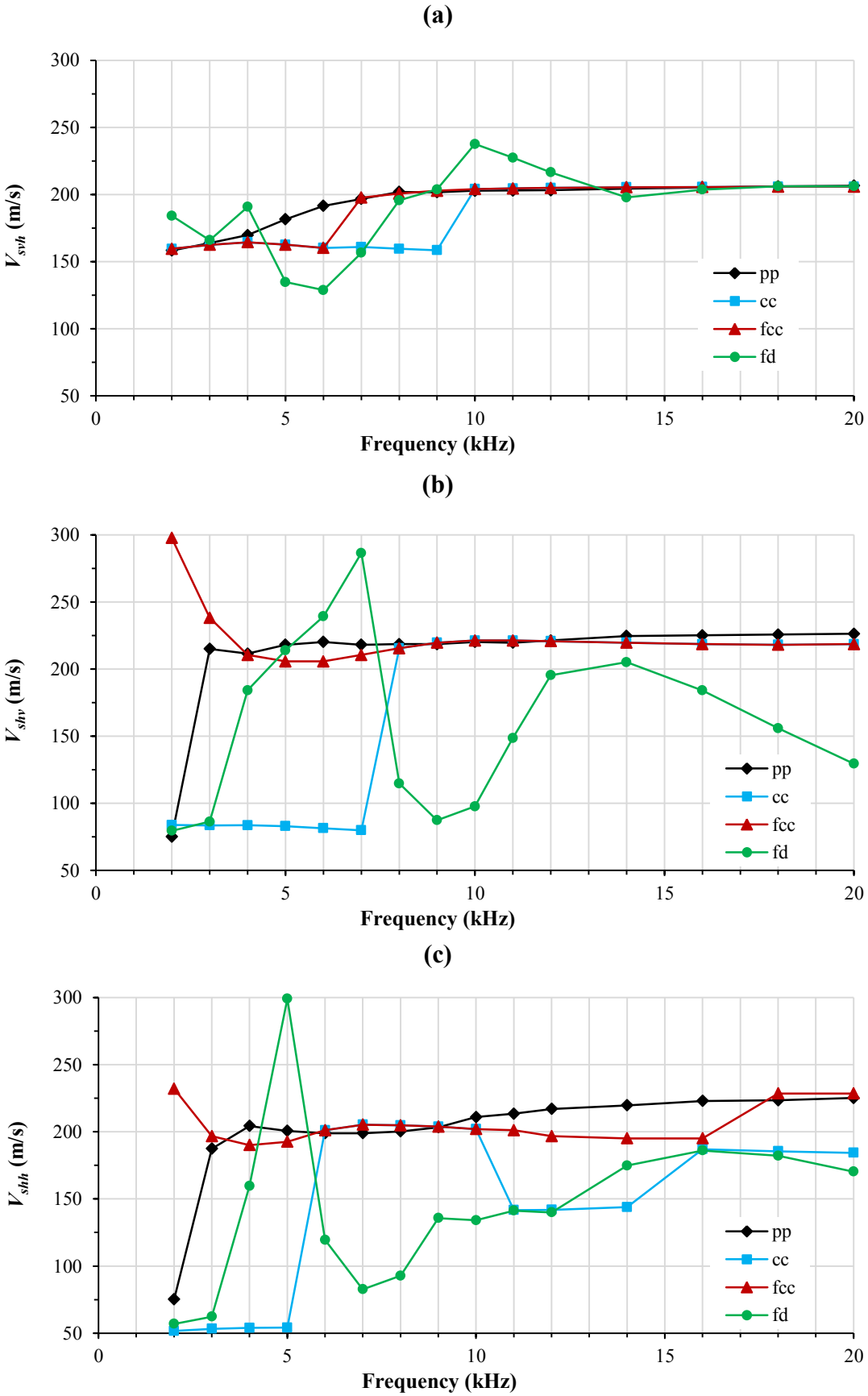

Figure 5.5: Variations of (a) V_{svh} (b) V_{shv} (c) V_{shh} with frequency

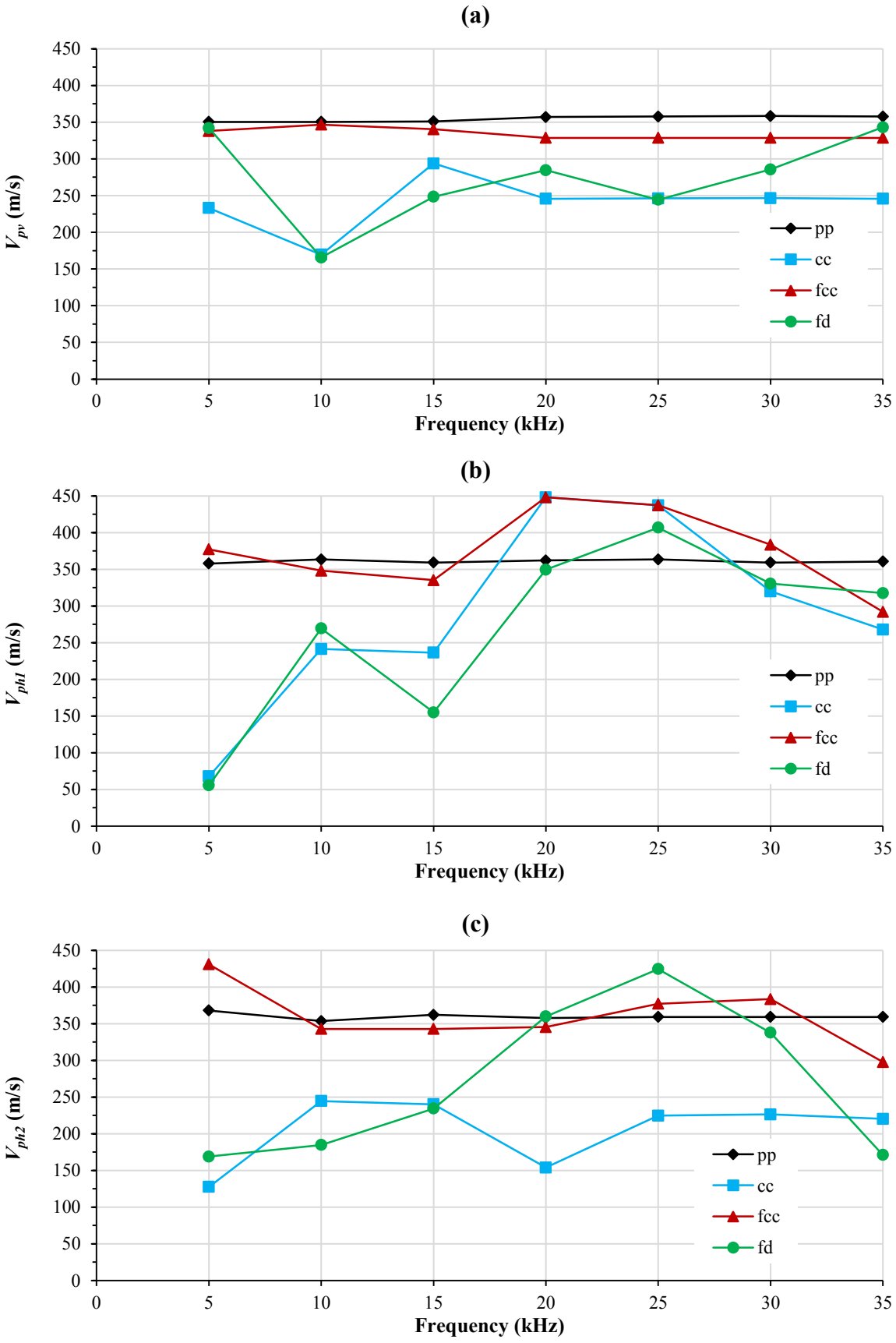

Figure 5.6: Variations of (a) V_{pv} (b) V_{ph1} (c) V_{ph2} with frequency

Figure 5.7 shows, for the *pp* interpretation method, the measured shear wave velocity ratios V_{shh}/V_{shv} and V_{shh}/V_{svh}. For frequencies above 16kHz, when both vertical and horizontal transmission methods produced frequency-independent measurements using the *pp* technique (see Section 5.1.2), the measured values of V_{shh} and V_{shv} (which both involved horizontal transmission) were almost identical (within 1%). Over the same frequency range, the measured value of V_{svh} (which involved vertical transmission) was however consistently about 9% lower than V_{shh} or V_{shv}.

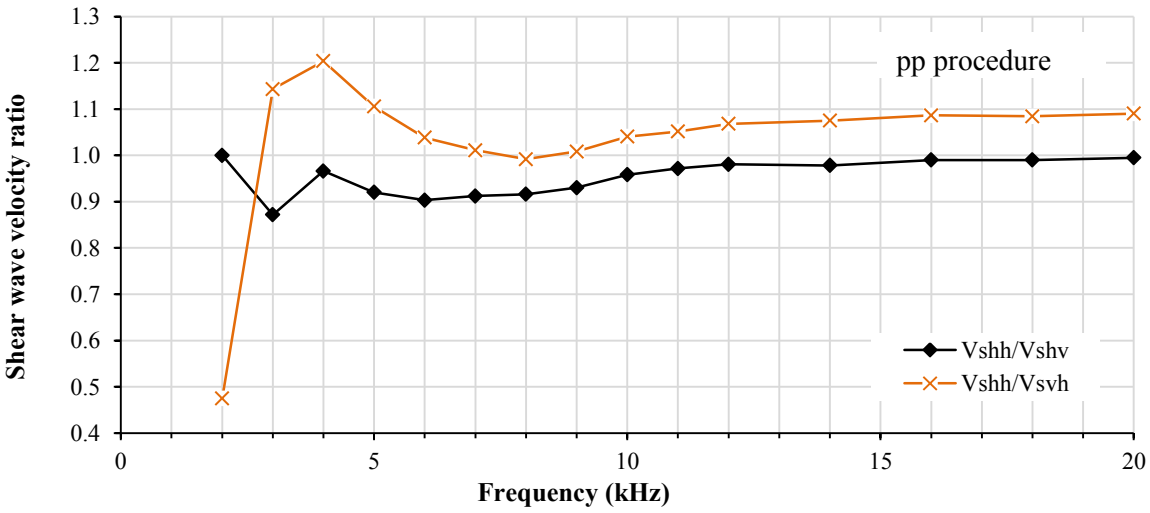

Figure 5.7: Measured shear wave velocity ratios

All values of V_s would be expected to be identical in these isotropic samples, and, in particular, V_{svh} would theoretically be expected to always have the same value as V_{shv} (even in anisotropic samples), because thermodynamic considerations require that the elastic shear moduli G_{vh} and G_{hv} are identical (Love, 1927). The results shown in Figure 5.7 therefore suggest that in bender element tests performed in a triaxial apparatus, measurements of shear wave velocity can be affected by the different boundary conditions for vertical and horizontal transmission. Pennington et al. (2001) arrived at the same conclusion.

Figure 5.8 shows, for all four interpretation techniques, the measured shear wave velocity ratio (V_{shh}/V_{shv}), which is not influenced by any difference of boundary conditions. The *pp* method gives values of V_{shh} and V_{shv} that are very similar over the full range of frequencies and, as stated previously, gives values that agree within 1% for frequencies above 16kHz (when the individual results are essentially frequency-independent). In contrast, Figure 5.8 shows that the other three interpretation methods give values of V_{shh} and V_{shv} that are often very different, and with a ratio V_{shh}/V_{shv} that varies with frequency in an erratic fashion.

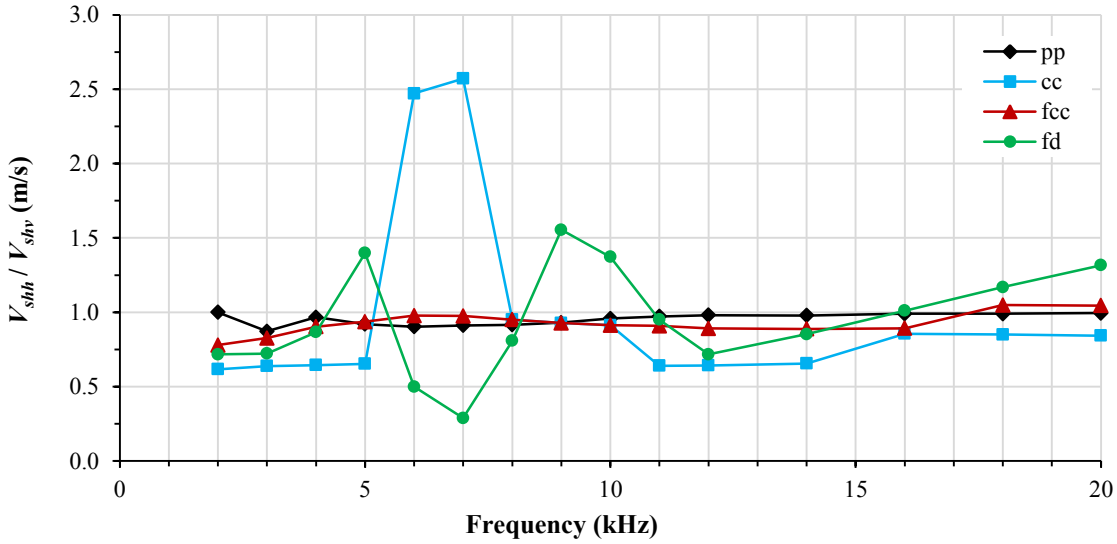

Figure 5.8: Measured shear wave velocity ratio

Figure 5.9 shows, for all four interpretation procedures, the measured ratio V_{ph}/V_{pv} of compression wave velocities with different transmission directions. Each value of V_{ph} was taken as the average of the two independent measurements (these were essentially identical for the *pp* interpretation method at frequencies above 10kHz, but showed some differences for the other three interpretation methods). Figure 5.9 shows that for the *pp* interpretation method, the measured values of V_{ph} and V_{pv} were almost identical (within 1%). This indicates that, unlike the corresponding shear wave velocity measurements, measurements of compression wave velocity with bender/extender elements in a triaxial apparatus are unaffected by the different boundary conditions for horizontal and vertical transmission.

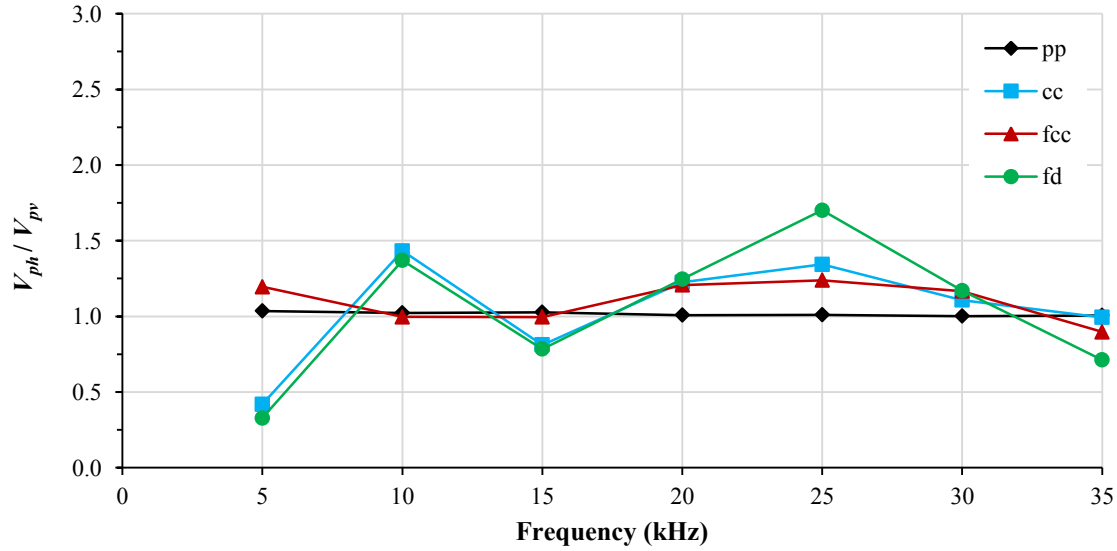

Figure 5.9: Measured compression wave velocity ratio

Inspection of Figure 5.9 shows that, whereas the *pp* interpretation method gives identical values of V_{ph} and V_{pv} (within 1%), the other three interpretation methods give values of V_{ph} and V_{pv} that are often very different, and with a ratio V_{ph}/V_{pv} that varies with frequency in an erratic fashion.

For these four particular techniques described above, it was concluded that simple measurement of peak-to-first-peak in the time domain gave the most reliable measurements of travel time for both shear and compression waves. This conclusion was based on two considerations. Firstly, that this procedure, unlike the other three, gave shear and compression wave velocities that were almost independent of frequency (less than 2.5% variation) over an appropriate range of frequencies, corresponding to wavelengths less than 25% of the transmission path length for shear waves and less than 70% of the transmission path length for compression waves. Secondly, that this procedure, unlike the other three, gave shear or compression wave velocities in an isotropic sample that were the same for different directions of wave transmission or wave polarisation, after excluding shear waves transmitted in the vertical direction, where the measured wave velocity was affected by a difference in boundary conditions.

5.1.4 Final confirmation of choice of technique

On the basis of the results presented above, it was decided that determination of travel time in the main test programme would be by measurement of peak-to-first-peak in the time domain and that transmitted wave frequencies of 20kHz and 35kHz would be used for measurement of V_s and V_p respectively.

As final confirmation of the choice of technique for determining travel time, the results for the isotropic loading stage of Test A (the first test in the main test programme) were interpreted using all four methods of determining travel time. Test A was performed in the suction-controlled double wall triaxial apparatus (as described in Section 4.2.2) on an unsaturated isotropically compacted sample and it involved "isotropic" loading (i.e. $\eta \approx 0$, with $q = 2$kPa) up to a mean net stress $\bar{p}$ of 300kPa under a constant suction of 300kPa. The expectation was that the values of shear wave velocity V_{shv} and V_{shh} would increase monotonically during the loading stage, due to the increase of $\bar{p}$ and the decrease of v.

Figure 5.10 shows the variations of measured shear wave velocities V_{shv} and V_{shh} with mean net stress $\bar{p}$ during the isotropic loading stage of Test A with each of the four different procedures for determining travel time. Inspection of Figure 5.10 shows that, of the four methods for determining travel time, the simple measurement of peak-to-first-peak in the time domain (shown as "*pp*" in Figure 5.10) gave results that varied

in a smooth logical fashion, with both V_{shv} and V_{shh} increasing monotonically with increasing $\bar{p}$. In contrast, each of the other three methods suggested more erratic and non-monotonic variation of shear wave velocities. This provided confirmation of the conclusion from the preliminary test that the measurement of peak-to-first-peak in the time domain was the most appropriate method of determining travel time in the BEE tests of this research programme.

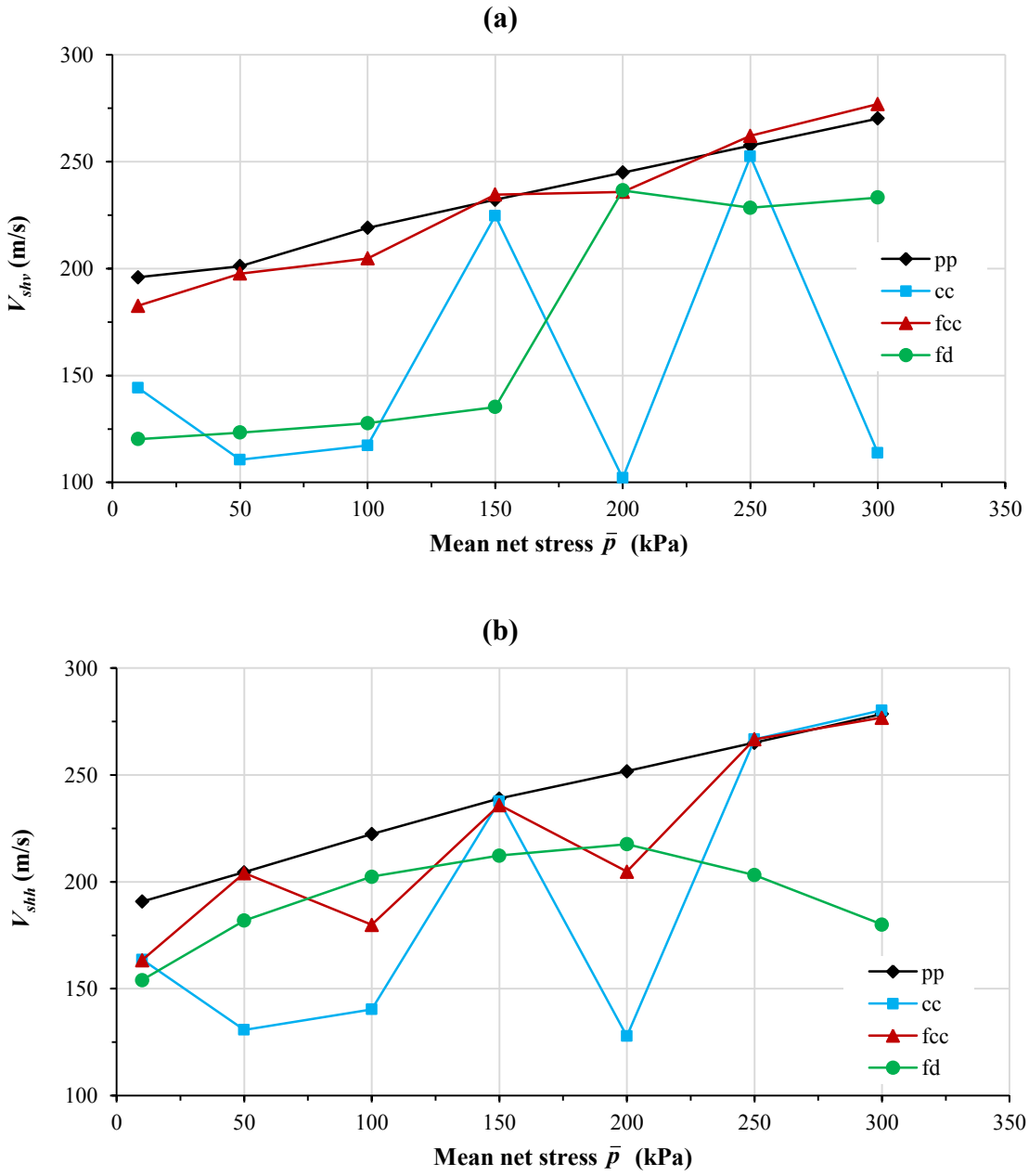

Figure 5.10: Variations of (a) V_{shv} (b) V_{shh} during isotropic loading stage of Test A

It is worth noting that selection of the best technique for measuring travel times may depend upon soil type, stress state and testing systems (including both the soil testing equipment (such as oedometer cell, shear box or triaxial cell) and the BEE

testing system). It should not therefore be concluded that peak-to-first-peak in the time domain will always be the best method of travel time determination, and other methods may provide more reliable results when testing other soils or using different testing systems.

5.2 Influence of sample preparation procedure

A series of 6 preliminary tests was performed on 6 samples prepared by 6 different methods. 5 samples were unsaturated, formed by different methods of compaction. The final sample was saturated, formed by reconstitution from a slurry in a mould. All were tested under unconfined conditions $\sigma_r = 0$, without suction control. BEE testing was performed with the samples at their initial state (at the as-compacted water content, or the water content produced by reconstitution). Only horizontal BEE pairs were used. The aim of this test series was to investigate the influence of different sample preparation methods on the initial anisotropy of elastic behaviour, as indicated by BEE tests performed with different directions of wave polarisation.

5.2.1 Sample preparation techniques

Speswhite kaolin clay was used for all 6 soil samples. The five unsaturated compacted samples were all prepared at a compaction water content of 25% (approximately 4% dry of the optimum from the standard Proctor compaction test, see Section 4.1.1). The five unsaturated compacted samples were all 50mm diameter and 100mm high. The single saturated reconstituted sample was 38mm diameter and 76mm high.

Anisotropic static compaction in a triaxial cell

This type of compaction was the type of anisotropic compaction used for the main test programme and described in Section 4.1.3. It involved two-stage static compaction of a larger sample in a triaxial apparatus, followed by coring of a 50mm diameter sample. The first stage of static compaction was under an isotropic stress state, to a mean total stress p of 100kPa, whereas the second stage was under an anisotropic stress state, with a mean total stress p of 250kPa and a deviator stress q of 300kPa.

Isotropic static compaction in a triaxial cell

The second type of compaction was similar to the isotropic compaction method used in the main test programme (see Section 4.1.3), but the final compaction stress was lower.

The method used in this preliminary test involved a first isotropic compaction stage to a mean total stress p of 100kPa and then a second isotropic compaction stage to $p = 250$kPa (compared to a $p = 390$kPa used for the isotropically compacted samples in the main test programme see Section 4.1.3). As a consequence, the value of v for the isotropically compacted sample used in this preliminary test was higher than for the equivalent anisotropically compacted sample.

Anisotropic static compaction in a mould

The third type of compaction involved static compaction directly into a 50 mm diameter split former in 9 layers, each subjected to a vertical total stress of 400kPa, following the same procedure as employed by Wheeler & Sivakumar (1995). This corresponded to anisotropic compaction under a prescribed strain path (zero lateral strain), rather than a prescribed stress path, as in the anisotropic static compaction in a triaxial cell.

Modified Proctor dynamic compaction

The fourth type of compacted sample was prepared by conventional Modified (heavy) Proctor dynamic compaction according to BS part 4 (1990) into a 1000cm^3 mould, followed by coring of a 50mm diameter sample.

Extra heavy dynamic compaction

The fifth type of compaction was an even heavier form of dynamic compaction (referred to hereafter as "extra heavy dynamic compaction") employing 56 hammer blows on each soil layer, rather than the 27 blows employed in the British Standard Modified Proctor dynamic compaction method.

Reconstituted from slurry in a mould

The final sample was prepared to a saturated reconstituted state, by consolidating one-dimensionally in a cylindrical mould (38mm internal diameter) from a slurry with an initial water content of 1.8 times the liquid limit. The applied force during this procedure corresponded to a vertical total stress of 70kPa, but friction between the cylinder wall and the porous filter placed above the soil meant that the vertical total stress applied to the soil was significantly lower than 70kPa.

The second type of compaction was intended to produce isotropic samples; whereas the other five methods of sample preparation were expected to produce different types of anisotropic samples.

5.2.2 Test results

BEE measurements of shear wave velocity were performed at a transmitted signal frequency of 20kHz, using a single sinusoidal pulse (as shown in Figures 5.11 - 5.13). Travel times were determined using the peak-to-first-peak method in the time domain (see Section 5.1). Elastic anisotropy of the samples was investigating by examining the shear modulus ratio G_{hh}/G_{hv}, determined from the shear wave velocities V_{shh} and V_{shv}. The shear wave velocity V_{svh} was not measured or included in the comparison, because an earlier test on an isotropic sample had indicated that this wave velocity was affected by the difference in boundary conditions between horizontal transmission and vertical transmission (see Section 5.1.1).

Figures 5.11 - 5.13 show typical test results of travel times (t_{hv} and t_{hh}), corresponding to samples produced by anisotropic static compaction in a triaxial cell, isotropic static compaction in a triaxial cell and extra heavy dynamic compaction respectively. The overall results for all 6 samples are given in Table 5.1. As expected, the values of elastic shear moduli measured on the samples prepared by Modified Proctor dynamic compaction and extra heavy dynamic compaction were much greater than for the other compacted samples, because these are much higher energy forms of compaction, which produced much lower values of v than the other compaction methods. Conversely, the reconstituted sample had the lowest values of shear moduli, because of the saturated state and high value of v of this sample.

Inspection of Table 5.1 shows that, as expected, isotropic static compaction in a triaxial cell produced an isotropic sample, with values of G_{hh} and G_{hv} agreeing within 1% (i.e. within the measurement accuracy indicated by the previous consistency check of the two bender element pairs see Section 3.2.6), whereas the samples prepared by the other five methods were all anisotropic, with significantly different values of G_{hh} and G_{hv}.

What is most significant in the results presented in Table 5.1 is that, whereas the samples prepared by Modified Proctor dynamic compaction and extra heavy dynamic compaction and the saturated reconstituted sample all showed G_{hh} greater than G_{hv}, the samples produced by static compaction in a mould or by anisotropic static compaction in a triaxial cell both showed G_{hh} less than G_{hv}. Repeat tests consistently confirmed this pattern of behaviour. Results from the literature generally show values of G_{hh} greater than G_{hv} for saturated reconstituted samples (e.g. Jovicic & Coop, 1998), saturated natural clay samples (e.g. Jovicic & Coop 1998 and Nash et al., 2000) and unsaturated dynamically compacted samples (e.g. Ng & Yung, 2008). It is therefore the form of results shown in Table 5.1 for the samples produced by static compaction in a mould or static compaction in a triaxial cell that is relatively unusual.

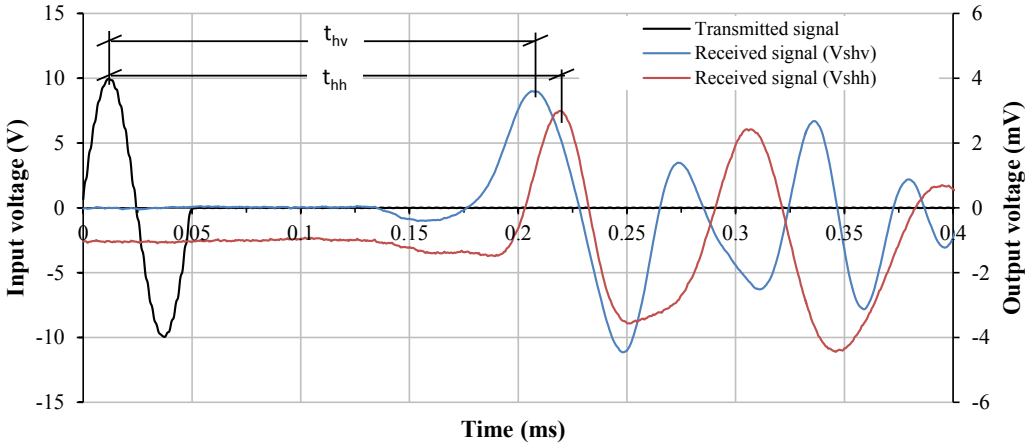

Figure 5.11: Bender element test results for sample prepared by anisotropic static compaction in a triaxial cell.

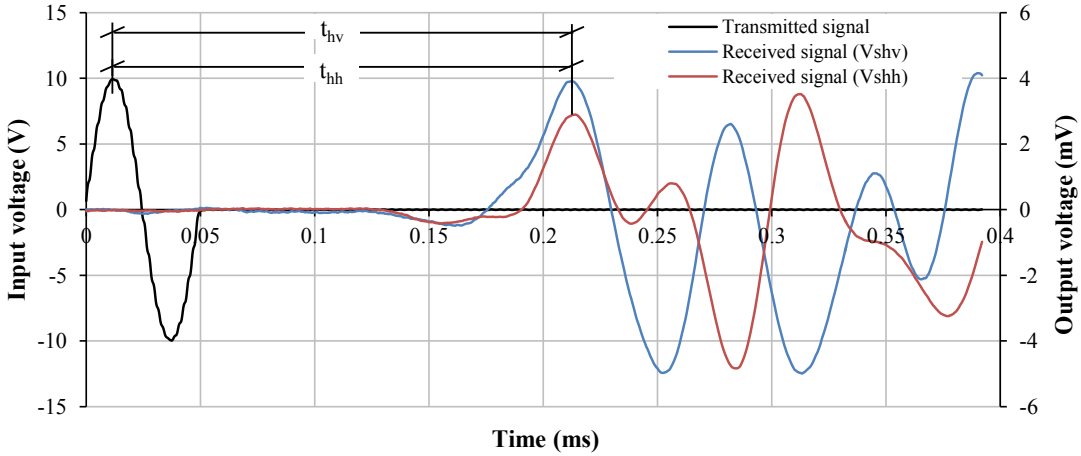

Figure 5.12: Bender element test results for sample prepared by isotropic static compaction in a triaxial cell.

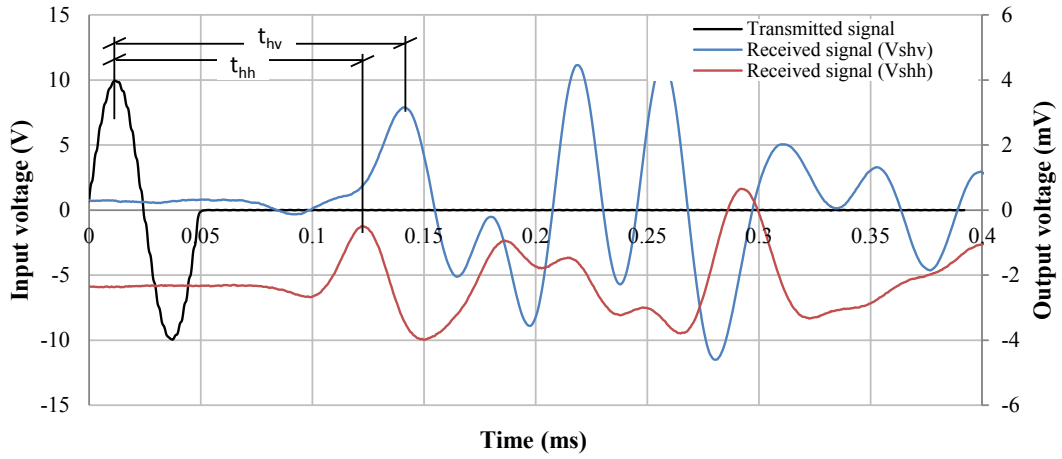

Figure 5.13: Bender element test results for sample prepared by extra heavy dynamic compaction

Table 5.1: Bender element test results for different methods of sample preparation

Sample preparation method	G_{hh} (MPa)	G_{hv} (MPa)	$\frac{G_{hh}}{G_{hv}}$
Anisotropic static compaction in a triaxial cell	72.6	81.4	0.89
Isotropic static compaction in a triaxial cell	75.9	76.7	0.99
Anisotropic static compaction in a mould	52.1	77.0	0.68
Modified Proctor dynamic compaction	206.9	177.8	1.16
Extra heavy dynamic compaction	326.6	241.8	1.35
Reconstituted from slurry in a mould	9.7	7.0	1.39

Comparing the values of the shear modulus ratio G_{hh}/G_{hv} produced by the four different methods of anisotropic compaction, it is not possible to state precisely the roles of different aspects of the compaction procedure in determining this ratio (which describes the degree of elastic anisotropy). Clearly, a change from dynamic to static compaction may have an impact, as will the nature of the lateral boundary condition during compaction (a stress-controlled boundary for the static compaction in a triaxial cell compared with zero lateral displacement for the other three types of anisotropic compaction). It appears likely, however, from inspection of Table 5.1, that the compaction energy is an important factor, given that the ratio G_{hh}/G_{hv} increases consistently with increasing compaction energy (and decreasing v) for the four types of anisotropic compaction shown in Table 5.1. Compaction water content is obviously another factor which may affect the ratio G_{hh}/G_{hv}, but this was not examined in the current work.

It is illuminating to compare the forms of small strain elastic anisotropy of the various types of sample, shown in Table 5.1, with the initial forms of large strain plastic anisotropy produced by different types of sample preparation. It is widely observed that both saturated reconstituted samples (e.g. Karstunen & Koskinen, 2008) and saturated natural clay samples (e.g. Graham et al., 1983 and Wheeler et al., 2003a) have an initial positive inclination of the yield curve in the $q : p'$ plane. Similarly, authors such as Cui & Delage (1996) showed positive inclinations of constant suction cross-sections of the yield surface in the $q : \bar{p}$ plane for unsaturated compacted samples prepared by static compaction. Finally, Al-Sharrad (2013) showed that the two types of static compaction in a triaxial cell used here produced constant suction cross-sections of the yield surface that were symmetric about the axis for the isotropic form of compaction and showed a positive inclination in the $q : \bar{p}$ plane for the anisotropic form of compaction.

It is clear therefore that whereas the five different types of anisotropic sample preparation used here produced two opposite forms of small strain elastic anisotropy (with G_{hh} either greater or less than G_{hv}), all these types of anisotropic sample preparation have been shown to produce a single form of large strain plastic anisotropy (with a positive inclination of the yield curves in the $q : p$ plane). This strongly suggests that anisotropy of small strain elastic behaviour and anisotropy of large strain plastic behaviour are controlled by different aspects of the soil fabric (each represented by a different fabric tensor).

Chapter 6

Main test programme

In this chapter, experimental results from the 11 tests in the main test programme are presented and discussed. Section 6.1 presents soil properties measured immediately after compaction, covering soil state variables v, w and S_r, as well as wave velocities (and corresponding very small strain elastic moduli) determined from BEE test results. Section 6.2 presents equivalent results after initial equalization stages. Sections 6.3–6.9 cover the behaviour observed in the main loading/unloading and wetting/drying stages, with each sub-section exploring the role of a particular test variable (such as form of compaction, suction during loading/unloading or stress ratio η during loading/unloading) on both large strain plastic behaviour and very small strain elastic behaviour (as indicated by BEE testing).

6.1 Soil properties after compaction

Table 6.1 shows test data measured in the as-compacted state (after setting up in the triaxial cell but prior to initial stress adjustment and initial equalization stage described in Section 4.5.1). Each of the 11 tests (A-K) also has a test code (as shown in Table 6.1). The first letter of the test code indicates whether the test was on an isotropically compacted sample (I) or an anisotropically compacted sample (A). This is followed by a number (300, 50 or 0), which indicates the value of suction during loading and unloading stages. Finally, a number in brackets indicates the value of stress ratio η (0, 1 or -1) during loading and unloading stages. For example, Test A has a code of I300(0), indicating that this was a test on an isotropically compacted sample, with loading and unloading stages performed at a suction of 300kPa with $\eta \simeq 0$ (i.e. at $q = 2$kPa, as explained in Section 4.5.2). The final R in the code for Test G (see Table 6.1) indicates that this was a test with a reduced length of loading path (see Section

4.5.2), to differentiate it from Test E. Finally, WD(10) and WD(100) at the end of the codes for Tests J and K (see Table 6.1) indicate that these two tests included a wetting-drying cycle performed either at $\bar{p} = 10$kPa (Test J) or at $\bar{p} = 100$kPa (Test K), as explained in Section 4.5.2.

6.1.1 Specific volume, water content and degree of saturation

One of the intentions in selecting the forms of isotropic and anisotropic compaction described in Section 4.1.3 was to produce soil samples with the same initial conditions of specific volume v, water content w and degree of saturation S_r. Therefore, it was expected that all the isotropically and anisotropically compacted soil samples would have approximately the same values of v, w and S_r.

Inspection of Table 6.1 shows that the average specific volume v of the 7 isotropically compacted samples was 2.161 (with a standard deviation of 0.010), whereas the average value of v of the 4 anisotropically compacted samples was 2.168 (with a standard deviation of 0.008). The average values of water content w were 23.35% (with a standard deviation of 0.22%) and 23.56% (with a standard deviation of 0.12%), for isotropically and anisotropically compacted samples respectively. Finally, the corresponding average values of degree of saturation S_r were 52.29% (with a standard deviation of 0.81%) and 52.46% (with a standard deviation of 0.59%). This confirms that, as intended, the as-compacted values of v, w and S_r were sensibly repeatable for both compaction methods and were the same for both compaction methods (within the range of repeatability).

The average value of v for the anisotropically compacted samples (2.168) was almost identical to the average value of v reported by Al-Sharrad (2013) (2.169, with a standard deviation of 0.008), who used the same anisotropic compaction procedure. This provides further confirmation of the repeatability of the sample preparation procedure. However, the average initial water content in this study (23.43%) for isotropically and anisotropically compacted samples combined was slightly lower than the result reported by Al-Sharrad (24.74%) because in this study the samples were subjected to the room temperature for a longer time period during setting-up than was the case in the Al-Sharrad (2013) study, producing more evaporation of water from the samples. This was due to the time required for forming the slots on the samples for mounting the bender/extender elements (see Section 4.2.2).

Table 6.1: Soil properties after compaction

Test	Test code	v	w (%)	S_r (%)	Shear wave velocities (m/s)			$\frac{G_{hh}}{G_{hv}}$	Compression wave velocities (m/s)			$\frac{M_h}{M_v}$
					V_{svh}	V_{shv}	V_{shh}		V_{pv}	V_{ph1}	V_{ph2}	
A	I300(0)	2.181	22.96	50.56	220.9	230.1	229.2	0.99	364.9	364.1	365.1	1.00
B	I300(1)	2.164	23.51	52.52	215.1	226.7	225.0	0.99	360.3	359.5	359.7	1.00
C	I300(-1)	2.148	23.25	52.60	223.1	226.7	225.1	0.99	365.3	363.9	364.9	1.00
D	A300(0)	2.163	23.50	52.54	220.1	225.6	218.1	0.93	355.9	360.0	361.9	1.03
E	A300(1)	2.179	23.50	51.84	218.5	222.2	215.5	0.94	365.9	370.1	372.2	1.03
F	A300(-1)	2.172	23.48	52.11	215.9	226.1	217.0	0.92	361.5	361.3	363.7	1.01
G	A300(1)R	2.157	23.77	53.39	213.7	221.2	212.5	0.92	362.1	368.9	369.1	1.04
H	I50(0)	2.154	23.63	53.25	221.4	230.0	227.5	0.98	376.7	376.6	375.5	1.00
I	I0(0)	2.159	23.57	52.87	-	232.6	230.5	0.98	-	365.9	365.1	-
J	I300(0)WD10	2.160	23.37	52.38	216.3	229.5	228.0	0.99	365.1	365.9	364.9	1.00
K	I300(0)WD100	2.162	23.18	51.86	215.9	226.6	227.1	1.00	363.0	362.9	361.5	1.00

6.1.2 Wave velocities

Table 6.1 shows measurements of shear and compression wave velocities immediately after compaction and setting-up.

Investigation of Table 6.1 shows that the average values of shear wave velocities V_{svh}, V_{shv} and V_{shh} for the 7 isotropically compacted samples were 218.8m/s (with a standard deviation of 3.1m/s), 228.9m/s (with a standard deviation of 1.6m/s), and 227.5m/s (with a standard deviation of 1.5m/s), respectively. The average values of V_{shv} and V_{shh} were very similar (within 0.6%), confirming the isotropic behaviour of these isotropically compacted samples. However, the average value of V_{svh} was almost 5% lower than the average values of V_{shv} and V_{shh}, despite the fact that thermodynamic considerations imply that V_{svh} and V_{shv} should be identical, irrespective of any material anisotropy (Love, 1927). This confirms the conclusion from the preliminary tests reported in Section 5.1.3. that the different boundary conditions for vertical and horizontal transmission has a significant influence on measured shear wave velocity. The small standard deviation of each individual shear wave velocity provides further confirmation of the repeatability of the sample preparation technique.

For the 4 anisotropically compacted samples, the average values of V_{svh}, V_{shv} and V_{shh} were 217.1m/s (with a standard deviation of 2.5m/s), 223.8m/s (with a standard deviation of 2.1m/s) and 215.8m/s (with a standard deviation of 2.1m/s), respectively. As expected, the average values of V_{shv} and V_{shh} were different (by about 4%). This was not due to the boundary conditions, but it seems that the anisotropic form of compaction produced soil samples with anisotropic elastic behaviour (indicating anisotropic fabric).

Table 6.1 also shows that the average values of compression wave velocities V_{pv}, V_{ph1} and V_{ph2} for the 7 isotropically compacted samples were 365.9m/s (with a standard deviation of 5.1m/s), 365.5m/s (with a standard deviation of 4.9m/s), and 365.2m/s (with a standard deviation of 4.6m/s), respectively. These results also confirm that the isotropic compaction technique in this study was able to produce isotropic samples in terms of compression wave velocities (all within about 0.2%). For anisotropically compacted samples, the average values of V_{pv}, V_{ph1} and V_{ph2} were 361.4m/s (with a standard deviation of 3.6m/s), 365.1m/s (with a standard deviation of 4.5m/s) and 366.7m/s (with a standard deviation of 4.1m/s), respectively. The average values of V_{ph1} and V_{ph2} were very similar (as expected), whereas the average values of V_{pv} was slightly lower (by about 1%), consistent with anisotropy of soil fabric produced by the anisotropic compaction procedure.

6.1.3 Elastic anisotropy

Investigation of the initial elastic anisotropy of the samples produced by the two different methods of compaction was performed by considering the shear modulus ratio G_{hh}/G_{hv} and the constrained modulus ratio M_h/M_v , with the various elastic moduli calculated from the corresponding shear or compression wave velocities using Equations 4.19 and 4.22. The shear modulus G_{vh} was excluded from this exercise, because of the indication that the difference in boundary conditions affected the measurement of shear wave velocity V_{svh}. The horizontal constrained modulus M_h was calculated from the horizontal compression wave velocity V_{ph}, taken as the average of the two independent measurements V_{ph1} and V_{ph2}.

Inspection of Table 6.1 indicates that the average values of elastic shear modulus ratio G_{hh}/G_{hv} and elastic constrained modulus ratio M_h/M_v for the 7 isotropically compacted soil samples were 0.99 and 1.00 respectively. This provides further confirmation that the isotropic compaction procedure produced isotropic samples, in terms of their elastic behaviour. In contrast, the average values of G_{hh}/G_{hv} and M_h/M_v for the 4 anisotropically compacted samples were 0.93 and 1.03 respectively. Clearly, the anisotropic compaction procedure produced samples that were anisotropic in their elastic behaviour. The degree of elastic anisotropy produced by the anisotropic compaction procedure was, however, relatively modest (for example, compare with some of the values of G_{hh}/G_{hv} reported in Table 5.1 for other forms of anisotropic sample preparation procedure).

6.2 Soil properties after initial equalization

6.2.1 Specific volume, water content and degree of saturation

Table 6.2 shows the values of $\bar{p}$, q and s after the initial equalization stage described in Section 4.3.2 for the 11 samples in the main test programme. For all tests except H and I, equalization took place at s =300kPa, $\bar{p}$ = 10kPa and a deviator stress q of 2kPa, 10kPa or -10kPa (see Table 6.2 and Section 4.5.1). For Test H the equalization was performed in two stages, with initial wetting to s = 300kPa then immediately followed by wetting to s = 50kPa, with $\bar{p}$ = 10kPa and q = 2kPa throughout (see Table 6.2). For the saturated sample Test I, the stress state at the end of equalization corresponded to p' = 5kPa (shown in Table 6.2 as $\bar{p}$ = 5kPa and s = 0) and q = 2kPa, as described in Section 4.5.1.

Figure 6.1 shows the measured variation of v plotted against time during the initial equalization stage for all samples. For the majority of tests, the variation of v shown

in Figure 6.1 corresponded to equalization at a suction of 300kPa. For Test H, the variation of v shown in Figure 6.1 covers both parts of the equalization stage, with initial wetting to $s = 300$kPa followed by subsequent wetting to $s = 50$kPa. Also, shown in Figure 6.1, for comparison, was the wetting stage of the wetting-drying cycle of test J, which also involved wetting from $s = 300$kPa to $s = 50$kPa at $\bar{p} = 10$kPa. For the saturated sample of Test I, the variation of v shown in Figure 6.1 corresponds to the saturation stage described in Section 4.2.3. This was in two parts, with a flushing process followed by an air dissolution process (see Section 4.2.3), and the transition from the flushing process to the air dissolution process is indicated by point X in Figure 6.1. Figure 6.2 shows the corresponding measured variation of w during the initial equalization stage of all tests except Test I on the saturated sample. It was not possible to monitor the variation of w during the saturation stage of test I, because the flushing process involved water inflow at the base of the sample but also an unmeasurable water outflow at the top of the sample (where a mixture of water and air was exiting). Figure 6.3 shows the corresponding calculated variation of S_r during the initial equalization stage of all tests except Test I on the saturated sample.

Inspection of Figure 6.2 shows a significant water inflow during equalization for all tests at $s = 300$kPa and additional water inflow for tests at $s = 50$kPa (the second part of equalization of Test H or the wetting stage of Test J). This confirms that the as-compacted value of suction (at the start of equalization) was significantly higher than 300kPa (Al-Sharrard (2013) reported an as-compacted suction of approximately 650kPa).

Investigation of Figure 6.1 shows that during the initial equalization stage, significant wetting-induced swelling occurred in all samples brought to a suction of 300kPa, with increased magnitude of swelling on wetting to $s = 50$kPa (Test H and J) and the greatest magnitude of swelling on wetting to a saturated state (Test I). There was no indication of wetting-induced collapse compression in any tests. This was expected, because the initial equalization process was performed under low stress state conditions ($\bar{p} = 10$kPa), such that the stress path was expected to remain inside the LC yield curve (see Wheeler & Sivakumar, 1995).

Table 6.2 shows that the average value of v at the end of equalization stage, for the 10 samples equalized at $s = 300$kPa (including the first part of equalization of Test H) was 2.214, with a standard deviation of 0.011. Detailed examination of results in Table 6.2 indicated that the difference between isotropic compaction and anisotropic compaction, and small differences in the value of q (2kPa, 10kPa or -10kPa), had no consistent effect on the values of v at the end of equalization at $s = 300$kPa. Inspection of Figure 6.1 shows that the main reason for the variation of v at the end

Table 6.2: Soil properties after initial equalization stage

Test	Test code	$\bar{p}$ (kPa)	q (kPa)	s (kPa)	v	w (%)	S_r (%)	Shear wave velocities (m/s)			$\frac{G_{hh}}{G_{hv}}$	Compression wave velocities (m/s)			$\frac{M_h}{M_v}$
								V_{svh}	V_{shv}	V_{shh}		V_{pv}	V_{ph1}	V_{ph2}	
A	I300(0)	10	2	300	2.232	28.95	61.11	174.1	196.1	197.0	1.01	315.0	316.1	314.6	1.00
B	I300(1)	10	10	300	2.220	29.27	62.39	179.1	194.0	191.0	0.97	311.6	319.3	319.0	1.05
C	I300(-1)	10	-10	300	2.206	28.58	61.64	175.1	190.6	199.6	1.10	292.3	316.1	313.5	1.16
D	A300(0)	10	0	300	2.208	28.79	61.99	193.5	202.0	197.5	0.96	314.0	319.1	313.1	1.01
E	A300(1)	10	10	300	2.233	29.26	61.71	177.6	192.0	187.9	0.96	305.2	307.5	308.0	1.02
F	A300(-1)	10	-10	300	2.220	28.21	60.10	180.1	188.3	186.1	0.98	304.0	303.0	307.0	1.01
G	A300(1)R	10	10	300	2.204	29.03	62.71	182.0	191.8	187.0	0.95	312.7	320.2	318.0	1.04
H	I50(0)	10	2	300	2.208	28.96	62.40	181.1	198.7	195.1	0.96	315.0	320.8	317.0	1.02
		10	2	50	2.266	40.32	82.81	130.0	147.9	149.0	1.01	297.5	302.3	304.6	1.04
I	I0(0)	5	2	0	-	-	-	-	83.7	83.9	1.00	-	-	-	-
J	I300(0)WD10	10	2	300	2.200	28.97	62.78	182.7	193.2	192.2	0.99	314.7	316.5	318.0	1.02
K	I300(0)WD100	10	2	300	2.209	28.41	61.13	180.1	192.7	195.5	1.03	309.4	313	315.8	1.03

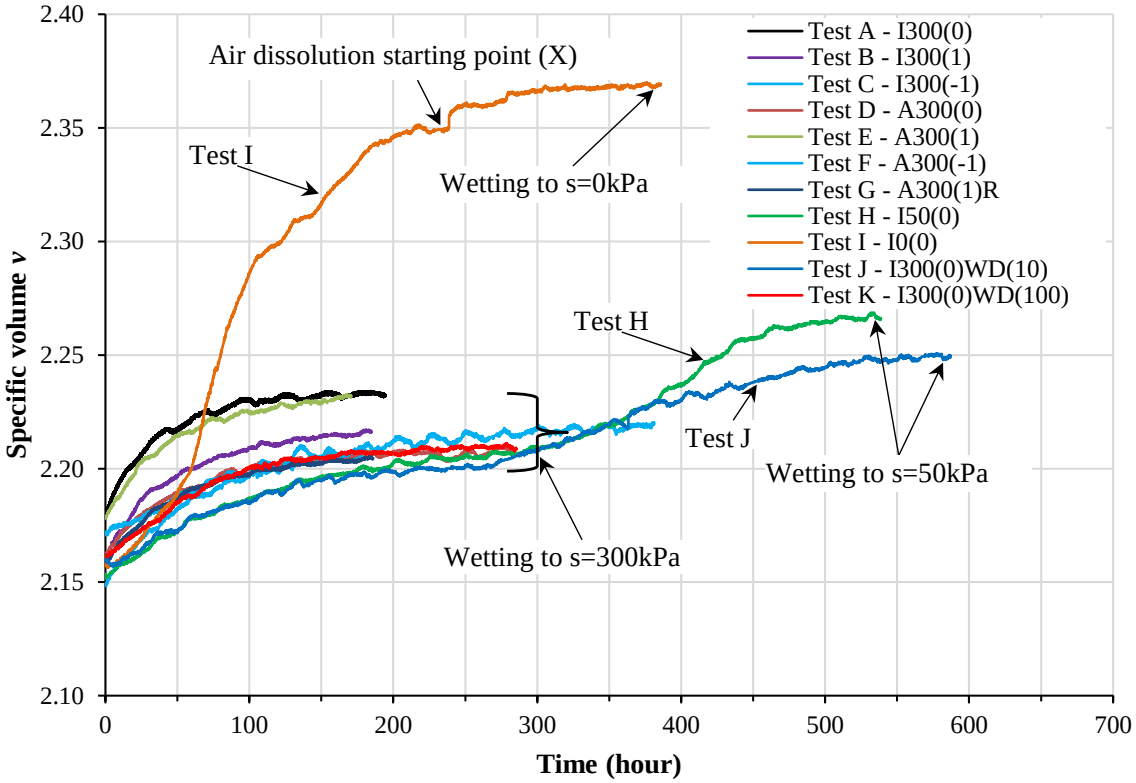

Figure 6.1: Variation of specific volume v during initial equalization stage for all samples

of the equalization stage for these tests was the variation in the measured values of v at the start of equalization (i.e. the changes in v during equalization were very similar for all these 10 tests). This was thought to be largely a measurement error, due to the difficulty in accurately determining sample volume at the start of equalization (an error analysis indicated that the variations of v between the 10 samples shown in Table 6.2 could have been produced by errors of less than $\pm$0.2mm in the measurements of initial sample height and diameter). It was therefore decided, to use an adjusted sample volume at the end of equalization at $s = 300$kPa for each of these 10 tests, corresponding to the average value of specific volume of $v = 2.214$ in all 10 tests, such that the variations of v (and the corresponding variations of S_r) during subsequent loading and unloading stages or wetting and drying stages were all adjusted to start at the same value of v.

Figure 6.1 shows that the rate of increase of v in the saturation stage of Test I was initially slower than in the equalization stages of other tests, even though the final increase of v was greatest in Test I. This is attributable to the fact that during the saturation stage of Test I water inflow was allowed only from the base of the sample (see Section 4.2.3), whereas in the equalization stages of the remaining tests water inflow occurred at both bottom and top of the sample (see Section 4.3.2).

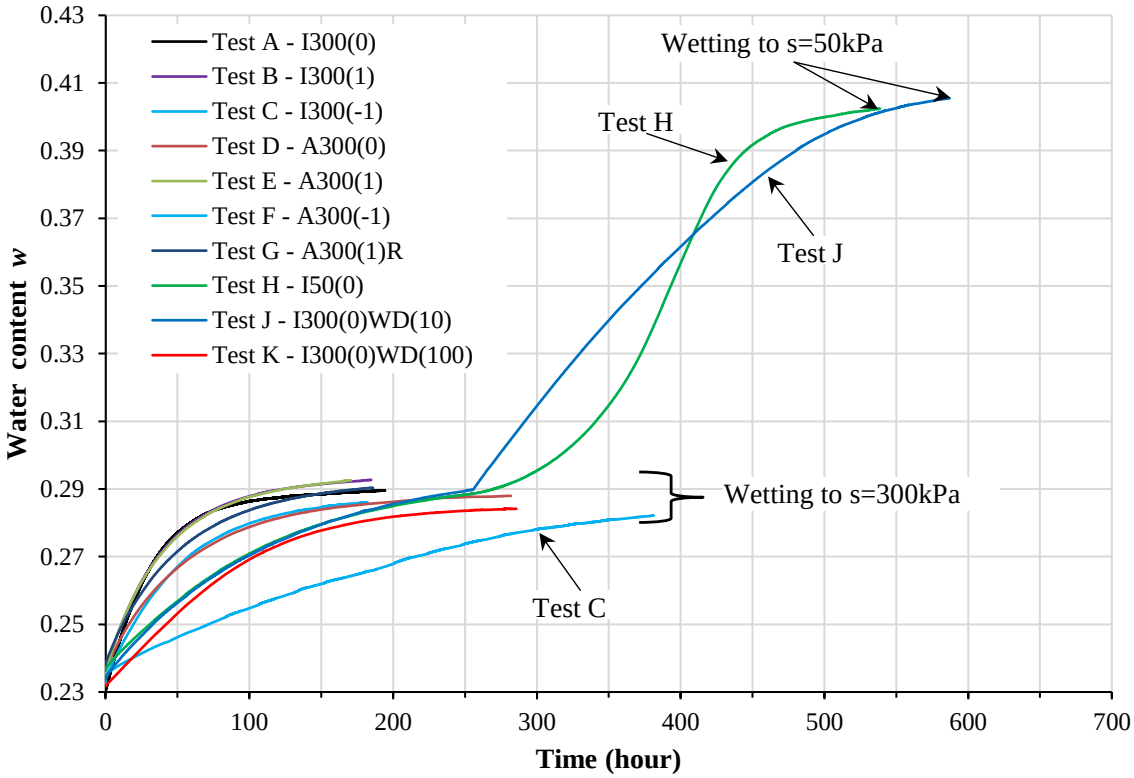

Figure 6.2: Variation of water content w during initial equalization stage for all samples

Table 6.2 shows that the average value of w at the end of the equalization stages performed at s = 300kPa was 28.84%, with a standard deviation of 0.28%. The corresponding average value of S_r was 61.80%, with a standard deviation of 0.65%.

Inspection of Figure 6.2 and Figure 6.3 shows that the variations of w and S_r during equalization were significantly slower in Test C than in other equivalent tests. This was attributed to poor initial contact between the soil sample and the HAE ceramic filter in either the base pedestal or top cap in Test C. For the other 9 tests wetted to s =300kPa, the rate of variation of w and S_r with time was generally slower for tests conducted later in the test programme than for those conducted early in the programme. This was attributed to gradual clogging of pores in the HAE ceramic filters by soil particles during the period of the test programme, with consequent gradual reduction in the permeability of the HAE ceramic filters.

Inspection of Figures 6.2 and 6.3 shows that in Tests H and J the variation with time of w and S_r during wetting from s = 300kPa to s = 50kPa was noticeably different in the two tests. This was because the change of suction (from s = 300kPa to s = 50kPa) was applied to the boundary of the sample as almost a step change in the case of Test J, whereas it was applied over a period of 125 hours (at 2kPa/hr) in the case of Test H.

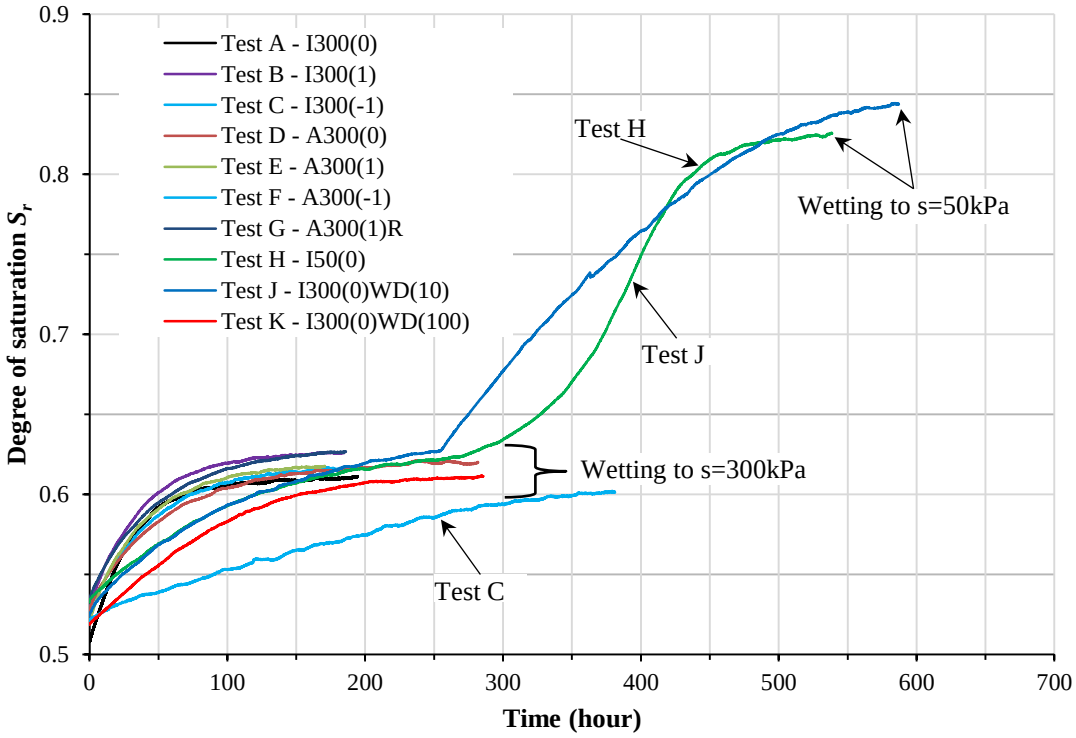

Figure 6.3: Variation of degree of saturation S_r during initial equalization stage for all samples

6.2.2 Wave velocities

Figures 6.4 and 6.5 show the variations of shear wave velocities V_{svh}, V_{shv} and V_{shh} and compression wave velocities V_{pv}, V_{ph1} and V_{ph2} plotted against time during the initial equalization stage of Test E, a typical test involving equalization to $s = 300$kPa. The BEE measurements were performed at 24 hour intervals throughout the initial equalization stage of Test E. Figures 6.4 and 6.5 indicate that all shear and compression wave velocities showed monotonic decrease throughout the equalization stage and had stabilised prior to the end of the stage. Figures 6.6 and 6.7 show typical raw BEE test results from Test E for the start and end of the equalization stage, demonstrating the increase of travel time (and hence reduction of wave velocity) that was observed during the equalization stage for both shear and compression waves.

Table 6.2 shows for all tests, the measured values of all shear and compression wave velocities at the end of the equalization stages. Also shown are the corresponding values of G_{hh}/G_{hv} and M_h/M_v which provide an indication of elastic anisotropy.

Measurements of V_{svh} and V_{pv} were not performed for the saturated sample I, because the modified base pedestal and top cap (with HAE ceramic filters and vertical BEEs) were replaced by conventional base pedestal and top cap in this test to allow saturation of the sample by flushing water through the sample from the base pedestal to the top cap (see Section 4.2.3). It was also not possible to measure V_{ph} at the end of the

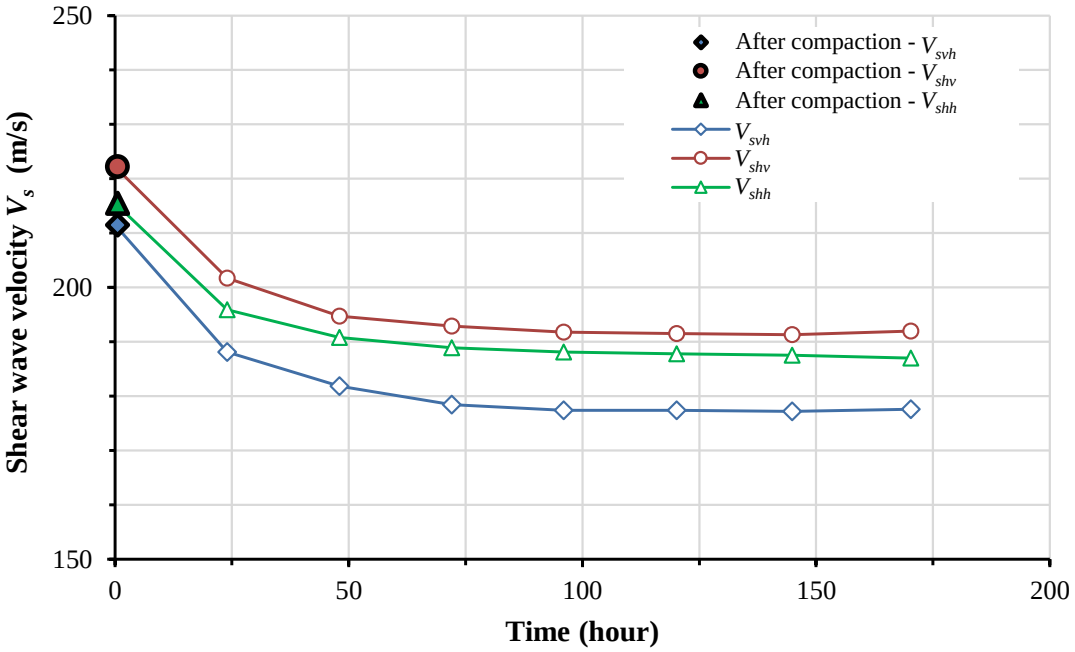

Figure 6.4: Variation of shear wave velocity V_s during initial equalization stage for sample E

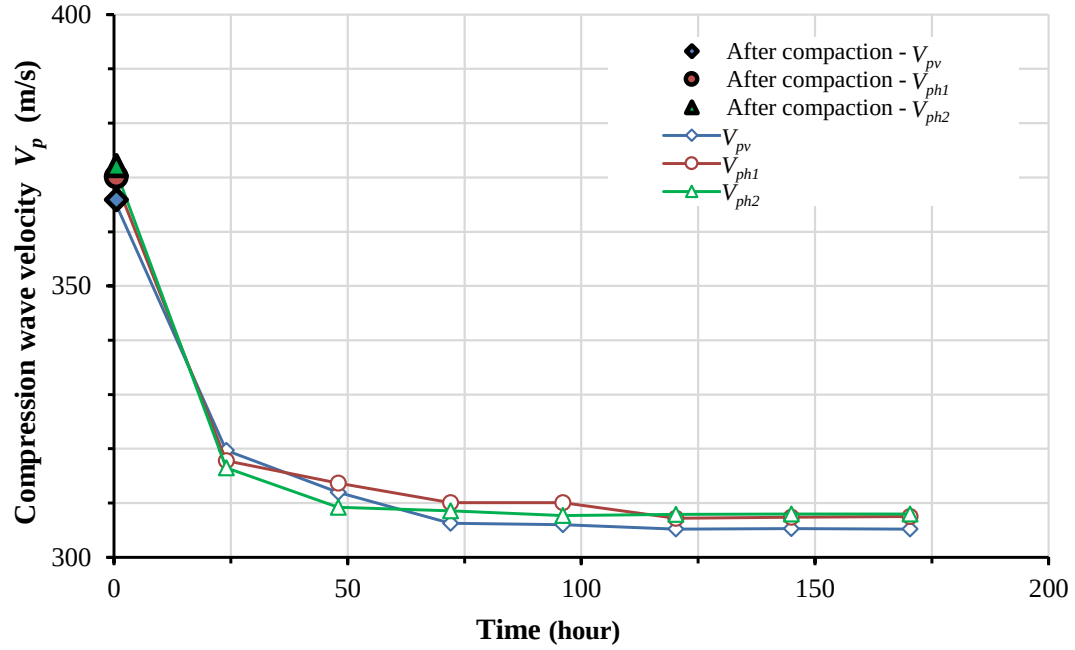

Figure 6.5: Variation of compression wave velocity V_p during initial equalization stage for sample E

saturation stage of test I, because the received signal was very noisy.

Inspection of Table 6.2 shows that the average values of V_{svh}, V_{shv} and V_{shh} for isotropically compacted samples after initial equalization to $s = 300$kPa were 178.7m/s (with a standard deviation of 3.1m/s), 194.2m/s (with a standard deviation of 2.6m/s) and 195.1m/s (with a standard deviation of 2.9m/s), respectively. Comparison with the results presented in Section 6.1.2 and Table 6.1 indicates the average values of V_{svh}, V_{shv} and V_{shh} for isotropically compacted samples reduced by 18%, 15% and 14% respectively during equalization to $s = 300$kPa. These reductions in the values of shear wave velocity V_s (and hence shear modulus) can be attributed to the combined effect of the wetting itself (reduction of s and increase of S_r) and the wetting-induced swelling (the increase of v shown in Figure 6.1).

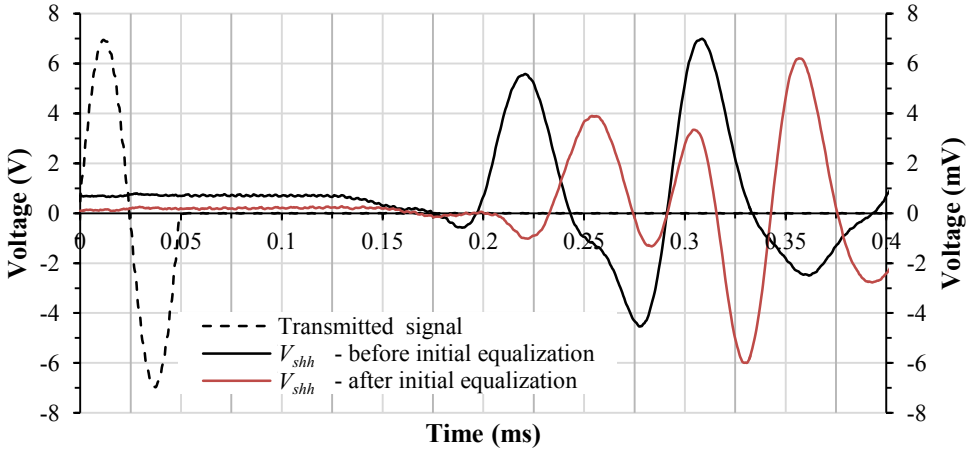

Figure 6.6: BEE test results for shear wave velocityV_s before and after initial equalization stage for sample E

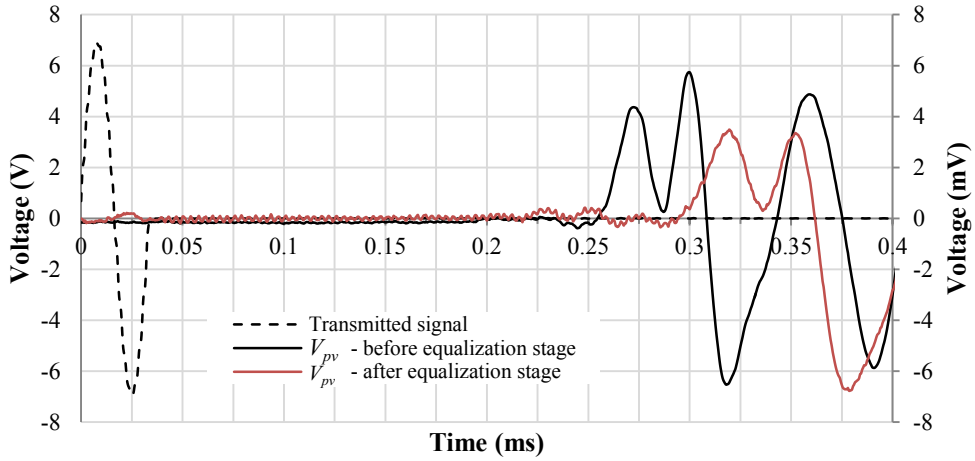

Figure 6.7: BEE test results for compression wave velocity V_p before and after initial equalization stage for sample E

For anisotropically compacted samples, Table 6.2 shows that the average values of V_{svh}, V_{shv} and V_{shh} after initial equalization to s = 300kPa were 183.3 m/s (with a standard deviation of 6.1m/s), 193.5 m/s (with a standard deviation of 5.1m/s) and 189.6 m/s (with a standard deviation of 4.6m/s) respectively. These represent reductions of 16%, 14% and 12% respectively during equalization, which again can be attributed to the combined direct effect of the wetting (reduction of s and increase of S_r) and the wetting-induced swelling (the increase of v).

Inspection of Table 6.2 shows that for the single sample equalized at a suction of 50kPa (Test H), the vales of V_{svh}, V_{shv} and V_{shh} after equalization were 130.0m/s, 147.9m/s and 149.0m/s respectively, representing reductions of 41%, 36% and 35% during equalization. For the single sample brought to a saturated state (Test I), the reduction in the values of shear wave velocity was even greater, to 83.7m/s and 83.9m/s for V_{shv} and V_{shh} respectively. This pattern of behaviour confirms that increased wetting (to lower values of s and higher values of S_r) and increased wetting-induced swelling led to greater reduction of shear wave velocity.

Values of compression wave velocity V_p (taken as the mean of V_{pv}, V_{ph1} and V_{ph2}) after equalization to s = 300kPa averaged 314m/s for isotropically compacted samples and 311.0m/s for anisotropically compacted samples (see Table 6.2). This represents reductions of 14% and 15% respectively from the corresponding values before equalization. Compression wave velocities would be expected to increase with an increase in degree of saturation (because of the likely increase of undrained bulk modulus) but decrease with an increase of v. The observed decreases of V_p therefore suggest that the influence of wetting-induced swelling (the increase of v) outweighed the influence of the wetting itself (the increase of S_r).

In Test H, values of compression wave velocity V_p (taken as the mean of V_{pv}, V_{ph1} and V_{ph2}) after equalization to s = 50kPa averaged 302m/s for isotropically compacted sample H (see Table 6.2). This represents a reduction of 16% from the corresponding value before equalization.

In Test I, for the saturated sample, values of compression wave velocity V_p were not recorded after saturation I, due to very noisy received signals.

6.2.3 Elastic anisotropy

Investigation of Table 6.2 shows that for isotropically compacted soil samples equalized under a very small deviator stress q of 2kPa (Tests A, H, I, J and K), the value of shear modulus ratio G_{hh}/G_{hv} after equalization averaged 1.00 (ranging from 0.96

to 1.03). This was almost unchanged from the average value of 0.99 before equalization. Similarly, the average value of constrained modulus ratio M_h/M_v for these samples was 1.02 (ranging from 1.00 to 1.03), showing very little change from the corresponding average value of 1.00 before equalization. This suggests that equalization of these isotropically compacted samples under an (almost) isotropic stress state had maintained the isotropy of elastic behaviour.

In contrast, the results from Tests B and C suggest that when a deviator stress of $\pm$10kPa was applied to an isotropically compacted sample during equalization this produced some anisotropy of elastic behaviour. For Test B (q = 10kPa), the values of G_{hh}/G_{hv} and M_h/M_v after equalization were 0.97 and 1.05 respectively. More markedly, for Test C ($q = -10$kPa), the values of G_{hh}/G_{hv} and M_h/M_v after equalization were 1.10 and 1.16 respectively. This suggests that the application of even a relatively modest value of deviator stress (well below the large strain yield value) can lead to anisotropy of small strain elastic behaviour (suggesting stress-induced anisotropy, rather than strain-induced anisotropy). This suggestion of stress-induced anisotropy, however, should be viewed with a degree of caution, because the effect was seen clearly only in Test C, and it can be dangerous to rely too strongly on a result from a single test.

For anisotropically compacted soil samples (Tests D, E, F and G) the average value of G_{hh}/G_{hv} after equalization was 0.97 (ranging from 0.96 to 0.98). This was an increase from the corresponding average value of 0.93 before equalization, suggesting that the small strain elastic behaviour had become closer to isotropic during equalization. The increase in the value of G_{hh}/G_{hv} during equalization was greatest for the case with $q = -10$kPa (Test F), where G_{hh}/G_{hv} increased from 0.92 to 0.98 during equalization. For these anisotropically compacted samples, there was relatively little change in the values of constrained modulus ratio M_h/M_v during equalization, averaging 1.03 before equalization and 1.02 after equalization (with no apparent influence of the value of q during equalization).

6.3 Loading/unloading stages: investigation of repeatability

Figure 6.8 shows the stress paths followed in the $q : \bar{p}$ plane during the loading and unloading stages of Tests E and G, which both involving loading with $\eta = 1$ at s =300kPa on anisotropically compacted samples. Also shown in Figure 6.8 is the estimated location of the critical state line in triaxial compression at s =300kPa, taken from the work of Al-Sharrad (2013).

In Figure 6.8 E_1 and G_1 represent the start of the loading stage (at the end of the previous equalization stage), E_2 and G_2 represent the end of the loading stages, E_3 and G_3 are the end of the subsequent 24 hour rest stages and E_4 and G_4 represent the end of the final unloading stages. Test E involved loading to $\bar{p}$ =250kPa, q =250kPa, whereas Test G involved loading to $\bar{p}$ =150kPa, q =150kPa. Comparison of results from the loading stage G_1G_2 from Test G with the corresponding results from the first part of the loading stage E_1E_2 from Test E therefore provides a means of investigating the repeatability of the test procedures and test results, given that the compaction procedure, stress history and loading stress paths were identical for these two tests up to $\bar{p}$ =150kPa, q =150kPa.

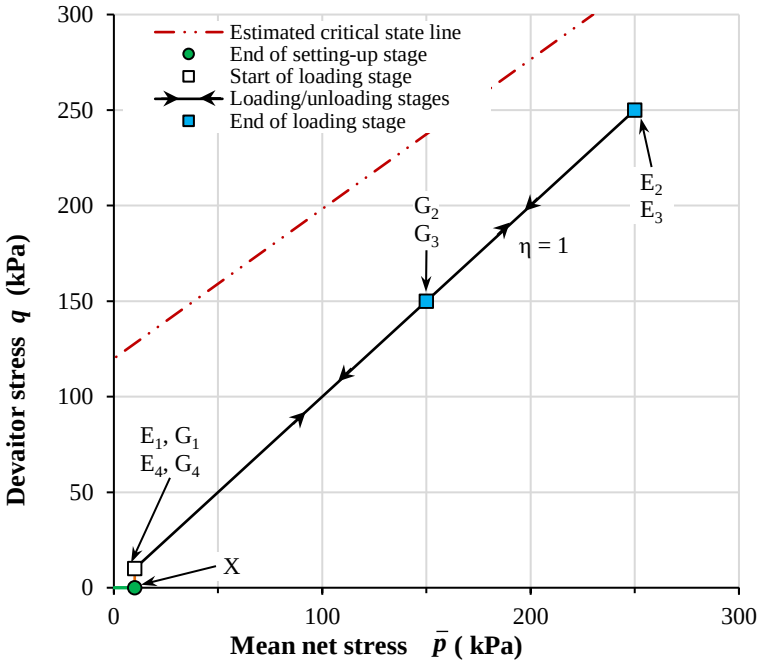

Figure 6.8: Stress paths for Tests E and G at s =300kPa

6.3.1 Large strain behaviour

Figure 6.9 shows the variations of deviator stress q with shear strain ϵ_s during the anisotropic ($\eta = 1$) loading and unloading stages of Tests E and G. Figure 6.10 shows the corresponding variations of volumetric strain ϵ_v against shear strain ϵ_s for these two tests. Inspection of Figures 6.9 and 6.10 shows an excellent level of repeatability between the results from loading stage G_1G_2 and corresponding results from the first part of the loading stage E_1E_2. At G_2 ($\bar{p}$ =150kPa, q =150kPa), the shear strain ϵ_s and volumetric strain ϵ_v were 3.39% and 4.60% respectively. At $\bar{p}$ =150kPa and q =150kPa the corresponding values of ϵ_s and ϵ_v during the loading stage E_1E_2 of Test E were 3.90% and 4.75% respectively. The shapes of the $q : \epsilon_s$ and $\epsilon_v : \epsilon_s$ curves up to this point were also very similar for Tests E and G.

Figure 6.11 shows the variations of specific volume v, water content w and degree of saturation S_r during the loading and unloading stages of Tests E and G, all plotted against $\bar{p}$ (with $\bar{p}$ on a logarithmic scale). In Figure 6.11a both tests are shown as starting from the same value of v, following the small adjustment to the assumed values of sample volume at this point, as described in Section 6.2.1. Inspection of Figure 6.11 shows that the variations of v, w and S_r during loading stage G_1G_2 were very similar to the variations of v, w and S_r during the first part of loading stage E_1E_2 (up to $\bar{p}$ =150kPa). Although values of w during the two tests may appear significantly different, this is simply because of the expanded scale used for plotting of w in Figure 6.11b and the slight difference in measured initial values of w (at E_1 and G_1).

Figures 6.9, 6.10 and 6.11 provide a high level of confidence that the tests procedures and measurement techniques produced an excellent level of repeatability of the large strain behaviour.

6.3.2 Wave velocities

Figure 6.12 shows the variations of shear wave velocities V_{svh}, V_{shv} and V_{shh} plotted against mean net stress $\bar{p}$ (with $\bar{p}$ on a logarithmic scale) for the loading and unloading stages of Tests E and G. Figure 6.13 shows the corresponding plots for the compression wave velocities V_{pv} and V_{ph} (with V_{ph} taken as the average of the independent measurements V_{ph1} and V_{ph2}).

Figures 6.12 and 6.13 show an excellent level of agreement between the wave velocities measured during loading stage G_1G_2 and those measured during the first part of loading stage E_1E_2 (up to $\bar{p}$ =150kPa). The shapes of the various curves of V_s or V_p against $ln\bar{p}$ were always very similar for stage G_1G_2 and the corresponding part of stage E_1E_2. In addition, the value of each shear velocity at G_2 differed by less than 2% from the corresponding shear wave velocity at $\bar{p}$ =150kPa in stage E_1E_2, and the value of each compression wave velocity at G_2 differed by less than 2.5% from the corresponding compression wave velocity at $\bar{p}$ =150kPa in stage E_1E_2.

Figures 6.12 and 6.13 give a high level of confidence that the test procedures and measurement techniques provided excellent repeatability of very small strain behaviour measured by shear and compression wave velocities. This means that it is realistic to examine the influence of different variables (such as stress ratio η during loading/unloading, isotropic or anisotropic compaction, suction value during loading or the existence of previous wetting and drying cycles) on the very small strain behaviour investigated with the BEEs. These issues are all examined in the remainder of this chapter.

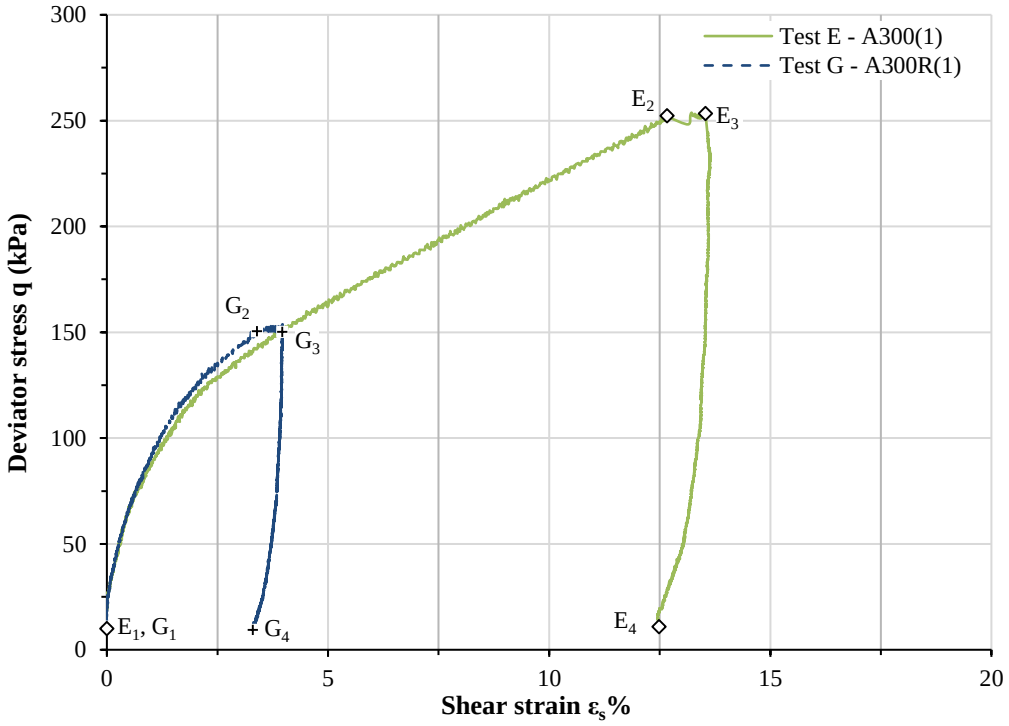

Figure 6.9: Variation of deviator stress q with shear strain ϵ_s in Tests E and G

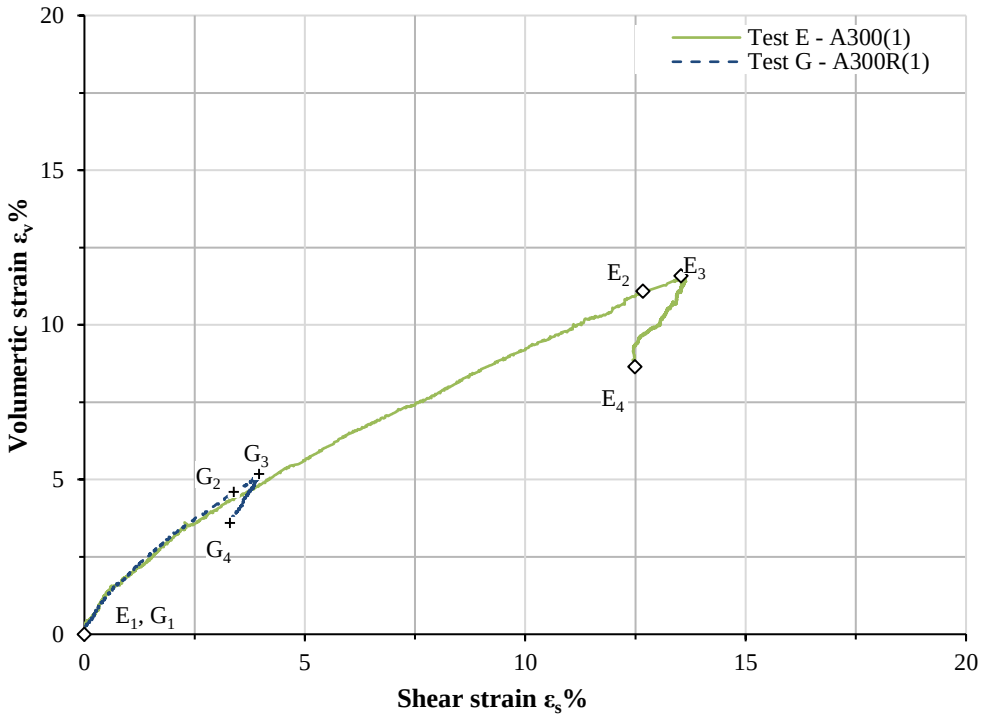

Figure 6.10: Variation of volumetric strain ϵ_v with shear strain ϵ_s in Tests E and G

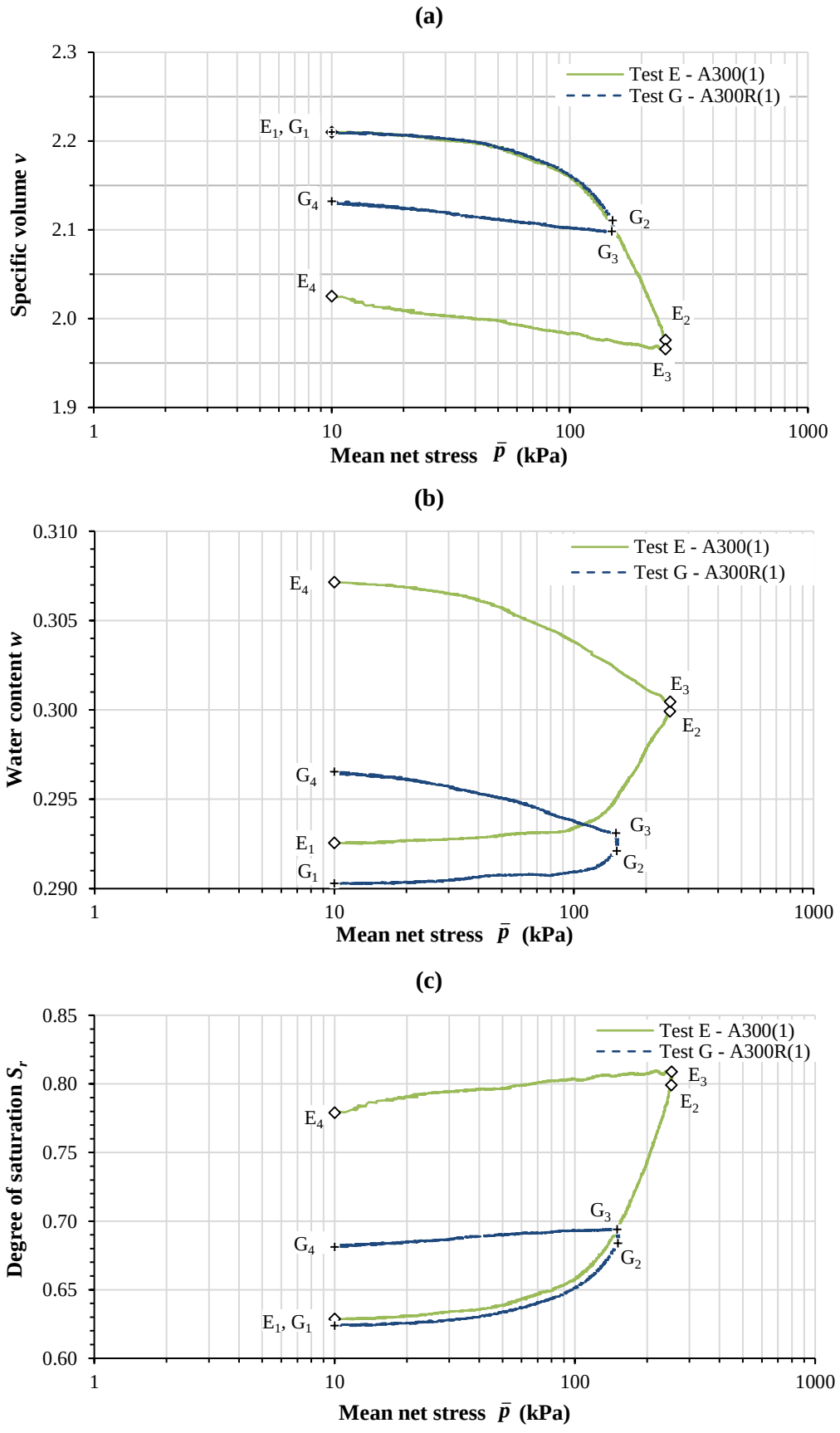

Figure 6.11: Variations of (a) specific volume v (b) water content w (c) degree of saturation S_r in Tests E and G

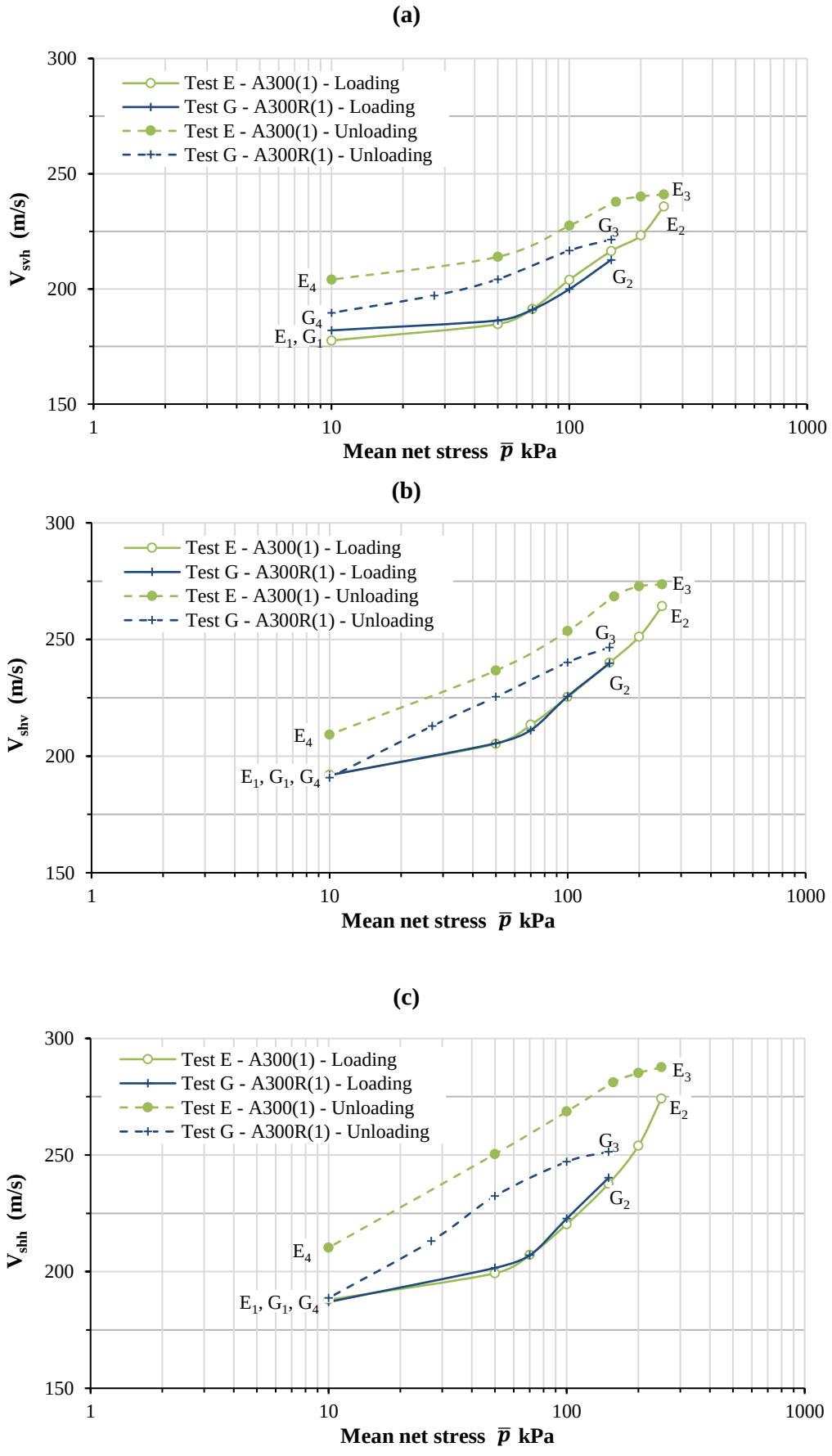

Figure 6.12: Variations of shear wave velocities in Tests E and G

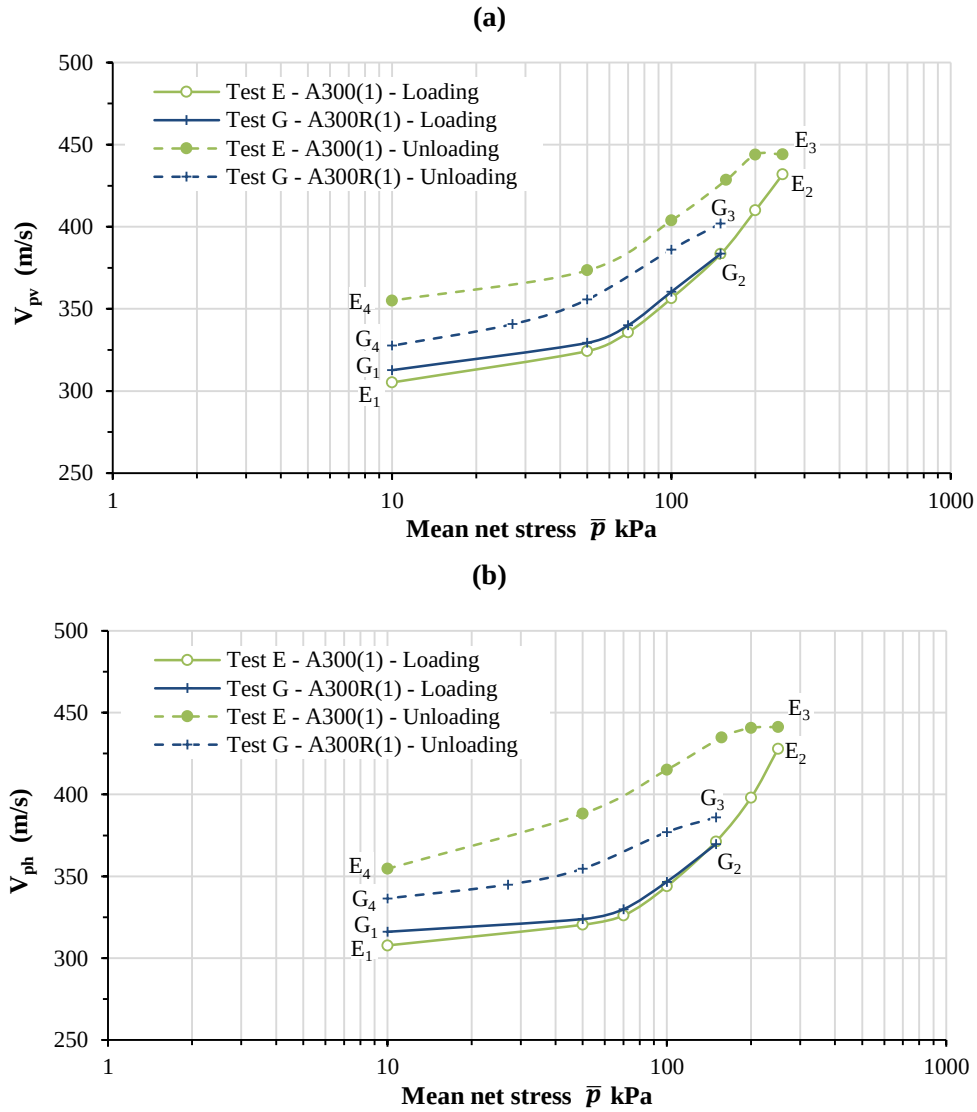

Figure 6.13: Variations of compression wave velocities in Tests E and G

6.4 Loading/unloading stages: influence of η on isotropically compacted samples

Figure 6.14 shows the stress paths followed in the $q : \bar{p}$ plane during the loading and unloading stages of Tests A, B and C, all performed at $s = 300$kPa on isotropically compacted samples. Also shown in Figure 6.14 are the estimated locations of the critical state lines in triaxial compression and triaxial extension at $s = 300$kPa (estimated from the work of Al-Sharrad, 2013).

In Test A, loading and unloading were performed at $\eta \approx 0$ (with $q = 2$kPa) to a maximum stress of $\bar{p} = 300$kPa, as described in Section 4.5.2. In Figure 6.14, A_1 represents the start of the loading stage (the end of the previous equalization stage),

A_2 is the end of the loading stage, A_3 is the end of the subsequent 24 hour rest stage (see Section 4.3.5) and A_4 is the end of the unloading stage. B_1, B_2, B_3 and B_4 are corresponding points in Test B, which involved loading and unloading at $\eta = 1$, to a maximum loading point of $\bar{p} = 250$kPa, $q = 250$kPa (see Section 4.5.2). Test C involved loading at $\eta = -1$. Unfortunately, there was no unloading stage in Test C, because shear failure occurred unintentionally in this test (see Section 6.4.1), with C_2 in Figure 6.14 representing the peak negative value of deviator stress achieved.

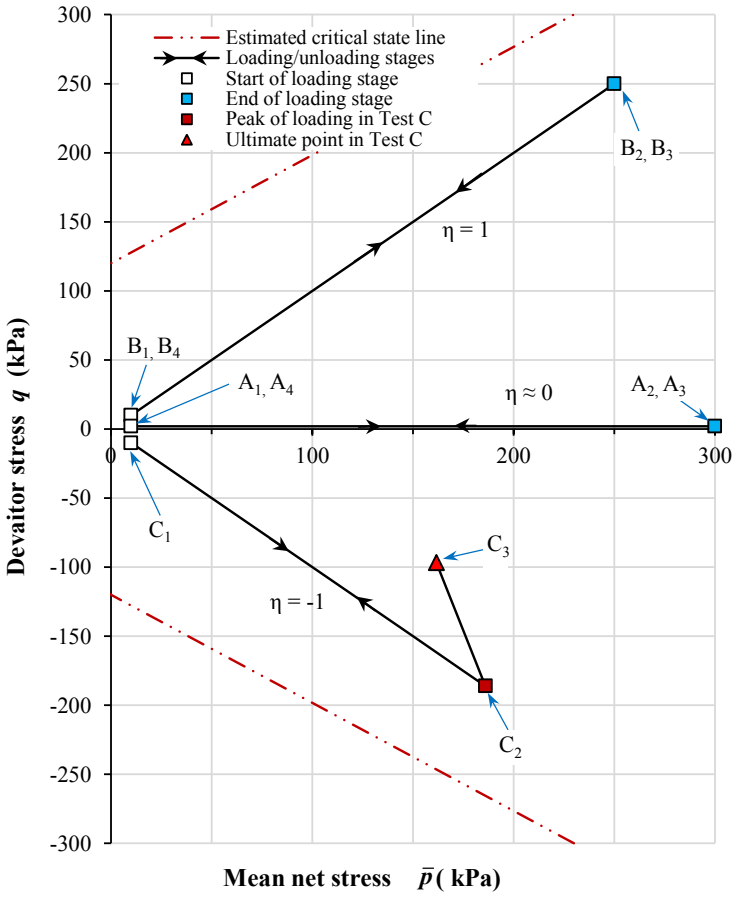

Figure 6.14: Stress paths for Tests A, B and C at $s = 300$kPa

The results from Tests A, B and C are presented together in this section, in order to investigate, for isotropically compacted samples, the influence of stress ratio η during loading and unloading stages on both large strain behaviour and very small strain elastic response indicated by BEE test results.

6.4.1 Large strain behaviour

Figure 6.15 shows the variation of deviator stress q with shear strain ϵ_s during the loading and unloading stages of Tests A, B and C, and Figure 6.16 shows the corresponding

plots of volumetric strain ϵ_v against shear strain ϵ_s.

Figures 6.15 and 6.16 show that a small positive shear strain occurred during the loading stage A_1A_2 of Test A, despite the fact that this was essentially isotropic loading ($\eta \approx 0$, with $q = 2$kPa) of an isotropically compacted sample. This may indicate some anisotropy of soil behaviour or, more likely, it may simply indicate experimental difficulties with accurate measurement of shear strainϵ_s, given that values of ϵ_s were determined from separate measurements of volumetric strain ϵ_v and axial strain ϵ_a (see Equations 4.12 and 4.11), and the latter was only measured with an external displacement transducer (see Section 3.3.5 and Figure 3.8) and hence was susceptible to bedding errors and errors due to compliance of the loading system.

The $q : \epsilon_s$ plot (Figure 6.15) for Test B ($\eta = 1$) shows that development of irreversible shear strain over the loading-unloading cycle and the clear suggestion of a yield point during the loading stage B_1B_2.

For Test C ($\eta = -1$), Figure 6.15 shows a clear suggestion of a yield point during the loading stage and the loading stage then unintentionally brought the sample to shear failure in triaxial extension, with deviator stress q reaching a peak negative value at C_2 (at $q = -186$kPa). After reaching this peak negative value of deviator stress, it was impossible for the Clisp logging/control software to keep the test on the pre-defined stress path, given that this was a stress-controlled test, with both $\bar{p}$ and the negative value of q required to increase at the standard rate of 2kPa/hr (see Section 4.3.3). As a consequence, post-peak response from C_2 to C_3 followed an uncontrolled stress path with both $\bar{p}$ and the negative value of q decreasing but $\eta \neq -1$ (see Figure 6.14) and the shear strain ϵ_s increasing rapidly until the control software terminated the stage at a limit value of axial displacement corresponding to point C_3. The peak negative value of deviator stress at point C_2 occurred well inside the estimated position of the critical state line in triaxial extension for $s = 300$kPa, taken from the results of Al-Sharrad (2013) (see Figure 6.14). It is unclear whether this indicates a significant difference between the compacted speswhite kaolin samples produced in the current study and those produced by Al-Sharrad (2013).

Figure 6.16 shows that significant positive (compressive) values of volumetric strain ϵ_v occurred during the loading stages of Tests A, B and C. Partial recovery of this volumetric strain occurred during the subsequent unloading stages of Tests A and B (A_3A_4 and B_3B_4), but leaving significant irreversible positive volumetric strain at the end of the loading-unloading cycle. In Test C, no further occurrence of volumetric strain occurred during the rapid post-peak shearing from C_2 to C_3.

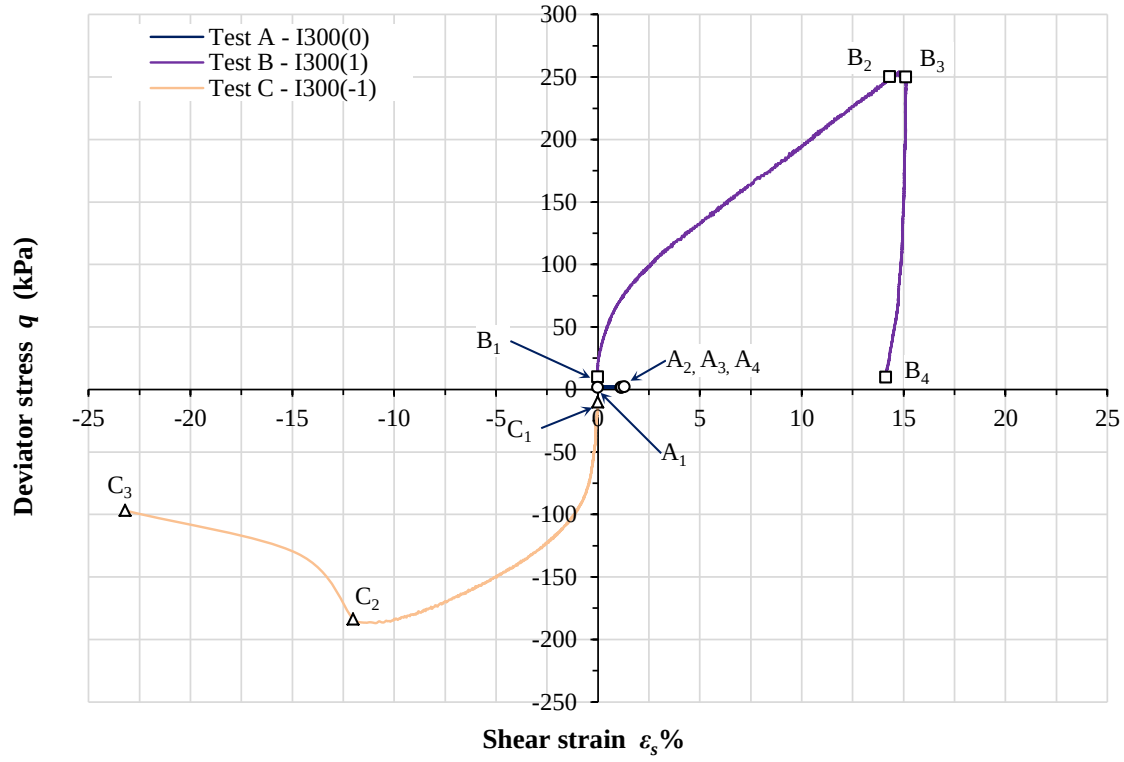

Figure 6.15: Variation of deviator stress q with shear strain ϵ_s in Tests A, B and C

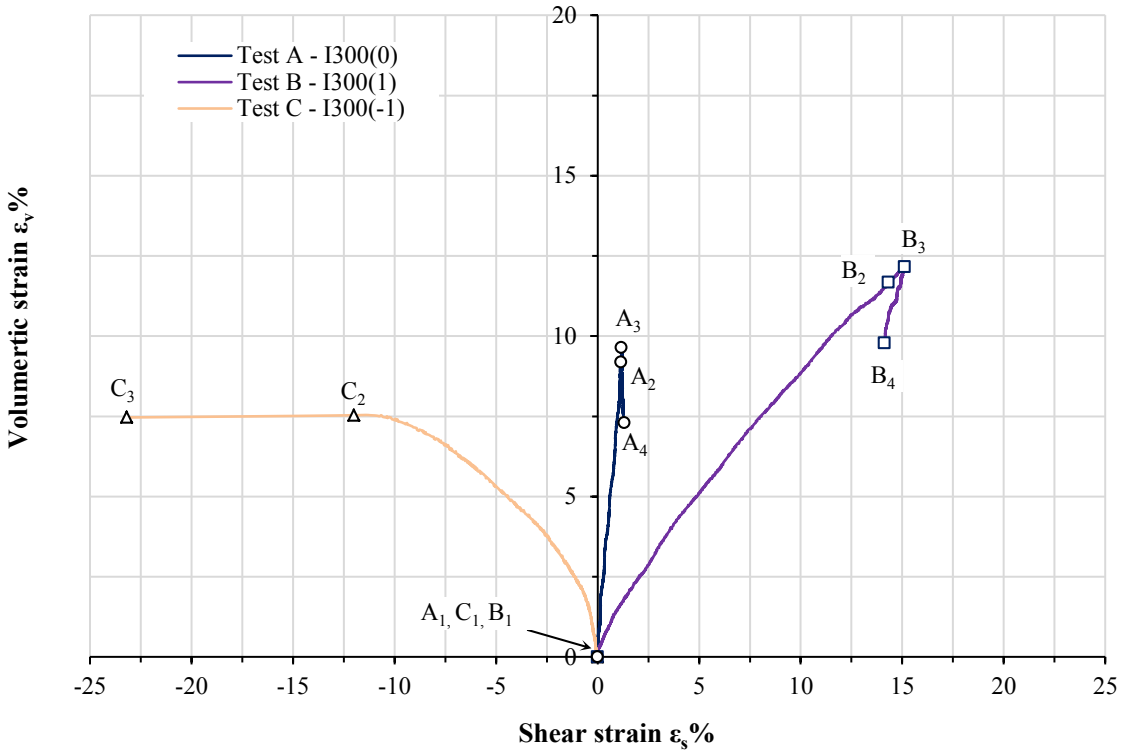

Figure 6.16: Variation of volumetric strain ϵ_v with shear strain ϵ_s in Tests A, B and C

Figure 6.17 shows the variations of specific volume v, water content w and degree of saturation S_r during the loading and unloading stages of Tests A, B and C, all plotted against $\bar{p}$ (with $\bar{p}$ on a logarithmic scale). In Figure 6.17a, all three tests are shown as starting from the same value of v, following the small adjustment to the assumed values of sample volume at this point, as described in Section 6.2.1.

Inspection of Figure 6.17a confirms significant irreversible compression over the loading-unloading cycles of Tests A and B, and clear suggestions of yield points during the loading stages of all three tests. The yield value of $\bar{p}$ appears greatest in Test A (at $\eta \approx 0$) and the post-yield compression curve (in the $v : \bar{p}$ plot) for Test A lies above the corresponding compression curves for the other two tests (at $\eta = 1$ and $\eta = -1$). This is consistent with expected behaviour under saturated and unsaturated conditions. Yield points are discussed further in Section 6.5.4.

Figure 6.17b shows that the initial water content in the three tests (at A_1, B_1 and C_1) varied by about 0.007 (0.7%). These small differences of initial w may be attributable to the small differences in initial values of deviator stress q (2kPa, 10kPa and -10kPa), but it is also possible that they simply reflect slight scatter between different tests.

Figure 6.17b shows relatively modest variations of water content w during the loading and unloading stages of all three tests, but it is clear that the fact that suction remained constant did not mean that w remained precisely constant. In particular, there was a clear evidence of net increase of w over the loading-unloading cycles of Tests A and B. During the loading stages of all three tests, the water content w showed very little variation during the early part of loading, but then more significant variation in the later part of loading, with particularly notable increase of w in the later part of loading in Tests B and C.

The experimental results of Sivakumar (1993) also showed that increases of w could occur on loading at constant suction, even if the soil was simultaneously decreasing in volume. Wheeler (1996) attributed this behaviour to the existence of two levels of soil fabric, with unsaturated macro-voids between soil packets reducing in volume and saturated micro-voids within soil packets increasing in volume (due to dilation of the dense packets). Toll (1990) provided a similar explanation (based on the two levels of soil fabric) for his observations of apparently contradictory changes of suction and changes of soil volume during constant water content tests.

Figure 6.17c shows small differences in initial values of S_r between the three tests (at A_1, B_1 and C_1), arising from the differences in initial values of w. Figure 6.17c shows significant irreversible increase of S_r over the loading-unloading cycles of Tests A and B, and the clear suggestion of yield points during the loading stages of all three tests.

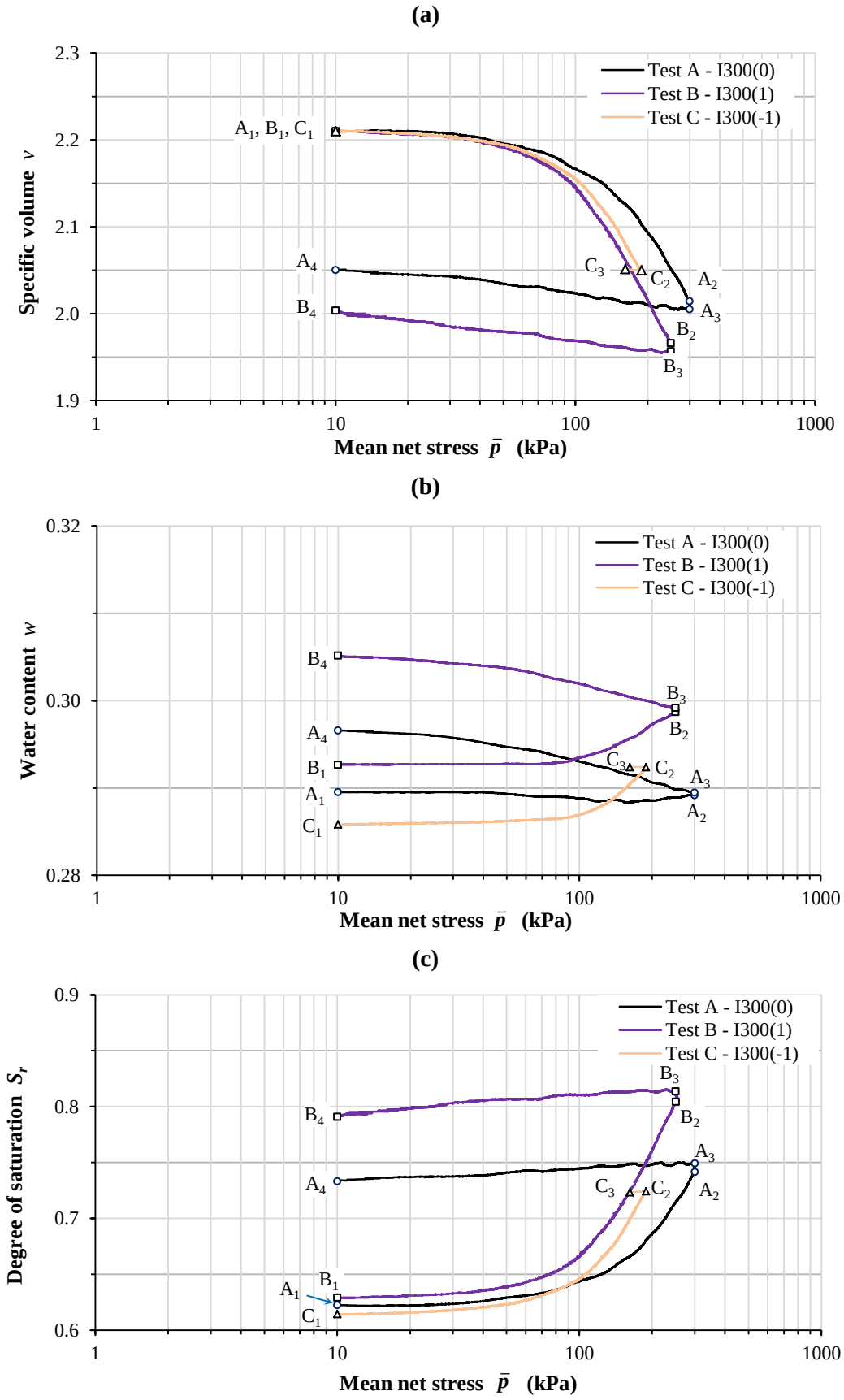

Figure 6.17: Variations of v,w and S_r for Tests A, B and C at $s = 300$kPa

6.4.2 Wave velocities

Figure 6.18 shows the variations of shear wave velocities V_{svh}, V_{shv} and V_{shh} plotted against mean net stress $\bar{p}$ for the loading and unloading stages of Tests A, B and C.

Thermodynamic considerations (Love, 1927) require that the values of V_{svh} and V_{shv} should be identical. However, the results of the preliminary tests reported in Section 5.1.3 indicated that measurements of V_{svh} were affected by the difference in boundary conditions between horizontal and vertical transmission of shear waves. The remaining discussion here and in Section 6.4.3 therefore focuses on V_{shv} and V_{shh}, and for all further test comparisons presented in Sections 6.5 – 6.9, the values of V_{svh} are omitted.

In Tests A, B and C, there were large increases in the shear wave velocities V_{shv} and V_{shh} during the loading stages (A_1A_2, B_1B_2 and C_1C_2) (see Figures 6.18b and 6.18c), as $\bar{p}$ increased, s remained constant, v decreased (Figure 6.17a) and S_r increased (Figure 6.17c). The variations of V_s followed qualitatively similar trends to the variations of v and S_r shown in Figures 6.17a and 6.17c respectively, suggesting that changes to one or both of these state variables may have contributed significantly to the variation of V_s. Established experience for saturated soils (see Equation 2.17) suggests that the increase of $\bar{p}$ and the decrease of v would both have contributed to the increase of V_s during the loading stages, whereas previous experience gives little indication of whether the increase of S_r (at constant s) could also have contributed to the increase of V_s or instead could have partially offset the effects of the changes to $\bar{p}$ and v. This issue will be discussed here and also more in the following sections.

During the unloading stages (A_3A_4 and B_3B_4) in Tests A and B, there was a decrease in the shear wave velocity V_s , as $\bar{p}$ decreased, s remained constant, v slightly increased (Figure 6.17a) and S_r slightly decreased (Figure 6.17c). There was a net increase of V_s over the full loading-unloading cycle in both Tests A and B (compare A_4 with A_1 and B_4 with B_1 in Figures 6.18b and 6.18c). This net increase of V_s is consistent with the decrease of v over the loading–unloading cycle of each of these tests (see Figure 6.17a), but it is not clear whether the simultaneous net increase of S_r (see Figure 6.17c) also contributed to the net increase of V_s or partially offset the influence of the decrease of v.

Comparison of Figure 6.18b with Figure 6.18c shows that the influence of stress ratio η on shear wave velocity variation was different for V_{shv} and V_{shh}. Whereas values of V_{shv} during the loading stage of Test C ($\eta = -1$) were consistently lower than in Test A ($\eta \approx 0$) or Test B ($\eta = 1$) (see Figure 6.18b), values of V_{shh} in Test C were consistently higher than in Tests A and B. This clearly indicates difference in elastic

anisotropy at $\eta = -1$ compared to the anisotropy at $\eta \approx 0$ or $\eta = 1$. This is discussed further in Section 6.4.3.

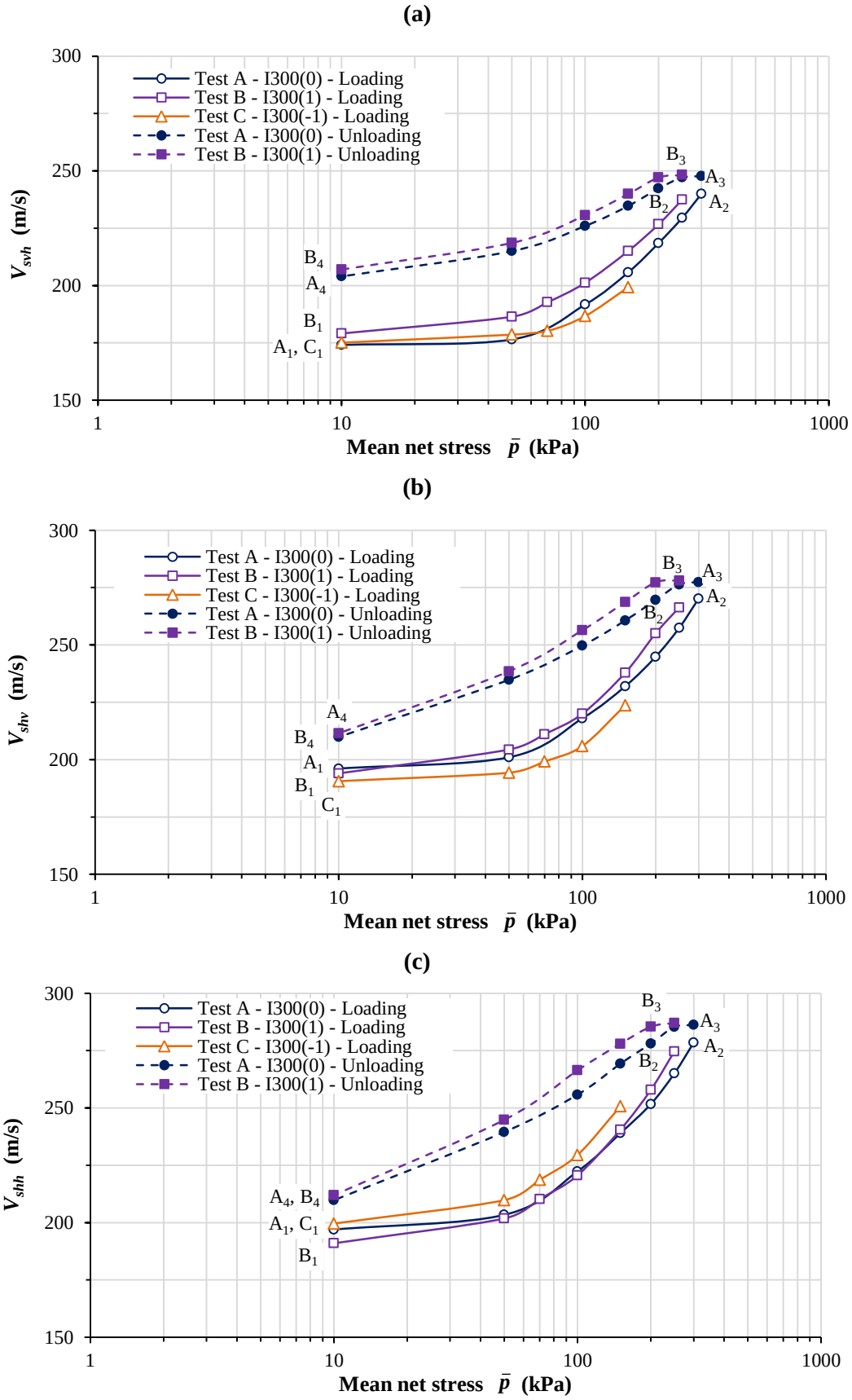

Figure 6.18: Variations of shear wave velocities in Tests A, B and C

Figure 6.19 shows the variations of compression wave velocities V_{pv}, V_{ph1} and V_{ph2} for the loading and unloading stages of Tests A, B and C. In all three tests the values of the two independent measurements of horizontal compression wave velocity (V_{ph1} and V_{ph2}) were always very similar. Therefore, in all subsequent sections, only the average horizontal compression wave velocity V_{ph} (the mean of V_{ph1} and V_{ph2}) is presented.

Figure 6.19 shows that significant increases of compression wave velocities V_{pv} and V_{ph} occurred during the loading stages of all three tests, with smaller decreases during the unloading stages of Tests A and B. The increase of $\bar{p}$, decrease of v and increase of S_r occurring during the loading stages would all be expected to contribute to the observed increase of V_p.

Comparison of Figure 6.19a with Figures 6.19b and 6.19c shows that the influence of stress path η is very different for V_{pv} and V_{ph}. For the horizontal compression wave velocity V_{ph} (Figures 6.19b and 6.19c) the results during the loading stages of Tests A, B and C were all very similar. In contrast, for the vertical compression wave velocity V_{pv} (Figure 6.19a) the results from the three tests diverge significantly during the loading stages, with V_p greatest for Test B ($\eta = 1$) and least for Test C ($\eta = -1$). This means that the variation of the ratio V_{ph}/V_{pv} during loading is significantly different for $\eta \approx 0$, $\eta = 1$ and $\eta = -1$, indicating that elastic anisotropy develops differently along the three different stress paths. This is discussed further in Section 6.4.3.

6.4.3 Elastic moduli and elastic anisotropy

Figures 6.20 and 6.21 show the variations of shear moduli G_{hv} and G_{hh} and constrained moduli M_h and M_v during the loading and unloading stages of Tests A, B and C, with values of G_{hv} and G_{hh} calculated from the shear wave velocities V_{shv} and V_{shh} respectively (using Equation 4.19) and values of M_v and M_h calculated from the compression wave velocities V_{pv} and V_{ph} respectively (using Equation 4.22).

Comparison of the variations of V_{shv} (in Figure 6.18b) and V_{shh}(in Figure 6.18c) with the corresponding variations of G_{hv} (in Figure 6.20a) and G_{hh} (in Figure 6.20b), shows that the variation of V_{shv} and V_{shh} are very similar to the corresponding variations of G_{hv} and G_{hh}, suggesting that the variation of bulk density ρ of the soil had little impact on the form of variation of G_{hv} and G_{hh} (compared to the variation of V_{shv} and V_{shh}). Similarly, the variation of ρ has little impact on the form of variations of M_v (in Figure 6.21a) and M_h (in Figure 6.21b) compared to the variation of V_{pv} (in Figure 6.19b) and V_{ph} (in Figure 6.19c).

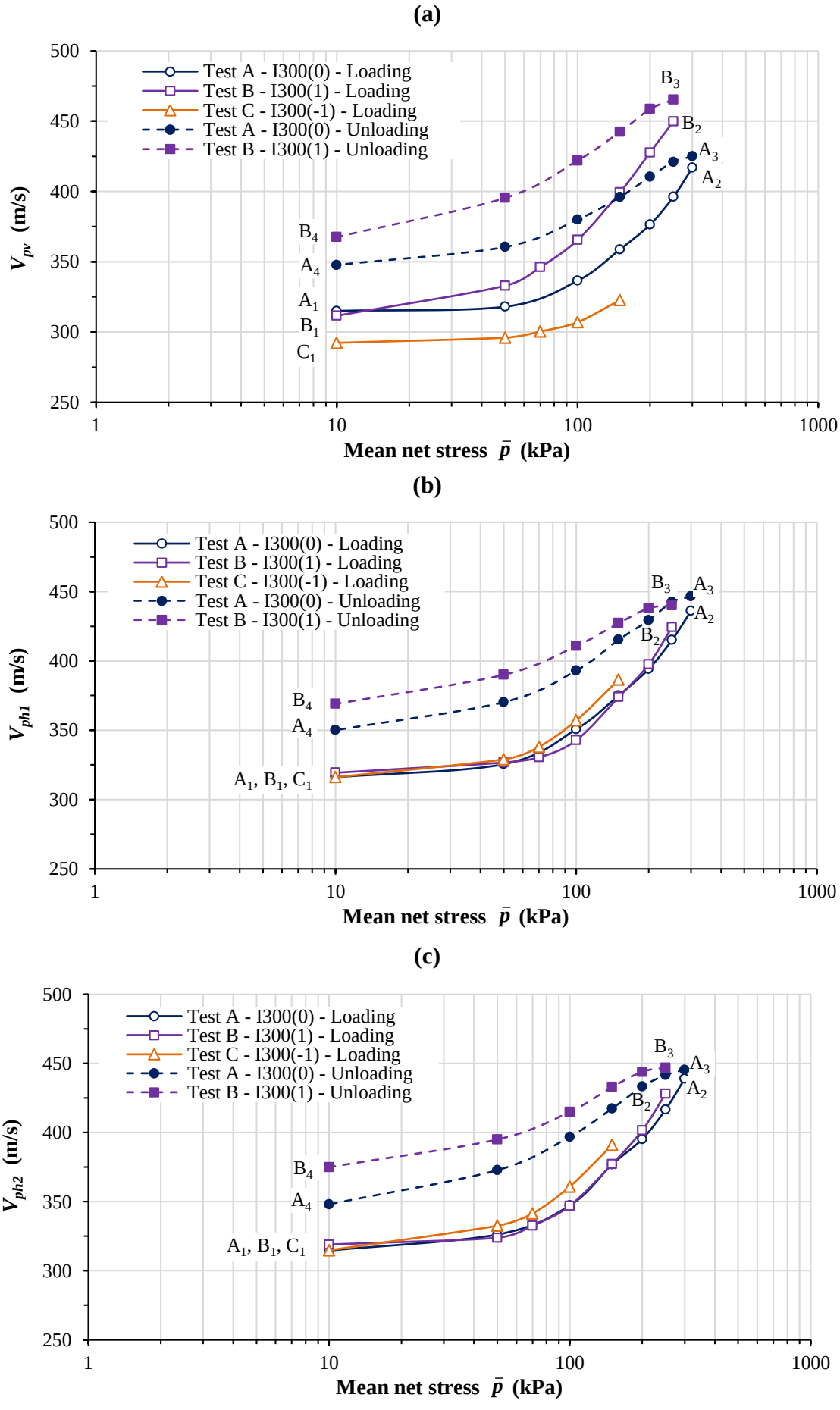

Figure 6.19: Variations of compression wave velocities in Tests A, B and C

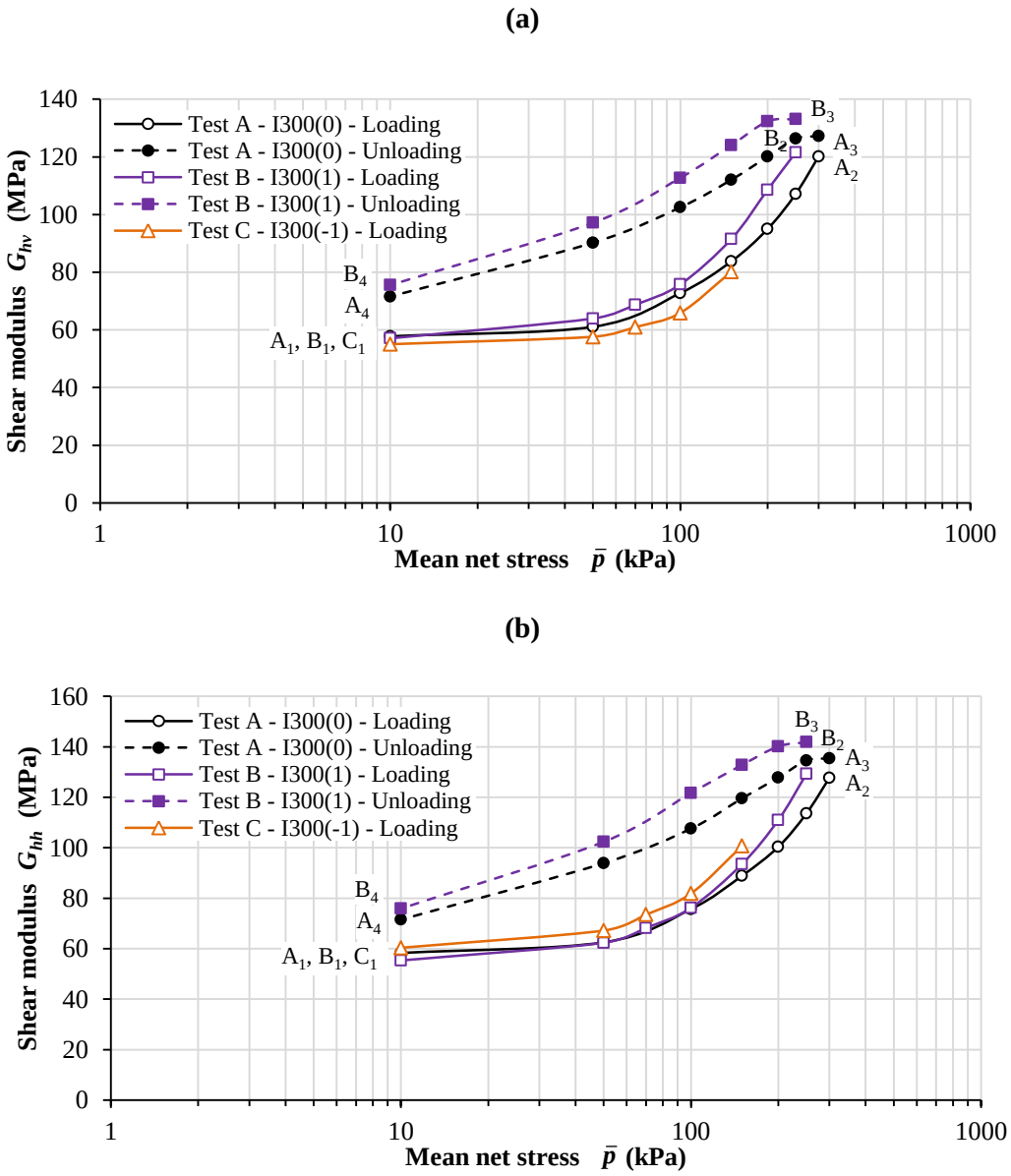

Figure 6.20: Variations of shear modulus in Tests A, B and C

Figures 6.22 and 6.23 show the variations of shear modulus ratio G_{hh}/G_{hv} and constrained modulus ratio M_h/M_v during the loading and unloading stages of Tests A, B and C.

In Test A the soil sample was isotropically compacted and then "isotropically" loaded ($\eta \approx 0$) and hence it was expected that the values of G_{hh}/G_{hv} and M_h/M_v would be 1 throughout the loading and unloading stages, indicating isotropy of elastic behaviour. Inspection of Figure 6.22 indicates, however, that in Test A the value of G_{hh}/G_{hv} increased from 1.01 to 1.06 during the early part of the loading and then remained approximately constant at 1.06 until the end of the loading stage at A_2. Similarly, Figure 6.23 shows that in Test A the value of M_h/M_v increased from 1.00 to about 1.10 during the early part of the loading and then remained approximately constant

at 1.10 through to the end of the loading stage.

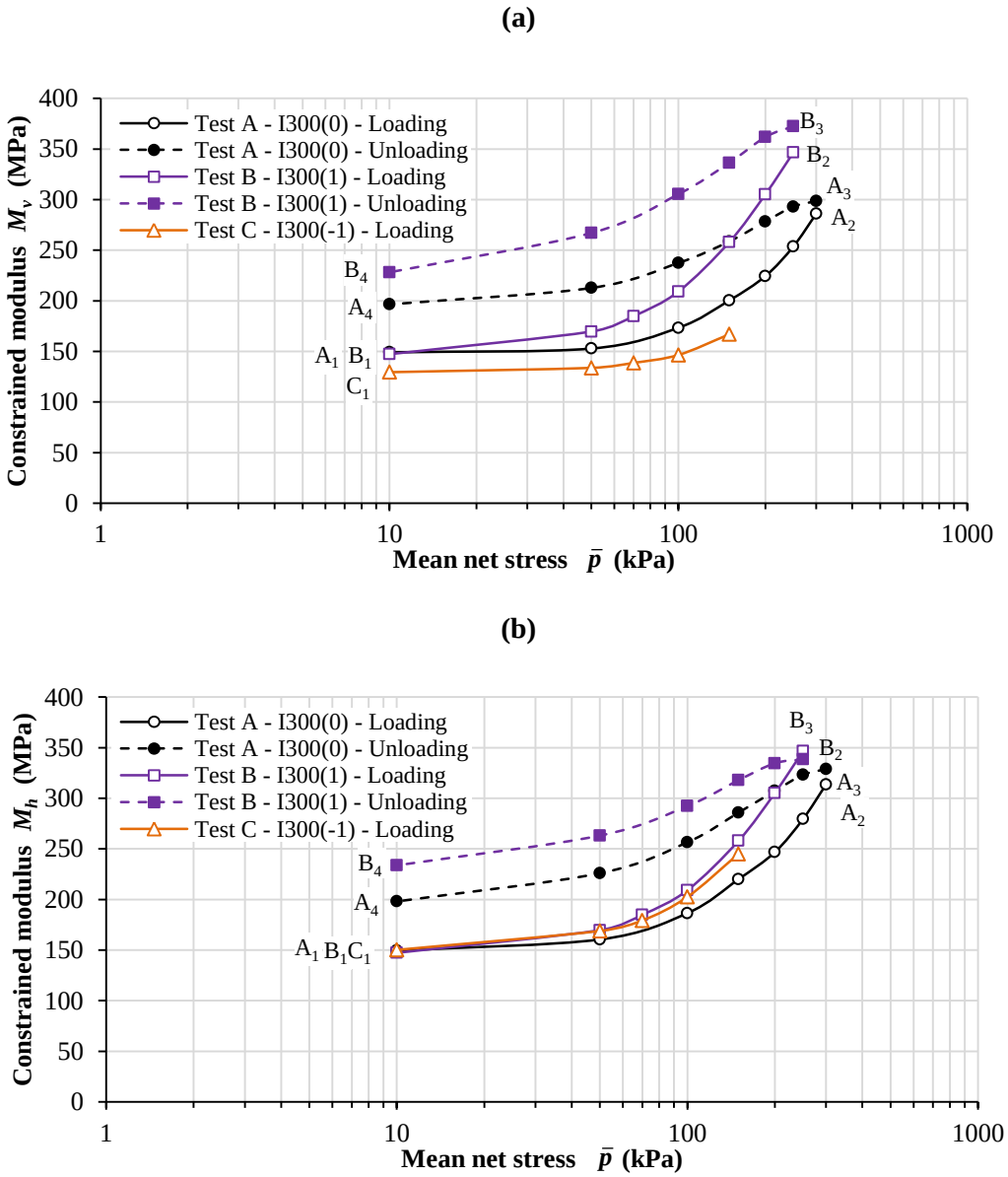

Figure 6.21: Variations of constrained moduli in Tests A, B and C

Interestingly, the variations of both G_{hh}/G_{hv} and M_h/M_v during the unloading stage of Test A appeared to indicate almost reversible variation of these modulus ratios, even though the individual moduli G_{hv}, G_{hh}, M_v and M_h did not vary in a reversible fashion during loading and unloading.

It is difficult to be sure why the measured values of G_{hh}/G_{hv} and M_h/M_v shown in Figures 6.22 and 6.23 did not remain constant at 1 during Test A. This would seem to indicate development of anisotropic elastic behaviour even for an isotropically compacted sample subjected to an isotropic stress state. This is probably because the difference in boundary conditions on the various boundaries of the triaxial test speci-

men (a stress-controlled boundary, with zero shear stress, on the cylindrical boundary, but a displacement-controlled boundary, with the possibility of shear stress, on the top and bottom boundaries) meant that a truly isotopic and uniform stress state was not maintained within the soil sample. The value of M_h/M_v was calculated from measurements involving both horizontal and vertical BEEs, and hence could have been affected by non-uniformity of the soil sample (with the soil state at the top and bottom of the sample different to that at the sample mid-height) as well as anisotropy of the soil state. In contrast, the value of G_{hh}/G_{hv} was calculated entirely from measurements from horizontal BEEs, and hence a value of G_{hh}/G_{hv} other than 1 suggests anisotropy of soil state even at the mid-height of the soil sample.

Inspection of Figures 6.22 and 6.23 shows that during Test B, with loading and unloading at $\eta = 1$, the value of G_{hh}/G_{hv} increased from 0.97 to 1.06 during loading stage, whereas the values of M_h/M_v decreased from 1.05 to 0.90 during the loading stage, with the changes to both modulus ratios occurring predominately during the early part of the loading. The variations of G_{hh}/G_{hv} and M_h/M_v during unloading, showed a return towards the values at the start of loading. This suggests that strain-induced anisotropy had a negligible effect on the elastic anisotropy, and the changes of G_{hh}/G_{hv} and M_h/M_v during the loading and unloading stages were predominantly due to stress-induced anisotropy.

Figures 6.22 and 6.23 show that the most significant variations of modulus ratios G_{hh}/G_{hv} and M_h/M_v occurred in Test C, where loading was performed at $\eta = -1$ and the loading was taken through to shear failure in triaxial extension. The final data points shown for Test C in Figures 6.22 and 6.23 correspond to the last BEE measurement before attainment of the peak negative value of deviator stress. In Test C, the value of G_{hh}/G_{hv} increased significantly during the loading stage (from 1.10 to 1.25) and the value of M_h/M_v increased even more dramatically (from 1.16 to 1.47).

Consideration of Figure 6.23 shows that the constrained modulus M (or compression wave velocity V_p) was greatest when the direction of compression wave transmission and polarisation coincided with the direction of the major principal stress (vertical in Test B, where $\eta = 1$, and horizontal in Test C, where $\eta = -1$). The picture is less clear for the shear response shown in Figure 6.22. Results from Test C in Figure 6.22 indicate that the shear modulus G (or shear wave velocity V_s) was greatest when the direction of shear wave polarisation coincided with the direction of the major principal stress (horizontal in Test C, where $\eta = -1$). However, this is less clear for Test B.

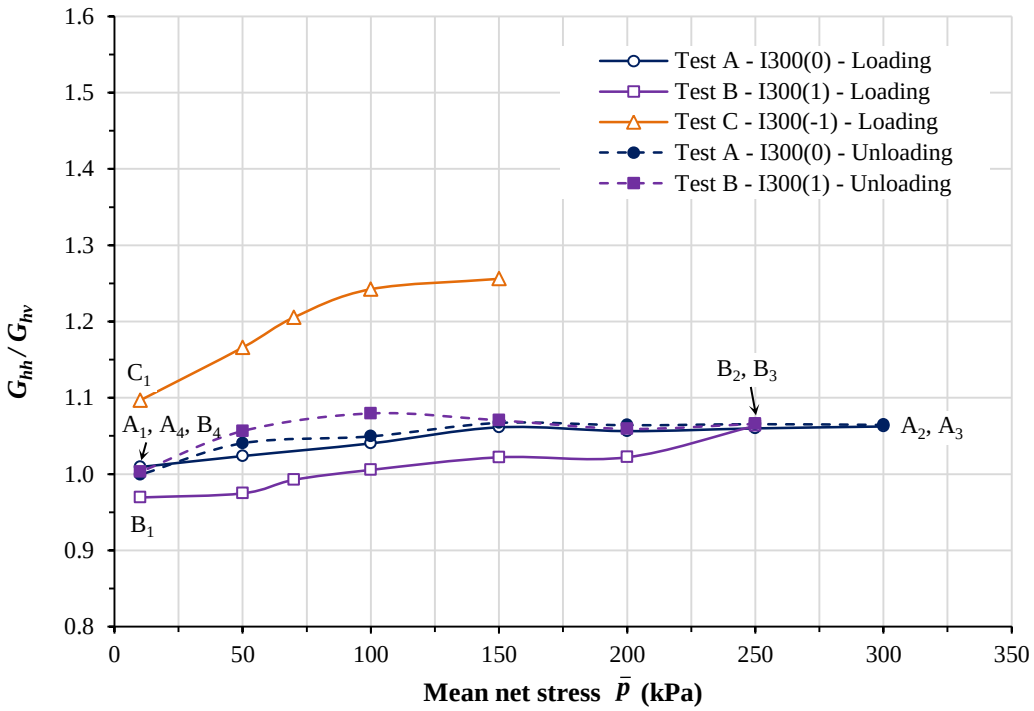

Figure 6.22: Variations of shear modulus ratio G_{hh}/G_{hv} in Tests A, B and C

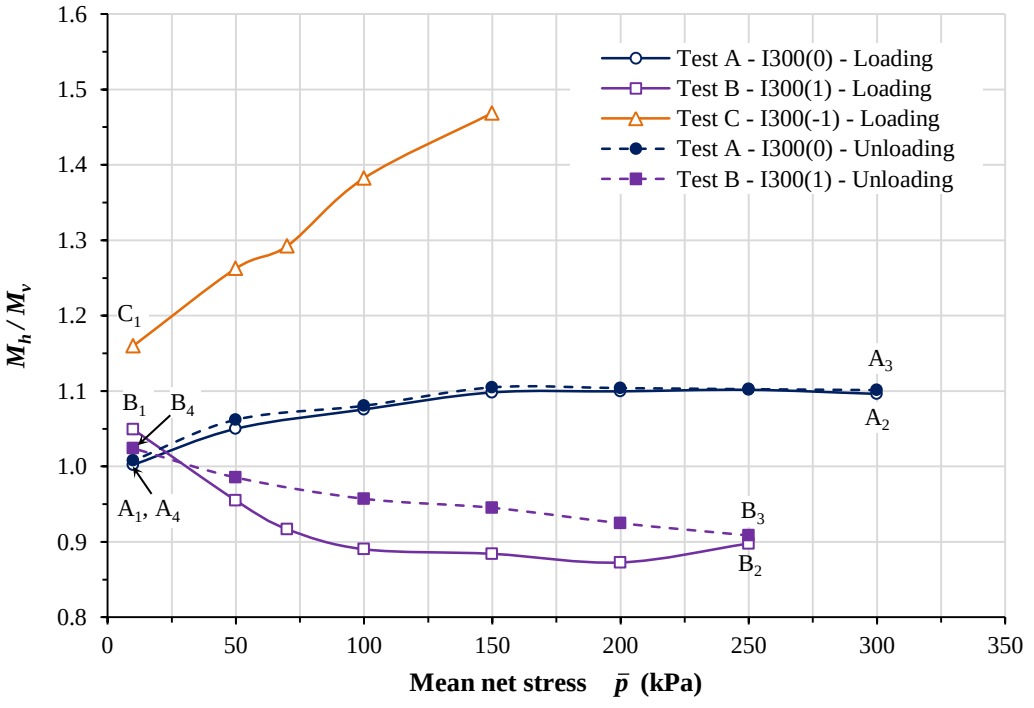

Figure 6.23: Variations of constrained modulus ratio M_h/M_v in Tests A, B and C

6.5 Loading/unloading stages: influence of compaction procedure on large strain behaviour

Tests D, E and F involved loading/unloading stages at s =300kPa (with $\eta \approx 0$, $\eta = 1$ and $\eta = -1$, respectively) performed on anisotropically compacted samples. Results from these tests can be compared with the corresponding results from Tests A, B and C on isotropically compacted samples (already presented in Section 6.4), to investigate the influence of compaction procedure on subsequent behaviour. Comparisons of large strain behaviour are presented in this section and comparisons of wave velocities and elastic anisotropy are presented in Section 6.6.

Figure 6.24 shows the stress paths followed in the $q : \bar{p}$ plane during loading and unloading stages of Tests D, E and F, all performed at s =300kPa on anisotropically compacted samples. Also shown in Figure 6.24 are the estimated locations of the critical state lines in triaxial compression and triaxial extension at s =300kPa (estimated from the work of Al-Sharrad, 2013).

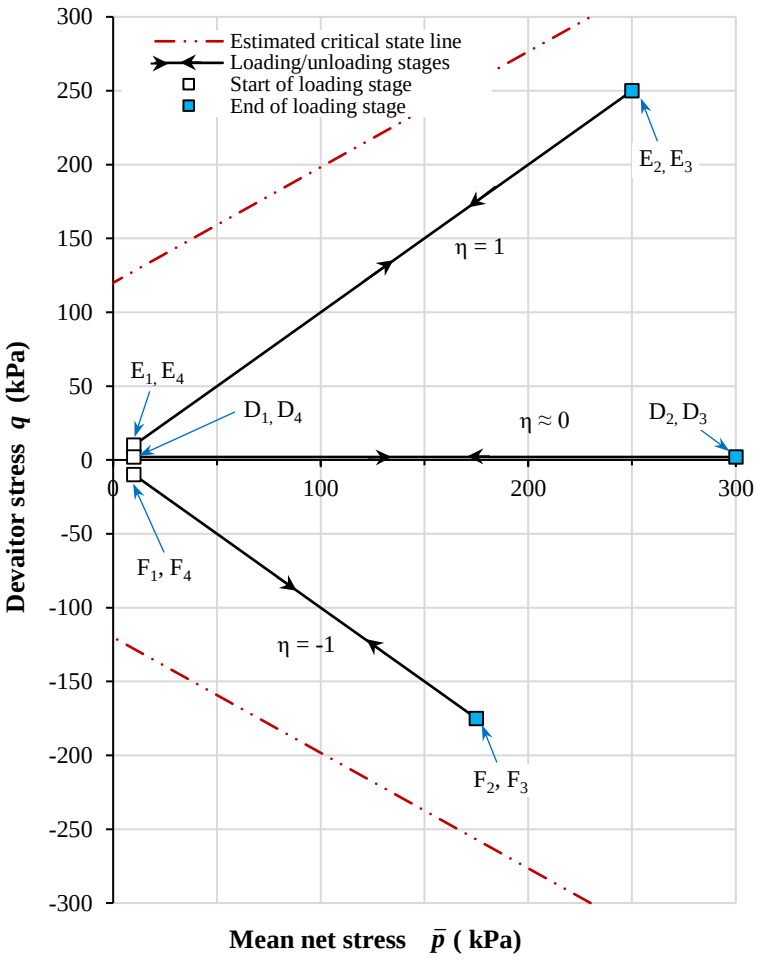

Figure 6.24: Stress paths for Tests D, E and F at s =300kPa

During Test D, loading and unloading were performed at $\eta \approx 0$ (with q =2kPa) to a maximum stress of $\bar{p}$ =300kPa. Test E involved loading and unloading at $\eta = 1$, to a maximum loading point of $\bar{p}$ =250kPa, q =250kPa. In Test F, involving loading and unloading $\eta = -1$, the sample was loaded to $\bar{p}$ =175kPa and $q = -175$kPa at point F_2 (i.e. to a lower negative value of q than caused failure in Test C (−186kPa), see Section 6.4.1). After a 24 hr rest period at F_3, the sample was unloaded to F_4.

6.5.1 Loading/unloading at $\eta \approx 0$

Tests A and D both involved "isotropic" loading and unloading at $\eta \approx 0$ (q =2kPa) to $\bar{p}$ =300kPa at s =300kPa, with Test A on an isotropically compacted sample and Test D on an anisotropically compacted sample.

Figure 6.25 shows the variations of specific volume v, water content w and degree of saturation S_r plotted against $\bar{p}$ (on a logarithmic scale) for loading and unloading stages of Tests A and D. Inspection of Figure 6.25 shows that the variations of v, w and S_r for Tests A and D appeared essentially identical. In particular, the curves for v and S_r (Figure 6.25a and 6.25c) for the two tests are very close, suggesting similar values of yield stress (discussed further in Section 6.5.4 below) and similar locations of the normal compression line for the isotropically and anisotropically compacted samples, when loaded isotropically. The initial values of w were slightly different for Tests A and D (see Figure 6.11b), but this is probably just attributable to imperfect repeatability between tests (compare with Figure 6.17 for two supposedly identical tests) and the shapes of the curves showing the subsequent variations of w were very similar for Tests A and D.

During loading and unloading stages of Test D, the axial deformation of the sample was not recorded, because the load cell was under repair and hence no deviator load was applied (meaning that it was not possible to monitor axial displacement of the soil sample by measuring the displacement of the loading ram).

6.5.2 Loading/unloading at $\eta = 1$

Tests B and E both involved loading and unloading at $\eta = 1$ to $\bar{p}$ =250kPa, q =250, with s =300kPa. Test B was on an isotropically compacted sample whereas Test E was on an anisotropically compacted sample.

Figure 6.26 shows the variations of deviator stress q with shear strain ϵ_s during the loading and unloading stages of Tests B and E. Figure 6.27 shows the corresponding plot of volumetric strain ϵ_v against shear strain ϵ_s.

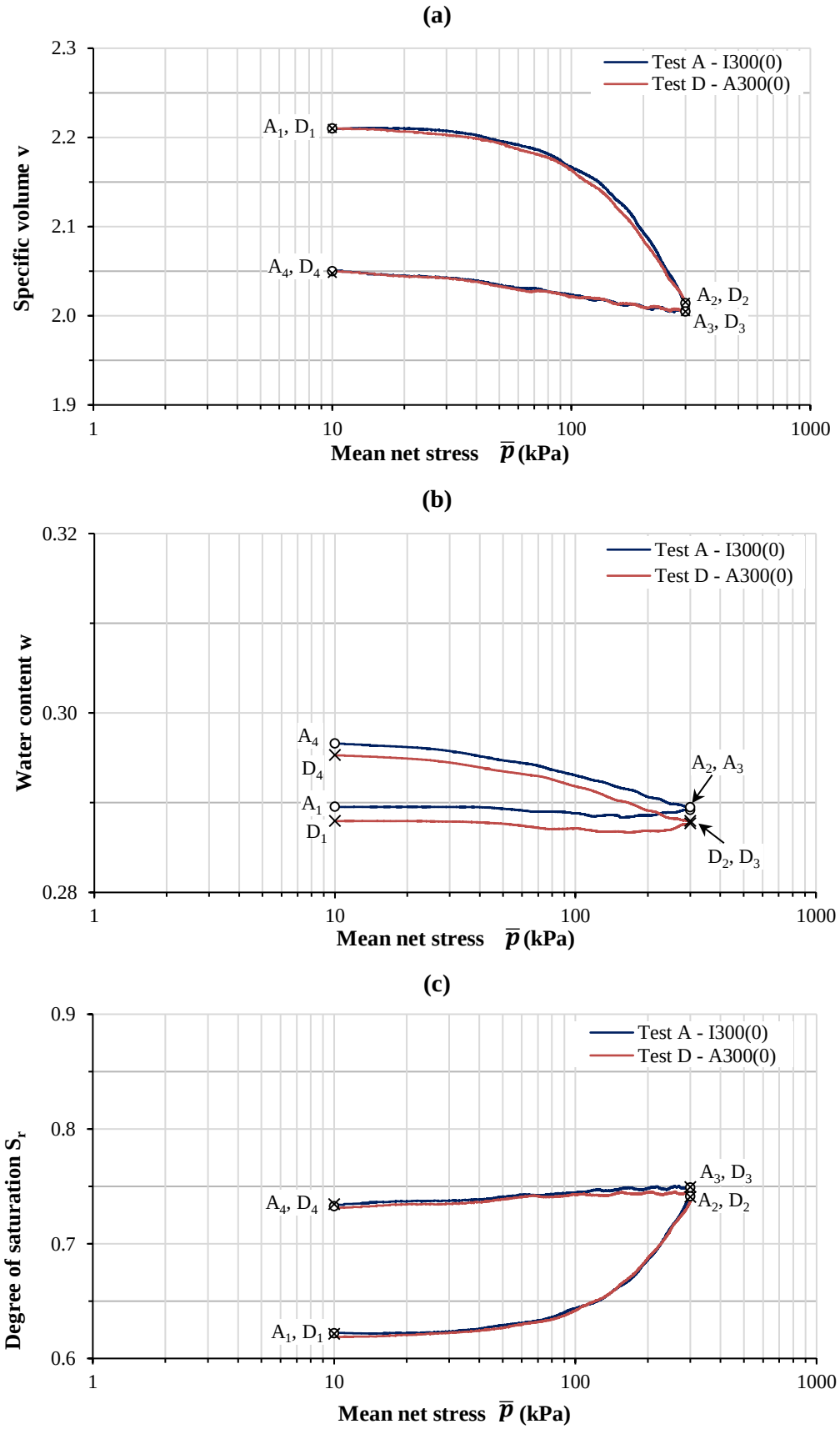

Figure 6.25: Variations of (a) specific volume v (b) water content w (c) degree of saturation S_r in Tests A and D

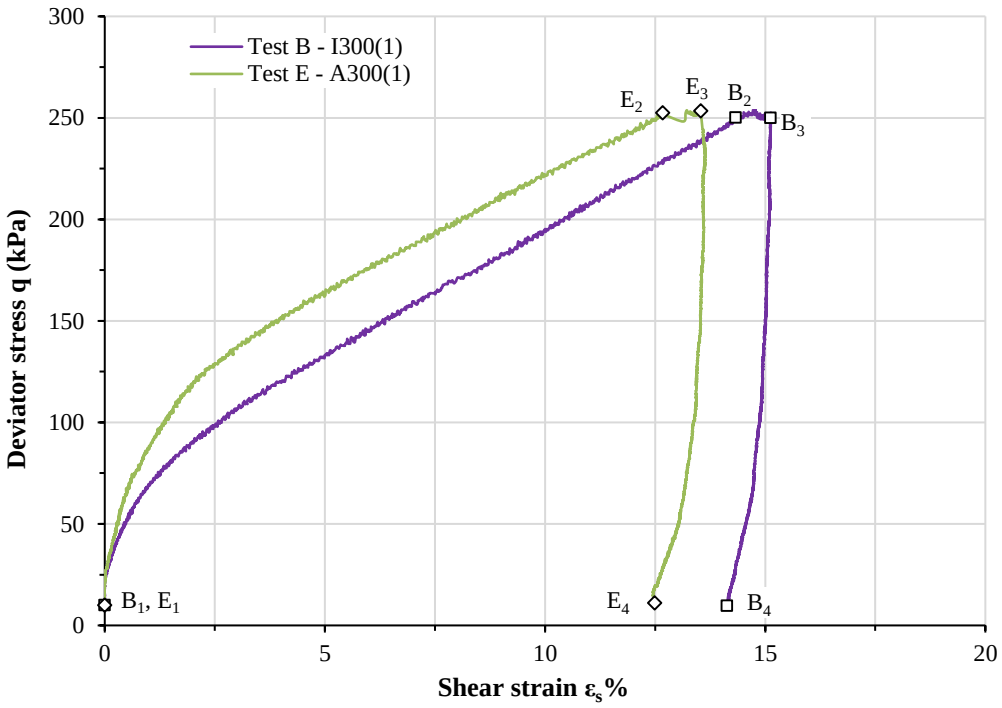

Figure 6.26: Variation of deviator stress q with shear strain ϵ_s in Tests B and E

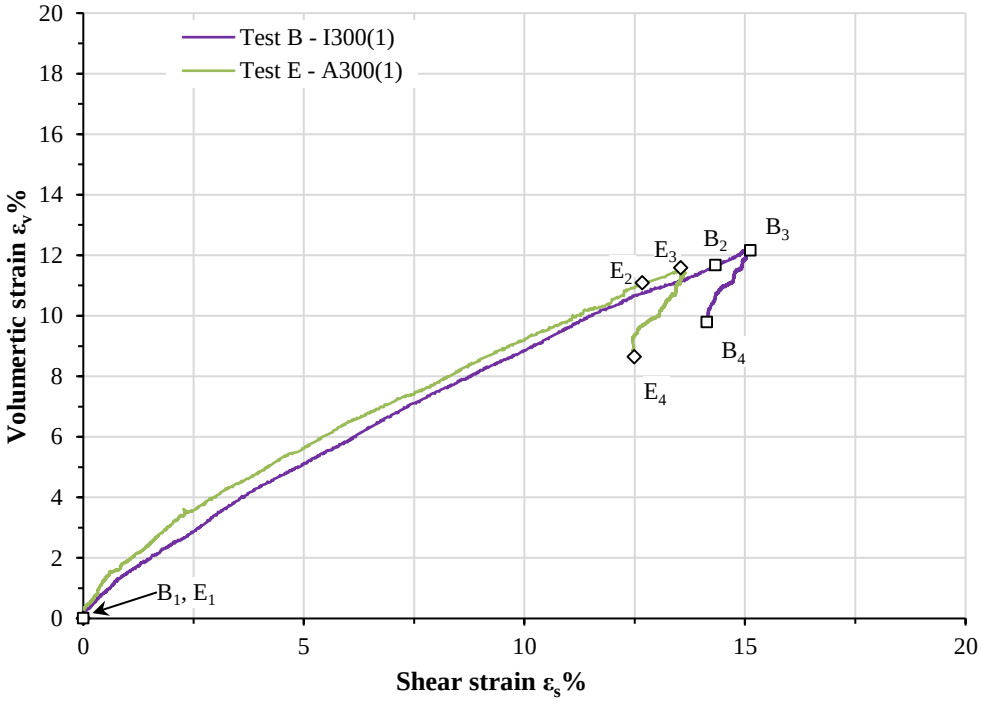

Figure 6.27: Variation of volumetric strain ϵ_v with shear strain ϵ_s in Tests B and E

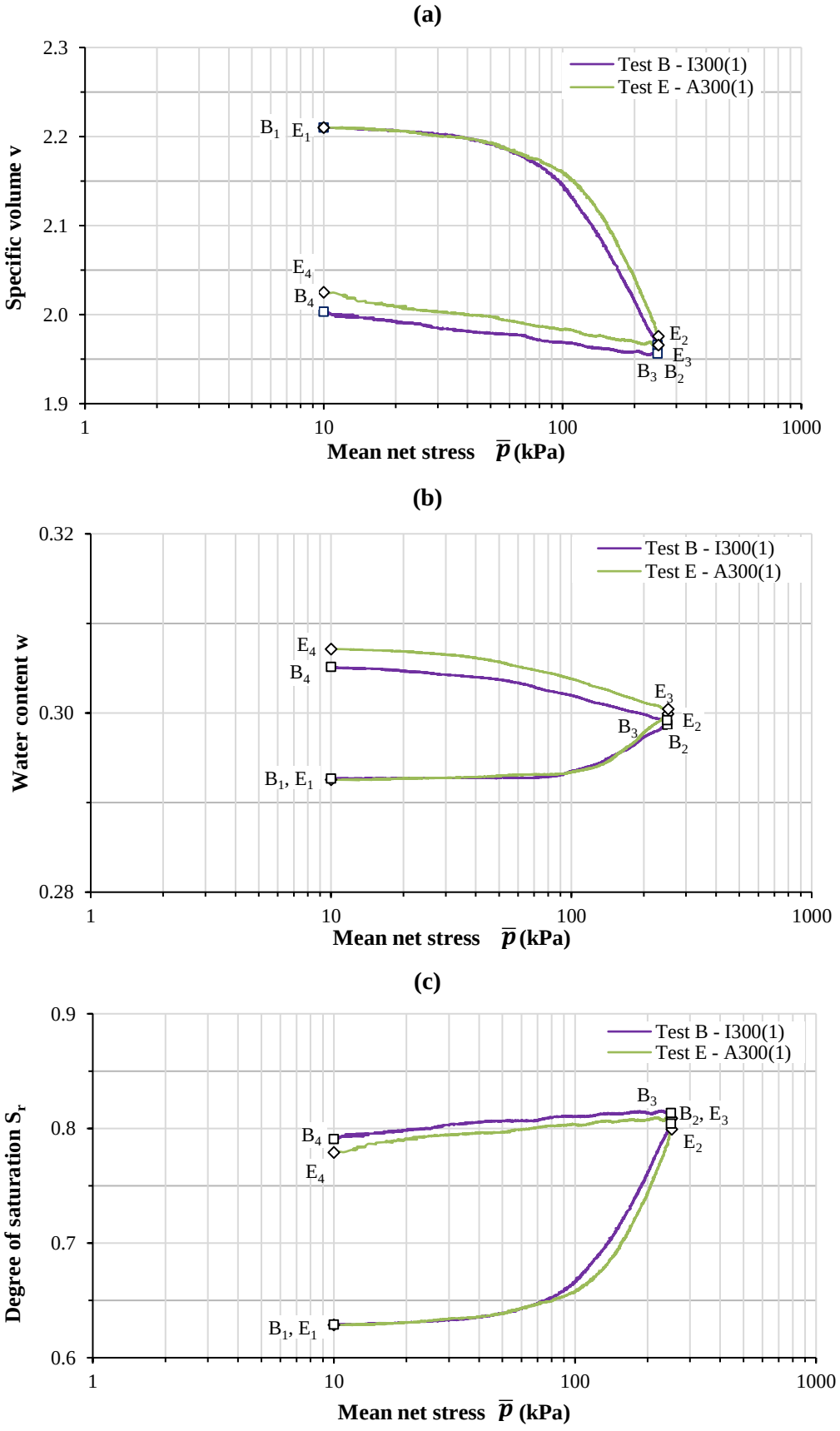

Figure 6.28: Variations of (a) specific volume v (b) water content w (c) degree of saturation S_r in Tests B and E

Inspection of Figure 6.26 suggests that, on loading at $\eta = 1$, the anisotropically compacted sample (Test E) yielded at a higher deviator stress than the isotropically compacted sample (Test B). This is discussed further in Section 6.5.4 below. After yielding the gradient of the $q : \epsilon_s$ plot was similar in the two tests, but the consequence of the higher yield stress in Test E was that shear strains ϵ_s at any given value of q remained lower than in Test B. At the end of the loading, the shear strain ϵ_s was 12.66% in Test E (E_2) compared to 14.33% in Test B (B_2). The variation of shear strain ϵ_s during subsequent unloading (B_3B_4 and E_3E_4) was similar in Tests B and E.

Figure 6.27 shows similar variations of ϵ_v with ϵ_s during Tests B and E. At the end of loading, the shear strain ϵ_s was slightly lower in Test E than in Test B (as discussed in the previous paragraph), but the volumetric strain ϵ_v was also slightly lower in Test E than in Test B (compare E_2 and B_2 in Figure 6.27). The form of ϵ_v:ϵ_s plot during subsequent unloading was similar in Tests B and E (compare E_3E_4 and B_3B_4 in Figure 6.27).

Figure 6.28 shows the variations of specific volume v, water content w and degree of saturation S_r during the loading and unloading stages of Tests B and E. Inspection of Figures 6.28a and 6.28c confirms that, during loading at $\eta = 1$, the yield stress was higher for the anisotropically compacted sample (Test E) than for the isotropically compacted sample (Test B), as discussed further in Section 6.5.4 below. As a consequence the post-yield compression curve for the anisotropically compacted sample lies above the corresponding curve for the isotropically compacted sample in the $v : ln\bar{p}$ plane (see Figure 6.28a). There is also some suggestion in Figure 6.28a that the post-yield compression curves for the two samples were gradually converging as $\bar{p}$ increased. This would be consistent with gradual erasure of the effects of differences in initial anisotropy during a process of plastic straining (see Wheeler et al., 2003a). At the end of loading, however, the value of v for sample E was still slightly higher than for sample B (compare E_2 and B_2) and this small difference remained throughout unloading (E_3E_4 and B_3B_4).

Figure 6.28b shows that, despite the lower yield stress, the increase of water content w was slightly greater during the loading stage of Test E than during the loading stage of Test B. This difference in w remained essentially constant during the unloading stages.

6.5.3 Loading/unloading at $\eta = -1$

Test C involved loading to C_2 (Figure 6.29) at $\bar{p}$ =186kPa, $q = -186$kPa, at which point unintentional shear failure occurred, and then an uncontrolled post-peak stage (C_2C_3 in Figure 6.29) (for more details, see Section 6.4.1), with s =300kPa on an

isotropically compacted sample, whereas Test F involved loading and unloading at $\eta = -1$ to $\bar{p}$ =175kPa, $q = -175$kPa, with s =300kPa, on an anisotropically compacted sample. Figure 6.29 shows the variations of deviator stress q with shear strain ϵ_s during the loading stage of Test C and the loading and unloading stages of Test F. Figure 6.30 shows the corresponding plots of volumetric strain ϵ_v against shear strain ϵ_s.

Inspection of Figure 6.29 suggests that, on loading at $\eta = -1$, the anisotropically compacted sample (Test F) yielded at a lower value of negative deviator stress than the isotropically compacted sample (Test C), as expected (see Section 6.5.4). After yielding, however, the gradient of the $q : \epsilon_s$ plot for Test C was significantly lower than that in Test F, so that, at a given value of deviator stress q, the value of negative shear strain in Test C was significantly higher than in Test F (for example at $q = -150$kPa, $\epsilon_s \approx -5\%$ in Test C whereas $\epsilon_s \approx -2\%$ in Test F). In addition, of course, shear failure occurred at $q = -186$kPa in Test C, whereas the results presented in Figure 6.29 suggest that failure was not imminent in Test F when the loading stage was terminated at $q = -175$kPa (F_2).

Inspection of Figure 6.30 shows that the maximum values of volumetric strain ϵ_v for Tests C and F were very similar (approximately 7.5% in both cases), whereas, as already seen, the values of negative shear strain ϵ_s were very different in the two tests.

Figure 6.31 shows the variations of specific volume v, water content w and degree of saturation S_r during the loading and unloading stages of Tests C and F, plotted against $\bar{p}$ (on a logarithmic scale). Inspection of Figures 6.31a and 6.31c shows that, during the loading stages of Tests C and F, the yield stress of the isotropically compacted sample (in Test C) was slightly higher than that of the anisotropically compacted sample (in Test F). This confirms the suggestion from Figure 6.29 and, as discussed below in Section 6.5.4, fits with expected behaviour. It can also be observed from Figures 6.31a and 6.31c that by the end of the loading stages, the values of v and S_r for Tests C and F had almost converged again, even though the two samples had experienced very different magnitudes of negative shear strain ϵ_s (see Figure 6.30).

6.5.4 Initial locations of yield curve

In this subsection yield values of $\bar{p}$ and q from the various loading stages are plotted, in order to investigate the initial shape and size of the yield curve (at a suction of 300kPa) for isotropically compacted samples (Tests A, B and C) and anisotropically compacted samples (Tests D, E and F).

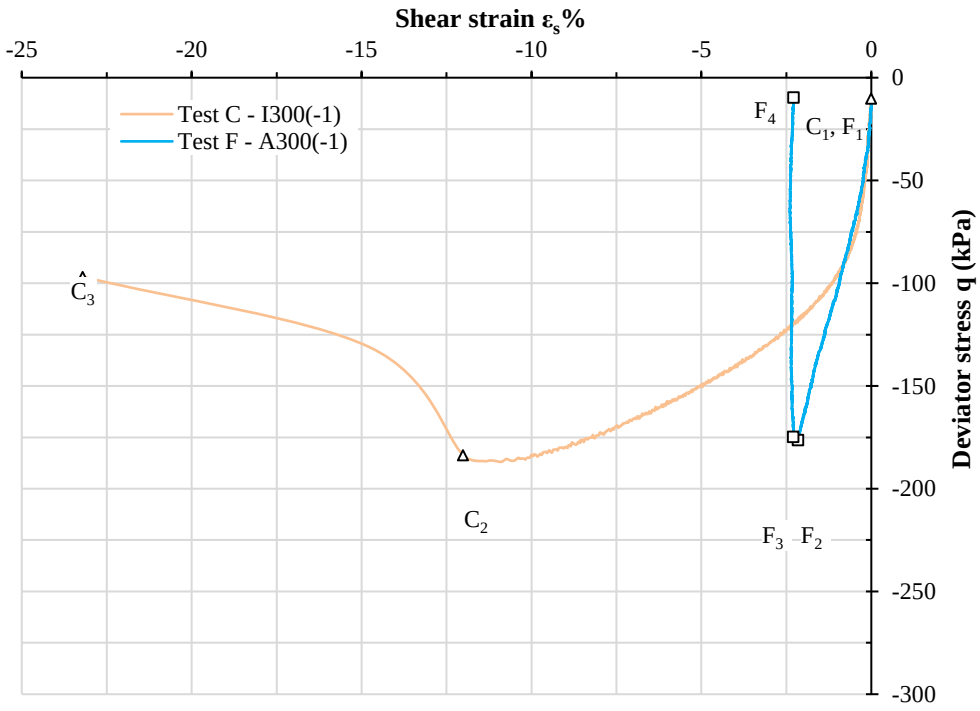

Figure 6.29: Variation of deviator stress q with shear strain ϵ_s in Tests C and F

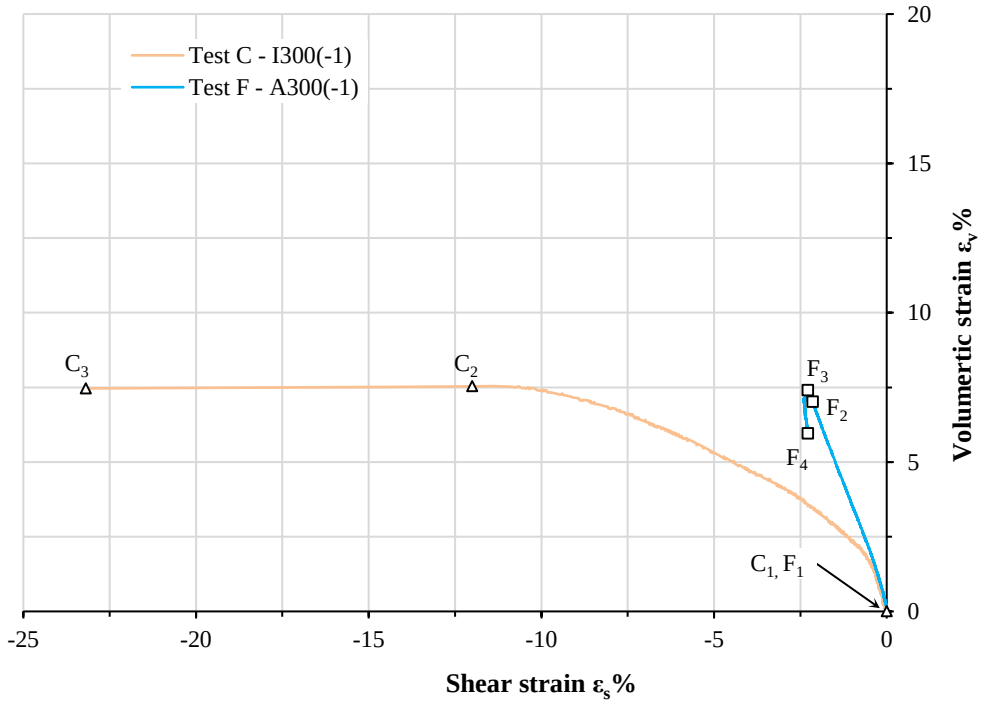

Figure 6.30: Variation of volumetric strain ϵ_v with shear strain ϵ_s in Tests C and F

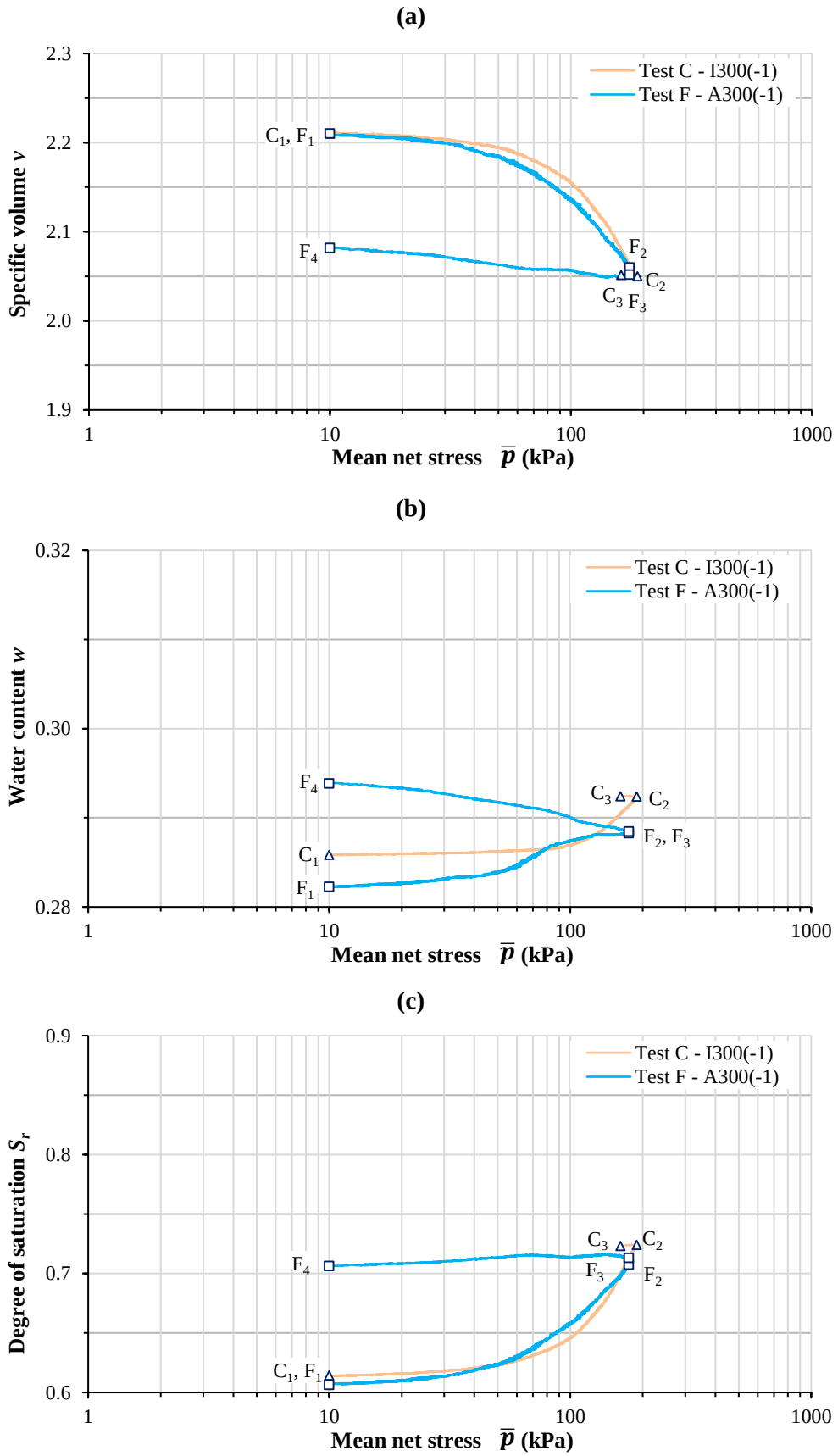

Figure 6.31: Variations of (a) specific volume v (b) water content w (c) degree of saturation S_r in Tests C and F

Yield points were identified from a bi-linear approximation in the $v : ln\bar{p}$ plot, as discussed in Section 2.5.2. As examples, Figure 6.32 shows the $v : ln\bar{p}$ plots for Tests D, E and F). In performing the bi-linear approximation, each post-yield compression curve was approximated by a straight line (see the dashed lines in Figure 6.32), with location and gradient selected to best-fit the later part of the individual post-yield compression curve. Two possible alternatives were investigated for constructing a linear approximation to the pre-yield compression curve. In the first case, shown by the dotted lines in Figure 6.32, a straight line was constructed with a gradient κ_e selected to give a best-fit line to the individual pre-yield compression curve. In the second case, shown by the continuous lines in Figure 6.32, a straight line was constructed with a gradient κ selected as the average gradient from all the various unloading stages (e.g. see Figure 6.32a). Values of κ_e were consistently lower than the value of κ, so that use of κ_e consistently resulted in lower values of yield stress than use of κ (see Figure 6.32). Use of κ_e would appear logical if the sole aim of the bi-linear approximation was to determine a value of yield stress for an individual test, whereas use of κ would make more sense if the yield point determination was part of a process of determining soil constants and initial state (including initial size and shape of yield surface) within a constitutive model as part of a numerical modelling exercise.

Figure 6.33 shows the estimated yield points from the loading stages on isotropically compacted samples (Tests A, B and C) and anisotropically compacted samples (Tests D, E and F), plotted in the $q : \bar{p}$ plane. These yield points were determined using the bi-linear approximation with the pre-yield compression curve approximated as a straight line of gradient κ (rather than κ_e). Yield curves defined by the ABBM1 expression of Equation 2.96 proposed by D'Onza et al. (2011a) are fitted to the two sets of experimental yield points in Figure 6.33. Within Equation 2.96, the value of M was taken as 0.752 and the value of $f(s)$ for s =300kPa was taken as 154kPa, based on the experimental critical state data for the same compacted speswhite kaolin from Al-Sharrad (2013). Values of $\bar{p}_m(s)$ and α, defining the size and shape of each yield curve, were selected to best-fit each set of experimental yield points. This gave $\bar{p}_m(s)$ =154kPa, $\alpha = -0.04$ for the isotropically compacted samples and $\bar{p}_m(s)$ =152kPa, α =0.47 for the anisotropically compacted samples.

Inspection of Figure 6.33 shows that the ABBM1 yield curve expression of Equation 2.96 provides a reasonable match to both sets of experimental yield points. For the isotropically compacted samples the best-fit yield curve inclination was approximately zero ($\alpha = -0.04$), confirming isotropy of plastic behaviour in the initial state. In contrast, for the anisotropically compacted samples the yield curve is inclined (α =0.47). Similar conclusions arise if the experimental yield points are determined using the alternative bi-linear approximation (using κ_e instead of κ for the gradient of the straight

line approximation to the pre-yield compression curve), with the yield curves simply of smaller size.

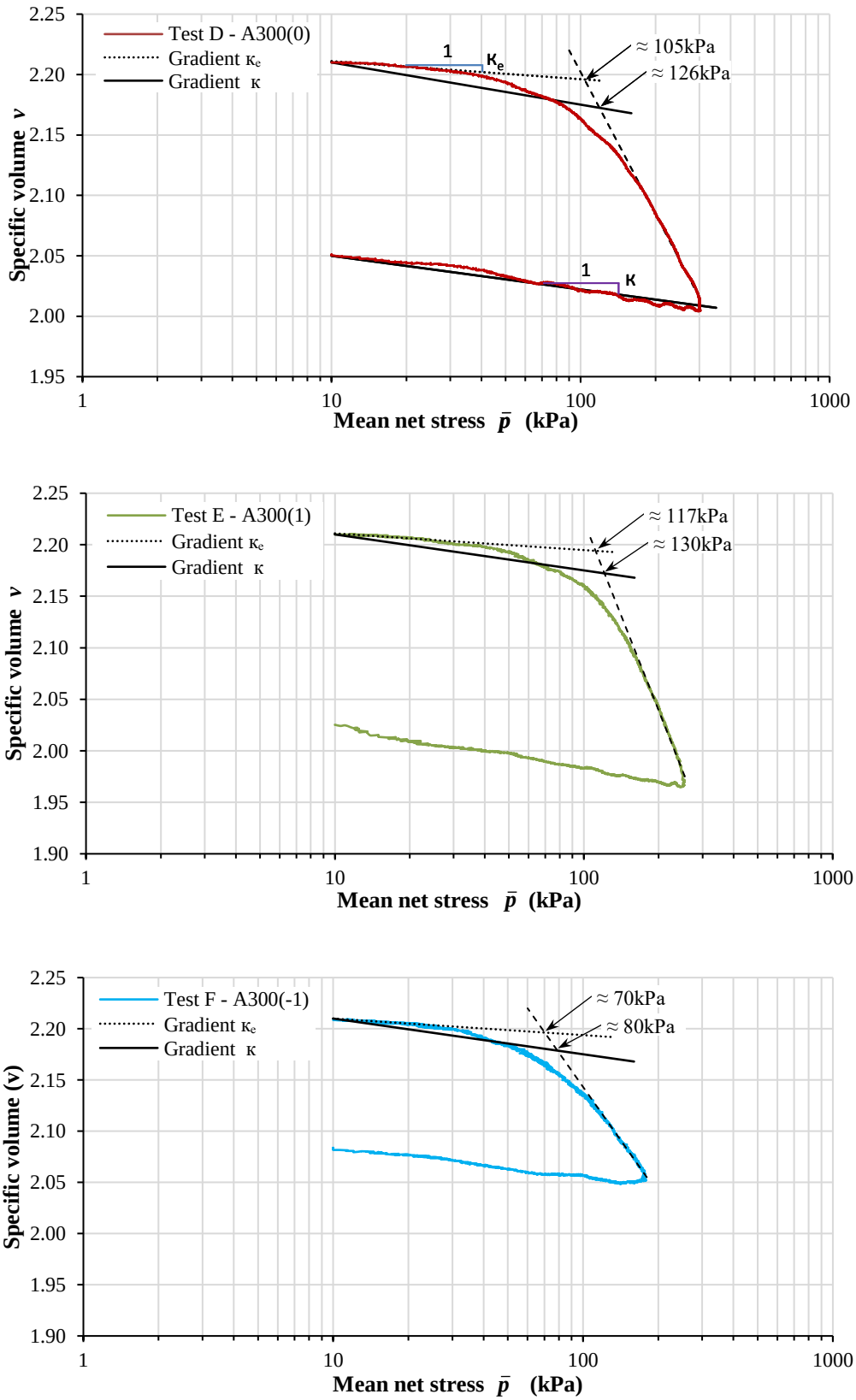

Figure 6.32: Estimation of yield stresses for anisotropically compacted samples in Tests D, E and F

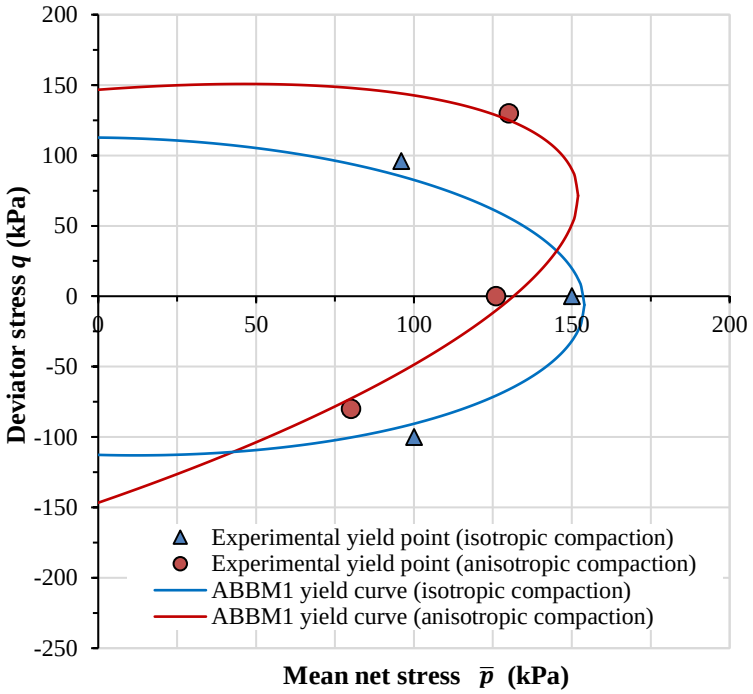

Figure 6.33: Estimated cross-sections of initial yield surface in $q : \bar{p}$ plane at s =300kPa for iotropically compacted samples (Tests A, B and C) and anisotropically compacted samples (Tests D, E and F)

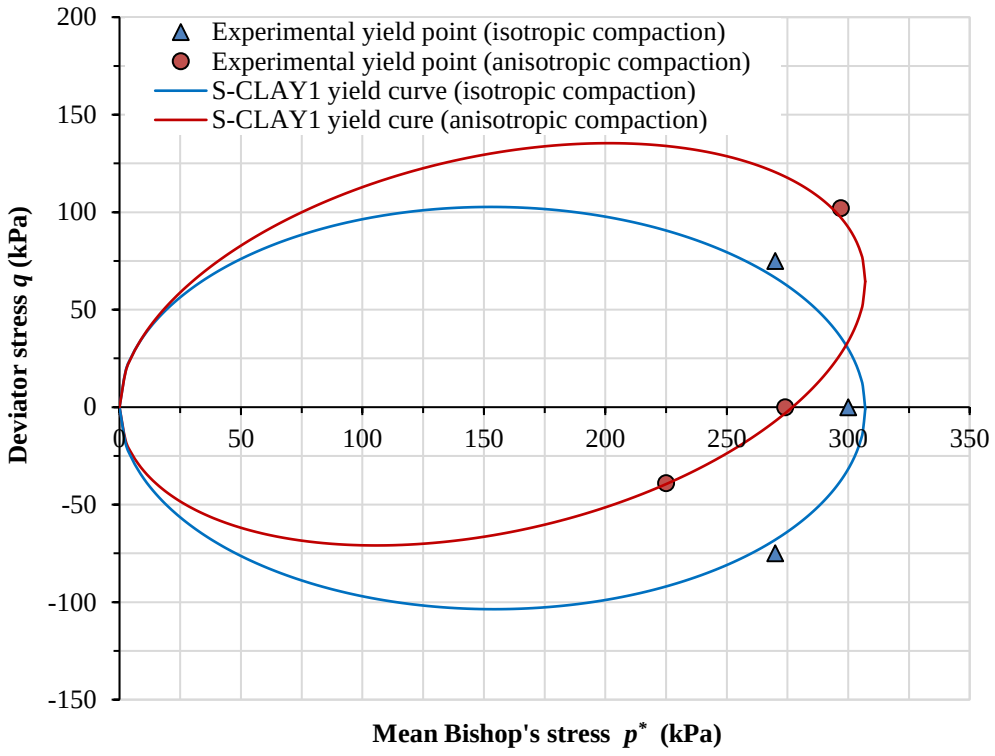

Figure 6.34: Estimated cross-sections of initial yield surface in $q : p^*$ plane at s =300kPa for iotropically compacted samples (Tests A, B and C) and anisotropically compacted samples (Tests D, E and F)

Figure 6.34 shows yield points from Tests A, B, C, D, E and F re-plotted in the $q : p^*$ plane, where p^* is the mean Bishop's stress (see Equation 2.77). Yield points were re-calculated using an equivalent bi-linear approximation in the $v : lnp^*$ plane. Yield curves are fitted to each set of three yield points in Figure 6.34 using the S-CLAY1 yield curve expression for anisotropic saturated soils of Equation 2.95, but with p' replaced by p^* and M replaced by M^* (the critical state stress ratio in the $q : p^*$ plane). The value of M^* was taken as 0.672, based on the experimental critical state data for the same compacted speswhite kaolin from Al-Sharrad (2013). Note that plotting in the $q : p^*$ plane (rather than in the $q : \bar{p}$ plane) has the advantage that, even for unsaturated conditions, each constant suction yield curve passes through the origin. Al-Sharrad (2013) reached the same conclusion in interpreting his experimental yield points (see Section 2.5.4). Best-fit values for α used in Figure 6.34 were $\alpha = 0.00$ for the isotropically compacted samples and $\alpha = 0.21$ for the anisotropically compacted samples (with p^*_m =307kPa in both cases).

6.6 Influence of compaction procedure on wave velocities and elastic anisotropy

This section compares shear and compression wave velocities and elastic anisotropies G_{hh}/G_{hv} and M_h/M_v for the isotropically compacted samples (Tests A, B and C) and the anisotropically compacted samples (Tests D, E and F).

6.6.1 Loading/unloading at $\eta \approx 0$

Figure 6.35 shows the variations of shear wave velocities V_{shv} and V_{shh} during loading and unloading stages of Tests A and D plotted against mean net stress $\bar{p}$. Figure 6.36 shows the corresponding variations of compression wave velocities V_{pv} and V_{ph}.

Inspection of Figures 6.35 and 6.36 shows that the variations of all shear and compression wave velocities were similar in Tests A and D, during both loading and unloading. V_{shv} was slightly higher in Test D than in Test A throughout loading and unloading (Figure 6.35a). V_{shh} was almost identical in Tests A and D in the early part of loading, but became slightly higher in Test D than in Test A during the later part of loading and throughout the subsequent unloading (Figure 6.35b). A similar pattern to V_{shh} can be seen when comparing compression wave velocities V_{pv} and V_{ph} from Tests A and D (Figure 6.36). It is difficult to know how much significance to attribute to the relatively small differences in wave velocities between Tests A and D. This is particularly true given that expected behaviour would be initial differences in wave velocities

between Tests A and D, due to differences in initial anisotropy, but then these differences gradually disappearing as memory of initial anisotropy was progressively erased during plastic straining (exactly the opposite of what is observed for V_{shh}, V_{pv} and V_{ph} in Figures 6.35 and 6.36).

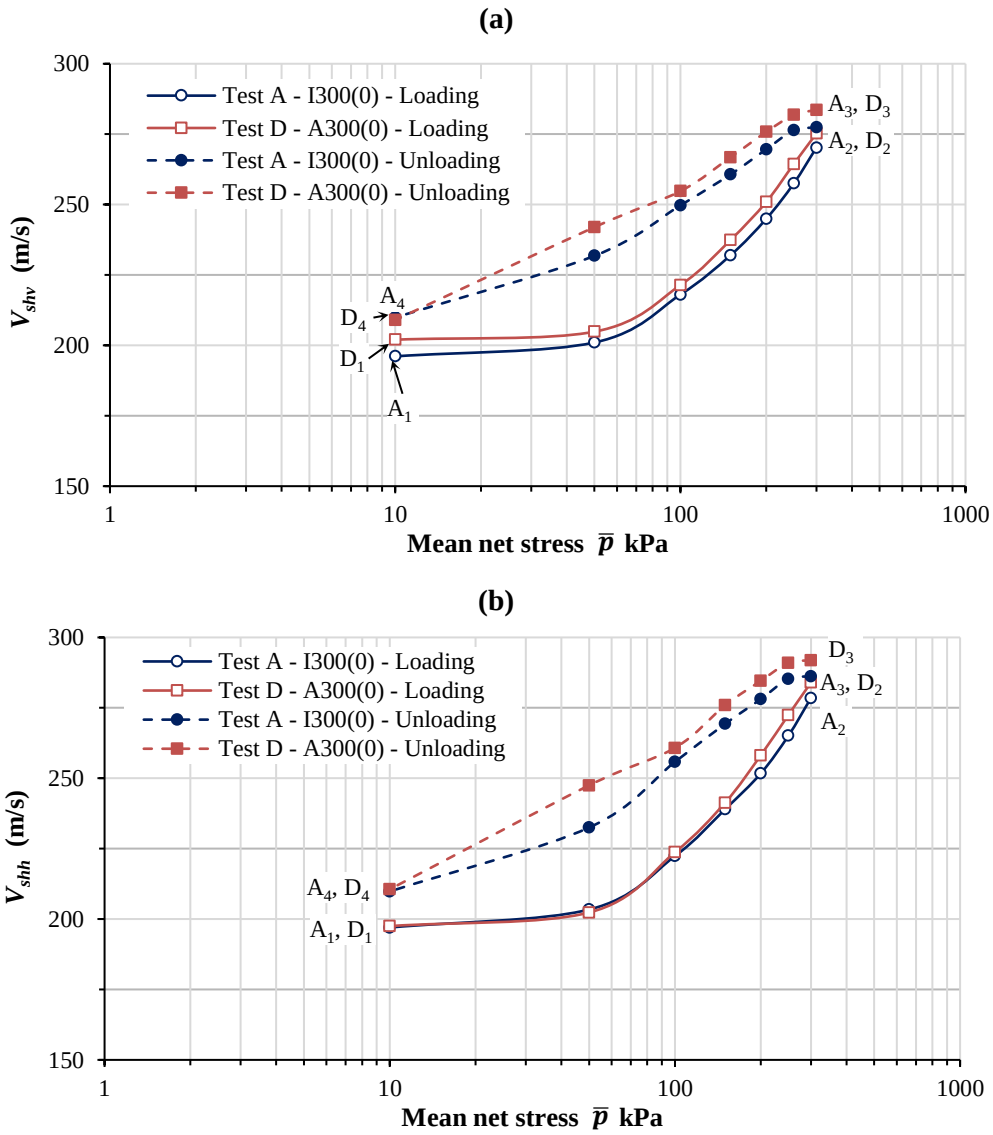

Figure 6.35: Variations of shear wave velocities in Tests A and D

Figures 6.37 and 6.38 show the variations of shear modulus ratio G_{hh}/G_{hv} and constrained modulus ratio M_h/M_v for Tests A and D. At the start of loading, the ratio of G_{hh}/G_{hv} was slightly higher in Test D than in Test A, but this difference disappeared during loading, so that G_{hh}/G_{hv} was essentially the same for Tests A and D during the later part of loading and throughout the subsequent unloading (Figure 6.37). This fits with expected behaviour, of a small difference of intial anisotropy being gradually erased during plastic straining. Values of ratio M_h/M_v (Figure 6.38) started very similar in Tests A and D, and remained very similar throughout loading and unloading.

6.6.2 Loading/unloading at $\eta = 1$

Figures 6.39 and 6.40 show the variations of shear wave velocities and compression wave velocities for Tests B and E.

Figure 6.39 shows that the variations of shear wave velocities were very similar in Test B (isotropically compacted sample) and Test E (anisotropically compacted sample). Figure 6.40 shows that, at the start of loading, both compression wave velocities were slightly lower in Test E than in Test B. The slight initial difference in V_{pv} remained throughout loading and unloading, whereas the slight initial difference in V_{ph} had essentially disappeared by part way through the loading stage.

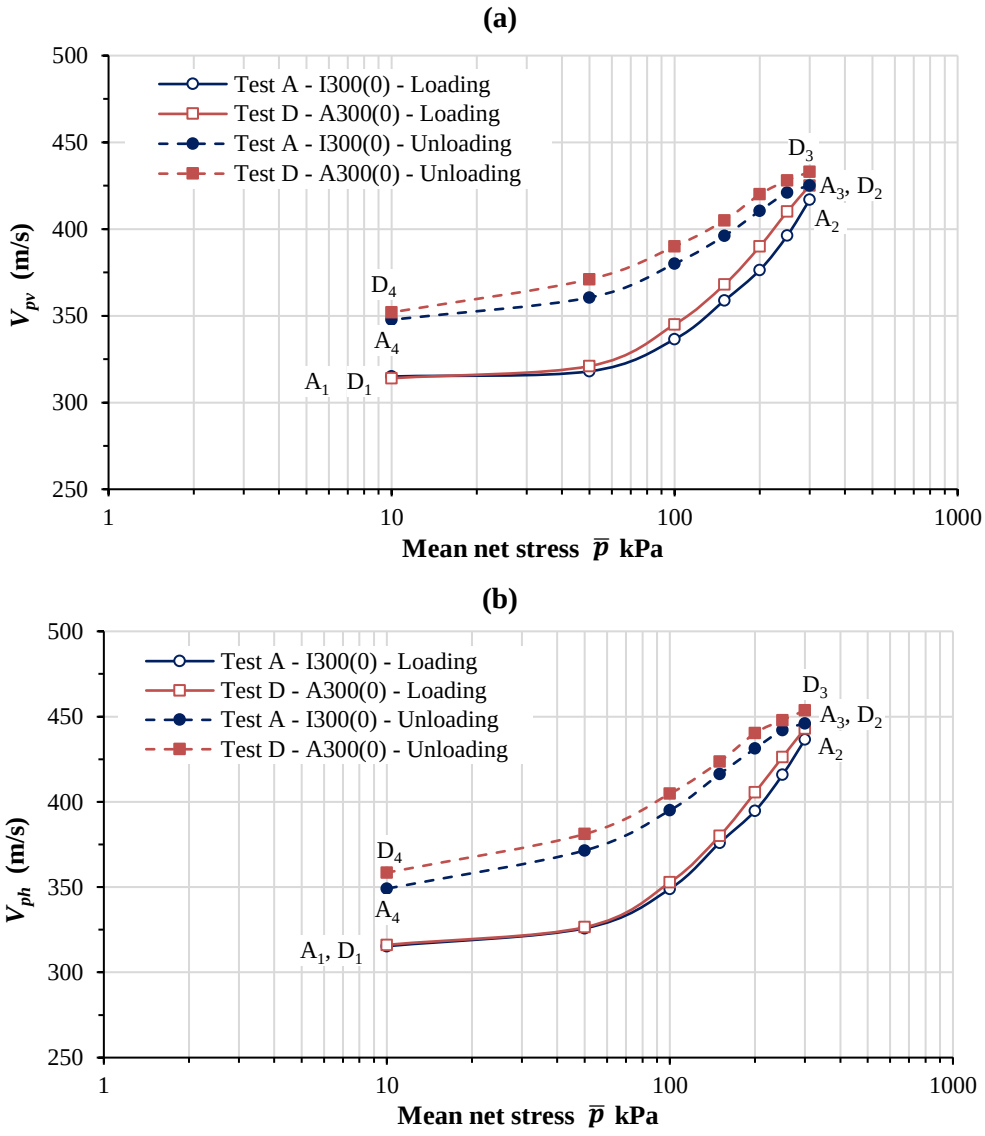

Figure 6.36: Variations of compression wave velocities in Tests A and D

Figures 6.41 and 6.42 show the variations of G_{hh}/G_{hv} and M_h/M_v in Tests B and E. Inspection of Figures 6.41 and 6.42 shows that the variations of G_{hh}/G_{hv} and M_h/M_v

were similar in Tests B and E, and no clear pattern emerges from any small differences between the two tests.

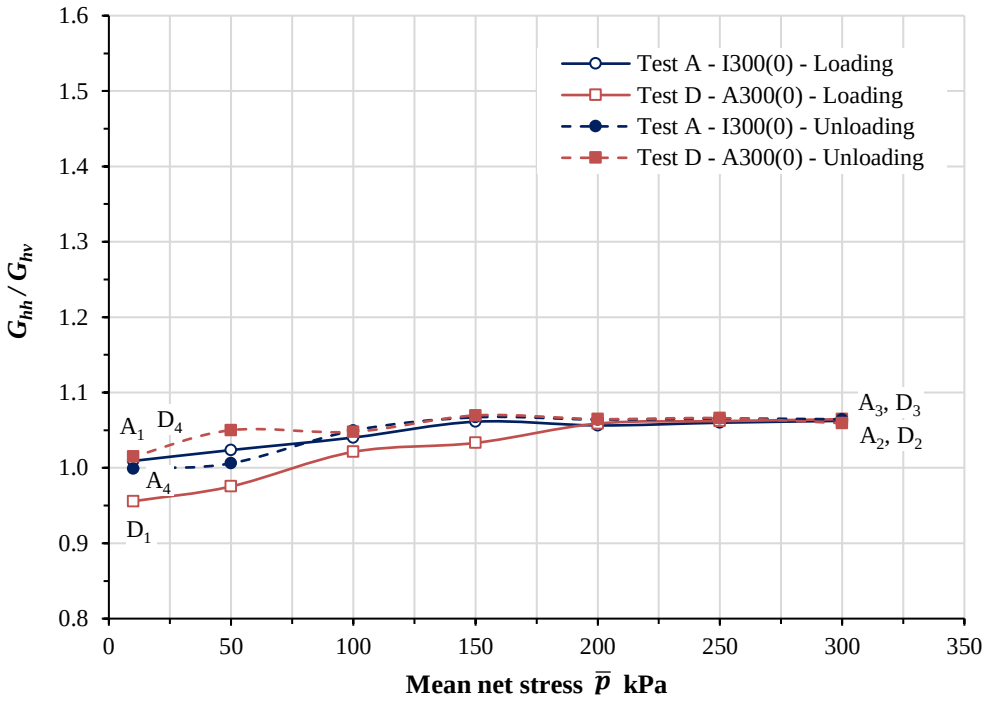

Figure 6.37: Variations of shear modulus ratio G_{hh}/G_{hv} in Tests A and D

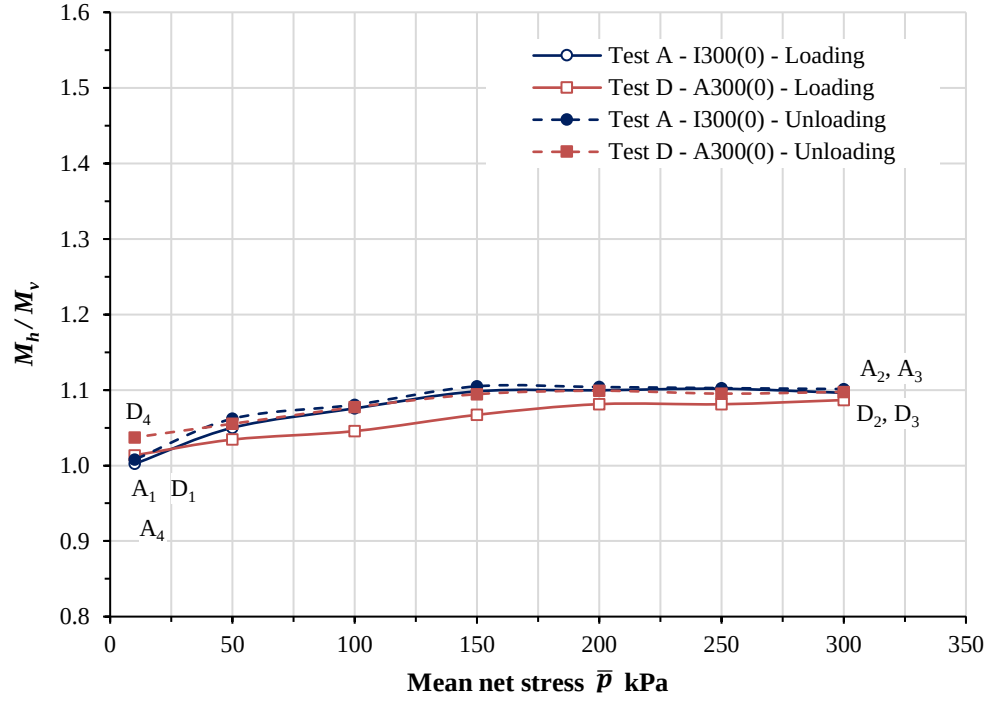

Figure 6.38: Variations of constrained modulus ratio M_h/M_v in Tests A and D

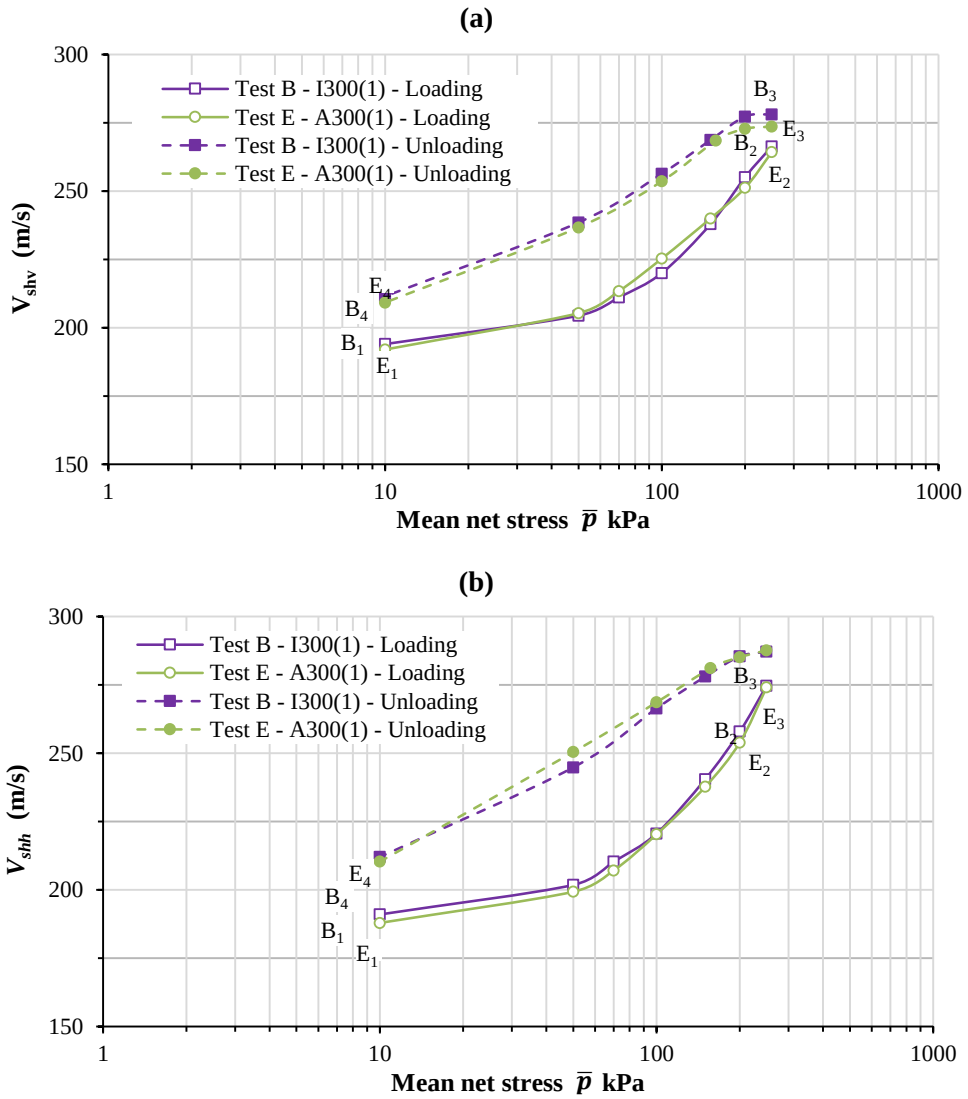

Figure 6.39: Variations of shear wave velocities in Tests B and E

6.6.3 Loading/unloading at $\eta = -1$

Figures 6.43 and 6.44 show the variations of shear wave velocities for Tests C and F. It appears that, under loading at $\eta = -1$, significant differences of shear wave velocity V_{shv} and compression wave velocity V_{pv} developed during the loading stages of these tests (with both V_{shv} and V_{pv} becoming significantly greater in Test F than in Test C). In contrast, values of shear wave velocity V_{shh} and compression wave velocity V_{ph} were similar in the two tests (at the start of loading, V_{shh} was lower in Test F than in Test C, but the values of V_{shh} converged during loading). It therefore appears that, in these tests at $\eta = -1$, where the vertical stress was the minor principal stress, there were significant differences between Tests C and F in terms of shear or compression wave velocities with a direction of wave transmission or polarisation in the vertical direction, but no differences between Tests C and F in terms of wave velocities with wave transmission and polarisation limited to horizontal directions.

The significant differences between the values of V_{shv} and V_{pv} in Test C and the values of V_{shv} and V_{pv} in Test F are consistent with the substantial differences in large strain behaviour observed in these two tests (see Figures 6.29 and 6.30), in particular the fact that shear failure occurred in Test C whereas shear failure did not appear to be imminent in Test F. It can be therefore tentatively be concluded that loading at $\eta = -1$ caused significant differences in both large strain behaviour and very small strain behaviour (in terms of V_{shv} and V_{pv}) between an isotropically compacted sample (Test C) and an anisotropically compacted sample (Test F). This conclusion should, however, be viewed with a degree of caution, given that no significant differences were observed between the behaviour of isotropically compacted and anisotropically compacted samples under loading at $\eta \approx 0$ and $\eta = 1$. An alternative explanation is simply that an experimental problem occurred in Test C, resulting in the unexpected shear failure and hence significant changes in both large strain and very small strain response. To eliminate this possibility, it would be useful to conduct a repeat of Test C.

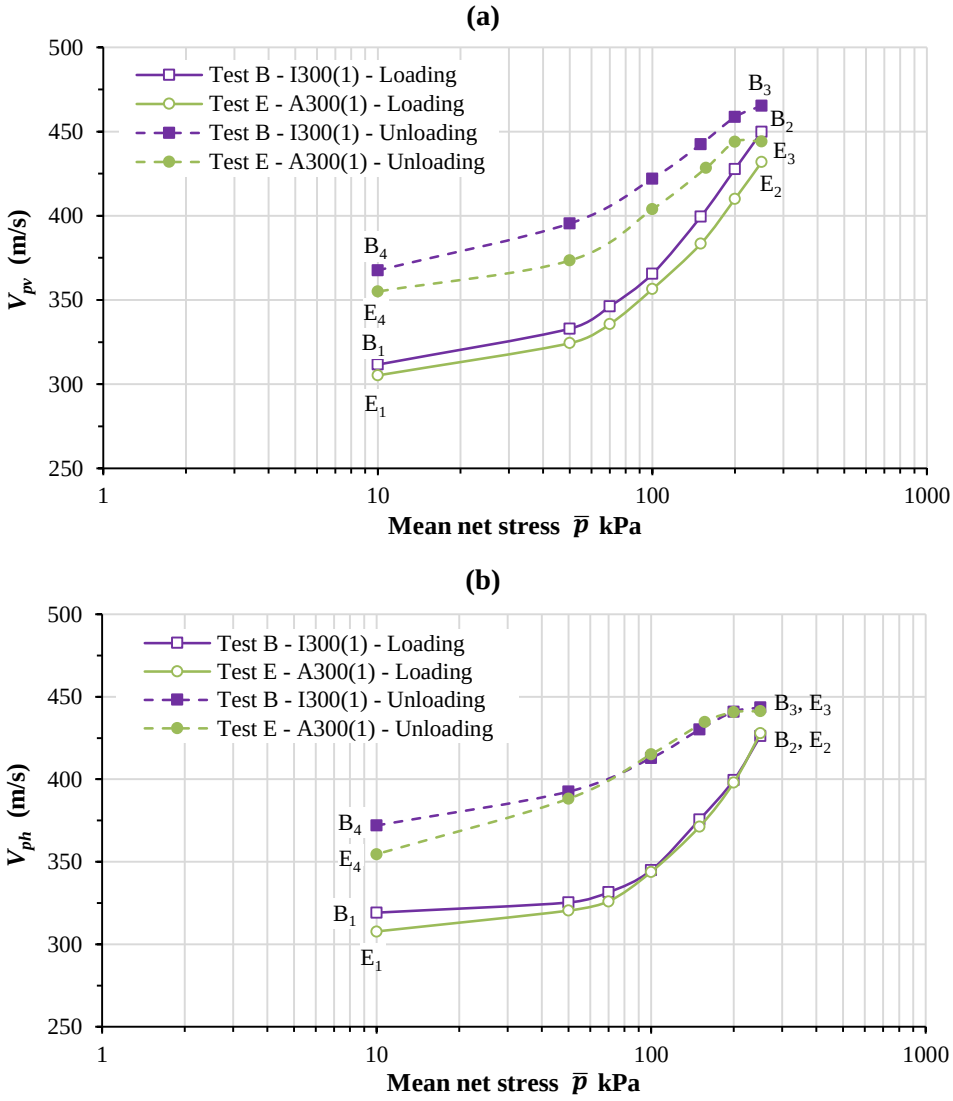

Figure 6.40: Variations of compression wave velocities in Tests B and E

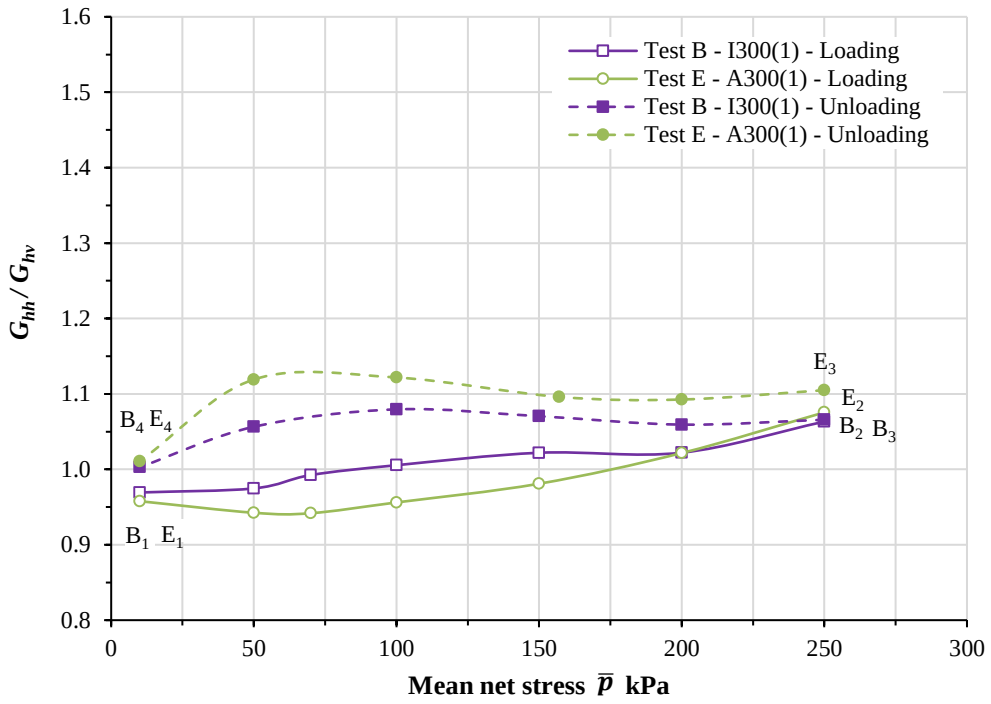

Figure 6.41: Variations of shear modulus ratio G_{hh}/G_{hv} in Tests B and E

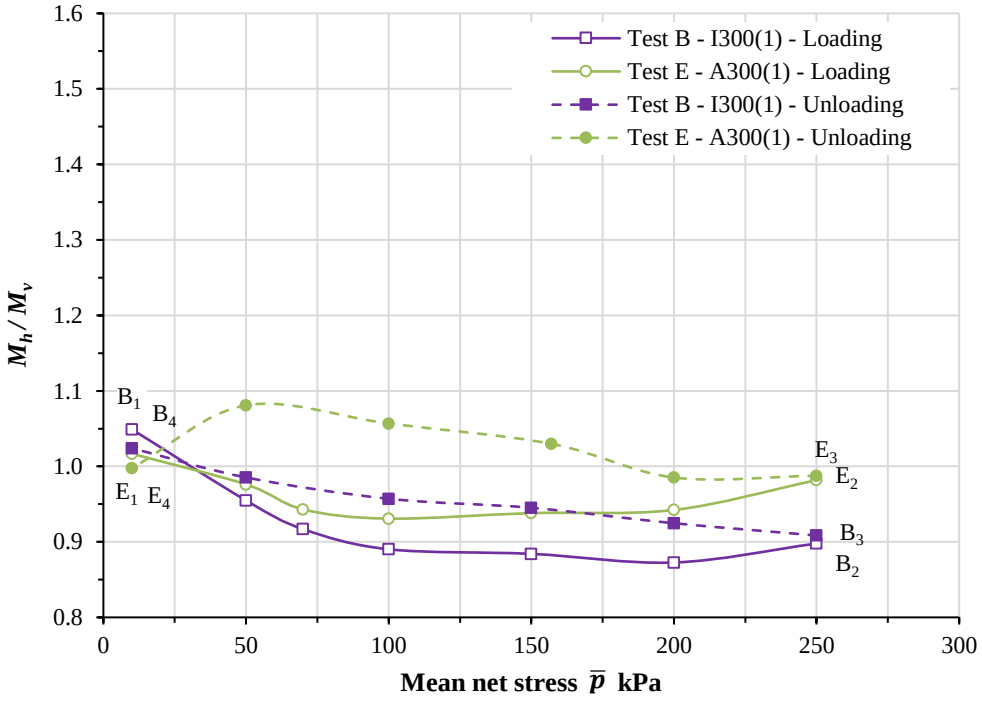

Figure 6.42: Variations of constrained modulus ratio M_h/M_v in Tests B and E

Figures 6.45 and 6.46 show the variations of G_{hh}/G_{hv} and M_h/M_v in Tests C and F. As expected from the values of various wave velocities, there are significant differences of both G_{hh}/G_{hv} and M_h/M_v between Tests C and F. It is predominantly the values of G_{hv} and M_v (rather than G_{hh} and M_h) that differ between the two tests.

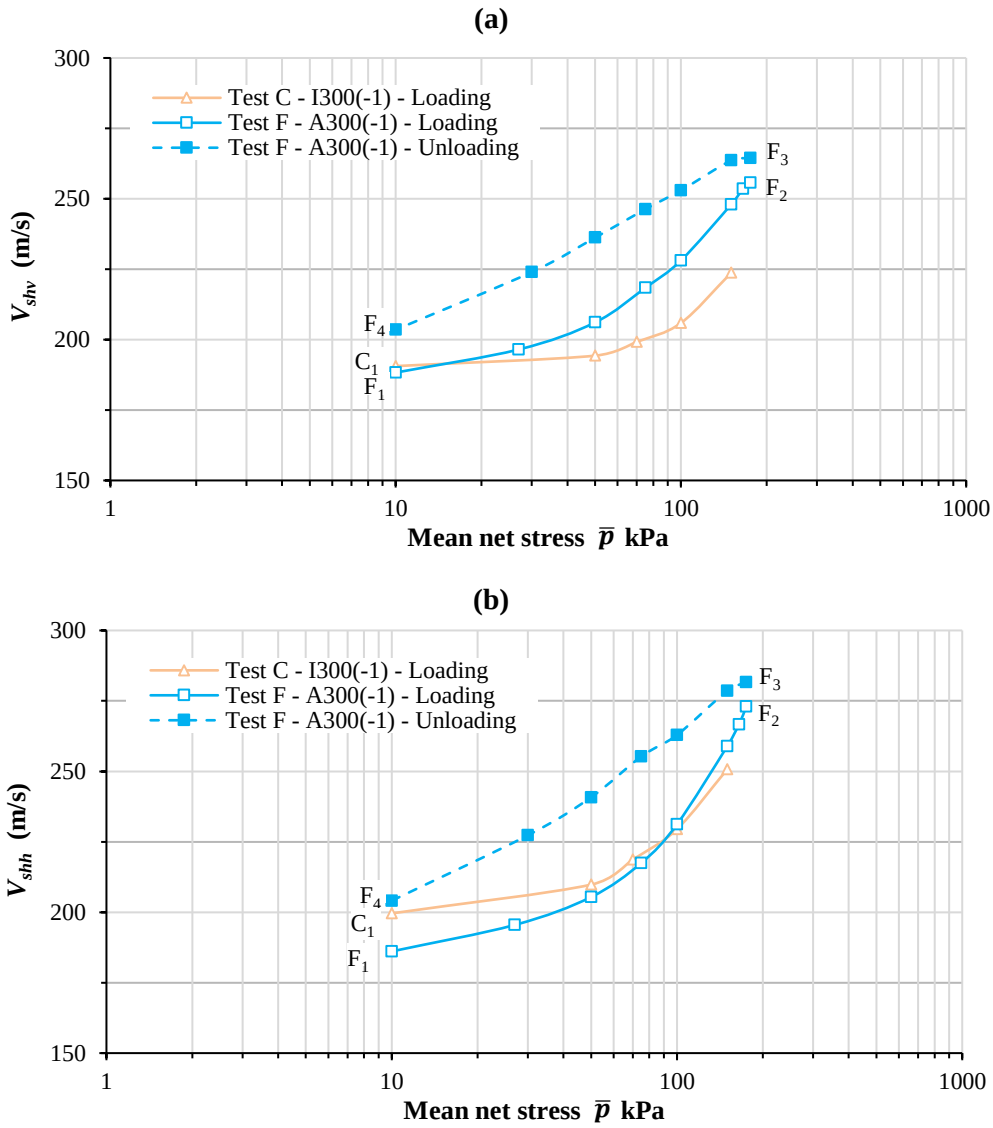

Figure 6.43: Variations of shear wave velocities in Tests C and F

6.7 Influence of cyclic loading and unloading

Test F involved a second loading-unloading cycle at the same stress ratio ($\eta = -1$) as the first loading-unloading cycle. The intention was to explore the variation of wave velocities and elastic anisotropies during elastic unloading-reloading as well as during plastic loading stages.

Figure 6.47 shows the stress path for Test F plotted in the $q : \bar{p}$ plane. The first loading-unloading cycle ($F_1F_2F_3F_4$) involved loading to $\bar{p}$ =175kPa, $q = -175$kPa, whereas the second loading-unloading cycle ($F_5F_6F_7F_8$) involved loading to $\bar{p}$ =300kPa, $q = -300$kPa. Also shown in Figure 6.47 is the estimated position of the critical state line in triaxial extension at s =300kPa, taken from the work of Al-Sharrad (2013).

6.7.1 Large strain behaviour

Figure 6.48 shows the variation of deviator stress q plotted against shear strain ϵ_s for Test F and Figure 6.49 shows the corresponding plot of volumetric strain ϵ_v against shear strain ϵ_s. Inspection of Figures 6.48 and 6.49 indicates that the large strain behaviour was essentially reversible during unloading F_3F_4 and the first part of the subsequent second loading stage F_5F_6 (up to the previous maximum stress of $q = -175$kPa). In addition, the later part of the second loading stage F_5F_6 (from $q = -175$kPa to $q = -300$kPa) plots as a simple continuation of the first loading stage F_1F_2, in terms of development of both shear strain and volumetric strain. Overall, therefore, Figures 6.48 and 6.49 confirm that the large strain behaviour can be approximated by an elasto-plastic form of behaviour (involving hardening). It is also interesting that there is no suggestion from Figure 6.48 that shear failure was imminent, even at $q = -300$kPa, in contrast to the equivalent test on the isotropically compacted sample (Test C), where unexpected failure occurred at $q = -186$kPa (see Sections 6.4.1 and 6.5.3).

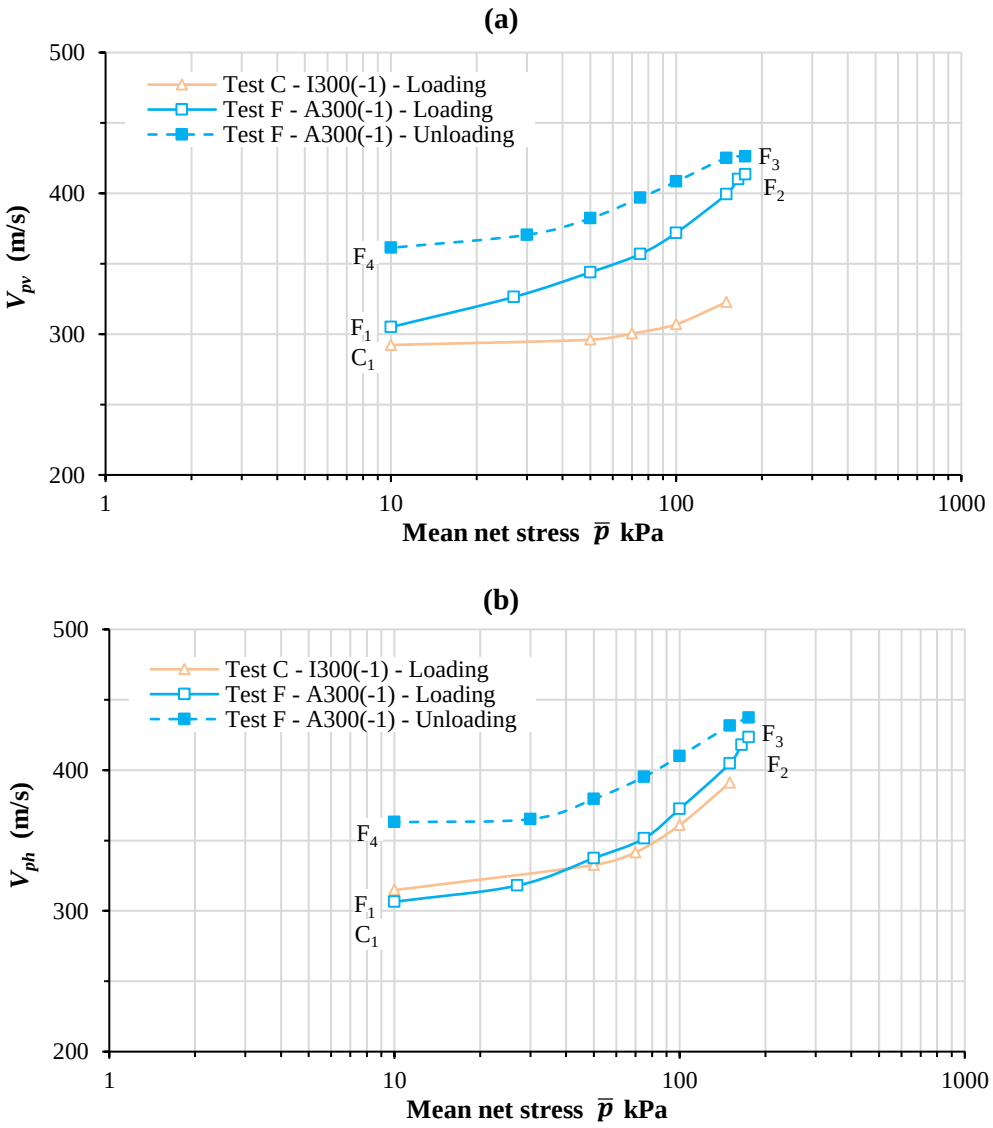

Figure 6.44: Variations of compression wave velocities in Tests C and F

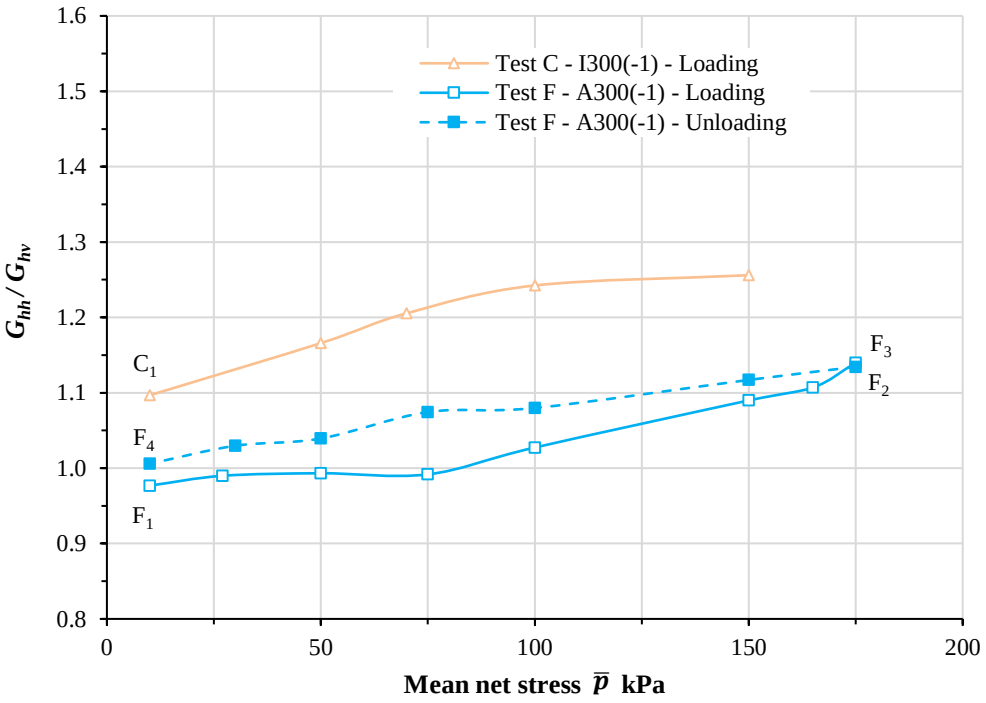

Figure 6.45: Variations of shear moduli ratio G_{hh}/G_{hv} in Tests C and F

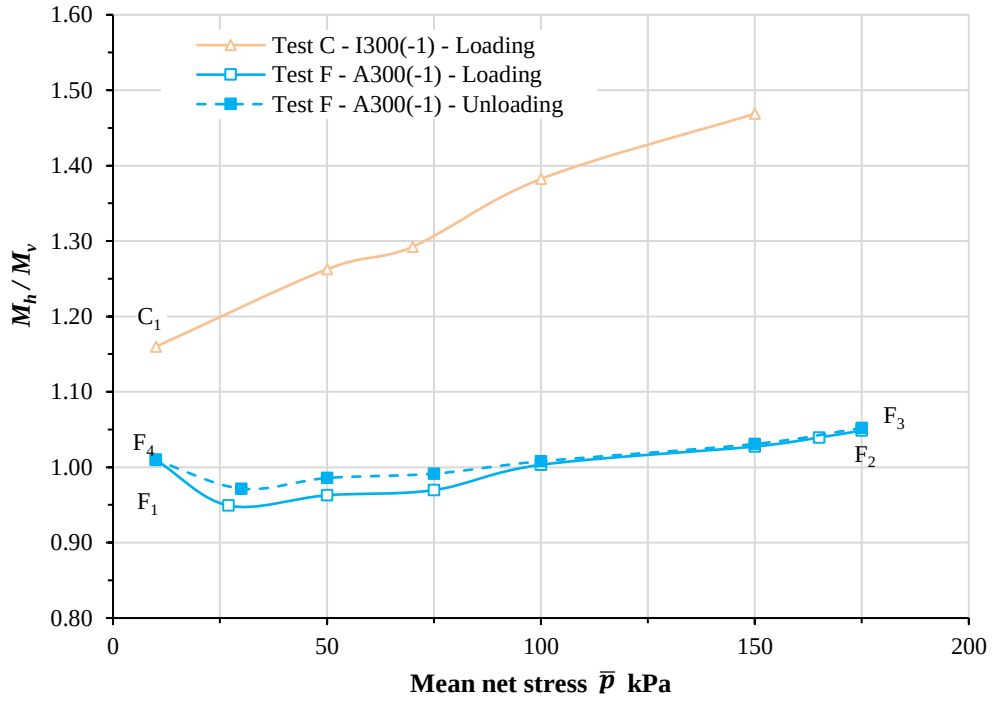

Figure 6.46: Variations of constrained modulus ratio M_h/M_v in Tests C and F

Figures 6.50 shows the variations of specific volume v, water content w and degree of saturation S_r during Test F. Inspection of Figures 6.50a and 6.50c confirms that the variations of v and S_r were essentially reversible during unloading (F_3F_4) and subsequent re-loading (the first part of F_5F_6) and that during the later part of the

second loading stage F_5F_6 the variations of both v and S_r followed continuations of the corresponding curves from the first loading stage F_1F_2. Finally, the variations of v and S_r during the second unloading stage F_7F_8 were approximately parallel to the corresponding curves from the first unloading stage F_3F_4. Overall, therefore, Figure 6.50 confirms that the large strain behaviour can be idealised by a hardening form of elasto-plasticity.

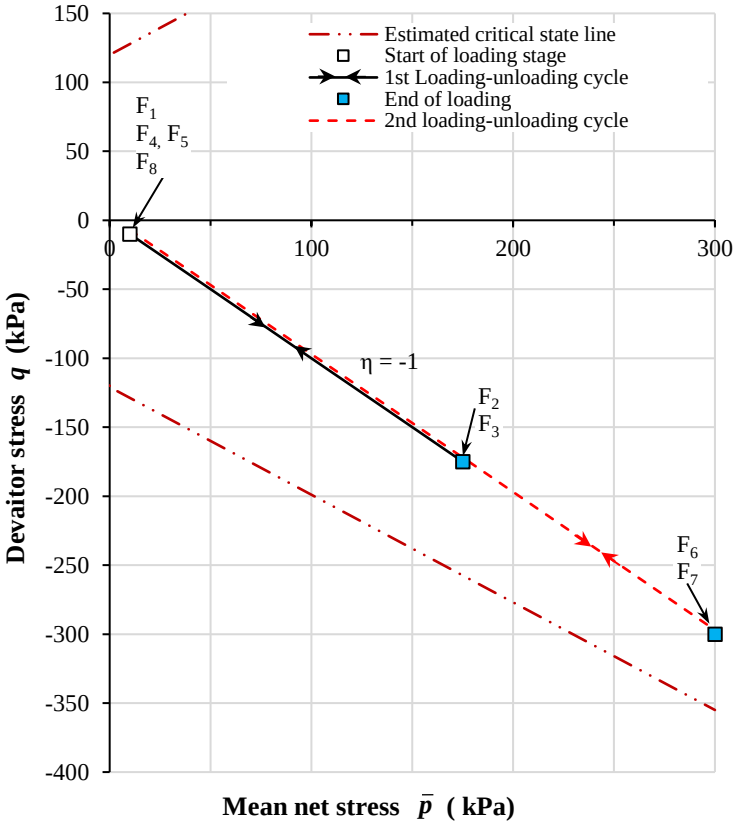

Figure 6.47: Stress paths for Test F at $s = 300$kPa

6.7.2 Wave velocities and elastic anisotropy

Figure 6.51 shows the variations of shear wave velocities V_{shv} and V_{shh} from Test F and Figure 6.52 shows the corresponding variations of compression wave velocities V_{pv} and V_{ph}. Inspection of Figures 6.51 and 6.52 shows that the variations of all wave velocities were essentially reversible during the first unloading stage F_3F_4 and subsequent re-loading (the first part of the second loading stage F_5F_6) and that the variations of all wave velocities during the later part of the second loading stage F_5F_6 plot as simple continuations of the corresponding curves from the first loading stage F_1F_2. In addition, the variations of all wave velocities in the second unloading stage F_7F_8 plot as parallel to the corresponding curves from the first unloading stage F_3F_4. Overall, therefore, the variations of wave velocities shown in Figures 6.51 and 6.52 are

qualitatively consistent with the large strain behaviour shown in Figures 6.48, 6.49 and 6.50.

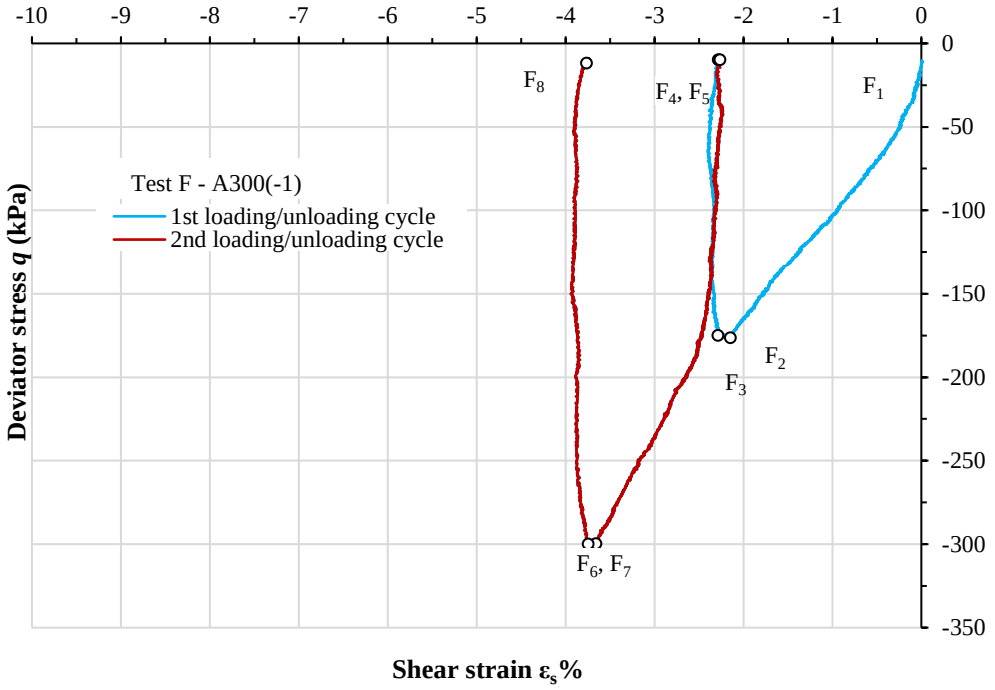

Figure 6.48: Variation of deviator stress q with shear strain ϵ_s in Tests F

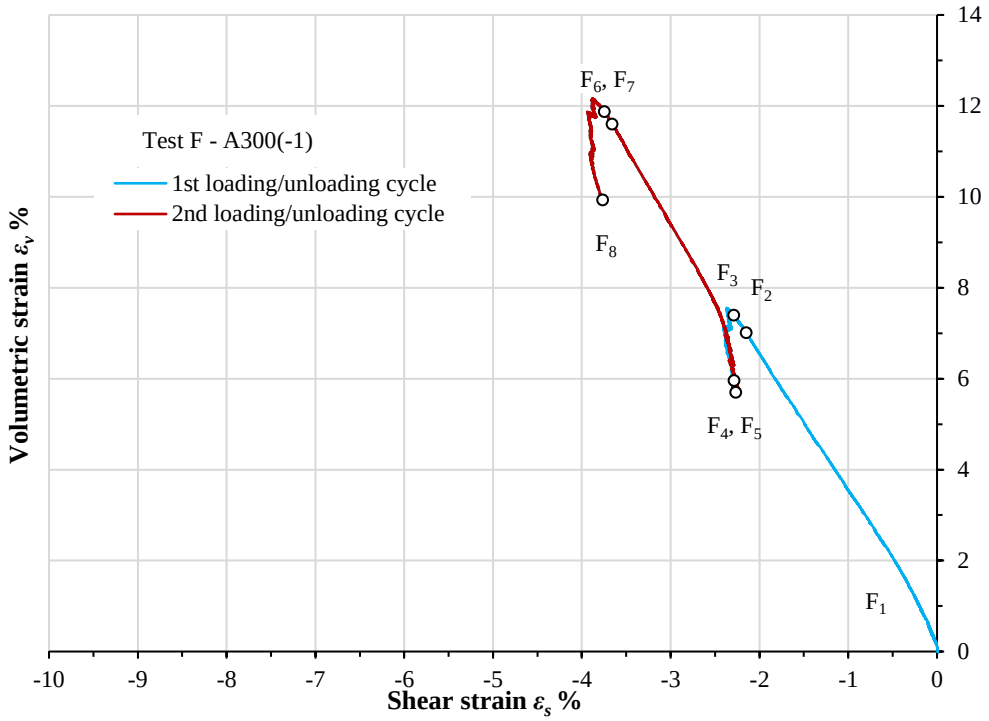

Figure 6.49: Variation of volumetric strain ϵ_v with shear strain ϵ_s in Tests F

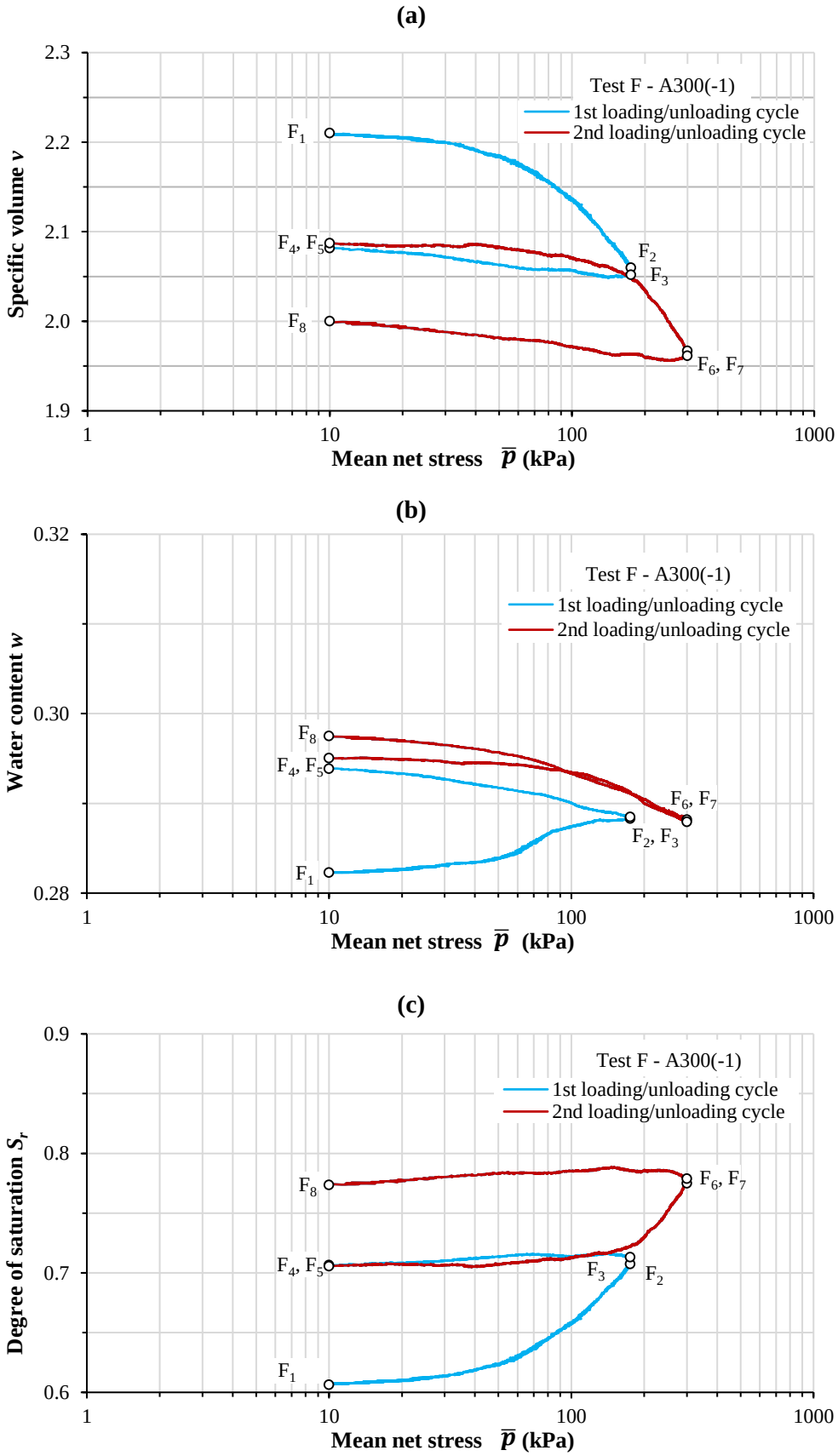

Figure 6.50: Variations of (a) specific volume v (b) water content w (c) degree of saturation S_r in Test F

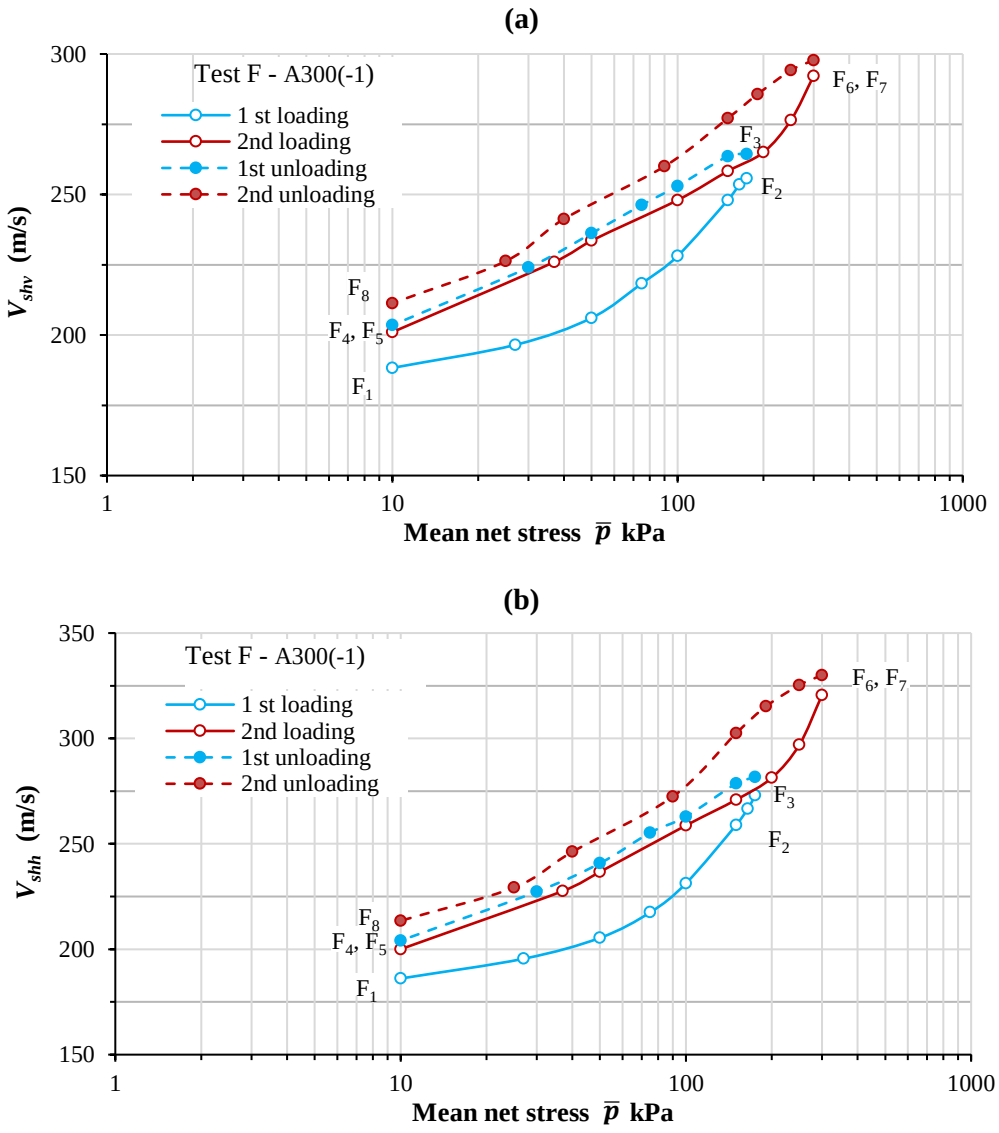

Figure 6.51: Variations of shear wave velocities in Test F

Figures 6.53 and 6.54 show the variations of G_{hh}/G_{hv} and M_h/M_v in Test F. Figure 6.53 shows that the variation of G_{hh}/G_{hv} was reversible during the first unloading stage F_3F_4 and subsequent re-loading (the first part of the second loading stage F_5F_6). Indeed, the entire variation of G_{hh}/G_{hv} during all loading and unloading stages was approximately reversible. Figure 6.54 shows that there was very little variation of the ratio M_h/M_v, but what little variation did occur was approximately reversible during all loading and unloading stages. The behaviour shown in Figures 6.53 and 6.54 therefore suggests that any development of elastic anisotropy during Test F was predominantly stress-induced, rather than strain-induced, because the latter would have been expected to produce irreversible variation of G_{hh}/G_{hv} or M_h/M_v. It is also useful to note that the significant variation of the value of G_{hh}/G_{hv} during the various loading and unloading stages of Test F suggests that stress-induced anisotropy may be controlled by the stress ratio η^* (where $\eta^* = q/p^*$ is expressed in terms of Bishop's

stresses) rather than the stress ratio η (expressed in terms of net stresses), because η^* varied significantly during loading and unloading stages (see Section 7.2), whereas η remained constant throughout ($\eta = -1$).

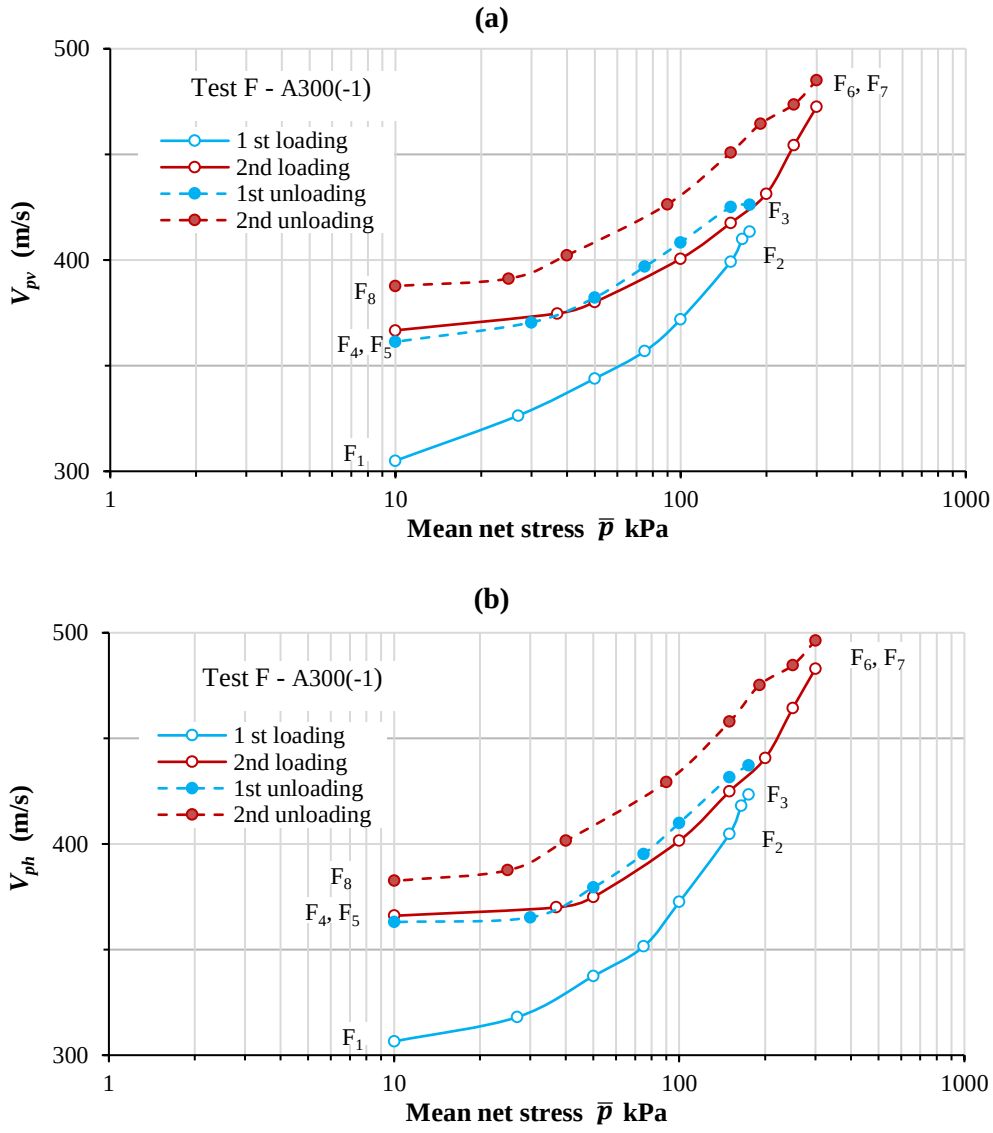

Figure 6.52: Variations of compression wave velocities in Test F

6.8 Loading/unloading: influence of suction

Tests A, H and I all involved isotropic loading and unloading ($\eta \approx 0$, with q =2kPa) on isotropically compacted samples, but at different values of suction (s =300kPa in Test A, s =50kPa in Test H and s =0 (saturated conditions) in Test I). Results from Tests A, H and I can therefore be compared to show the influence of suction on behaviour during loading and unloading, in terms of large strain behaviour and very small strain elastic response indicated by BEE test results.

Figure 6.55 shows the stress paths for Tests A, H and I plotted in the $s : \bar{p}$ plane, including the initial equalisation stages (from X) and the subsequent loading and unloading stages. Test A (at s =300kPa) involved loading to $\bar{p}$ =300kPa, and Test I (under saturated conditions) involved loading to p' =300kPa. In contrast, loading in Test H (at s =50kPa) was only to $\bar{p}$ =200kPa.

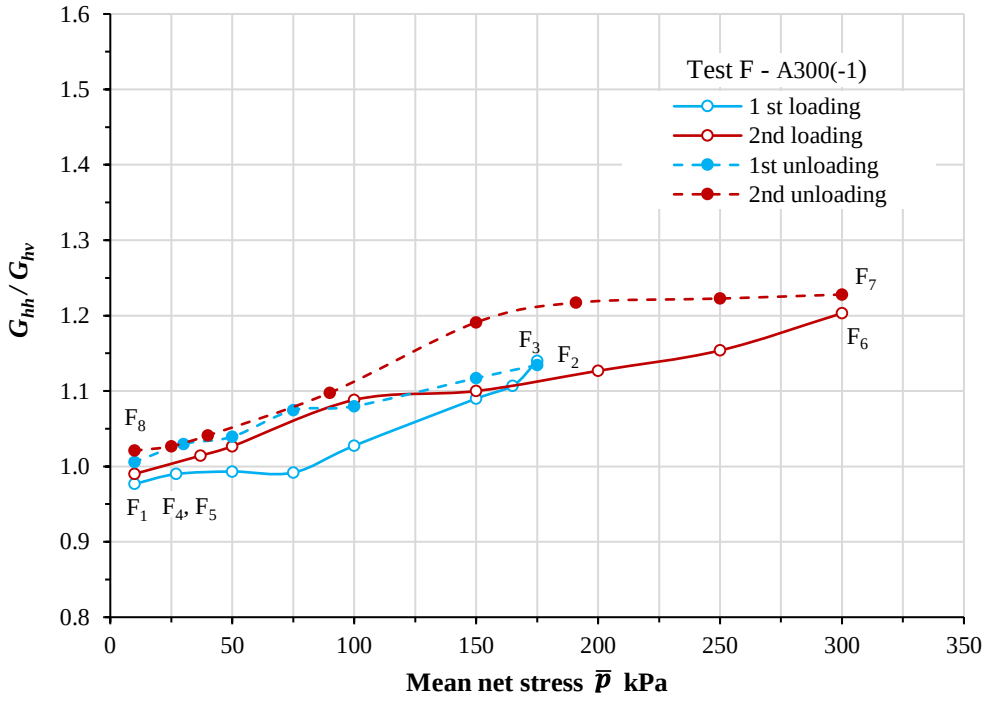

Figure 6.53: Variation of shear modulus ratio G_{hh}/G_{hv} in Test F

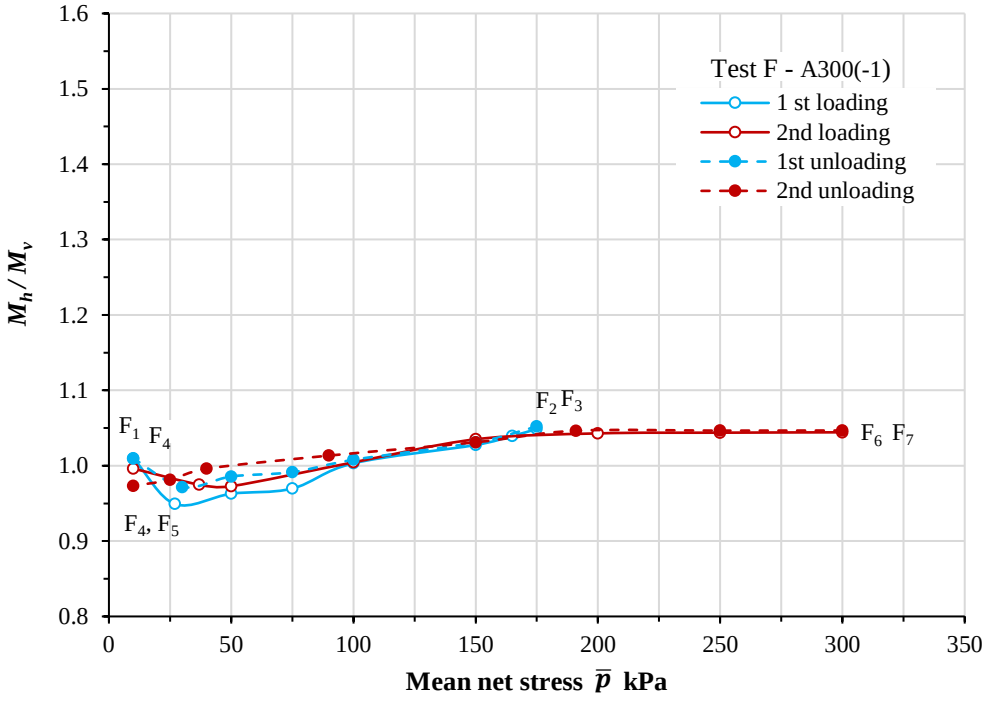

Figure 6.54: Variation of constrained modulus ratio M_h/M_v in Test F

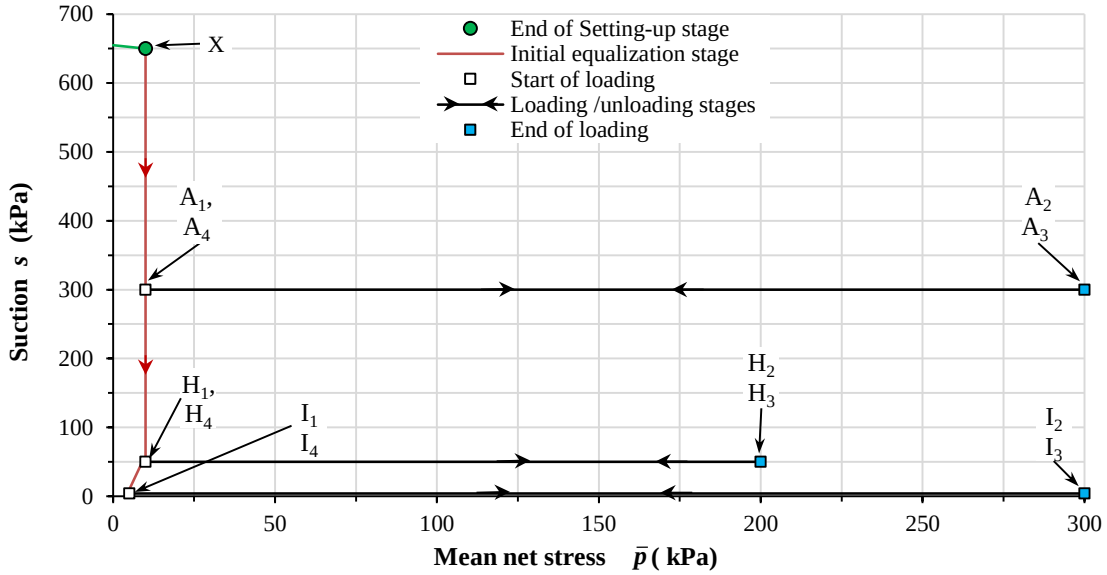

Figure 6.55: Stress paths for Tests A, H and I

6.8.1 Large strain behaviour

Figure 6.56 shows the variations of specific volume v, water content w and degree of saturation S_r in the loading and unloading stages of Tests A, H and I. The initial values of v for the three tests were significantly different, due to the different amount of wetting-induced swelling in the preceding equalisation stages, with wetting to a lower value of s producing a larger amount of swelling (see Section 6.2.1).

Inspection of Figure 6.56a shows that the yield value of $\bar{p}$ during isotropic loading at constant suction was greatest in Test A (s =300kPa) and least in Test I (saturated conditions). This fits with expected behaviour and the concept of a LC yield curve in the $s : \bar{p}$ plane (see Section 2.3.6).

Figure 6.56a also shows that the normal compression lines for the three different values of suction (the three post-yield compression curves) are in different locations. As expected, the normal compression line at the highest value of suction (s =300kPa in Test A) lies above the normal compression lines for the two lower values of suction (see Section 2.3.6). However, the normal compression line at s =50kPa (Test H) is slightly below the saturated normal compression line (Test I). This is explainable by the fact that the degree of saturation S_r was relatively high in Test H (see Figure 6.56c), reaching almost saturated conditions at the end of loading (S_r =0.961 at H_2). Under saturated (or almost saturated) conditions the relevant stress variable is $p' = \bar{p} - u_w = \bar{p} + s$, rather than $\bar{p}$. This means that if Tests H and I are compared at the same value of $\bar{p}$ (say $\bar{p}$ =200kPa), then the value of p' is 50kPa higher in Test H than in Test I (say p' =250kPa in Test H, compared to p' =200kPa in Test I) and hence, if both

samples were saturated, the value of v would be expected to be slightly lower in Test H than in Test I. This emphasises the problems that occur in attempting to interpret behaviour in terms of net stresses and suction if saturated conditions are approached at a non-zero value of suction. Use of Bishop's stresses avoids these problems, because Bishop's stresses tend naturally to saturated effective stresses as degree of saturation S_r approaches 1, even of the value of suction is not zero (see Section 2.3.4).

6.8.2 Wave velocities

Figure 6.57 shows the variations of shear wave velocities V_{shv} and V_{shh} for Tests A, H and I. Throughout loading and unloading stages, shear wave velocities were highest in Test A (at s =300kPa) and lowest in Test I (saturated conditions). This indicates that shear wave velocities were increased by increase of suction s or decrease of degree of saturation S_r, and this influence of s or S_r was sufficient to over-ride any influence of specific volume v on shear wave velocities (given that by the end of loading stage, the value of v was highest in Test A, which would suggest a low value of shear modulus G and hence shear wave velocity).

Figure 6.58 shows the variations of compression wave velocities V_{pv} and V_{ph} during Tests A, H and I. V_{pv} was not measured in Test I, because the base pedestal and top cap housing the vertical BEE pair had to be replaced with a conventional base pedestal and top cap, in order to saturate the sample (see Section 4.2.3). Also, values of horizontal compression wave velocity V_{ph} could not be determined during the early part of the loading stage of Test I because the received signal was very noisy.

Inspection of Figure 6.58 shows that values of compression wave velocities were very similar in Tests A and H at the start of loading (there were no equivalent measurements in Test I), but that during loading the compression wave velocities became very different in the three tests, with the highest value in Test I (saturated conditions) and the lowest value in Test A (s =300kPa). These substantial differences in compression wave velocities between the three tests remained throughout the subsequent unloading stages. The fact that compression wave velocities were highest in Test I and lowest in Test A is consistent with the crucial influence of degree of saturation S_r on compression wave velocity (through the strong influence of S_r on undrained bulk modulus K_u and hence on undrained constrained modulus M_u (see Equation 2.9) and thus on compression wave velocity (see Equation 2.2)). The fact that there were very large differences between Tests H and I in the values of V_{ph} at the end of loading and throughout subsequent unloading (see Figure 6.58b), even though the values of S_r were relatively similar (S_r above 0.95 in Test H, see Figure 6.56c, and S_r =1.00 in Test I)

illustrates the very large effect on compression wave velocity of changes of S_r between 0.95 and 1.00, as shown, for example, by Eseller-Bayat et al. (2013) (see Figure 2.32).

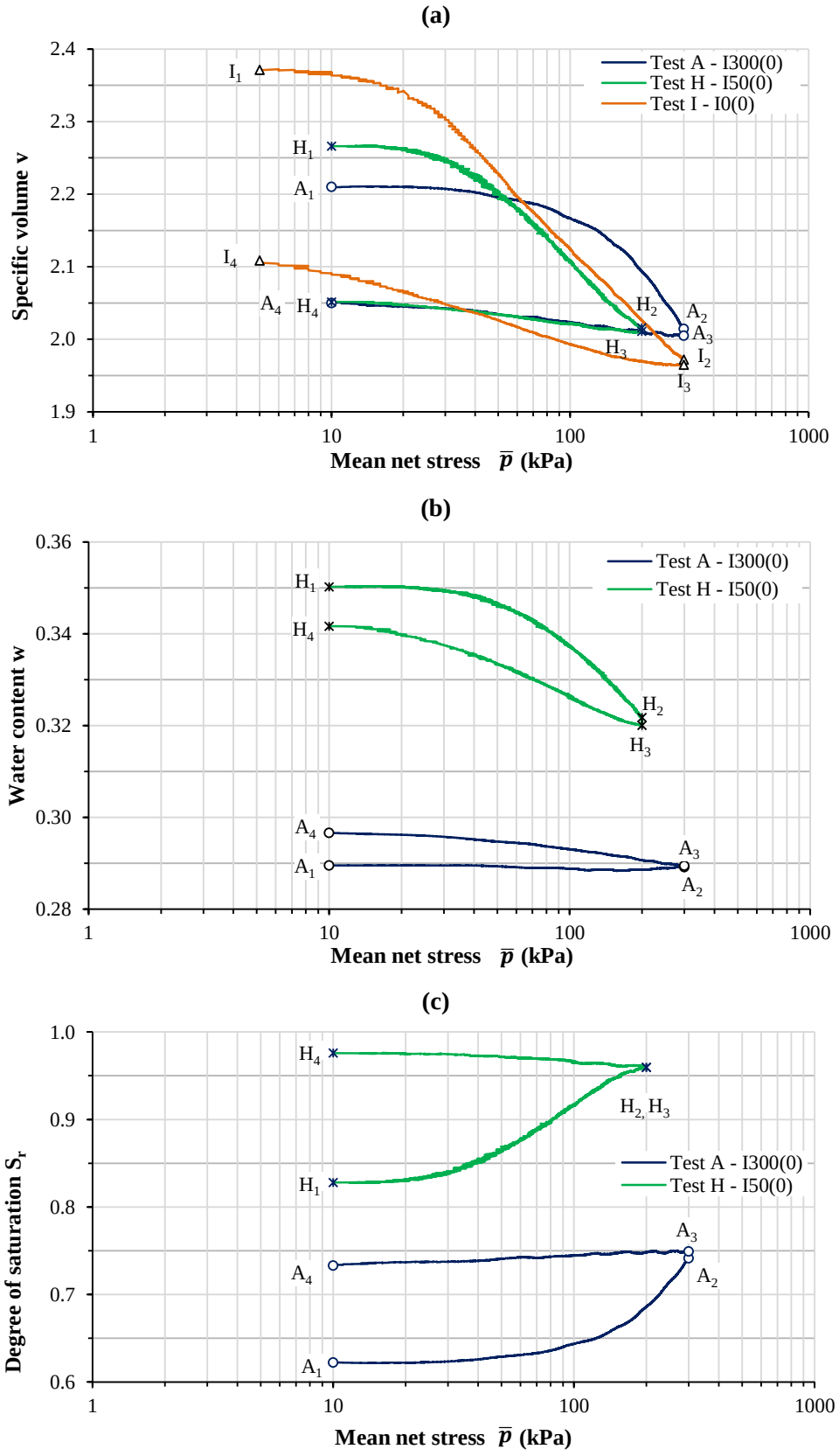

Figure 6.56: Variations of (a) specific volume v (b) water content w (c) degree of saturation S_r in Tests A, H and I

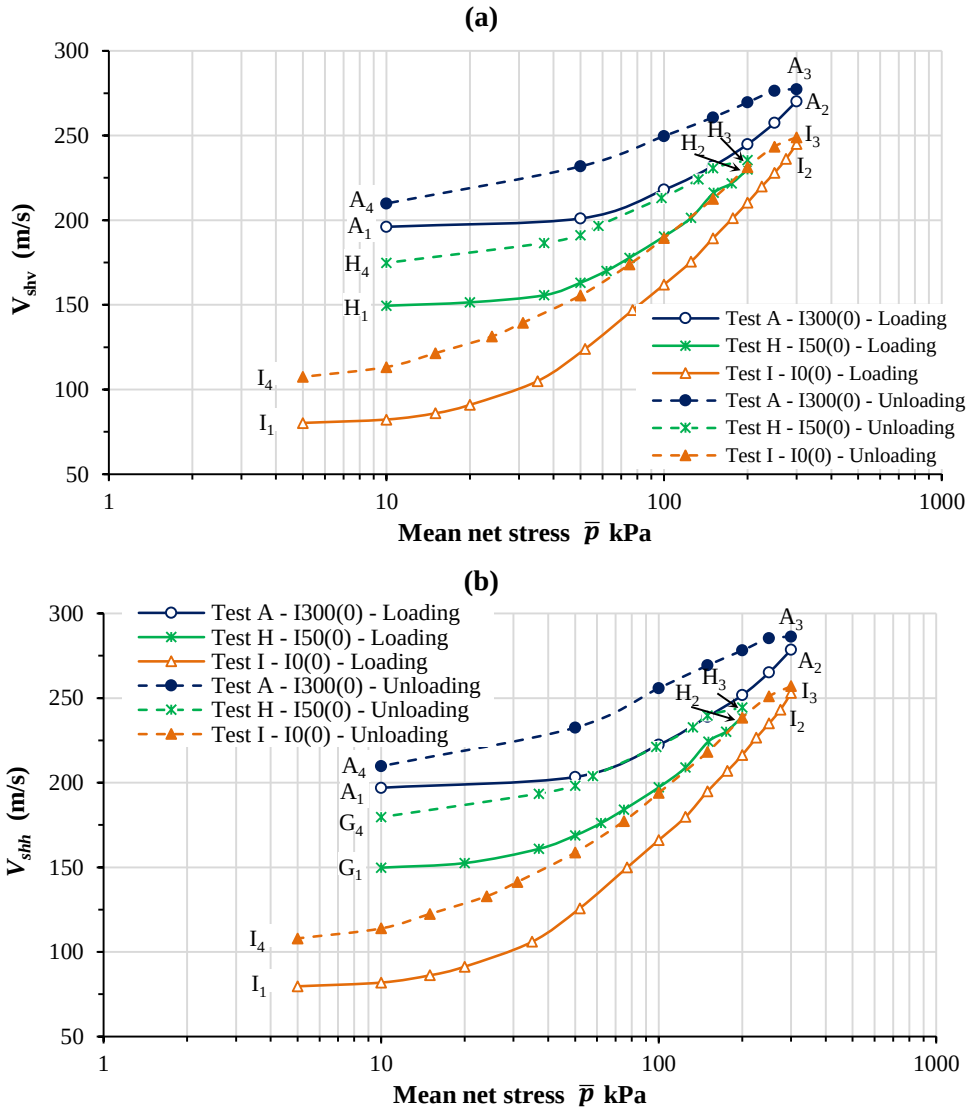

Figure 6.57: Variations of shear wave velocities in Tests A, H and I

6.9 Influence of wetting and drying

Comparison of Tests A, J and K provides information on the role of wetting and drying stages on both large strain behaviour and the very small strain behaviour explored by BEE testing. In particular, an objective in performing these tests was to investigate the separate influences of S_r and s on the variations of shear and compression wave velocities (in addition to the roles of $\bar{p}$ and v).

Figure 6.59 shows the stress paths followed in Tests A, J and K in th $s : \bar{p}$ plane. In all three tests, after mounting in the triaxial cell, a mean net stress of 10 kPa was applied (point X in Figure 6.59) and then samples were wetted to a suction of 300 kPa (points A_1, J_1 and K_1) (see Section 4.5.1).

Test A involved isotropic loading (A_1A_2) at constant suction (s =300kPa) to $\bar{p}$ =300kPa, followed by isotropic unloading (A_3A_4) to $\bar{p}$ =10kPa. Test J involved a wetting-drying cycle ($J_1J_2J_3$) at $\bar{p}$ =10kPa to a minimum suction of 50 kPa, followed by isotropic loading-unloading ($J_3J_4J_5J_6$) at s =300kPa. Finally, Test K involved isotropic loading (K_1K_2) at s =300kPa to $\bar{p}$ =100kPa, followed by a wetting-drying cycle ($K_3K_4K_5$) at $\bar{p}$ =100kPa to a minimum suction of 50 kPa and then isotropic loading and unloading ($K_5K_6K_7K_8$) at s =300kPa.

The purpose of the wetting-drying cycles in Tests J and K was to ensure that during subsequent isotropic loading and unloading the values of S_r were different for samples A, J and K (due to hysteresis in the water retention behaviour), even though the suction value was identical at 300 kPa in all three cases. For sample K the wetting-drying cycle was expected to produce collapse compression, whereas collapse compression was not expected in the wetting-drying cycle performed in Test J, so that the subsequent stages of Tests J and K were expected to be at different values of v.

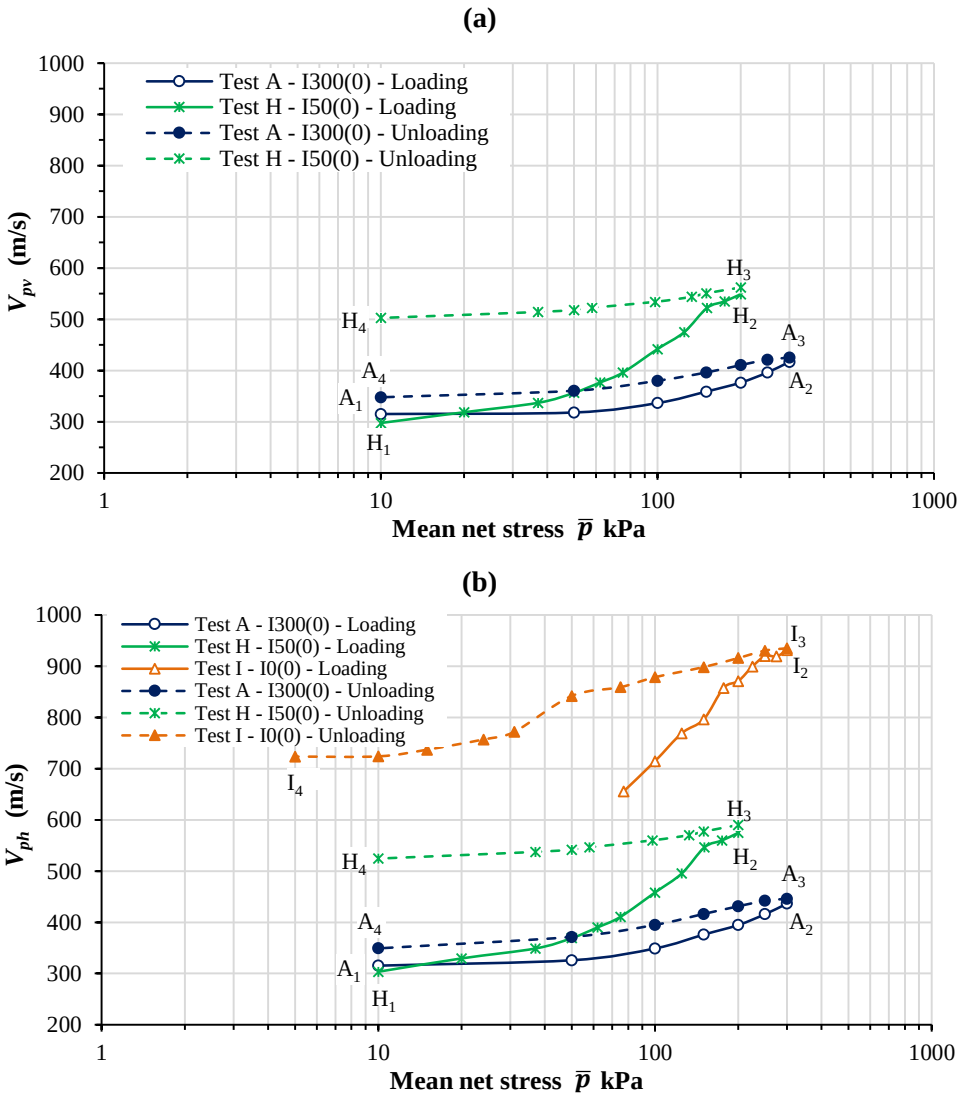

Figure 6.58: Variations of compression wave velocities in Tests A, H and I

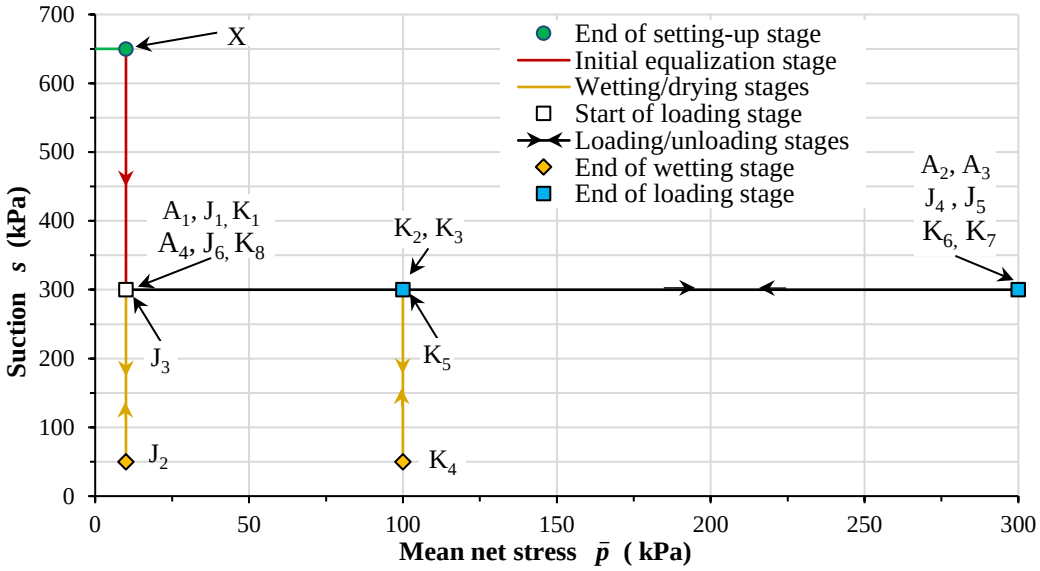

Figure 6.59: Stress paths for Tests A, J and K

6.9.1 Large strain behaviour

Figure 6.60 shows the variation of specific volume v , water content w and degree of saturation S_r for Tests A, J and K, during loading and unloading stages and wetting-drying cycles.

During Test J, swelling was observed during the wetting stage J_1J_2 (see Figure 6.60a), with no indication of any wetting-induced collapse compression. This was followed by shrinkage during the drying stage J_2J_3, with a net reduction of v over the wetting-drying cycle $J_1J_2J_3$. During the subsequent isotropic loading stage J_3J_4 the compression curve gradually converged with the curve from Test A, and during subsequent unloading J_5J_6 the variation of v was very similar to Test A.

For Test K, Figure 6.60a shows that the variation of v during the initial loading K_1K_2 was, as expected, almost identical to that from Test A. The subsequent wetting stage (K_3K_4) produced significant reduction of v (collapse compression), and this was followed by further shrinkage in the drying stage K_4K_5. The final isotropic loading (K_5K_6) and unloading (K_7K_8) stages produced irreversible compression, with the suggestion of yielding during loading. By the end of the loading stage (K_5K_6) the compression curve had not fully converged with the curves from Tests A and J, and the final value of v after unloading to K_8 was still significantly lower than in Tests A and J.

Figure 6.60c shows that the initial values of S_r for the three samples (at A_1, J_1 and K_1) were all very similar. In Test J there was significant net increase of S_r during the wetting-drying cycle $J_1J_2J_3$, as a consequence of hysteresis in the water retention

behaviour, so that the value of S_r at the start of the subsequent loading stage was higher than in Test A (compare J_3 and A_1 in Figure 6.60c). By the end of the loading stages (J_4 and A_2 in Figure 6.60c) the difference between the values of S_r in Tests J and A had reduced, and this difference in S_r then remained almost unchanged during the final unloading stages (A_3A_4 and J_5J_6).

In Test K the variation of S_r (see Fig 6.60c) during the first loading stage K_1K_2 was very similar to that in Test A, as expected. A large increase of S_r occurred during the wetting stage K_3K_4, with a smaller reduction of S_r during the subsequent drying stage K_4K_5, as a consequence of hysteresis in the water retention behaviour. Little further change of S_r occurred during the final loading stage K_5K_6 and unloading stage K_7K_8, and the value of S_r remained higher than in Tests A and J.

6.9.2 Wave velocities and elastic anisotropy

Figures 6.61 shows the variations of shear wave velocities V_{shv} and V_{shh} for all three samples A, J and K.

Inspection of Figure 6.61 shows that a significant decrease of V_s occurred during the wetting stage J_1J_2 of Test J. This decrease of V_s can be partially attributed to the increase of v during the wetting stage (Figure 6.60a), but this increase of v was relatively small and it is therefore likely that the combined decrease of s and increase of S_r (Figure 6.60c) during the wetting stage also contributed to the significant decrease of V_s. It is not, however, possible to separate the influences of the decrease of s and the increase of S_r. The value of V_s at the end of the drying stage J_2J_3 was higher than at the start of the wetting-drying cycle (compare J_3 and J_1 in Figure 6.61). This is consistent with the net reduction of v over the wetting-drying cycle (Figure 6.60a), but it is not clear whether the net increase of S_r over the wetting-drying cycle also contributed to the increase of V_s or partially offset the effect of the decrease in v.

During the isotropic loading stage J_3J_4 of Test J, values of V_s were initially slightly higher than in Test A, but by the end of the loading stage and during subsequent unloading J_5J_6 the values of V_s were very similar to those from Test A (see Figure 6.61). This pattern of behaviour is entirely consistent with the difference of v between Tests A and J at the start of loading and the gradual erasure of this difference as loading progressed (see Figure 6.60a). The fact that values of V_s were very similar during the unloading stages of Tests A and J, when values of v were very similar but values of S_r were significantly different (see Figure 6.60c), suggests that the change of S_r (at constant s) had relatively little influence on the value of V_s.

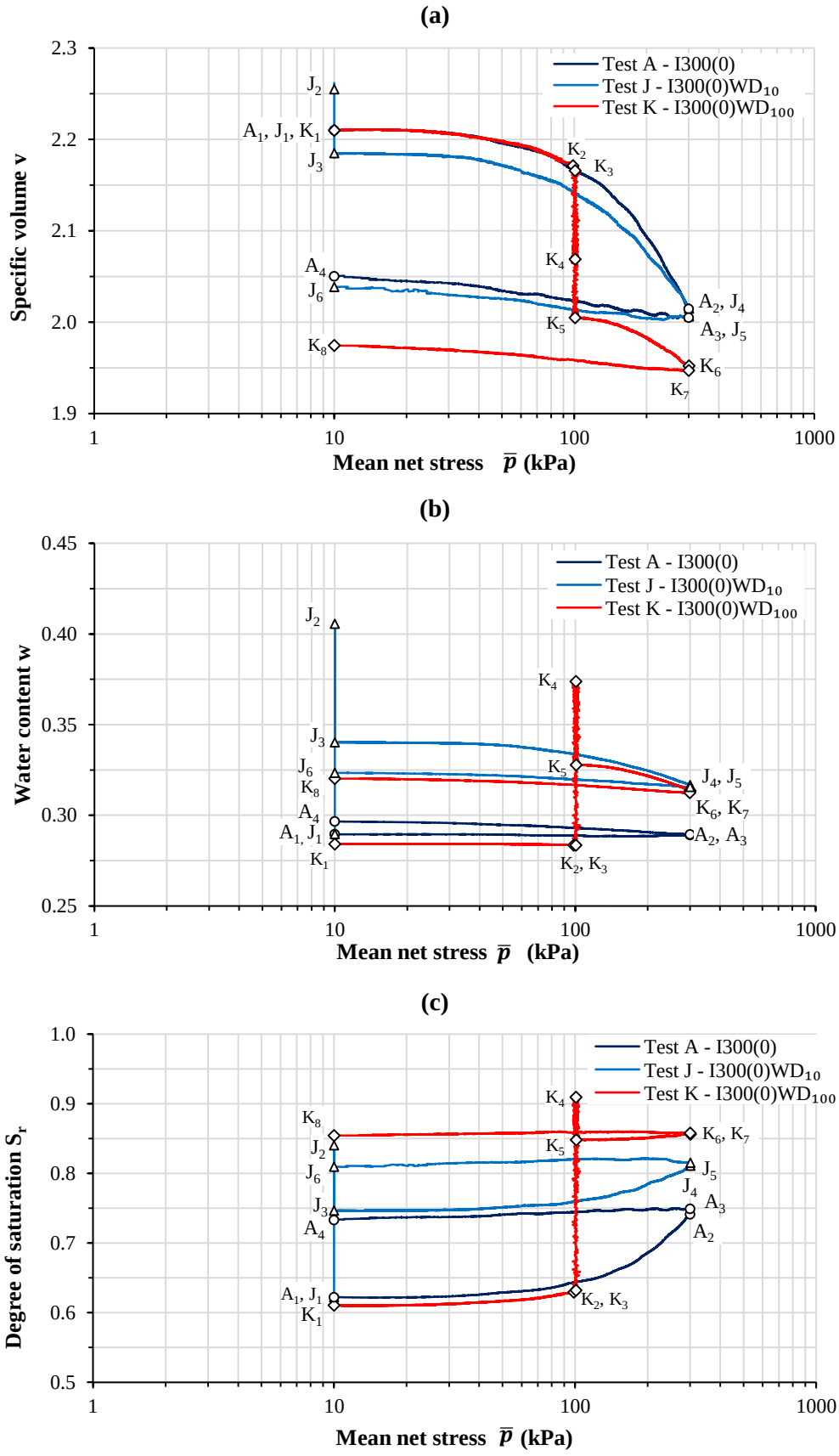

Figure 6.60: Variations of (a) specific volume v (b) water content w (c) degree of saturation S_r in Tests A, J and K

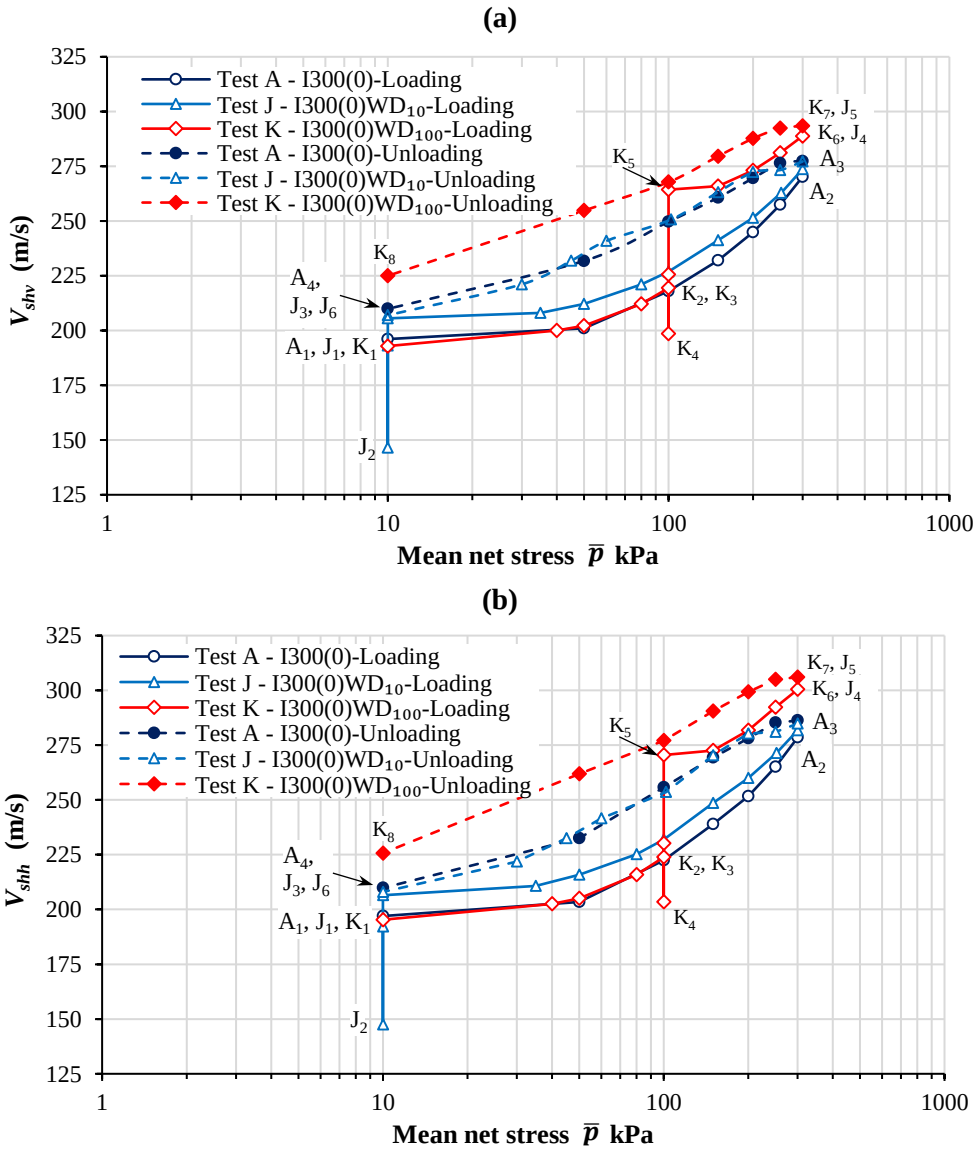

Figure 6.61: Variations of shear wave velocities in Tests A, J and K

A noteworthy point from Test J is that the value of V_s at the end of the loading-unloading cycle was very similar to the value measured at the beginning of the cycle (compare J_6 and J_3 in Figure 6.61), despite the fact that the value of v was substantially lower at the end of the cycle than at the beginning (see Figure 6.60a). This reduction of v would have been expected to produce a significant increase of V_s, so the fact that V_s was almost unchanged at the end of the loading-unloading cycle suggests that the influence of the decrease of v must have been offset by the influence of the increase of S_r between J_3 and J_6 (see Figure 6.61). This suggestion, that an increase of S_r (at constant s) could lead to a decrease of V_s , is contradictory to the suggestion arising from the comparison of Tests A and J, that an increase of S_r has little effect on V_s (see previous paragraph).

In Test K, the variation of V_s during the initial loading stage K_1K_2 was, as expected,

very similar to that observed in Test A (see Figure 6.61).

During the wetting stage K_3K_4 of Test K, there was a decrease in the value of V_s , suggesting that the combined influence of the decrease of s and increase of S_r (tending to produce a decrease of V_s) was stronger than the influence of the decrease of v (which would be expected to produce an increase of V_s). The drying stage K_4K_5 then produced a large increase of V_s , consistent with the fact that the decrease of v (Figure 6.60a) would be expected to produce an increase of V_s and so would the combined influence of the increase of s and the decrease of S_r (Figure 6.60c). The value of V_s at the end K_5 of the wetting-drying cycle was significantly greater than the value at the beginning K_2 (see Figure 6.61), consistent with the net decrease of v over the cycle, with the influence of the net increase of S_r (at constant s) being unclear.

At the end of the final isotropic unloading stage of Test K, the value of V_s was higher than in Tests A and J (compare K_8 with A_4 and J_6 in Figure 6.61). This is consistent with the lower final value of v in Test K (see Figure 6.60a), and it is unclear whether this was enhanced or partially offset by the higher value of S_r (see Figure 6.61).

Further contradictory evidence on the influence of a change of S_r (at constant s) on the value of V_s emerges from comparing other points within Test K with appropriate points in Tests A and J. For example, the value of V_s at K_5 is noticeably higher than at $\bar{p}$ =100kPa within unloading stages A_3A_4 and J_5J_6, and it seems unlikely that this can be attributed solely to a slightly lower value of v (see Figure 6.60a). This suggests that the higher value of S_r at K_5 (see Figure 6.61) may also have contributed to the higher value of V_s i.e. a suggestion that an increase of S_r (at constant s) leads to an increase of V_s, whereas previous suggestions were either that an increase of S_r (at constant s) has little effect on V_s or leads to a decrease of V_s.

Figure 6.62 shows the variation of compression wave velocity V_{pv} and V_{ph} for all three samples A, J and K. Inspection of Figure 6.62 suggests that increases of V_p are caused by increases of $\bar{p}$, decreases of v and increases of S_r, whereas the separate influence of a change of s (at constant S_r) is unclear. Note that a combined decrease of s and increase of S_r (wetting) produces an increase of V_p , whereas it produces a decrease of V_s.

Simple illustrations of the influences of v and S_r on compression wave velocity V_p are given by considering the wetting-drying cycles in Tests J and K. During the wetting stage J_1J_2 of Test J, there was a small decrease in the value of V_p , because the effect of the increase of v was partially offset by the effects of the increase of S_r. In the wetting stage K_3K_4 of Test K, there was a large increase of V_p , caused by a combination of the decrease of v and the increase of S_r. Further small increase of V_p occurred during the

subsequent drying stage K_4K_5 of Test K, suggesting that the influence of the decrease of v outweighed the influence of the decrease of S_r. In both Tests J and K there was significant net increase of V_p over the wetting-drying cycle $J_1J_2J_3$ and $K_3K_4K_5$), because of the net decrease of v and net increase of S_r over the cycle.

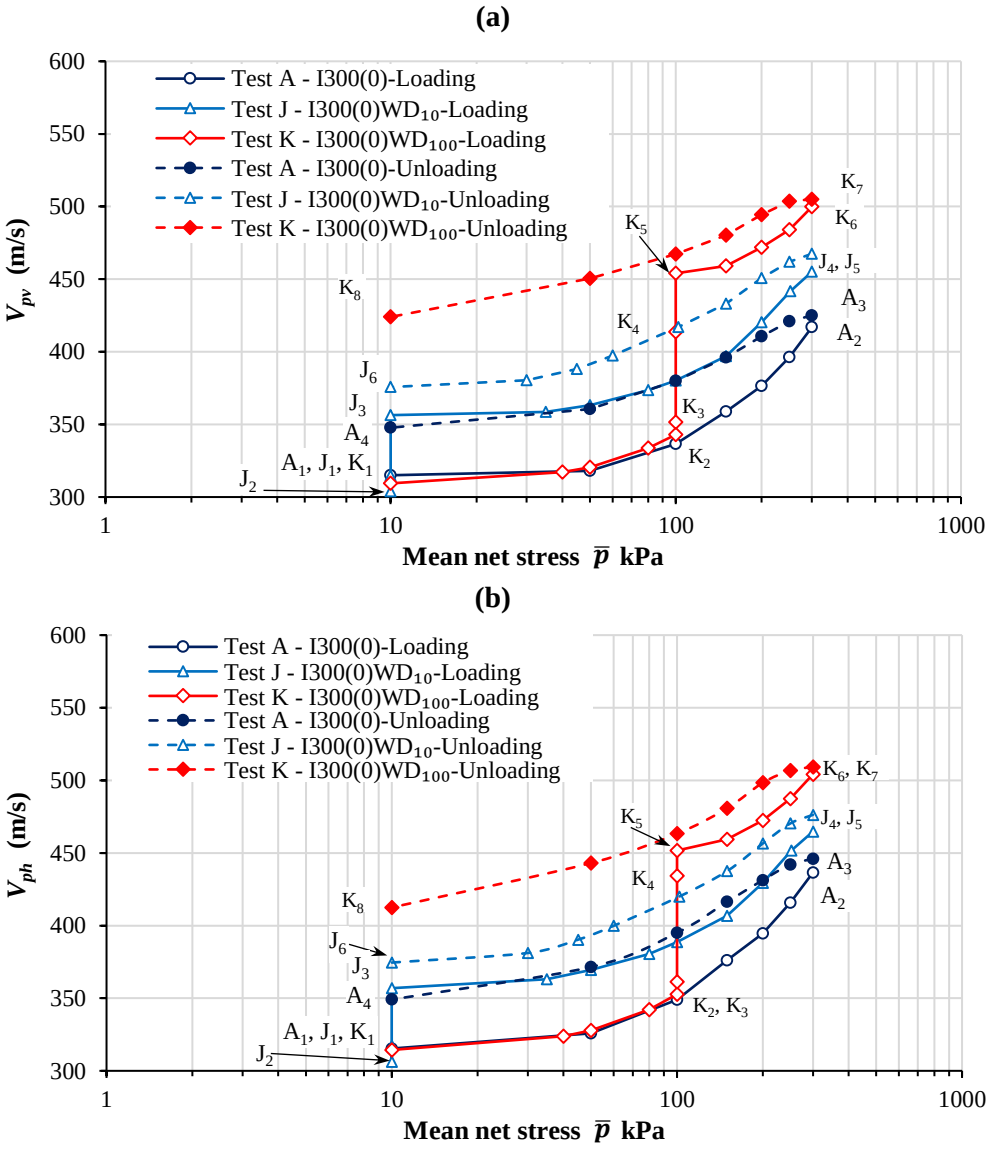

Figure 6.62: Variations of compression wave velocities in Tests A, J and K

It can be concluded from bender/extender element test results that, for a soil under unsaturated conditions and isotropic stress states, increases of shear wave velocity V_s are caused by increases of $\bar{p}$ and decreases of v. Combined increases of s and decreases of S_r during drying also lead to increases of V_s, whereas combined decreases of s and increases of S_r during wetting lead to decreases of V_s. The experimental evidence on the separate influences of s and S_r on V_s is, however, contradictory, so that it is unclear whether an increase of S_r at constant s leads to a decrease or increase of V_s or to no significant effect on V_s. The experimental results also suggest that increases of

compression wave velocity V_p are caused by increases of $\bar{p}$, decreases of v and increases of S_r , but the separate influence of a change of s (at constant S_r) is unclear.

Given the contradictory evidence on the separate influences of s and S_r on V_s, when interpreted in a framework employing $\bar{p}$, s, v and S_r as unsaturated state variables, it may be useful to examine whether interpretation in terms of alternative unsaturated stress state parameters (such as the mean Bishop's stress employed in the constitutive framework of Wheeler et al. (2003b)) would be advantageous. This might also mean that it would be easier to establish explicit expressions describing the variations of V_s and V_p (or G and M) with unsaturated state variables, if this alternative approach resulted in the formulation of expressions for V_s and V_p (or G and M) involving fewer variables. As a consequence, in Chapter 7 the variations of G and M are interpreted in terms of both conventional ($\bar{p}$, v, s and S_r) and alternative (p^*, v and S_r) unsaturated state variables.

Figure 6.63 shows the variations of G_{hh}/G_{hv} in Tests A, J and K, during wetting, drying, loading and unloading stages. Figure 6.63 shows only modest changes of the ratio G_{hh}/G_{hv} in all tests and the variations are approximately the same in all tests. As described in Section 6.4.3, behaviour would be expected to be isotropic throughout Tests A, J and K (G_{hh}/G_{hv} =1), because these were tests involving solely isotropic loading ($\eta \approx 0$) on isotropically compacted samples, so there was no reason for the soil to develop either stress -induced anisotropy or strain-induced anisotropy. As discussed in Section 6.4.3, it therefore seems likely that the small amount of anisotropy apparent in all of these tests in Figure 6.63 was probably due to experimental issues associated with sample non-uniformity (due to end-effects at the boundaries with the base pedestal and top cap).

Figure 6.64 shows the variations of M_h/M_v during Tests A, J and K. Again, isotropic behaviour (M_h/M_v =1) would be expected throughout, whereas the experimental results in Figure 6.64 show modest amounts of anisotropy, probably as a consequence of sample non-uniformity due to end effects. One feature that is apparent in Figure 6.64 is that, whereas values of M_h/M_v rise above 1 in Test A, the values of M_h/M_v remained at approximately 1 after the wetting-drying cycle of Test J or dropped back to approximately 1 after the wetting-drying cycle in Test K. It is unclear what, if any, significance should be read into this observation.

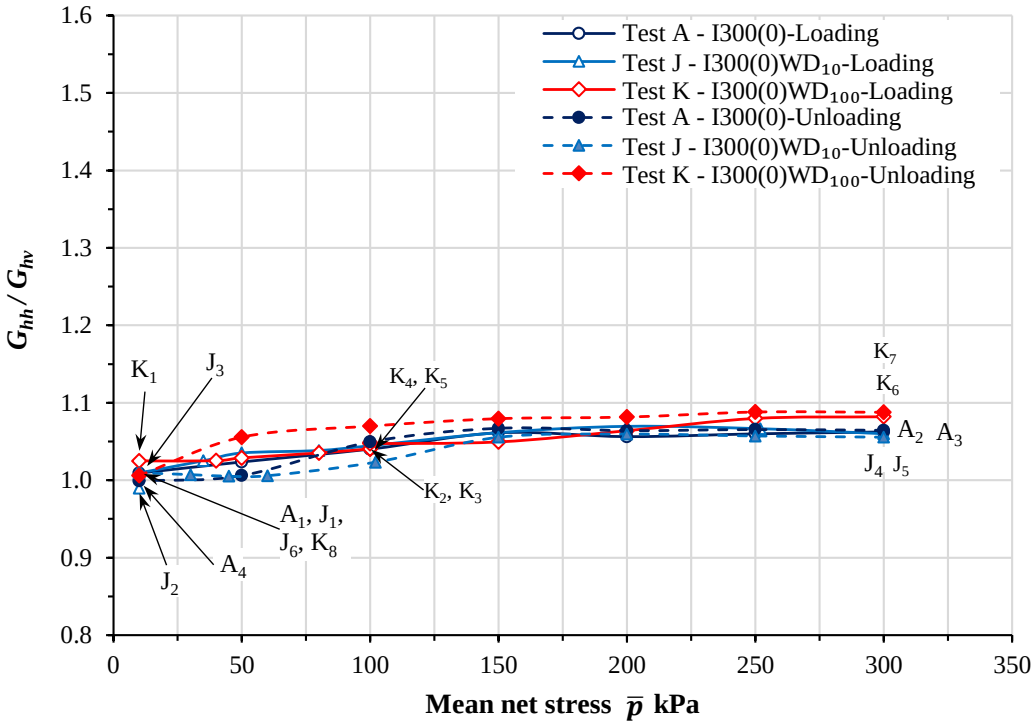

Figure 6.63: Variations of shear modulus ratio G_{hh}/G_{hv} in Tests A, J and K

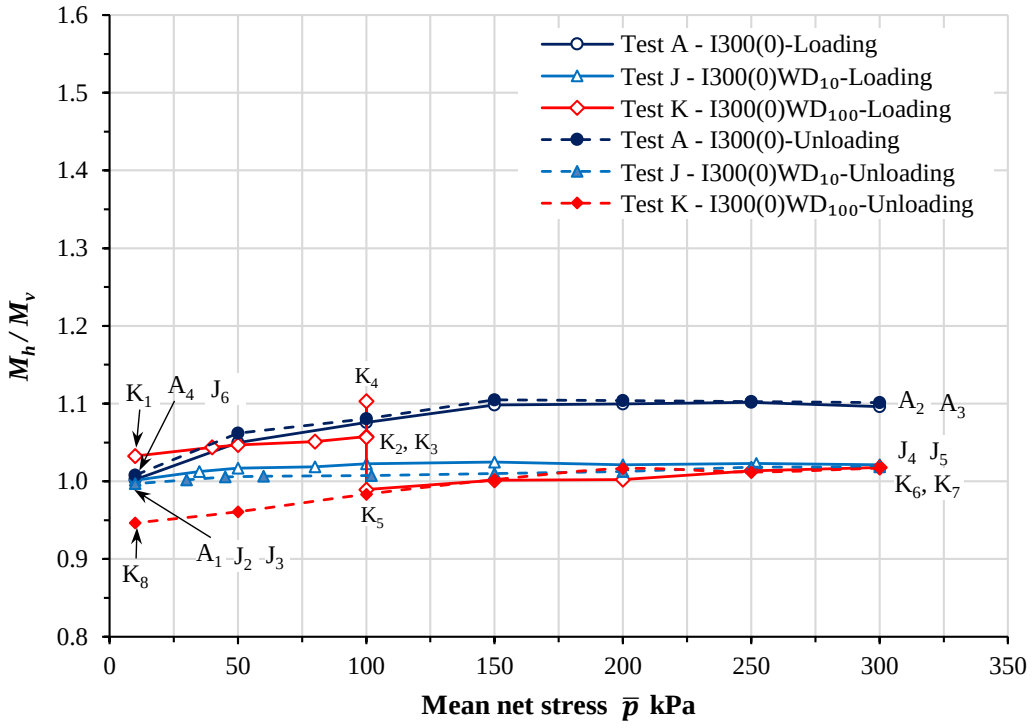

Figure 6.64: Variations of constrained modulus ratio M_h/M_v in Tests A, J and K

Chapter 7

Influence of unsaturated state variables on shear modulus G

In order to propose and validate expressions for elastic shear modulus G of the unsaturated compacted kaolin, under isotropic and anisotropic stress conditions, the experimental test results from Chapter 6 have been interpreted in terms of both conventional and alternative unsaturated state variables. The ability of the proposed expressions to match the experimental measurements of G was then compared with other proposed expressions in the literature.

In this chapter results from only isotropically compacted samples under isotropic and anisotropic stress states are investigated. It is assumed that anisotropic elastic behaviour of isotropically compacted samples was developed only due to stress-induced anisotropy and any role of strain-induced anisotropy of very small strain elastic behhaviour has been ignored. This assumption was based on the fact that experimental results on isotropically compacted samples (see, for example, Section 6.6) suggested that any development of anisotropy of very small strain elastic response during anisotropic stress paths was predominantly due to stress-induced anisotropy and the role of strain-induced anisotropy of small strain elastic behaviour was less significant. Interpretation of experimental results is limited to the isotropically compacted samples, to also remove the influence of any initial (intrinsic) strain-induced anisotropy.

7.1 Variation of G under isotropic stress states

5 experimental tests involved isotropic loading ($\eta \approx 0$) on isotropically compacted samples (Tests A, H, I, J and K) and results from these 5 tests were used to investigate

potential expressions for very small strain shear modulus G under isotropic stress states. Test I involved isotropic loading and unloading under saturated conditions (s =0), Test H involved isotropic loading and unloading under unsaturated conditions with s = 50kPa, and Tests A, J and K involved isotropic loading and unloading under unsaturated conditions with s = 300kPa. Tests J and K also involved a wetting-drying cycle (at $\bar{p}$ = 10kPa and $\bar{p}$ = 100kPa respectively).

Figure 7.1 shows the variations of v and S_r during Tests A, H, I, J and K (both plotted against $\bar{p}$, with $\bar{p}$ on a logarithmic scale). Figures 7.2 and 7.3 show the corresponding measurements of shear moduli G_{hv} and G_{hh}, calculated from the corresponding shear wave velocities V_{shv} and V_{shh} and the bulk density ρ of the soil (see Equation 2.1). The variations of G_{hv} and G_{hh} shown in Figures 7.2 and 7.3 follow very similar patterns to the corresponding variations of V_{shv} and V_{shh}, which were fully discussed in Chapter 6 (see Sections 6.8 and 6.9).

Comparison of Figures 7.2 and 7.3 shows that values of G_{hv} and G_{hh} were always very similar for these isotropically compacted soil samples loaded to isotropic stress states (as expected). Therefore, throughout the remainder of Section 7.1, experimental values of shear modulus G were simply taken as the average of G_{hv} and G_{hh}.

7.1.1 Interpretation in terms of $\bar{p}$, v, s and S_r

Ng and Yung (2008) proposed Equation 2.87 for the shear modulus of a soil under unsaturated conditions, as a function of $\bar{p}$, s and void ratio e. Based on experience for saturated soils (see Section 2.2.2), it seems logical to assume that the function $f(e)$ in Equation 2.87 takes the form of a power function of v, (rather than the power function of e proposed by Ng & Yung, 2008), so that Equation 2.87 becomes:

$$G = Cv^{-m}\left(\frac{\bar{p}}{p_r}\right)^n\left(\frac{s+p_r}{p_r}\right)^k \tag{7.1}$$

where C, m, n and k are soil constants. p_r is a reference pressure and the use of $s+p_r$ (rather than simply s) as the numerator of the last part of Equation 7.1 was to allow the expression to be used down to s =0 (saturated conditions). Ng and Yung (2008) suggested using p_r=1kPa, however this was entirely arbitrary and a different choice of p_r would result in different predictions from Equation 7.1. This is clearly a weakness of Equation 7.1.

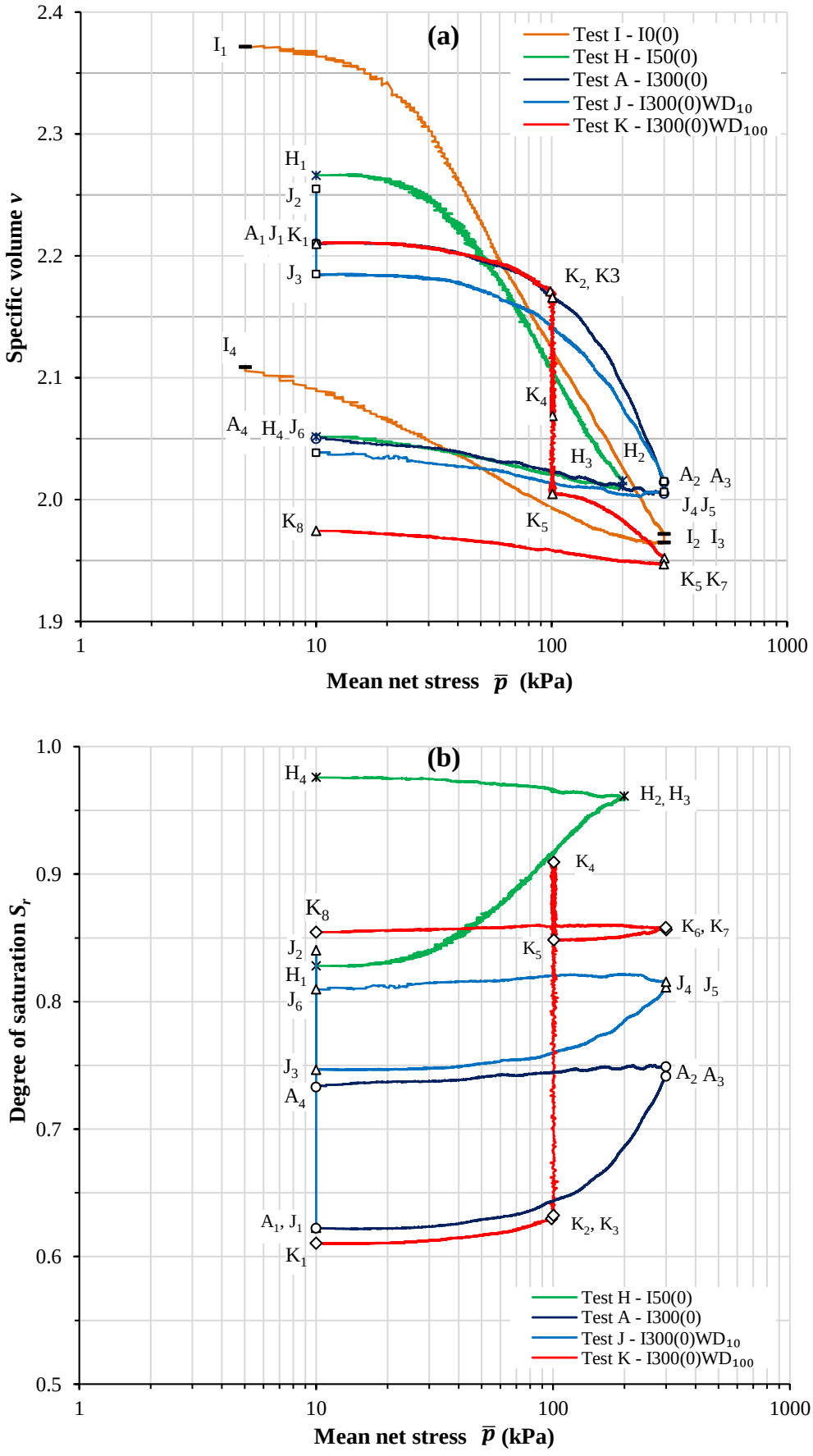

Figure 7.1: Variation of specific volume v and degree of saturation S_r in Tests A, H, I, J and K

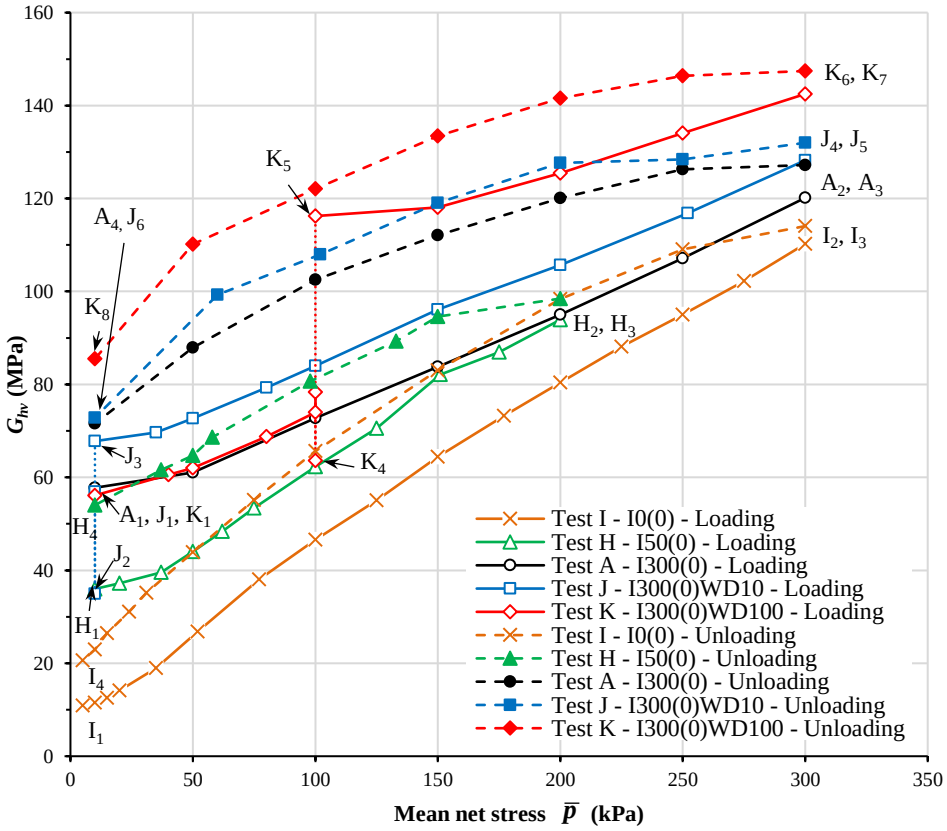

Figure 7.2: Variation of G_{hv} in Tests A, H, I, J and K

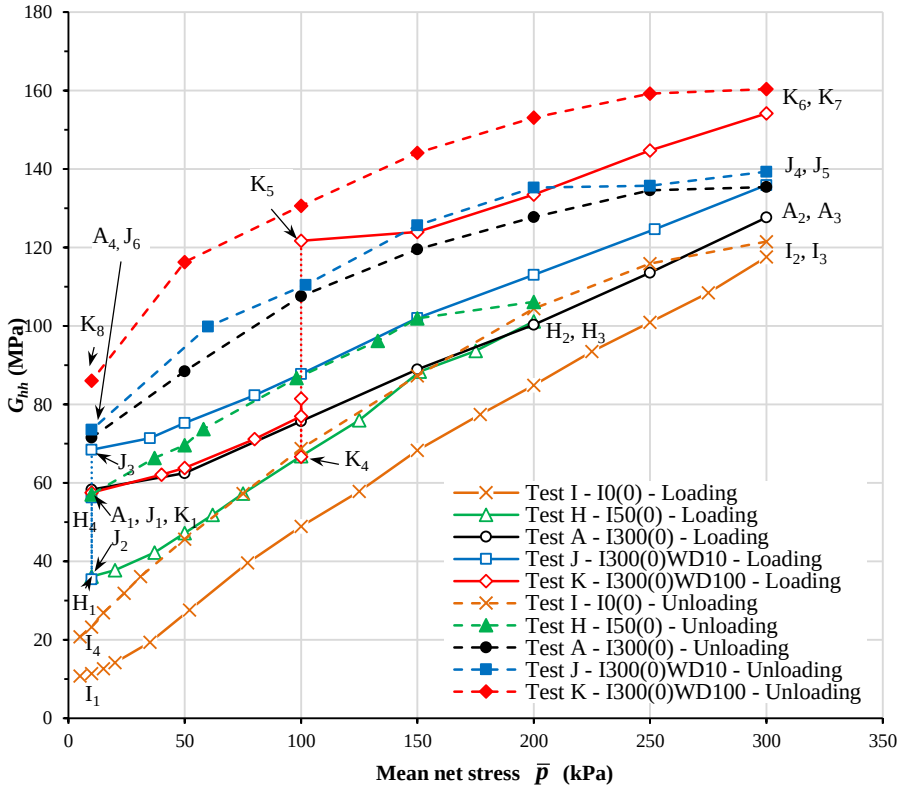

Figure 7.3: Variation of G_{hh} in Tests A, H, I, J and K

A multi-variate regression analysis was performed, using all experimental values of G from Tests A, H, I, J and K to determine best-fit values of the soil constants C, m, n and k in Equation 7.1, using a value of reference pressure p_r=100kPa. This regression analysis was performed using the multi-variate non-linear regression tool within the IBM Statistical Package for the Social Sciences version 22 software (IBM, 2013). The regression analysis software varies the equation coefficients (C, m, n and k in the case of Equation 7.1) to find a set of values that minimises the sum of the squares of the errors between predicted and measured values of the dependent variable (G in the case of Equation 7.1). To do this, the user must specify initial trial values of all coefficients. It is important to repeat the regression analysis with a number of different sets of initial trial values of coefficients, to confirm that the analysis has robustly identified the "global minimum" of the sum of the squares of the errors corresponding to the best-fit between predicted and measured values.

The regression analysis provided the following best-fit values for the soil constants in Equation 7.1 (using p_r =100kPa): C =2747MPa, m =5.12, n =0.16, k =0.26. The corresponding value for the coefficient of determination R^2 was 0.9611.

Equation 7.1 does not include dependency on degree of saturation S_r (separately from suction s). To explore whether the inclusion of S_r as an additional independent variable would significantly improve the fit between predicted and measured vales of G, an alternative expression to Equation 7.1 was also investigated:

$$G = Cv^{-m}\left(\frac{\bar{p}}{p_r}\right)^{n}\left(\frac{s+p_r}{p_r}\right)^{k} S_r^{x} \tag{7.2}$$

The choice of a power function of S_r for the final part of Equation 7.2 was essentially arbitrary, chosen simply to match the power forms of the dependencies on v, $\bar{p}$ and $s + p_r$.

The regression analysis using all experimental vales of G from Tests A, H, I, J and K and p_r =100kPa, gave the following best-fit values for the soil constants in Equation 7.2: C =3115MPa, m =5.28, n =0.15, k =0.25, $x = -0.08$. The corresponding value of R^2 was 0.9612. Inclusion of S_r as an additional independent variable (at least in the form of a power function) had therefore produced negligible improvement in the fit between predicted and measured values of G (increasing R^2 only from 0.9611 to 0.9612, with the value of the exponent of S_r very close to zero ($x = -0.08$)). It was therefore concluded that there was no merit to using Equation 7.2 over Equation 7.1. Of course, it is possible that including the influence of S_r through an alternative expression other

than simply by multiplication by a power function of S_r, would have shown greater improvement.

The results from the regression analysis using Equation 7.1 were somewhat surprising, in that the best-fit value of the soil constant n (n =0.16) was much lower than the range of values of n typically suggested for saturated soils (see Section 2.2.2). The regression analysis was repeated, but with the value of n enforced at n =0.5 (as suggested for saturated soils, by for example, Oztoprak & Bolton, 2013), but this resulted in a significantly worse fit between predicted and measured vales of G (R^2 =0.179). The fact that the best-fit value of n for Tests A, H, I, J and K (one saturated test and four unsaturated tests) was so different to the value of n =0.5 generally employed for saturated conditions suggests that Equation 7.1 will struggle to successfully match experimental values of G under both saturated and unsaturated conditions.

Figure 7.4 shows the predicted variations of G for Tests I, H, A, J and K from Equation 7.1, using p_r =100kPa and the corresponding best-fit values of soil constants (C =2747MPa, m =5.12, n =0.16, k =0.26), plotted against $\bar{p}$, together with the corresponding experimental values of G. Figure 7.5 shows the corresponding comparisons of predicted and experimental values of G for the wetting-drying cycles in Tests J and K, plotted against s.

Inspection of Figure 7.4 shows that Equation 7.1 provides a good match between predicted and experimental values of G during loading and unloading stages performed under unsaturated conditions at either s =50kPa (Test H in Figure 7.4b) or s =300kPa (Tests A, J and K in Figures 7.4c, 7.4d and 7.4e). However, the fit is less good for loading and unloading stages under saturated conditions (Test I in Figure 7.4a).

In addition, inspection of Figure 7.5 shows that the fit between the predicted and measured variations of G is also less good during wetting and drying stages. In Test J (Figure 7.5a), with the wetting-drying cycle performed at $\bar{p}$ =10kPa, Equation 7.1 provides a reasonable prediction of the observed decrease of G during the wetting stage J_1J_2, but it significantly underpredicts the greater increase of G during the subsequent drying stage J_2J_3 (incorrectly predicting only a very small net increase of G over the wetting-drying cycle). In Test K (Figure 7.5b), with the wetting-drying cycle performed at $\bar{p}$ =100kPa, Equation 7.1 incorrectly predicts that G remains almost constant during the wetting stage K_3K_4 (whereas a noticeable decrease of G is actually observed), although it does give a reasonable prediction of the net increase of G observed over the wetting-drying cycle.

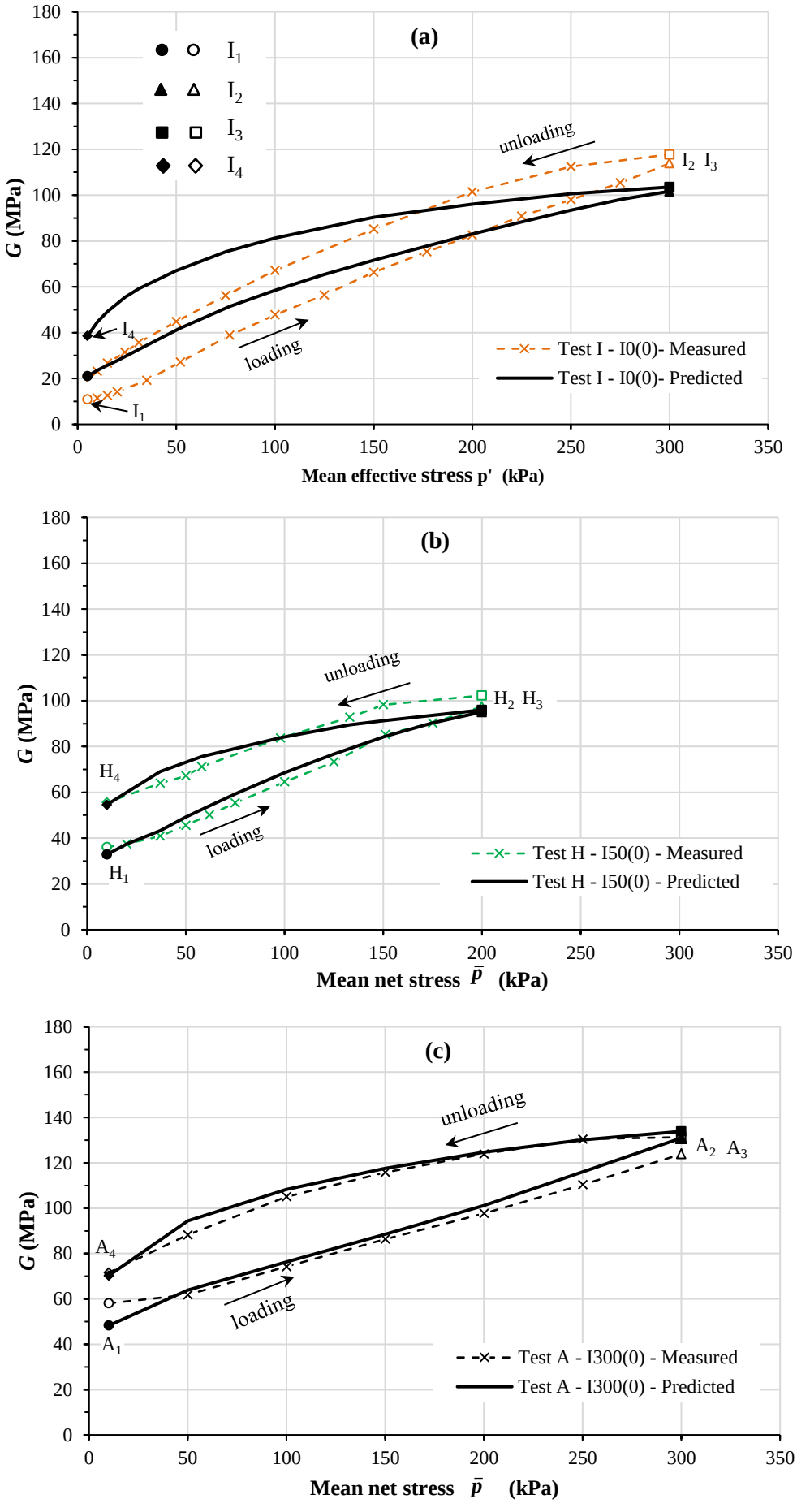

Figure 7.4: Continued.....

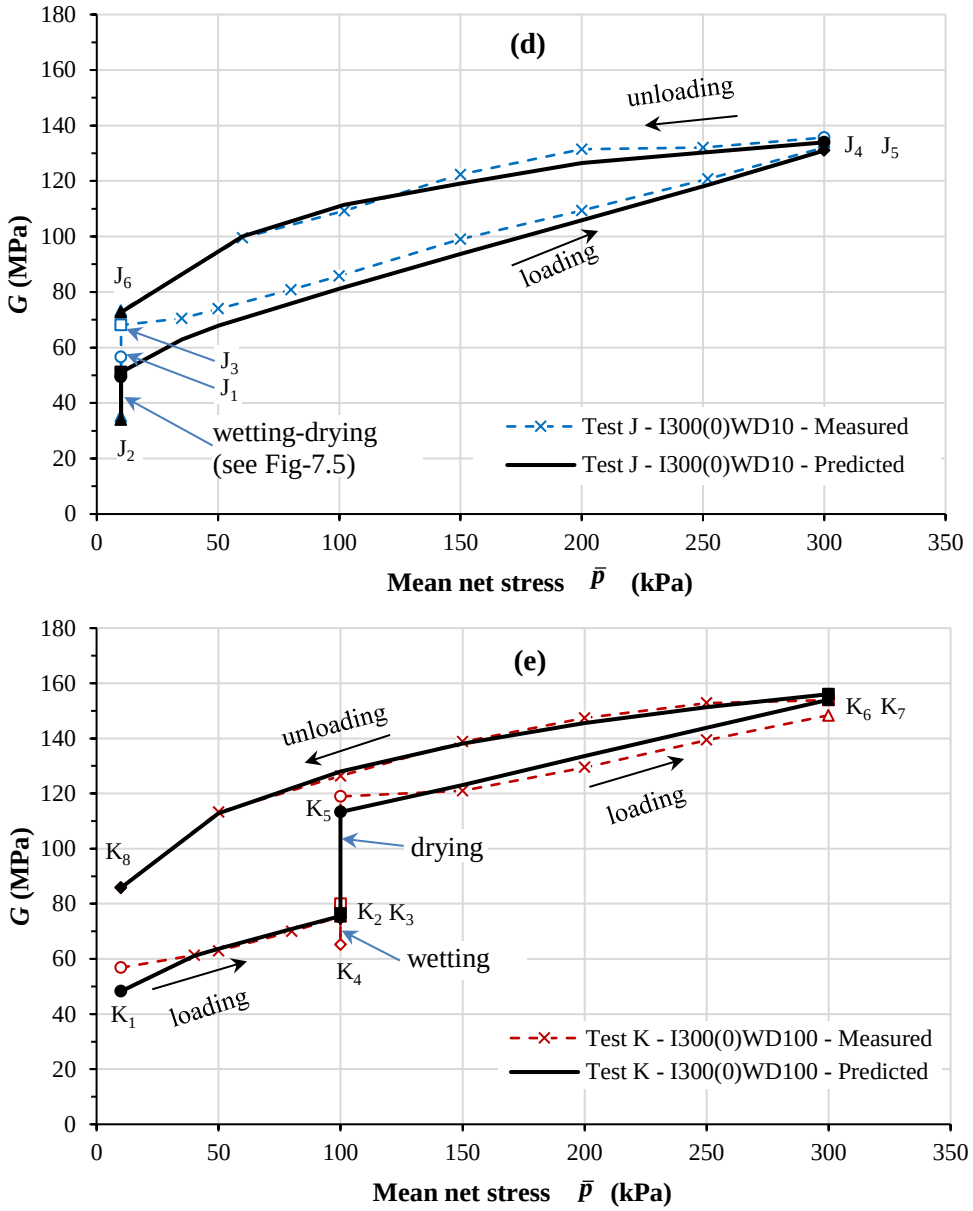

Figure 7.4: Measured and predicted (Eq.7.1) variation of G with of $\bar{p}$ for (a) Test I (b) Test H (c) Test A (d) Test J and (e) Test K

In order to investigate the influence of choosing different values of reference pressure p_r on the ability of Equation 7.1 to accurately represent observed variations of G, the regression analysis on the experimental results of Tests A, H, I, J and K was repeated, but using a value of reference pressure of p_r =1kPa, as recommended by Ng & Yung (2008), instead of p_r =100kPa. New versions of Figures 7.4 and 7.5 were then plotted, using the new values of soil constants in Equation 7.1 (determined from the new regression analysis). The results showed that there was a slight deterioration of the prediction of G, with reduction of R^2 from 0.961 (using p_r =100kPa) to 0.945 (using p_r =1kPa).

7.1.2 Interpretation in terms of p^* and v

Several authors (e.g. Wheeler et al., 2003b; Khalili et al., 2008; and Nuth & Laloui, 2008) have argued that, whereas yielding and plastic behaviour under unsaturated conditions depends upon two independent stress state variables, elastic behaviour under unsaturated conditions can be related to a single (tensorial) stress state variable, such as the Bishop's stress tensor (see Equation 2.75). This raises the possibility that, for isotropic behaviour, the variables governing the value of very small strain elastic shear modulus G need include only a single stress variable, the mean Bishop's stress p^* (defined in Equation 2.77), rather than two separate stress state variables of mean net stress $\bar{p}$ and suction s.

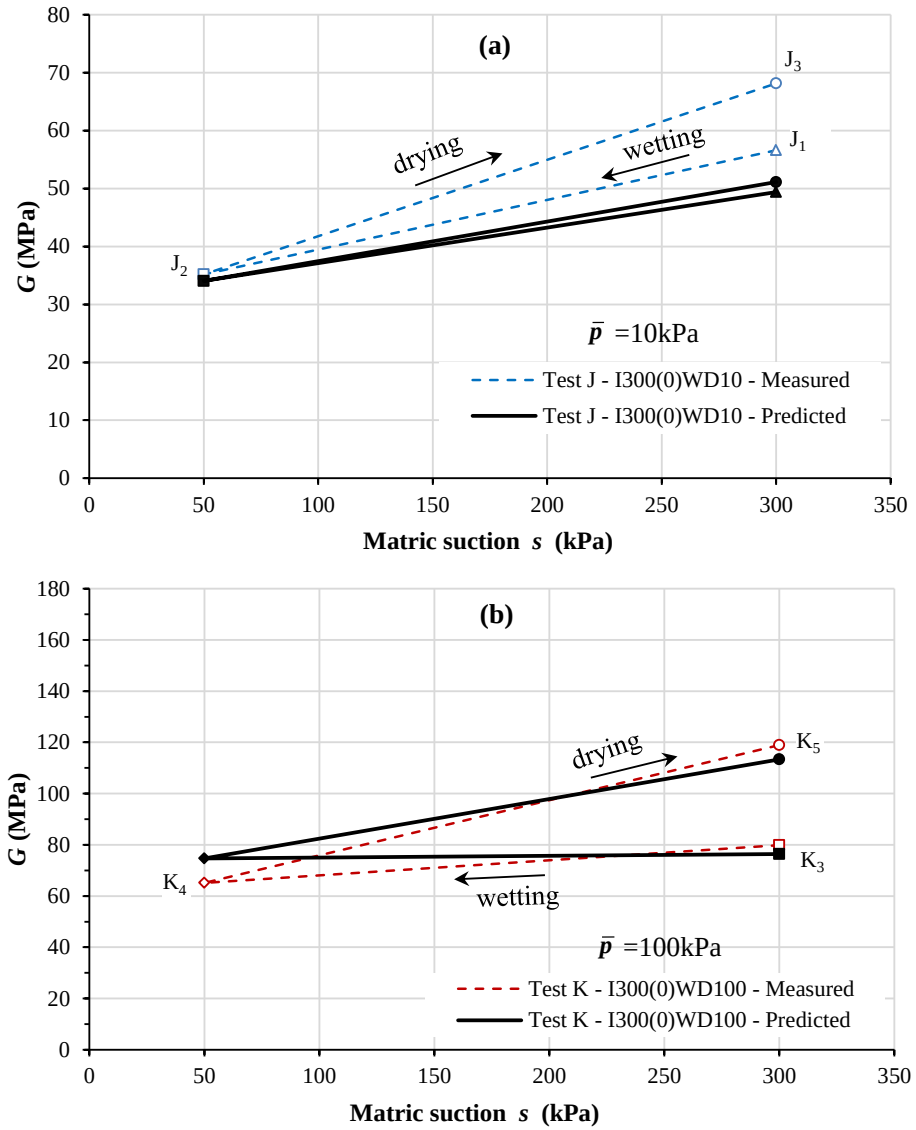

Figure 7.5: Measured and predicted (Eq.7.1) variation of G with s during wetting-drying cycles (a) Test J at $\bar{p}$ =10kPa (b) Test K at $\bar{p}$ =100kPa

The proposal is, therefore, that by analogy with saturated soils (see Equation 2.17),

very small strain elastic shear modulus of an isotropic soil under unsaturated conditions can be expressed as a function of only p^* and void ratio e:

$$G = f(e, p^*) \tag{7.3}$$

The experimental results from Tests A, H, I, J and K were re-interpreted in terms of Equation 7.3. To illustrate the variation of p^* during a typical test including loading and unloading stages and also wetting and drying stages, Figure 7.6 shows the stress path of Test K plotted in the $s : p^*$ plane. Note that p^* reduced during the wetting stage K_3K_4 and increased during the subsequent drying stage K_4K_5, with a net increase of p^* over the wetting-drying cycle (because of the net increase of S_r).

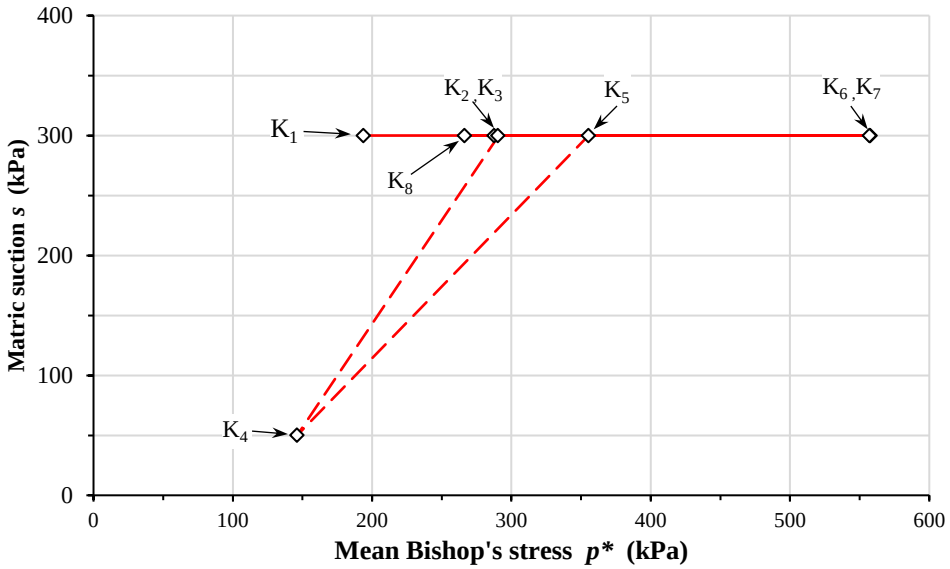

Figure 7.6: Stress path for Test K in $p^* : s$ plane.

Figure 7.7 shows the experimental measurements of G (taken as the average of G_{hv} and G_{hh}) from Tests A, H, I, J and K plotted in three-dimensional $p^* : v : G$ space. The experimental data seem to define a unique surface in this three-dimensional space, consistent with the proposal of Equation 7.3.

Inspection of Equation 2.17 for saturated conditions, suggests the following specific mathematical form for the relationship linking G, v and p^*:

$$G = Cv^{-m}\left(\frac{p^*}{p_r}\right)^n \tag{7.4}$$

where C, m and n are soil constants and p_r is a reference pressure.

Regression analysis to the data of Tests A, H, I, J and K, using p_r =100kPa, gave the following best-fit values for the soil constants in Equation 7.4: C =1356MPa, m =4.32, n =0.41, with R^2 =0.974. Encouragingly, the best-fit value of n (n =0.41) was within the range of values typically suggested in the equivalent expression for saturated soils (see Section 2.2.2). Some authors (e.g. Oztoprak & Bolton, 2013) suggest always using n =0.5 in the equivalent expression for saturated soils. The regression analysis was therefore repeated with the value of n enforced as 0.5, so that Equation 7.4 became:

$$G = Cv^{-m}\left(\frac{p^*}{p_r}\right)^{0.5} \tag{7.5}$$

This gave the following modified best-fit values for the soil constants C and m: C =636MPa, m =3.37, with R^2 =0.699. Note that enforcing n =0.5 had resulted in some deterioration in the fit between predicted and measured value of G (with R^2 reducing from 0.974 to 0.699).

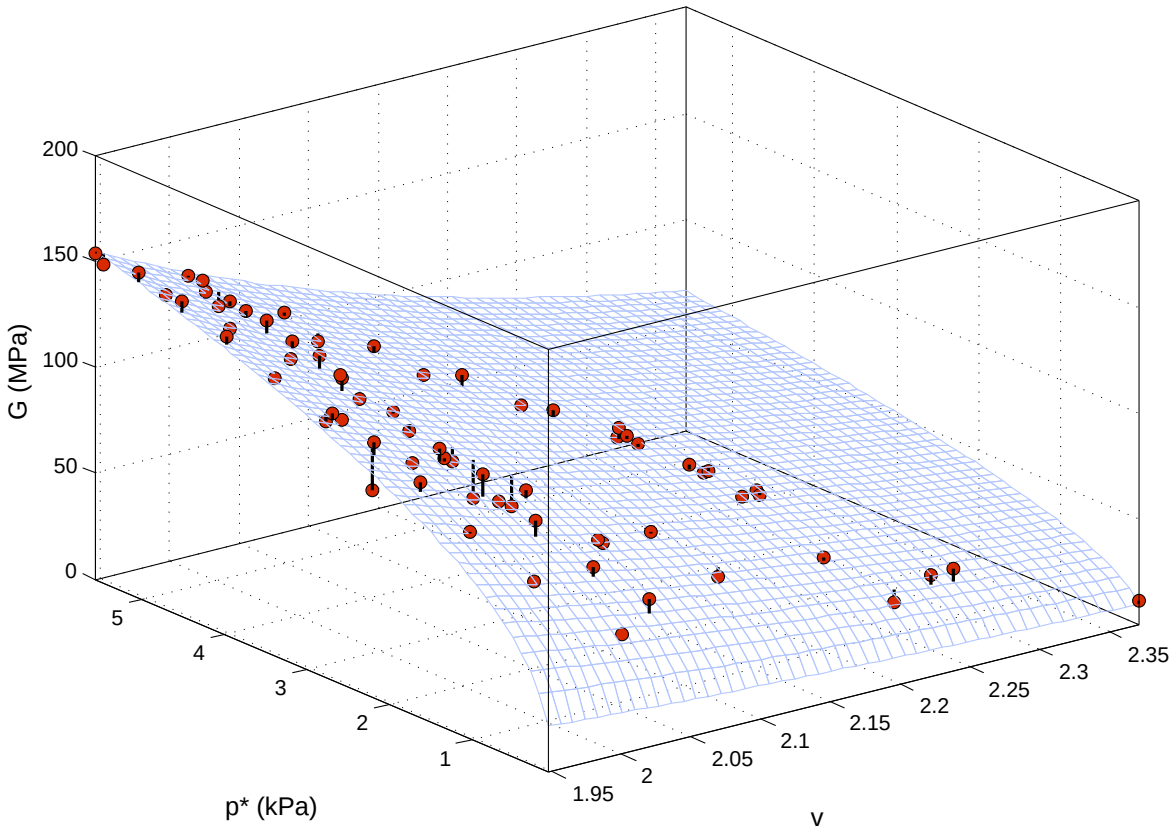

Figure 7.7: Variation of G in $p^* : v : G$ space for Tests A, H, I, J and K

Figure 7.8 shows the predicted variations of G for Tests A, H, I, J and K from Equa-

tion 7.4, using p_r =100kPa, C =1356MPa, m =4.32 and n =0.41, plotted against p^*, together with the corresponding experimental values of G. Figure 7.9 shows the corresponding comparisons of predicted and experimental values of G for the wetting-drying cycles of Tests J and K, plotted against s. Figure 7.8 shows that Equation 7.4 provides a reasonable match to loading-unloading stages performed under saturated conditions at s =0 (Test I, in Figure 7.8a), under unsaturated conditions at s =50kPa (Test H, in Figure 7.8b) and under unsaturated conditions at s =300kPa (Tests A, J and K, in Figures 7.8c, 7.8d and 7.8e). Probably, the most significant mis-matches occur at the end of unloading stages performed at s =300kPa, when Equation 7.4 consistently under-predicts the very large reduction of G observed in the very last part of the unloading stage (see Figures 7.8c, 7.8d and 7.8e). Figure 7.9 shows that Equation 7.4 provides an excellent match to the variation of G observed during wetting and drying stages.

It is very encouraging to see that Equation 7.4, which involves only a single stress state variable, the mean Bishop's stress p^*, is capable of providing a good match to the experimentally observed variation of elastic shear modulus G under unsaturated and saturated conditions. Wheeler et al (2003b) suggested that elastic behaviour is governed by Bishop's stresses only (see Section 2.3.8), and the results presented here provide the first experimental confirmation of this proposal.

Figures 7.10 and 7.11 show the predicted variations of G for the Tests A, H, I, J and K from Equation 7.5 (i.e. with the value of n enforced at 0.5), together with the corresponding experimental values of G. Comparison of Figures 7.10 and 7.11 with Figures 7.8 and 7.9 shows that the deterioration in the fit between predicted and measured values of G produced by enforcing $n = 0.5$ appears relatively small, despite the significant reduction in the value of R^2 (from R^2=0.974 to R^2=0.699).

7.1.3 Comparison between the two alternative approaches

In order to compare between Equation 7.1 (where G is expressed as a function of $\bar{p}$, s and v) and Equation 7.4 (where G is expressed as a function of p^* and v), Figures 7.12 and 7.13 show the predictions of both expressions plotted together for Tests A, H, I, J and K, together with the corresponding experimental values of G. Figure 7.12 shows results for all 5 tests plotted against $\bar{p}$, whereas Figure 7.13 shows results for the wetting-drying stages of Tests J and K plotted against s.

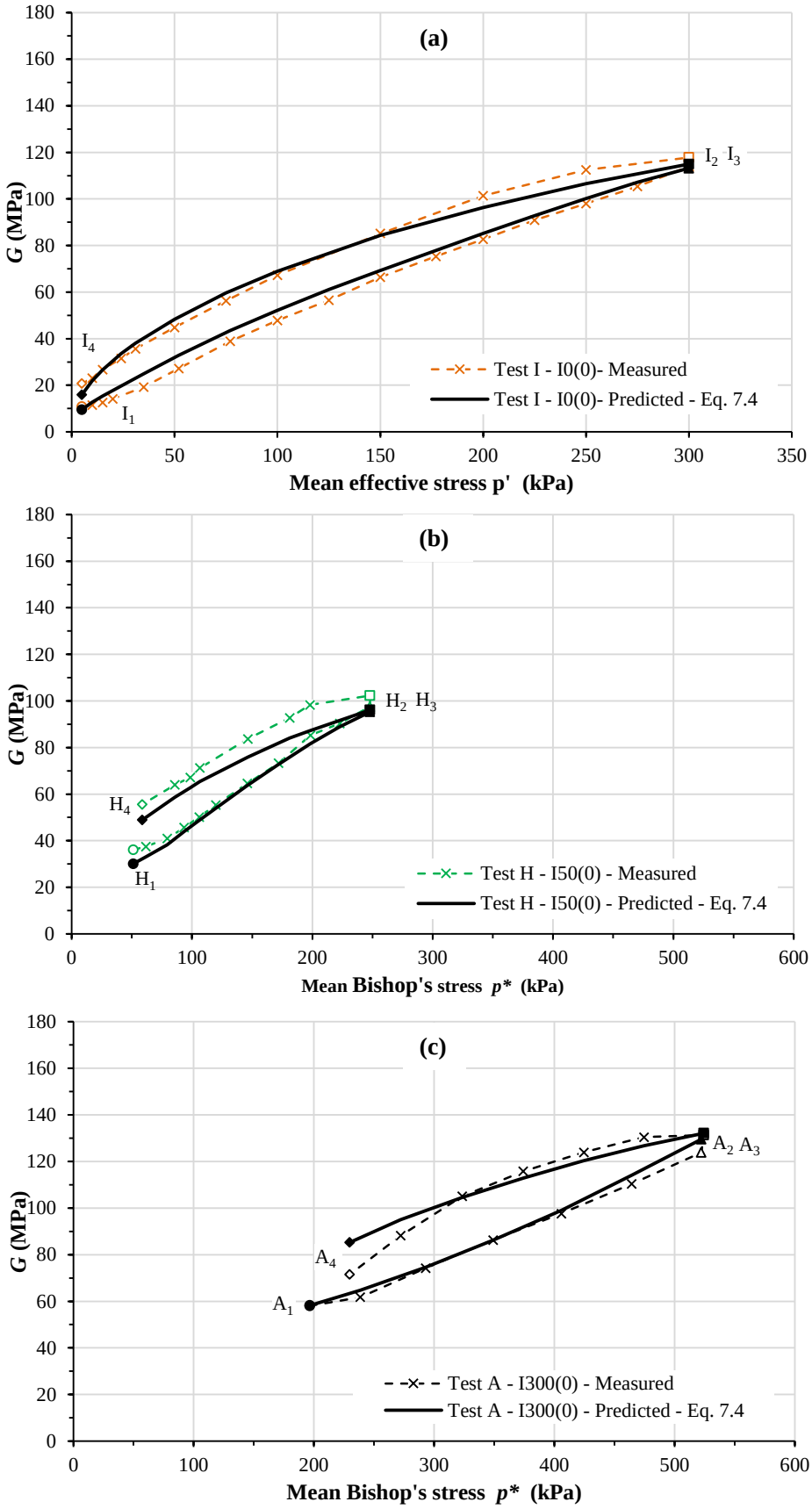

Figure 7.8: Continued.....

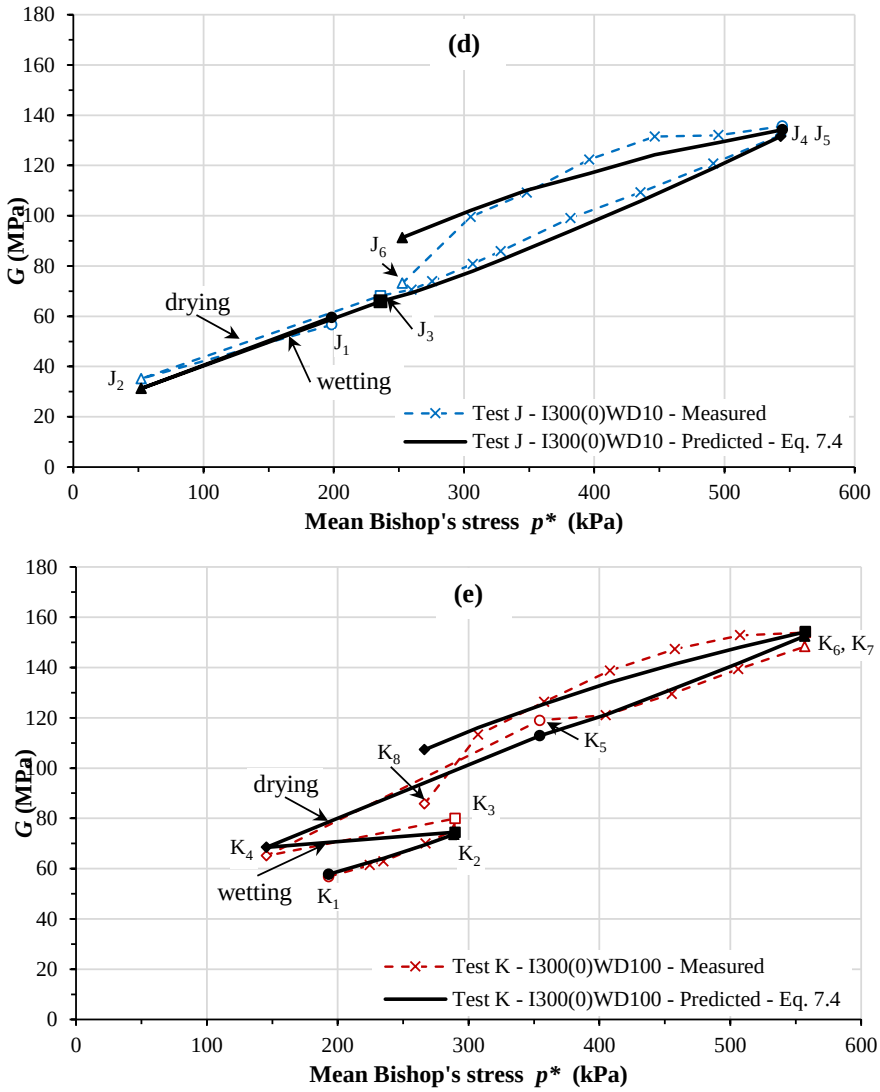

Figure 7.8: Measured and predicted (Eq.7.4) variation of G with p^* for (a) Test I (b) Test H (c) Test A (d),(e) Test J and (e) Test K

Figure 7.12a shows that Equation 7.4 (employing p^* and v) does significantly better than Equation 7.1 (employing $\bar{p}$, s and v) in matching the experimental results for loading and unloading stages performed under saturated conditions. Figure 7.12b shows, however, that Equation 7.1 does marginally better than Equation 7.4 in matching experimental results for loading and unloading stages performed under unsaturated conditions at s =50kPa. Inspection of Figures 7.12c, 7.12d and 7.12e shows that the two expressions provide similar qualities of fit to the experimental results for loading and unloading stages performed under unsaturated conditions at s =300kPa. For loading stages performed at s =300kPa, Equation 7.1 generally provides a worse fit than Equation 7.4 to the value of G at the start of the loading stage (see A_1, J_3, and K_1 in Figures 7.12c, 7.12d and 7.12e respectively). This is because Equation 7.1 provides a relatively poor representation of the variations of G during the preceding equalization or wetting stages (see next paragraph). In contrast, for unloading stages

performed at s =300kPa), Equation 7.4 generally provides a worse fit than Equation 7.1 to the value of G at the end of the unloading stages (see A_4, J_6, and K_8 in Figures 7.12c, 7.12d and 7.12e respectively). This is because Equation 7.4 fails to capture the very large reduction of G observed in the very last part of the unloading stage of each of these tests. The reason that Equation 7.1 predicts a much bigger drop in G in the last part of unloading than Equation 7.4 (fitting better to the experimental results) is that the percentage reduction of $\bar{p}$ during this last part of unloading (as $\bar{p}$ reduces to only 10kPa) is much larger than the percentage reduction of p^*.

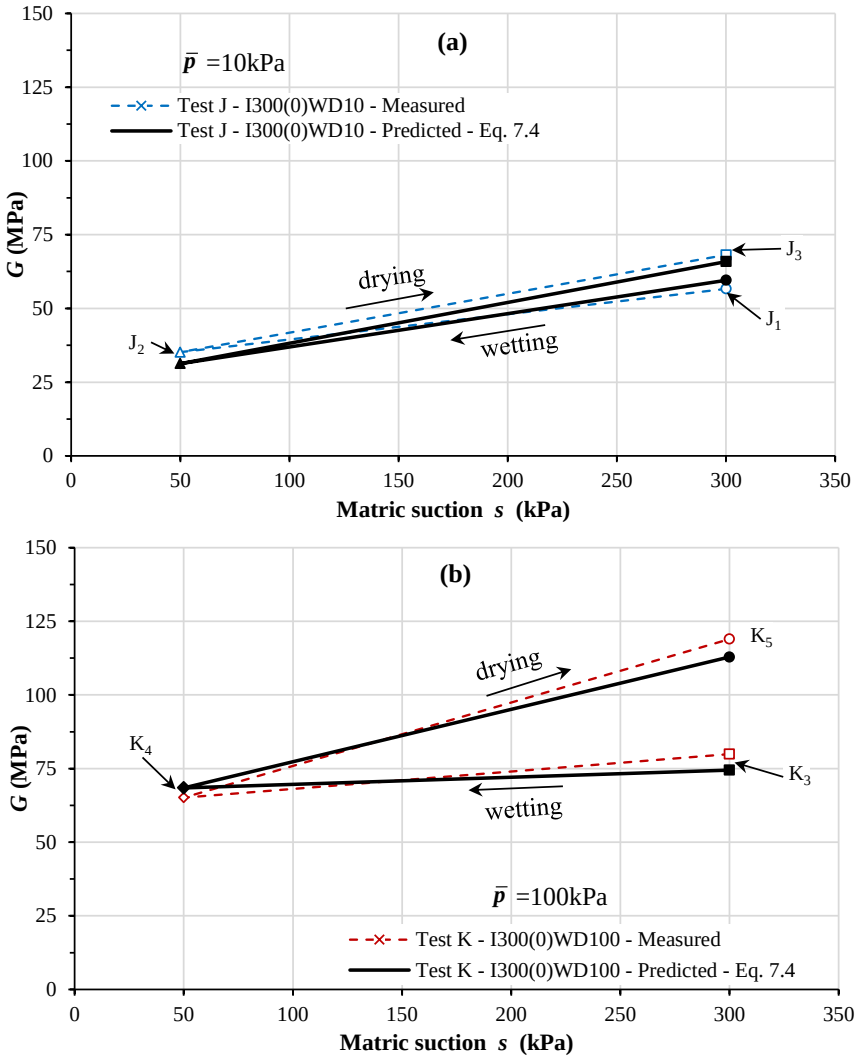

Figure 7.9: Measured and predicted (Eq.7.4) variation of G with s during wetting-drying cycles (a) Test J at $\bar{p}$ =10kPa (b) Test K at $\bar{p}$ =100kPa

Figure 7.13 shows that Equation 7.4 does significantly better than Equation 7.1 in predicting the observed variations of G during wetting and drying stages.

Inspection of Figure 7.13 shows that Equation 7.4 (employing p^* and v) provides a significantly better match than Equation 7.1 (employing $\bar{p}$, s and v) to the experimentally

observed variations of G during the wetting-drying cycles of Tests J and K.

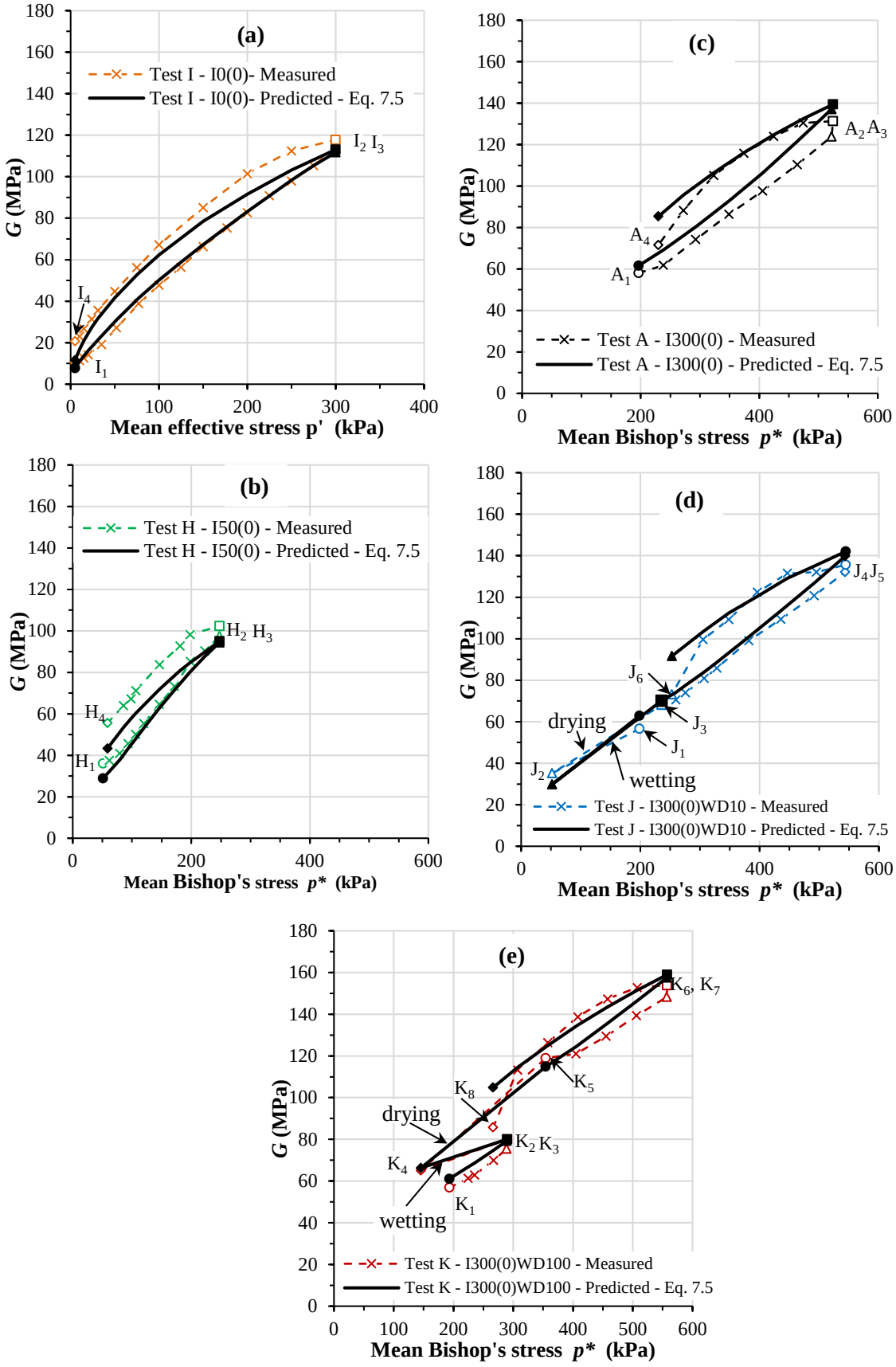

Figure 7.10: Measured and predicted (Eq.7.5) variation of G with p^* for (a) Test I (b) Test H (c) Test A (d),(e) Test J and (e) Test K

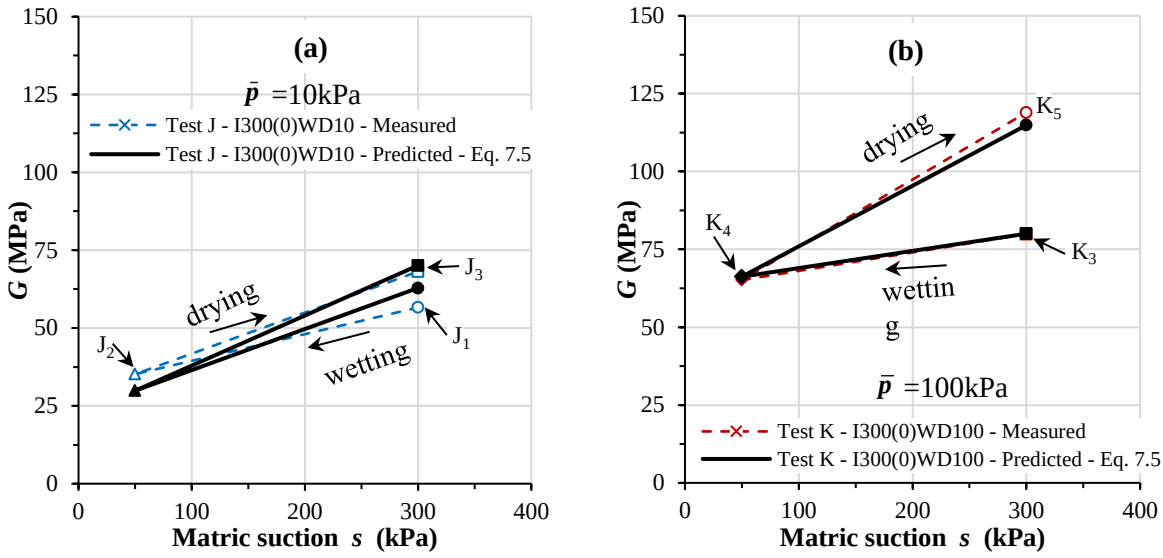

Figure 7.11: Measured and predicted (Eq.7.5) variation of G with s during wetting-drying cycles (a) Test J at $\bar{p}$ =10kPa (b) Test K at $\bar{p}$ =100kPa

Overall, therefore, it appears that, for Tests A, H, I, J and K, Equation 7.4 (employing p^* and v) provides a slightly better match to the full set of observed variations of G than Equation 7.1 (employing $\bar{p}$, s and v). Given that Equation 7.4 is also simpler than Equation 7.1 (involving one fewer state variable and one fewer soil constant), it can be concluded that Equation 7.4 has significant advantages over Equation 7.1. A further advantage of Equation 7.4 over Equation 7.1 is that it is potentially possible to determine the values of all constants in Equation 7.4 (C, m and n) from experimental tests performed under saturated conditions, whereas if using Equation 7.1 it will always be necessary to also perform experimental tests under unsaturated conditions, in order to determine the value of the soil constant k. This issue is examined further in the next sub-section.

7.1.4 Calibration of proposed expression using only data from saturated test

If Equation 7.4 is to be used to predict the variation of G for a given soil under saturated and unsaturated conditions, then the values of the soil constants C, m and n can, in principle, be determined solely from experimental data from tests performed under saturated conditions. To examine this possibility, regression analysis was performed on Equation 7.4 using only the data from the saturated test (Test I). This resulted in the following best-fit values of soil constants (using p_r =100kPa): C =4040MPa, m =5.89 and n =0.40 (compared to C =1356MPa, m =4.32, n =0.41 when the

regression analysis was performed using experimental data from Tests A, H, I, J and K).

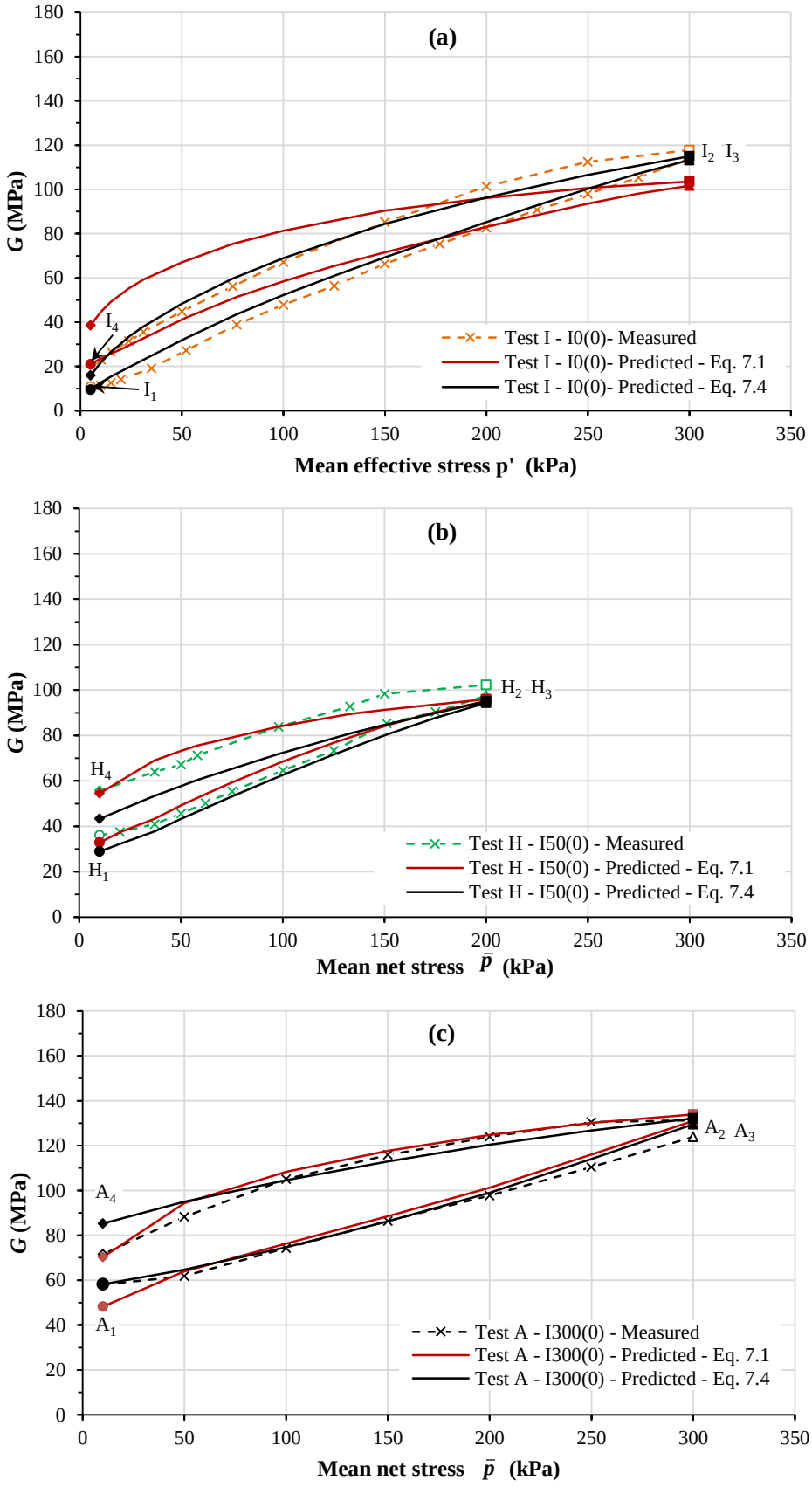

Figure 7.12: Continued.....

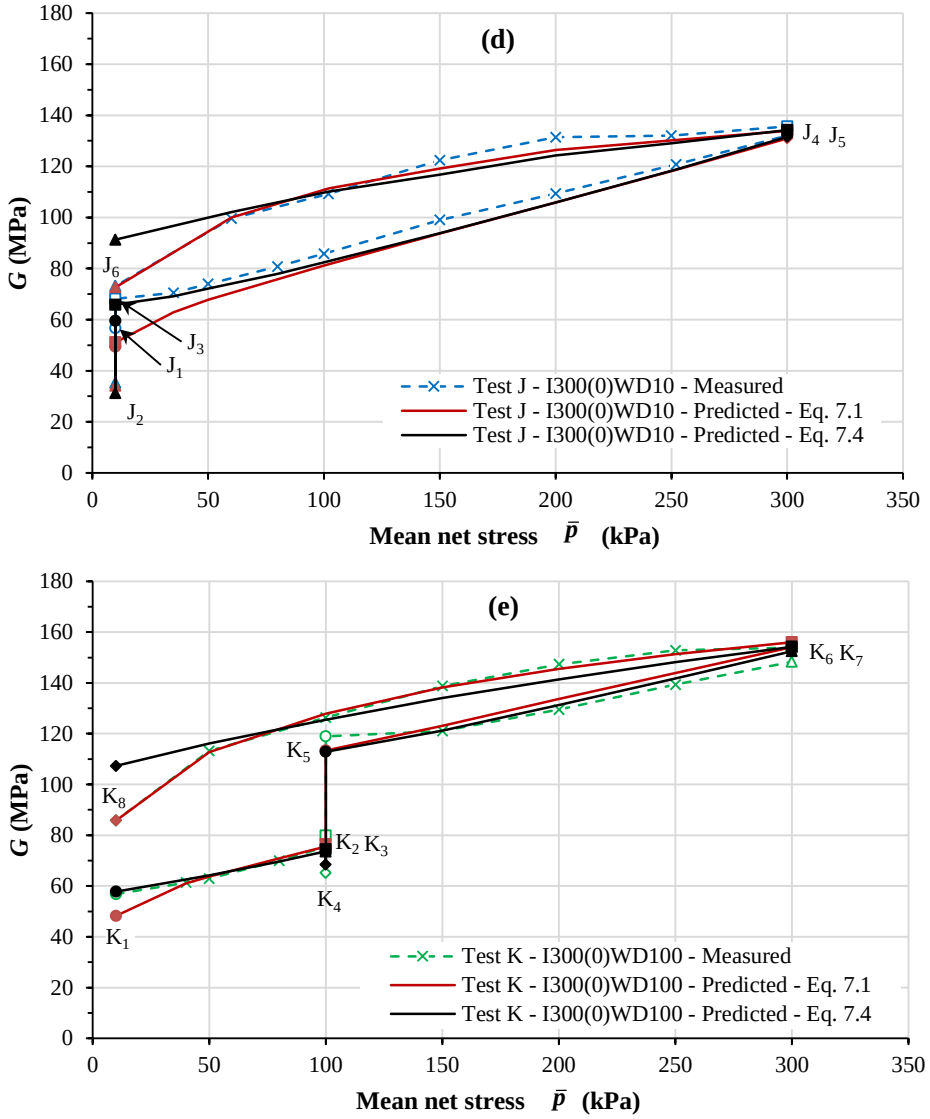

Figure 7.12: Comparison between Eq.7.1 and Eq.7.4 in predicting variation of G with $\bar{p}$ for (a) Test I (b) Test H (c) Test A (d),(e) Test J and (e) Test K

Figures 7.14 and 7.15 show the predicted variations of G in Tests A, H, I, J and K from Equation 7.4, using C =4040MPa, m =5.89 and n =0.40, together with the corresponding experimental results. Inspection of the two figures shows that determination of the values of C, m and n in Equation 7.4 from the single saturated test has resulted in satisfactory prediction of the variation of G in the 4 unsaturated tests (including the wetting and drying stages in Tests J and K). Indeed, comparison of Figures 7.14 and 7.15 with Figures 7.8 and 7.9 shows that determining the values of C, m and n from the single saturated test has resulted in predictions for the 4 unsaturated tests (Figures 7.14 and 7.15) that are only marginally worse than if the results from these unsaturated tests were also used in the determination of the values of C, m and n (Figures 7.8 and 7.9).

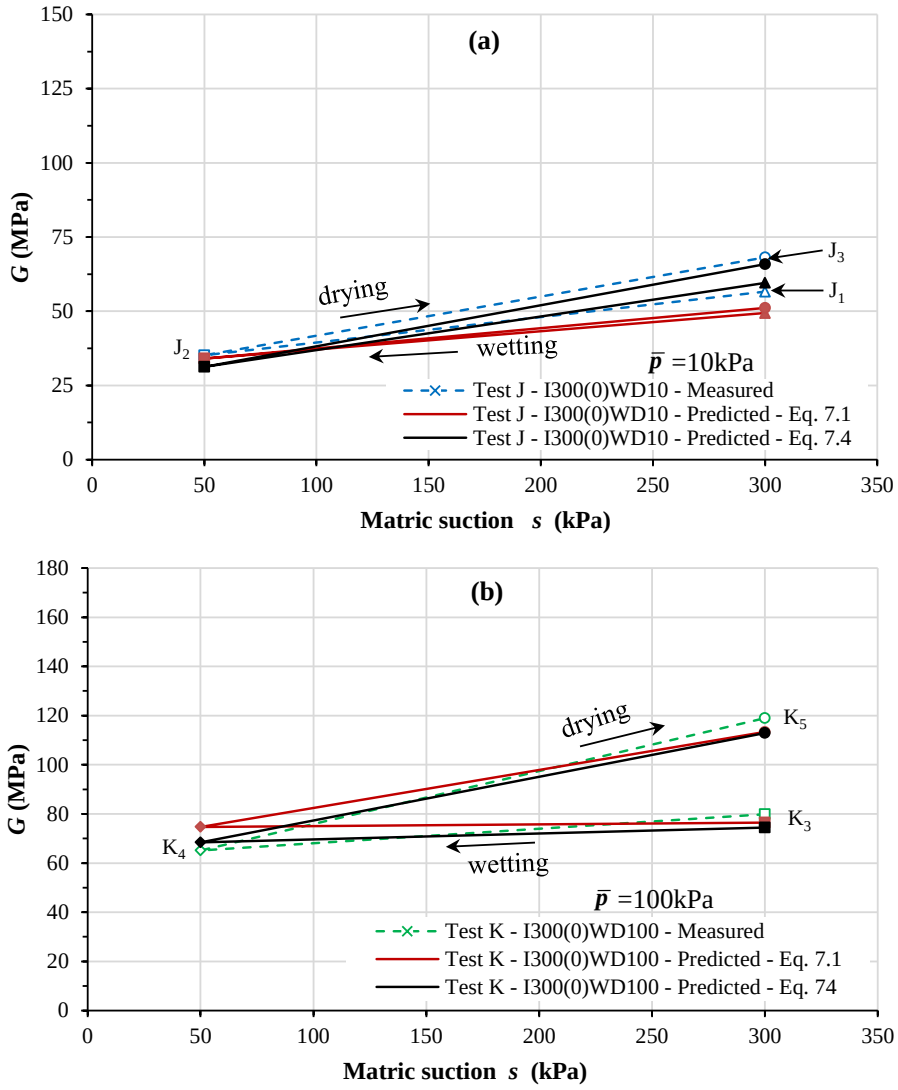

Figure 7.13: Comparison between Eq.7.1 and Eq.7.4 in predicting variation of G with s during wetting-drying cycles (a) Test J at $\bar{p}$ =10kPa (b) Test K at $\bar{p}$ =100kPa

7.1.5 Comparison with other expressions from the literature

In order to compare the proposed expression derived in the current study (Equation 7.4) with expressions proposed by other researchers for the variation of G under unsaturated conditions, two recently proposed expressions of Wong et al. (2014) (Equation 2.88) and Zhou (2014) (Equation 2.90) were selected from the literature.

Equation 2.88 of Wong et al (2014) relates G to $\bar{p}$, s, v and S_r and involves 5 soil constants (C, m, n, k and λ_p). Wong et al (2014) compared their equation with three other expressions proposed by Ng & Yung (2008), Sawangsuriya et al. (2009) and Biglari et al. (2011). They concluded that their expression was able to predict the variation of G for most stress paths as well as the more complex expression of Biglari et al. (2011) (and with fewer parameters) and better than the expressions of Ng &

Yung (2008) and Sawangsuriya et al. (2009).

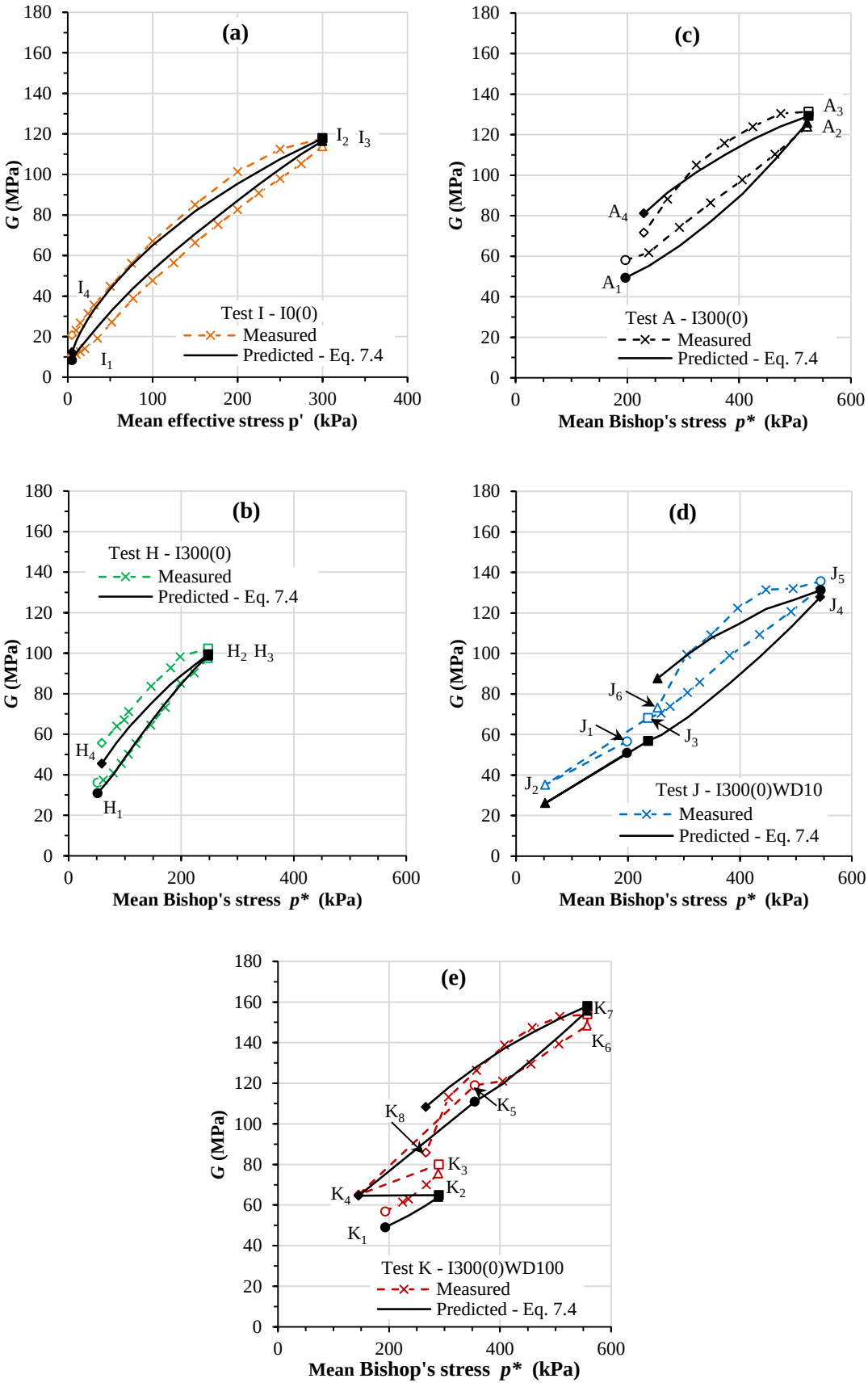

Figure 7.14: Measured and predicted variations of G using Equation 7.4 and values of soil constants from saturated test

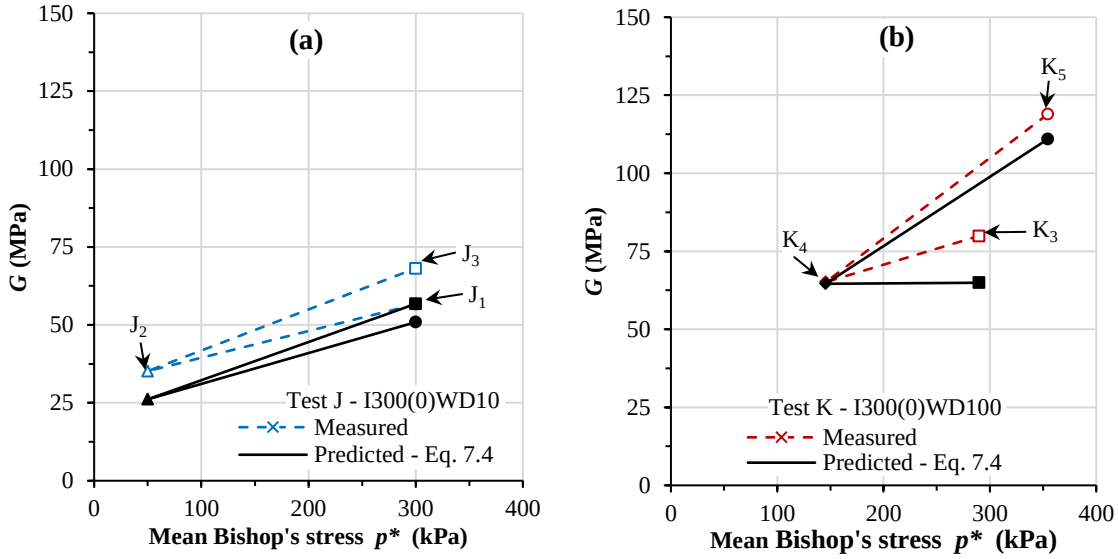

Figure 7.15: Measured and predicted variations of G during wetting and drying in Tests J and K using Equation 7.4 and values of soil constants from saturated test

The expression proposed by Zhou (2014) (Equation 2.90) relates G to p^*, s, S_r and v, with dependency on s and S_r incorporated through the bonding parameter ξ (see Equation 2.89) introduced by Gallipoli et al. (2003b). In Equation 2.89, the function $f(s)$ is derived from the work of Fisher (1926) for the additional normal inter-particle force caused by the presence of a meniscus water bridge (see Section 2.3.3) between two identical spherical soil particles of radius R. This leads to:

$$f(s) = \frac{3}{2} - \frac{9T_s}{8sR}\left[\left(1 + \frac{8sR}{9T_s}\right)^{1/2} - 1\right] \tag{7.6}$$

where T_s is the value of surface tension at the air-water interface. The derivation of Equation 7.6 is given in Appendix B. The validity of Equation 7.6, which assumes spherical soil particles of radius R, is highly questionable for clay soils (involving platy particles), and for these soils selection of an appropriate value of R is likely to be problematic. After inserting for $f(s)$ from Equation 7.6, Equation 2.90 involves 6 soil constants (C_1, C_2, m, n_1, n_2 and R), although Zhou (2014) suggests that it is possible to assume default values for three parameters, m =3, n_1 =0.5, n_2 =0.5 for all soils. Zhou (2014) verified his expression on the basis of experimental test results from Ng & Yung (2008), Khosravi & McCartney (2012), Mancuso et al. (2002) and Nyunt et al. (2011) on sand and clay soils under saturated and unsaturated conditions.

Table 7.1 shows the values of the various soil constants for the compacted speswhite kaolin tested in this study, derived from the experimental results of Tests A, H, I,

J and K, for the three expressions for G of Equation 7.4 (current study), Equation 2.88 (Wong et al., 2014) and Equation 2.90 (Zhou, 2014), using a value of reference pressure p_r =100kPa in all three cases. Values of C, m, λ_p, n and k in Equation 2.88 were derived from the experimental data using the multi-variate non-linear regression tool software (IBM, 2013), with a value of 0.55 used for γ (as stated for all soils by Khalili & Khabbaz, 1998). The value of λ_p was determined from the regression analysis, rather than independently from the gradient of the water retention curve in the $lnS_r : lns$ plot (as recommended by Wong et al., 2014). In Equation 2.90, the value of $f(s)$ at each value of suction was calculated from Equation 7.6, with the soil particle radius R taken as 0.001mm and the surface tension T_s at an air-water interface taken as 0.07N/m. A subsequent check confirmed that the results were very insensitive to the value selected for R. Values of m, n_1 and n_2 in Equation 2.90 were taken as 3, 0.5 and 0.5 respectively (as recommended by Zhou, 2014) and values of C_1 and C_2 were determined using the regression tool. The best-fit value of C_2 was negative ($C_2 = -0.342$), which is surprising (see Equation 2.90), because an increase of the value of the bonding parameter ξ would be expected to produce an increase of G.

Table 7.1: Soil constants in Equations 7.4, 2.88 and 2.90 for the compacted speswhite kaolin of the current study

(a) Equation 7.4

C	m	n
1356MPa	4.32	0.41

(b) Equation 2.88 (Wong et al., 2014)

C	m	λ_p	n	k
68MPa	1.89	0.25	0.43	0.03

(c) Equation 2.90 (Zhou, 2014)

C_1	C_2	m	n_1	n_2	R
519MPa	−0.342	3	0.5	0.5	0.001mm

Figures 7.16 and 7.17 show the predicted variations of G from Equations 7.4, 2.88 and 2.90 for Tests A, H, I, J and K, using the values of soil constants from Table 7.1. Inspection of Figures 7.16 and 7.17 shows that all three equations provide a similar quality of fit to the experimentally observed variations of G. Given that the new proposed expression of Equation 7.4 is simpler than Equations 2.88 or 2.90, involves fewer state variables, fewer soil constants and, uniquely, the values of all soil constants can be determined solely from saturated tests, Equation 7.4 would appear to have significant advantages over existing expressions from the literature such as Equation 2.88 (Wong et al., 2014) or Equation 2.90 (Zhou, 2014).

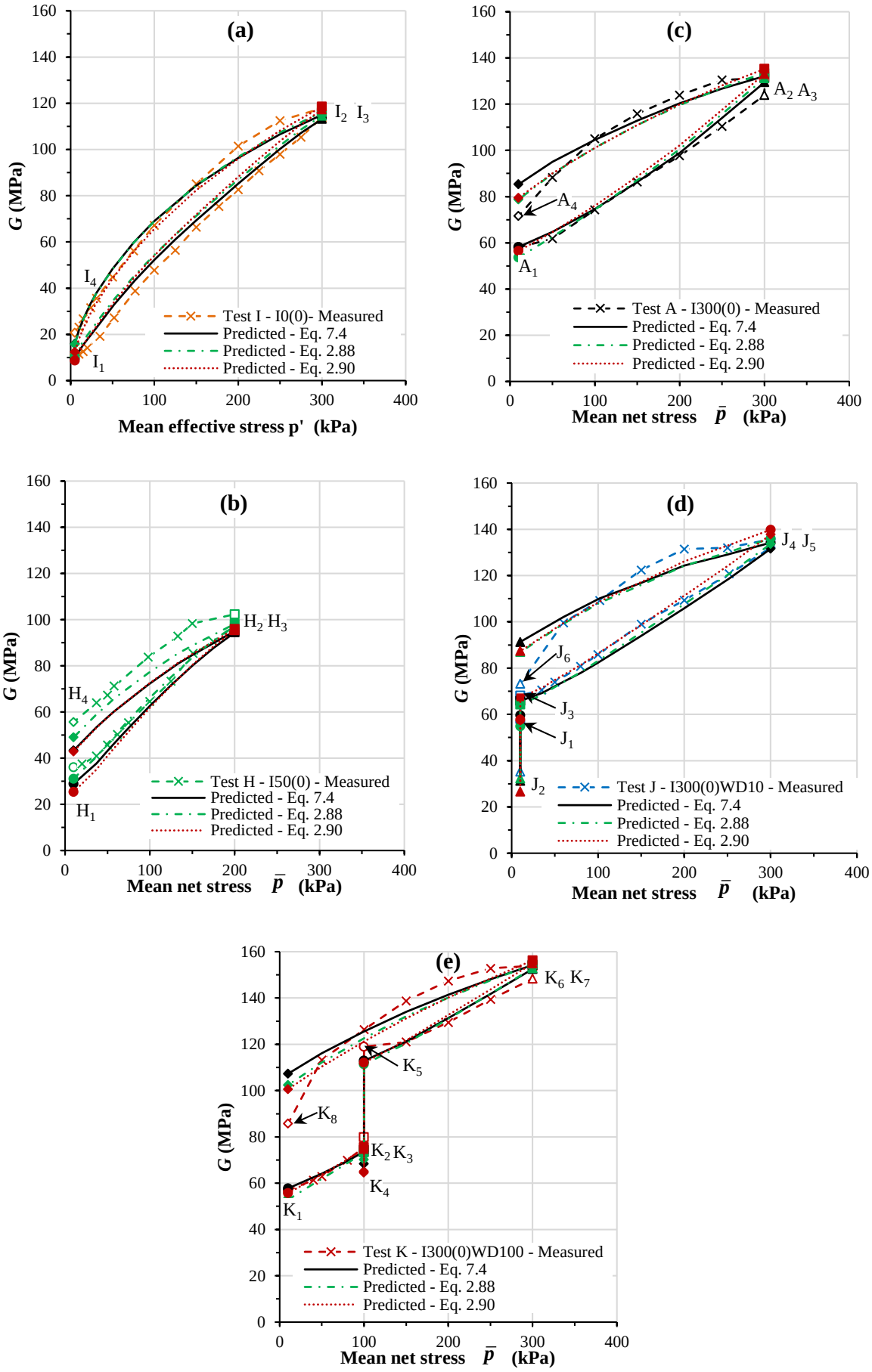

Figure 7.16: Comparison between predictions of Eq.7.4 (current study), Eq. 2.88 (Wong et al., 2014) and Eq. 2.90 (Zhou, 2014) for variation of G during Tests A, H, I, J and K

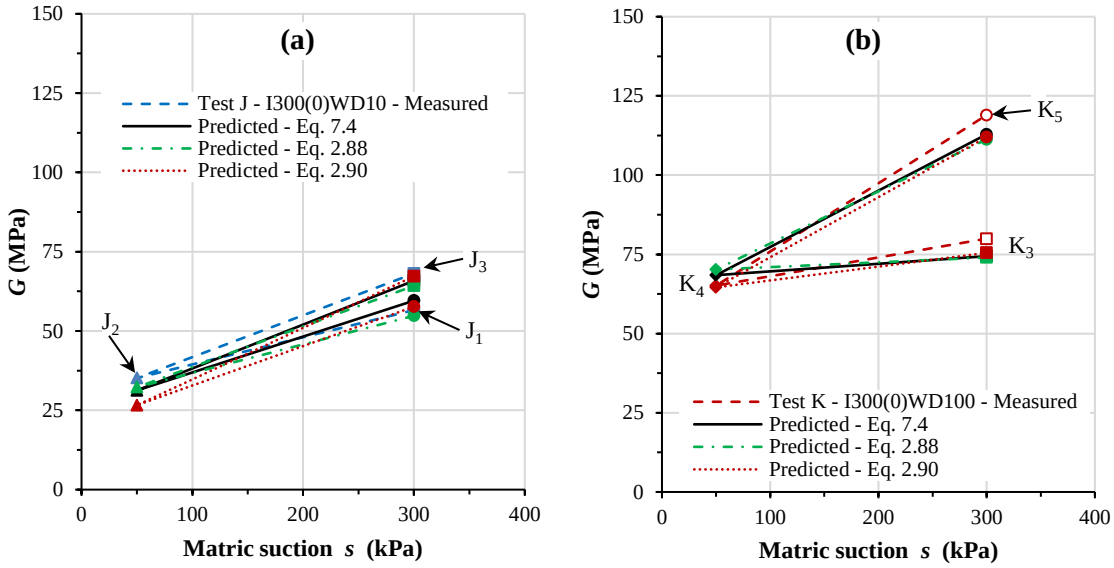

Figure 7.17: Comparison between predictions of Eq.7.4 (current study), Eq. 2.88 (Wong et al., 2014) and Eq. 2.90 (Zhou, 2014) for variation of G with s during wetting-drying cycles (a) Test J at $\bar{p}$ =10kPa (b) Test K at $\bar{p}$ =100kPa

7.1.6 Comparison against other experimental data sets

To investigate further the validity of the proposed expression of Equation 7.4, it was used to predict the variation of G observed in three other experimental data sets from the literature, with Equations 2.88 and 2.90 also used to provide alternative predictions for comparison. The three experimental data sets were for Po silt, a clayey sandy silt tested by Vassallo at al. (2007a), Zenoz kaolin clay, a commercial Iranian kaolin clay tested by Biglari et al. (2011, 2012) and Completely Decomposed Tuff (CDT), a clayey sandy silt from Hong Kong tested by Ng & Yung (2008). Index properties for all these soils are given in Table 7.2.

The tests on CDT involved measurements of very small strain shear modulus G with bender elements, whereas the tests on Po silt and Zenoz kaolin clay involved measurements of very small strain shear modulus G with a resonant column apparatus. These tests included loading-unloading cycles at constant suction and wetting-drying cycles. Table 7.3 shows the values of the soil constants determined for each of the three expressions for G (Equations 7.4, 2.88 and 2.90) for the Po silt. Tables 7.4 and 7.5 show the corresponding information for the Zenoz kaolin clay and the CDT respectively. Values of the various soil constants were determined in a similar fashion to that employed for the speswhite kaolin tested in this study (see Sections 7.1.2 and 7.1.5), except that for the Po silt, Zenoz kaolin clay and CDT the value of the soil constant λ_p in the Wong et al. (2014) expression (Equation 2.88) was determined from the gradient of the water retention curve in the $lnS_r : lns$ plot (rather than as part of

the main regression analysis). This independent determination of the value of λ_p was not possible for the speswhite kaolin tested in this study, as no water retention test was performed.

Table 7.2: Index properties of Po silt, Zenoz kaolin and CDT (Wong et al. 2014)

Parameter	Po silt	Zenoz kaolin	CDT
Maximum dry unit weight (kN/m^3)	15.5	17.4	17.3
Optimum water content (%)	23.1	15.4	16.3
Percentage of sand (%)	33	22	24
Percentage of silt (%)	40	60	72
Percentage of clay (%)	27	18	4
Specific gravity	2.74	2.65	2.73
Liquid limit (%)	51	29	43
Plastic limit (%)	33	17	29
Plasticity index (%)	18	12	14
Classification (USCS)	ML/MH	CL	ML

Table 7.3: Soil constants in Equations 7.4, 2.88 and 2.90 for the Po silt tested by Vassallo et al. (2007a)

(a) Equation 7.4

C	m	n
5627MPa	7.32	0.29

(b) Equation 2.88 (Wong et al., 2014)

C	m	λ_p	n	k
19MPa	4.56	0.11	0.19	0.22

(c) Equation 2.90 (Zhou, 2014)

C_1	C_2	m	n_1	n_2	R
321MPa	1.43	3	0.5	0.5	0.001mm

Figures 7.18, 7.19 and 7.20 show the predicted variations of G from the three expressions (Equations 7.4, 2.88 and 2.90) for the tests on Po silt, Zenoz kaolin clay and CDT respectively, together with the corresponding experimental results. Inspection of Figures 7.18, 7.19 and 7.20 shows that all three expressions capture the main trends of the experimental results but that the fit of all three expressions to the experimental results is generally not as good as it was for the speswhite kaolin tested in the current study (compare with Figures 7.16 and 7.17). For all three soils, Equation 7.4 (proposed in this study) provides as good a match to the experimental results as Equations 2.88

and 2.90 from the literature. Given that Equation 7.4 is significantly simpler than the other two expressions (involving fewer state variables and fewer soil constants) and that, unlike the other two expressions, the values of the soil constants within Equation 7.4 can be determined solely from saturated tests, it is clear that Equation 7.4 has substantial advantages over the two expressions from the literature.

Table 7.4: Soil constants in Equations 7.4, 2.88 and 2.90 for the Zenoz clay tested by Biglari et al. (2011, 2012)

(a) Equation 7.4

C	m	n
89MPa	1.04	0.59

(b) Equation 2.88 (Wong et al., 2014)

C	m	λ_p	n	k
12MPa	3.28	0.18	0.29	0.25

(c) Equation 2.90 (Zhou, 2014)

C_1	C_2	m	n_1	n_2	R
240MPa	0.79	3	0.5	0.5	0.001mm

When using Equation 2.90, there was considerable uncertainty in the most appropriate value of soil particle radius R to use in the determination of $f(s)$ from Equation 7.6. The regression analysis for Equation 2.90 was therefore repeated using a larger value of R (0.005mm) for each of the four soils, and revised versions of Figures 7.16, 7.17, 7.18, 7.19 and 7.20 were plotted. The results showed that there was a very marginal difference with the corresponding predictions using R =0.001mm.

Table 7.5: Soil constants in Equations 7.4, 2.88 and 2.90 for the CDT tested by Ng & Yung (2008)

(a) Equation 7.4

C	m	n
690MPa	4.56	0.65

(b) Equation 2.88 (Wong et al., 2014)

C	m	λ_p	n	k
33MPa	1.63	0.54	0.64	0.17

(c) Equation 2.90 (Zhou, 2014)

C_1	C_2	m	n_1	n_2	R
394MPa	0.43	3	0.5	0.5	0.001mm

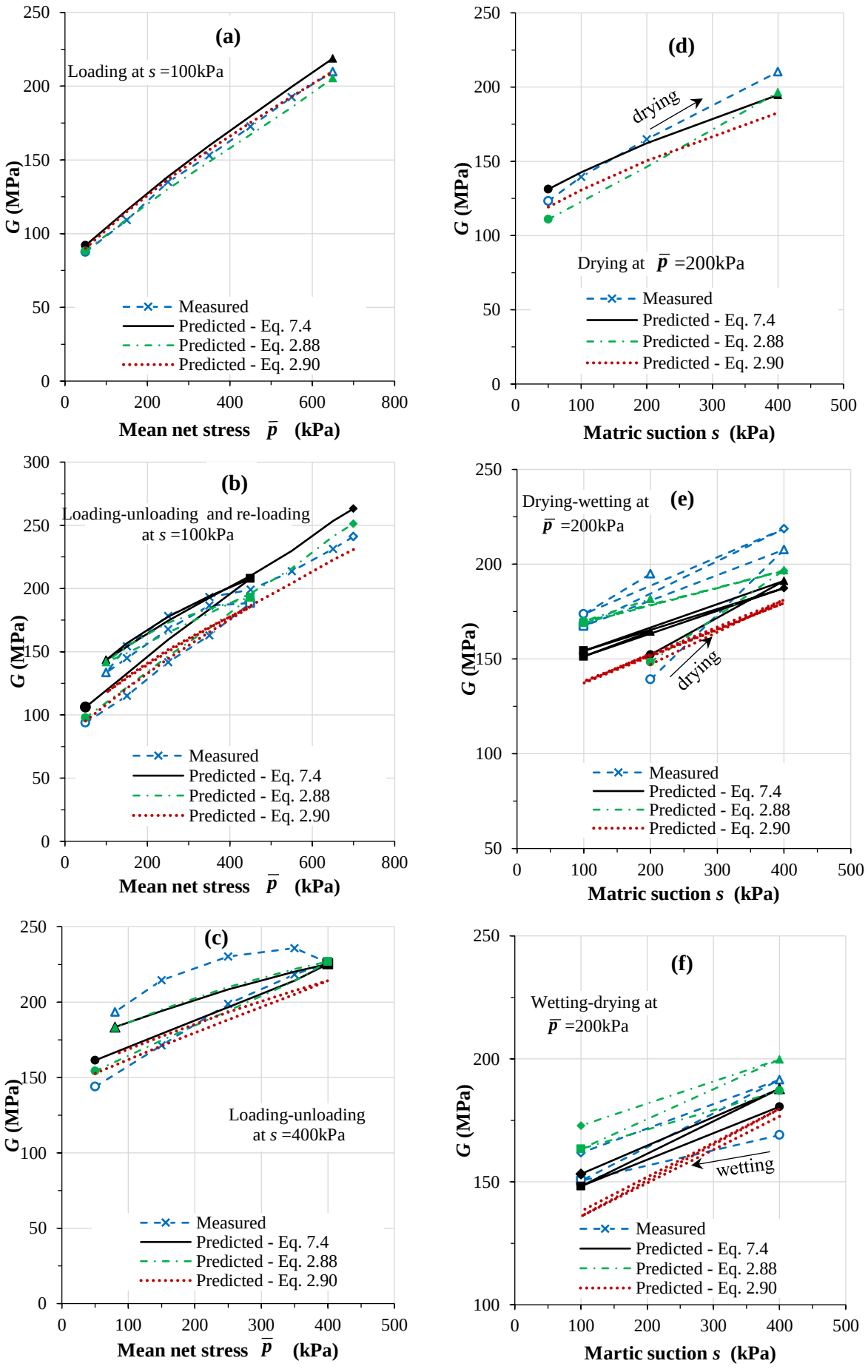

Figure 7.18: Comparison between predictions of Eq.7.4 (current study), Eq. 2.88 (Wong et al., 2014) and Eq. 2.90 (Zhou, 2014) for variation of G in tests of Vassallo et al. (2007a) on Po silt

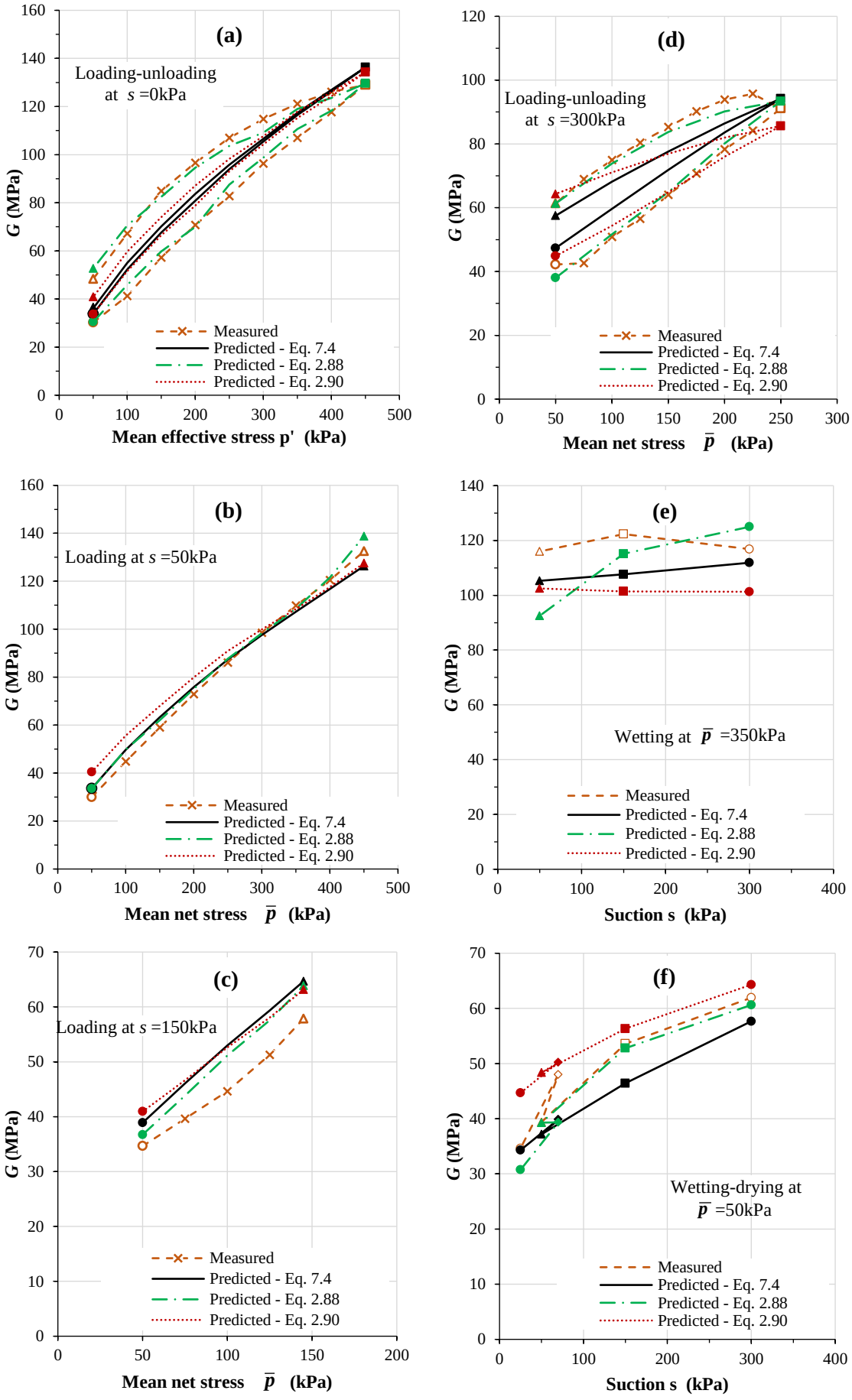

Figure 7.19: Comparison between predictions of Eq.7.4 (current study), Eq. 2.88 (Wong et al., 2014) and Eq. 2.90 (Zhou, 2014) for variation of G in tests of Biglari et al. (2011, 2012) on Zenoz kaolin clay

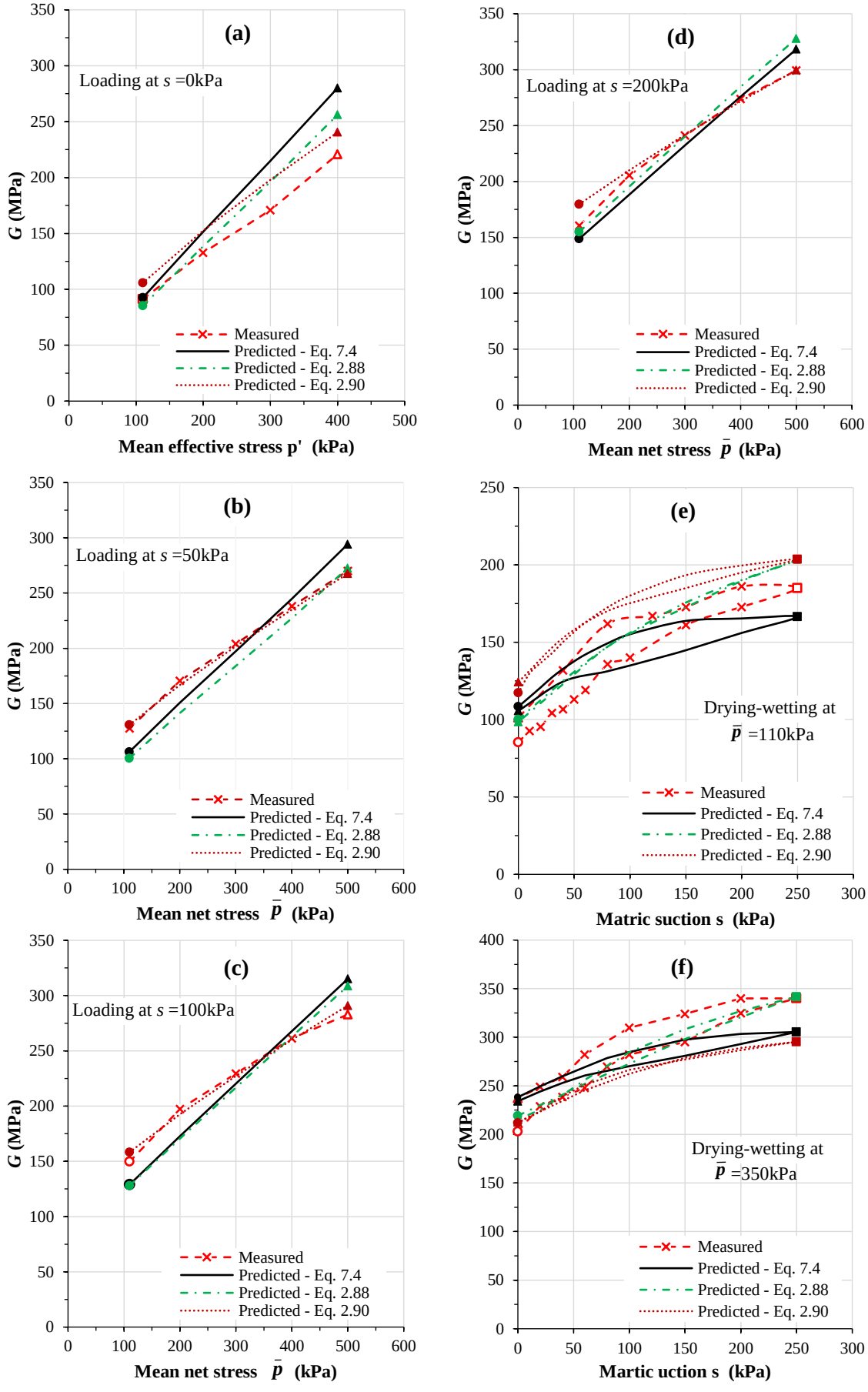

Figure 7.20: Comparison between predictions of Eq.7.4 (current study), Eq. 2.88 (Wong et al., 2014) and Eq. 2.90 (Zhou, 2014) for variation of G in tests of Ng & Yung. (2008) on CDT

7.2 Variation of G_{hv} and G_{hh} under anisotropic stress states

As described in Section 2.2.3, expressions for G for saturated soils under isotropic stress states can be extended to include the effect of stress-induced anisotropy, to predict the values of G_{ij} under anisotropic stress states (see Equation 2.42). Similarly, in the current study under unsaturated conditions, the proposed expression for G under isotropic stress states (Equation 7.4) can be extended to predict values of G_{ij} under anisotropic stress states.

Experimental evidence on the variations of G_{hv} and G_{hh} under anisotropic stress states was taken from Tests A, B and C. All three of these tests were on isotropically compacted samples, so that there was no strain-induced anisotropy at the start of loading. All three tests involved loading stages performed under unsaturated conditions at s =300kPa. In Test A, the loading was performed under (almost) isotropic stress states ($\eta \approx 0$, with q =2kPa), whereas in Tests B and C loading was performed at $\eta = 1$ (triaxial compression) and $\eta = -1$ (triaxial extension) respectively. In interpreting the results, it was assumed that there was no development of strain-induced anisotropy during the loading stages of Tests B and C, so that only stress-induced anisotropy was considered.

Figure 7.21 shows the experimental variations of G_{hv} and G_{hh}, plotted against p^*, during the loading stages of Tests A, B and C. For Test C there was no subsequent unloading stage, because the soil unexpectedly failed during the loading stage, as described in Section 6.4. Unloading stages from Tests A and B have also been omitted in Figure 7.21, in the interests of clarity.

Inspection of Figure 7.21a shows that, at any given value of p^*, the value of G_{hv} was highest in Test B ($\eta = 1$) and lowest in Test C($\eta = -1$). In contrast, Figure 7.21b shows that, at any given value of p^*, the value of G_{hh} was highest in Test C ($\eta = -1$). It is however clear from Figure 7.21 that the influence of η on both G_{hv} and G_{hh} was relatively small. This may be because the anisotropy of the stress state was relatively modest when expressed in terms of Bishop's stresses rather than net stresses. For example, in Test B, whereas the stress ratio in terms of net stress was given by $\eta = q/\bar{p} = 1$, the stress ratio in terms of Bishop's stress ($\eta^* = q/p^*$) varied from η^* =0.05 at the start of loading (B_1) to η^* =0.51 at the end of the loading stage (B_2). Similarly, in Test C, whereas $\eta = -1$, η^* varied from -0.05 at the start of loading (C_1) to -0.42 at the final point of bender/extender element measurement before shear failure.

Equation 7.4 represents the proposed expression for the elastic shear modulus G for isotropic soil under isotropic stress conditions including unsaturated states. This can be extended to anisotropic soil under anisotropic stress states using the same logic as presented for saturated soils in Section 2.2.3 (see Equation 2.42), to give:

$$G_{ij} = C_{ij} v^{-m} \left(\frac{\sigma_i^*}{p_r}\right)^{n_i} \left(\frac{\sigma_j^*}{p_r}\right)^{n_j} \left(\frac{\sigma_k^*}{p_r}\right)^{n_k} \tag{7.7}$$

In Equation 7.7, if G_{ij} is determined from a shear wave velocity V_{sij} , then subscript i represents the direction of wave transmission, subscript j represents the direction of wave polarisation and subscript k represents the third mutually perpendicular direction. σ_i^* is the principal Bishop's stress in the direction of wave propagation, σ_j^* is the principal Bishop's stress in the direction of wave polarisation and σ_k^* is the principal Bishop's stress in the third mutually perpendicular direction. Thermodynamic considerations require that $G_{ji} = G_{ij}$ (Love, 1927), so that $C_{ji} = C_{ij}$ and $n_i = n_j$ in Equation 7.7. In addition, if strain-induced anisotropy is ignored, then C_{ij} has the same value for all directions i and j ($C_{ij} = C$). Equation 7.7 then becomes:

$$G_{ij} = C v^{-m} \left(\frac{\sigma_i^*}{p_r}.\frac{\sigma_j^*}{p_r}\right)^{n_i} \left(\frac{\sigma_k^*}{p_r}\right)^{n_k} \tag{7.8}$$

For example, for testing in a triaxial apparatus, expressions for G_{hv} and G_{hh} are:

$$G_{hv} = C v^{-m} \left(\frac{\sigma_h^*}{p_r}\right)^{(n_i+n_k)} \left(\frac{\sigma_v^*}{p_r}\right)^{n_i} \tag{7.9}$$

$$G_{hh} = C v^{-m} \left(\frac{\sigma_h^*}{p_r}\right)^{2n_i} \left(\frac{\sigma_v^*}{p_r}\right)^{n_k} \tag{7.10}$$

where σ_h^* and σ_v^* are:

$$\sigma_h^* = \bar{\sigma}_h + S_r s \tag{7.11}$$

$$\sigma_v^* = \bar{\sigma}_v + S_r s \tag{7.12}$$

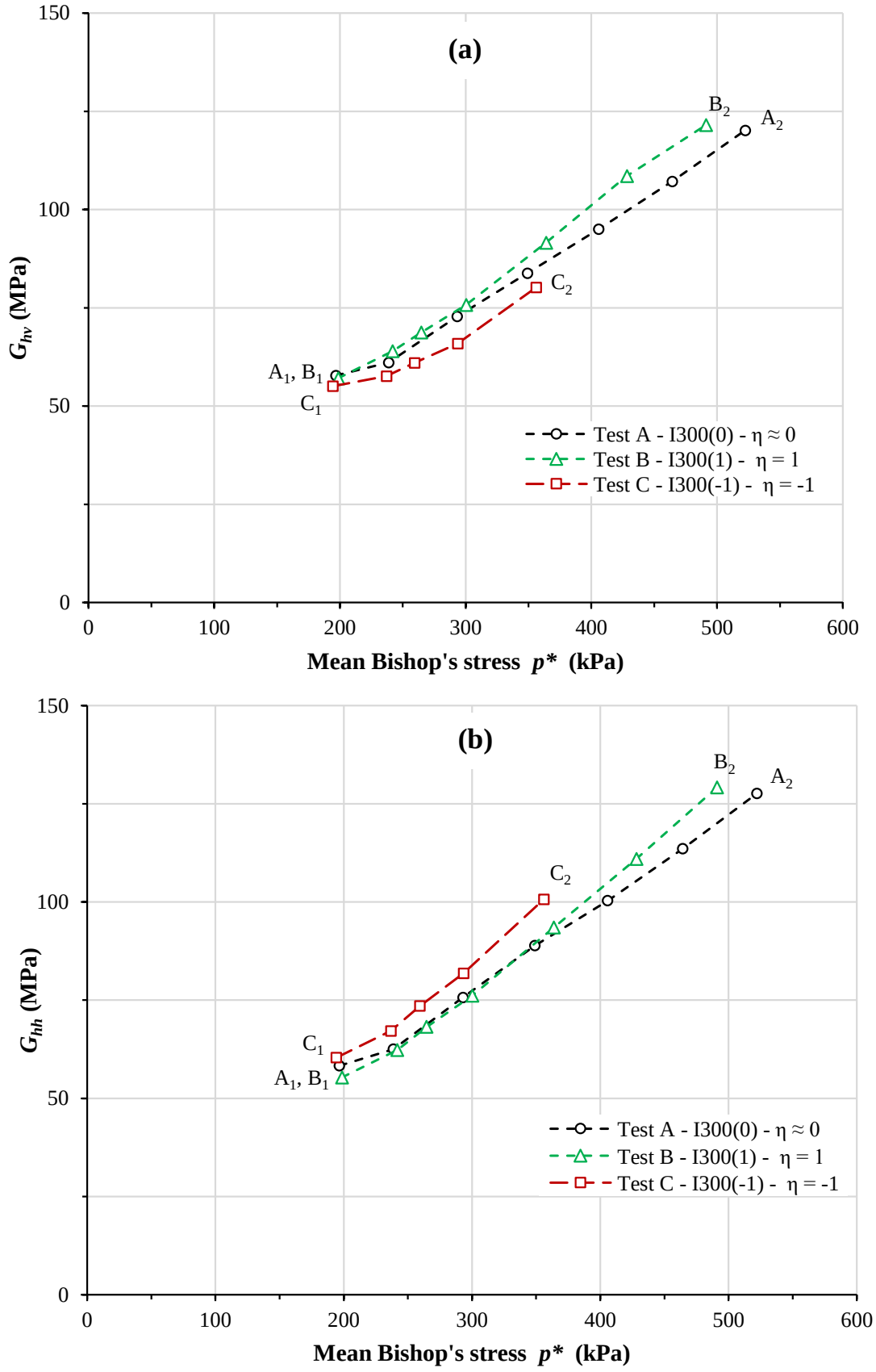

Figure 7.21: Experimental variations of G_{hv} and G_{hh} during loading stages of Tests A, B and C

Equations 7.8, 7.9 and 7.10 involve four soil constants (C, m, n_i and n_k). If Equation 7.8 is to converge to Equation 7.4 for isotropic stress states, the values of C and m in Equation 7.8 should be the same as those in Equation 7.4 and the following relation should hold between the values of n_i and n_k in Equation 7.8 and the value of n in Equation 7.4:

$$2n_i + n_k = n \tag{7.13}$$

The experimental values of G_{hv} and G_{hh} from the loading stages of Tests A, B and C were used with the regression tool (in a single regression analysis, using Equation 7.8 and all values of both G_{hv} and G_{hh}) to determine best-fit values of C, m, n_i and n_k (using p_r =100kPa). This gave C =675MPa, m =3.62, n_i =0.17 and n_k =0.19. Interestingly, the best-fit value of n_k (n_k =0.19) is very similar to the best-fit value of n_i (n_i =0.17), suggesting that the stress σ_k^* in the third mutually perpendicular direction has a similar influence on G_{ij} as the stresses σ_i^* and σ_j^* in the shear wave transmission and polarisation directions. This confirms the suggestion of Jung et al. (2007) for saturated tests that n_k is non-zero in clays (see Section 2.2.3), whereas Stokoe et al. (1995) concluded that n_k is zero for tests on dry sand. However, the best-fit values of n_i and n_k do not satisfy Equation 7.13: $2n_i + n_k$ =0.53, whereas the best-fit value of n from Tests A, H, I, J and K (isotropic loading) was 0.41 (see Section 7.1.2). As a consequence of this, the best-fit values of C and m from Equation 7.8 and Tests A, B and C do not match the best-fit values of C and m from Equation 7.4 and Tests A, H, I, J and K.

Figure 7.22 shows the predicted values of G_{hv} and G_{hh} for the loading stages of Tests A, B and C, using Equations 7.9 and 7.10, with the best-fit values of C, m, n_i and n_k from Tests A, B and C (C =675MPA, m =3.62, n_i =0.17 and n_k =0.19), together with the corresponding experimental results. It is clear that Equations 7.9 and 7.10 (based on Equation 7.8) have not been able to fully capture the influence of η on G_{hv} and G_{hh}. In particular, it is not possible with Equations 7.9 and 7.10 (whatever choice of n_i and n_k is selected) to correctly predict that values of G_{hv} are lowest in Test C ($\eta = -1$) and values of G_{hh} are highest in Test C ($\eta = -1$) while at the same time correctly predicting the relative magnitudes of G_{hv} and G_{hh} in Tests A and B ($\eta \approx 0$ and $\eta = 1$ respectively). This may be consistent with the conclusions of Viggiani & Atkinson (1995) for saturated clays, when they reported that the exponent n_k appeared to take different values depending upon whether the stress state was triaxial compression or triaxial extension. Viggiani & Atkinson (1995) reported that n_k was non-zero in triaxial extension but approximately zero in triaxial compression (see Section 2.2.3). This means that the value of n_k (and possibly also the value of n_i)

may be influenced by the Lode angle (i.e. the intermediate principal stress in triaxial compression is the same as the minor principal stress, whereas in triaxial extension it is the same as the major principal stress). By including the influence of Lode angle in Equation 7.8, it is possible that Equation 7.8 could properly predict the sequences of the three curves in Tests A, B and C in Figure 7.22.

Based on the regression analysis results under isotropic stress states reported in Section 7.1.2, the sum of the three exponents ($2n_i$ and n_k) was enforced to be equal to 0.41 (to agree with the best-fit value of n from Tests A, H, I, J and K) and similarly the values of C and m were enforced as 1356MPa and 4.32 respectively and a new regression analysis was then performed, using the experimental results from Tests A, B and C, to determine the values of the exponents n_i and n_k (where $n_k = 0.41 - 2n_i$). Results from the regression analysis showed that the best-fit values of n_i and n_k were 0.14 and 0.13, respectively. Note that values of n_i and n_k were very similar.

Figure 7.23 shows the predicted values of G_{hv} and G_{hh} for the loading stages of Tests A, B and C, using Equations 7.9 and 7.10, with the best-fit values of C, m and $(2n_i + n_k)$ from the 5 isotropic tests (C =1356MPa, m =4.32, ($2n_i$+$n_k = 0.41$)) (see Section 7.1.2) and individual values of n_i and n_k from Tests A, B and C, (n_i =0.14 and n_k =0.13), together with the corresponding experimental results of G. Comparison of Figure 7.23 with Figure 7.22 shows very little difference between the two sets of predictions. This means that it is possible to assume that $n_i = n_k$ and then to calibrate the soil constants (C, m and n) in Equation 7.4 using only saturated data under isotropic stress states and then to use Equations 7.9 and 7.10 to predict G under isotropic and anisotropic stress states and saturated and unsaturated conditions.

7.3 Variation of M under isotropic and anisotropic stress states

Attempts were made by the author to interpret results of Tests A, H, I , J and K to propose expressions for constrained modulus M under isotropic stress states, in terms of both conventional and alternative unsaturated stress state variables. Unfortunately, no real success was achieved with this exercise within the time constraints and therefore no proposed expressions are presented here. As a consequence, no attempts were made to interpret results of Tests A, B and C to propose expressions for M_i under anisotropic stress states.

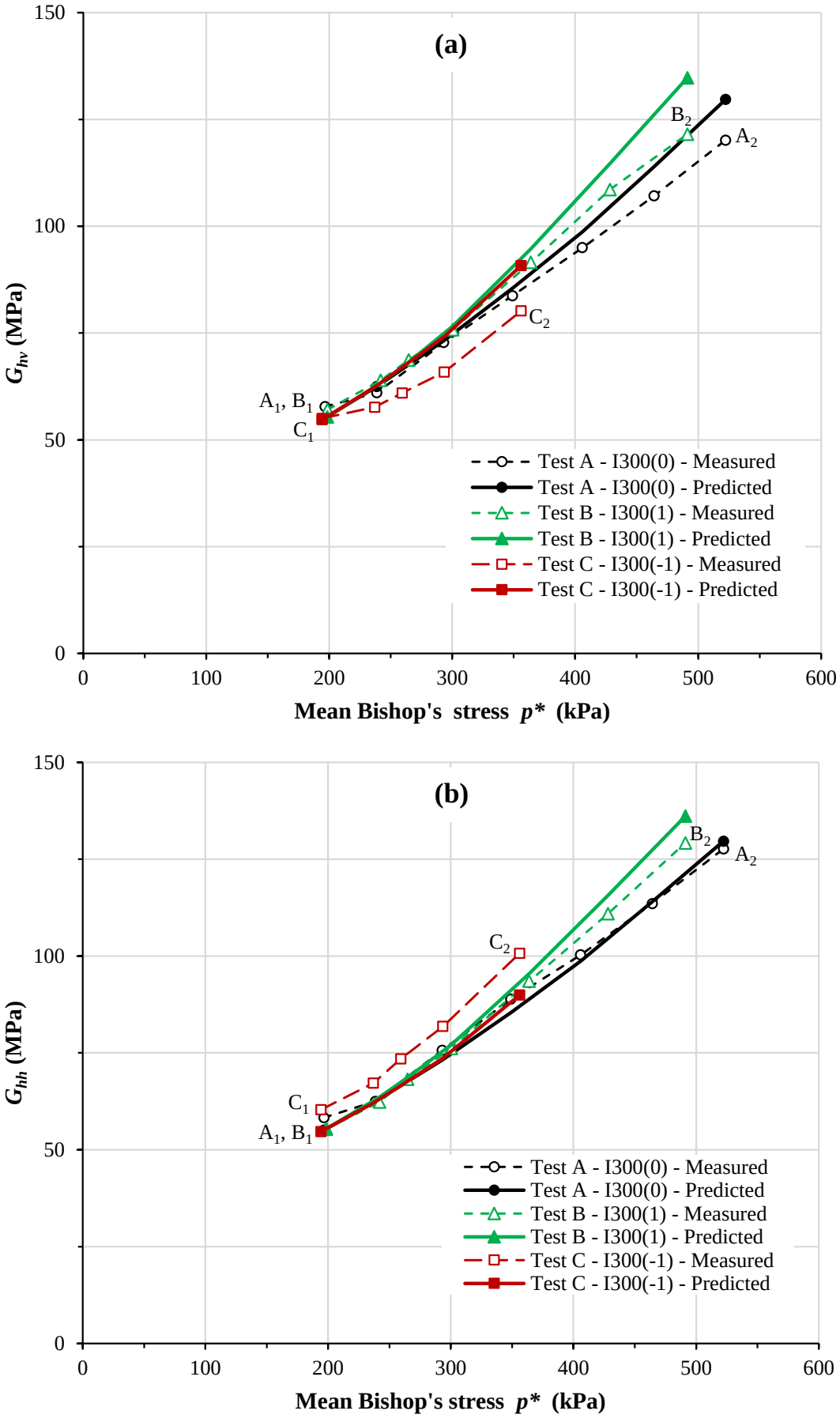

Figure 7.22: Measured and predicted (Eq.7.9 and 7.10) variations of (a) G_{hv} and (b) G_{hh} during loading stages of Tests A, B and C

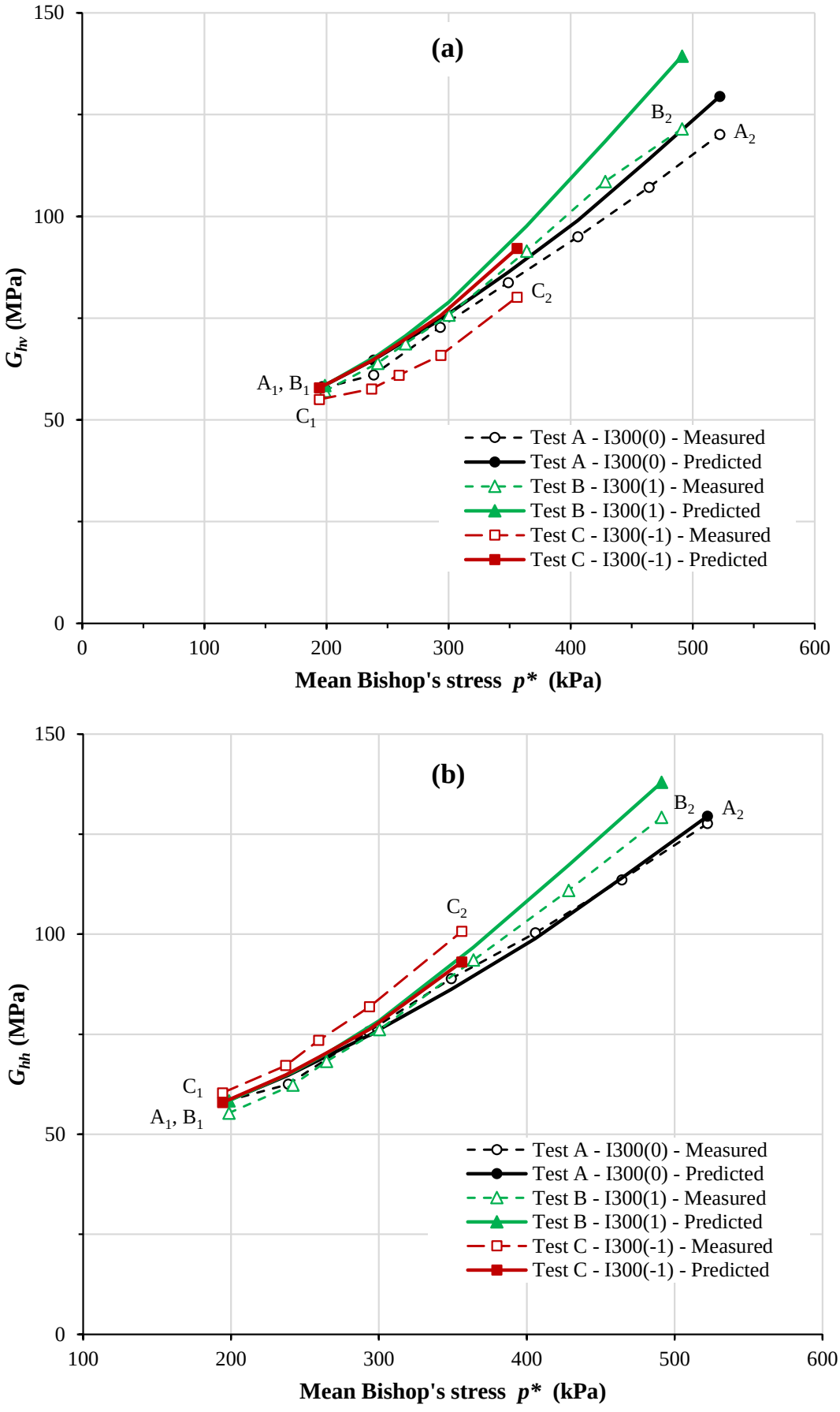

Figure 7.23: Measured and predicted (Eq.7.9 and 7.10, with C =1356MPa, m =4.32, $2n_i + n_k = 0.41$) variations of (a) G_{hv} and (b) G_{hh} during loading stages of Tests A, B and C

Chapter 8

Conclusions and recommendations

During the last two decades, several expressions have been proposed by researchers such as Mancuso et al. (2002) and Wong et al. (2014) to predict shear modulus G at very small strains under unsaturated conditions. However, some of these existing expressions include rather arbitrary assumptions about their form and all of them are relatively complex, meaning that practical determination of the values of the various soil constants within these expressions is likely to be problematic.

In order to derive a new and simple expression for shear modulus G at very small strain under unsaturated conditions, including smooth convergence with saturated conditions, avoiding the shortcomings of existing expressions, a set of experimental tests was designed and performed using a modified suction-controlled double wall triaxial apparatus incorporating three pairs of bender/extender elements. These tests covered various different testing aspects, including two different forms of sample compaction (isotropic and anisotropic), three different values of suction (covering both unsaturated and saturated conditions), loading and unloading stages at three different values of stress ratio η, and wetting and drying stages (including both wetting-induced swelling and wetting-induced collapse compression). In addition to the derivation and validation of the new proposed expression for G, changes of elastic anisotropy were investigated, including the possibilities of both strain-induced anisotropy and stress-induced anisotropy.

Interpretation of the test results was performed in terms of both conventional unsaturated state variables ($\bar{p}$, q, s, v and S_r, where $\bar{p}$ is mean net stress) and alternative unsaturated state variables (p^*,q , v and S_r, where p^* is mean Bishop's stress).

8.1 Experimental systems and procedures

- An existing suction-controlled double wall triaxial apparatus was successfully modified to incorporate three pairs of bender/extender elements. The modifications predominantly involved re-design of the base pedestal and top cap. In mounting the high air-entry (HAE) ceramic filters within the steel body of the base pedestal and top cap it was found that the choice of glue was very important, because it was possible for the glue to swell and cause radial cracks in the HAE ceramic filters (see Section 3.3.3). In addition, the surface roughness of the steel body of the base pedestal and the top cap was another very important issue that reduced the influence of any tendency for vertical swelling of the glue that might damage the HAE ceramic filters.

- It was very important to check the re-designed base pedestal and top cap for seal quality and to check the air-entry value of the HAE ceramic filters. This was performed through rigorous test procedures described in Section 3.3.4.

- Sample volume change was measured by monitoring the inflow or outflow of water to the inner glass-walled cell of a double wall triaxial cell. Even with the double wall cell, accuracy of the measurement of sample volume change was substantially improved by employing a test procedure where the cell pressure remained constant throughout, with radial net stress and matric suction controlled by appropriate variation of pore air pressure and pore water pressure respectively (see Section 3.5.1).

- A temperature correction was applied to the measurements of water inflow or outflow to the inner cell, to improve the accuracy of sample volume change measurement. It was concluded that, in future, it would be better to mount the thermocouple within the inner cell (rather than within the outer cell), to improve further the accuracy of sample volume change measurement and to reduce small spurious temperature-induced oscillations in the calculated variation of sample volume (see Section 3.5.2).

- To avoid desaturation of the HAE ceramic filter in the base pedestal during the long period required for setting-up an unsaturated soil sample with BEEs (see Section 4.2.2), a slotted cylindrical mould was designed and successfully used for mounting the horizontal BEE pairs. It was very important to make sure that the BEEs were properly aligned and contacted with the soil sample through the pre-slotted locations on the sample during the setting-up process, because improper contact between the BEEs and the soil sample has a great influence on the measurements of shear wave velocity and compression wave velocity.

- In order to select a reliable technique for measuring travel times in the bender/extender element tests, four different interpretation procedures were examined, involving both time and frequency domains (see Section 5.1). It was concluded that simple measurement of peak-to-first-peak in the time domain gave the most reliable measurements of travel time for both shear and compression waves. It is worth noting that selection of the best technique for measuring travel times may depend upon soil type, stress state and testing systems (including both the soil testing equipment (such as oedometer cell, shear box or triaxial cell) and the BEE testing system). It should not therefore be concluded that peak-to-first-peak in the time domain will always be the best method of travel time determination, and other methods may provide more reliable results when testing other soils or using different testing systems.

8.2 Experimental results

8.2.1 General points

- After sample compaction and setting-up in the triaxial apparatus, the values of specific volume v, water content w and degree of saturation S_r for isotropically compacted samples and anisotropically compacted samples were very similar, as intended (see Section 4.1.3).

- After compaction and setting-up of isotropically compacted samples, the values of V_{shv} and V_{shh} were very similar, confirming isotropic behaviour of these isotropically compacted samples. However, values of V_{svh} and V_{shv} were significantly different, whereas they should always be identical (for isotropic and anisotropic soils), because of thermodynamic considerations. This showed that measurements of shear wave velocity were affected by differences in the boundary conditions between vertical transmission and horizontal transmission (see Section 5.1.3). It was therefore decided not to use values of V_{svh} in the investigation of elastic anisotropy.

- In contrast, values of the compression wave velocities V_{pv} and V_{ph} after compaction and setting-up were essentially identical in the isotropically compacted samples (see Section 5.1.3), confirming that values of V_{pv} and V_{ph} could be used in the investigation of elastic anisotropy.

- After compaction and setting-up, the average values of G_{hh}/G_{hv} (based on measurements of V_{shv} and V_{shh}) was 0.99 for isotropically compacted samples, and the corresponding values of M_h/M_v (based on V_{pv} and V_{ph}) was 1.00, thus confirming initially isotropic behaviour of these isotropically compacted samples. In

contrast, the corresponding average initial values of G_{hh}/G_{hv} and M_h/M_v for anisotropically compacted samples were 0.93 and 1.03 respectively. Hence, the anisotropically compacted samples showed initial anisotropy of elastic behaviour, but the degree of initial anisotropy was relatively modest (see Section 6.2.3).

- During the initial equalization stages to the three different values of suctions (0, 50 and 300kPa), the water content increased, meaning that the suction of the as-compacted samples was higher than 300kPa. All samples showed an increase of v during the equalization stage (wetting-induced swelling).

- In order to examine the quality of repeatability of tests in terms of both large strain plastic behaviour and very small strain elastic behaviour, Tests E and G both involved loading with η =1 at s =300kPa on anisotropically compacted samples. Experimental results from these two tests demonstrated excellent repeatability of large strain behaviour (variations of ϵ_v, ϵ_s, v and S_r) and very small strain elastic behaviour (measured values of V_s and V_p) (see Sections 6.3.1 and 6.3.2).

8.2.2 Large strain behaviour

- Large strain behaviour observed during loading and unloading stages and wetting and drying stages was consistent with established behaviour from other research programmes on unsaturated soils. For example, behaviour was consistent with hardening elasto-plasticity (see Section 6.7.1), including the existence of a LC yield curve in the $s : \bar{p}$ plane, such that the yield value of $\bar{p}$ increased with increasing s (see Section 6.8.1) and wetting caused swelling at low values of $\bar{p}$ and collapse compression at high values of $\bar{p}$ (see Section 6.9.1).

- For anisotropically compacted samples, large strain behaviour observed during loading and unloading at different values of stress ratio η (where $\eta = q/\bar{p}$ is expressed in terms of net stresses) was qualitatively and quantitatively consistent with corresponding results on the same anisotropically compacted speswhite kaolin reported by Al-Sharrad (2013) (see Section 6.5).

- The large strain behaviour observed (at s =300kPa) for isotropically compacted samples was very similar to that observed for anisotropically compacted samples during loading at $\eta = 0$ or $\eta = 1$, whereas the large strain behaviour of an isotropically compacted sample and an anisotropically compacted sample showed major differences on loading in triaxial extension at $\eta = -1$. In particular, the isotropically compacted sample unexpectedly suffered shear failure at $q = -186$kPa, whereas there was no indication that shear failure was imminent for

the anisotropically compacted sample even on loading to $q = -300$kPa (see Sections 6.5.3 and 6.7.1). This could mean that isotropically compacted samples and anisotropically compacted samples behave very differently when loaded in triaxial extension, but it is also possible that an experimental problem caused the unexpected shear failure of the isotropically compacted sample (a repeat test would be useful).

- Yield points observed during loading at different values of η (at s =300kPa) were consistent with an initial shape of constant suction yield curve in the $q : \bar{p}$ plane that was not inclined (isotropic) for the isotropically compacted samples and inclined (anisotropic) for the anisotropically compacted samples (see Section 6.5.4). In both cases, the yield points fitted well to the anisotropic unsaturated ABBM1 yield curve expression of D'Onza et al. (2011a). When plotted in the $q : p^*$ plane the yield points could be fitted by the anisotropic saturated S-CLAY1 yield curve expression of Wheeler at al. (2003a), by simply replacing p' by p^* (see Section 6.5.4). Plotting in the $q : p^*$ plane (rather than in the $q : \bar{p}$ plane) has the advantage that all yield curves pass through the origin (as reported by Al-Sharrad, 2013).

- Isotropic loading at three different values of suction produced normal compression lines with different locations, when plotted in the $v : ln\bar{p}$ plane (see Section 6.8.1). As expected, the normal compression line for the highest value of suction (s =300kPa) lies above the normal compression lines for the two lower values of suction (s =50kPa and s =0). However the normal compression line at s =50kPa lies below the saturated normal compression line (s =0) when plotted in the $v : ln\bar{p}$ plane. This is explainable (see Section 6.8.1) when it is appreciated that the soil is almost saturated at s =50kPa. This emphasises the problems that occur in attempting to interpret behaviour in terms of net stresses and suction if saturated conditions are approached at a non-zero value of suction. These problems are avoided by use of Bishop's stresses.

8.2.3 Very small strain elastic behaviour

- Bender/extender element results during loading, unloading and re-loading stages show that shear and compression wave velocities (V_s and V_p), and hence very small strain shear modulus G and constrained modulus M, vary in a reversible fashion during unloading and subsequent re-loading, with irreversible changes of V_s and V_p (and hence G and M) occurring during loading to higher stress than previously applied (see Section 6.7.2).

- Bender/extender element test results suggest that, for the compacted speswhite kaolin clay soil under isotropic stress states, increases of shear modulus G are caused by increases of $\bar{p}$ and decreases of v. Combined increases of s and decreases of S_r during drying also lead to increases of G whereas combined decreases of s and increases of S_r during wetting lead to decreases of G (see Sections 6.8.2 and 6.9.2). The experimental evidence on the separate influences of s and S_r on G is, however, contradictory, so that it is unclear whether an increase of S_r at constant s leads to a decrease or increase of G or to no significant effect on G.

- Given the contradictory evidence on the separate influences of s and S_r on G , when interpreted in a framework employing $\bar{p}$, s , v and S_r as unsaturated state variables, it was useful to examine alternative unsaturated stress state parameters (such as the mean Bishop's stress p^*). The experimental measurements of G from saturated and unsaturated tests on isotropically compacted samples loaded to isotropic stress states can all be fitted by a single surface in three-dimensional $p^* : v : G$ space, suggesting that, for an isotropic soil, G can be expressed as a unique function of only p^* and v (see Section 7.1.2), with G increasing as p^* increases or v decreases. Wheeler et al (2003b) suggested that elastic behaviour is governed by Bishop's stresses only (no other stress variables are required), and the results presented here provide the first experimental confirmation of this proposal.

- The experimental results suggest that increases of constrained modulus M are caused by increases of $\bar{p}$, decreases of v and increases of S_r , but the separate influence of a change of s (at constant S_r) is unclear (see Sections 6.8.2 and 6.9.2).

8.2.4 Anisotropy of very small strain elastic behaviour

- BEE measurements suggested development of modest amounts of apparent anisotropy of very small strain elastic behaviour, as represented by values of G_{hh}/G_{hv} and M_h/M_v not equal to 1, even for isotropically compacted samples subjected to isotropic stress states (see Sections 6.4.3 and 6.9.2). This was attributed to non-uniformity of sample state caused by end effects at the boundaries with the base pedestal and top cap. More significant development of anisotropy of very small strain behaviour occurred during anisotropic loading, particularly in triaxial extension at $\eta = -1$ (see Section 6.4.3).

- In all tests (at all values of suction and both on isotropically compacted samples and on anisotropically compacted samples) the variation of the shear modulus

ratio G_{hh}/G_{hv} and constrained modulus ratio M_h/M_v during loading and unloading was approximately reversible (see, for example, Section 6.7.2), even though the individual moduli (G_{hh}, G_{hv}, M_h and M_v) showed irreversible variation during loading and unloading. In addition, there was generally little difference in the variation of G_{hh}/G_{hv} and M_h/M_v between isotropically compacted samples and anisotropically compacted samples (see Sections 6.6.1 and 6.6.2), with the single exception of loading at $\eta = -1$ (see Section 6.6.3) (which may have been due to an experimental problem in Test C producing unexpected premature shear failure). Together, these two observations suggest that the variations of G_{hh}/G_{hv} and M_h/M_v were predominantly attributable to stress-induced anisotropy, rather that strain-induced anisotropy.

- Significant variation of G_{hh}/G_{hv} and M_h/M_v during loading and unloading stages where the value of η was held constant suggests that stress-induced anisotropy of very small strain elastic behaviour may be controlled by the stress ratio η^* (where $\eta^* = q/p^*$ is expressed in terms of Bishop's stresses) rather than being controlled by the stress ratio η (expressed in terms of net stresses) because, unlike η, η^* varied significantly during loading and unloading stages (see Sections 6.7.2 and 7.2).

- Preliminary tests described in Section 5.2 involved 5 different types of anisotropic sample preparation. Three of these produced values of G_{hh}/G_{hv} greater than 1, whereas the other two produced values of G_{hh}/G_{hv} less than 1. In contrast, evidence from the literature suggests that all 5 methods of anisotropic sample preparation would have produced positive inclinations of constant suction yield curves in the $q : \bar{p}$ plane. This suggests that intrinsic (strain-induced) anisotropy of very small strain elastic behaviour and anisotropy of large strain plastic behaviour are controlled by different aspects of soil fabric (each represented by different fabric tensor).

8.3 Proposed expressions for G under isotropic and anisotropic stress states

8.3.1 Isotropically compacted samples under isotropic stress states

- The experimental variation of shear modulus G for isotropic conditions (isotropically compacted samples subjected to isotropic stress states) was interpreted in

terms of conventional unsaturated state variables by comparison with the predictions of Equation 7.1 (based on the proposal of Ng and Yung, 2008), which relates G to $\bar{p}$, s and v. The comparisons showed that Equation 7.1 struggled to represent variation of G under both saturated and unsaturated conditions (with a single set of soil constants) and also struggled to match the observed variation of G during wetting-drying cycles (see Section 7.1.1). An attempt to improve the fitting by adding additional dependence on S_r (Equation 7.2) resulted in little improvement (see Section 7.1.1).

- A new expression, employing an alternative unsaturated stress state variable, was proposed to describe the variation of shear modulus G under saturated and unsaturated conditions. This new expression (Equation 7.4) is relatively simple, relates G to only p^* and v, and converges with a well-established expression for the variation of G under saturated conditions (Equation 2.17) as S_r tends to 1. Comparison with the experimental results (see Section 7.1.3) showed that the proposed new expression (Equation 7.4) provided a better match than the more conventional expression of Equation 7.1, even though Equation 7.4 was simpler (involving one less state variable and one less soil constant).

- The three soil constants in the proposed new expression for G (Equation 7.4) can be determined solely from data from a saturated test. It was shown that determination of the soil constants in Equation 7.4 in this way resulted in excellent prediction of the variation of G under saturated and unsaturated conditions.

- Equation 7.4 was compared with two other proposed expressions from the literature (Equations 2.88 and 2.90), using experimental results from the current study and from three other soils: Po silt (Vassallo at al., 2007a), Zenoz kaolin clay (Biglari et al., 2011, 2012) and Completely Decomposed Tuff (CDT) (Ng & Yung, 2008) (see Sections 7.1.5 and 7.1.6). It was concluded that all three expressions capture the main trends of the experimental results but that the fit of all three expressions to the experimental results of the other three soils was generally not as good as it was for the speswhite kaolin tested in the current study. For all three soils, Equation 7.4 (proposed in this study) provides as good a match to the experimental results as Equations 2.88 and 2.90 from the literature. Given that Equation 7.4 is significantly simpler than the other two expressions (involving fewer state variables and fewer soil constants) and that, unlike the other two expressions, the values of the soil constants within Equation 7.4 can be determined solely from saturated tests, it is clear that Equation 7.4 has substantial advantages over the two expressions from the literature.

8.3.2 Isotropically compacted samples under anisotropic stress states

- Equation 7.4, which describes the variation of G for an isotropic soil, was extended to include the effect of stress-induced anisotropy, to produce Equation 7.8 (see Section 7.2). In Equation 7.8, for the shear modulus G_{ij}, the value of the exponent n_i applied to the Bishop's stresses in the directions of shear wave transmission and polarisation can be different to the value of the exponent n_k applied to the Bishop's stress in the direction of the third mutually perpendicular direction. Regression analysis to the experimental values of G_{hh} and G_{hv} from tests involving loading at different values of η suggested that the best-fit value of n_k was very similar to the best-fit value of n_i. This confirms the suggestion of Jung et al. (2007) from saturated tests (see Section 2.2.3) that n_k is non-zero in clays.

- Equation 7.8 did not fully capture the experimentally observed variations of G_{hh} and G_{hv} during loading at different values of η (see Section 7.2). This suggested it might be necessary to also include the influence of Lode angle (i.e. the intermediate principal stress ratio) on the variations of the various shear moduli under non-isotropic stress states.

8.4 Recommendations for future work

- The test results presented in Chapter 6 provide a substantial experimental database. Although significant interpretation and analysis of these experimental results are presented in Chapters 6 and 7, there is still scope for further analysis and interpretation.

- One aspect of further interpretation would be to include the influence of Lode angle in the proposed expression for shear modulus G_{ij} accounting for stress-induced anisotropy (Equation 7.8), to see whether this would produce improved matching of the experimental results for G_{hh} and G_{hv} during loading at different values of η.

- Another aspect of analysis and interpretation of the experimental results presented in Chapter 6 that would be worth pursuing would be to try to develop an expression relating the variation of constrained modulus M to the various unsaturated state variables. An initial attempt proved unsuccessful (see Section 7.3), but this only involved exploration of a limited range of possible mathematical

functions. The investigation should cover both saturated and unsaturated conditions and should consider both conventional and alternative unsaturated state variables. The initial focus would be on developing an expression for constrained modulus under isotropic conditions and, if this was successful, it could be subsequently extended to account for the influence of stress-induced anisotropy on M.

- In addition to further analysis and interpretation of the experimental results from Chapter 6, further experimental testing would also be useful. Firstly, it would be desirable to perform a repeat of Test C, to see whether the unexpected shear failure in this test was repeatable (indicating a substantial difference in behaviour between isotropically compacted samples and anisotropically compacted samples when loaded in triaxial extension) or whether there was simply an experimental problem in Test C (see Sections 6.5.3 and 6.6.3).

- Even the tests on anisotropically compacted samples reported in Chapter 6 showed only modest amounts of initial anisotropy of very small strain elastic behaviour (as indicated by the initial values of G_{hh}/G_{hv} and M_h/M_v). Subsequently there appeared little further development of strain-induced anisotropy of very small strain elastic behaviour. As a consequence, it was not possible to properly explore the possible influence of initial strain-induced anisotropy and how this strain-induced anisotropy of very small strain elastic behaviour evolved during plastic straining. It would therefore be desirable to perform further experimental testing using an alternative sample preparation technique, which resulted in a more significant initial degree of elastic anisotropy (i.e. initial values of G_{hh}/G_{hv} and M_h/M_v more significantly different to 1). Results from the literature (see Section 5.2.2) clearly show that it is possible to produce soil samples that show greater initial anisotropy of elastic behaviour than was achieved in this programme.

- Given that conditions in the ground often involve a K_0 strain history (zero lateral straining), it would be informative to explore the variation of the various values of G and M (and the ratios G_{hh}/G_{hv} and M_h/M_v) under conditions of zero lateral straining (covering unsaturated and saturated conditions and including loading, unloading, wetting and drying). Given the difficulties of performing BEE testing in an oedometer apparatus (because shear and compression waves would travel faster through the stiff confining ring than through the soil sample), this K_0 testing with BEE measurements could be performed in the double wall triaxial apparatus, using feedback control to maintain conditions of zero lateral strain.

- The experimental research on the very small strain behaviour under unsaturated conditions presented in this project could in the future be extended to cover different soil types. The compacted speswhite kaolin tested in the current project was a non-expansive clay, whereas different patterns of behaviour might be observed in a highly expansive clay or in a coarse-grained soil (i.e. a sand).

- Finally, the improved understanding of very small strain elastic behaviour (e.g. the proposed expression for G of Equation 7.4) could be incorporated within constitutive models for soil behaviour under unsaturated conditions. A comprehensive model would, of course, need to model the entire stiffness degradation behaviour, from the very small strain values of G given by Equation 7.4 to large strain values. This perhaps could be achieved using either a multiple yield surface approach or a bounding surface approach (see Section 2.2.1). If a constitutive model incorporating this improved understanding was implemented within a finite element code, this should lead to improved numerical modelling of geotechnical problems where prediction of ground movements under saturated and unsaturated conditions was required.

Appendix A

Cross-anisotropic elasticity

A.1 Derivation of expression for M_v (Eq. 2.36)

The stress-strain relations of a cross-anisotropic elastic material can be expressed (see Equation 2.33 in Section 2.2.3) as:

$$\begin{bmatrix} \Delta\epsilon_{xx} \\ \Delta\epsilon_{yy} \\ \Delta\epsilon_{zz} \\ \Delta\gamma_{xy} \\ \Delta\gamma_{yz} \\ \Delta\gamma_{zx} \end{bmatrix} = \begin{bmatrix} \frac{1}{E_h} & -\frac{\nu_{hh}}{E_h} & -\frac{\nu_{vh}}{E_v} & & & \\ -\frac{\nu_{hh}}{E_h} & \frac{1}{E_h} & -\frac{\nu_{vh}}{E_v} & & & \\ -\frac{\nu_{vh}}{E_v} & -\frac{\nu_{vh}}{E_v} & \frac{1}{E_v} & & & \\ & & & \frac{1}{G_{hv}} & & \\ & & & & \frac{1}{G_{hv}} & \\ & & & & & \frac{2(1+\nu_{hh})}{E_h} \end{bmatrix} \begin{bmatrix} \Delta\sigma'_{xx} \\ \Delta\sigma'_{yy} \\ \Delta\sigma'_{zz} \\ \Delta\tau_{xy} \\ \Delta\tau_{yz} \\ \Delta\tau_{zx} \end{bmatrix} \tag{A.1}$$

For the conditions of the triaxial test, Equation A.1 gives:

$$\Delta\epsilon_v = \frac{1}{E_v}\Delta\sigma'_v - \frac{2\nu_{vh}}{E_v}\Delta\sigma'_h \tag{A.2}$$

$$\Delta\epsilon_h = \left(\frac{1}{E_h} - \frac{\nu_{hh}}{E_h}\right)\Delta\sigma'_h - \frac{\nu_{vh}}{E_v}\Delta\sigma'_v \tag{A.3}$$

where $\Delta\epsilon_{xx} = \Delta\epsilon_{yy} = \Delta\epsilon_h$, $\Delta\epsilon_{zz} = \Delta\epsilon_v$, $\Delta\sigma_{xx} = \Delta\sigma_{yy} = \Delta\sigma_h$ and $\Delta\sigma_{zz} = \Delta\sigma_v$.

If a stress increment $\Delta\sigma'_v$ is applied in a vertical direction, to produce a corresponding strain increment $\Delta\epsilon_v$ in that direction, while strains are prevented in the horizontal direction (i.e. $\Delta\epsilon_h = 0$). Equation A.3 can be re-arranged to give:

$$\Delta\sigma'_h = \frac{E_h}{E_v}\frac{\nu_{vh}}{(1-\nu_{hh})}\Delta\sigma'_v \tag{A.4}$$

By inserting Equation A.4 into Equation A.2:

$$\Delta\epsilon_v = \left(\frac{1}{E_v} - \frac{2\nu_{vh}}{E_v}\frac{E_h}{E_v}\frac{\nu_{vh}}{(1-\nu_{hh})}\right)\Delta\sigma'_v \tag{A.5}$$

For this situation of no horizontal strain, the vertical constained modulus M_v is defined by:

$$\Delta\epsilon_v = \frac{\Delta\sigma'_v}{M_v} \tag{A.6}$$

Comparing Equation A.5 and A.6:

$$M_v = \frac{E_v}{1 - 2\nu_{vh}\dfrac{E_h}{E_v}\dfrac{\nu_{vh}}{(1-\nu_{hh})}} \tag{A.7}$$

Equation A.7 corresponds to Equation 2.36. This simplifies to the standard result for the constrained modulus of an isotropic elastic material (see Equation 2.8) if $E_v = E_h = E$ and $\nu_{vh} = \nu_{hh} = \nu$.

A.2 Derivation of expression for M_h (Eq. 2.37)

Consider a situation where a stress increment $\Delta\sigma'_{xx}$ is applied in one horizontal direction (x), to produce a corresponding strain increment ($\Delta\epsilon_{xx}$) in that direction, while strains are prevented in the other horizontal direction ($\Delta\epsilon_{yy} = 0$) and in the vertical direction ($\Delta\epsilon_{zz} = 0$). Equation A.1 now gives:

$$\Delta\epsilon_x = \frac{1}{E_h}\Delta\sigma'_x - \frac{\nu_{hh}}{E_h}\Delta\sigma'_y - \frac{\nu_{vh}}{E_v}\Delta\sigma'_z \tag{A.8}$$

$$\Delta\epsilon_y = \frac{-\nu_{hh}}{E_h}\Delta\sigma'_x + \frac{1}{E_h}\Delta\sigma'_y - \frac{\nu_{vh}}{E_v}\Delta\sigma'_z = 0 \tag{A.9}$$

$$\Delta\epsilon_z = \frac{-\nu_{vh}}{E_v}\Delta\sigma'_x - \frac{\nu_{vh}}{E_v}\Delta\sigma'_y + \frac{1}{E_v}\Delta\sigma'_z = 0 \tag{A.10}$$

Solving the two simultaneous equations of Equations A.9 and A.10 for $\Delta\sigma'_y$ and $\Delta\sigma'_z$ gives:

$$\Delta\sigma'_y = \left(\frac{\nu_{hh}E_v + \nu_{vh}^2 E_h}{E_v - \nu_{vh}^2 E_h}\right)\Delta\sigma'_x \tag{A.11}$$

$$\Delta\sigma'_z = \left(\frac{(1+\nu_{hh})\nu_{vh}E_v}{E_v - \nu_{vh}^2 E_h}\right)\Delta\sigma'_x \tag{A.12}$$

Inserting for $\Delta\sigma'_y$ and $\Delta\sigma'_z$ from Equations A.11 and A.12 in Equation A.8 and re-arranging:

$$\Delta\epsilon_x = \left[\frac{(1-\nu_{hh}^2)E_v - 2\nu_{vh}^2(1+\nu_{hh})E_h}{E_h(E_v - \nu_{vh}^2 E_h)}\right]\Delta\sigma'_x \tag{A.13}$$

For this situation of zero strain in the y (horizontal) and z (vertical) directions, the horizontal constrained modulus M_h is defined by:

$$\Delta\epsilon_x = \frac{\Delta\sigma'_x}{M_h} \tag{A.14}$$

Comparing Equations A.13 and A.14:

$$M_h = \frac{E_h(E_v - \nu_{vh}^2 E_h)}{(1-\nu_{hh}^2)E_v - 2\nu_{vh}^2(1+\nu_{hh})E_h} \tag{A.15}$$

Equation A.15 corresponds to Equation 2.37. This simplifies to the standard result for the constrained modulus of an isotropic elastic material (Equation 2.8) if $E_v = E_h = E$

and $\nu_{vh} = \nu_{hh} = \nu$.

A.3 Derivation of expressions for E_h, E_v and ν_{vh} (Eqs. 2.38, 2.39 and 2.40)

One of the five independent elastic moduli of a cross-anisotropic soil ($G_{hv} = G_{hv}$) can be measured directly from one of the measurements provided by the standard arrangement of three BEE pairs. None of the other 4 independent elastic moduli of a cross-anisotropic soil (E_h, E_v, ν_{vh} and ν_{hh}) can be determined from this standard arrangement of three BEE pairs, however if the value of one of them (say ν_{hh}) is known or assumed, then it is possible to determine the values of the other three (say E_h, E_v and ν_{vh}) from the other three parameters measured by the standard arrangement of three BEE pairs (G_{hh}, M_v and M_h).

Equation 2.32 gives:

$$G_{hh} = \frac{E_h}{2(1+\nu_{hh})} \tag{A.16}$$

Re-arranging:

$$E_h = 2(1+\nu_{hh})G_{hh} \tag{A.17}$$

Inserting Equation A.17 into Equation A.7 and re-arranging:

$$(1-\nu_{hh})(M_v - E_v)E_v = 4\nu_{vh}^2(1+\nu_{hh})M_v G_{vhh} \tag{A.18}$$

Similarly, inserting Equation A.17 into Equation A.15:

$$\left[(1-\nu_{hh})M_h - 2G_{hh}\right]E_v = 4\nu_{vh}^2(1+\nu_{hh})(M_h - G_{hh})G_{vhh} \tag{A.19}$$

If G_{hh}, M_v and M_h are known, and ν_{hh} is either known or assumed, Equations A.18 and A.19 form two simultaneous equations in 2 unknowns (E_v and ν_{vh}). Solving:

$$E_v = \frac{(1+\nu_{hh})M_v G_{hh}}{(1-\nu_{hh})(M_h - G_{hh})} \tag{A.20}$$

$$\nu_{vh} = \frac{1}{2(M_h - G_{hh})}\left[\frac{M_v\left((1-\nu_{hh})M_h - 2G_{hh}\right)}{(1-\nu_{hh})}\right]^{1/2} \tag{A.21}$$

Equations A.17, A.20 and A.21 provide expressions for the independent elastic moduli E_h, E_v and ν_{vh} in terms of three of the moduli measured by the standard arrangement of three BEE pairs (G_{hh}, M_v and M_h) and the final independent elastic modulus ν_{hh}, the value of which must be either known independently or assumed. Equations A.17, A.20 and A.21 correspond to Equations 2.38, 2.39 and 2.40.

Appendix B

Derivation of $f(s)$ in Eq. 7.6

As described in Section 2.3.2, it is possible to express matric suction s in terms of the surface tension T_s at the air-water interface and the principal radii of curvature (r_1 and r_2) of this interface:

$$s = u_a - u_w = T_s \left(\frac{1}{r_1} + \frac{1}{r_2} \right) \tag{B.1}$$

where r_1 and r_2 are positive if measured on the air side of the interface.

Figure B.1 shows a meniscus water bridge between two identical spherical soil particles of radius R, as considered by Fisher (1926). In this case, the radius r_1 is measured on the water side of the interface, so Equation B.1 becomes:

$$s = T_s \left(\frac{1}{r_1} - \frac{1}{r_2} \right) \tag{B.2}$$

Assuming, for simplicity, that the profile of the meniscus water bridge seen in Figure B.1 is a circular arc of radius r_1 (as assumed by Fisher, 1926), application of Pythagoras rule shows that r_1 can be related to r_2 and R through:

$$r_1 = \frac{r_2^2}{2(R - r_2)} \tag{B.3}$$

Inserting B.3 into B.2, gives:

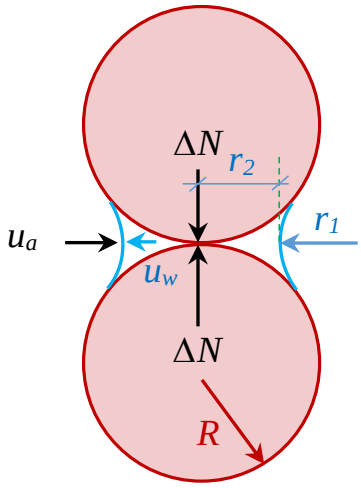

Figure B.1: Additional inter-particle force ΔN at a contact between two ideal spherical soil particles

$$s = \frac{T_s}{R}\left[\frac{2 - 3\left(\frac{r_2}{R}\right)}{\left(\frac{r_2}{R}\right)^2}\right] \tag{B.4}$$

Equation B.4 can be re-arranged to form a quadratic equation in terms of the ratio r_2/R:

$$\left(\frac{r_2}{R}\right)^2 + \frac{3T_s}{sR}\left(\frac{r_2}{R}\right) - \frac{2T_s}{sR} = 0 \tag{B.5}$$

Solving Equation B.5, with only the positive result for r_2/R valid, gives:

$$\frac{r_2}{R} = \frac{3T_s}{2sR}\left[\left(1 + \frac{8sR}{9T_s}\right)^{1/2} - 1\right] \tag{B.6}$$

Following the logic of Fisher (1926), by considering force equilibrium, the additional normal inter-particle force ΔN due to presence of the meniscus water bridge is given by:

$$\Delta N = (u_a - u_w)\pi r_2^2 + T_s 2\pi r_2 = s\pi r_2^2 + T_s 2\pi r_2 \tag{B.7}$$

Replacing s in Equation B.7 with the expression from Equation B.4 and then re-arranging gives an expression for ΔN in terms of the ratio r_2/R:

$$\Delta N = \pi T_s R \left(2 - \frac{r_2}{R}\right) \tag{B.8}$$

Inserting for r_2/R from B.6 into B.8:

$$\Delta N = \pi T_s R \left(2 - \frac{3T_s}{2sR}\left[\left(1 + \frac{8sR}{9T_s}\right)^{1/2} - 1\right]\right) \tag{B.9}$$

As suction tends to zero, Equation B.9 gives:

$$(\Delta N)_{s=0} = \frac{4}{3}\pi T_s R \tag{B.10}$$

The function $f(s)$ in Eq. 7.6 is defined by:

$$f(s) = \frac{\Delta N}{(\Delta N)_{s=0}} \tag{B.11}$$

Therefore inserting for ΔN and $(\Delta N)_{s=0}$ from Equations B.9 and B.10 gives:

$$f(s) = \frac{3}{2} - \frac{9T_s}{8sR}\left[\left(1 + \frac{8sR}{9T_s}\right)^{1/2} - 1\right] \tag{B.12}$$

In order to determine the variation of $f(s)$ with s for any values of soil particle radius R and surface tension T_s, $f(s)$ can be plotted against the non-dimensional parameter sR/T_s, as shown in Figure B.2. The value of $f(s)$ varies from $f(s) = 1$ at $sR/T_s = 0$ to $f(s) = 1.5$ at $sR/T_s = \infty$.

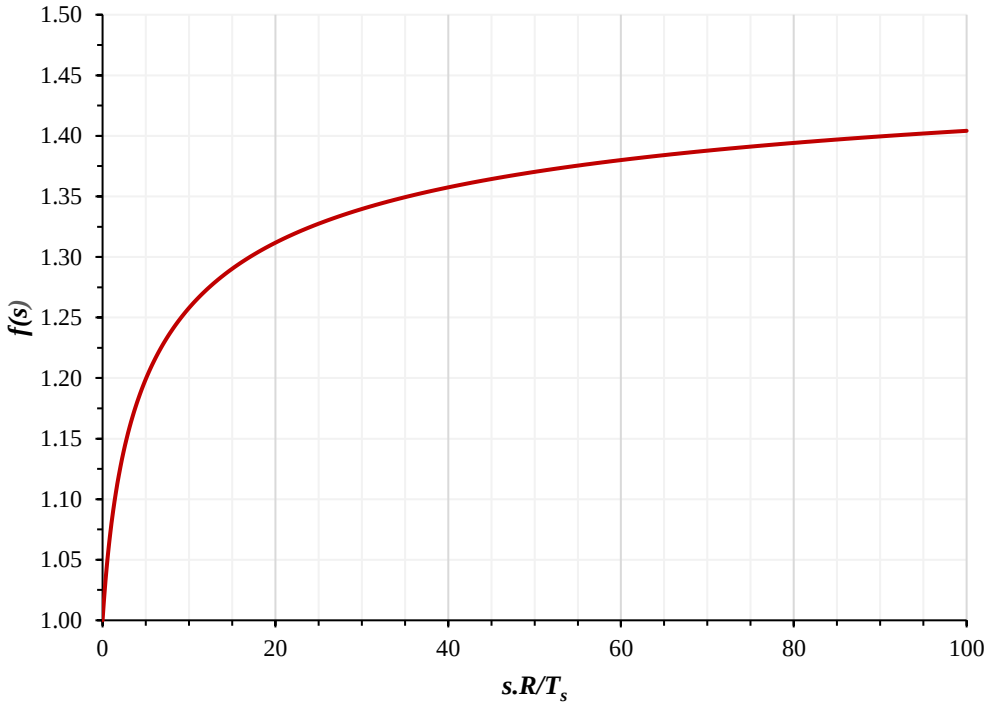

Figure B.2: Variation of $f(s)$ with non-dimensional suction parameter sR/T_s

References

[1] Abbiss, C. P., 1981. Shear wave measurements of the elasticity of the ground. Géotechnique, 31 (1), 721–726.

[2] Ackerley, S. K., Standing, J. R. & Hosseini Kamal, R., 2016. A system for measuring local radial strains in triaxial apparatus. Géotechnique, 66 (6), 515–522.

[3] Ackerley, S. K. Hellings, J. E. & Jardine, R., 1987. Discussion on A new device for measuring local axial strains on triaxial specimens. Géotechnique, 37 (3), 414–415.

[4] Airey, D. &., Mohsin, A. K. M., 2013. Evaluation of shear wave velocity from bender elements using cross-correlation. Geotechnical Testing Journal, 36 (4), 1–9.

[5] Al-Karni, A. A. & Al-Shamrani, M. A., 2000. Study of the effect of soil anisotropy on slope stability using method of slices. Computers and Geotechnics, 26 (2), 83–103.

[6] Al-Sharrad, M. A., 2013. Evolving anisotropy in unsaturated soils: Experimental investigation and constitutive modelling. PhD Thesis, The University of Glasgow, UK.

[7] Al-Tabbaa, A. & Wood, D., 1989. An experimental based "bubble" model for clay. Proceedings of the Third Conference on Numerical Models in Geomechanics, Niagara Falls, Canada, 91–99.

[8] Allen, J. C. & Stokoe, K. H., 1982. Development of resonant column apparatus with anisotropic loading. Geotechnical Engineering Report GR82-28, Civil Engineering Dept., University of Texas at Austin.

[9] Alonso, E. E. Gens, A. & Hight, D. W., 1987. Special problem soils. General Rep. Proc., 9th European Conf. Soil Mechanics and Foundation Engineering, Dublin, 3, 1087–1146.

[10] Alonso, E. E. Gens, A. & Josa, A., 1990. A constitutive model for partially saturated soils. Géotechnique, 40 (3), 405–430.

[11] Alonso, E. E. Vaunat, J. & Gens, A., 1999. Modelling the mechanical behaviour of expansive clays. Engineering Geology, 54 (1-2), 173–183.

[12] Alonso, E.E. Lloret, A. Gens, A. & Yang, D., 1995. Experimental behaviour of highly expansive double-structure clay. Proc. 1st Int. Conf. on Unsaturated Soils, Paris, 1, 11–16.

[13] Alonso, E.E. Vaunat, J. Pereira, J. M. & Olivella, S., 2010. A microstructurally based effective stress for unsaturated soils. Géotechnique, 60 (12), 913–925.

[14] Alramahi, B. Alshibli, K. A. Fratta, D. & Trautwein, S., 2008. A suction-control apparatus for the measurement of P and S wave velocity in Soils. Geotechnical Testing Journal, 31 (1), 12–23.

[15] Anderson, D. G. & Stokoe, K. H., 1978. Shear modulus: a time dependant soil property. Dynamic Geotechnical Testing, ASTM, 654,, 66–90.

[16] Arroyo, M. Muir Wood, D. & Greening, P. D., 2003. Source near-field effects and pulse tests in soil samples. Géotechnique, 53 (3), 337–345.

[17] Arroyo, M. Muir Wood, D. Greening, P. D. Medina, L. & Rio, J., 2006. Effects of sample size on bender-based axial G 0 measurements. Géotechnique, 56 (1), 39–52.

[18] Arulnathan, R. Boulanger, R.W. & Riemer, M., 1998. Analysis of bender element tests. Geotechnical Testing Journal, 21 (2), 120–131.

[19] ASTM, 1997. Testing materials, laboratory determination of pulse velocities and ultrasonic elastic constants of rock. American Society for Testing Materials ASTM, Standard D2845, West Conshhocken, Pa,.

[20] ASTM, 2000. Standard Test Methods for Modulus and Damping of Soils by the Resonant-Column. American Society for Testing Materials ASTM, Standard D4015, West Conshhocken, Pa,.

[21] Atkinson, J. H. & Evans, J. S., 1985. Discussion on: Jardine, R.J., Symes, M.J.R.P., and Burland, J.B., (1984). The measurement of soil stiffness in the triaxial apparatus. Géotechnique, 35 (3), 378–382.

[22] Atkinson, J. H. & Sällfors, G., 1991. Experimental determination of stress-strain-time characteristics in laboratory and in-situ tests. Proc. 10th Eur. Conf. Soil Mech. Florence, 915–956.

[23] Atkinson, J. H. Coop, M. R. Stallebrass, S. E. & Viggiani, G., 1993. Measurement of stiffness of soils and weak rocks in laboratory tests. Proc. 26th Conf. Eng. Grp. Geological Society, Leeds, Cripps et al. (eds), Balkema Rotterdam the Engineering Geology Group, 21–27.

[24] Atkinson, J. H. Richardson, D. & Stallebrass, S. E., 1990. Effect of recent stress history on the stiffness of overconsolidated soil. Géotechnique, 40 (4), 531–540.

[25] Banerjee, P. K. & Yousif, N. B., 1986. A plasticity model for the mechanical behaviour of anisotropically consolidated clay. International Journal for Numerical and Analytical Methods in Geomechanics, 10, 521–541.

[26] Bates, C. R., 1989. Dynamic soil property measurements during triaxial testing. Géotechnique, 39 (4), 721–726.

[27] Bellotti, R. Jamiolkowski, M. Lo Presti, D. C. F. & O'Nell, D. A., 1996. Anisotropy of small strain stiffness in Ticino sand. Géotechnique, 46 (1), 115–131.

[28] Biglari, D'Onofrio, A. M. Mancuso, C. Jafari, M. K. Shafiee, Al. & Ashayeri, I., 2012. Small-strain stiffness of Zenoz kaolin in unsaturated conditions. Canadian Geotechnical Journal, 49, 311–322.

[29] Biglari, M. Mancuso, C., D'Onofrio, A. Jafari, M. K. & Shafiee, A., 2011. Modelling the initial shear stiffness of unsaturated soils as a function of the coupled effects of the void ratio and the degree of saturation. Computers and Geotechnics, 38 (5), 709–720.

[30] Bishop, A. W., 1959. The principle of effective stress. Teknisk Ukeblad, 39, 859–863.

[31] Bishop, A. W. & Blight, G., 1963. Some aspects of effective stress in saturated and partly saturated soils. Géotechnique, 13 (3), 177–197.

[32] Bishop, A.W. & Donald, I., 1961. The experimental study of partly saturated soil in the triaxial apparatus. Proceedings of the 5th International Conference on Soil Mechanics and Foundation Engineering, Paris, 1, 13–21.

[33] Blewett, J. Blewett, I. J. & Woodward, P. K., 1999. Measurement of shear-wave velocity using phase-sensitive detection techniques. Canadian Geotechnical Journal, 36 (5), 934–939.

[34] Blewett, J. Blewett, I. J. & Woodward, P. K., 2000. Phase and amplitude responses associated with the measurement of shear-wave velocity in sand by bender elements. Canadian Geotechnical Journal, 37, 1348–1357.

[35] Bolzon, G. Schrefler, B. A. & Zienkiewicz, O. C., 1996. Elasto-plastic soil constitutive laws generalized to partially saturated states. Géotechnique, 46 (2), 279–289.

[36] Brignoli, E. G. M. Gotti, M. & Stokoe, K. H., 1996. Measheárment of Shear Waves in Laboratory Specimens by Means of Piezoelectric Transducers. Geotechnical Testing Journal, 19 (4), 384–397.

[37] British Standard 1377, 1990. British standard for test of soils for Civil Engineering purposes. London (British Standards Institution).

[38] Brooks, R. H. & Corey, A. T., 1964. Hydraulic properties of porous media. Hydrology Paper No.3, Colorado State Univ., Fort Collins.

[39] Bui, M., 2009. Influence of some particle characteristics on the small strain response of granular materials. PhD thesis, University of Southampton, UK.

[40] Buisson, M. S. R. & Wheeler, S. J., 2000. Inclusion of hydraulic hysteresis in a new elasto-plastic framework for unsaturated soils. Experimental evidence and theoretical approaches in unsaturated soils, Eds. A. Tarantino and C. Mancuso, Rotterdam: Balkema„ 109– 119.

[41] Burland, J., 1989. Ninth Laurits Bjerrum Memorial Lecture: "Small is beautiful" the stiffness of soils at small strains. Canadian Geotechnical Journal, 26 (4), 499–516.

[42] Burland, J. B. & Symes, M., 1982. A simple axial displacement gauge for use in the triaxial apparatus. Géotechnique, 32 (1), 62–65.

[43] Butterfield, R., 1979. A natural compression law for soils (an advance on e-log p'). Géotechnique, 29 (4), 469–480.

[44] Cabarkapa, Z. & Cuccovillo, T., 2005. Automated triaxial apparatus for testing unsaturated soils. Geotechnical Testing Journal, 29 (1), 1–9.

[45] Camacho-Tauta, J. F. Cascante, G. Viana da Fonseca, A. & Santos, J. A., 2015. Time and frequency domain evaluation of bender element systems. Géotechnique, 65 (7), 548–562.

[46] Casagrande, A., 1936. The determination of the pre-consolidation load and its practical significance. Proceedings of the 1st International Conference on Soil Mechanics and Foundation Engineering. Cambridge, 3, 60–64.

[47] Castillo, L. & Rampello, L., 2002. Shear strength and small strain stiffness of a natural clay under general stress conditions. Géotechnique, 52 (8), 547–560.

[48] Chan, K. H. Boonyatee, T. & Mitachi, T., 2010. Effect of bender element installation in clay samples. Géotechnique, 60 (4), 287–291.

[49] Chiu, C. F. & Ng, C. W. W., 2003. A state-dependent elasto-plastic model for saturated and unsaturated soils. Géotechnique, 53 (9), 809–829.

[50] Clayton, C., 2011. Stiffness at small strain: research and practice. Géotechnique, 61 (1), 5–37.

[51] Clayton, C. R. I. & Khatrush, S., 1987. A new device for measuring local axial strains on triaxial specimens. Géotechnique, 36 (4), 593–597.

[52] Clayton, C. R. I. Khatrush, S. A. Bica, A. V. D. & Siddique, A., 1989. The use of Hall effect semiconductors in Geotechnical instrumentation. Geotechnical Testing Journal, 12 (1), 69–76.

[53] Costa-Filho, L. M., 1985. Measurements of axial strains in triaxial tests on London clay. Geotechnical Testing Journal, 8 (1), 3–13.

[54] Cuccovillo, T. & Coop, M. R., 1997. The measurement of local axial strains in triaxial tests using LVDTs. Géotechnique, 47 (1), 167–171.

[55] Cui, Y. J. & Delage, P., 1996. Yielding and plastic behaviour of an unsaturated compacted silt. Géotechnique, 46 (2), 291–311.

[56] Dafalias, Y., 1987. Anisotropic critical state clay plasticity model. 2nd International Conference on Constitutive Laws for Engineering Materials. Tucson, Arizona, 1, 513–521.

[57] Dafalias, Y. F. & Herrmnn, L. R., 1982. Bounding surface formulation of soil plasticity. Soil Mechanics -Transient and Cyclic Loads, (London)„ 253–282.

[58] Dangla, P. Malinsky, L. & Coussy, O., 1997. Plasticity and imbibition-drainage curves for unsaturated soils: a unified approach. Proc. 6th Int. Symp. Numer. Models Geomech., VI, Montreal„ 141–146.

[59] Davies, M. C. R. & Newson, T., 1993. A critical state constitutive model for anisotropic soils. Proceedings of the Wroth memorial Symposium. Oxford, Thomas Telford, London„ 219–229.

[60] Delage, P. & Cui, Y. J., 2008. An evaluation of the osmotic method of controlling suction. Geomechanics and Geoengineering, 3 (1), 1–11.

[61] Delage, P. Suraj De Silva, G. P. R. & Vicol, T., 1992. Suction controlled testing of non saturated soils with an osmotic consolidometer. 7th Int. Conf. Expansive Soils, Dallas„ 206–211.

[62] Della Vecchia, G. Jommi, C. & Romero, E., 2012. A fully coupled elastic-plastic hydromechanical model for compacted soils accounting for clay activity. International Journal for Numerical and Analytical Methods in Geomechanics, 10, 1002–1116.

[63] Di Benedetto, H. Geoffroy, H. & Sauzéat, C., 1999. Sand behaviour in very small to medium strain domain,. Proceedings of the 2nd Int. Conference on Pre-failure Deformation Characteristics of Geomaterials. Eds, Jamiolkowski, Lancellotta and Lo Presti, Balkema, Rotterdam,, 89–96.

[64] Diaz-Rodriguez, J. A. Leroueil, S. & Aleman, J. D., 1992. Yielding of Mexico city clay and other natural clays. Journal of Geotechnical Engineering, ASCE, 118 (7), 981–995.

[65] Dobrin, M. B. & Savit, C. H., 1988. Introduction to geophysical prospecting. McGraw-Hill.

[66] Dong, Y. Lu, N. & McCartney, J. S., 2016. Unified model for small strain shear modulus of variably saturated soil. Journal of Geotechnical and Geoenvironmental Engineering, ASCE,, 1–10.

[67] D'Onza, F., Gallipoli, D., Wheeler, S., Casini, F., Vaunat, J., Khalili, N., Laloui, L., Mancuso, C., Mašín, D., Nuth, M., Pereira, J., Vassallo, R., 2011. b. Benchmark of constitutive models for unsaturated soils. Géotechnique 61 (4), 283–302.

[68] D'Onza, F. Gallipoli, D. & Wheeler, S. J., 2011. a. Effect of anisotropy on the prediction of unsaturated soil response under triaxial and oedometric conditions. Proceedings of the 5th International Conference on Unsaturated Soils. Barcelona, Spain, 2, 787–794.

[69] D'Onza, F. Wheeler, S. J. Gallipoli, D. Barrera Bucio, M. Hofmanne, M. Lloret-Cabot, M. Lloret Morancho, A. Mancuso, C. Pereira, J. M. Romero, M. E. Sánchez, M. Solowski, W. Tarantino, A. Toll, D. G. & Vassallo, R., 2015. Benchmarking selection of parameter values for the Barcelona Basic Model. Engineering Geology, 196, 99–118.

[70] Duffy, S. M. Wheeler, S. J. & Bennell, J., 1994. Shear modulus of Kaolin containing Methane bubbles. Journal of Geotechnical Engineering, ASCE, 120 (5), 781–796.

[71] Dyvik, R. & Madshus, C., 1985. Laboratory measurements of Gmax using bender elements. In: Advances in the Art of Testing Soils Under Cyclic Conditions. (Proceedings of a session Sponsored by the Geotechnical Engineering Division in Conjunction with the ASCE Convention in Detroit, Michigan.) ASCE, New York,, 186–196.

[72] Dyvik, R. & Olsen, T. S., 1989. Gmax measured in oedometer and DSS tests using bender elements. Proceedings of the Twelfth International Conference on Soil Mechanics and Foundation Engineering, Rio de Janeiro, 1, 39–42.

[73] Escario, V. & Saez, J., 1986. The Shear Strength of Partly Saturated Soils. Géotechnique, 36 (3), 453–456.

[74] Eseller-Bayat, E. Gokyer, S. Yegian, M. K. Deniz, R. O. & Alshawabkeh, A., 2013. Bender elements and bending disks for measurement of shear and compression wave velocities in large fully and partially saturated sand specimens. Geotechnical Testing Journal, 36 (2), 1–8.

[75] Fam, M. & Santamarina, C., 1995. Study of geoprocesses with complementary mechanical and electromagnetic wave measurements in an oedometer. Geotechnical Testing Journal, 18 (3), 307–314.

[76] Fam, M. A. Cascante, G. & Dusseault, M. B., 2002. Large and small strain properties of sands subjected to local void increase. ournal of Geotechnical and Geoenvironmental Engineering, ASCE, 128 (12), 1018–1025.

[77] Ferreira, C., 2008. The use of seismic Wave Velocities in the Measurement of Stiffness of a Residual Soil. PhD thesis, University of Porto, Portugal.

[78] Ferreira, C. Viana da Fonseca, A. & Santos, J., 2007. Comparison of simultaneous bender elements and resonant column tests on Porto residual soil, Soil Stress-Strain Behavior: Measurement, Modeling and Analysis. A Collection of Papers of the Geotechnical Symposium in Rome, Eds.: Ling, Callisto, Leshchinsky & Koseki, Springer, 523–535.

[79] Fioravante, V. & Capoferri, R., 2001. On the use of multi-directional piezoelectric transducers in triaxial testing. Geotechnical Testing Journal, 24 (3), 243–255.

[80] Fisher, R. A., 1926. On the capillary forces in an ideal soil: correction of formulae given by W. B. Haines. Journal of Agricultural Science, 16 (3), 492–505.

[81] Fredlund, D., 1975. A diffused air indicator for unsaturated soils. Canadian Geotechnical Journal, 12, 533–539.

[82] Fredlund, D., Xing, A., 1994. Equations for the soil-water characteristic curve. Canadian Geotechnical Journal, 31 (6), 1026–1026.

[83] Fredlund, D. G. & Morgenstern, N. R., 1977. Stress State Variables for Saturated and Unsaturated Soils. Journal of the Geotechnical Engineering Division, ASCE, 103 (5) , 447-466.

[84] Fredlund, D. G. Morgenstern, N. R. & Widger, R. A., 1978. The shear strength of unsaturated soils. Canadian Geotechnical Journal, 15, 316–321.

[85] Fredlund, D. G. Rahardjo, H. & Gan, J. K. M., 1987. Nonlinearity of strength envelope for unsaturated soils. Proceedings of the 6th International Conference on Expansive Soils. New Delhi, India„ 49–54.

[86] Gachet, P. Geiser, F. Laloui, L. & Vulliet, L., 2007. Automated Digital Image Processing for Volume Change Measurement in Triaxial Cells. Geotechnical Testing Journal, 30 (2), 98–103.

[87] Gallipoli, D. Gens, A. Sharma, R. & Vaunat, J., 2003. b. An elasto-plastic model for unsaturated soil incorporating the effects of suction and degree of saturation on mechanical behaviour. Géotechnique, 53 (1), 123–135.

[88] Gallipoli, D. Wheeler, S. & Karstunen, M., 2003. a. Modelling the variation of degree of saturation in a deformable unsaturated soil. Géotechnique, 53 (1), 105–112.

[89] Gan, J. K. M. & Fredlund, D. G., 1988. Multistage direct shear testing of unsaturated soils. Geotechnical Testing Journal, 11 (2), 132–138.

[90] Gens, A., 1996. Constitutive laws. Modern issues in non-saturated soils. Wien: Springer-Verlag„ 129–158.

[91] Gens, A. Sanchez, M. & Sheng, D., 2006. On constitutive modelling of unsaturated soils. Acta Geotachnica, 1, 137–147.

[92] Geoffroy, H. Di Benedetto, H. Duttine, A. & Sauzéat, C., 2003. Dynamic and cyclic loadings on sands: results and modelling for general stress strain conditions. Proceedings of Deformation Characteristics of Geomaterials, Lyon, France, Lyon, France. Balkema„ 353–363.

[93] Goto, S. Tatsuoka, F. Shibuya, S. Kim, Y. S. & Sato, T., 1991. A simple gauge for local small strain measurements in the laboratory. Soils and Foundations, 31 (1), 169–180.

[94] Graham, J. & Houlsby, G. T., 1983. Anisotropic elasticity of a natural clay. Géotechnique, 33 (3), 354–354.

[95] Graham, J. Noonan, M. L. & Lew, K. V., 1983. Yield states and stress-strain relationships in a natural plastic clay. Canadian Geotechnical Journal, 20 (3), 502–516.

[96] Grammatikopoulou, A. Schroeder, F. C. Gasparre, A. Kovacevic, N. & Germano, V., 2014. The influence of stiffness anisotropy on the behaviour of a stiff natural clay. Geotechnical and Geological Engineering, 32, 1377–1387.

[97] Greening, P. D. & Nash, D. F. T., 2004. Frequency domain determinantion of Go using bender elements. Geotechnical Testing Journal, 27 (3), 1–7.

[98] Grolewski, B. & Zeng, X., 2001. Measurement of Gmax and Ko of saturated clay using bender elements. Proceedings of the Fourth International Conference on Recent Advances in Geotechnical Earthquake Engineering and Soil Dynamics, San Diego, California, No. 1.47.

[99] Hall, J. R. & Richart, F. E., 1963. Dissipation of elastic wave energy in granular soils. Journal of Soil Mechanics and Foundation Division, ASCE, 89 (SM6), 27–56.

[100] Han, Z., Vanapalli, S. K., 2016. Stiffness and shear strength of unsaturated soils in relation to soil-water characteristic curve. Géotechnique, (March), 1–21.

[101] Hanks, R.J. Klute, A. & Bresler, E., 1969. A numerical method for estimating infiltration redistribution, drainage, and evaporation of water from soil. Water Resources Research, 13, 992–998.

[102] Hardin, B., 1978. The nature of stress-strain behaviour of soils. Proceedings of the Earthquake Engineering and Soil Dynamics Conference ASCE, Pasadena, California, 1, 3–39.

[103] Hardin, B. O. & Black, W. L., 1966. Sand stiffness under various triaxial stresses. Journal of Soil Mechanics and Foundation Division, ASCE, 92 (SM2), 27–42.

[104] Hardin, B. O. & Black, W. L., 1968. Vibration modulus of normally consolidated clays. Journal of Soil Mechanics and Foundation Division, ASCE, 94 (SM2), 353–369.

[105] Hardin, B. O. & Black, W. L., 1969. Closure to: Vibration modulus of normally consolidated clays. J. Journal of Soil Mechanics and Foundation Division, ASCE, 95 (6), 1531–1537.

[106] Hardin, B.O. & Blandford, G., 1989. Elasticity of articulate materials. Journal of Geotechnical Engineering, ASCE, 115 (6), 788–805.

[107] Hardin, B.O. & Richart, F., 1963. Elastic wave velocities in granular soils. Journal of Soil Mechanics and Foundation Division, ASCE, 89 (1), 33–65.

[108] Heitor, A. Indraratna, B. &., Rujikiatkamjorn, C., 2013. Laboratory study of small-strain behavior of a compacted silty sand. Canadian Geotechnical Journal, 50 (2), 179–188.

[109] Hilf, J., 1956. An investigation of pore-water pressure in compacted cohesive soils. Tech. Memo. 654. U.S. Bureau of reclamation, Design and construction Div. Denver, USA.

[110] Hird, C. C. & Yung, P., 1987. Discussion on: A new device for measuring local axial strains on triaxial specimens. Géotechnique, 37 (3), 413–417.

[111] Hird, C. C. & Yung, P., 1989. The use of Proximity transducers for local strain measurements in triaxial tests. Geotechnical Testing Journal, 12 (4), 292–296.

[112] Hoffman, K. Varuso, R. & Fratta, D., 2006. The use of low-cost MEMS accelerometers in near-surface travel-time tomography. GeoCongress Conference, Atlanta, GA„ 1–6.

[113] Hoffmann, C. Romero, E. & Alonso, E., 2005. Combining different suction controlled techniques to study the volume change response of expansive clays. International symposium on Advanced Experimental Unsaturated Soil Mechanics-EXPERUS„ 61–67.

[114] Houlsby, G. T., 1997. The work input to an unsaturated granular material. Géotechnique, 47 (1), 193–196.

[115] Houlsby, G. T. & Wroth, C. P., 1991. The variation of shear modulus of a clay with pressure and overconsolidation ratio.

[116] Hu, R. Chen, Y. F. Liu, H. H. & Zhou, C. B., 2013. A water retention curve and unsaturated hydraulic conductivity model for deformable soils: consideration of the change in pore-size distribution. Géotechnique, 63 (16), 1389–1405.

[117] Huang, A. B. Huang, Y. T. & Ho, F. J., 2005. Assessment of liquefaction potential for a silty sand in Central Western Taiwan. Proceedings of 16th ICSMGE, Osaka., 2653–2657.

[118] IBM, 2013. IBM SPSS Regression 22.
URL http://www.sussex.ac.uk/its/pdfs/SPSS{_}Regression{_}22.pdf

[119] Ismail, M. A. & Hourani, Y., 2003. An innovative facility to measure shear-wave velocity in centrifuge and 1-g models,. Proceedings of Deformation Characteristics of Geomaterials, Lyon, France, Balkema„ 21–29.

[120] Jamiolkowski, M. Lancellotta, R. & Lo Presti, D., 1995. Remarks on the stiffness at small strains of six Italian clays. Pre-failure Deformation of Geomaterials. Eds: Shibuya, Mitachi & Miura . Balkema, Rotterdam,, 817–836.

[121] Jamiolkowski, M. Leroueil, S. & Lo Presti, D., 1991. Design parameters from theory to practice. Theme Lecture. Proceedings of Geo-Coast, Yokohama, 2, 877–917.

[122] Jardine, R. J. Potts, D. M. John, H. D. & Hight, D. W., 1991. Some practical applications of a non-linear ground model. Xth ECSMFE, 1 Florence,, 223–228.

[123] Jardine, R. J. Symes, M. J. & Burland, J. B., 1984. The measurement of soil stiffness triaxial apparatus. Géotechnique, 34 (3), 323–340.

[124] Jennings, J. E. B. & Burland, J., 1962. Limitations to the Use of Effective Stresses in Partly Saturated Soils. Géotechnique, 12 (2), 125 –144.

[125] Jommi, C., 2000. Remarks on the constitutive modelling of unsaturated soils. Proceedings of the international workshop on unsaturated soils, Trento,, 139–153.

[126] Jommi, C. & Di Prisco, C., 1994. Un semplice approccio teorico per la modellazione del comportamento meccanico dei terreni granulari parzialmente saturi (in Italian). In Atti Convegno sul Tema: Ruolo deiFluidi nei Problemi di Ingegneria Geotecnica, Mondovi,, 167–188.

[127] Josa, A., 1988. Un modelo eslastoplirstico para suelos no saturados. PhD Thesis. Universitat Politecnica de Catalunya, Barcelona.

[128] Josa, A. Balmaceda, A. Gens, A. & Alonso, E. E., 1992. An elasto-plastic model for partially saturated soils exhibiting a maximum of collapse. Proc. 3rd International Conf. Computational Plasticity, Barcelona, 1, 815–826.

[129] Jovcic, V., 1997. The measurement and interpretation of small strain stiffness of soils. PhD thesis, City University London, UK.

[130] Jovicic, V. & Coop, M., 1998. The measurement of stiffness anisotropy in clays with bender element tests in triaxial apparatus. Geotechnical Testing Journal, 21 (1), 3–10.

[131] Jovicic, V. Coop, M. R. & Simic, M., 1996. Objective criteria for determining Gmax from bender element tests. Géotechnique, 46 (2), 357–362.

[132] Jung, Y. Cho, W. &. F. R. J., 2007. Defining yield from bender element measurements in triaxial stress probe experiments. Journal of Geotechnical and Geoenvironmental Engineering ASCE, 133 (7), 841–849.

[133] Kang, X., Kang, G. C., Bate, B., 2014. Measurement of stiffness anisotropy in kaolinite using bender element tests in a floating wall consolidometer. Geotechnical Testing Journal, 37 (5), 1–15.

[134] Karstunen, M. & Koskinen, M., 2008. Plastic Anisotropy of Soft Reconstituted Clays. Canadian Geotechnical Journal, 45 (3), 314–328.

[135] Kassiff, G. & Ben Shalom, A., 1971. Experimental relationship between swell pressure and suction. Géotechnique, 21 (3), 245–255.

[136] Kato, S., 1998. Deformation characteristics of a compacted clay in collapse under isotropic stress state and its shear deformation after collapse. Journal of the Japan Society of Civil Engineers [In Japanese], (III-43), 596, 271–281.

[137] Kawaguchi, T. Mitachi, T. & Shibuya, S., 2001. Evaluation of shear wave travel time in laboratory bender element test. 15th International Conference on Soil Mechanics and Geotechnical Gngineering, Istanbul, Turkey, 1, 155–158.

[138] Khalili, N. & Khabbaz, M. H., 1998. A unique relationship for X for the determination of shear strength of unsaturated soils. Géotechnique, 48 (5), 681–688.

[139] Khalili, N. Habte, M. A. & Zargarbashi, S., 2008. A fully coupled flow deformation model for cyclic analysis of unsaturated soils, including hydraulic and mechanical hystresis. Computers and Geotechnics, 35 (6), 872–889.

[140] Khosravi, A. & McCartney, J. S., 2012. Impact of Hydraulic Hysteresis on the Small Strain Shear Modulus of Low Plasticity Soils. Journal of Geotechnical and Geoenvironmental Engineering, ASCE, (November), 445.

[141] Kim, T. & Finno, R. J., 2012. Anisotropy Evolution and Irrecoverable Deformation in Triaxial Stress Probes. Journal of Geotechnical and Geoenvironmental Engineering, ASCE, 138 (2), 155–165.

[142] Kohgo, Y. Nakano, M. & Miyazaki, T., 1993. Theoretical Aspects of Constitutive Modelling for Unsaturated Soils. Soils and Foundations, 33 (4), 49–63.

[143] Korhonen, K. H. & Lojander, M., 1987. Yielding of Perno clay. Proceedings of the 2nd International Conference on Constitutive Laws for Engineering Materials. Tucson, Arizona, 2, 1249–1255.

[144] Kumar, J. & Madhusudhan, B. N., 2010. A note on the measurement of travel times using bender and extender elements. Soil Dynamics and Earthquake Engineering, 30 (7), 630–634.

[145] Kuwano, R. Connolly, T. M. & Kuwano, J., 1999. Shear stiffness anisotropy measured by multidirectional bender element transducers. Proc., Int. Symp. on Pre-Failure Deformation of Geomaterials. Eds: Jamiolkowski et al., 1 (205-212).

[146] Lambe, T. W. & Whitman, R. V., 1979. Soil Mechanics, SI version. Wiley.

[147] Lawrence, F., 1963. Propagation of ultrasonic waves through sand. Research report R63- 8. Massachusetts Institute of Technology, Cambridge, MA.

[148] Lawrence, F., 1965. Ultrasonic shear wave velocity in sand and clay. Research report R65-05, Soil Publication No. 175. Massachusetts Institute of Technology, Cambridge, MA.

[149] Lee, J. & Santamarina, C., 2005. Bender Elements: Performance and Signal Interpretation. Journal of Geotechnical and Geoenvironmental Engineering, ASCE, 131 (9), 1063–1070.

[150] Lee, J. & Santamarina, C., 2006. Discussion "Measuring Shear Wave Velocity Using Bender Elements" By Leong,E.C., Yeo,S.H.,and Rahardjo,H. Geotechnical Testing Journal, 29 (5), 1–5.

[151] Lee, K. M. & Rowe, R., 1989. Deformation caused by surface loading and tunnelling: the role of elastic anisotropy. Géotechnique, 39 (1), 125–14.

[152] Leong, E. C. & Rahardjo, H., 1997. Review of soil water characteristic curve equations. ournal of Geotechnical and Geoenvironmental Engineering, ASCE, 123 (12), 1106–1117.

[153] Leong, E. C. Cahyadi, J. &., Rahardjo, H., 2009. Measuring shear and compression wave velocities of soil using bender extender elements. Canadian Geotechnical Journal, 46 (7), 792–812.

[154] Leong, E. C. Cahyadi, J. & Rahardjo, H., 2006. Stiffness of a compacted residual soil. Unsaturated soils: Geotechnical Special Publications, 147, Eds Gerald A. Miller, Claudia E. Zapata, Sandra L. Houston, and Delwyn G. Fredlund,, 1168–1180.

[155] Leong, E. C. Yeo, S. H. & Rahardjo, H., 2005. Measuring shear wave velocity using bender elements. Geotechnical Testing Journal, 28 (5), 488–498.

[156] Lings, M. L., 2001. Drained and undrained anisotropic elastic stiffness parameters. Géotechnique, 51 (6), 555–565.

[157] Lings, M. L. & Greening, P. D., 2001. A novel bender / extender element for soil testing. Géotechnique, 51 (8), 713–717.

[158] Lloret-cabot, M., Wheeler, S. J., Pineda, J. A., Sheng, D., Gens, A., 2014. Relative performance of teo unsaturated soil models using different constitutive variables. Canadian Geotechnical Journal, 51, 1–15.

[159] Lloret-Cabot, M. Sanchez, M. & Wheeler, S. J., 2013. Formulation of a three-dimentional constitutive model for unsaturated soils incorporating mechanical-water retention coupling. International Journal for Numerical and Analytical Methods in Geomechanics, 37 (17), 3008–3035.

[160] Lo Presti, D., 1995. General report: Measurement of shear deformation of geomaterials in the laboratory. Pre-failure Deformation of Geomaterials. Shibuya, Mitachi & Miura (eds). Balkema, Rotterdam,, 1067–1088.

[161] Lo Presti, D. C. F. Pallara, O. Lancellotta, R. Armandi, M. & Maniscalco, R., 1993. Monotonic and cyclic loading behaviour of two sands at small strains. Geotechnical Testing Journal, 16 (4), 409–424.

[162] Loret, B. & Khalili, N., 2000. A three phase model for unsaturated soils. International Journal for Numerical and Analytical Methods of Geomechanics, 24 (11), 893–927.

[163] Lourenço, S. D N. Gallipoli, D. Augarde, C. E. Toll, D. G. & Evans, F. D., 2011. Towards a Tensiometer Based Suction Control System for Laboratory Testing of Unsaturated Soils. Geotechnical Testing Journal, 34 (6), 755–764.

[164] Love, A., 1927. A treatise on the Mathematical theory of elasticity. University Press, Cambridge.

[165] Mair, R. J., 1993. Developments in geotechnical engineering research: applications to tunnels and deep excavations. Unwin Memorial Lecture , Proc. Institution of Civil Engineers Civ. Engng 93, 27–41.

[166] Mancuso, C. Simonelli, A.L. & Vinale, F., 1989. Numerical analysis of in-situ S-wave measurements. In Proceedings of the 12th International Conference on Soil Mechanics and Foundation Engineering, Rio de Janeiro, 3, 277–280.

[167] Mancuso, C. Vassallo, R. & D'Onofrio, A., 2002. Small strain behavior of a silty sand in controlled-suction resonant column torsional shear tests. Canadian Geotechnical Journal, 39 (1), 22–31.

[168] Marinho, E. A. M. Chandler, R. J. & Crilly, M. S., 1995. Stiffness measurements on an high plasticity clay using bender elements. Unsaturated Soils: Advances in Geo-Engineering, Proceedings of the First International Conference on Unsaturated Soils, Paris, France, 1, 535–539.

[169] Masin, D. & Khalili, N., 2008. A hypoplastic model for mechanical response of unsaturated soils. International Journal for Numerical and Analytical Methods of Geomechanics, 32 (15), 1903–1926.

[170] Matyas, E. L. & Radhakrishna, H. S., 1968. Volume change characteristics of partially saturated soils. Géotechnique, 18, 432–448.

[171] McDowell, G. R. & Bolton, M. D., 2001. Micro mechanics of elastic soil. Soils and Foundations, 41 (6), 147–152.

[172] Mendoza, C. E. & Colmenares, J. E., 2006. Influence of the suction on the stiffness at very small strains. ASCE, Proc., of the 4th Int. Conf. on Unsaturated Soils, Unsaturated Soils,, 529–540.

[173] Mitaritonna, G. Amorosi, A. &., Cotecchia, F., 2014. Experimental investigation of the evolution of elastic stiffness anisotropy in a clayey soil. Géotechnique, (6), 1–13.

[174] Mohsin, A. K. M. & Airey, D. W., 2003. Automating Gmax measurements in triaxial tests,. Proceedings of the 3rd International Symposium on Deformation Characteristics of Geomaterials, Lyon, France,, 73–80.

[175] Moore, W. M., 1966. Effects of variations in Poisson's ratio on soil triaxial testing. Highway Research Record, (108), 19–30.

[176] Mroz, Z. Norris, V. & Zienkiewicz, O. C., 1979. Application of an anisotropic hardening model in the analysis of elasto-plastic deformation of soils. Géotechnique, 29 (1), 1–34.

[177] Mualem, Y., 1974. A conceptual model of hysteresis. Water Resources Research, 10, 514–520.

[178] Nakagawa, K. Soga, K. & Mitchell, J., 1997. Observation of Biot compressional wave of the second kind in granular soils. Géotechnique, 47 (1), 133–147.

[179] Nash, D. F. T. Pennington, D. S. & Lings, M. L., 2000. Anisotropic stiffness parameters and their measurement in a stiff natural clay. Géotechnique, 50 (2), 109–125.

[180] Nash, D. Sukolrat, J. Greening, P. & Benahmed, N., 2007. Comparison of shear wave velocity measurements in different materials using time and frequency domain techniques. Rivista Italiana di Geotechnica, (2), 56–68.

[181] Ng, C. W. W. & Leung, E. H. Y., 2007. Determination of shear-wave velocities and shear moduli of completely decomposed tuff. Journal of Geotechnical and Geoenvironmental Engineering, ASCE, 133, 630–640.

[182] Ng, C. W. W. & Yung, S. Y., 2008. Determination of the anisotropic shear stiffness of an unsaturated decomposed soil. Géotechnique, 58 (1), 23–35.

[183] Ng, C. W. W. Leung, E. H. Y. & Lau, C. K., 2004. Inherent anisotropic stiffness of weathered geomaterial and its influence on ground deformations around deep excavations. Canadian Geotechnical Journal, 41 (1), 12–24.

[184] Ng, C. W. W. Xu, J. & Yung, S. Y., 2009. Effects of wetting-drying and stress ratio on anisotropic stiffness of an unsaturated soil at very small strains. Canadian Geotechnical Journal, 46 (9), 1062–1076.

[185] Ng, C. W. W. Zhan, L. T. & Cui, Y. J., 2002. A New Simple System for Measuring Volume Changes in Unsaturated Soils. Canadian Geotechnical Journal, 39, 757–764.

[186] Nuth, M. & Laloui, L., 2008. Effective stress concept in unsaturated soils: clarification and validation of a unified framework. International Journal for Numerical and Analytical Methods in Geomechanics, 32 (7), 771–801.

[187] Nyunt, T. Leong, E. & Rahardjo, H., 2011. Strength and Small-Strain Stiffness Characteristics of Unsaturated Sand. Geotechnical Testing Journal, 34 (5), 551–561.

[188] Oztoprak, S. & Bolton, M. D., 2013. Stiffness of sands through a laboratory test database. Géotechnique, 63 (1), 54–70.

[189] Pennington, D., 1999. The anisotropic small strain stiffness of Cambridge Gault clay. PhD thesis, University of Bristol, UK.

[190] Pennington, D. S. Nash, D. F. T. & Lings, M. L., 2001. Horizontally-mounted bender elements for measuring anisotropic shear moduli in triaxial clay specimens. Geotechnical Testing Journal, 24 (2), 133–144.

[191] Pereira, J. M. Wong, H. Dubujet, P. & Dangla, P., 2005. Adoption of existing behaviour models to unsaturated states: application to CJS model. International Journal for Numerical and Analytical Methods in Geomechanics, 29 (1), 1127–1155.

[192] Philip, J., 1964. Similarity hypothesis for capillary hysteresis in porous materials. Journal of Geophysical Research, 69, 1553–1562.

[193] Pickering, D. J., 1970. Anisotropic elastic parameters for soil. Géotechnique, 20 (3), 271–276.

[194] Pierce, S. J. & Charlie, W. A., 1990. High-intensity compressive stress wave propagation through unsaturated sands. A final report, Engineering Research Division, Air force Engineering & Service Centre, Florida„ 32403.

[195] Puzrin, A. M. & Burland, J. B., 1998. Non-linear model of small-strain behaviour of soils. Géotechnique, 48 (2), 217–213.

[196] Rampello, S. Viggiani, G. M. & Amorosi, A., 1997. Small-strain stiffness of reconstituted clay compressed along constant triaxial effective stress ratio paths. Géotechnique, 47 (3), 475–489.

[197] Raveendiraraj, A., 2009. Coupling of mechanical behaviour and water retention behaviour in unsaturated soils. PhD thesis, University of Glasgow, UK.

[198] Raymond, G. P., 1970. Discussion on stress and displacements in a cross-anisotropic soil. Géotechnique, 20 (4), 456–458.

[199] Rees, S. Le Compte, A. & Snelling, K., 2013. A new tool for the automated travel time analyses of bender element tests. 18th ICSMGE, Paris, France 4, 2843–2846.

[200] Ridley, A. M. & Burland, J. B., 1993. A new instrument for the measurement of soil moisture suction. Géotechnique, 43 (2), 321–324.

[201] Rojas, J. C. Gallipoli, D. & Wheeler, S. J., 2012. Image analysis of strains in soils subjected to wetting and drying. Geotechnical Testing Journal, 35 (1), 60–73.

[202] Romero, E., 1999. Characterisation and thermo-hydro-mechanical behaviour of unsaturated Boom clay: an experimental study. PhD thesis, Universitat Politècnica de Catalunya, Spain.

[203] Romero, E. Lloret, F. Gen, J. A. & Alonso, E. E., 1997. A new suction and temperature controlled triaxial apparatus. Proceedings of the 14th International Conference on Soil Mechanics and Foundation Engineering, Hamburg, 1, 185–188.

[204] Roscoe, K. H. & Burland, J. B., 1968. On the generalised stress-strain behaviour of wet clay. Cambridge University Press, Cambridge, Engineering Plasticity„ 535–609.

[205] Rosler, S. K., 1979. Anisotropic shear modulus due to stress anisotropy. JFredlund, D.G. & Morgenstern, N.R., 1977. Stress state variables for unsaturated soils, 105 (7), 871–880.

[206] Rowe, P. W. & Barden, L., 1964. The importance of free-ends in the triaxial test. Journal of Soil Mechanics and Foundation Engineering Division, ASCE, 90, 1–27.

[207] Salgado, R. Bandini, P. & Karim, A., 2000. Shear strength and stiffness of silty sand. Journal of Geotechnical and Geoenvironmental Engineering, ASCE, 126, 451–462.

[208] Sanchez-Salinero, I. Roesset, J. M. & Stokoe, K. H., 1986. Analytical studies of body wave propagation and attenuation. Geotechnical report No GR86-15, Civil Engineering Department, University of Texas at Austin.

[209] Santagata, M. Germaine, J. T. & Ladd, C. C., 2005. Factors affecting the initial stiffness of cohesive soils. Journal Geotechnical and Geoenvironmental Engineering, ASCE, 131 (4), 430–441.

[210] Sawangsuriya, A., Edil, T. B. &., Bosscher, P. J., 2008. Modulus-suction-moisture relationship for compacted soils. Canadian Geotechnical Journal, 45 (7), 973–983.

[211] Sawangsuriya, A. Edil, T. B. &., Bosscher, P. J., 2009. Modulus-suction-moisture relationship for compacted soils. Canadian Geotechnical Journal, 45 (7), 973–983.

[212] Scholey, G. K. Frost, J. D. Lo Presti, D. C. F. & Jamiolkowski, M., 1995. A review of instrumentation for measuring small strains during triaxial testing of soil specimens. Geotechnical Testing Journal, 18 (2), 137–156.

[213] Schultheiss, P. J., 1981. Simultaneous measurement of P & S wave velocities during conventional laboratory soil testing procedures. Marine Geotechnology, 4, 343–367.

[214] Sheng, D. Fredlund, D. G. & Gens, A., 2008. A new modelling approach for unsaturated soils using independent stress variables. Canadian Geotechnical Journal, 45 (4), 511–534.

[215] Shibuya, S. & Tanaka, H., 1996. Estimate of elastic shear modulus in Holocene soil deposit. Soils and Foundations, 36 (4), 45–55.

[216] Shibuya, S. Hwang, S. & Mitachi, T., 1997. Elastic shear modulus of soft clays from shear wave velocity measurement. Géotechnique, 47 (3), 593–601.

[217] Shibuya, S. Tatsuoka, F. Teachavorasinskun, S. Kong, X. J. Abe, F. Kim, Y. S. & Park, C. S., 1992. Elastic deformation properties of geomaterials. Soils and Foundations, 32 (3), 26–46.

[218] Shirley, D. J., 1978. An improved shear wave transducer. Journal of Acoustic Society of America, 63 (5), 1643–1645.

[219] Shirley, D. J., Hampton, L. D., 1978. Shear-wave measurements in laboratory sediments. The Journal of the Acoustical Society of America, 63 (2), 607.

[220] Simpson, B. Atkinson, J. H. & Jovicic, V., 1996. The infuence of anisotropy on calculations of ground settlements above tunnels. Proceedings of the international symposium on geotechnical aspects of underground construction in soft ground, Rotterdam: Balkema,, 591–594.

[221] Simpson, B. O'Riordan, N.J. & Croft, D., 1979. A computer model for the analysis of ground movements in London Clay. Géotechnique, 29 (2), 149–175.

[222] Sivakumar, R., 2005. Effects of anisotropy on the behaviour of unsaturated compacted clay. PhD. thesis, Queen's University of Belfast, UK.

[223] Sivakumar, V., 1993. A critical state framework for unsaturated soil. PhD thesis, University of Sheffield, UK.

[224] Sivakumar, R. Sivakumar, V., Blatz, J. & Vimalan, J., 2006. Twin-cell stress path apparatus for testing unsaturated soils. Geotechnical Testing Journal, 29 (2), 175–179.

[225] Sivakumar, V. & Wheeler, S. J., 2000. Influence of compaction procedure on the mechanical behaviour of an unsaturated compacted clay. Part 1: Wetting and isotropic compression. Géotechnique, 50 (4), 359–368.

[226] Smith, P. R. Jardine, R. J. & Hight, D., 1992. The yielding of Bothkennar clay. Géotechnique, 42 (2), 257–274.

[227] Souto, A. Hartikainen, J. & Ozudogru, K., 1994. Measurement of dynamic parameters of road pavement materials by the bender element and resonant column tests. Géotechnique, 44 (3), 519–526.

[228] Stallebrass, S. E. & Taylor, R. N., 1997. The development and evaluation of a constitutive model for the prediction of ground movements in overconsolidated clay. Géotechnique, 47 (2), 235–253.

[229] Stallebrass, S. E. Richardson, D. & Atkinson, J. H., 1990. Effect of recent stress history on the stiffness of overconsolidated soil. Géotechnique, 40 (4), 531–540.

[230] Stokoe, K. H. Hwang, S. K. Lee, N. K. J. & Andrus, R. D., 1995. Effect of various parameters on the stiffness and damping of soils at small to medium strains. Keynote Lecture. Proc. 1st Int. Symp. on Pre-Failure Deformation of Geomaterials, Hokkaido, 2, 785–816.

[231] Stropeit, K. Wheeler, S. J. & Cui, Y. J., 2008. An anisotropic elasto-plastic model for unsaturated soils. Unsaturated Soils: Advances in Geo-Engineering, 1st European Conference for Unsaturated Soils, Durham, 2 (1), 625–632.

[232] Styler, M. A. & Howie, J. A., 2013. Combined time and frequency domain approach to the interpretation of bender-element tests on sand. Geotechnical Testing Journal, 36 (5).

[233] Sultan, N. Cui, Y. J. & Delage, P., 2010. Yielding and plastic behaviour of Boom clay. Géotechnique, 60 (9), 657–666.

[234] Tarantino, A., 2009. A water retention model for deformable soils. Géotechnique, 59 (9), 751–762.

[235] Tarantino, A. & Mongiovi, L., 2000. Experimental investigations on the stress variables governing unsaturated soil behaviour at medium to high degrees of saturation. Experimental Evidence and Theoretical Approaches in Unsaturated Soils, Proc. of an International Workshop, Trento, Italy. Rotterdam: Balkema,, 3–20.

[236] Tatsuoka, F. Shibuya, S. Goto, S. Sato, T. & Kong, X., 1990. Discussion on: The use of effect semiconductors in Geotechnical instrumentation. Geotechnical Testing Journal, 13 (1), 63–67.

[237] Terzaghi, K., 1936. The shearing resistance of saturated soils and the angle between the planes of shear. Proc. 1st Int. Conf. Soil Mech. Found. Engng, Cambridge, MA, 1, 54–56.

[238] Thomann, T. G. & Hryciw, R. D., 1990. Laboratory measurement of small strain shear modulus under ko conditions. Geotechnical Testing Journal, 13 (2), 97–105.

[239] Toll, D. G., 1990. A framework for unsaturated soil behaviour. Géotechnique, 40 (1), 31–44.

[240] Valle-Molina, C. &., Stokoe, K. H., 2012. Seismic measurements in sand specimens with varying degrees of saturation using piezoelectric transducers. Canadian Geotechnical Journal, 49 (6), 671–685.

[241] Van Genuchten, M. T., 1980. A closed-form equation for predicting the hydraulic conductivity of unsaturated soil. Soil Science Society of America Journal, 44 (5), 892–898.

[242] Vassallo, R. Mancuso, C. & Vinale, F., 2007. a. Effects of net stress and suction history on the small strain stiffness of a compacted clayey silt. Canadian Geotechnical Journal, 44 (4), 447–462.

[243] Vassallo, R. Mancuso, C. & Vinale, F., 2007. b. Modelling the influence of stress-strain history on the initial shear stiffness of an unsaturated compacted silt. Canadian Geotechnical Journal, 44 (4), 463–472.

[244] Viana da Fonseca, A. Ferreira, C. & Fahey, M., 2009. A framework interpreting bender element tests, combining time-domain and frequency-domain methods. Geotechnical Testing Journal, 32 (2), 91–107.

[245] Viggiani, J. & Atkinson, J. H., 1995. Interpretation of Bender Element Tests. Géotechnique, 45 (1), 149–154.

[246] Wang, Y. & Ng, C. W. W., 2005. Effects of stress paths on the small-strain stiffness of completely decomposed granite. Canadian Geotechnical Journal, 42 (4), 1200–1211.

[247] Wang, Y. H. Lo, K. F. Yan, W. M. & Dong, X. B., 2007. Measurement Biases in the Bender Element Test. Journal of Geotechnical and Geoenvironmental Engineering, ASCE, 133 (5), 564–574.

[248] Wei, Z. L., 2012. Influence of Anisotropic Internal Friction Angle on the Stability of Uniform Soil Slopes. Applied Mechanics and Materials, 170, 270–273.

[249] Wheeler, S., 1986. The stress-strain behavior of soils containing gas bubbles. Ph.D. thesis, Oxford University, Oxford, U.K.

[250] Wheeler, S. J., 1996. Inclusion of specific water volume within an elasto-plastic model for unsaturated soil. Canadian Geotechnical Journal, 33, 42–57.

[251] Wheeler, S. J. & Karube, D., 1996. Constitutive modelling. Proc. 1st Int. Conf. Unsaturated Soils, Paris, 3, 1323–1356.

[252] Wheeler, S. J. & Sivakumar, V., 1995. An elasto-plastic critical state framework for unsaturated soil. Géotechnique, 45 (1), 35–53.

[253] Wheeler, S. J. Näätänen, A. Karstunen, M. & Lojander, M., 2003. a. An anisotropic elasto-plastic model for natural soft clays. Canadian Geotechnical Journal, 40 (2), 403–418.

[254] Wheeler, S. J. Sharma, R. S. & Buisson, M. S. R., 2003. b. Coupling of hydraulic hysteresis and stress-strain behaviour in unsaturated soils. Géotechnique, 53 (1), 41–54.

[255] Whittle, A. J. & Kavvadas, M., 1994. Formultion of MIT-E3 constitutive model for overconsolidated clays. Journal of Geotechnical Engineering, ASCE, 120 (1), 173–198.

[256] Wong, K. S. Mašín, D. Ng, C. W. W., 2014. Modelling of shear stiffness of unsaturated fine grained soils at very small strains. Computers and Geotechnics, 56, 28–39.

[257] Wongsaroj, J. Soga, K. Yimsiri, S. &. M. R. J., 2004. Stiffness anisotropy of London clay and its modelling: laboratory and field. Advances in geotechnical engineering: the ICE, Proceedings of the Skempton conference, 1, London, UK.

[258] Wroth, C. P. & Houlsby, G. T., 1985. Soil mechanics property characterisation and analysis. Proc. 11th Conf. Soil Mech. San Francisco, 1, 1–55.

[259] Yamashita, S. & Suzuki, T., 2001. Small strain stiffness on anisotropic consolidated state of sands by bender element and cyclic loading tests. 15th International Conference on Soil Mechanics and Geotechnical Gngineering, Istanbul, Turkey, 1, 325–328.

[260] Yamashita, S. Kawaguchi, T. Nakata, Y. Mikami, T., Fujiwara, T. & Shibuya, S., 2009. Interpretation of international parallel test on the measurement of Gmax using bender elements. Soils and Foundations, 49 (4), 631–650.

[261] Yang, J. & Gu, X. Q., 2013. Shear stiffness of granular material at small strains: does it depend on grain size? Géotechnique, 63 (2), 165–179.

[262] Yang, J. and Liu, X., 2016. Shear wave velocity and stiffness of sand : the role of non-plastic fines. Géotechnique, 66 (6), 500–514.

[263] Zakaria, I., 1994. Yielding of unsaturated soil. PhD thesis, University of Sheffield, UK.

[264] Zdravković, L. Potts, D. M. & Hight, D. W., 2002. The effect of strength anisotropy on the behaviour of embankments on soft ground. Géotechnique, 52 (6), 447–457.

[265] Zeng, X. & Ni, B., 1998. Application of bender elements in measuring Gmax of sand under Ko conditions. Geotechnical Testing Journal, 21 (3), 251–263.

[266] Zhou, C., 2014. Experimental study and constative modelling of cyclic behaviour of at small strains of unsaturated soil at various temperatures. PhD thesis, Hong Hong University of Science and Technology.